Université Paul Sabatier

HABILITATION A DIRIGER DES RECHERCHES

Spécialité

SPÉCIALITÉ ASTROPHYSIQUE ET TECHNIQUES SPATIALES

par

Nadège MEUNIER

⟶⟵

Analyse multi-échelle et dynamique du champ magnétique solaire

Soutenue le 21 Juin 2007

Jury composé de

Jean Arnaud	Président du jury
Karine Bocchialini	Rapporteur
Lidia van Driel-Gesztelyi	Rapporteur
Gianna Cauzzi	Rapporteur
Françoise Génova	Examinateur
Frédéric Paletou	Examinateur
Michel Rieutord	Examinateur

Laboratoire d'Astrophysique de Toulouse-Tarbes, Observatoire Midi-Pyrénées

Regarder le Soleil ?
Pourquoi il faut travailler pour regarder le Soleil ?
Gabrielle, 4 ans

Table des matières

Annexes

Remerciements

Je voudrais tout d'abord remercier Jean Arnaud, qui a accepté de diriger mon Habilitation à diriger des Recherches. Je remercie également l'ensemble des membres du Jury, en premier lieu mes rapporteurs Karine Bocchialini, Lidia van Driel et Gianna Cauzzi, ainsi que Michel Rieutord, Frédéric Paletou et Françoise Génova. J'ai une pensée toute particulière pour Karine qui vit des moments difficiles.

Je souhaite remercier ensuite les personnes avec lesquelles j'ai travaillé au cours de ces années depuis ma soutenance de thèse, à l'Université de Stanford et à Tarbes. Les travaux présentés dans ce document couvrent les 2 ans que j'ai passé dans le groupe SOI à l'Université de Stanford. Merci à tous pour leur accueil et les bons moments passés ensemble: Brian, Jesper, John, Tom, Jeneen et les autres ... Merci également à Stuart pour son accueil à Maui.

Je remercie Thierry pour son soutien. Merci à Martine, Patrick et Franck pour le travail fructueux au sein de BASS2000. Je regretterai en quittant Tarbes notre travail ensemble et leur efficacité. Merci à tous ceux qui ont participé au projet CALAS, et tout particulièrement Sylvain, Michel, Thierry, et Francis, ainsi que Ruben. Merci enfin à Jean pour son soutien lors de nos efforts de traitement de données THEMIS. Je remercie également Sami, Andreas et Tom pour avoir mis leurs code à ma disposition. Merci à Jacques-Clair, David, Odile et toute l'équipe des Observateurs Associés pour leur enthousiasme inébranlable.

Enfin, merci à David pour tout ...

Chapitre 1

Introduction

> *Il est vrai qu'on ne peut trouver la pierre philosophale,*
> *mais il est bon qu'on la cherche*
> Bernard de Bovier de Fontenelle, Dialogue des morts

1.1 La photosphère solaire : quelques problématiques

1.1.1 La dynamo solaire

La Fig. 1.1, tirée de Schüssler (2005), illustre de manière schématique le contexte dans lequel se place ce travail. Il est maintenant bien accepté que la dynamo solaire opère à la base de la zone convective, dans la tachocline. Le mécanisme dynamo va transformer de l'énergie cinétique en énergie magnétique. Le flux magnétique émerge ensuite vers la surface pour former les régions actives. Les tubes de flux sont ensuite soumis essentiellement à la dynamique de la surface ou proche de la surface, de manière probablement passive. Il est en général admis que les tubes de flux se déconnectent du bas de la zone convective (voir Schüssler 2005 pour une discussion sur la nécessité de cette déconnexion et les processus possibles) : en surface, ils renseignent ainsi surtout sur la dynamique de surface. L'héliosismologie permet d'avoir accès à la dynamique de l'intérieur du Soleil, avec certaines limites (il n'est par exemple pas encore possible de mesurer directement le champ magnétique interne ni d'estimer l'amplitude éventuelle de la circulation méridienne[1] attendue vers l'équateur), et une possibilité pour étudier la dynamo solaire est d'étudier les propriétés de la dynamique et du champ magnétique en surface, qui sont eux directement observables. Bien sûr, ce ne sont pas des mesures directes de ce qui se passe en profondeur, et des distorsions peuvent se produire, ce qui complique les interprétations.

Les principales observations qui permettent de contraindre les modèles de dynamo sont généralement des propriétés globales comme le diagramme papillon et d'autres observations essentiellement liées aux taches solaires et aux polarités du champ magnétique

---

[1] La circulation méridienne est une circulation dirigée dans la direction Nord-Sud, observée vers les pôles en surface. On s'attend à un mouvement vers l'équateur en profondeur (voir Fig. 1.2, Nandy & Choudhuri 2002), mais ce champ de vitesse n'a pas encore été observé, probablement à cause de sa faible amplitude

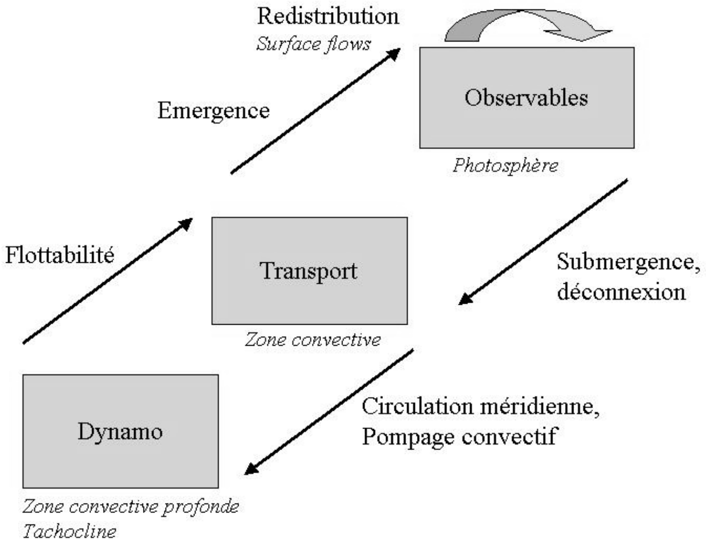

Figure 1.1 : Illustration schématique des processus connectant le flux magnétique généré par la dynamo solaire avec les observables dans la photosphère. D'après Schüssler (2005).

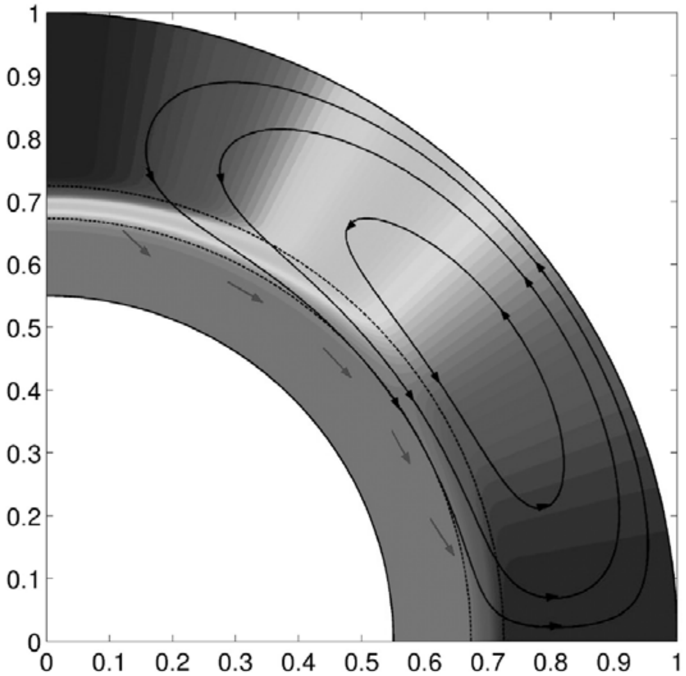

Figure 1.2 : Coupe dans la circulation méridienne du Soleil (simulation de Nandy et Chouduri 2002), vers les pôles en surface (R$\sim$1) et vers l'équateur au bas de la zone convective (R$\sim$0.7). Les niveau de gris représentent la rotation différentielle. L'équateur est en bas et le pôle en haut.

global, comme les lois de Joy et de Hale. Cependant, le champ magnétique se présente sous des formes extrêmement diverses, avec des échelles spatiales et temporelles très variables. De nombreux groupes travaillent à caractériser du mieux possible les variations de la photosphère au cours du cycle solaire, afin 1/ d'apporter davantage de contraintes aux modèles de dynamo d'une part, et 2/ d'obtenir des indices permettant de comprendre l'origine de ses structures (réseau magnétique photosphérique ou supergranulation par exemple) d'autre part. L'objectif est de mieux comprendre les interactions entre la dynamique et le champ magnétique et par suite les structures dynamiques elles-mêmes.

Enfin, il apparaît que de nombreuses composantes de la dynamique solaire sont essentielles pour comprendre la dynamo. La rotation différentielle a longtemps été considérée comme un élément clé, mais dans les modèles de dynamo fondés sur le transport de flux (voir entre autres Dikpati et al. 2004; Dikpati et al. 2006; Rempel 2006) la circulation méridienne et la diffusion supergranulaire jouent également un rôle clé. La variabilité temporelle de ces champs de vitesse est essentielle pour raffiner les modèles.

Le Soleil n'est qu'une étoile parmi d'autres, d'un type bien particulier et à une certaine phase de sa vie. Les avantages du Soleil sont sa proximité, permettant d'accéder à de nombreux détails de la surface (haute résolution spatiale, associée à une cadence élevée d'observations très utile du fait du très grand dynamisme des structures magnétiques) ainsi que la grande couverture temporelle : on voit bien par exemple qu'une observation sur quelques dizaines d'années du Soleil n'aurait pas permis la mise en évidence des cycles à long terme ni de l'existence sporadique de périodes comme le minimum de Maunder montrant une réduction drastique de l'activité pendant plusieurs décennies. D'un autre côté, l'étude des autres étoiles permet d'explorer l'espace des paramètres, ce qui peut ensuite être comparé aux résultats de modèles. L'étude du magnétisme des autres étoiles est donc essentiel pour avoir une vue plus large des différents régimes de dynamo en fonction de la masse des étoiles, de leur dynamique (par exemple de leur gradient de rotation différentielle) ou de leur âge.

1.1.2 Formation et évolution des régions actives

Les régions actives ont des durées de vie assez longues, pouvant atteindre plusieurs mois. Il est également maintenant établi que l'activité magnétique a tendance à perdurer aux mêmes longitudes durant de longues périodes, à l'échelle de l'année ou davantage (pour des travaux récents voir Berdyugina & Usoskin 2003; Usoskin et al. 2005). Les structures formant ces régions, en particulier les tubes de flux formant les plages, ont par contre des durées de vie beaucoup plus courtes.

Les modèles d'émergence de flux du bas de la zone convective vers la surface s'attachent surtout à l'étude de structures simples simulant les taches (émergence d'un seul tube de flux), sans s'intéresser à la complexité des régions actives de manière réaliste. La distribution spatiale du champ magnétique contient pourtant de nombreuses informations qui doivent être prises en compte pour comprendre la formation de ces régions actives et leur évolution au cours du temps. Dans ce contexte, un certain nombre de questions restent d'actualité, en particulier la profondeur à laquelle les structures magnétiques sont ancrées (dans la zone convective) au cours de leur vie, qu'est ce qui produit la complexité des régions actives, et pourquoi certaines sont plus actives (en terme d'éruptions) que d'autres.

De même que pour les différents régimes de dynamo possibles, l'étude d'autres étoiles montrent des régions actives ayant des caractéristiques très différentes de celles du Soleil, en terme de taille notamment. Il n'est par exemple pas évident que la loi de Hale sur les polarités soit universelle. A court terme, ces études ne permettront surement pas d'accéder au niveau de détail que l'on peut avoir pour le Soleil, néanmoins la caractérisation la plus approfondie possible permettra d'obtenir davantage d'informations pour nourrir les modèles de dynamo, par exemple sur les loi de polarité ou les cycles stellaires. La question de la profondeur d'ancrage devrait également pouvoir être abordée, comme le montre les mesures de rotation différentielle des structures stellaires (voir par exemple Collier Cameron et al. 2002).

1.1.3 Formation du réseau magnétique et des structures inter-réseau

Depuis les années 1960 et les premières simulations de transport de flux magnétique à la surface du Soleil (Leighton 1964), de nombreuses simulations de plus en plus complexes ont été effectuées pour modéliser le transport du flux magnétique et le renversement de polarité au cours du cycle, ainsi que sur les bilans de flux magnétique et les échelles temporelles typiques pour le renouvellement du flux en fonction de la phase du cycle. La formation du réseau magnétique et des structures inter-réseau se situe dans ce contexte. Le réseau est le mieux connu, étant beaucoup plus facile à observer : il s'agit de structures assez concentrées constituées de tubes de flux à champ fort (supérieur au kGauss), ce qui est très facilement observable à l'aide des magnétographes usuels. Leur caractérisation complète et leur dynamique globale reste encore à étudier en détail cependant. Les champs inter-réseau, plus faibles, sont bien moins connus, bien que de nombreuses observations depuis une douzaine d'années aient bien exploré ce sujet. L'origine de ces champs magnétiques en particulier reste une question ouverte : résidus des régions actives (et donc indirectement de la dynamo opérant à la base de la zone convective) ou bien dynamo locale ?

1.1.4 Origine de la supergranulation

La supergranulation, découverte en 1954 (Hart 1954), correspond à une organisation des champs de vitesse photosphérique à l'échelle de $\sim$30000 km. Ces champs de vitesse sont observés très facilement sur des Dopplergrammes, et le pic de la supergranulation est bien visible dans le spectre de puissance des vitesses photosphériques (Hathaway et al. 2000). La supergranulation joue un rôle essentiel dans la diffusion du champ magnétique à la surface solaire, en parallèle avec la circulation méridienne. Elle contribue ainsi fortement au transport du flux magnétique des régions actives vers le Soleil calme et à la formation du réseau magnétique. La supergranulation a longtemps été interprêtée comme une échelle convective de la photosphère solaire, au même titre que la granulation[2]. L'échelle typique de la supergranulation serait associée à la profondeur à laquelle se produit la transition He^{++} – He^{+} (Simon & Leighton 1964; van der Borght

---

[2] La granulation est constituée de cellules convectives ayant une taille horizontale de l'ordre de 1000 km à la surface du Soleil, plus chaudes au centre et plus froides au bord.

1979). Cette interprétation est cependant de plus en plus contestée (Rieutord et al. 2000; Rast 2003) et la question de la nature même de la supergranulation se pose. En outre, les travaux de Del Moro et al. (2004) ont montré que l'organisation spatiale des granules et des supergranules étaient différentes. De la même manière, du fait de sa forte interaction avec le champ magnétique, l'évolution de ses propriétés en fonction du niveau d'activité reste également à éclaircir. La supergranulation est une échelle extrêmement intéressante car elle se situe entre les petites échelles, qui sont assez bien connues (tubes de flux magnétique avec des diamètres inférieurs à 300 km, granules à l'échelle de 1000 km), et l'échelle globale (rotation différentielle circulation méridienne), elle aussi bien étudiée. Elle joue un rôle essentiel dans l'organisation du champ magnétique à la surface solaire, en contribuant à diffuser le flux magnétique provenant des régions actives à la surface. De plus, la compréhension des interactions entre la dynamique à différentes échelles est cruciale pour bien comprendre un milieu turbulent. L'observation directe de la supergranulation sur d'autres étoiles sera difficile, cependant il est possible de prendre en compte ce facteur dans les modèles de dynamo (diffusion du champ magnétique à la surface) et ainsi d'obtenir une information indirecte sur ses caratéristiques.

1.2 Contexte instrumental

L'étude des questions ci-dessus se situe dans un contexte instrumental très favorable. J'ai ainsi pu suivre plusieurs approches : l'utilisation de données existantes, l'acquisition de données en utilisant des instruments existants et, pour finir, la mise en place d'une nouvelle instrumentation.

En ce qui concerne l'utilisation de données existantes, j'en ai fait une exploitation intensive, tant pour des données sol (spectrohéliographe de Meudon pendant ma thèse) que pour des données spatiales (données de l'instrument MDI - Michelson Doppler Imager - sur la sonde SOHO, pendant mon post-doc et depuis mon recrutement). Je détaille ce dernier point car ce sont les données sur lesquelles j'ai le plus travaillé. L'objectif initial de l'instrument MDI était d'acquérir des images de la photosphère solaire de la manière la plus continue possible afin d'exploiter au maximum les techniques d'héliosismologie, globale et locale. A ce titre le principal mode observationnel consiste en l'acquisition de Dopplergrammes, en particulier disque entier (cadence 1 minute, résolution spatiale 4 secondes d'arc). Si j'ai peu abordé cet aspect de l'instrument (voir cependant Meunier & Jefferies 2000 et chapitre 3), je me suis concentrée sur les autres données fournies par MDI de manière complémentaire, les magnétogrammes et les cartes d'intensité, soit en mode disque entier également, soit en mode haute résolution (champ typique de 600×300 arcsec^2, cadence 1 minute ou 96 minutes, résolution spatiale 1.2 secondes d'arc). Ces données sont exploitées dans les chapitres 2 à 4.

J'ai également effectué des observations sur des installations existantes, pendant ma thèse (télescope McMath, Observatoire de Kitt Peak) et depuis mon recrutement, au télescope THEMIS (Tenerife). Dans ce dernier cas, j'ai effectué 4 campagnes d'observations en 2000 et 2001, dans le mode spectropolarimétrie multi-raies. Ces données sont exploitées dans le chapitre 2.

Pour finir, nous avons démarré le développement d'une nouvelle instrumentation pour la Lunette Jean Rösch (LJR) sur une ACI (Action Concertée Incitative) “jeune chercheur” dont je suis le PI (voir chapitre 4) : le projet CALAS (CAmera for the LArge Scales of the solar surface). Il s’agit d’une caméra grand champ, qui permet d’observer la surface solaire à la fois sur un très grand champ et avec une excellente résolution spatiale, ce qui en fait un instrument unique. Une contrainte supplémentaire est la haute cadence temporelle demandée : une haute cadence doit permettre d’améliorer la qualité des images en compensant leur dégradation par les turbulences atmosphériques.

1.3 Plan du document

Le fil conducteur de mon approche observationnelle est une étude multi-échelle d’un milieu turbulent et magnétisé, soit en se concentrant sur une échelle particulière (à petite échelle : le réseau magnétique, le champ inter-réseau, et à grande échelle : la dynamique globale), soit en étudiant de nombreuses échelles simultanément (étude de la dynamique, analyse fractale permettant l’étude de la distribution du champ magnétique à toutes les échelles disponibles). Mes travaux se sont déroulés à l’Université de Stanford (post-doctorat) puis au Laboratoire d’Astrophysique de Toulouse-Tarbes (Observatoire Midi-Pyrénées), au sein de l’équipe Magnétisme Solaire et Stellaire et de l’équipe du Service d’Observation BASS000.

Cette approche se situe dans le contexte de l’évolution du champ magnétique photosphérique, incluant la formation des régions actives et la diffusion du champ magnétique à la surface (réseau magnétique, champs inter-réseau). Je présente tout d’abord (*chapitre 2*) plusieurs études “statiques” du champ magnétique solaire, dans la majeure partie des cas en étudiant les propriétés statistiques d’un grand nombre de structures (analyse fractale, propriétés des structures du réseau au cours du cycle solaire).

Il apparaît clairement que ces propriétés sont très liées à la dynamique et qu’il est nécessaire de caractériser et de comprendre celle-ci. Le *chapitre 3* présente donc plusieurs études de la dynamique globale de la photosphère déterminée à partir des structures magnétiques, et ce à plusieurs échelles (rotation différentielle, circulation méridienne). Le lien entre la dynamique globale, telle qu’observée dans la photosphère, et la dynamique de la zone convective est également discutée dans ce chapitre, notamment sur la problématique de l’ancrage des structures magnétiques en profondeur.

La dynamique à plus petite échelle, concernant essentiellement la supergranulation, est présentée dans le *chapitre 4*, avec plusieurs études de la dynamique associée à la supergranulation et le lien entre supergranulation et activité magnétique.

Dans tous ces travaux, mon approche a été essentiellement observationnelle, et j’ai utilisé de nombreux outils et approches : mesure de la dynamique (imagerie et spectropolarimétrie), analyse fractale, traitement d’images, lois de puissance, héliosismologie.

Enfin, le *chapitre 5* présente mon implication dans le service d’observation BASS2000, dont je suis responsable depuis 2002 : je présente en particulier les développements que j’ai suscités et auxquels j’ai participé activement.

Enfin, les perspectives dérivant des travaux discutés dans ce document sont présentées dans le *chapitre 6*.

Je présente les autres éléments de mon dossier en annexe : mes tâches au service de la communauté (*annexe I*), ma liste complète de publications (*annexe II*), mes enseignements et encadrements de thèses (*annexe III*), mes collaborations (*annexe IV*). La plupart de mes articles dans des revues à comité de lecture, y compris ceux publiés durant ma thèse, sont indiqués dans les différents chapitres, cependant seuls mes travaux effectués après la fin de ma thèse sont discutés en détail. Les articles à comité de lecture publiés depuis la fin de ma thèse (*annexe V*) sont indiqués dans le texte en italiques.

Chapitre 2

Analyse multi-échelles du champ magnétique solaire

Dans ce chapitre, je m'intéresse à l'organisation du champ magnétique à la surface solaire. La distribution spatiale du champ magnétique, et en particulier son évolution au cours du cycle solaire, donne des informations précieuses sur le mécanisme dynamo et le lien entre le champ magnétique et la dynamique. J'étudie cette organisation en utilisant plusieurs approches, tout d'abord à l'aide d'une analyse multi-échelles du champ magnétique solaire et ensuite en étudiant les propriétés des structures magnétiques, du champ inter-réseau aux régions actives.

2.1 Analyse multi-échelle du champ magnétique solaire

Articles :

- *Meunier N., Complexity of active regions: flares and cycle phase dependence, 2004, A & A, 420, 333*
- *Meunier N., Fractal analysis of MDI magnetograms: a contribution to the study of the formation of solar active regions, 1999, Astrophys. J., 515, 801*
- Nesme-Ribes E., Meunier N. & Collin B., Fractal analysis of magnetic patterns from Meudon spectroheliograms, 1996, A & A 308, 213

2.1.1 Analyse fractale: pourquoi et comment ?

Pourquoi ?

Pourquoi utiliser une analyse multi-échelles, par exemple une analyse fractale, pour étudier la complexité des régions actives ? Considérons tout d'abord une image à très haute résolution d'une tache solaire ou d'une région active. De très nombreuses structures, à diverses échelles et avec des formes variées, y sont présentes. Une approche habituelle pour essayer de modéliser ces observations serait de décrire physiquement ces structures (champ magnétique, densité, température etc.). Une analyse fractale peut cependant compléter une telle approche plus physique de manière très intéressante : plusieurs raisons montrent qu'une approche purement physique n'est pas possible ou très difficile.

- Une première raison est qu'il est très difficile, voire impossible, de simuler la formation d'une région active qui va ressembler exactement à la tache observée. Au mieux, il sera possible de reproduire de manière statistique des structures qui y ressembleront, mais elles n'auront jamais la forme exacte des structures observées. Ceci signifie que si l'on veut comparer le résultat de modèles de régions actives à des observations, il faudra utiliser des outils statistiques qui permettront d'étudier un large éventail de données de manière automatisée. La dimension fractale des structures observées ou modélisées est un exemple d'outil possible.

- Des propriétés assez simples des régions actives ou d'autres structures solaires comme les granules ont été utilisées dans le passé. Bien sûr, pour les structures magnétiques, on peut mentionner par exemple la loi de Hale[1], la loi de Joy[2] ou bien le diagramme papillon[3] : c'est ce que cherchent à reproduire en premier les modèles de dynamo. La distribution en taille des structures a également été utilisée, par exemple par Harvey (1993), Wentzel & Seiden (1992) and Seiden & Wentzel (1996), en particulier afin d'effectuer des comparaisons avec des modèles. Il est cependant intéressant d'aller plus loin pour mieux les contraindre, en utilisant davantages de critère : les travaux présentés ici ont montré que c'était même nécessaire (voir plus loin).

- Une troisième raison est que lorsque l'on regarde par exemple la distribution en taille des régions actives, on observe en général des lois de puissance. Il faut rappeler que la turbulence est partout en astrophysique, et elle est observée directement dans la photosphère solaire. Il est possible de l'y observer en utilisant des observations à très haute résolution spatiale par exemple. Dans un milieu où la turbulence est pleinement développée (très grand nombre de Reynolds, comme dans le Soleil), la turbulence est souvent décrite comme une hiérarchie de structures à différentes échelles. Dans la turbulence de Kolmogorov par exemple, de l'énergie est injectée à grande échelle, puis elle cascade vers les petites échelles où cette énergie est dissipée. L'énergie cinétique du fluide considéré obéit alors à une loi de puissance en fonction de l'échelle, avec une pente bien connue de -5/3. Il faut noter que dans le cas du Soleil, le spectre de puissance de la vitesse a été observé, par exemple par Komm et al. (1990), qui ont bien trouvé une pente en -5/3. Avec ce type de milieu, il est très naturel d'utiliser des lois de puissances pour décrire les observations.

Comment ?

Une propriété importante des structures associées à la turbulence est leur auto-similarité : si l'on fait un gros plan sur une petite région, il ressemblera à l'objet vu à échelle

---

[1] Les polarités de tête et de queue des taches solaires sont opposée dans un même hémisphère, les polarités de tête sont oppposées entre les deux hémisphères et leur signe change à la fin du cycle de 11 ans, créant ainsi un cycle de 22 ans.

[2] Les taches de tête d'une région active sont statistiquement plus proches de l'équateur que les taches de queue.

[3] Les taches solaires apparaissent à moyenne latitude au début du cycle, puis de plus en plus proche de l'équateur au cours du cycle.

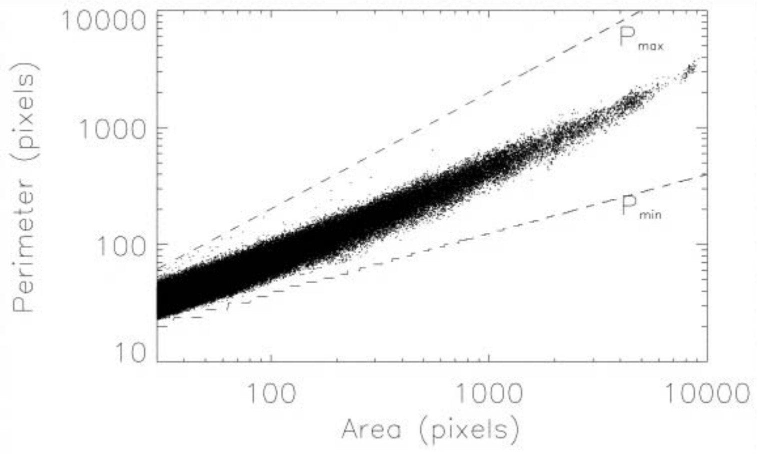

Figure 2.1 : Périmètre en fonction de la taille des structures définies sur les magnétogrammes MDI avec un seuil de 40 G (2 ans de données), pour les structures ayant une surface supérieure à 30 pixels. Les courbes en pointillés représentent les valeurs possibles minimum et maximum du périmètre en fonction de la taille. D'après Meunier (1999).

plus grande. Outre les lois de puissance correspondant à diverses variables physiques (taille des structures, vitesses), un outil très utile est l'analyse fractale, permettant de caractériser le système à l'aide d'une dimension fractale. Les fractales ont été introduites par Mandelbrot (1975) pour décrire la longueur de la côte de Bretagne. Il a montré que la longueur mesurée L dépendait en fait de l'échelle δ à laquelle on la mesurait, avec une variation du type $L \sim \delta^{1-D}$ où D est la dimension fractale de l'objet. Avec cette définition, une courbe "ordinaire" a une dimension fractale de 1 et un objet très complexe aux différentes échelles a une dimension fractale proche de 2.

Plusieurs méthodes pour mesurer la dimension fractale ont été utilisées dans la littérature. Dans mes travaux, j'en ai utilisé trois, et plus particulièrement la relation classique aire-périmètre (Fig. 2.1) et la relation $N(\varepsilon)$, où N représente le nombre de pixels définis à l'échelle ε couvrant l'objet ou bien la frontière délimitant l'objet. Sur la Fig. 2.1 par exemple, la pente entre le logarithme de l'aire et le logarithme du périmètre va fournir la dimension fractale. Ces définitions, qui s'appliquent à des structures observées ou simulées, ont toutes des limitations, que je liste ici (certaines seront détaillées plus loin car elles influencent nos résultats, elles sont également discutées par Meunier 1999a) :

- En général il faut définir le contour de la structure, c'est-à-dire segmenter l'image. Cette opération est toujours délicate et dans tous les cas des seuils différents montrent un objet différent.
- Sur des données avec une résolution "apparente" limitée (la taille du pixel), une taille ou un périmètre ne peut pas prendre toutes les valeurs possibles (Brandt et al. 1991; Criscuoli et al. 2007). Pour une taille donnée, le périmètre est ainsi limité, en particulier pour les petites tailles (par exemple pour une taille de 1 pixel le périmètre

ne peut valoir que 4). Ceci limite la validité du calcul de la dimension fractale pour les petites structures (Fig. 2.1).

- Un corollaire est que si la résolution spatiale réelle sur l'image est moins bonne que la taille du pixel, utiliser celui-ci comme plus petite échelle peut conduire à des erreurs sur le calcul de la dimension fractale (Janßen, Vögler, & Kneer 2003).
- Lorsque l'on utilise une définition telle que la relation aire-périmètre, il faut un grand nombre de points pour pouvoir la calculer, autrement dit il n'est possible de la calculer que de manière statistique et pas pour une structure donnée à un instant t donné. Cet inconvénient disparait pour des définitions de type $N(\varepsilon)$ vs. ε.
- Le bruit sur les données devra être pris en compte lors du choix du seuil pour segmenter les images, car il aura tendance à biaiser le résultat vers des structures trop complexes.
- Les distorsions des images, par exemple les effets de projections, doivent être pris en compte attentivement, car les mesures de longueur (périmètre) et de surface (aire) sont affectées différement.

Il faut noter qu'en astrophysique l'analyse fractale a été très largement utilisée par de nombreuses équipes, non seulement en physique solaire (granulation, supergranulation, série temporelle de l'activité solaire) mais aussi dans d'autres domaines : nuages moléculaires, poussières interplanétaires, surfaces planétaires, distribution à grande échelle des galaxies.

2.1.2 Propriétés générales

Les principaux travaux existants sur la dimension fractale des régions actives avaient été effectués par Schrijver et al. (1992) et Balke et al. (1993). Ces travaux avaient concerné une observation à haute résolution spatiale, ce qui permettait d'avoir une très grande dynamique. Par contre, la statistique n'était pas très bonne car il n'y avait qu'une seule région active.

J'ai effectué une première analyse fractale d'un nombre significatif de régions actives à partir de spectrohéliogrammes dit $\mathrm{K}_{1\mathrm{v}}$ obtenus à l'Observatoire de Meudon (Nesme-Ribes, Meunier, & Collin 1996). Ces images montrent en particulier les facules dans la haute photosphère. Cette analyse a par la suite été approfondie en utilisant les nombreux magnétogrammes de MDI, tout d'abord sur la période 1996-1998 (Meunier 1999a) puis sur 8 ans de données (Meunier 2004).

Les premiers résultats ont montré que la façon dont on définit la dimension fractale était critique si l'on veut comparer des résultats provenant de diverses sources ou comparer une observation avec le résultat d'un modèle. Dans ce premier travail, trois définitions ont été utilisées, afin de permettre des comparaisons avec des résultats théoriques correspondant à des situations assez générales, comme la théorie de la percolation[4]

---

[4] La thérie de la percolation décrit le comportement de structures dont le remplissage a été aléatoire dans un espace donné. Selon le taux de remplissage, la théorie prédit des propriétés différentes, par exemple une dimension fractale différente. Dans le cas solaire, l'espace donné pourrait être les zones entre les granules ; un remplissage aléatoire de cet espace par des tubes de flux magnétique, donne des structures dont les propriétés dépendent du facteur de remplissage.

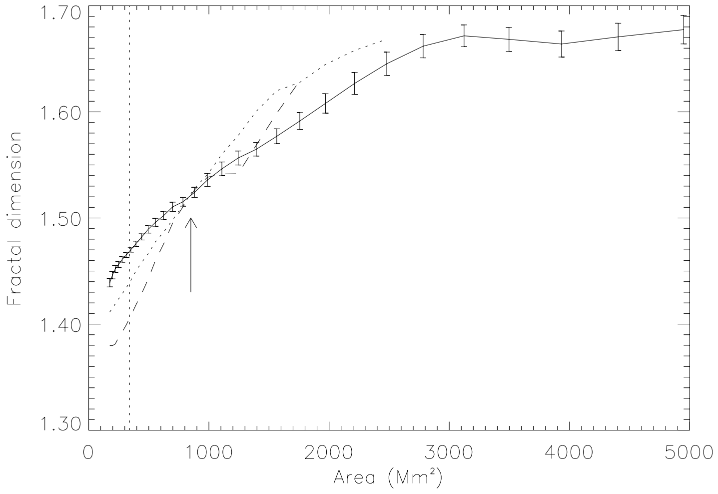

Figure 2.2 : Dimension fractale en fonction de la taille définie pour des structures identifiées à partir de 8 ans de données MDI, pour différents seuils en champ magnétique : 40 G (trait plein), 80 G (pointillés), 120 G (tirets). Les barres d'erreur ne sont montrées que pour 40 G. La flèche indique la taille critique discutée dans le texte. La ligne pointillée verticale indique la taille minimum au-dessus de laquelle le calcul n'inclut aucune structure plus petite que 30 pixels. D'après Meunier (2004).

(Stauffer 1985) ou la turbulence de Kolmogorov. Ces travaux ont permis de montrer que la turbulence de Kolmogorov permettait de bien décrire les facules à l'échelle de la supergranulation, et que la distribution d'intensité dans les facules pouvait être due à un processus de remplissage aléatoire de la surface par les tubes de flux. La dimension fractale des facules étaient aussi compatible avec des prévisions de la dynamo $\alpha - \omega$ (Ruzmaikin, Sokoloff, & Tarbell 1991).

Un autre résultat important a été que les facules ne sont en fait pas auto-similaires : selon le domaine de taille pour lequel le calcul est effectué, la dimension fractale mesurée est différente, les structures plus grandes étant plus complexes. Ceci a principalement deux conséquences. Bien qu'il soit dans ce cas toujours possible de calculer une dimension fractale et d'utiliser cet outil, il faut être davantage attentif à toutes les conditions du calcul si l'on souhaite effectuer des comparaisons. L'autre conséquence est bien sûr que les facules n'étant pas exactement auto-similaires, tout modèle visant à expliquer leur structure doit pouvoir expliquer ce fait. Ceci exclut donc tout modèle trop “simpliste”.

Le travail sur les données MDI a permis de travailler sur un échantillon significativement plus grand, même en ne se cantonnant dans un premier temps qu'aux deux premières années d'observations dans une première analyse. Celle-ci a permis de confirmer les résultats obtenus avec les spectrohéliogrammes, à savoir la variabilité de la dimension fractale calculée avec la taille des structures. En outre, j'ai pu étudier de manière approfondie la variabilité de la dimension fractale avec le seuil en champ magnétique utilisé pour déterminer les structures. Autrement dit, lorsqu'on se place à des niveaux de flux magnétique différents, l'organisation spatiale du champ magnétique diffère. L'examen de l'ensemble des courbes montrant la dimension fractale en fonction de l'échelle, pour différents seuils, montrent un point pivot, une échelle typique, pour laquelle toutes les dimensions fractales mesurées sont les mêmes, soit environ 1.52 (Fig. 2.2). Ceci a été confirmé avec l'analyse des 8 ans de données. Cette échelle correspond à peu près à l'échelle de la supergranulation, les régions actives plus petites ayant un comportement radicalement différent des grandes régions, le seuil entre les deux comportements illustrés sur la Fig. 2.2 étant dans le domaine 550–800 Mm^2 : en dessous de cette taille, la dimension fractale diminue lorsque le seuil en champ magnétique utilisé pour définir les structures augmente, c'est le contraire au dessus. Pour les structures les plus grandes, qui ont pu être étudiées dans le dernier article (Meunier 2004), la dimension fractale atteint un plateau au-dessus de 3000 Mm^2. Les structures d'une taille donnée sont également plus complexes quand elles contiennent des taches.

En parallèle avec l'analyse des données MDI, il a été possible de modéliser la formation de régions actives à l'aide d'un modèle simple inspiré des travaux de Wentzel & Seiden (1992) et Seiden & Wentzel (1996). Ces travaux sont fondés sur une approche de type percolation, avec un modèle simple de formation de structures fonctionnant sur deux couches : une couche en profondeur où se produit un processus de percolation, avec possibilité de stimuler l'émergence de flux à partir de flux existant, et un processus de diffusion en surface. Dans ce type de modele très simple, un “pixel” représente un “tube de flux”, et les 2 polarités sont prises en compte. Les résultats ont montré que les structures observées étaient moins complexes que les structures modélisées, et qu'il était impossible de trouver des paramètres du modèle qui reproduisent à la fois la distribution en taille des structures et leur dimension fractale, en particulier si l'on souhaite qu'ils incluent la variation de la dimension fractale mesurée avec la taille.

2.1.3 Variations au cours du cycle

L'étude de la variation au cours du cycle (Meunier 2004) a été faite en couvrant 8 ans du cycle 23, soit 3 phases : le minimum du cycle (pour lequel très peu de grandes régions sont présentes), la phase ascendante du cycle et le maximum (Fig 2.3). Cette figure est similaire à celle de la Fig. 2.2, mais en montrant les différentes phases du cycle séparément. Un premier résultat, illustré sur ces figures, est que l'échelle typique observée sur les courbes couvrant la période complète augmente en même temps que le niveau d'activité. La dimension fractale elle-même varie au cours du temps, avec une amplitude atteignant 0.17 entre la phase ascendante et le maximum du cycle. Le détail des variations est assez complexe, du fait de l'influence du seuil utilisé pour déterminer les structures. Les structures avec taches sont également plus complexes au début du cycle alors que les structures sans tache sont plus complexes au maximum du cycle.

L'origine des variations de la dimension au cours du cycle est une question ouverte. Elle pourrait être due à une variation de paramètres contrôlant la dynamo en profondeur (par exemple une variation avec la profondeur), ou bien à des effets de surface contrôlant la désintégration des régions actives (par exemple la supergranulation). Les grandes variations avec l'amplitude du champ magnétique et la présence ou non de taches aurait plutôt tendance à favoriser une explication faisant intervenir la dynamo. La variation non mono-

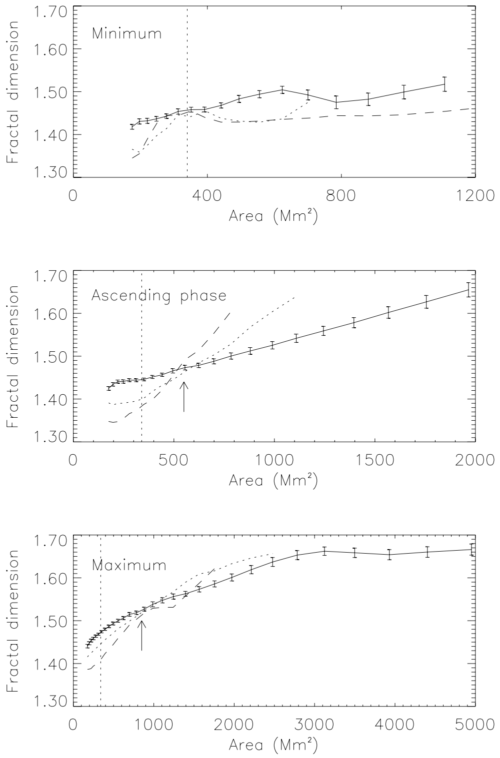

Figure 2.3 : Dimension fractale en fonction de la taille pour les 3 périodes observées du cycle solaire, sur la même échelle: le minimum du cycle (en haut), la phase ascendante (au milieu) et le maximum du cycle (en bas). Les traits pleins correspondent au seuil de 40 G, les pointillés au seuil de 80 G et les tirets au seuil de 120 G. La flèche indique la taille critique discutée dans le texte. La ligne pointillée verticale indique la taille minimum au-dessus de laquelle le calcul n'inclut aucune structure plus petite que 30 pixels. D'après Meunier (2004).

tone pourrait être due à l'influence de deux processus qui ne seraient pas en phase (parmi lesquels la supergranulation, le flux magnétique disponible, la circulation méridienne, etc.). D'un autre côté, les flots de surface pourraient affecter différemment des structures ayant des propriétés différentes. Par exemple, Harvey (1993) a montré qu'au maximum du cycle, les structures ont une durée de vie plus longue, quelle que soit la taille des régions actives. Ceci pourrait entrainer une phase de désintégration plus longue au maximum du cycle et donc des structures plus diluées et ayant ainsi une morphologie plus complexe. Les flots convergents et divergents à diverses profondeurs (Zhao, Kosovichev, & Duvall 2001) pourraient aussi jouer un rôle : à grande échelle, des flots convergents sont observés (Meunier 1999b; Chou & Dai 2001; Beck, Gizon, & Duvall 2002) alors que des flots divergents sont observés plus proches des structures (effet Evershed). Une étude separée des régions jeunes et vieilles devraient pouvoir permettre de séparer les différentes contributions.

2.1.4 Eruptions et analyse fractale

J'ai utilisé les données MDI précédentes pour étudier une éventuelle variation de la dimension fractale des régions actives durant une éruption. De nombreuses tentatives, en général sur de petits échantillons, avaient été effectuées précédemment par d'autres équipes, sans détection positive. Le travail réalisé sur les données MDI concerne le champ magnétique longitudinal seulement. Cependant, le volume de données est énorme et permet donc d'obtenir des résultats plus significatifs statistiquement. J'ai montré qu'à faible distance (quelques degrés) des éruptions les variations étaient négligeables. De petites modifications ont été observées cependant à plus grande distance des éruptions (10 degrés), ce qui suggère des modifications à grande échelle comme celles observées par Yurchyshyn et al. (2000). Les variations très faibles confirment cependant les résultats d'Adams et al. (1997) par exemple, obtenus avec une méthode différente, et montrent que la dimension fractale des régions actives obtenue à partir du champ magnétique longitudinal n'est pas adaptée pour prédire l'occurence des éruptions.

McAteer et al. (2005) ont par la suite montré que l'on pouvait établir une relation entre la dimension fractale des régions actives et la classe des éruptions sous forme d'un seuil : une dimension fractale minimale est nécessaire pour qu'une région produise une éruption d'une classe donnée. Mais la dispersion reste large et le seuil finalement assez bas (1.2 pour obtenir des éruptions de classe M et 1.25 pour des éruptions de classe X). A noter qu'ils ont également tenté d'établir une relation entre la dimension fractale des régions actives et leur classe dans la classification du Mont Wilson, mais cela ne s'est pas avéré concluant.

Une extension des modèles mentionnés ci-dessus (de type percolation) a été réalisée par Fragos et al. (2004) et Vlahos & Georgoulis (2004) afin de déterminer où se produit l'émergence de flux magnétique et de reproduire la distribution en énergie des éruptions, là aussi avec l'objectif de mieux comprendre l'évolution de la complexité des régions actives au cours des éruptions.

2.2 Contribution à une caractérisation physique des structures magnétiques solaires

Articles :

- *Meunier N., Statistical properties of magnetic structures: their dependence on scale and solar activity, 2003, A & A 405, 1107*
- *Meunier N. & Kosovichev A., Fast photospheric flows and magnetic field in a flaring active region, 2003, A & A 412, 541*
- *Meunier N., Arnaud J. & Vigneau J., Observations of intranetwork magnetic fields with THEMIS, 2002, Il Nuovo Cimento 25C (5-6), in "THEMIS and the new frontiers of solar atmosphere dynamics", Rome, March 19-21, 2001, 659*
- Meunier N., Solanki S.K. & Livingston W.C., Infared lines as probes of solar magnetic features. XIII. The magnetic flux in weak and strong quiet-sun fields, 1998, A & A, 331, 771

Mes travaux concernant une caractérisation physique des structures magnétiques solaires ont surtout porté sur les champs magnétiques inter-réseau (IN dans la suite, pour "intranetwork") et sur le réseau magnétique. Le premier travail est plus ancien, et depuis, de nombreux travaux ont été réalisés dans ce domaine par d'autres équipes. Je le replace dans ce contexte. Mon plus gros travail a été la caractérisation approfondie du réseau magnétique, effectuée conjointement avec l'étude des régions actives pour comparaison. Les régions actives sont effectivement les structures qui ont été les plus étudiées, et de nombreuses études existent sur ce sujet. Je renvoie en particulier à la thèse de Harvey (1993) qui étudie en détail un certain nombre de propriétés statistiques des régions actives. Mon travail sur le réseau se situe dans cette lignée, mais appliqué à des structures qui bien que connues depuis longtemps, n'ont jamais été étudiées de cette manière auparavant. Les questions qui se posaient étaient en effet les suivantes : comment varie le flux magnétique des structures du réseau en fonction de leur taille ? Comment cette variation se compare-t-elle avec celle des régions actives ? La fin de cette section présente quelques résultats obtenus dans une région active, et qui représente un travail plus ponctuel.

2.2.1 Détection et caractérisation des champs magnétiques IN

Le champ magnétique solaire se présente sous des formes très diverses, les plus connues et les plus étudiées étant les structures à champ magnétique fort (1–3 kG au niveau photosphérique) telle que les régions actives et, dans une moindre mesure, le réseau magnétique. Cependant, plusieurs travaux datant des années 1970 (Livingston & Harvey 1971; Livingston & Harvey 1975; Harvey 1977) ont montré que des champs plus faibles étaient probablement présents un peu partout à la surface du Soleil. Ces observations se sont raffinées dans les années 1980, notamment avec les travaux de Livi et al. (1985), de Zirin (1987) et de Martin (1988) ainsi que ceux de Stenflo (1982) en utilisant l'effet Hanle près de limbe solaire. Des observations plus approfondies ont par la suite confirmé ces conclusions (Rüedi et al. 1992; Faurobert-Scholl 1993; Keller et al. 1994; Faurobert-Scholl et al. 1995; Lin 1995; Wang et al. 1995; Lites et al. 1996; Solanki et al.

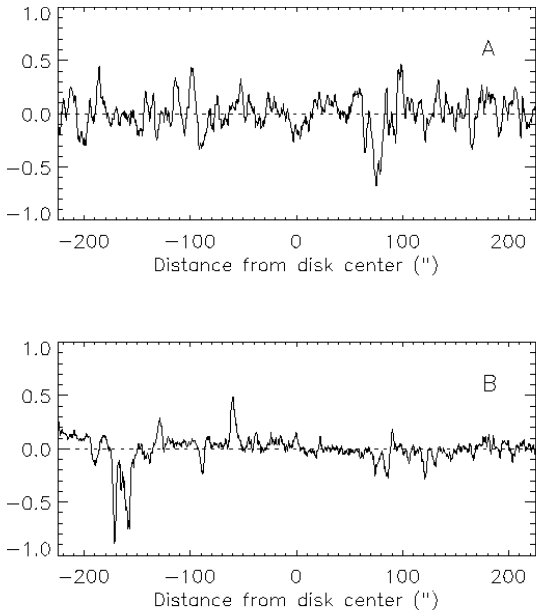

Figure 2.4 : Deux balayages spatiaux à Fe I 1.5648 μm, proche du centre de la raie (en haut) et dans l'aile de la raie (en bas) montrant le pourcentage de polarisation en fonction de la position. Le taux de polarisation indiqué n'est pas calibré et correspond à une polarisation d'origine solaire entièrement linéaire. Il faut diviser par un facteur 1.4 si la polarisation d'origine solaire est entièrement circulaire, le taux réel étant intermédiaire selon les pourcentages de polarisation linéaire et circulaire observés. D'après Meunier et al. (1998).

1996). A la date du début de mes travaux sur les champs IN, plusieurs articles fournissant des indications sur la structure physique de ces champs IN avaient été publiés. Il n'y avait cependant pas de travaux étudiant en détail les proportions relatives de flux magnétique à la surface du Soleil sous forme de champs faibles et forts : il est important d'établir la contribution des champs faibles au flux total comparé au flux émergent dans les régions actives.

Des observations menées à l'Observatoire de Kitt Peak en 1995 et 1996 nous ont permis de répondre à cette question. L'utilisation de raies du fer dans l'infrarouge, à 1.56 μm, avec un facteur de Landé de 3, était bien sûr très favorable à l'étude des champs faibles. Ces observations ont été effectuées durant une période calme du cycle solaire, proche du minimum. Nous avons montré qu'environ 2/3 du flux était sous la forme de champs faibles, ce qui a constitué le principal résultat de cette analyse. C'est la première fois que des observations avec une modulation rapide entre les deux polarisation circulaires (300 Hz) étaient effectuées à cette longueur d'onde. Les balayages, effectués séparement aux diverses longueurs d'onde dans la raie, ont montré une structure spatiale très différente dans le centre de la raie (sensible seulement aux champs faibles) et dans les ailes (sensible surtout aux champs forts), comme illustré sur la Fig. 2.4 : les champs forts observés correspondent au réseau magnétique, distribué à la surface du Soleil à l'échelle de la supergranulation (bien visible en bas de la figure avec des pics toutes les quelques dizaines de secondes d'arc ou plus), et les champs faibles sont présents partout à la surface (par exemple sur le balayage du haut).

La mise en service du télescope THEMIS en 1999 (Arnaud, Briand, & Ceppatelli 1998; Paletou & Molodij 2001; Paletou 2001), qui permet d'effectuer des observations spectro-polarimétriques dans plusieurs domaines de longueurs d'onde simultanément, était très prometteuse pour poursuivre ce type d'étude. La résolution spatiale annoncée devait permettre d'aborder également l'étude de la distribution spatiale des champs IN à la surface du Soleil (ce qui n'a pas été le cas). La caractérisation fine des structures IN restaient en effet à faire à cette date, en terme de taux de remplissage, orientation du champ magnétique, valeur des champs magnétiques, durée de vie, distribution spatiale, car les travaux des années 1990 avaient amené à des résultats apparemment incohérents entre les différentes études (par exemple en terme d'orientation du champ magnétique, de taille de structure ou de durée de vie). Notre objectif était également de replacer ces champs IN dans le contexte de la supergranulation.

Nous avons donc effectué une série d'observations en 2000 et 2001 avec THEMIS dans plusieurs domaines spectraux, en mesurant tous les paramètres de Stokes et avec diverses conditions instrumentales afin d'optimiser les balayages entre la résolution polarimétrique et l'évolution temporelle des structures. Les raies choisies devaient permettre d'observer à plusieurs hauteurs dans l'atmosphère solaire, de prendre en compte les effets de température et de microturbulence et, pour les champs forts, de déterminer l'intensité du champ et le facteur de remplissage. Un bilan sur les observations de Juin 2000, qui avaient présenté le meilleur seeing, a été publié (Meunier, Arnaud, & Vigneau 2002). Il a malheureusement mis en évidence des problèmes de fond dans ces données qui n'ont pas permis d'effectuer les analyses escomptées. Le principal problème provenait de la différence de co-spatialité entre les deux voies d'analyse polarimétrique. Les observations que nous avons effectuées en Juillet 2001 ont d'ailleurs permis de caractériser ce problème assez précisément. Le manque d'amélioration du télescope au cours des années suivantes sur ces aspects a conduit à l'abandon de ce programme avec THEMIS. Il est cependant probable que THEMIS soit à l'heure actuelle capable d'aborder à nouveau cette thématique difficile.

Cette thématique a cependant été abordée par plusieurs groupes avec d'autres instruments depuis quelques années et qui ont amené des résultats extrêmements intéressants. On peut noter en particulier les résultats de Domínguez Cerdeña et al. (2003) et de Domínguez Cerdeña et al. (2003) qui ont observé des champs IN avec une excellente résolution spatiale (0.5 arcsec). Ceci leur a permis, outre la caractérisation du champ magnétique (distribution avec une queue longue au delà de 1kG, 75% des pixels ayant un champ magnétique supérieur à 500 G, 25% des pixels montrant des polarités opposées), de montrer la présence de “patchs” de champs IN localisés dans les intergranules. Khomenko et al. (2003) ont également analysé en détail les paramètres de Stokes associés aux champs IN et leur localisation par rapport aux granules. Plusieurs travaux ont également été effectués dans l'infrarouge, en particulier des simulations pour mieux comprendre les mesures effectuées sur ces champs faibles (Socas-Navarro & Sánchez Almeida 2003; Bellot Rubio & Collados 2003). Ces simulations permettent d'interpréter les différences entre les mesures effectuées dans l'infrarouge et le visible : les mesures ne sont pas sensibles aux mêmes composantes du champ magnétique, le visible fournissant surtout une mesure des champs supérieurs au kG, et l'IR une mesure des champs plus faibles.

2.2.2 Caractérisation complète du réseau magnétique et lien avec les régions actives

Contexte

Une bonne connaissance des propriétés du réseau magnétique est essentielle pour appréhender correctement la diffusion du flux magnétique en provenance des régions actives et la façon dont ce flux évolue (disparition par rencontre de structures de polarités opposées, enfouissement dans la zone convective par exemple). Elle doit fournir des informations sur les processus à l'origine de la concentration du champ magnétique dans les tubes de flux formant le réseau et l'interaction du réseau avec la dynamique à petite et moyenne échelle. Il faut noter que la contribution du réseau magnétique aux variations de l'éclairement solaire a longtemps été un sujet controversé (White & Livingston 1981; Labonte & Howard 1982; Muller & Roudier 1984; Foukal & Lean 1988; Foukal, Harvey, & Hill 1991; Nishikawa 1994; Lean et al. 1998) et sera discutée plus loin. Les propriétés du réseau ont souvent été étudiées via la mesure du coefficient de diffusion de ces structures à la surface du Soleil (voir par exemple Schrijver et al. 1996 et références), mais ceci n'a été fait que ponctuellement et jamais au cours du cycle. D'un autre côté, l'étude de Harvey (1993) sur les régions bipolaires a porté entre autres sur les durées de vie et le tilt (angle donnant l'inclinaison entre l'équateur et la ligne formée par les structures de polarité opposée dans une région active), mais pas sur le flux magnétique. Les structures du réseau étaient exclues de cette analyse. Les propriétés du réseau magnétique sont donc principalement connues via quelques études spectropolarimétriques portant sur un faible nombre de structures sans analyse à large échelle simultanée (Sánchez Almeida & Lites 2000; Sigwarth 2001; Socas-Navarro & Sánchez Almeida 2002).

Résumé des résultats

Il était donc nécessaire d'étudier ces propriétés à l'aide de données permettant d'obtenir une excellente statistique. Ceci a été possible grâce aux magnétogrammes “disque entier” de MDI. L'étude a porté sur 6 ans de données (Meunier 2003), représentant près d'une dizaine de milliers d'images. Elle a permis d'étudier la distribution en taille des structures allant du réseau magnétique jusqu'aux régions actives, et en particulier les asymétries nord-sud et est-ouest de cette distribution en fonction de la polarité. Les propriétés des structures telles que le flux magnétique moyen par pixel, le flux magnétique total, le champ magnétique maximum et le rapport entre champ magnétique maximum et flux magnétique moyen ont été étudiées en fonction de la taille des structures, de même que

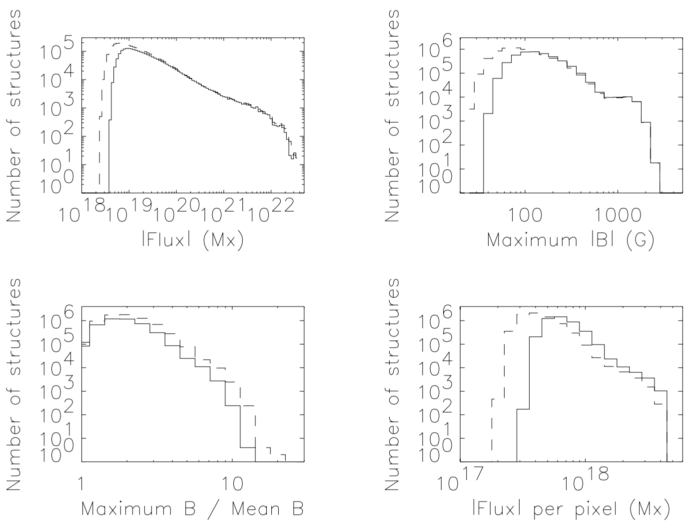

Figure 2.5 : Distribution du flux magnétique (en haut à gauche), du champ magnétique maximum (en haut à droite), du rapport maximum / champ moyen dans les structures (en bas à gauche) et de la densité de flux magnétique (en bas à droite) pour toutes les structures et pour des seuils de 40 G (trait plein) et 25 G (tirets). D'après Meunier (2003).

leur distribution et leurs variations au cours du cycle solaire. En outre, il a été possible de considérer, pour les petites structures du réseau (taille en dessous de 80 Mm^2), les variations de propriétés en fonction de leur distance à une région active et en fonction de la latitude. De nombreux résultats nouveaux ont été obtenus, résumés ainsi :

- Les distributions en taille et flux magnétique montrent trois régimes : le domaine en dessous de 40 Mm^2 (3 10^{19} Mx), le domaine 40–400 Mm^2 (3 10^{19}–10^{21} Mx) où les distributions sont des lois de puissance, et le domaine supérieur 400-700 Mm^2 ($\sim$ 10^{21} Mx). Cette dernière échelle, proche de l'échelle de la supergranulation, augmente du minimum du cycle au maximum. Les distributions du flux magnétiques et des autres paramètres sont montrés sur la Fig. 2.5. En outre, la forme de la distribution en taille n'est pas un invariant au cours du cycle solaire, comme le montre la Fig. 2.6.
- Une loi de puissance du flux magnétique en fonction de leur taille suggère une continuité des petites échelles (petites structures du réseau) aux grandes échelles (régions actives), voir Fig. 2.7. La pente supérieure à 1 (Table 2.1) montre que la densité de flux est également dépendante de la taille. La dépendence du flux magnétique en fonction de la taille est cependant moins prononcée durant le maximum d'activité, surtout pour les petites structures. Les résultats suggèrent qu'il y a plus de flux par unité de surface au maximum du cycle. Un comportement assez similaire est observé pour les autres paramètres physiques mesurés.
- L'asymétrie nord-sud du nombre de structures se renverse pour les petites structures pour le seuil à 25 G mais pas pour le seuil à 40 G (pour les structures en dessous

Table 2.1 : Pente de Log(paramètre) en fonction de Log(A), avec A la taille des structures, après avoir moyenné Log(paramètre) sur de petits domaines en taille (ΔLog$A$=0.1). Les paramètres étudiés sont le flux magntétique ($|\Phi|$), le champ magnétique maximum ($|B_m|$), le rapport champ maximum sur champ moyen ($B_m/\overline{B}$) et la densité de flux magnétique ($|\Phi|/A$). D'après Meunier (2003).

Paramètre	25 G	40 G
$\lvert\Phi\rvert$	1.210±0.007	1.175±0.006
$\lvert B_m\rvert\_$	0.429±0.009	0.384±0.007
B_m/B	0.222±0.005	0.209±0.004
$\lvert\Phi\rvert/A$	0.184±0.006	0.161±0.005

de 40 Mm^2), ce qui suggère une origine différente des plus petites structures. Les différences entre polarités sont compatibles avec le fait que la polarité de tête est plus facile à détecter pour les structures de toutes tailles incluant le réseau.

- L'asymétrie est-ouest est compatible avec une inclinaison vers l'est des tubes de flux, y compris pour le réseau magnétique bien qu'il résulte de la désintégration des régions actives et ne correspondent a priori pas à du flux nouvellement émergent. Les deux polarités (de tête et de queue) présenteraient des inclinaisons légèrement différentes.
- Le flux magnétique des petites structures du réseau dépend fortement du niveau d'activité environnant, à la fois à petite échelle et à grande échelle. Leur flux et leur densité de flux décroit quand on s'éloigne d'une région active.
- La distribution en latitude des structures de diverses tailles ainsi que le diagramme papillon confirme que les petites structures apparaissent en plus grand nombre dans les régions de haut niveau d'activité. Cependant, le flux magnétique par structure dans les petites structures (en dessous de 40 Mm^2), est maximal à des latitudes plus hautes. Une asymétrie nord-sud est également observée.
- Les variations au cours du cycle du flux intégré sur l'ensemble des structures de diverses tailles ou de divers domaines de flux sont similaires (Fig. 2.8), sauf pour l'amplitude qui est bien plus faible pour les petites structures. Pour toutes les tailles, la variation est corrélée avec le cycle solaire. L'amplitude pour le réseau semble plus élevée que ce qui a été obtenu dans des travaux précédents, par exemple ceux de Foukal et al. (1991), avec un facteur $\sim$7 au lieu de $\sim$1.5. Ceci pourrait être dû à une meilleure sensibilité dans la détermination du réseau magnétique : le nombre d'images utilisé par Foukal et al. (1991) était beaucoup plus faible que dans Meunier (2003).
- Au minimum du cycle, le flux dans les régions actives est du même ordre de grandeur que celui dans le réseau, comme le montre la Fig. 2.9.

Discussion

Ces résultats suggèrent une certaine continuité entre les propriétés des structures des régions actives jusqu'aux structures du réseau les plus petites. Cependant, on observe une

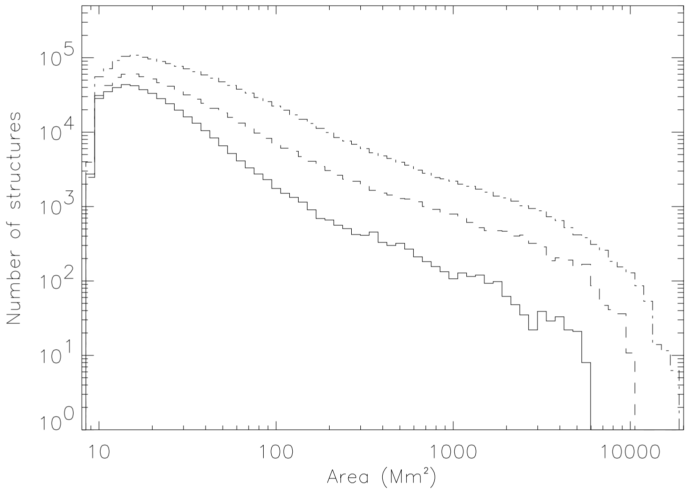

Figure 2.6 : Distribution en taille des structures allant du réseau magnétique aux régions actives pour les 3 phases étudiées du cycle solaire : minimum du cycle (trait plein), phase ascendante (tirets) et maximum du cycle (pointillés), pour le seuil de 40 G. D'après Meunier (2003).

échelle typique, autour de la supergranulation, à laquelle certaines propriétés changent, et ce avec diverses approches (voir également la section ci-dessus sur l'analyse fractale des régions actives). Les variations au cours du cycle sont toutes cohérentes entre elles, avec une augmentation de cette échelle au cours du cycle.

Dans tous les cas, le flux est toujours plus large quand c'est plus actif, que ce soit en terme de phase du cycle ou de proximité aux régions actives. Cependant, le détail des variations diffère selon le cas, suggérant l'influence de plusieurs processus. Les variations pour le réseau pourraient être dues à la granulation ou à la supergranulation. Dans le cas des régions éphémères ou des régions actives, il est plus probable que cela soit dû à une variation du processus de dynamo, par exemple avec des propriétés différentes au bas de la zone convective, et une forte relation entre la présence d'un "nid" ("nest") autour de la région active et ses propriétés.

Les régions actives ont en effet des propriétés différentes selon qu'elles sont proches les unes des autres ou isolées. Il est bien connu que le flux magnétique des régions actives émerge préférentiellement dans les zones occupées précédemment par des régions actives. La présence de longitudes actives ou "nids" a été observée par divers auteurs (Gaizauskas et al. 1983; Harvey & Zwaan 1993; Harvey 1993; Schrijver & Zwaan 2000). J'observe que ceci va en fait plus loin que l'existence de longitudes actives, car le flux est également plus concentré dans ces structures que dans les structures isolées. Une indication de propriétés différentes pour les structures isolées ou non avait été notée par Harvey (1993), qui avait observé une corrélation entre le tilt des régions émergentes avec celui des régions précédentes. Le flux plus large au maximum du cycle pourrait avoir une origine similaire, car elle a observé que les régions dans des "nids" étaient plus nombreuses

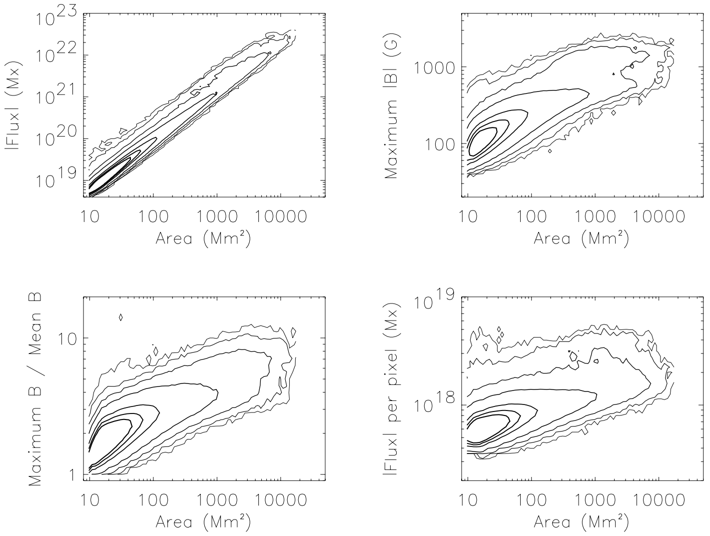

Figure 2.7 : Nombre de structures en fonction de leur taille et en fonction du flux magnétique (resp. du champ magnétique maximum, du rapport maximum / champ moyen dans les structures, et de la densité de flux magnétique). Les structures sont définies par le seuil à 40 G. Les courbes correspondent à 1, 10, 100, 10^3, 10^4, 2×10^4 et 3×10^4 structures (de l'extérieur vers l'intérieur des distributions). D'après Meunier (2003).

durant le maximum du cycle solaire (50% des régions) que durant le minimum du cycle (30%).

Deux observations pourraient sembler contradictoire. D'une part, le flux dans les petites structures décroit lorsque la distance à une région active augmente. Par ailleurs, j'observe que le flux magnétique moyen dans ces structures n'est pas maximal aux latitudes où le niveau d'activité est maximum. D'après la première observation, on pourrait s'attendre à ce qu'il le soit, puis décroissent vers les basses et hautes latitudes, celles-ci correspondant statistiquement à des structures plus loin des régions actives. Ceci n'est cependant pas incohérent. Dans le premier cas, la dépendence est en effet moyennée dans toutes les directions. Ceci suggère que la diffusion n'est peut-être pas isotrope, par exemple à cause de la présence de la circulation méridienne, qui est essentiellement dirigée vers les pôles. Une interprétation possible de cette observation pourrait être la suivante : à la latitude de forte activité, la diffusion due à la supergranulation pourrait être moins efficace, entrainant des structures de flux magnétique plus petit. A haute latitude, la supergranulation pourrait devenir plus efficace pour concentrer le flux, probablement disponible en quantité un peu plus importante que du côté de l'équateur à cause de la circulation méridienne. Il est cependant étonnant que ceci ne soit pas vrai pour les structures du réseau dans le domaine 40–80 Mm^2, car elles résultent aussi de la dispersion du flux à la surface.

J'ai également suggéré que l'anti-corrélation entre le nombre de points brillants du réseau avec le cycle solaire observée par Muller & Roudier (1984) pourrait être due à

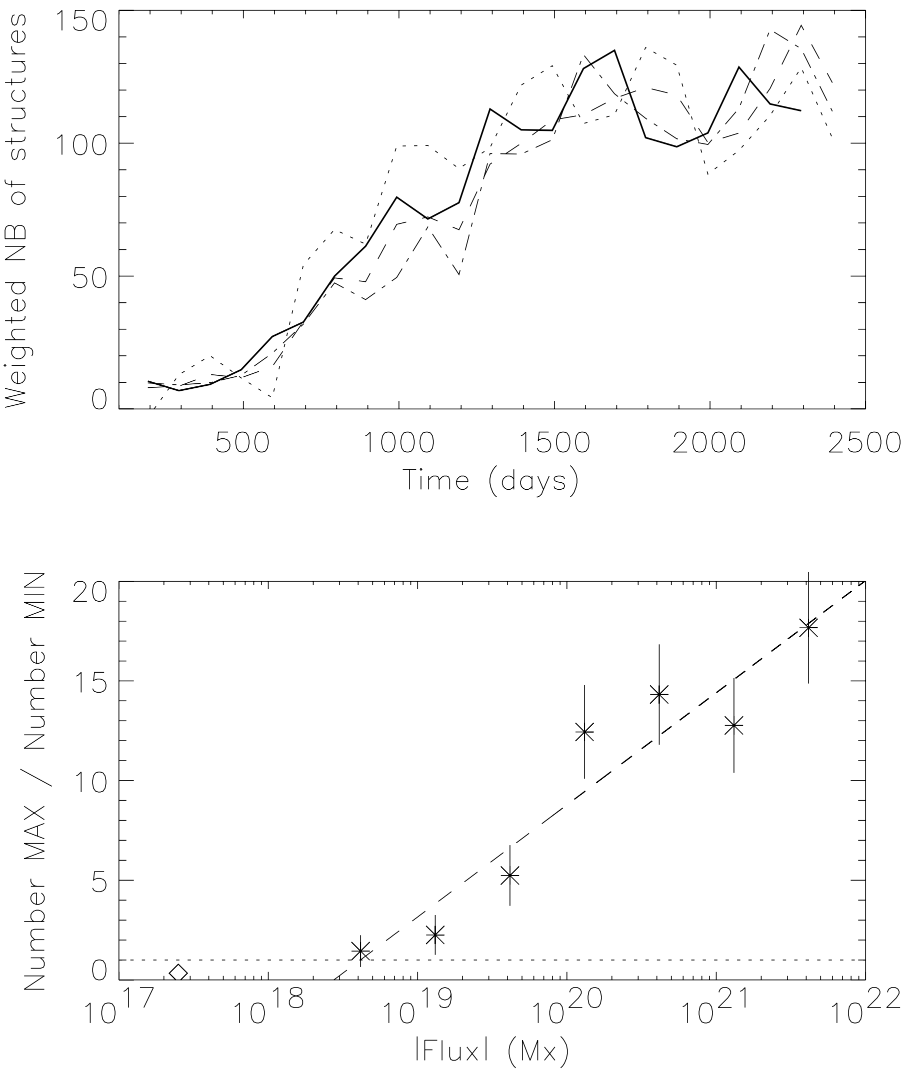

Figure 2.8 : En haut : Nombre de structures ayant des flux inférieurs à 3 × 10^{19} Mx (pointillés), entre 3 × 10^{19} et 10^{21} Mx (tirets) et au-dessus de 10^{21} Mx (tiret-pointillé). La courbe en trait épais représente le nombre de Wolf. Les courbes ont été normalisées de manière à avoir le même nombre moyen de structures durant le minimum du cycle et durant le maximum du cycle. La normalisation tient également compte du nombre d'images différent d'une période à l'autre. En bas : rapport entre le nombre de structures au minimum d'activité et au maximum d'activité (étoiles), pour différents domaines de flux magnétiques (calcul dans un domaine couvrant Log Φ=0.5, avec Φ le flux magnétique). La courbe en tirets est un ajustement linéaire sur ces points. La ligne horizontale en pointillés correspond au rapport 1 (renversement du sens de variation au cours du cycle). Le carré en bas à gauche représente le résultat de Muller et Roudier (1984), avec l'hypothèse d'un flux de 2.5 × 10^{17} par NPB individuel. D'après Meunier (2003).

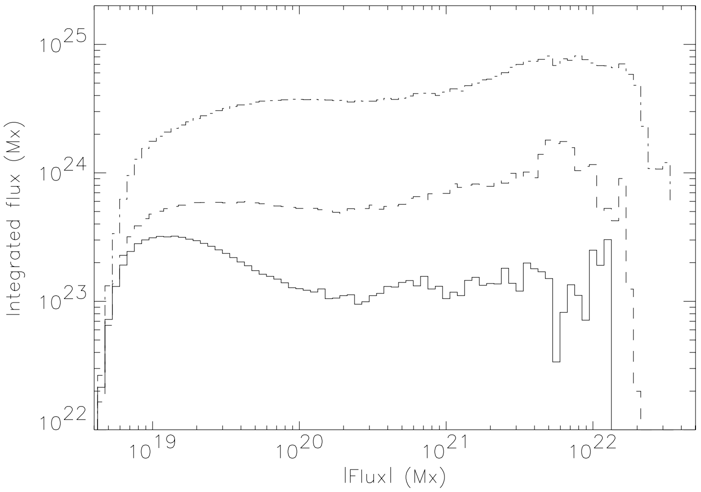

Figure 2.9 : Distribution du flux magnétique pour les trois phases étudiées du cycle solaire : minimum du cycle (trait plein), phase ascendante (tirets) et maximum du cycle (pointillés), pour un seuil de 40 G. D'après Meunier (2003).

la fois à un effet de sélection (les régions les plus calmes à un instant donné ayant été choisies, on pourrait imaginer que la plus grande concentration du flux dans certaines régions rendent ces zones les plus calmes non représentatives de l'ensemble de la surface) et à une plus grande concentration du flux dans les structures du réseau durant le maximum du cycle. La variation des propriétés magnétiques des structures du réseau pourrait également être liée aux différences de contrastes entre réseau et plages observées par Ortiz et al. (2002). Ces résultats sont essentiels pour l'étude des variations de l'éclairement solaire. La contribution du réseau à ces variations pourrait en effet être plus grande que celle obtenue jusqu'à maintenant.

2.2.3 Champs de vitesse supersoniques dans les régions actives

Des observations conjointes entre THEMIS et MDI/SOHO ont permis d'observer dans de bonnes conditions une région active présentant de nombreuses éruptions (NOAA 9236). L'avantage de THEMIS était de permettre une analyse spectropolarimétrique fine, en fournissant les profils à haute résolution, et ce dans plusieurs raies simultanément (toutes au niveau photosphérique). D'un autre côté, les données MDI étaient continues, avec une cadence de 1 minute, ce qui a permis d'observer l'évolution des champs de vitesse et du flux magnétique au cours du temps, et plus particulièrement au cours d'une éruption. Nous avons observé deux régions avec des vitesses très particulières dans cette région active (Meunier & Kosovichev 2003) :

- Tout d'abord, un flot descendant supersonique d'environ 10 km/s a été observé, principalement dans le profil de Stokes V, incliné d'environ 51° par rapport à la

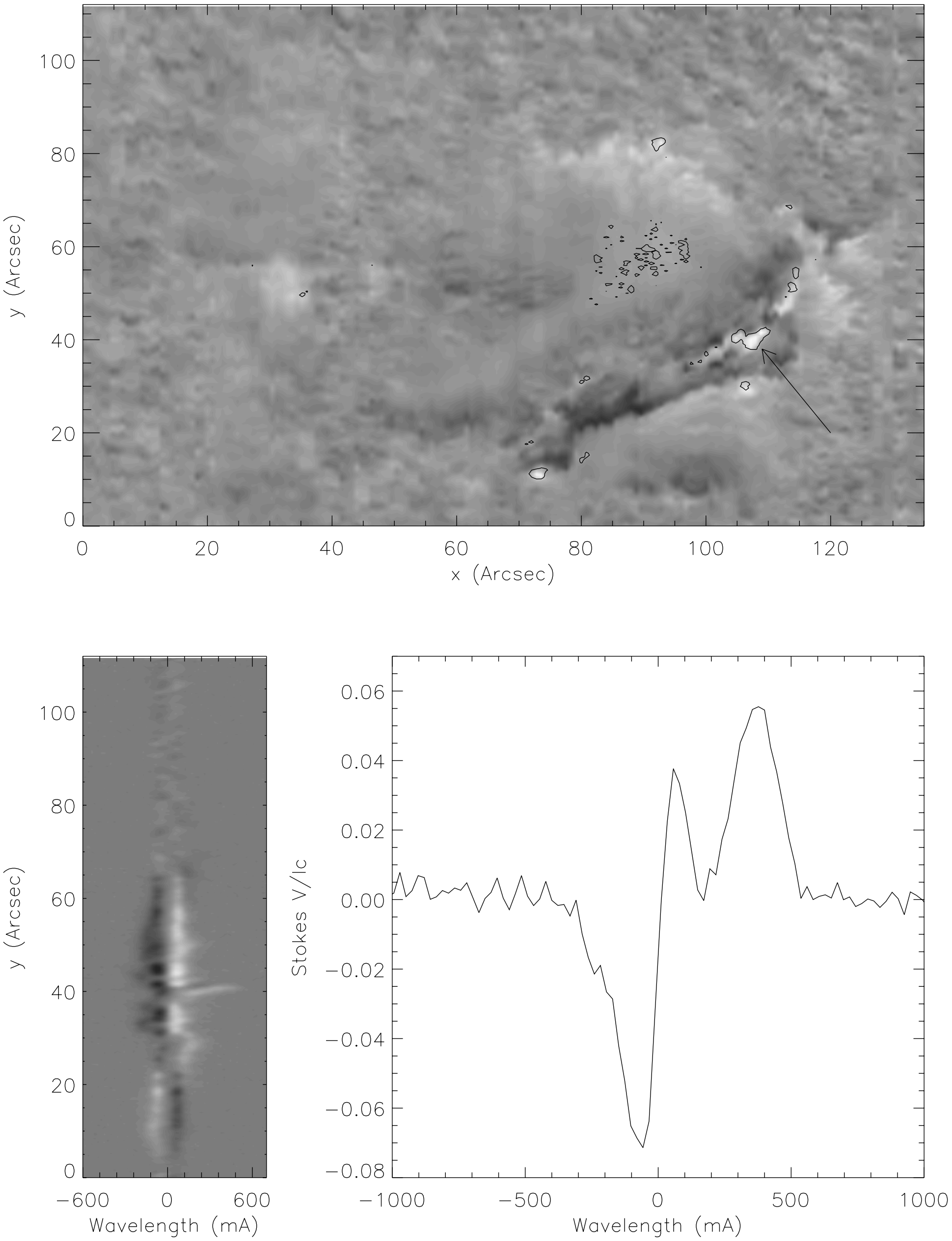

Figure 2.10 : En haut : Les contours délimitent les régions ayant un Stokes V de forte amplitude à environ 300 mÅ du centre de la raie, superposé sur une carte Doppler (raie du Ni, observations THEMIS), le 26 Novembre 2000 (8h24 TU). Les contours au centre de la taches sont dûs à une contamination par des raies faibles. La région qui nous intéresse est indiquée par une flèche. Un exemple de profil de Stokes V (à la position x=105 arcsec) est montré en bas à gauche, ainsi qu'une coupe à la position y=40 arcsec, montrant un profil anormal (en bas à droite). D'après Meunier & Kosovichev (2003).

verticale locale. Ceci est illustré sur la Fig. 2.10 : la carte montre la localisation des régions avec fort décalage Doppler, et le spectre montre clairement la présence de deux composantes dans le profil de Stokes V, l'un avec un décalage Doppler pratiquement nul, et l'autre très fortement décalé. Ce décalage vers le rouge est également visible en Stokes I, y compris pour la raie insensible au champ magnétique. L'azimuth et l'inclinaison de cette composante sont différents de la composante magnétique non décalée, et présente une topologie très complexe. Il faut noter que ce champ de vitesse n'a été observé que sur un balayage effectué avec THEMIS (il n'était pas présent la veille), aucune autre observation THEMIS de la tache du même jour n'ayant été conservée. Par contre, MDI a observé ce champ de vitesse, avec une amplitude réduite (du fait de la moyenne sur toutes les composantes en un pixel donné), de l'ordre de 1.5–2 km/s. Il y est présent pendant au moins 8 heures, ce qui suggère que ce flot a une longue durée de vie. L'interprétation de ce flot n'est pas claire. Il pourrait être liée à l'éruption Hα qui s'est produite 5 heures auparavant, ou bien pourrait également être relié à la très forte émission X observée au même moment. Il n'a cependant pas été possible de relier avec certitude cette très forte émission X avec cette région active, car les observations Hα (Learmonth Observatory) ne montrent pas d'embrillancement à ce moment-là dans cette région active ni dans l'autre région active présente sur le disque, alors que les observations radio de Nancay montrent un embrillancement dans les deux régions ! Nous remarquons cependant une décroissance du flux magnétique, et ceci dans les deux polarités, dès le matin précédent l'observation THEMIS, et ce jusqu'au début de l'éruption Hα. Ceci est surprenant, car on s'attendrait plutôt à une augmentation du flux magnétique dans un fort flot descendant (cependant, aucun flot convergent n'est visible).

- Un autre champ de vitesse important est observé, décalé vers le bleu et adjacent à un flot décalé vers le rouge, proche de la ligne neutre. Pour les mêmes raisons que ci-dessus, les données MDI suggèrent qu'il s'agit d'une structure de longue durée. De plus, il a été possible d'observer cette zone particulière avec THEMIS (une fois avec un balayage, comme pour le résultat précédent, et une fois avec la fente fixe sur cette zone, au moment d'une éruption Hα) à 9 heures d'intervalle, avec une évolution significative de la configuration du champ de vitesse au cours de la journée. Avec l'hypothèse que ces flots suivent des lignes de champ magnétique, et avec la topologie magnétique déduite des observations de l'ensemble des paramètres de Stokes avec THEMIS, on déduit que ces deux flots sont proches de l'horizontale et en sens contraires, ce qui peut être interprété comme un cisaillement horizontal, avec l'une des 2 composantes supersoniques sur une échelle spatiale de 2–3 arcsec. Un cisaillement de cette amplitude n'a jamais été observé auparavant dans la photosphère. L'origine de ce flot pourrait être indépendante de l'éruption. Cependant, la composante décalée vers le rouge augmente de 800 m/s après l'éruption, et ce sur une longue échelle de temps. Il est donc probable que ce flot ait été influencé par l'éruption et pourrait jouer un rôle dans la restructuration de la configuration magnétique au cours de l'éruption.

Des vitesses supersoniques ont été observées dans la photosphère auparavant, mais très rarement. Pillet et al. (1994) en ont observé dans une tache de configuration δ, à savoir des flots descendant au niveau de la ligne neutre avec une longue durée de vie (raison pour laquelle ils ont suggéré que ces flots n'avaient rien à voir avec les processus de reconnection). Les polarités de la composante décalée en vitesse et de la composante à vitesse nulle sont les mêmes ou opposées selon le pixel. D'un autre coté, del Toro Iniesta et al. (2001) ont également observé un flot descendant supersonique dans la pénombre d'une tache simple, avec une polarité opposée pour la composante décalée en vitesse. Ce que nous avons observé est donc différent de cette configuration, et également différent des "moustaches", qui sont des structures à très courte durée de vie, 5–10 minutes (voir par exemple Beckers & Artzner 1974 pour une description de ces phénomènes chromosphériques associés à des vitesses très élevées), et des bombes Ellerman (structures à l'échelle de 1–2 arcsec). Les inclinaisons des flots sont également très différentes, avec des structures de longue durée de vie et un lien avec l'éruption. A noter que des vitesses ascendantes ou descendantes avaient été observées par Sigwarth (2001) assez proches des nôtres du point de vue du stokes V, de la même polarité ou de polarité opposée. Ses observations étaient cependant associées à une émergence de flux et était interprétées comme un pré-choc décalé vers le rouge et un post-choc décalé vers le bleu. Le processus est probablement différent dans le cas de nos observations.

Il pourrait sembler surprenant que des flots d'une telle amplitude n'aient que très rarement été détectés auparavant au niveau photosphérique. Cependant, les observations spectropolarimétrique d'éruptions ne sont pas très courantes, surtout en utilisant des raies photosphériques comme c'était le cas pour ce travail. L'origine de ces flots reste cependant à éclaircir. Ceci nécessiterait davantage d'observations, avec une bonne coordination entre observations spectropolarimétriques (qui ont typiquement une cadence faible du fait de la nécessité de balayer la région active) et des observations de type magnétographie qui, bien que fournissant des données partielles, permettent de suivre les phénomènes avec une bonne cadence temporelle par rapport à l'échelle caractéristique des éruptions.

La rareté de ce type d'observation est peut-être due à la mauvaise résolution spatiale de la plupart des observations spectropolarimétriques (typiquement la seconde d'arc). Les premières observations de Hinode, qui pallie à cette limitation, ont en effet montré la présence très courante de champs de vitesse très grands au niveau photosphérique : nous pourrions avoir observé un événement particulièrement étendu se situant en queue d'une distribution centrée sur des événements beaucoup moins étendus.

2.3 Conclusion

La caractérisation de la complexité des régions actives en utilisant l'analyse fractale est maintenant très exhaustive (grand échantillon, influence du seuil en champ magnétique, variation au cours du cycle, influence de la présence de taches), et de nombreux résultats nouveaux ont ainsi été obtenus. Cette technique continue à être utilisée, ainsi que ses biais possibles : Criscuoli et al. (2007) a par exemple montré que l'estimation de la dimension fractale des structures les plus petites pouvaient être sous-estimées à cause de l'échantillonnage par les pixels. Le principal travail restant à faire, à mon avis, est cependant d'améliorer significativement les modèles de régions actives en y ajoutant davantage de processus physiques, sur plusieurs aspects : introduire des champs de vitesse réalistes en profondeur (bas de la zone convective) et en surface (diffusion supergranulaire), introduire une remontée des tubes de flux vers la surface plus réaliste (par exemple Fan et al. 2003), en tenant compte notamment de plusieurs profondeurs d'ancrage selon le type de structure (voir prochain chapitre également). A ce stade, les observations ont permis de fournir des outils et des résultats permettant une caractérisation très fine, et les modèles se doivent d'arriver à faire se rejoindre les processus physiques élémentaires et l'approche statistique afin d'être validés en utilisant ces mêmes outils.

Le réseau magnétique a également été caractérisé de manière assez exhaustive, dans la limite de la résolution spatiale des observations actuelles. Ces travaux devront être poursuivis avec l'étude à très haute résolution spatiale, si possible en spectropolarimétrie (par exemple avec Hinode lancé en 2006) ou sur de grands champs (par exemple avec CALAS, voir chapitre 4, à la fois en bande G et en magnétométrie). Ce type d'observation devra être poursuivi au cours du cycle solaire. En parallèle, des simulations comme celles de Simon et al. (2001) et Krijger & Roudier (2003), qui consistent à utiliser des “bouchons” passifs pour reproduire le réseau magnétique à partir d'un champ de vitesse, devront également être poussées plus loin afin de prendre en compte les variations au cours du cycle de paramètres comme la taille de la supergranulation. Ceci devrait aider à interpréter certains des résultats obtenus. La comparaison avec des modèles globaux de Schrijver (2001) et Schrijver et al. (2002) devra être faite également, ou bien avec un modèle de tapis magnétique comme celui de Parnell (2002). Il serait également très utile d'étudier la différence d'efficacité entre la diffusion supergranulaire et la circulation méridienne pour le transport du flux, et leur importance relative au cours du cycle.

La caractérisation des champs IN, bien qu'ayant fortement progressé ces dernières années, souffre encore du faible volume d'observation. Cette étude reste donc à approfondir afin de permettre d'avoir une vue cohérente des différents types de structures coexistants. Les observations prochaines de Hinode seront sans nul doute les plus adaptées pour effectuer un bond significatif vers la compréhension de ces champs faibles. Des perspectives d'études par effet Hanle des champs turbulents proches du limbe avec résolution spatiale (Malherbe et al. 2007) constitueront une approche complementaire très intéressante.

Un élément important qui est apparu au cours de l'analyse de ces divers résultats est le besoin crucial de mieux connaitre la dynamique de la photosphère, que ce soit à grande échelle (rotation différentielle et surtout ici circulation méridienne) ou à petite échelle (supergranulation). L'étude de cette dynamique fait l'objet des deux prochains chapitres.

Chapitre 3

Dynamique globale de la photosphère

La connaissance de la dynamique solaire à différentes échelles temporelles et spatiales est un élément clé des théories de la dynamo visant à reproduire le comportement du Soleil au cours du cycle solaire. Le couplage entre les champs magnétiques solaires et la dynamique de la zone convective est essentiel pour comprendre les éventuelles rétroactions du champ magnétique sur la dynamique à l'origine de la dynamo. Avec la diffusion supergranulaire, la rotation différentielle et la circulation méridienne sont également des ingrédients essentiels pour expliquer la distribution du flux magnétique solaire à la surface du Soleil (voir par exemple Wang & Sheeley 1990). Dans ce chapitre, je présente une caractérisation de la dynamique photosphérique obtenue à partir des structures magnétiques, des régions actives jusqu'au réseau. L'influence de nombreux facteurs a été étudiée : la taille des structures et le flux magnétique associé, la polarité, la phase du cycle, la présence de trous coronaux.

3.1 Caractérisation de la dynamique photosphérique

Articles :

- *Meunier N., Roudier T., The superrotation of supergranules, 2007, A & A 466, 691*
- *Meunier N., Temporal variations in the magnetic network large-scale dynamics, 2005, A & A 442, 693*
- *Meunier N., Large-scale dynamics and polarities of magnetic structures, 2005, A & A 437, 303*
- *Meunier N., Magnetic network dynamics: activity level, feature size and anchoring depth, 2005, A & A 436, 1075*
- *Meunier N. & Jefferies S.M., Two-Dimensional Modeling of the Solar Oscillation* l-ν *Power Spectrum, 2000, Astrophys. J., 530, 1016*
- *Meunier N., Large scale dynamics of active regions and small photospheric magnetic features, 1999, Astrophys. J., 527, 967*
- Meunier N., Nesme-Ribes E. & Collin B., Cycle 19 facula dynamics II. Meridional circulation, rms velocity and Reynolds stresses, 1997, A & A 319, 683
- Meunier N., Nesme-Ribes E. & Grosso N., Cycle 19 facula dynamics I. Angular rotation, 1997, A & A 319, 673

- Nesme-Ribes E., Meunier N., & Vince I., 1997, Solar dynamics over cycle 19 using sunspots as tracers, 1997, A & A 321, 323

Approches possibles

Plusieurs approches complémentaires ont été utilisées par divers groupes pour étudier cette dynamique (voir également Beck 2000) :

- Les *Dopplergrammes* fournissent les champs de vitesse du plasma non magnétisé à la surface du Soleil (Hathaway 1992; Hathaway 1996). Les images brutes contiennent une information sur la dynamique globale (telle que la rotation différentielle ou la circulation méridienne) mais aussi sur la dynamique à petite échelle (granulation ou supergranulation), sujet qui sera abordé dans le prochain chapitre.
- L'*héliosismologie* permet d'accéder à la dynamique interne du Soleil. Les données de base peuvent être des Dopplergrammes identiques à ceux mentionnés ci-dessus ou bien des images en intensité. Une analyse globale des séries temporelles fournit en général une dynamique à grande échelle symétrisée entre les deux hémisphères (par exemple Schou et al. 1998). Cette dynamique est généralement à faible résolution spatiale et ne permet pas bien d'accéder à la circulation méridienne, par contre elle fournit des informations sur les couches très profondes, y compris la zone radiative. Par ailleurs, les analyses locales (par exemple Duvall et al. 1993; Duvall et al. 1996) fournissent cette dynamique avec une meilleure résolution spatiale dans les couches proches de la surface. La résolution temporelle reste généralement moyenne (plusieurs heures). L'analyse locale permet d'accéder à toutes les composantes du champ de vitesse, y compris la circulation méridienne ou la supergranulation.
- Le *suivi de structures* de différents types, soit magnétiques (taches, facules, réseau), soit dynamiques (supergranulation) permet également d'accéder à la dynamique globale : ces structures sont ainsi considérées comme des traceurs des mouvements photosphériques. Plusieurs techniques sont possibles, soit le suivi de structures bien déterminées, soit la corrélation entre images successives, effectuée à diverses échelles. Selon les structures concernées, elles fournissent des résultats différents, simplement parce que les structures ont des dynamiques différentes en fonction de leur nature, de leur taille, de leur âge, de la phase du cycle, etc. C'est cette complexité qui permet d'utiliser la dynamique comme diagnostic pour comprendre leur nature et les processus à l'oeuvre.

Mes contributions

Toutes ces approches sont donc nécessaires et complémentaires pour appréhender la dynamique solaire. Je me suis plus particulièrement intéressée à la troisième approche, le suivi de structures et, de manière indirecte, à la deuxième.

J'ai abordé l'héliosismologie (Meunier & Jefferies 2000) en élaborant un algorithme d'ajustement du spectre de puissance $\ell - \nu$ [1] dans les deux dimensions simultanément, en

---

[1] ℓ est le degré des modes, représentant le nombre de lignes nodales à la surface du Soleil, et ν leur fréquence temporelle.

prenant en compte un grand domaine de fréquences ν et de degrés ℓ. Nous avons montré qu'une telle méthode fournissait une meilleure représentation du spectre observé que les méthodes traditionnelles à une dimension. L'utilisation d'une plus grande partie du signal disponible, ainsi qu'une prise en compte du fond et des fuites entre les différents modes, permettent un gain significatif (ce gain est très variable selon le domaine du spectre, mais la méthode peut conduire à une réduction du maximum de vraisemblance d'un ordre de grandeur dans certains cas). Cette méthode s'est avérée très lourde en temps de calcul, ce qui la rend difficile à utiliser de manière systématique. Elle a cependant permis de quantifier des biais présents dans les méthodes traditionnelles. J'ai aussi utilisé la dynamique dérivée de l'héliosismologie fournie par d'autres équipes (voir plus loin).

A la date du début de mes travaux, les structures les plus étudiées, de loin, étaient les taches solaires. De nombreux travaux avaient été réalisés par plusieurs groupes à partir d'observations synoptiques provenant de plusieurs observatoires. L'abondance de données avait permis de fournir beaucoup de détails sur leur dynamique, en permettant de prendre en compte la taille et l'âge des structures. Ce dernier point est essentiel car il est probablement l'élément clé qui permet d'expliquer les contradictions apparentes entre les différents auteurs. J'ai participé à cet effort, en travaillant sur des données du cycle 19 (spectrohéliogrammes de Meudon), travaux qui représentent la poursuite du travail d'E. Nesme-Ribes sur ce sujet (Nesme-Ribes E., Ferreira E. and Vince I. 1993). Ce travail a en particulier confirmé les résultats originaux qu'elle avait déjà obtenus à partir de données d'une autre période, à savoir une circulation méridienne complexe des taches solaires au cours du cycle (Nesme-Ribes, Meunier, & Vince 1997).

Paradoxalement, les autres manifestations du champ magnétique solaire, en particulier les facules, constituants essentiels des régions actives, n'avaient été que très peu étudiées, bien que d'abondantes données existent également. Le réseau magnétique quant à lui n'avait fait l'objet que de très peu de travaux. Un suivi des facules avait été effectué par Belvedere et al. (1977) mais avec de grandes barres d'erreur. Des magnétogrammes quotidiens obtenus au sol avaient également été utilisés, en particulier par Snodgrass & Ulrich (1990), Komm et al. (1993b) et Komm et al. (1993a), sur un cycle solaire. Dans tous les cas, une rotation des régions actives plus rapide que le plasma environnant a été observée, ainsi qu'une circulation méridienne vers les pôles.

J'ai donc concentré mes travaux sur ces structures magnétiques, à l'aide de deux jeux de données. J'ai tout d'abord utilisé des spectrohéliogrammes de Meudon, qui non seulement montrent les taches solaires, mais également les facules et le réseau magnétique en intensité. Un inconvénient majeur de ces données, comme de toutes celles qui avaient été utilisées jusqu'à présent d'ailleurs, était d'une part une cadence temporelle faible (1 journée) et d'autre part des différences de qualité d'image d'un jour à l'autre. Pour pallier à ce dernier problème, une sélection drastique des images avait été faite, réduisant ainsi l'échantillon. Les structures magnétiques se déformant beaucoup d'un jour à l'autre, le problème de la cadence devient crucial, tout particulièrement pour le réseau magnétique étant donnée la durée de vie typique des structures individuelles. C'est pourquoi j'ai ensuite entamé une analyse exhaustive des magnétogrammes de MDI, qui ont été obtenus avec une cadence de 96 minutes. Dans ce cas, les déformations entre les images sont très faibles, d'autant qu'il n'y a pas non plus de distorsion atmosphérique. Ceci permet une analyse beaucoup plus fine que celles effectués précédemment sur des magnétogrammes du Mont Wilson par Snodgrass & Ulrich (1990), Komm et al. (1993b), et Komm et al. (1993a) car ils avaient dû moyenner fortement leurs résultats spatialement et temporellement afin d'obtenir des résultats significatifs.

Dans les deux sections suivantes, je détaille mes résultats récents sur la rotation différentielle puis sur la circulation méridienne et enfin les variations au cours du cycle. Auparavant, il est utile de préciser les deux méthodes employées, qui seront également évoquées dans les section 3.3 (ancrage des structures dans la zone convective) et 3.4 (rotation et trous coronaux) :

- Le suivi par corrélation (dénommé CT pour "Correlation Tracking" dans la suite du chapitre) : Les corrélations entre 2 images consécutives sont calculées sur des boites ayant des tailles similaires à l'échelle de la supergranulation. **Elles couvrent donc un grand nombre de structures, dont les mouvements sont ainsi moyennés avec des pondérations diverses. Autrement dit, elle fournit le déplacement d'un "motif" formé par plusieurs structures** : on s'attend donc à ce qu'elle fournisse les mouvements associés aux structures associées à la supergranulation. Elle permet l'accès à la détermination de la dynamique avec une bonne résolution spatiale, en latitude notamment.

- Le suivi de structures individuelles (dénommé FT pour "Feature Tracking" dans la suite du chapitre) : Les structures sont identifiées sur chaque image (voir chapitre 2), puis une idenfication automatique entre paires d'images est effectuée. Ceci permet d'avoir accès à une meilleure résolution spatiale ainsi qu'au **mouvement des structures individuelles**. Par structure individuelle, il ne s'agit pas ici des tubes de flux individuels formant le réseau bien sûr, étant donnée la résolution spatiale de l'instrument, mais des structures formées par des groupes de tubes de flux. Dans la suite, le mot "structure" représente un groupe de tubes de flux apparaissant comme une seule structure à cette résolution spatiale.

3.1.1 La rotation différentielle

Rotation en fonction de la méthode

L'étude approfondie des spectrohéliogrammes de Meudon a permis de dériver la rotation différentielle des petites structures constituant les facules et le réseau (Meunier, Nesme-Ribes, & Grosso 1997; Meunier, Nesme-Ribes, & Collin 1997). J'ai obtenu dans ce travail une rotation très asymétrique par rapport à l'équateur, avec une rotation plus rapide et plus rigide dans l'hémisphère nord. Il faut noter que ce cycle était très actif et présentaient une très forte asymétrie entre les niveaux d'activité des deux hemisphères, ce qui explique peut-être nos observations.

Les travaux sur les données MDI, tout d'abord sur deux ans de données (Meunier 1999b) puis sur 8 ans (Meunier 2005c) couvrant pratiquement un cycle solaire, ont permis d'affiner fortement la connaissance de la dynamique des régions actives en dehors des taches. J'ai confirmé une rotation plus rapide des facules par rapport au plasma en dehors des régions actives, avec une rotation à l'équateur de $14.390 \pm 0.001^\circ$/jour en utilisant une

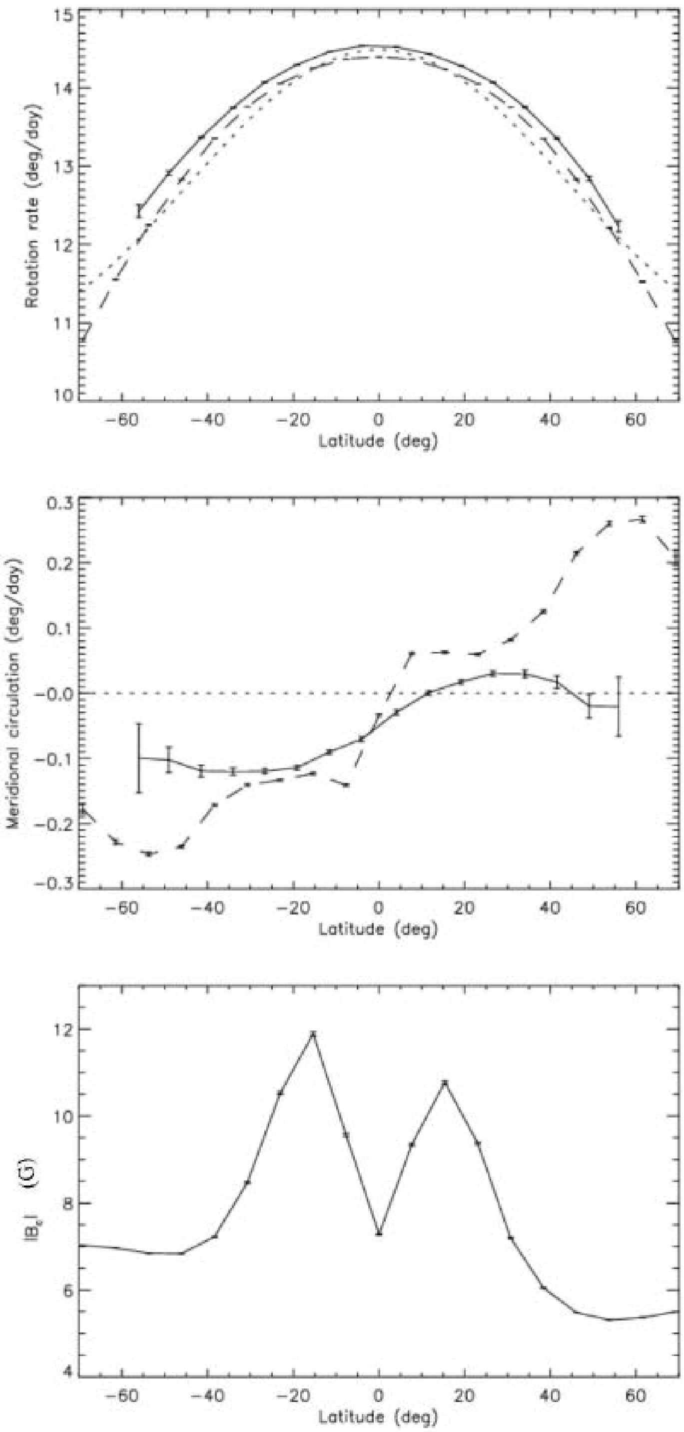

Figure 3.1 : En haut : rotation en fonction de la latitude pour la technique FT (trait plein) et CT (tirets), pour 8 ans de données MDI. La courbe en pointillés représente la rotation de référence autour de laquelle on cherche la bonne rotation. Au milieu : idem pour la circulation méridienne. En bas : champ magnétique moyen dans les boites (technique CT), montrant les latitudes actives. 0.1°/jour correspond à 14 m/s. D'après Meunier (2005a).

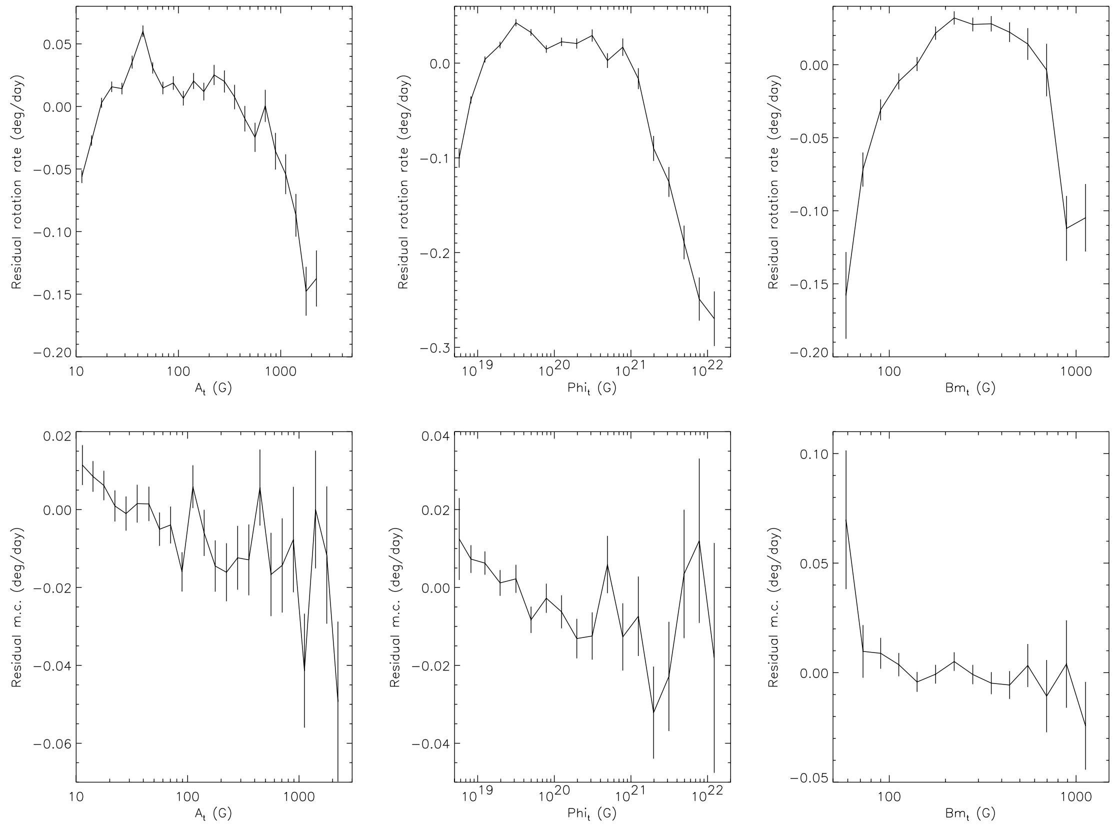

Figure 3.2 : En haut : résidus de rotation FT par rapport à la rotation différentielle moyenne. En bas : résidu de circulation méridienne FT. Résidus en fonction de la taille des structures (à gauche), du flux magnétique dans les structures (au milieu) et du champ magnétique maximum dans les structures (à droite). D'après Meunier (2005a).

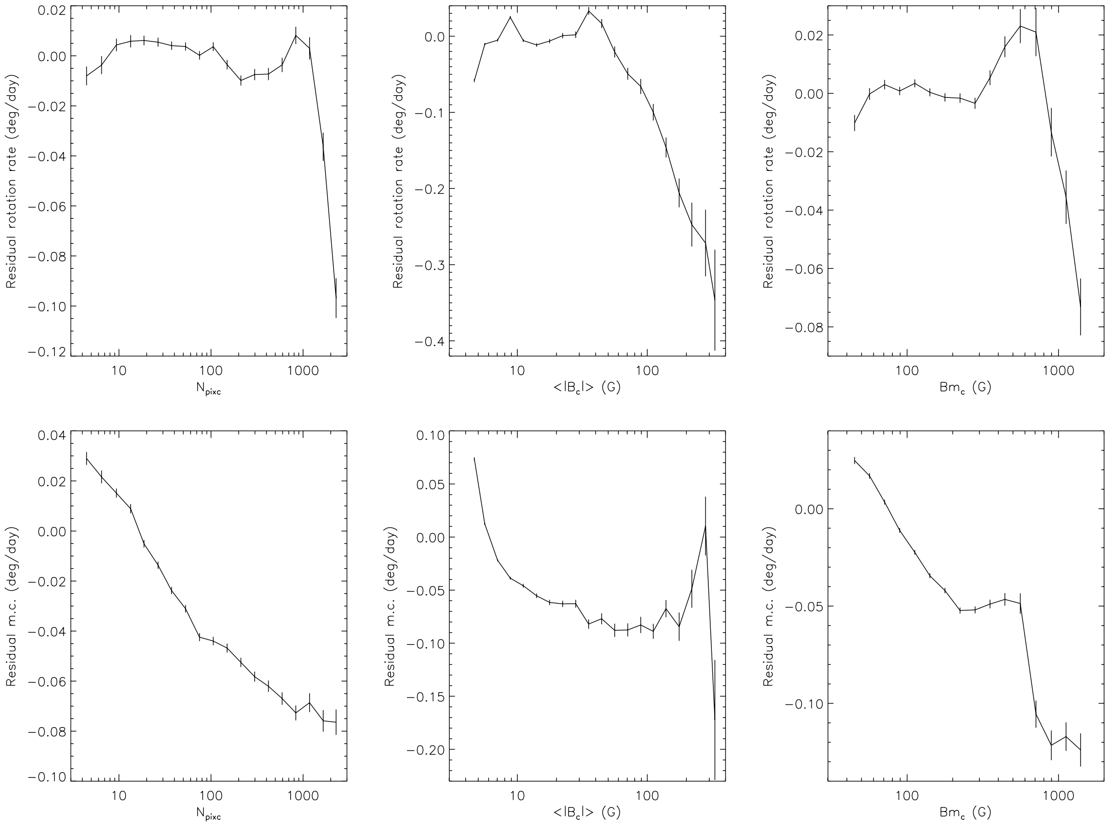

Figure 3.3 : En haut : résidus de rotation CT par rapport à la rotation différentielle moyenne. En bas : résidu de circulation méridienne CT. Résidus en fonction du nombre de pixels de la boite au-dessus de 40 G (à gauche), du champ magnétique moyen dans la boite (au milieu) et du champ magnétique maximum dans la boite (à droite). D'après Meunier (2005a).

Table 3.1 : Rotation équatoriale (en deg/jour) dans la littérature : structures magnétiques photosphériques utilisant une corrélation locale (CT) ou un suivi de structures (FT), sauf pour le travail de Brajša et al. (2004), qui concerne les points brillants coronaux (la méthode 1 est interactive et sélectionne moins de structures dans le domaine de latitude 10–40° que la méthode 2, automatique). Le travail de Meunier et al. (1997) est effectué à partir d'images Ca II au niveau photosphérique. La rotation de la supergranulation (SG) est estimée à partir de corrélation entre Dopplergrammes. Les coefficients A_2 et A_4 sont les coefficients de Legendre d'un ajustement sur la rotation en fonction de la latitude.

Référence	Période	Rotation	B	C
CT Meunier (2005a)	1996–2004	14.390±0.001	-2.568±0.003	-0.552±0.003
CT Meunier (1999)	1996–1998	14.33±0.02	-2.671±0.005	-0.630±0.005
CT Komm et al. (1993a)	1975–1991	14.43±0.02	-2.53±0.12	-0.48±0.03
CT Snodgrass & Ulrich (1990)	1967–1987	14.25±0.01	-2.49±0.07	-0.55±0.02
SG Duvall (1980)	1979	14.72±0.07	-	-
SG Snodgrass & Ulrich (1990)	1967–1987	14.71±0.05	-2.62±0.19	-0.41±0.06
FT Meunier (2005a)	1996–2004	14.562±0.002	-2.21±0.03	-0.34±0.02
FT Meunier et al. (1997)	1957–1964	14.42±0.02	-1.85±0.51	0.16±0.20
Cor. BP (Brajša et al. 2004^1)	1998–1999	14.454±0.027	-2.65±0.36	-0.32±0.11
Cor. BP (Brajša et al. 2004^2)	1998–1999	14.677±0.033	-2.52±0.42	-0.63±0.13

technique de corrélation (CT dans la suite) et 14.562±0.002°/jour en utilisant une technique de suivi de structures individuelles (FT dans la suite). La rotation différentielle obtenue est illustrée Fig. 3.1. J'obtiens aussi avec une précision meilleure que 1 σ que la rotation CT est plus différentielle que la rotation FT : les structures magnétiques individuelles ont donc une rotation relativement rigide, tandis que le motif représenté par plusieurs structures présente une rotation plus différentielle. Il faut noter que j'ai aussi étudié en détail les biais potentiels de l'analyse, ainsi que la correspondance entre les deux approches.

Une comparaison de ces résultats avec d'autres travaux est présentée dans la Table 3.1. La différence de rotation entre les méthodes CT et FT est de l'ordre de 0.17°/jour. Dans le cas CT, les résultats sont compatibles avec ceux obtenus précédemment avec une technique similaire (Snodgrass & Ulrich 1990; Komm, Howard, & Harvey 1993b; Meunier 1999b). Dans le cas FT, le seul travail au niveau photosphérique était celui de Meunier et al. (1997) qui avaient trouvé une rotation plus faible, mais incluait une grande proportion de petites structures à l'intérieur des facules (alors que dans le cas présent une grande facule compte une fois, donc l'influence du réseau sur le résultat est beaucoup plus grande). Mes résultats sont cependant assez proches des estimations faites sur des points brillants coronaux (Brajša et al. 2004).

Au vu des définitions, on pourrait s'attendre à ce que la rotation derivée de la technique CT soit assez proche de la rotation de la supergranulation (pour les régions calmes du réseau magnétique), qui est plus élevée que celle des structures magnétiques (Duvall 1980; Beck & Schou 2000), tandis que la rotation dérivée de FT pourrait être assez

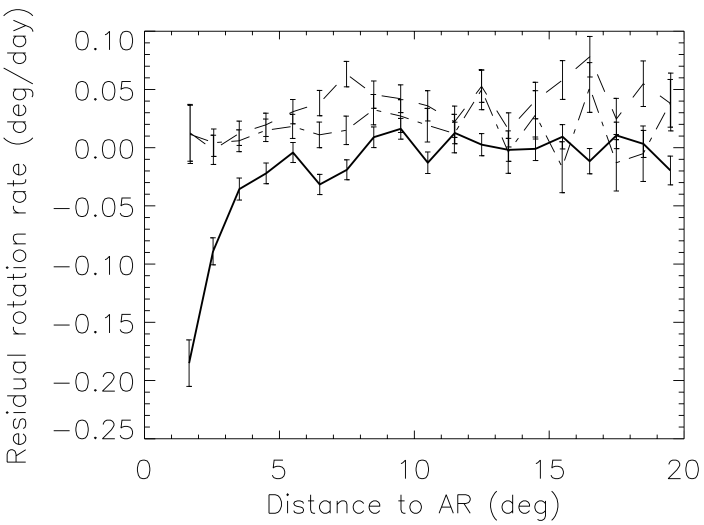

Figure 3.4 : Résidu de rotation FT en fonction de la distance à la région active la plus proche, pour les structures plus petites que 40 Mm^2 (trait plain épais), dans le domaine 40–80 Mm^2 (tirets) et 80-6200 Mm^2 (tiret-pointillés). D'après Meunier (2005a).

proche de la rotation des régions actives, voire même inférieure. Il est cependant surprenant de voir qu'au contraire, la rotation FT, c'est-à-dire des structures individuelles, est plus élevée que la rotation CT, c'est-à-dire de l'organisation à plus grande échelle de ces structures, à toutes les latitudes et pour toutes les tailles de structures.

Analyse de détails

Le grand échantillon disponible m'a permis d'analyser en détail la variation de la rotation en fonction de plusieurs caractéristiques des structures :

- Dans le cas FT : la taille des structures, du flux total et du champ magnétique maximum dans les structures (Fig. 3.2).
- Dans le cas CT : le nombre de pixels au-dessus de 40 G (seuil utilisé pour déterminer les structures dans la technique FT) dans la boite de corrélation, le champ magnétique moyen et le champ magnétique maximum dans la boite (Fig. 3.3).

Dans le cas FT, j'obtiens que les structures les plus grandes (régions actives) tournent le plus lentement. En regardant des structures de plus en plus petites, la rotation passe par un maximum autour d'une taille de l'ordre de 40 Mm^2. C'est ainsi la première fois qu'une telle étude descend jusqu'au réseau magnétique. Le même type de courbe est observé pour la variation de la rotation avec le flux magnétique et le champ magnétique maximum, avec des valeurs critiques qui correspondent bien les unes avec les autres. Dans le cas CT, une forte décroissance de la rotation est également observée pour les “boites” les plus actives. Pour les zones les plus calmes, la variation observée est plus complexe, avec à nouveau une rotation plus petite.

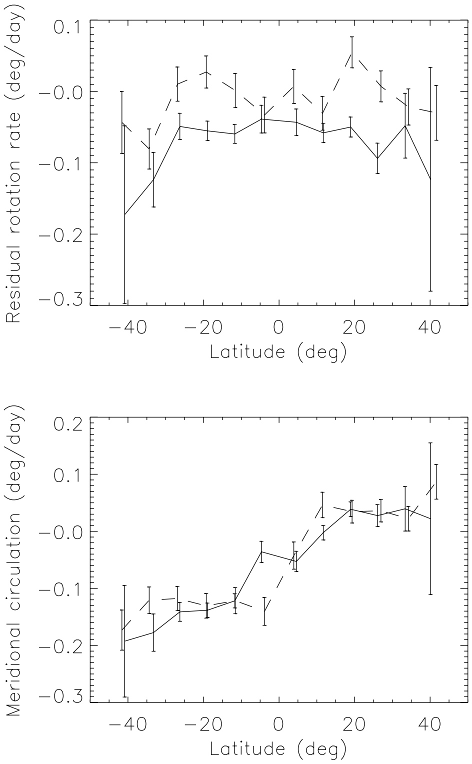

Figure 3.5 : Résidu de rotation FT (en haut) et circulation méridienne FT (en bas) en fonction de la latitude pour petites structures proches d'une région active (trait plein) et loin d'une région active (tirets). D'après Meunier (2005a).

Comme c'était la première fois que la dynamique du réseau était étudiée en permettant d'accéder à autant de détails, il a été possible d'étudier sa dynamique en fonction de sa distance aux régions actives. Ceci est très important pour comprendre le chemin que suit le flux magnétique des régions actives jusqu'au réseau magnétique. Pour les structures les plus petites (en dessous de 40 Mm^2), la rotation FT a été trouvée moins rapide à grande distance d'une région active que proche d'elle. Ceci ne s'observe pas pour les structures de taille supérieure, y compris les grosses structures du réseau (Fig. 3.4). Par ailleurs, une analyse de voisinage a montré une rotation plus rapide des structures incluses dans un groupe par rapport aux structures isolées (Fig. 3.5).

Rotation en fonction de la polarité des structures

Dans le passé, des résultats intéressants sur la rotation des taches de tête et des taches de queue avait été obtenus (voir Howard 1996 pour une revue). Pour les régions actives peu de choses avaient été faites, et rien pour le réseau. Cette approche est très importante pour comprendre l'émergence des régions actives et leur désintégration. J'avais tenté d'étudier la variation de rotation avec la polarité sur les deux premières années de MDI, sans grand succès. Par contre, avec 8 ans de données, l'échantillon est devenu suffisant

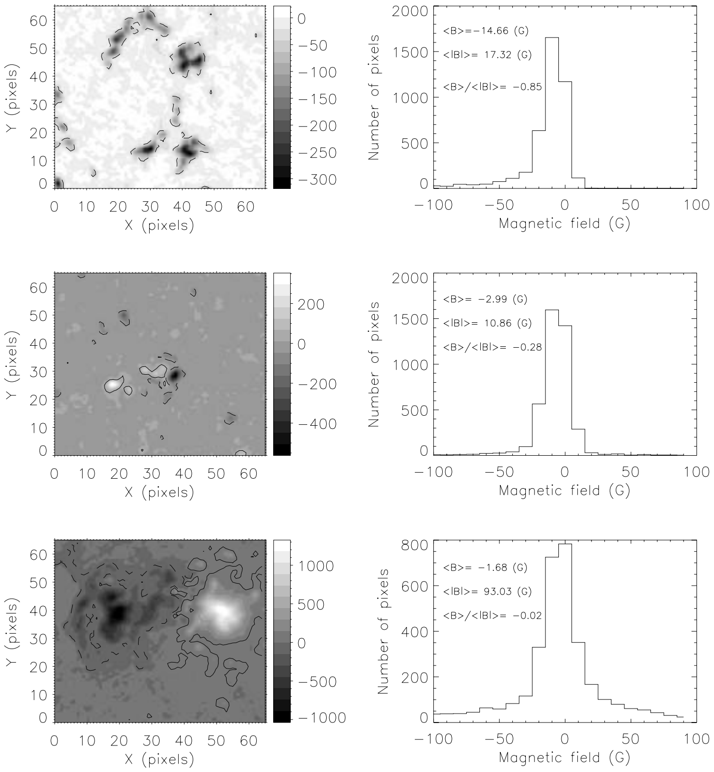

Figure 3.6 : A gauche : Exemples de boites CT. Les contours représentent la limite à 40 G, qui est le seuil utilisé pour l'analyse FT (trait plein pour les champ magnétiques positifs et tirets pour les champs négatifs). A droite : Distribution correspondante du champ magnétique dans ces boites, avec indication du champ magnétique moyen, de la valeur absolue moyenne du champ magnétique et du rapport des deux. D'après Meunier (2005b).

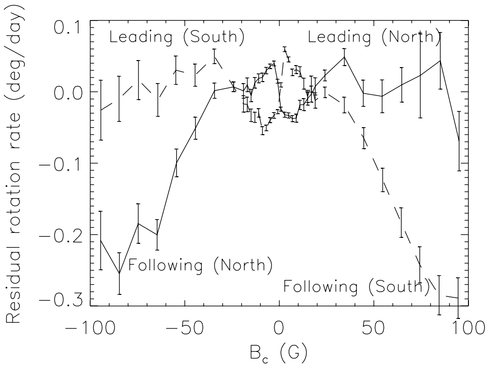

Figure 3.7 : Résidu de rotation CT en fonction du champ magnétique moyen (signé) pour l'hémisphère nord (trait plein) et pour l'hémisphère sud (tirets). D'après Meunier (2005b).

pour obtenir des résultats significatifs (Meunier 2005a). Les boites CT avec les calculs de champ magnétique signés et en valeur absolue sont illustrés sur la Fig. 3.6. Le principal résultat est obtenu avec la méthode CT. Dans ce cas, non seulement les régions actives de tête tournent plus vite (comme observé précédemment pour les taches), mais, au contraire, les structures du réseau correspondant à la polarité de tête tournent moins vite, c'est-à-dire qu'il y a un renversement par rapport aux régions actives (Fig. 3.7). En parallèle à ces travaux, et de manière indépendante, Zhao et al. (2004) ont observé, à l'aide d'une analyse temps-distance en héliosismologie, une rotation du plasma plus rapide lorsque des polarités de queue étaient présentes, ce qu'ils ont interprété par une localisation préférentielle des polarités de queue au bord est des supergranules. Cependant, je n'ai pas observé ceci avec la technique FT, ce qui remet cette interprétation en question. Si elle est correcte, ceci veut dire que les structures elles-même ne sont absolument pas influencées par la dynamique de la supergranulation, ce qui serait un peu surprenant. Parce que je ne l'observe que pour la CT, cela veut dire que des ensembles de structures (à l'échelle de la supergranulation) d'une certaine polarité ont ce comportement. De plus, les différences de vitesse maximum que j'observe sont de l'ordre de 7 m/s, alors que Zhao et al. (2004) ont trouvé des différences atteignant 10-40 m/s à 300 G, ce qui est significativement plus grand. Ces différents résultats pourraient avoir la même origine mais avec des amplitudes différentes du fait d'ancrages des structures (au sens large) à différentes profondeurs. Il faut noter cependant que les variations au cours du cycle sont assez différentes entre les deux travaux.

La façon dont le flux disparaît dans les zones de polarité mixte n'est pas complètement comprise (Zwaan 1987). Si ces régions correspondent à des zones frontières entre zones unipolaires, on pourrait s'attendre à ce que ces zones aient une rotation intermédiaire entre les rotations de queue et de tête, ce qui n'est pas observée (Fig. 3.8).

Une rotation plus rapide des taches de tête a été observée auparavant (Gilman & Howard 1985; Howard 1992c; Howard 1992a). Cependant, Howard (1992a) a montré que ceci est vrai pour les groupes de taches dans leur phase croissante seulement, et a ob-

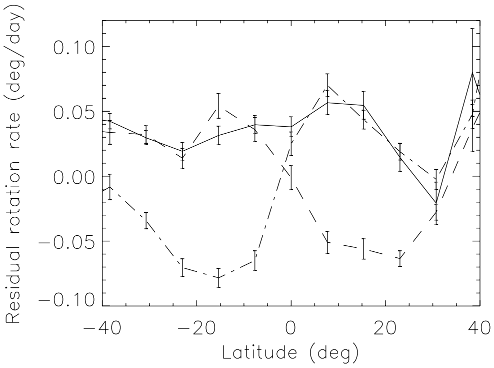

Figure 3.8 : Résidu de rotation CT pour un champ magnétique moyen (en valeur absolue) dans le domaine 9–12 G. La courbe en trait plein représente les domaine de polarité mixte (champ moyen signé entre -4 G et 4 G), la courbe en tiret-pointillé les champs inférieurs à -4 G et la courbe en tiret les champs supérieurs à 4 G. D'après Meunier (2005b).

servé un renversement pour les régions en train de se désintégrer. Howard (1996) trouve aussi que les plages de tête et de queue ont la même rotation proche de l'équateur, mais que les plages ayant la polarité de queue tournent plus vite à plus haute latitude. Son interprétation est la suivante : durant la phase croissante, une boucle émergente intercepte la surface en 2 endroits, ce qui entraîne deux régions de polarités opposées qui s'éloignent l'une de l'autre, entrainant ainsi une rotation apparente plus rapide pour la structure en tête. Ceci suggère que durant la phase de désintégration, les 2 parties de la boucle se rapprochent l'une de l'autre, entrainant le renversement. Ceci peut sembler plausible pour les taches, mais n'est probablement pas adapté au réseau magnétique, car il ne s'agit pas de flux en émergence.

Une possibilité pour la rotation plus rapide des polarités de queue pourrait être une orientation différente des tubes de flux correspondants. Plusieurs auteurs ont en effet publié des variations avec les caractéristiques de ces structures (van Driel-Gesztelyi & Petrovay 1990; Howard 1991; Howard 1992b; Meunier 2003), ce qui pourrait entrainer un biais sur la position des structures (il faut rappeler que nous ne mesurons que le champ le long de la ligne de visée). Cependant, si un tel biais devait entrainer une différence de rotation, elle serait similaire pour les deux techniques, et pas seulement avec la technique CT. Il est également possible qu'une différence d'inclinaison puisse entrainer une différence d'interaction avec la supergranulation, mais ceci reste entièrement à explorer.

Une autre possibilité serait une différence d'ancrage différente des polarités, avec les polarités de queue ancrées plus profondément. Cette interprétation doit être prise avec précaution (voir section suivante) mais un tel effet pourrait néanmoins être présent. Par exemple, parce que la partie de queue des régions actives se désintègre en général plus vite que la partie de tête, elle pourrait avoir plus de temps pour être entrainée en profondeur. Ceci serait également cohérent avec la rotation plus rapide des petites structures situées loin des régions actives. Ce n'est par contre pas cohérent avec une circulation méridienne de plus grande amplitude, car celle-ci semble décroitre vers l'intérieur du Soleil (Haber et al. 2002; Komm et al. 2004; Zhao & Kosovichev 2004).

3.1.2 La circulation méridienne

La circulation méridienne des facules, obtenue à partir des mêmes spectrohéliogrammes que les travaux de Nesme-Ribes et al. (1997) sur les taches, est bien différente de celle des taches. Elle est en effet toujours dirigée vers les pôles, sans indication de complexité particulière. Ceci est très similaire aux résultats de Komm et al. (1993a). Les résultats obtenus avec les magnétogrammes permettent d'aller beaucoup plus loin dans l'analyse, pour les mêmes raisons que pour la rotation différentielle : meilleure cadence temporelle, faible distorsion des images, information sur le champ magnétique.

Comme pour la rotation différentielle, la circulation méridienne obtenue avec les deux méthodes, FT et CT, est assez différente. Dans le cas de la CT, on confirme les résultats obtenus par Meunier (1999b), avec une structure assez complexe au niveau des latitudes actives (Fig. 3.1, milieu), à savoir une convergence vers les latitudes actives (on peut noter que ceci est opposé à ce qui a été trouvé pour les taches : une divergence aux latitudes d'émergence de celles-ci). Ceci n'est pas observé avec la FT, qui présente une circulation méridienne simple vers les pôles, et de beaucoup plus faible amplitude. Elle présente un maximum vers 30° de latitude alors le maximum pour la CT se situe vers 50–60°. Une analyse temporelle montre que l'organisation des mouvements observée avec la CT suit bien les latitudes actives, et n'est donc pas dû à la superposition de plusieurs composantes décalées au cours du temps par exemple. Les résultats de Meunier (1999b) montrent d'ailleurs qu'en longitude, ce flot convergent est bien localisé au niveau des régions actives.

Avec les deux techniques, la circulation méridienne des grandes structures est plus faible que celle des petites structures, tout en restant dirigée vers les pôles. On observe une variation complexe dans le cas de la dépendance avec le champ magnétique moyen, due à la présence du flot convergent. En regardant cette variation avec la latitude, on s'aperçoit qu'elle est en fait très complexe, car elle se renverse près de l'équateur. Ceci serait compatible avec les résultats récents de Komm et al. (2004) obtenus avec l'héliosismologie. A noter que le flot convergent n'est présent que pour les boites à fort champ magnétique, et disparait lorsque le champ magnétique est calme, ce qui confirme le résultat de Meunier (1999b) sur une plus longue période.

A noter que les petites structures proches des régions actives ne présentent pas non plus ce flot. Par contre, la circulation méridienne des petites structures proches des régions actives est de plus grande amplitude à haute latitude (au-delà de 20°) et de plus faible amplitude proche de l'équateur, que celle des petites structures loin d'une région active.

Enfin, comme pour la rotation différentielle, la variabilité avec la polarité a également été étudiée. Pour les petites structures, aucune différence systématique n'a été observée, car elle varie selon les hémisphères, ce qui reste à comprendre. Par contre, dans les régions actives, j'observe une circulation méridienne plus grande dans les zones de polarité de queue, toujours avec la technique CT. Ceci ressemble au résultat de Ward (1973) obtenus sur les taches solaires.

3.1.3 Variations au cours du cycle solaire

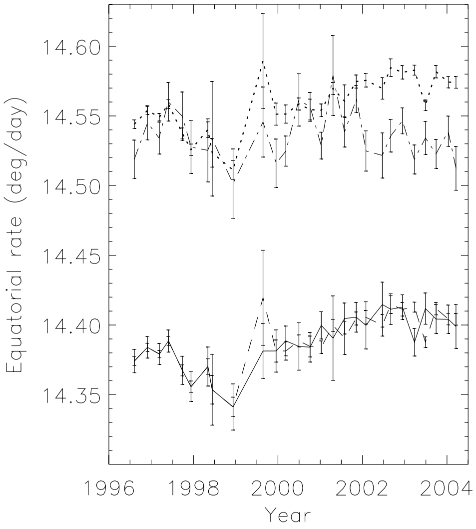

Figure 3.9 : Rotation équatoriale en fonction du temps (deg/jour), pour CT, dérivée d'un ajustement en polynôme de Legendre de degré 5 sur la rotation en fonction de la latitude (trait plein), pour CT, dérivée d'un ajustement en $\sin^i(\theta)$ avec θ la latitude (tirets) et pour FT, dérivée d'un ajustement en $\sin^i(\theta)$ (tiret-pointillés). La courbe en pointillé est la même que la courbe en tiret mais décalée de 0.17 deg/jour afin de correspondre à la même rotation FT au minimum du cycle. D'après Meunier (2005c).

L'échantillon de données très volumineux fourni par MDI m'a permis de regarder en détail la variabilité au cours du cycle de la dynamique mesurée tant avec la méthode FT qu'avec la méthode CT (Meunier 2005d). Je la compare avec les résultats obtenus par d'autres groupes sur la variabilité de la dynamique des taches, qui a été bien étudiée dans le passé.

Rotation différentielle

Il y a un certain consensus pour une rotation plus rigide des taches durant le maximum du cycle (Balthasar & Wöhl 1980; Lustig & Hanslmeier 1987; Nesme-Ribes E., Ferreira E. and Mein P. 1993), en particulier à la fin du cycle. Ceci est consistant avec le résultat obtenu ici pour le réseau magnétique, avec également une rotation plus rigide au maximum du cycle. Cependant, la rotation équatoriale plus grande au maximum est dans le cas du réseau très étalée dans le temps, et est observée pour CT essentiellement, comme le montre la Fig. 3.9. L'amplitude de la rotation CT est également plus importante au maximum du cycle par rapport au minimum, ce qui n'est pas le cas des taches. Par comparaison, les résultats de Meunier et al. (1997) avaient montré une rotation des plages

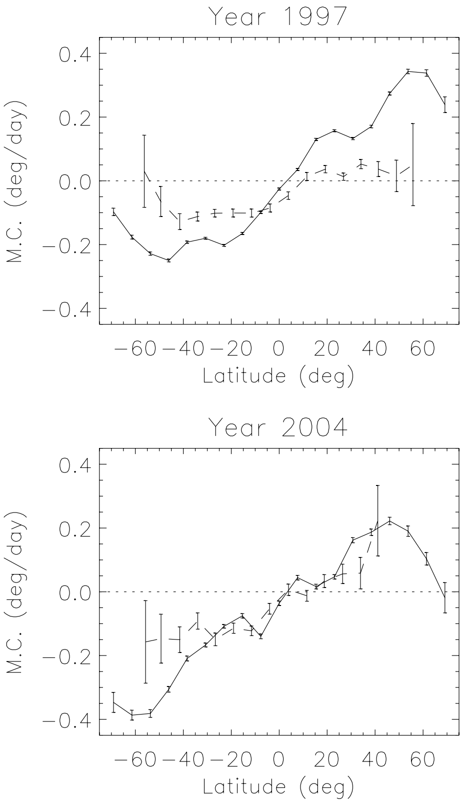

Figure 3.10 : Circulation méridienne CT (trait plein) et FT (tirets) en fonction de la latitude, en 1997 (en haut, période de minimum) et en 2004 (en bas, période de minimum). Une circulation méridienne est positive vers le pôle Nord. D'après Meunier (2005c).

et du réseau plus importante au maximum du cycle, tandis que Komm et al. (1993b) avait trouvé une rotation à peu près constante.

J'ai pu également étudier la variabilité de propriétés plus spécifiques au cours du cycle, en particulier la dépendance de la dynamique en fonction du champ magnétique ou de la taille des structures (Fig. 3.11), et en fonction de la polarité (voir section ci-dessus).

Circulation mérdienne

Concernant la circulation méridienne, Komm et al. (1993a) avait observé une amplitude plus importante au maximum du cycle, supérieure d'environ 30% à celle du minimum. D'un autre côté, Meunier et al. (1997) avait trouvé un résultat similaire dans l'hémisphère nord, avec une circulation méridienne constante dans l'hémisphère sud. Ceci est difficile à comparer avec les résultats obtenus ici sur les données MDI (Fig. 3.10), du fait en particulier de la présence du flot convergent dans la zone d'activité, qui varie évidemment au cours du cycle et domine la variation. J'observe surtout une grande variation de l'amplitude de la circulation méridienne CT à haute latitude, avec une très forte asymétrie entre les deux hémisphères. Il faut noter que l'étude de la variation de la cir-

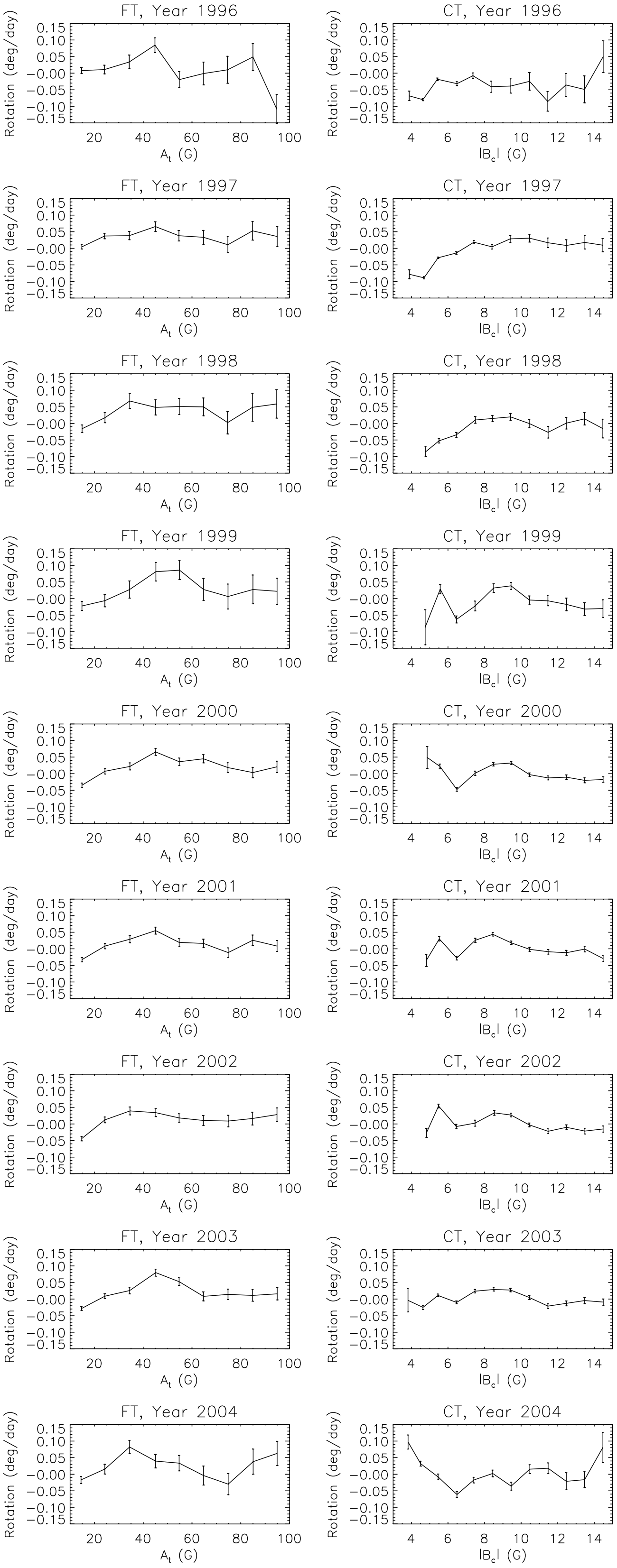

Figure 3.11 : A gauche : résidu de rotation FT en fonction de la taille des structures, de 1996 (en haut) à 2004 (en bas). A droite : même chose pour les résidus de rotation CT en fonction du champ magnétique dans la boite. D'après Meunier (2005c).

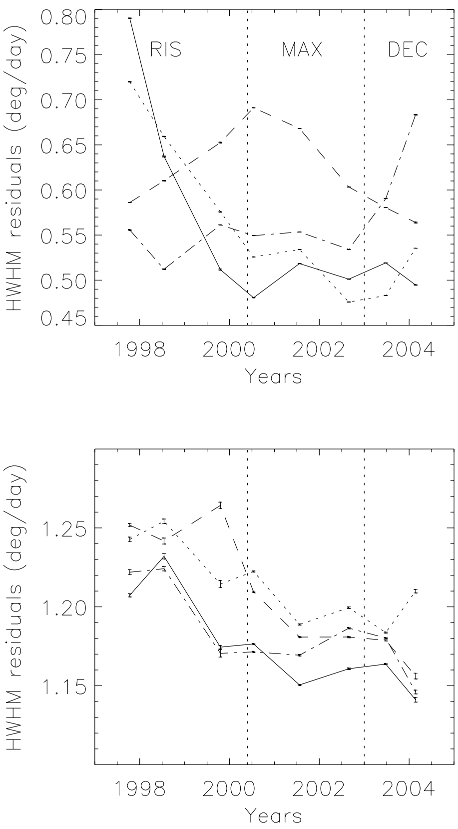

Figure 3.12 : En haut : HWHM sur la distribution des résidus de rotation en fonction du temps, pour la polarité de tête dans l'hémisphere Nord (trait plein), polarité de queue dans l'hémisphere Nord (tirets), polarité de tête dans l'hémisphere Sud (pointillés), polarité de queue dans l'hémisphere Sud (tiret-pointillés). En bas : même chose pour FT. D'après Meunier (2005c).

culation méridienne des taches au cours du cycle a toujours été compliquée et a montré une grande variabilité, ce qui est confirmé ici pour les plages et le réseau magnétique. En général, la circulation méridienne a un comportement plus complexe que la rotation. La très forte asymétrie nord-sud de la variation de la circulation méridienne montre qu'il est très difficile de dériver un comportement cyclique simple (sur 11 ans) pour la circulation méridienne, alors que c'est beaucoup plus facile pour la rotation.

Il est intéressant de comparer les résultats obtenus avec ceux issus de l'héliosismologie locales obtenus par divers groupes (Chou & Dai 2001; Haber et al. 2002; Basu & Antia 2003; Zhao & Kosovichev 2004). L'asymétrie nord-sud de la circulation méridienne à haute latitude décroit significativement au cours du cycle, ce qui est en bon accord avec les résultats de Basu & Antia (2003). Cependant, ils ont observé une décroissance de la circulation méridienne dans les deux hémisphères. Leur asymétrie nord-sud vient du fait que la décroissance est plus forte dans l'hémisphère nord, donc l'accord n'est pas entièrement bon. A noter que leur variation de circulation méridienne est visible jusqu'à 0.985 $R_\odot$ (10.5 Mm), les variations étant ensuite plus complexes en dessous. Par ailleurs, Zhao & Kosovichev (2004) ont étudié la période 1996-2002 en utilisant une analyse locale pour deux domaines de profondeur, 3–4.5 Mm et 6–9 Mm. Près de la surface et à la latitude de 50°, ils ont observé une augmentation suivie d'une décroissance vers zéro ; plus profondément, ils observent seulement une décroissance. Leur résultat correspond donc au nôtre dans l'hémisphère nord mais pas au sud ! A plus basse latitude, ils observent une décroissance significative que je n'observe pas. Haber et al. (2002) ont aussi étudié la période 1996–2001 avec une technique similaire. Les profondeurs étudiées étaient 0.9 Mm et 7.1 Mm. Près de la surface et à la latitude de 50°, ils ont observé une augmentation de la circulation méridienne cette fois, qui n'est pas compatible avec nos observations dans l'hémisphère nord. Plus profondément, ils observent un renversement que nous n'observons pas. Chou & Dai (2001) ont obtenu des résultats à plus grande profondeur, mais qui ne correspondent pas non plus aux nôtres.

Cette comparaison avec l'héliosismologie montre que la circulation méridienne dérivée avec cette technique donne des résultats diffférents de ceux obtenus avec FT et CT. Plusieurs limitations peuvent être à l'origine de ces incohérences apparentes. Tout d'abord, la profondeur concernée peut être différente, et Basu & Antia (2003) ont montré que la circulation méridienne était très variable avec la profondeur. C'est donc un paramètre très important. Par ailleurs, les processus à l'origine de la différence entre FT et CT ne sont pas bien identifiés, et ils pourraient également varier avec le temps et dominer le signal. De plus, la couverture temporelle au cours de l'année n'est pas exactement la même dans les différents travaux. Dans mon cas, la plus grande partie de l'année est couverte (à part la grande interruption de 1998), tandis que ces études héliosismiques ont souvent utilisé une couverture plus restreinte en temps (typiquement 30%).

Distributions en vitesse

Cependant, les distributions en vitesse (illustrées Fig. 3.12 pour la rotation) dans les deux cas, rotation et circulation méridienne, montrent une grande variabilité au cours du cycle, en particulier lorsque l'on sépare les polarités avec la technique CT. On observe notamment une avance de l'hémisphère nord de l'ordre d'un an sur l'hémisphère sud. Il est connu que le premier renversement de polarité aux pôle s'est produit en premier dans l'hémisphère nord (Harvey & Recely 2002; Wang, Sheeley, & Andrews 2002), et un an plus tard dans l'hémisphère sud. Il n'est pas exclu que les distributions en vitesse que j'observe soient reliées à ce renversement, même si ceci doit être confirmé. Nous observons en effet que les flots à grande échelle associés aux polarités de queue (qui jouent un rôle important dans le renversement du champ magnétique) augmentent plus vite dans l'hémisphère dans lequel le renversement a lieu en premier.

3.2 Ancrage des structures dans la zone convective

Articles :

- *Meunier N., Magnetic network dynamics: activity level, feature size and anchoring depth, 2005, A & A 436, 1075*

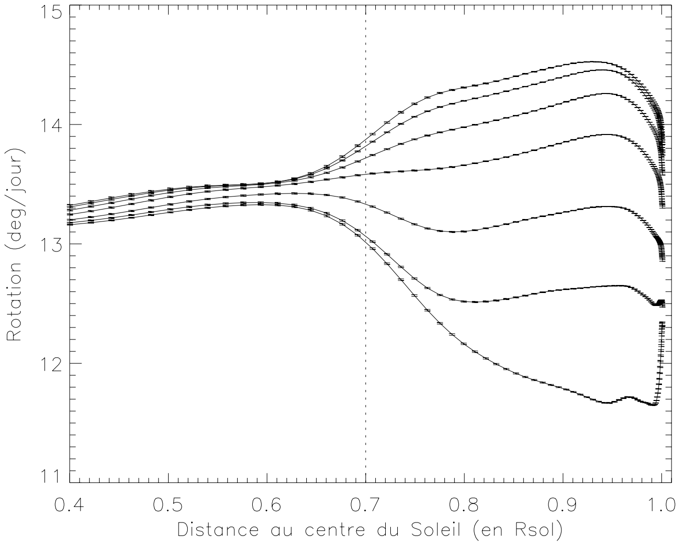

Figure 3.13 : Rotation interne du Soleil d'après les résultats obtenus en héliosismologie (MDI, inversion OLA, R. Howe). De la courbe du haut à la courbe du bas : latitude croissant de 0° à 60° environ, par pas de ∼10°. Le trait vertical en pointillé indique la position approximative de la tachocline (Basu & Schou 2000).

- Collin B., Nesme-Ribes E., Leroy B., Meunier N., Sokoloff D., La dynamique interne du Soleil à partir des traceurs magnétiques, 1995, C. R. Acad. Sci. Paris 321, Serie IIb, 111

Les différences de dynamique pour des taches solaires de différentes catégories ont souvent été interprêtées comme une différence de profondeur d'ancrage de ces structures dans la zone convective (Collin et al. 1995; Beck 2000 par exemple). En fait, avant l'avènement de l'héliosismologie, les différences de rotation différentielle étaient même utilisées pour déduire la variation de rotation interne dans la zone convective : les taches jeunes ayant tendance à tourner plus vite que les taches plus vieilles, il en était déduit une rotation plus rapide en profondeur. Ce gradient de vitesse, un élément clé des modèles de dynamo solaire, était alors utilisé dans ces modèles. Lorsque les premières estimations de la rotation interne fournies par l'héliosismologie ont été disponibles, elles ont remis tout ceci en cause. En effet, là où se trouve la source la plus probable pour la dynamo, la tachocline au bas de la zone convective (voir entre autres Basu & Schou 2000 pour une estimation de sa profondeur et des variations au cours du cycle), le gradient radial de rotation s'est avéré être en fait positif et non négatif (rotation plus faible à plus grande profondeur à basse latitude, c'est-à-dire dans la zone où l'on observe des taches), ainsi qu'illustré sur la Fig. 3.13.

A l'heure actuelle, il n'est donc plus question d'utiliser directement la dynamique des structures magnétiques comme paramètre d'entrée aux modèles de dynamos, car la dynamique interne dérivée de l'héliosismologie est la plus adaptée. Cependant, l'étude de la

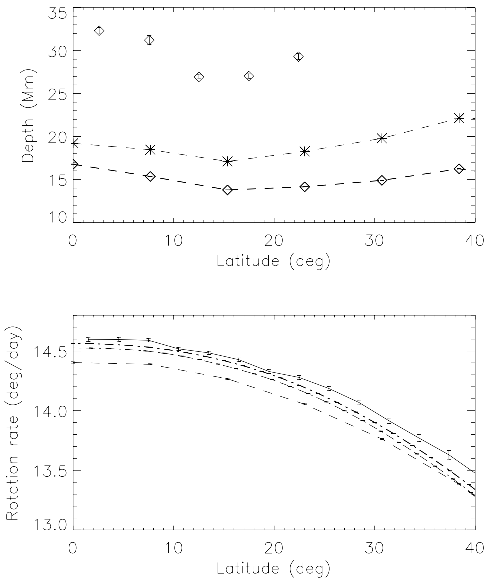

Figure 3.14 : En haut : profondeur correspondant à la rotation FT (carrés sans courbes : MDI) et à la rotation CT (carrés avec tirets épais : GONG ; étoiles avec tirets fins : MDI), en fonction de la latitude. La profondeur correspond à la première intersection avec la rotation dérivée de l'héliosismologie à partir de la surface. La rotation interne (MDI et GONG) a été fournie par R. Howe. En bas : rotation en fonction de la latitude pour FT (trait plein, structures dans le domaine 40–50 Mm^2), pour CT (tirets, champ magnétique dans le domaine 8–9 G), MDI (tiret-pointillé fin, valeur maximum dans la zone convective) et MDI (tiret-pointillé épais, valeur maximum dans la zone convective). D'après Meunier (2005a).

dynamique des structures reste essentielle, car elle permet d'étudier le comportement des structures magnétiques au sein d'un champ de vitesse donné. Elle informe sur les processus influant leur évolution, des variations éventuelles de localisation ou de condition dans laquelle la dynamo opère au cours du cycle, les effets de la dynamo sur les champs de vitesse plus proches de la surface.

Dans ce contexte, revenons sur les résultats obtenus. Etant donné la rotation observée par l'héliosismologie lorsque l'on descend en profondeur jusque $\sim$35-50 Mm, il est tentant d'attribuer une profondeur d'ancrage plus importante aux structures individuelles formant le réseau magnétique (au vu de la rotation différentielle obtenu par FT) qu'au motif formé par ces structures (résultats CT). La circulation méridienne décroissant avec la profondeur (Haber et al. 2002; Zhao & Kosovichev 2004; Komm et al. 2004) est cohérente avec cette interprétation préliminaire.

Une tentative d'attribution de profondeur d'ancrage à chaque type de structures est présentée sur la Fig. 3.14. La rotation interne a été fournie par R. Howe et est déduite d'une inversion des résultats obtenus avec GONG (inversion RLS) et MDI (inversion OLA). Je me concentre sur les résultats obtenus aux latitudes inférieures à 40°, car ces

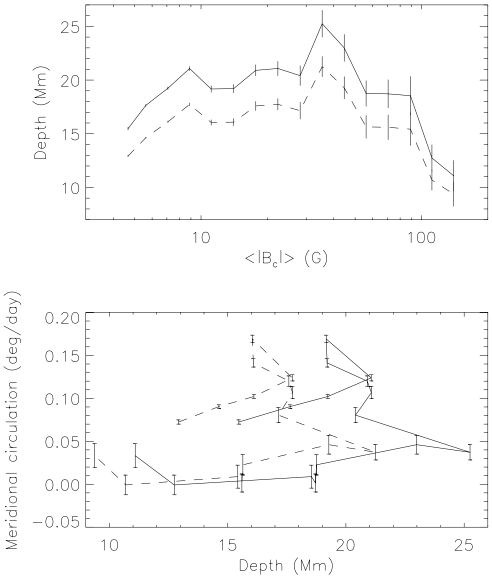

Figure 3.15 : En haut : Profondeur estimée en fonction du champ magnétique moyen à partir des rotation CT en fonction de ce champ, pour la latitude ±7.68° pour MDI (trait plein) et GONG (tirets). La rotation interne (MDI et GONG) a été fournies par R. Howe. En bas : circulation méridienne en fonction de la profondeur dérivée des courbes du haut (même convention) et de la circulation méridienne en fonction du champ magnétique moyen. D'après Meunier (2005a).

deux jeux de données diffèrent significativement à plus haute latitude (Schou et al. 2002). Pour cette discussion, les résults CT et FT ont été symétrisés par rapport à l'équateur. Si l'on utilise la rotation MDI, aucune profondeur d'ancrage ne peut être affectée aux structures FT car la rotation FT observée est trop grande. Il est possible de faire cette attribution pour GONG mais seulement pour les latitudes les plus basses, ce qui donne une profondeur de 27–33 Mm. La rotation CT étant plus faible, l'attribution peut se faire, avec une profondeur dans le domaine 13–17 Mm (MDI) et 18–22 Mm (GONG). Cependant, l'impossibilité d'"ancrer" les structures FT met considérablement en doute l'interprétation en terme d'ancrage. Le maximum de rotation dans la zone convective en fonction de la latitude montré sur la Fig. 3.14 confirme que les structures FT tournent plus vite que toutes les couches de la zone convective.

Il est possible de contraindre davantage l'estimation d'ancrage des structures CT en utilisant la circulation méridienne. En effet, il existe des structures ayant la même rotation mais une circulation méridienne bien différente. Ceci est illustré sur la Fig. 3.15, où une variation de la circulation méridienne avec la profondeur peut être déduite en utilisant plusieurs résultats : la variation de la circulation méridienne en fonction du champ magnétique, la variation de la rotation en fonction du champ magnétique, et la correspondance entre la rotation observée et celle déduite de l'héliosismologie. La figure montre qu'il est impossible d'établir une correspondance unique, car cela conduit à avoir des amplitudes de circulation méridienne différentes pour la même profondeur. Une possiblité pour contourner ce problème serait que des structures ayant circulation méridienne différente et même rotation soient en fait ancrées dans deux couches différentes ayant la même rotation. Ceci est a priori possible, car lorsque l'on s'enfonce vers l'intérieur du Soleil, en dessous de 35–50 Mm, la rotation diminue à nouveau jusque vers le bas de la zone convective. Il est cependant très improbable que les structures du réseau soient ancrées si profondément. En effet, d'autres travaux tendent plutôt vers des structures de surface, par exemple ceux de November (1994) sur la supergranulation.

En conclusion, les différences de dynamique entre les structures magnétiques et le plasma environnant ne peuvent s'expliquer entièrement par des profondeurs d'ancrage différentes dans la zone convective et un processus d'accéleration doit être trouvé pour expliquer l'ensemble des différences de manière cohérente.

3.3 Sur la rotation différentielle photosphérique et la rotation rigide des trous coronaux

Article :

- *Meunier N., Large-scale photospheric dynamics below coronal holes, 2005, A & A 443, 309*

Contexte

Les trous coronaux (CH dans la suite) sont définis comme des régions de champ magnétique ouvert (Wang, Hawley, & Sheeley 1996), par opposition aux lignes de champ fermées associées aux régions actives. Ils sont observés sous forme de régions sombres en X et EUV, et sous forme de régions brillantes dans la raie de He I 10380 Å. Ils sont également associées à des régions plutôt unipolaires de la photosphère. Des procédures d'identification des CHs ont été élaborées en utilisant des jeux de données complémentaires, par exemple par Harvey & Recely (2002) (combinaison de magnétogrammes photosphériques et de spectrohéliogrammes dans cette raie He I). Il y a 3 types de CHs : les CHs polaires, l'extension à basse latitude des CHs polaires et les CHs transitoires qui sont plus proches des régions actives. Leurs durées de vies respectives sont très variables, ainsi que leur distribution au cours du cycle solaire (Harvey & Recely 2002).

Cependant, toutes les propriétés des CHs ne sont pas connues ou bien comprises. Par exemple, toutes les régions unipolaires ne sont pas associées à un CH, et les différences entre des régions calmes avec et sans CH ne sont pas claires, malgré des études du champ magnétique en dehors des CHs et sous les CHs (Harvey, Harvey, & Sheeley 1982; Harvey & Recely 2002). De plus, les CHs polaires avec une extension vers les basses latitudes ont une rotation rigide par comparaison avec la rotation différentielle des structures de la photosphère mais également des points brillants coronaux par exemple (Antonucci et al. 1979; Brajša et al. 2004). Plusieurs travaux théoriques, par exemple ceux de Wang & Sheeley (1990), Wang & Sheeley (2004) et Fisk et al. (1999) ont essayé d'expliquer cette rotation rigide, qui est très probablement due à des processus se produisant à la frontière des CHs. L'étude des frontières des CHs est donc très importante. Kahler & Hudson (2002) ont ainsi étudié en détail leur morphologie. Des observations de la dynamique de la photosphère en lien avec les CHs n'avaient cependant jamais été réalisées.

Résumé des résultats

J'ai donc utilisé la dynamique obtenue ci-dessus (section 3.2) afin de déterminer si elle pouvait être différente sous les CHs et en dehors, pour des régions calmes avec des propriétés similaires (Meunier 2005b). Les CHs utilisés sont ceux déterminés par Harvey & Recely (2002) (base de données de Kitt Peak). Des différences significatives ont été obtenues entre la dynamique de la photosphère en dehors des CHs et en dessous, en général avec la technique CT. Ils peuvent être résumés ainsi :

- Une circulation méridienne CT plus faible dans les CHs, avec un flot convergent dans la zone de latitude active plus important.
- Une rotation différentielle plus importante dans les CHs à haute latitude.
- Une dynamique plus asymétrique entre les hémisphères à haute latitude pour les CHs.
- Une dynamique dépendant de la taille des CHs liée à leur distribution en latitude et à leur distribution en taille.
- Une variabilité temporelle différente de la circulation méridienne à haute latitude
- Une dispersion en vitesse CT dans les CHs au niveau des latitudes actives plus petite dans les CHs qu'en dehors, et une dispersion FT plus grande.
- Une rotation CT différente au centre des CHs par rapport à leur frontière, à haute latitude.
- Une dépendence de la circulation méridienne en fonction du champ magnétique différente, avec des variations plus fortes dans les CHs par rapport à l'extérieur des CHs, pour les champs magnétiques les plus faibles.

Discussion

Une rotation plus différentielle des structures magnétiques photosphériques dans les CHs peut apparaitre en contradiction avec la rotation relativement rigide des CHs eux-même. D'un autre côté, une circulation méridienne plus faible est compatible avec une rotation plus différentielle, ce qui pourrait expliquer la dynamique des CHs à haute latitude. La variabilité de la dynamique dans les CHs est aussi grande que celle en dehors des CHs, tandis que le champ magnétique moyen est moins variable dans notre échantillon. L'asymétrie nord-sud est déjà bien connue, comme le montre les asymétries de distribution en taille avec la latitude, mais ceci se manifeste aussi dans la dynamique.

La dispersion en circulation méridienne et rotation CT est principalement reliée aux flots à grande échelle tels que ceux dérivés par Ambrož (2001). J'obtiens des "rms" de l'ordre de 40–60 m/s, tandis qu'Ambrož (2001) a obtenu des "rms" de l'ordre de 40 m/s, ce qui est en bon accord. Cette circulation à grande échelle semble donc partiellement inhibée dans les CHs et à leur frontière. D'un autre côté, les dispersions FT, bien que contenant également la composante grande échelle, éventuellement à une profondeur différente, sont également fortement influencées par la diffusion des petites structures.

Les dispersions FT sont en effet supérieures aux dispersions CT, et sont également plus grandes dans les CHs. Ceci suggère que la diffusion des structures dans les CHs pourrait être plus importante. Cependant, il faut noter que ces “rms” correspondent à des coefficients de diffusion plus faibles que ceux publiés. Par exemple, Berger et al. (1998) et Hagenaar et al. (1999) ont mesuré des coefficients de diffusion de l’ordre de 50–70 km^2/s. Sur 90 minutes, ceci correspond à un déplacement moyen de 180–220 m/s, ce qui est plus grand que la dispersion FT (130 m/s à l’équateur). Ceci pourrait être dû au fait que le suivi des structure (approche FT) est dans mon cas biaisé vers les plus grosses structures du réseau, à cause de la relativement faible résolution spatiale des données MDI qui ne permet pas de résoudre les tubes de flux individuels.

Wang & Sheeley (2004) expliquent la rotation rigide des CHs par de la reconnexion entre petites structures magnétiques à la frontière des CHs. Les lignes de champs associées à ces structures changent de “statut” entre boucle fermée et boucle ouverte durant le processus et donc traversent la frontière, ce qui pourrait peut-être expliquer au final la rotation rigide. D’un autre côté, Fisk et al. (1999) ont expliqué cette rotation rigide par de larges excursions des lignes de champs en latitude créées par la rotation différentielle photosphérique et l’expansion non radiale du vent solaire. Le modèle de Wang & Sheeley (2004) était en bon accord avec les travaux de Madjarska et al. (2004), qui a trouvé des preuves de reconnexion au bord des CHs (observations SUMER/SOHO). Raju et al. (2005) a également trouvé des indices de reconnexion. Les résultats que j’ai obtenus sont compatibles avec une diffusion plus grande à la frontière des CHs comparée à celle à l’intérieur, mais elle n’est cependant pas plus grande qu’à l’extérieur ! Cette diffusion plus grande pourrait contribuer à une grande excursion des lignes de champ comme dans le modèle de Fisk et al. (1999). D’un autre côté, cette diffusion plus grande pourrait être due à des propriétés des supergranules différentes dans les CHs et en dehors.

Ces nouveaux résultats montrent que les flots à grande échelle dans les CHs sont plus faibles que les flots en dehors des CHs, et ils pourraient également jouer un rôle dans la rotation plus rigide des CHs, tandis que la dynamique à plus petite échelle pourrait être consistante avec des processus de reconnexion à la frontière des CHs. Il est possible que la frontière rigide des CHs puisse empêcher des flots à grande échelle de se développer à l’intérieur des CHs. Ceci doit etre étudié davantage ainsi que la dépendence avec la profondeur de cette dynamique. Il faudra surtout augmenter l’échantillon en couvrant plusieurs cycles solaires.

3.4 Conclusion

Les différences de dynamique entre les structures magnétiques de divers types ou tailles ont longtemps été interprétées comme étant dues à des ancrages à des profondeurs différentes dans la zone convective. La comparaison de la dynamique de surface et celle obtenue avec l’héliosismologie m’a permis de faire avancer ce sujet. L’étude détaillée de la dynamique globale des structures magnétiques, rotation différentielle et circulation méridienne, a en effet montré que cette explication n’était pas suffisante pour expliquer toutes les observations, et qu’un processus supplémentaire devait être présent. Ce processus, non identifié, doit permettre d’expliquer l’excès de vitesse des structures magnétiques, tant par rapport à leur environnement en surface qu'en profondeur. L'ordre de grandeur typique de cet excès est de 30–60 m/s si les structures étaient ancrées à une profondeur de 2–7 Mm.

L'analyse fine des variations montre que le comportement des structures est différent selon leur proximité aux régions actives. Une analyse de la dynamique des supergranules (voir chapitre suivant), naturellement liée à l'évolution du réseau magnétique, devrait permettre de comprendre davantage le comportement des structures du réseau. A noter que la comparaison avec l'héliosismologie devra être poursuivie de manière fine, car une grande variation temporelle est observée, en particulier pour la circulation méridienne.

Enfin, l'étude de la variation de la dynamique au cours du cycle solaire montre un exemple typique d'interaction entre champ magnétique et dynamique. Cependant, cette interaction est complexe, car la variation temporelle de la dynamique ne s'applique pas nécessairement à une couche entière de plasma, mais peut n'affecter que certains processus (par exemple supergranulation) modulant la dynamique des structures magnétiques.

Chapitre 4

De la dynamique globale à la dynamique à petite échelle : étude de la supergranulation

Dans les deux chapitres précédents, de nombreux résultats nouveaux ont été présentés concernant en particulier les propriétés du réseau magnétique au niveau photosphérique, à l'aide de différentes approches : distribution du champ magnétique à la surface solaire, caractérisation des structures magnétiques, dynamique globale. Dans tous les cas, les difficultés d'interprétation ont montré des lacunes en ce qui concerne la compréhension de la diffusion du champ magnétique à la surface et plus particulièrement les propriétés de la supergranulation. Ce chapitre présente les travaux réalisés ou en cours pour mieux comprendre l'origine de la supergranulation, ses propriétés et son interaction avec le champ magnétique du réseau.

4.1 Propriétés de la supergranulation

4.1.1 Un état des lieux sur la supergranulation

La supergranulation a été découverte par Hart en 1954 (Hart 1954). Elle est formée de structures en vitesse à l'échelle de 30000 km (pour un travail récent sur la taille des supergranules, voir Srikanth et al. 2000), au niveau photosphérique. Les principales caractéristiques de la supergranulation sont les suivantes :

- Champs de vitesse horizontaux de plusieurs centaines de m/s.
- Champs de vitesse verticaux de quelques dizaines de m/s, essentiellement au bord des cellules.
- Les cellules sont associées à une forte divergence horizontale, les flots étant descendant sur les bords des cellules, et peut-être ascendant au centre (ce sujet reste une question ouverte, les champs de vitesse étant faible : les Dopplergrammes doivent être extrêmement bien calibrés pour faire cette détermination).
- La durée de vie typique des cellules est de l'ordre de 24 h, avec des cellules pouvant survivre beaucoup plus longtemps (plus de 2 jours).

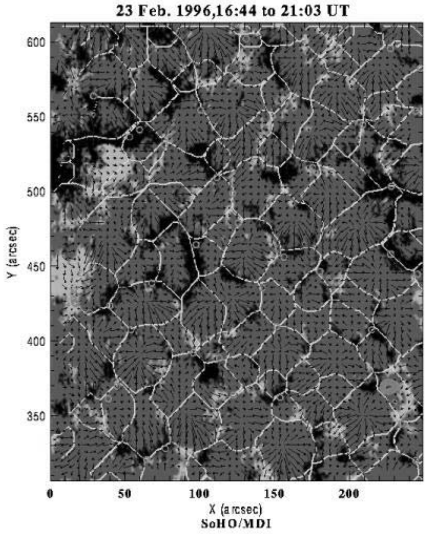

Figure 4.1 : Les niveaux de gris représentent le champ magnétique longitudinal, et et en particulier le réseau. Les petites flèches montrent le champ de vitesse supergranulaire horizontal et les contours des cellules sont indiqués en blanc. La taille typique des supergranules est de 30000 km. Image MDI/SOHO.

- Le réseau magnétique se trouve au bord des cellules, dans les zones de convergence, définissant ainsi de manière intermittente les bords des cellules. Ceci est illustré sur la Fig. 4.2 : le bord des cellules est bien défini par les champs de vitesse, par contre les structures du réseau magnétique ne sont pas présentes partout au bord.
- L'échelle verticale des cellules est peu connue. November (1994) a montré que la supergranulation était sûrement peu profonde (2 Mm), avec des flots descendants s'étendant plus profondément.
- Une vitesse de rotation des supergranules plus rapide que le plasma (d'environ 4%) et que les structures magnétiques (Duvall 1980; Snodgrass & Ulrich 1990) d'environ 2%. Cette rotation pourrait dépendre de l'échelle (Beck & Schou 2000), avec une rotation rapide pour les plus grandes échelles, et une rotation proche de celle des structures magnétiques à plus petite échelle.

Les travaux les plus récents sur la supergranulation ont insisté sur l'étude de la formation et l'évolution des supergranules, en particulier par Shine et al. (2000) et DeRosa & Toomre (2004). A noter la détection par Lisle et al. (2004) d'une tendance à l'alignement dans la direction Nord-Sud des supergranules. Roudier et al. (2003) ont montré qu'une fraction significative des granules étaient organisés en “Trees of Fragmenting Granules” (TFGs), qui consistent en des familles de granules pouvant vivre très longtemps (au moins 8 heures), ces familles étant corrélées avec les mésogranules, structures en vitesse observées à une échelle intermédiaire entre la granulation et la supergranulation ($\sim$8000 km) : ces résultats sont également très importants pour comprendre l'origine de la supergranulation.

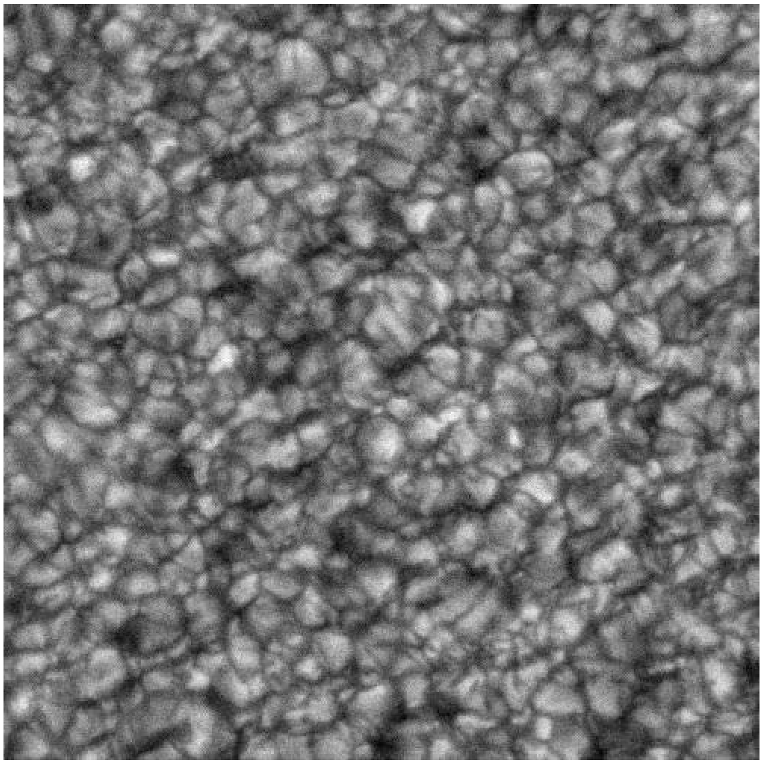

Figure 4.2 : Image de la granulation solaire obtenues à la Lunette Jean Rösch du Pic du Midi (R. Muller). La taille typique des granules est de 1000 km.

Parmi les questions ouvertes figurent la nature de la supergranulation (son origine convective étant de plus en plus remise en cause) et les relations entre propriétés des supergranules et champ magnétique. Dans le premier cas, plusieurs pistes d'étude s'offrent à nous afin de contribuer à répondre à cette question. Tout d'abord la détermination des lois de puissance éventuelles existant entre la taille des cellules et les champs de vitesse ainsi que les distributions de divergences horizontales, facile à déterminer, peuvent donner des indications sur la nature turbulente de la supergranulation et le type de turbulence associée à cette échelle de la dynamique solaire. Une autre piste est d'étudier l'éventuelle variation d'intensité entre les centres des cellules et les bords, une décroissance de cette intensité (et de la température) pouvant être associée à de la convection. Dans le deuxième cas, les relations entre taille des cellules et niveau d'activité, toujours controversé, restent à comprendre en détail, que ce soit à une époque donnée (variabilité dans le champ) ou au cours du cycle (variabilité temporelle). La dynamique des supergranules, en particulier leur rotation par rapport au champ magnétique, peut également aider à mieux appréhender la nature de la supergranulation et son interaction avec le réseau magnétique.

4.1.2 Approche suivie

Si l'on veut déterminer les propriétés de la supergranulation, il faut tout d'abord déterminer ces supergranules à partir des données. La supergranulation se manifeste sous diverses formes (champs de vitesse, réseau magnétique) et en conséquence plusieurs technique sont possibles. J'en ai testé plusieurs au cours des années, qui pour la plupart n'ont pas été entièrement satisfaisantes.

Une première approche a consisté à déterminer les supergranules à partir de Dopplergrammes moyennés sur une période de temps assez longue (par exemple 1 heure). Cette approche a déjà été utilisée dans la littérature (voir Krishan et al. 2002 par exemple). L'analyse Doppler est cependant délicate car les effets de projection dominent le signal, les champs de vitesse dominants étant essentiellement horizontaux. Le signal est donc très dépendant de la distance au centre disque, les supergranules n'étant pratiquement pas détectables au centre du disque. Typiquement, un supergranule donné apparaît alors sous la forme de deux structures, l'une correspondant à la partie s'éloignant de l'observateur, et l'autre s'en rapprochant (la plus proche du centre disque). Ceci est illustré sur la Fig. 4.3 (en bas) : on voit clairement l'allure différente des supergranules en fonction de leur position sur le disque. Cette approche s'est donc avérée délicate à utiliser et source de bon nombre d'incertitudes.

J'ai en paralèlle testé une approche adaptée de travaux effectuée dans un tout autre domaine, la distribution des galaxies dans l'univers. Celles-ci ne sont pas distribuées de manière homogène dans l'espace, et on peut définir des zones presque vides de galaxies, celles-ci étant réparties sur des nappes (en 3D). El-Ad et al. (1996) ont caractérisé ces "vides" en ajustant des sphères les plus grandes possibles afin qu'elles n'incluent aucune galaxie appartenant aux nappes. J'ai adapté cette technique à des magnétogammes de MDI, en 2D, en cherchant les cercles de taille maximum qui n'incluent pas de structure du réseau magnétique. Une illustration de cette technique est montrée sur la Fig. 4.4. Cette méthode a pu être appliquée à un grand nombre de magnétogrammes MDI disque entier, et j'ai pu commencé à étudier la variation de la taille des supergranules avec le champ magnétique et au cours du cycle par exemple, ce qui était très prometteur. J'ai ainsi obtenu que les cellules de supergranulation étaient plus grandes au minimum du cycle. Cependant, avec cette technique, l'épaisseur du réseau va influencer la taille des cellules déterminées, et elle doit être complétée par une squelettisation (remplissage de tout l'espace par des cellules). Au final, cette technique présente cependant les mêmes inconvénients que ce qui a été fait dans la littérature (à partir du champ magnétique ou d'images dans le calcium au niveau chromosphérique), à savoir que les supergranules étant définis à partir du champ magnétique, il est difficile d'étudier la variation des tailles des cellules avec le champ magnétique étant donné que les deux mesures ne sont pas indépendantes.

Le plus prometteur s'est donc révélé être l'utilisation de cartes de champs de vitesse horizontaux déterminées par corrélation locale (LCT) à partir d'images en intensité, puis des cartes de divergence (voir Fig. 4.3, milieu). Leur grand avantage est d'être indépendant de la présence de champ magnétique. Une telle technique a pu être appliquée à des données MDI haute résolution sans problème particulier. En outre, elle a l'avantage de préparer les observations de CALAS (voir plus bas) car il s'agira également d'observations

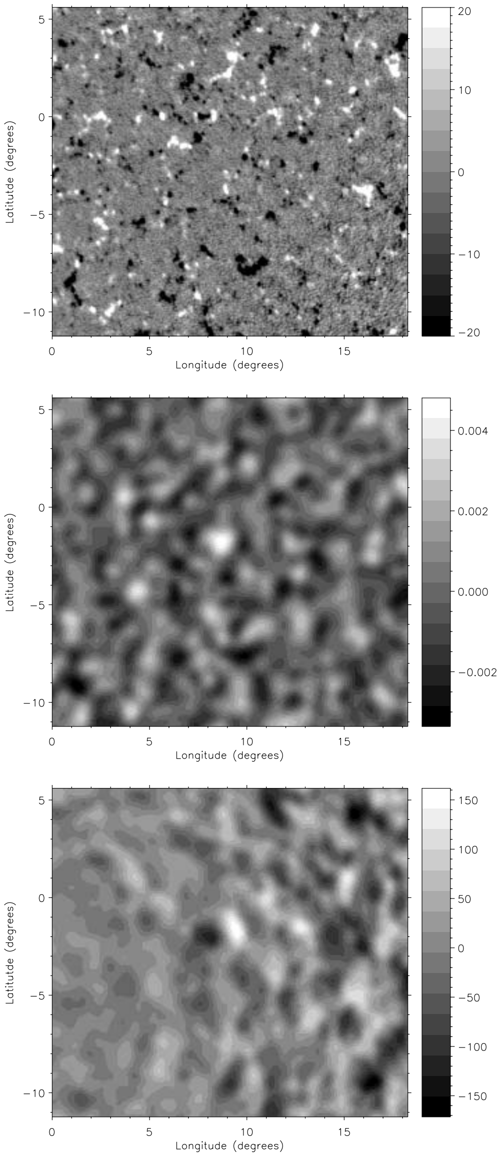

Figure 4.3 : Exemple de carte de champ magnétique montrant le réseau (en haut), divergence des champs de vitesse horizontaux déterminés par corrélation locale (au milieu) et Dopplergramme (en bas). D’après Meunier & Roudier (2007).

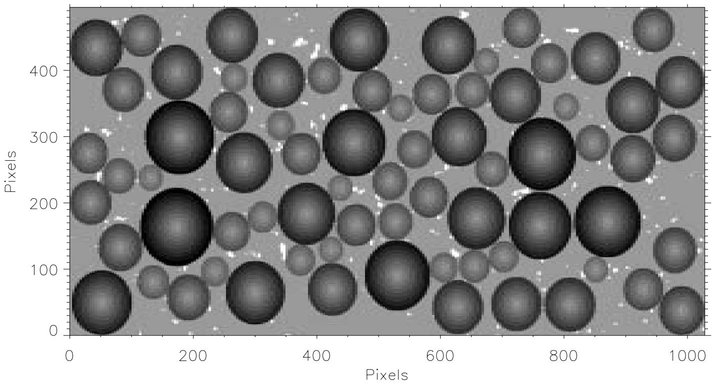

Figure 4.4 : Les petites structures blanches représentent le réseau magnétique (MDI/SOHO) saturé à 40 G. Les disques montrent l'identification des structures circulaires, symbolisant les cellules de supergranulation, les plus grandes possibles et ne recouvrant pas le réseau défini à ce seuil de 40 G.

d'intensités. Dans la suite de cette section, c'est donc cette approche "carte de divergence" qui a été suivie.

Nous avons utilisé des données fournies par l'instrument MDI sur la sonde SOHO, en opération depuis 1996. MDI fournit typiquement des cartes Doppler, de champ magnétique le long de la ligne de visée (magnétogrammes), et intensité (continu) Dans le mode haute résolution, la résolution spatiale est de 1.2 arcsec (pixel de 0.605 arcsec environ), ce qui permet de voir les granules (mais avec peu de précision), et le champ de ∼620x300 arcsec. La cadence est de une minute, ce qui permet par contre de très bien suivre les structures. Nous avons surtout utilisé deux séries temporelles datant de 1997, en période de minimum d'activité, ce qui permet de se concentrer sur l'étude du Soleil calme. L'exploitation de données au cours du cycle fait partie des travaux en cours. Pour analyser ces données, un travail de recentrage des images a été effectué ainsi que diverses corrections (en particulier un filtrage k-ω), puis des cartes de champs de vitesse ont été établies à partir d'un suivi par corrélation des granules sur les cartes d'intensité. A partir de ces champs de vitesse horizontaux, nous avons également calculé les cartes de divergence horizontale, qui sont les cartes qui vont nous permettre d'identifier les supergranules.

Il faut noter qu'une analyse similaire de données disque entier de MDI a été effectuée afin de contribuer à l'étude de la dynamique photosphérique associée à un filament, dans le cadre de la campagne d'observations coordonnées conduite par T. Roudier (JOP 178). Je ne détaille pas les résultats ici (voir Rondi et al. 2007).

4.2 La dynamique des supergranules

Articles :

- *Meunier N., Tkaczuk R., Roudier T., Rieutord M., Velocities and divergences as a function of supergranule size, 2007, A & A 461, 1141*

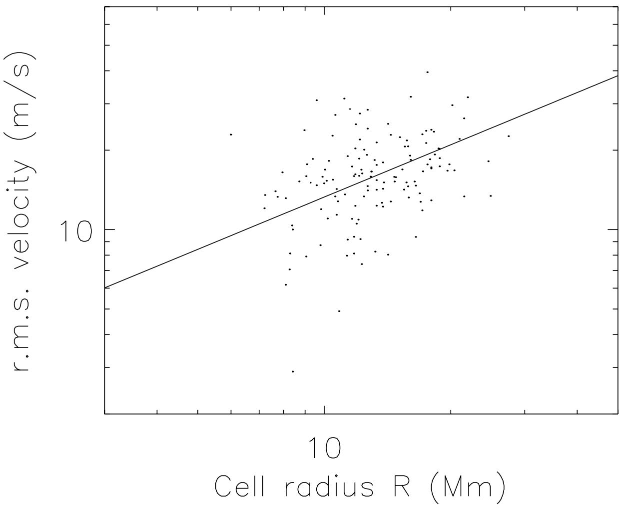

Figure 4.5 : R.m.s. des vitesses horizontales dans chaque cellule en fonction le taille des cellules définies à l'échelle de la supergranulation. L'axe des abscisses va de 3 à 50 Mm et l'axe des ordonnées de 2 à 70 m/s. La ligne droite est un fit linéaire sur les points. D'après Meunier et al. (2007).

- *Meunier N., Tkaczuk R., Roudier T., Rieutord M., Intensity variations accross supergranules, 2007, A & A 463, 745*
- *Meunier N., Roudier T., The superrotation of supergranules, 2007, A & A 466, 691*

4.2.1 Champs de vitesse et divergence horizontale à l'échelle supergranulaire

Une première piste pour discriminer entre les différents scénarios est d'étudier les propriétés des champs de vitesse et de divergences (dans notre cas les composantes horizontales) en fonction de l'échelle (mésogranulation ou supergranulation par exemple) et de la taille des cellules.

Le principal travail précédent existant sur les propriétés des champs de vitesse est celui de Krishan et al. (2002). Ils ont mis en évidence l'importance de comprendre la relation entre vitesse et échelle afin de mieux contraindre la dynamique de la supergranulation et la turbulence associée. Ils ont ainsi obtenu une pente compatible avec 1/3 (0.34 ± 0.05) entre $Log(V)$ et $Log(R)$ (V et R la vitesse maximale dans les cellules et leur taille linéaire). L'interprétation de ce résultat est que la supergranulation serait compatible avec une convection turbulente de Kolmogorov. Leurs travaux présentent cependant un certain nombre d'inconvénients. Outre le faible nombre de supergranules étudiés, ils ont déterminé les cellules à partir de Dopplergrammes et ont donc dû appliquer des corrections significatives à cause des effets de projection qui affectent fortement le signal. De plus, ils ont défini la vitesse typique comme étant la vitesse maximale dans la cellule et

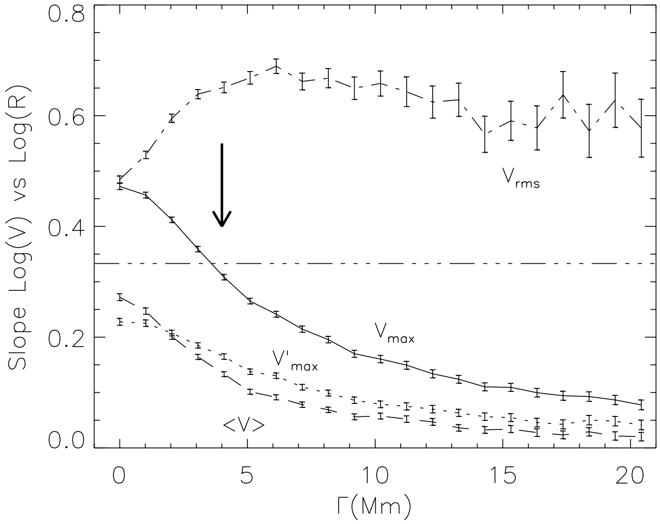

Figure 4.6 : Pente de Log(V) versus log(R) en fonction du lissage des cartes de vitesse, pour V la vitesse maximale $V_{\max}$ dans chaque cellule (trait plein), la vitesse moyenne $< V >$ (tirets), la dispersion de vitesse V_{rms} (trait tiret-pointillé) et la vitesse maximale des profils radiaux moyens de vitesse $V'_{\max}$ (trait tiret-pointillé-pointillé-pointillé). R représente le rayon des cellules. La droite horizontale correspond à une pente de 1/3. Les barres d'erreurs sont les incertitudes à 1 σ. D'après Meunier et al. (2007).

non la dispersion de vitesse, et ce à une échelle plus proche de la mésogranulation que de la supergranulation. Il était donc nécessaire de refaire ce travail en évitant ces biais et en définissant mieux les vitesses.

Nous avons donc refait cette étude de manière plus approfondie, en étudiant la pente de $Log(V)$ en fonction de $Log(R)$ pour différentes échelles et ce pour différentes définitions de la vitesse caractéristique dans une cellule (Meunier et al. 2007). La Fig. 4.5 montre un exemple de variation de la dispersion de vitesse en fonction de la taille des cellules pour l'échelle supergranulaire. Les pentes sont calculées sur ce type de variables. Les résultats sont illustrés sur la Fig. 4.6. Pour la supergranulation, nous trouvons une pente de 0.66 ± 0.02 entre $Log(Vrms)$ et $Log(R)$. Ceci est donc très significativement différent d'une turbulence de Kolmogorov et est en désaccord avec les résultats de Krishan et al. (2002). Cependant, en comparant avec la pente calculée pour la vitesse maximale determinée à leur échelle, on retrouve une pente similaire à la leur. En outre, nous avons étudié la distribution des vitesses dans les supergranules, et la vitesse maximale ne correspond pas toujours à la même chose selon la taille des supergranules (plutôt dans la cellule ou plutôt au bord selon le cas), ce qui rend cette variable très peu fiable.

Grâce à cette loi de puissance, nous avons donc mis en évidence la nature turbulente de la supergranulation. La loi d'échelle observée $V_{\mathrm{rms}} \sim R^{0.66}$ rappelle la loi de Bolgiano-Obukhov (0.6). Si c'était le cas, cette signature serait le signe d'un effet de stratification de la turbulence dans les couches de surface. Combiné à une instabilité à grande échelle

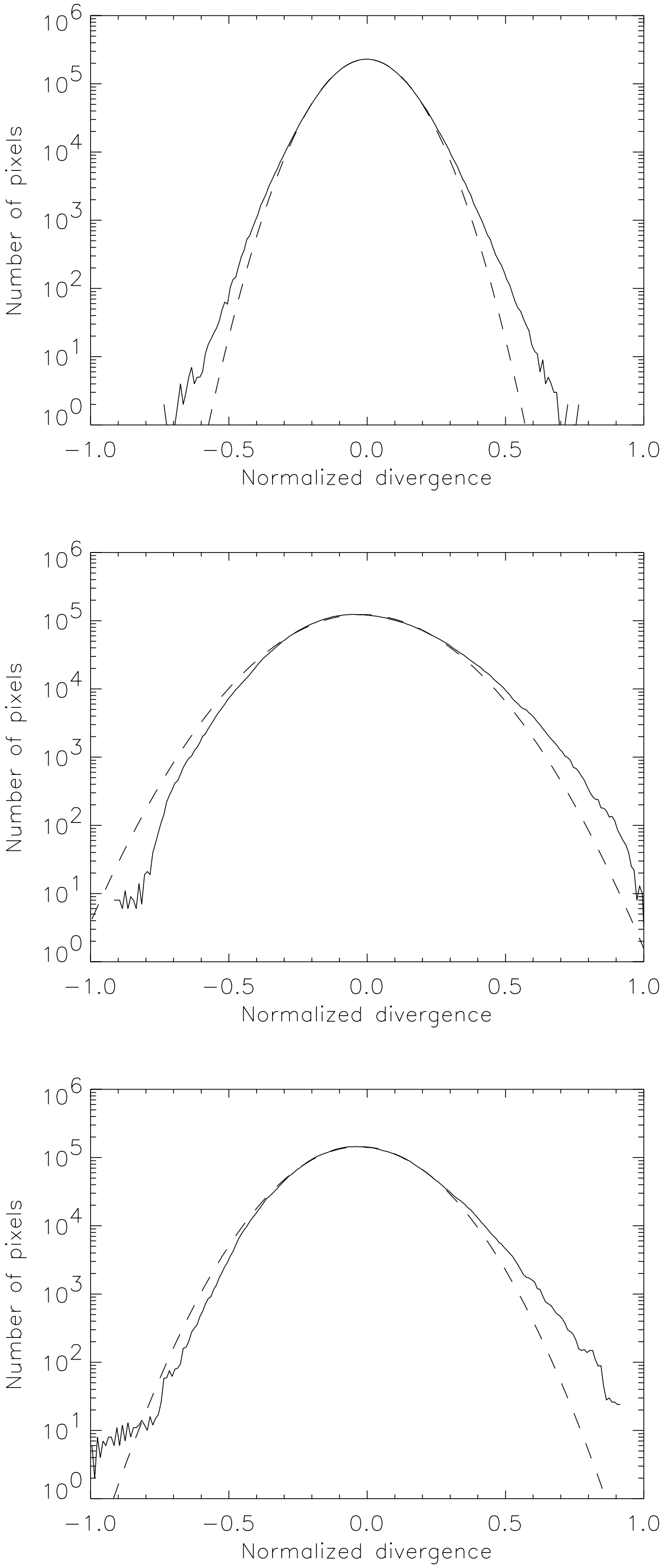

Figure 4.7 : *En haut :* Distribution des divergences normalisées pour les cartes de divergence non lissées (trait plein) et pour le fit d'une gaussienne sur cette distribution (tirets). *Au milieu :* Même chose pour un lissage de 10.2 Mm (supergranulation). *En bas :* Même chose pour un lissage de 20.4 Mm. D'après Meunier et al. (2007).

Table 4.1 : Vitesse de rotation sidérale (deg/jour) dérivée du suivi global pour le réseau magnétique ($\Omega_{\rm B}$) et pour les divergences horizontales ($\Omega_{\rm div}$). Le maximum de corrélation entre cartes adjacentes est également indiqué (respectivement $C_{\rm mag}$ et $C_{\rm div}$), ainsi que la différence entre $\Omega_{\rm div}$ et $\Omega_{\rm B}$ ($\Delta\Omega_{\rm div}$). D'après Meunier & Roudier (2007).

Série	# images	$\Omega_{\rm B}$	$C_{\rm B}$	$\Omega_{\rm div}$	$\Delta\Omega_{\rm div}$	$C_{\rm div}$
Janvier 1997	46	14.27±0.03	0.93	14.44±0.08	0.17±0.08	0.68
Mars 1997	15	14.11±0.03	0.82	14.46±0.11	0.35±0.11	0.67

Table 4.2 : Vitesse de rotation sidérale (deg/jour) dérivée du suivi des structures pour le réseau magnétique ($\Omega_{\rm B}$) et pour les divergences horizontales ($\Omega_{\rm div}$). Le maximum de corrélation entre cartes adjacentes est également indiqué (respectivement $C_{\rm mag}$ et $C_{\rm div}$), ainsi que la différence entre $\Omega_{\rm div}$ et $\Omega_{\rm B}$ ($\Delta\Omega_{\rm div}$). Les résultats sont montrés pour les flots divergents (Div) et convergents (Conv). D'après Meunier & Roudier (2007).

Série	Type	# cellules	$\Omega_{\rm B}$	$C_{\rm B}$	$\Omega_{\rm div}$	$\Delta\Omega_{\rm div}$	$C_{\rm div}$
Janvier 1997	Div	4979	14.18±0.01	0.79	14.35±0.07	0.26±0.07	0.73
Mars 1997	Div	1622	14.02±0.02	0.72	14.40±0.13	0.47±0.13	0.73
Janvier 1997	Conv	5327	14.19±0.01	0.80	14.38±0.07	0.30±0.06	0.73
Mars 1997	Conv	1775	14.03±0.02	0.73	14.67±0.12	0.61±0.12	0.73

qui pourrait résulter de divergences synchronisées[1] (Rieutord et al. 2000), ceci pointe vers un scénario ou la supergranulation résulterait d'une redistribution de l'énergie cinétique sur une large échelle à la surface du Soleil.

Nous nous sommes également intéressés à la distribution des divergences à différentes échelles. Les résultats sont montrés sur la Fig. 4.7. A l'échelle mésogranulaire, on observe clairement de l'intermittence, à la fois du côté des flots divergents et des flots convergents, comme le montrent les queues de distributions plus longues que celle d'une gaussienne. A l'échelle de la supergranulation on l'observe toujours du côté des flots divergents, mais une forte assymétrie est présente. Un moment d'ordre 3 différent de zéro avait déjà été observé par Duvall & Gizon (2000) par héliosismologie locale. Ceci pourrait être dû au fait que dans les cartes à plus petite échelle (mésogranulation), la taille des régions occupées par les zones de fortes divergences positives (centre des cellules) ont une aire plus grande que celle pour les fortes divergences négatives (flots convergeant) d'environ 30%. Lors du lissage, on écrête donc plus facilement les fortes valeurs des convergences d'où l'assymétrie de la distribution.

4.2.2 La rotation des supergranules

J'ai mentionné plus haut (section 4.1.1) la grande vitesse de rotation des supergranules, non seulement par rapport au plasma, mais également par rapport aux structures magnétiques dont le réseau. Ce dernier résultat a toujours étonné car le réseau est localisé sur les bords de ces cellules, bien que de façon intermittente, et on peut s'attendre à un comportement similaire. Par ailleurs, la vitesse de rotation mesurée était telle qu'il n'existait aucune couche de la zone convective tournant au même taux, ce qui posait des problèmes pour expliquer cette super-rotation par un ancrage en profondeur des supergranules (voir aussi Chap. 3 pour une discussion sur les profondeur d'ancrage). Très récemment, Hathaway et al. (2006) ont montré qu'en fait, tous les travaux antérieurs avaient été effectués à partir de Dopplergrammes (Duvall 1980; Snodgrass & Ulrich 1990), et que ceux-ci étaient très biaisés à cause des forts effets de projection affectant le signal en vitesse de la supergranulation. Ils ont donc effectué des simulations montrant qu'effectivement, le suivi de structures Doppler surestimait le taux de rotation.

Il était donc nécessaire de remesurer précisément la vitesse de rotation angulaire des supergranules, à partir de données fiables, afin de voir si les supergranules tournaient effectivement plus vite que le réseau magnétique ou pas. C'est ce que nous avons effectué à partir de nos cartes de divergences horizontales à l'aide de plusieurs approches, soit avec un suivi global (carte complète), soit avec un suivi local (une structure à la fois), dans tous les cas par corrélation (Meunier & Roudier 2007). L'intérêt de cette approche est que les mêmes calculs ont été appliqués aux cartes de champ magnétique, ce qui nous a permis de nous en servir comme *référence*. Ceci permet en particulier de s'affranchir de la variation temporelle importante de la rotation différentielle. Un résumé des résultats est montré dans les tables 4.1 et 4.2. Dans tous les cas, et pour deux séries indépendantes, nous obtenons que les cellules de supergranulation tournent effectivement plus vite que le réseau magnétique, mais dans une moindre mesure par rapport aux résultats précédents. L'interprétation en terme de profondeur d'ancrage est cependant toujours délicate (voir Chap. 3), car les supergranules continuent à tourner plus vite que la zone convective. Nous confirmons également que la dynamique déterminée à partir des structures Doppler est par contre très sensible aux effets de projection.

4.2.3 Variations d'intensité dans les supergranules

Une autre propriété très importante des supergranules est de savoir s'il y a des variations de températures dans les cellules. Pour les granules solaires, dont le caractère convectif est très bien établi, il y a une très forte corrélation entre l'intensité (correspondant à des variations de température) et le champ de vitesse. La question se pose donc pour les supergranules, et pourrait constituer un test très intéressant pour trancher entre diverses origines (convective ou non). Ce type de travail a été tenté à plusieurs reprises dans le passé (Beckers 1968; Frazier 1970; Foukal & Fowler 1984; Lin & Kuhn 1992). Cependant, c'est difficile à faire directement car les structures magnétiques du réseau, qui sont situées de manière prédominante sur les bords des cellules, ont tendance à être associées à

---

[1] Les divergences sur l'ensemble de la surface ne seraient pas indépendantes les unes des autres mais au contraire corrélées du fait de l'existence d'une instabilité à grande échelle

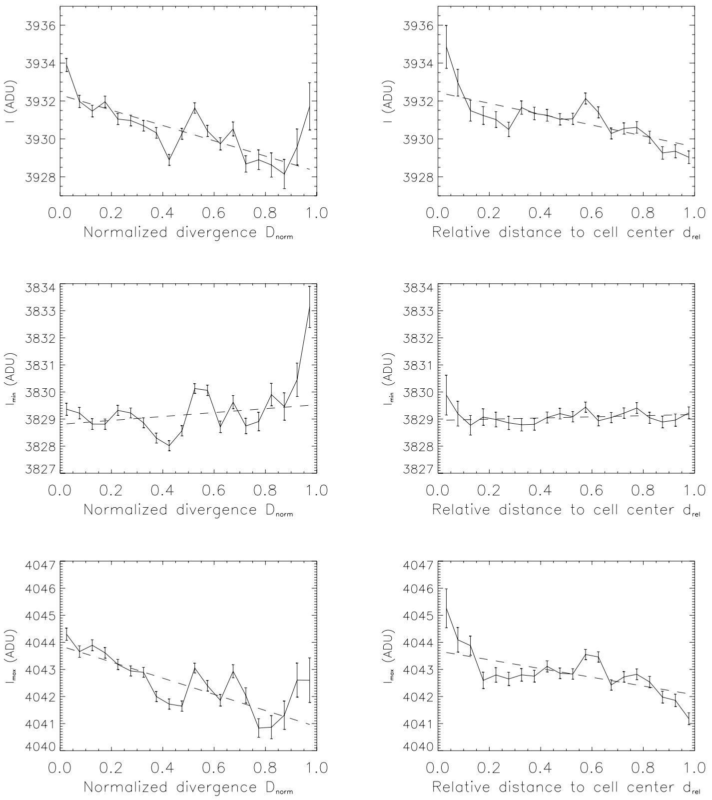

Figure 4.8 : A gauche : Intensités en fonction de la divergence normalisée D_{norm}, pour N_{box} supérieur à 40 et $|B| < 3$ G. *A droite :* même chose en fonction de la distance relative au centre des cellules d_{rel}. *De haut en bas :* Intensité I, I_{min}, et I_{max}. Les courbes en tirets sont des ajustements linéaires. D'après Meunier et al. (2007).

un embrillancement, ce qui fait que tous les résultats tendent vers une intensité plus élevée au bord qu'au centre. Ceci est le contraire de ce qui est attendu pour de la convection, mais c'est très fortement biaisé par l'embrillancement dû au réseau magnétique.

L'approche que nous avons suivie est la suivante (Meunier, Tkaczuk, & Roudier 2007) : A partir des cellules bien identifiées, il s'agit de caractériser tout d'abord la variation d'intensité en fonction du champ magnétique. Nous nous sommes aperçus qu'il fallait effectuer une sélection drastique sur le champ magnétique de chaque pixel courant *et* sur le champ magnétique environnant le pixel, afin d'arriver à éliminer au maximum l'influence du champ magnétique sur la mesure d'intensité. Quand on ne sélectionne que très peu, il reste bien sûr beaucoup de pixels, et dans ce cas la pente de l'intensité en fonction de la distance relative au centre de la cellule ou en fonction de la divergence est positive, comme les résultats précédents : l'intensité observée est alors plus élevée sur les bords. Quand on sélectionne davantage cependant, et que l'on s'affranchit au maximum du biais dû à la présence du réseau, la pente devient négative, ce qui correspond à des intensités plus faibles au bord des cellules dans ce cas. A noter que le pourcentage de pixels restants (quelques %) est faible mais ces pixels sont bien répartis dans les cellules. Par ailleurs nous avons étudié les biais possibles de cette sélection et les biais attendus sont dans le sens contraire des observations que nous faisons. Selon le mode de calcul, la pente qui correspond à la moyenne de ce qui se passe sur la cellule, ou la différence d'intensité entre centre et bord, on obtient des résultats un peu différents, mais toujours du même signe.

La Fig. 4.8 montre un récapitulatif de nos observations. Tout d'abord, on observe une décroissance de l'intensité du centre des cellules vers les bords. La variation de température correspondante est de l'ordre de 0.8–2.8 K. Le résultat est très robuste selon le critère utilisé pour définir la variation d'intensité. Il est également très robuste lorsque l'on considère plusieurs catégories indépendantes de cellules (différentes tailles). Il faut aussi noter que notre approche a permis de bien regarder ce qui se passait selon la partie des granules considérée. Lorsque l'on considère l'intensité minimale autour des pixels courants, i.e. l'intergranule, une faible variation est observée. Par contre, l'intensité maximale, correspondant au centre des granules, suit la même variation, une décroissance vers les bords.

Pour conclure, en première approximation, ce résultat va dans le sens d'une origine convective de la supergranulation. Par contre une analyse fine reste à faire pour comparer les variations des intensités minimales et maximales avec des simulations et vérifier si cela peut correspondre à de la convection ou non. Le problème est qu'il existe très peu de simulations réalistes de la supergranulation, à cause du grand nombre d'échelles en jeu pour modéliser correctement la dynamique des granules jusqu'à l'échelle de 30000 km. Ceci devrait cependant pouvoir être accessible dans un futur proche (voir en particulier la thèse de Rincon 2004).

4.3 Les supergranules et le champ magnétique

Article :

- *Meunier N., Roudier T., Tkaczuk R., Are supergranule sizes anti-correlated with magnetic activity ?, 2007, A & A 466, 1123*

Il est bien connu que les supergranules sont étroitement associés au réseau magnétique (voir Fig. 4.2) : les structures du réseau sont localisées au bord des cellules, de manière très intermittente car elles sont situées essentiellement dans les zones de convergence (elles ne remplissent pas complètement les frontières des cellules). On sait par ailleurs que pour les granules solaires, cellules convectives à l'échelle du Mm, on observe une taille plus petite des cellules près des régions actives. Ceci est attendu car un champ magnétique proche de la verticale devrait inhiber les mouvements horizontaux (force de Lorentz) et donc ainsi limiter la taille des granules dans les zones de plus forte activité. La variation de la taille des granules est quant à elle toujours controversée. Une question qui se pose donc depuis longtemps est la suivante : est-ce que la taille des supergranules est anti-corrélée avec le champ magnétique (comme attendu) ou corrélé ? Un certain nombre de travaux ont été effectués depuis le début des années 1970 par divers groupes (la Table 4.3 en donne un récapitulatif), soit en étudiant la variation de la taille des cellules à un instant donné (c'est-à-dire à une phase donnée du cycle solaire), soit en regardant

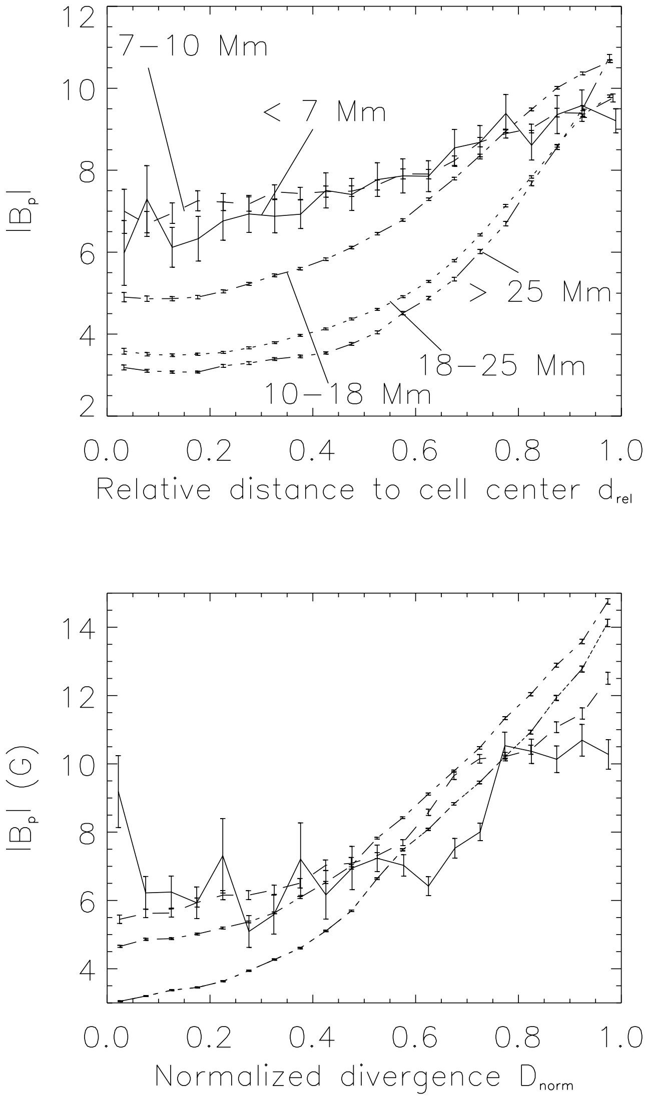

Figure 4.9 : *En haut :* Champ magnétique $|B_\mathrm{p}|$ en fonction de la distance relative au centre des cellules d_rel, pour différents domaines de taille : R inférieur à 7 Mm (trait plein), dans le domaine 7–10 Mm (tirets), dans le domaine 10–18 Mm (tirets-pointillés), dans le domaine 18–25 Mm (pointillés), et supérieur à 25 Mm (tiret-pointillés-pointillés-pointillés). *En bas :* même chose en fonction de la divergence normalisée D_norm. D'après Meunier et al. (2007).

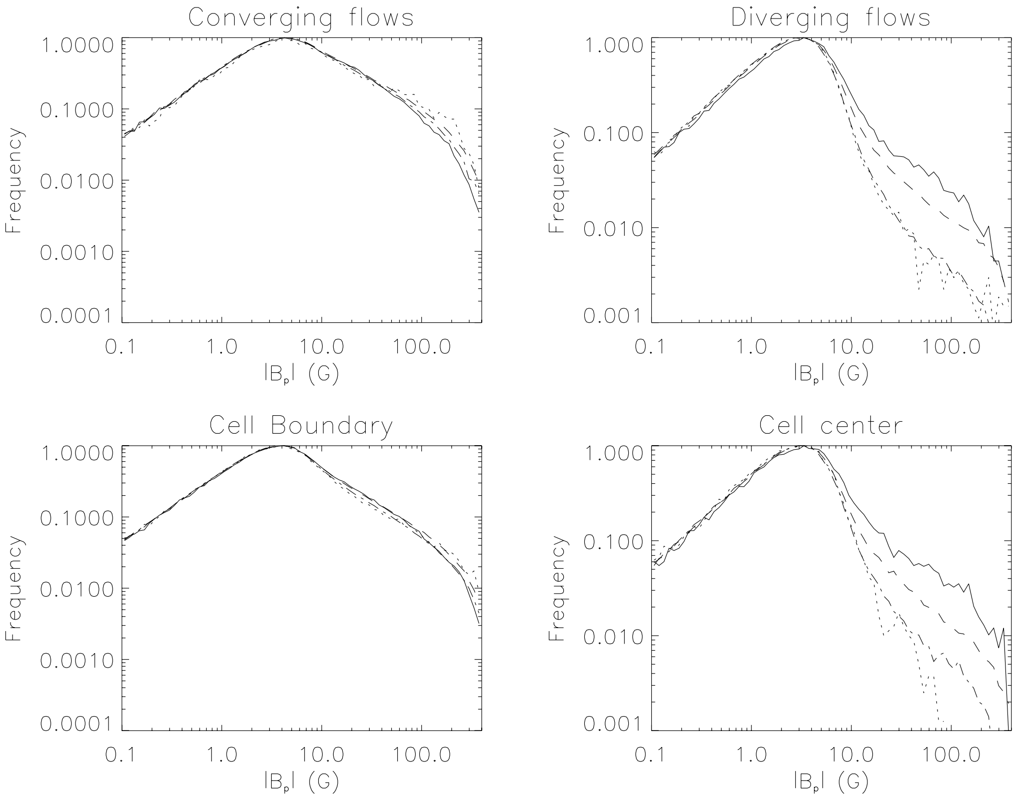

Figure 4.10 : Distribution du champ magnétique $|B_\mathrm{p}|$ pour différents domaine de taille : *R* inférieur à 10 Mm (trait plein), dans le domaine 10–16 Mm (tirets), dans le domaine 16–20 Mm (tirets-pointillés) et supérieur à 20 Mm (pointillés). Les champ magnétique est considéré dans différentes régions des cellules : dans les flots convergents (en haut à gauche), dans les flots divergents (en haut à droite), au bord des cellules (en bas à gauche), au centre des cellules (en bas à droite). D'après Meunier et al. (2007).

Table 4.3 : Variation de la taille des supergranules avec le niveau d'activité disponible dans la littérature. Les 5 premières références sont issues de l'études de la variation spatiale (à une phase donnée du cycle solaire) et les 6 dernières sont issues d'études de la variation temporelle (au cours du cycle solaire). FT veut dire transformée de Fourier. Le signe "+" veut dire une augmentation de la taille des supergranules avec le niveau d'activité, le signe "-" une décroissance et "0" pas de variation.

Référence	Données	Méthode	Variation
Sýkora (1970)	Ca II K images	auto-corrélation	+
Wang (1988)	magnetograms	auto-corrélation	+
Wang et al. (1996)	magnetograms	auto-corrélation	+
Hagenaar et al. (1997)	Ca II K images	segmentation	0
Raju & Singh (2002)	Ca II K images	auto-corrélation	-
Sýkora (1970)	CaII K images	auto-corrélation	+
Singh & Bappu (1981)	Ca II K images	auto-corrélation	-
Muenzer et al. (1989)	Ca II K images	2D TF	+
Komm et al. (1995)	magnetograms	auto-corrélation	+
Berrilli et al. (1999)	Ca II K images	segmentation	-
DeRosa & Toomre (2004)	Doppler	segmentation	-

la variation de la taille des cellules au cours du cycle. Dans pratiquement tous les cas (sauf un, DeRosa & Toomre 2004, mais l'analyse y est peu approfondie sur ce point, se concentrant surtout sur les durées de vie) les cellules avaient été déterminées en utilisant des cartes de champ magnétique ou des proxys du champ magnétique. La détermination des cellules n'étaient donc pas indépendante de celle du champ magnétique et l'étude de la relation entre les deux pouvait être fortement biaisée. Par conséquent, il était nécessaire de faire cette étude à l'aide d'une détermination des cellules indépendantes de la mesure du champ magnétique, ce qui est notre cas avec les cartes de divergences du champ de vitesse horizontal.

Nous utilisons donc la méthodologie suivante (Meunier, Roudier, & Tkaczuk 2007). A partir des cartes de divergences du champ de vitesse horizontal nous determinons les cellules et leur rayon typique. Les magnétogrammes quant à eux donnent des informations sur le champ magnétique dans le réseau et sur le champ magnétique inter-réseau, à l'intérieur des cellules. Nous avons utilisé deux approches : tout d'abord une approche globale, en caractérisant globalement le niveau d'activité dans chaque cellule (éventuellement en restreignant le calcul à certaines zones de la cellule), soit en regardant les distributions de champ magnétique pour l'ensemble des pixels ou les profils radiaux dans les cellules, pour différentes catégories de taille de cellules. Les résultats sont illustrés sur les Figs. 4.9 et 4.10 pour l'ensemble des pixels.

En résumé, on obtient qu'un champ magnétique plus élevé *à l'intérieur* les cellules (c'est-à-dire un champ inter-réseau important), est associé à une taille *maximale* des cellules plus petites, la taille moyenne étant peu affectée. Deux interprétations sont possibles : 1/ on peut imaginer que dans les régions avec plus de flux magnétique, où le champ IN serait plus fort, les champs de vitesse horizontaux soient inhibés et donc empêchent la formation de grandes cellules ; 2/ une autre possibilité serait que les grandes cellules, qui sont associées à des champs de vitesse plus grands et ont une durée de vie plus grande, auraient tendance à davantage concentrer le champ magnétique vers les bords des cellules et à vider davantage les cellules du flux magnétique. En regardant l'évolution du champ magnétique dans les cellules individuelles, nous n'avons observé que de petites variations au cours de la vie de la cellule, tandis que le champ magnétique au début de la vie des supergranules présente toujours une forte variation. Ceci tend à éliminer l'hypothèse 2. Par ailleurs, dans le deuxième cas, on s'attend à ce que dans les grandes cellules, du fait de davantage d'annihilation de flux de polarités opposées, on ait au final un champ davantage unipolaire. Nous avons observé une tendance à l'effet contraire. Ceci favorise également l'hypothèse 1.

Pour conclure, à la question : la taille des supergranules est-elle correlée ou anti-correlée avec le niveau d'activité, il semble y avoir *deux réponses* : 1/ tout d'abord l'amplitude du champ intranetwork dans les cellules limite la taille des cellules, soit une anti-corrélation ; 2/ ensuite, le réseau magnétique tend à être davantage présent dans les fortes convergences et grandes cellules, soit une corrélation. Pour finir, cela veut dire que ces deux effets, qui agissent en sens contraires, peuvent expliquer au moins en partie la variété de résultats obtenus jusqu'à maintenant, car selon la sensibilité magnétique, on verra plus ou moins l'influence du champ IN, qui est cruciale.

4.4 Le projet CALAS

Articles :

- *Tkaczuk, R., Rieutord, M., Meunier, N., Roudier, T., Tracking granules at the Sun's surface and reconstructing velocity fields. II. Error analysis, 2007, A&A, sous presse.*

4.4.1 Objectifs

Afin de caractériser davantage les propriétés de la supergranulation, et en particulier pour déterminer si elle est d'origine convective ou si elle résulte d'une instabilité à grande échelle, comme suggérée par Rieutord et al. (2000), il est nécessaire d'effectuer des observations présentant les deux principales caractéristiques suivantes. Tout d'abord, il est nécessaire d'avoir accès à la *haute résolution spatiale*, afin de pouvoir identifier et caractériser au mieux les granules explosifs, qui pourraient être à l'origine de l'instabilité. Ensuite, il est nécessaire d'avoir un grand champ permettant d'observer un très grand nombre de supergranules, non seulement pour des raisons statistiques, mais également pour avoir accès à la grande échelle de cette instabilité. Un certain nombre d'instruments existants, tant dans l'espace qu'au sol, possède l'une ou l'autre de ces propriétés, mais aucun ne possède les deux.

Nous avons donc proposé l'expérience CALAS (CAmera for the LArge Scales of the solar surface) pour la Lunette Jean Rösch du Pic du Midi, dans le cadre d'une ACI (Action Concertée Incitative) jeunes chercheurs dont je suis PI. CALAS a pour objectif d'observer la supergranulation à haute résolution spatiale et sur grand champ (typiquement 10'). Les observations se font en premier lieu en imagerie (afin de déterminer les supergranules via suivi de granules comme traceurs du champ de vitesse), ainsi qu'en mode magnétométrie et Doppler à l'aide d'un MOF (filtre magnéto-optique) dans la raie du potassium (niveau photosphérique). Les autres caractéristique de CALAS sont : cadence temporelle élevée (2 im/sec) pour permettre la restauration d'image et/ou sélection, rafales centre disque sur plusieurs heures dans de bonne conditions de seeing.

4.4.2 Mise en oeuvre

La réalisation technique de CALAS a été confiée au GIGT et à un étudiant en thèse, S. Rondi. Je renvoie à son manuscrit de thèse pour plus de détails (Rondi 2006). La plupart des tâches ont été effectuées par F. Beigbeder (IR GIGT, électronique principalement mais aussi informatique et suivi général du projet) et S. Rondi. D'autres ingénieur et techniciens ont participé à divers degrés à ce projet : G. Delaigue (électronique), L. Parès (optique), R. Dorignac (mécanique), F. Soulier, P. Saby, E. Bourrec (informatique). Le travail a été effectué en collaboration avec M. Rieutord et T. Roudier (responsable de la LJR).

Le choix du détecteur, au coeur de notre problématique, s'est porté sur des CMOS 4kx4k IBIS16000 de chez Fillfactory. Ces détecteurs n'étaient pas disponibles en mode standard, et était livrés “nus”. Ils étaient cependant les seuls à correspondre aux contraintes que nous nous étions fixées. L'ensemble de l'acquisition était à développer. Ce type de détecteur, dont nous possédons plusieurs exemplaires dont deux de qualité intéressante (peu de colonnes ou lignes mortes), étaient les seuls sur le marché permettant d'atteindre nos objectifs au moment où nous avons commencé le projet. De nombreux problèmes techniques, de natures diverses, ont contribué à le retarder, ce qui a entraîné en 2006 l'achat de détecteurs nouvellement disponibles et légèrement plus petits, IBIS14000, chez le même fournisseur. Ils avaient l'avantage d'être peu chers et de meilleure qualité (aucune ligne ni colonne morte). Nous avons acquis une cible pour laquelle l'acquisition serait la même que celle développée pour les IBIS16000, avec l'objectif de tester la chaîne d'acquisition avec une cible de meilleure qualité. Nous avons également acheté une caméra commerciale équipée de ce même détecteur et qui a pu être utilisée rapidement.

4.4.3 Préparation du traitement des données

Observations et calibrations

Les observations sont effectuées dans un mode assez simple, avec acquisition en continu ou par rafales en position fixe, en général au centre disque. Ces observations devront être effectuées en période de très bon seeing et au moins plusieurs heures afin de pouvoir étudier le signal supergranulaire. Les observations en imagerie se feront en bande G, ce qui permet d'étudier la granulation avec un bon contraste et de pouvoir également identifier les points brillants du réseau. La coordination avec la voie MOF permettra d'étendre le domaine de recherche, en particulier en appliquant de manière directe l'étude effectuée précédemment sur les variations d'intensité dans les supergranules. En attendant le MOF,

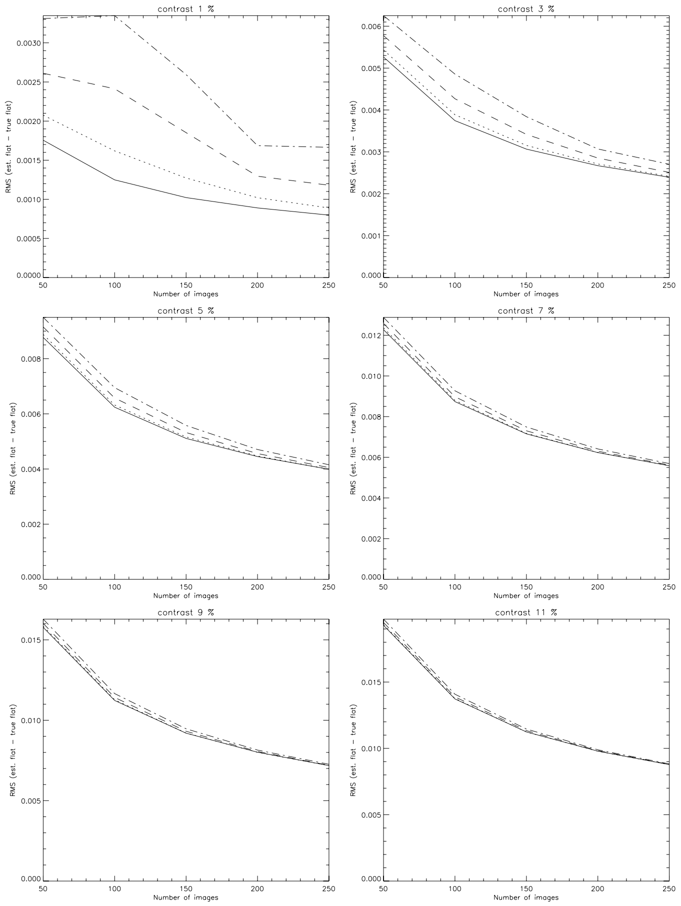

Figure 4.11 : RMS de la différence entre le flat-field estimé et le vrai flat-field en fonction du nombre d'images utilisées pour différents contrastes. Les courbes correspondent à différentes erreurs sur la position du centre disque : pas d'erreur (trait plein), pointillés (10 pixels), tirets (20 pixels) et tirets-pointillés (30 pixels). La simulation suppose une fonction d'assombrissement centre-bord parfaite.

une observation coordonnée avec MDI par exemple en mode disque entier devrait permettre de caractériser de manière au moins partielle la présence de champs magnétiques et de procéder à une sélection de pixels en conséquence.

La réalisation des flat-fields est un point délicat. Contrairement aux observations effectuées jusqu'à présent à la LJR, le grand champ ne permet pas de simplement balayer le disque solaire et de moyenner ensuite les images pour fournir une calibration. La présence de taches, pratiquement inévitables en dehors du minimum d'activité, et surtout l'assombrissement centre-bord, ne permettront pas d'obtenir directement un flat-field effectivement uniforme. Deux pistes ont été suivies. Tout d'abord, R. Tkaczuk (étudiant en thèse) a exploré la possibilité d'appliquer l'algorithme de Kuhn et al. (1991). Celui-ci consiste à ajuster un flat-field sur une série d'images (en faible nombre) décalées les unes par rapport aux autres avec un décalage connu. Les simulations effectuées montrent des effets de bords redhibitoires. Cette piste reste à approfondir. En parallèle, j'ai exploré une autre technique, qui consiste à corriger chaque image de flat-field individuelle (destinée à contribuer au flat-field final) d'un assombrissement centre-bord connu (à partir d'observations à la longueur d'onde qui nous intéresse) et à éliminer du calcul de la médiane en chaque pixel ceux qui sont dans une région active. Si la deuxième étape est assez facile à implémenter, la première nécessite une bonne connaissance de l'assombrissement centre-bord à la longueur d'onde de l'observation d'une part, et également une bonne connaissance de la position du centre du disque sur chaque image. Ce dernier point n'est pas facile à trouver en l'absence de structures telles que des taches sur le disque. Une solution consiste à faire des acquisition en partant d'un bord solaire, puis en laissant défiler le Soleil grâce à la rotation de la Terre, et ce jusqu'à l'autre bord solaire. En répétant ces balayages afin d'accumuler suffisement d'images, on peut reconstituer la position du centre disque sur chaque image. En outre, ceci doit fournir une taille du pixel assez fiable. J'ai effectué des simulations visant à déterminer l'incertitude sur le flat-field compte-tenu d'un certain nombre de paramètres : nombre d'images, signal solaire résiduel (type granulation, caracterisé par un certain contraste), erreur sur le positionnement. J'ai également inclus des taches réalistes dans cette simulation. Les résultats sont montrés sur la Fig. 4.11, qui montre la r.m.s. de la différence entre le flat-field estimé et le vrai flat-field en fonction du nombre d'images utilisées, et pour différents contrastes. Lors que le contraste est faible (1%), l'incertitude sur le flat-field est dominée à la fois par le nombre d'images et l'incertitude sur la position du centre du disque. A plus fort contraste, cette incertitude est complètement dominée par le nombre d'images.

Préparation d'une série d'images exploitable

L'étape suivante consiste à fabriquer une série d'images propres afin de calculer ultérieurement les champs de vitesses. Un recentrage et filtrage de type k-ω des rafales ou série temporelle plus longue doivent être effectués. Ce travail est actuellement essentiellement réalisé par M. Rieutord (codes validés).

Une première approche serait ensuite de sélectionner les meilleures images. Cette méthode ne permettra pas, en cas de seeing variable, de sélectionner des images complètement bonnes, car l'acquisition avec un CMOS se fait avec un balayage, dans notre cas sur une durée de l'ordre de 400 ms. Cette durée est bien supérieure à l'échelle de temps caractéristique sur laquelle évoluent les distorsions atmosphériques. Cependant, même dans ce cas, un seeing variable donne des images meilleures que d'autres. Les deux critères suivants sont pris en compte lors d'une sélection manuelle :

- Le contraste relatif sur l'ensemble de l'image : le plus grand possible.
- Nombre de boites pour lesquelles le contraste local est élevé : le plus grand possible.

Il est possible d'effectuer le même type d'opération lors d'une sélection automatisée. Ces deux critères s'avèrent cependant corrélés, et la technique consistant à prendre toutes les images dont le contraste moyen est supérieur à un certain seuil, et d'y ajouter la meilleure image (sur ce critère) de chaque rafale pour éviter les trous dans la série temporelle donne de bons résultats au vu de la comparaison avec la sélection manuelle. On peut aussi facilement déterminer des séries temporelles indépendantes. C'est cette technique que nous avons utilisée jusqu'à présent.

Une autre méthode consiste à tenter d'améliorer la qualité des images, éventuellement après élimination des plus mauvaises, afin de n'utiliser que la moyenne de la rafale ou la meilleure. Nous avons exploré la possibilité d'utiliser la technique développée par G. Molodij (LESIA) qui consiste à utiliser le signal présent dans l'image afin de calculer une MTF (Modulation Transfert Function) qui servira ensuite à déconvoluer chaque image : la MTF instrumentale ainsi que la turbulence atmosphérique vont contribuer à cette MTF. Cette technique doit s'appliquer sur des données recentrées filtrées les plus propres possibles afin de limiter le bruit introduit par la déconvolution. Nous avons effectué des observations petits champs qui ont contribué à la validation de la méthode. Ce travail se poursuit.

Analyse des données

Le calcul des champs de vitesse, qui serviront entre autre à déterminer les cellules de supergranulation, peut se faire selon deux types de techniques. Tout d'abord, une technique de corrélation locale comme celle utilisée ci-dessus sur les données MDI peut être appliquée. Une technique très prometteuse permettant le suivi des structures cohérentes (granules en l'occurence) a également été développée et utilisée (Roudier et al. 1999; Rieutord et al. 2000; Rieutord et al. 2001). Elle est décrite en détail dans Rieutord et al. (2007) et Tkaczuk et al. (2007). L'intérêt de cette technique est d'une part de permettre de quantifier les incertitudes sur les champs de vitesse (y compris sur les produits dérivés comme les divergences horizontales et la composante verticale du rotationnel), mais également de minimiser ces incertitudes en ne sélectionnant que les granules ayant une durée de vie supérieure à une certaine valeur. Ce travail, auquel j'ai participé, a été effectué essentiellement par M. Rieutord et R. Tkaczuk (Rieutord et al. 2007; Tkaczuk et al. 2007).

Une fois les champs de vitesse bien établis, nous pourrons reprendre certaines des études ci-dessus, en particulier l'étude des propriétés des champs de vitesse, cette fois sur un grand domaine d'échelle, ce qui sera inédit. De plus, T. Roudier a commencé à explorer la possibilité de déterminer de manière automatisée les granules explosifs : ce travail sera à mon avis crucial pour tester les instabilités à grande échelle, par exemple en étudiant les corrélations éventuelles entre le déclenchement de granules explosifs sur une grande échelle.

4.4.4 Premières images

Les premières séries d'images ont été obtenues en Octobre 2006. Un exemple est montré sur la Fig. 4.12. Ces deux séries ont été traitées et les champs de vitesse ont pu être calculés. Le spectre de puissance du champ de vitesse (Fig. 4.13) montre l'énergie liée à la supergranulation dans un spectre qui présente une très grande dynamique. Ces résultats sont encore préliminaires et nécessitent d'être approfondis. Deux séries d'observations ont également été effectuées en Février 2007 (N. Meunier et T. Roudier) et Mars 2007 (T. Roudier et M. Rieutord). Au cours de cette dernière campagne, plusieurs séries de très bonne qualité ont pu être obtenues, notamment une s̀equence de 7h35 d'observations en continue (10845 images). Ces données sont en cours d'analyse, et le pic de la supergranulation apparait très clairement dans le spectre de puissance.

4.5 Conclusion

Les résultats obtenus dans ce travail ont permis de conclure sur des questions ouvertes depuis longtemps, en particulier les variations d'intensité dans les supergranules et le lien entre taille des supergranules et champ magnétique local. Ce dernier point sera étendu naturellement au lien entre les propriétés des supergranules (taille mais aussi dynamique) au cours du cycle, permettant d'avoir accès à un domaine plus grand de champ magnétique ainsi qu'aux variations spécifiques possibles liées au niveau d'activité globale (et non pas seulement à l'échelle des cellules comme dans le travail présenté ici). Les analyses effectuées dans les sections précédentes pour deux séries temporelles proches du minimum du cycle peuvent effectivement être étendues facilement à d'autres séries correspondant à des phases différentes du cycle solaire. La principale difficulté est d'estimer les évolutions instrumentales au cours de cette période ainsi que leur influence sur les différents paramètres que nous souhaitons mesurer. Ce travail est en cours, toujours sur les données MDI/SOHO. Nous avons déjà des résultats préliminaires extrêmement intéressants, par exemple : une diminution significative de la taille des supergranules au maximum du cycle, une modification de la distribution du champ magnétique dans les cellules de supergranulation, un profil de variation de l'intensité dans les supergranules beaucoup mieux défini.

En ce qui concerne l'étude de la supergranulation dans le cadre du projet CALAS, un certain nombre d'études, tant du point de vue de l'instrumentation que de l'analyse des données restent à effectuer ou à terminer : La caractérisation de l'acquisition pour les cibles 16 Mpix est en cours de finalisation et l'acquisition avec la voie imagerie et la caméra 14 Mpix est déjà opérationnelle. La plus grosse opération reste probablement l'implémentation complète du filtre magnéto-optique (MOF) devant permettre de réaliser des Dopplergrammes et magnétogrammes en paralèlle avec la voie imagerie. Les observations obtenues en Octobre 2006 et début 2007 sont en cours d'analyse. Outre la détermination précise des champs de vitesse, pour lesquels les logiciels sont déjà développés, d'autres analyses originales seront faites, par exemple la détection automatique des granules explosifs et l'analyse de leur organisation spatio-temporelle, la recherche d'événements permettant de montrer si la supergranulation peut effectivement avoir pour origine une instabilité à grande échelle. L'analyse des champs de vitesse des petites échelles aux grandes échelles, permettra peut-être de caractériser la viscosité et la possiblité d'avoir des instabilité à grande échelle comme discuté par Gama et al. (1994).

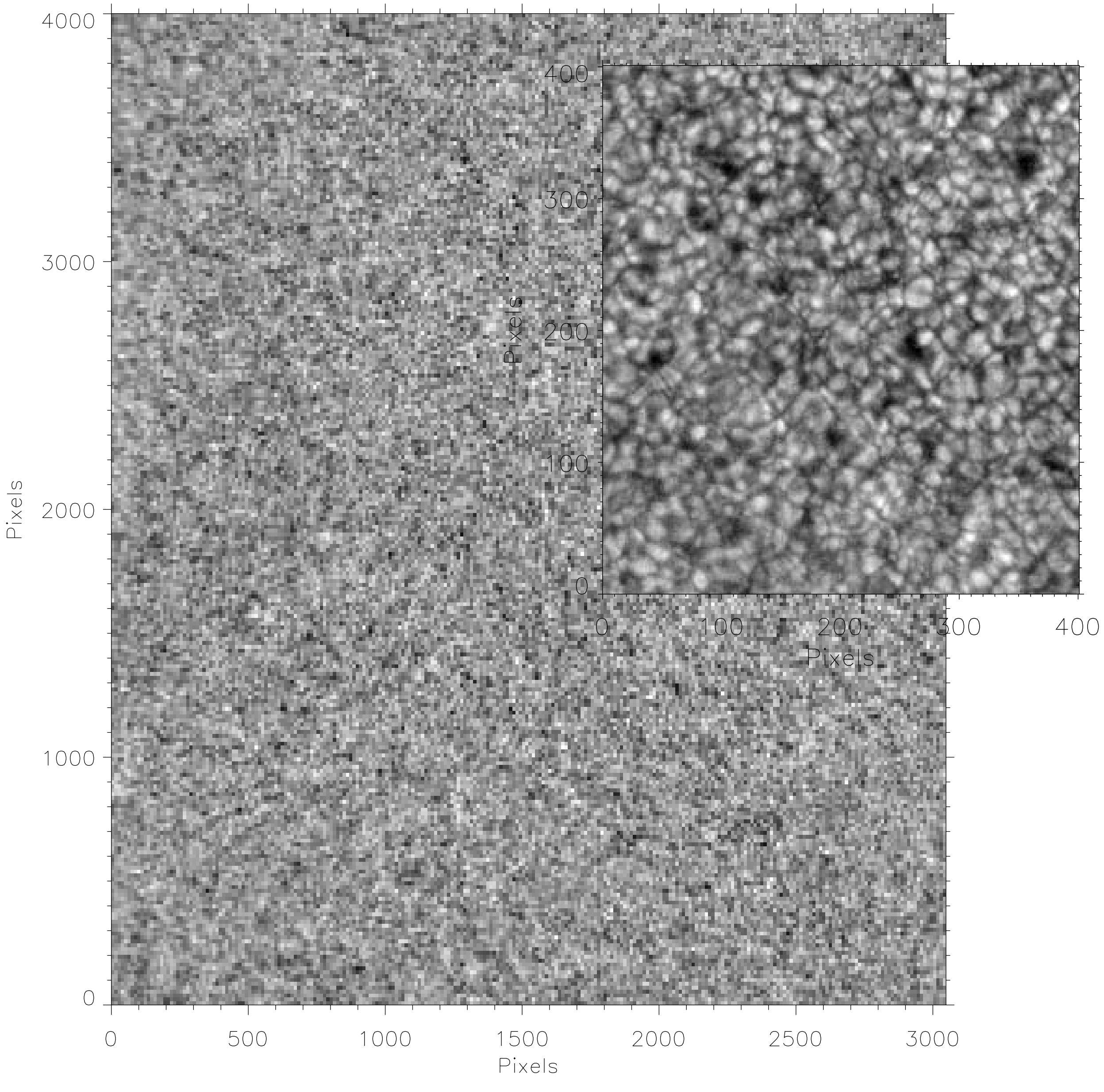

Figure 4.12 : Grande figure : champ complet observé le 29 Octobre 2006 avec CALAS, avec un pixel de 0.18 arcsec (observations S. Rondi et T. Roudier). En haut à droite : zoom sur une partie de l'image.

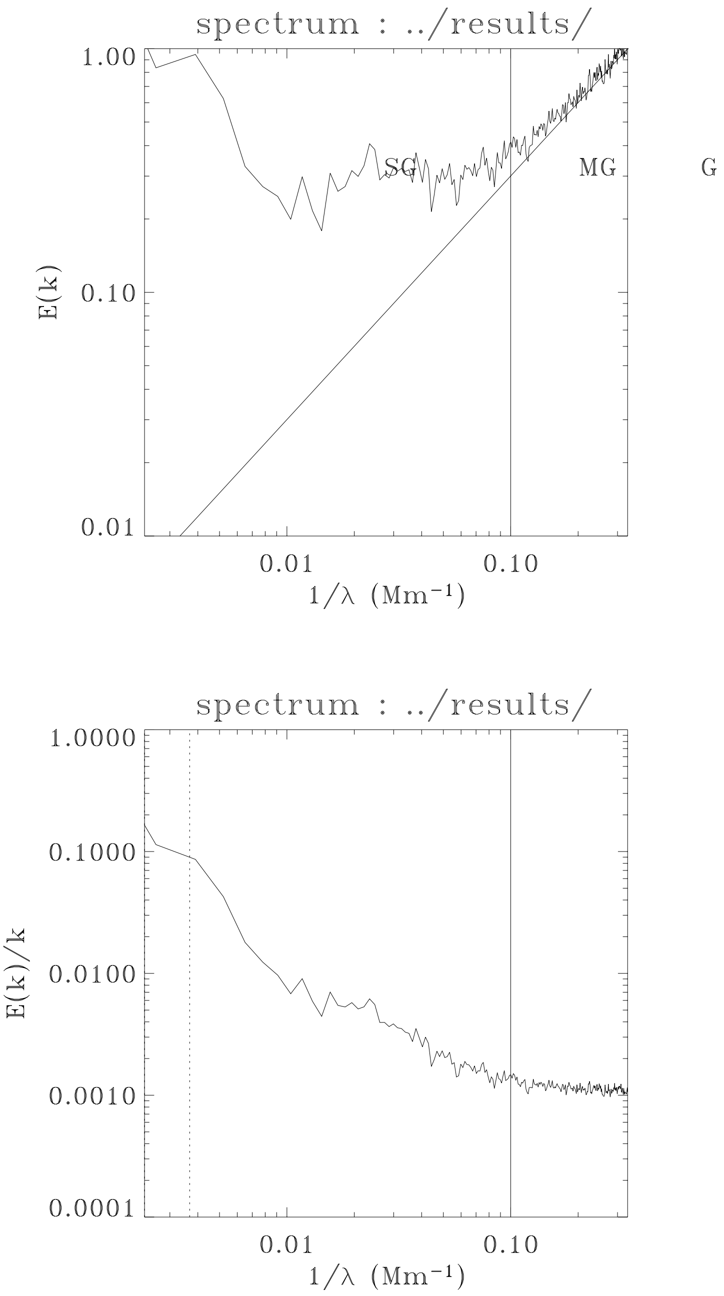

Figure 4.13 : Spectre de puissance de l’énergie cinétique en fonction de l’échelle.

Chapitre 5

La base de données solaires sol BASS2000

5.1 La responsabilité scientifique de BASS2000

J'effectue ma tâche de service au sein du service d'observation BASS2000 depuis mon recrutement en 2000 et en suis responsable depuis 2001. L'objectif de BASS2000 est d'archiver et pérenniser l'ensemble des données solaires sol françaises. La responsabilité scientifique de BASS2000, qui comprend les archives de Tarbes et de Meudon (cette dernière étant placée sous la responsabilité locale de J. Aboudarham), implique diverses taches administratives, en particulier les demandes de financement (PNST, Observatoire Midi-Pyrénées, Laboratoire d'Astrophysique de Toulouse-Tarbes), la gestion des comptes et des commandes, et le suivi des carrières du personnel. J'ai également eu une forte activité d'animation scientifique de BASS2000 : organisation des réunions de l'équipe, proposition de nombreux projets pour améliorer le retour scientifique de BASS2000 et pour rassembler la communauté autour de ces données. J'ai par ailleurs formé un nouveau Conseil Scientifique de BASS2000 en 2001, que je réunis annuellement. Dans ce cadre également, j'ai mis en place les statuts de BASS2000 ainsi qu'une convention THEMIS-BASS2000 adoptée part le CS de BASS2000 et le CA de THEMIS.

Les archives de Meudon et de Tarbes sont complémentaires. Dans le premier cas il s'agit de mettre en ligne des données, éventuellement partielles, mais qui seront disponibles très rapidement. Ceci est particulièrement utile pour la préparation d'observations avec d'autres instruments. Par ailleurs, la vocation de l'archive de Tarbes est de proposer un catalogue de gros volumes de données hors ligne, avec en contrepartie le maximum d'informations en ligne. Je me concentre dans ce qui suit sur les développements effectués à Tarbes sous ma responsabilité directe. Ce travail a été réalisé en collaboration avec l'équipe technique constituée de M. Lafon (responsable technique du service), P. Maeght et F. Grimaud.

5.2 Le formatage des données et l'archivage

Articles :

- *Romeuf D., Meunier N., Noëns J.-C., Koutchmy S., Jimenez R., Wurmser O., Rochain S., et al., Analysis of broad-band Hα coronagraphic observations, 2007, A & A 462, 731*

Le catalogue de données de l'archive de Tarbes était opérationnel à mon arrivée à Tarbes en septembre 2000. Cette archive fonctionnait sous Oracle et l'introduction des données THEMIS (données de la campagne 1999) ainsi que d'une séquence de données de la LJR (ex- Coupole Tourelle, Observatoire du Pic du Midi) avait commencé à cette date, sous la responsabilité scientifique de T. Roudier. Le volume actuellement archivé à BASS2000 est de plus de 8 To de données.

5.2.1 THEMIS

Etat des lieux en 2000

Les données THEMIS, correspondant aux modes MTR (spectro-polarimétrie) et DPSM (spectro-imagerie avec polarimétrie), nous sont envoyées par THEMIS sur DLT (depuis 1999 et jusqu'en 2005) puis sur LTO (à partir de 2005). A ce jour le catalogue contient plus de 7 To de données brutes DPSM et MTR. Lors de mon arrivée dans l'équipe BASS2000, je me suis tout d'abord attachée au bon formatage des données THEMIS. Dès la mise en fonction de l'archive, et ce malgré les efforts importants fournis par T. Roudier et l'équipe BASS2000 (et notamment M. Lafon) dès la création de BASS2000, les mots-clés dans les entêtes des fichiers FITS envoyés par THEMIS étaient souvent mal remplis. A cette date (2000), seuls 25 étaient obligatoires : ceci résultait d'un compromis entre le nombre de mots-clés souhaitables pour bien décrire les données (bien supérieur à 25) et ce qu'il était raisonnable d'obtenir dans un délai court de la part de THEMIS. Les erreurs dans les mots-clés ont plusieurs origines :

- Mauvais remplissage du mot-clé par l'observateur (par exemple OBJECT).
- Mauvais remplissage du mot-clé par le logiciel d'acquisition (mauvaise récupération d'un paramètre par exemple).
- Utilisation inappropriée du logiciel d'acquisition.

Au cours du temps, le nombre d'erreurs a diminué, en particulier grâce à l'introduction d'une interface observateur à THEMIS en 2001. Ces erreurs sont restées cependant à un niveau significatif depuis cette période, avec résolution de problèmes anciens et introduction de nouveaux problèmes.

Les mots-clés mal remplis sont à la source de plusieurs problèmes :

- Les données sont mal documentées et l'utilisateur des données risque de mal les interpréter. Par exemple les coordonnées peuvent être mauvaises, et dans la mesure du possible le pointage doit être vérifié à l'aide d'autres observations (comme MDI/SOHO par exemple). Dans certains cas (observation sur du Soleil calme par exemple), il est impossible de faire ces vérifications, ce qui est lourd de conséquence sur les résultats obtenus.
- Des informations manquantes peuvent empêcher l'utilisation de ces données, par exemple la configuration des lames du polarimètre au moment de l'observation (ces informations ne faisaient pas partie des mots-clés obligatoires en 2000).

- Les tables du catalogue sont mal remplies : ceci empêche les utilisateurs d'avoir accès à l'ensemble des données correspondant à leurs critères de requêtes. Par contre le résultat de requête est pollué par des séquences qui n'ont rien à voir avec ces mêmes critères.
- Lorsqu'un mot-clé est détecté comme étant mal rempli, il empêche l'intégration dans le catalogue, induit des échanges lourds avec THEMIS voire avec les observateurs et par conséquent une perte de temps et d'énergie importante pour tous.

A ces problèmes de formatage se sont ajoutés d'autres défauts qui ont rendu difficile le travail de l'équipe BASS2000 : organisation des données sur les bandes inadéquates, fichiers manquants ou bien au contraire en multiples exemplaires, etc. Ces défauts ont également été source de perte de temps dans le développement des projets.

Suivi du catalogue initial

Par conséquent, il a fallu implémenter des tests toujours plus nombreux pour vérifier la qualité du formatage des données lorsque des vérifications automatiques étaient possibles. J'ai par exemple mis en place une routine de vérification de la cohérence des coordonnées avec l'objet, des coordonnées centre-disque étant par exemple incompatibles avec l'objet “limbe”. Des vérifications manuelles ont également été faites. Des nombreux échanges avec l'équipe THEMIS ont eu lieu afin de leur signaler les problèmes rencontrés, et les convaincre de faire les modifications nécessaires. Il a fallu ensuite assurer le suivi des divers problèmes rencontrés et des modifications.

Sans modification du formatage ni du code d'intégration, il a été également possible de modifier les imagettes mises en ligne. Il faut rappeler que les données d'origine, sous forme de fichiers FITS, correspondant à de gros volumes, sont hors ligne. Le catalogue contient donc des informations sur les données : ceci inclut des extraits des entêtes (coordonnées, objet en particulier, mode d'observation) ainsi que la première image d'une séquence. Initialement, une seule “imagette” illustrait donc les données. J'ai développé une routine afin d'améliorer cette présentation afin que davantage d'informations soient présentées en ligne et permettent éventuellement à l'utilisateur de sélectionner les données (qualité selon la raie observée en particulier). Dans la nouvelle version, sont en ligne pour chaque balayage la première image pour chaque longueur d'onde observée, ainsi que pour les calibrations (flat-field, dark-current et, pour le mode DPSM, field-stop). A cela s'ajoute une coupe spatio-temporelle à longueur d'onde fixée dans le continu pour l'un des domaines de longueur d'onde observée, ce qui permet, outre la première image, de visualiser le champ couvert (présence du limbe ou de taches facile à vérifier).

Ajout d'informations dans le catalogue

Je me suis ensuite rendu compte que les critères de sélections choisis, bien que tout à fait pertinents et nécessaires, n'étaient pas suffisants pour faire une requête correcte. Ces critères étaient des critères de temps (date et heure), d'espace (coordonnées sur le Soleil), domaine de longueur d'onde, et objet. Si l'on a effectué des observations de manière indépendante avec un autre instrument et que l'on recherche a posteriori si THEMIS a observé simultanément, alors le résultat de la requête sera automatiquement très restreint.

Par contre, si l'on est uniquement interessé par un certain domaine de longueurs d'onde pour un type d'objet, sans contrainte de date, on recupère très facilement plusieurs centaines de Go de spectres bruts. Ceci va décourager sans aucun doute les utilisateurs potentiels. Afin de résoudre ce problème, j'ai proposé de rajouter des critères de requêtes supplémentaires afin de mieux contraindre ces requêtes. Ces critères sont les suivants : mode d'observation pour le MTR (2x2', 2x1', grille), nombre de pas du balayage (et en particulier l'information fente fixe / balayage spatial), seeing minimum (estimé à partir des valeurs fournis par un scintillomètre, sans calibration), séquence de Stokes observée, nombre d'images dans chaque burst, observation en imagerie simultanée. Il a fallu ensuite convaincre l'équipe THEMIS d'assurer la validité de ces mots-clés et leur suivi, et développer des routines pour les traiter (en particulier pour dériver des informations pertinentes à partir des données du scintillomètre à cadence régulière). Des statistiques sur le seeing au cours du temps à THEMIS ont ainsi pu être dérivées.

Ces mots-clés ont pu être pris en compte dans notre catalogue (moyennant des développements nouveaux de notre code d'intégration avec un schéma complémentaire du précédent) à partir de la campagne 2004. D'autres mots-clés proposés n'ont pas pu être pris en compte car ils n'ont pas été validés, en particulier le numéro NOAA des régions actives, pourtant bien utiles dans le contexte d'une interrogation future dans le cadre des Observatoires Virtuels.

Il faut noter que, comme pour les mots-clés obligatoires durant la première phase, et malgré leur validation initiale par THEMIS, de nombreux problèmes ont en pratique été rencontrés sur ces mots-clés. Il faut aussi savoir que le mot-clé concernant la configuration du mode MTR est associé à l'information sur les positions des lames du polarimètre. Cette information est nécessaire pour pouvoir corriger les paramètres de Stokes des cross-talks. Or ces informations ne sont disponibles qu'à partir de 2004 inclus. Pour les données antérieures, et ce malgré plusieurs demandes officielles depuis 2003, ces informations ne sont pas disponibles à BASS2000, ce qui empêche tout traitement sérieux de ces données.

Cette introduction de nouveaux critères de requêtes s'est accompagnée de la mise en ligne d'informations complémentaires. Outres les informations correspondant aux critères, l'ensemble des données du scintillomètre ont ainsi été mises en ligne, ainsi que les valeurs moyennes pour chaque balayage. Des fiches sous format électronique correspondant au bilan des séquences observées et bilan quotidien de la part de l'observateur sont également en ligne, ainsi que les listes d'heures correspondant à chaque image (les fichiers étant des cubes 3D, cette information est manquante dans les entêtes des fichiers FITS). L'ensemble de ces informations est accessible soit indépendamment soit à partir des résultats de requêtes. Des pages d'aide en ligne ont également été développées.

Plus récemment, et sur la proposition de L. Rossi membre du CA de THEMIS, nous avons élaboré des fiches correspondant à chaque séquence ayant donné lieu à au moins une publication. Le contenu de ces fiches a en partie été fourni par les observateurs quand ils ont repondu à nos requêtes. Pour la plupart nous avons travaillé avec les articles et les entêtes de fichiers. Ceci permet de visualier, lors d'une requête, les séquences qui ont été utilisées, et d'aller vers plus d'informations sur cette séquence (conditions d'observations, etc.) et les publications concernées. Dans le même état d'esprit, lorsqu'une séquence a été utilisée dans le cadre du service FROMAGE (G. Aulanier) pour effectuer une extrapolation du champ magnétique photosphérique, un lien vers ce service est indiqué.

Pour finir, et afin de perdre moins de temps lors de la rencontre des problèmes de formatage, la plupart des itérations avec THEMIS ont été supprimées en instaurant un délai d’une semaine, au-dela duquel les données à problèmes sont intégrées telles quelles avec indication d’un “flag” mentionnant le problème potentiel (objet, etc.). En 2005, 6% des séquences contenant des observations (i.e. après élimination des séquences ne contenant que des calibrations) ont été “flaguées”. Le pourcentage de séquences à problème est probablement supérieur à 10% dans la mesure où tous les problèmes ne peuvent pas être détectés de manière automatique. Il est clair également que si un tel mode de fonctionnement avait été mis en place en 2000, toutes les séquences auraient été “flaguées”, ce qui explique pourquoi cela a été fait tardivement.

5.2.2 Le Radiohéliographe de Nancay

Depuis la mise en fonction de l’archive de Meudon en 1996, deux cartes quotidiennes correspondant à deux domaines de fréquences sont obtenues à partis des observations du Radiohéliographe de Nancay et mise en ligne rapidement dans l’archive de Meudon. L’ensemble des données obtenues est cependant bien plus grand puisque 5 domaines de fréquences sont utilisées, et la cadence temporelle est élevée. En 2003, nous avons donc commencé à archiver à Tarbes l’ensemble des données brutes (visibilités). Actuellement notre catalogue contient l’ensemble des données du Radiohéliographe de Nancay obtenues depuis 1997.

5.2.3 Le Coronographe du Pic du Midi

De la même manière, quelques images représentatives sont selectionnées par les observateurs au Coronographe du Pic du Midi chaque jour et envoyée sur l’archive de Meudon pour mise en ligne immédiate. L’intérêt de cette mise en ligne rapide est qu’elle permet à des observateurs sur d’autres télescopes, en particulier à petit champ, de sélectionner des cibles de type protubérance ou jet. Là encore, un volume bien plus important de données est disponible, plus de 80000 images depuis 1994. Le formatage des données, effectué par l’équipe du Coronographe, a bénéficié de l’aide de BASS2000. J’ai fortement incité son responsable, J.-C. Noëns, à faire en sorte que ces données puissent etre intégrées dans le catalogue de BASS2000. S’en est ensuivi un certain nombre d’actions. Une machine achetée par l’equipe du Coronographe pour le dépouillement de ces images (en particulier calibration photométrique et extraction des structures) a été installée dans nos locaux à Tarbes et reliée par réseau aux machines BASS2000. Le dépouillement des données est effectué par l’équipe du Coronographe (D. Romeuf en particulier). Une routine additionnelle permet de mettre en ligne des films de détails sur des protubérances ou jet à plein resolution spatiale. Suite à des développements du code d’intégration par l’équipe technique de BASS2000, les données 1997-2001 ont pu être intégrées dans le catalogue BASS2000. En outre, un catalogue de structures (jets, protubérances) réalisé par l’équipe du Coronographe est en ligne sur cette machine. Le reste des données sera intégré prochainement.

Un article associé à ce travail a été écrit, et j’ai fortement contribué à sa rédaction (Romeuf et al. 2007). Nous avons pu étudié la variabilité de la luminosité observée des structures en fonction de leur taille sur plus de trois ordres de grandeur, ce qui nous a permis de dériver les lois de puissances correspondantes, ainsi que les distributions en taille et en luminosité. Une forte asymétrie du niveau d'activité est observée entre les 2 hémisphères, en particulier aux pôles. Nous observons également que la distribution des structures en fonction de la latitude présente un pic à haute latitude.

La mise en place du nouvel instrument CLIMSO en 2007 permettra de fournir des données de meilleure qualité (en particulier du point de vue photométrique) et plus complètes, avec des observations du disque solaire en Hα et CaII K, et des images du coronographes dans des longueurs d'onde autres que Hα (notamment des raies du Fer donnant accès à des structures plus chaudes).

5.2.4 La LJR - Pic du Midi

Dès la mise en ligne du catalogue contenant les premières données THEMIS, une séquence obtenue avec la LJR en 1988 avait été intégrée dans ce catalogue. Il s'agit d'une séquence de 3 heures environ d'excellente qualité, sous forme traitée (y compris un destretching). Lors de la refonte du catalogue avec l'introduction des données THEMIS dépouillées, cette séquence a été mise de côté pour pouvoir être réintégrée plus tard après avoir revu le mode d'integration des données de la LJR de manière plus globale. Actuellement, nous aidons au formatage de differents types de données de la LJR, qui seront intégrées prochainement. Outre cette séquence, il s'agit de :

- Images individuelles de la granulation obtenues depuis les années 70 par R. Muller, numérisées à la MAMA (Machine A Mesurer pour l'Astronomie) et calibrées. Ces données correspondent à une sélection drastique par rapport à l'ensemble des données d'origine (qui avaient été obtenues à une cadence de 24 im/sec), avec la qualité d'image comme critère de sélection.
- Des observations récentes de la granulation effectuées par R. Muller, toujours en imagerie, correspondant à des rafales de 50 images en diverses positions sur le disque solaire. Ces données sont brutes et fournies avec flat-field et dark-current.
- Une séquence dépouillée de données DPSM fournie par T. Roudier.

A court terme les données CALAS seront également intégrées dans le catalogue.

5.3 Le traitement de données THEMIS par BASS2000 et leur introduction dans le catalogue

Les observateurs ne repartant pas du télescope avec l'ensemble de leurs données, la majorité des requêtes de données THEMIS qui sont faites auprès de BASS2000 émanent d'observateurs demandant leur propres données. Par ailleurs, ces données sont brutes et, étant de type spectro-polarimétriques, elles sont assez compliquées à dépouiller. Selon le niveau de réduction, les données intéresseront des utilisateurs spécialisés en spectropolarimétrie (profils de Stokes) ou bien des utilisateurs spécialisées sur d'autres types d'instruments (SOHO par exemple) et recherchant des informations complémentaires.

Partant de ce constat, j'ai proposé que l'équipe BASS2000 dépouille ces données de manière standard, les intègrent dans le catalogue et mettent ainsi à disposition de la communauté des paramètres de Stokes et des cartes (champ magnétique en particulier) pratiquement prêtes à l'emploi. La mise en place du dépouillement pour un mode donné implique un certain nombre d'étapes :

- Définition des niveaux de dépouillement
- Organisation du dépouillement
- Recherche des informations éventuellement manquantes sur les données
- Choix du code de traitement le cas échéant
- Développement d'un code d'interfaçage à BASS2000
- Tests de robustesse du code sur un jeu de données limité
- Figer les choix (conditions du calcul, niveaux hors ligne / en ligne, etc.)
- Choix du mode de sélection éventuel des données
- Dépouillement des données et vérifications visuelles
- Intégration dans le catalogue et sauvegardes

5.3.1 Le dépouillement de données DPSM-THEMIS

Nous avons commencé par la mise en place du dépouillement de données DPSM, car il existe un seul code pour ces données (développé par P. Mein) et ce code était disponible immédiatement (en fait, il était en ligne sur notre site). J'ai élaboré en 2004 un cahier des charges portant sur l'introduction de données dépouillées en général (tous instruments confondus) dans notre catalogue. J'y ai en particulier proposé des niveaux de traitements à conserver pour le mode DPSM. Le choix final a été fait en collaboration avec P. Mein. Nous avons également travaillé avec lui afin de tester la robustesse du code et d'identifier les points à modifier afin d'éviter des interruptions intempestives du code dans le cas du traitement d'un gros volume de données.

Il était également très important de bien définir un mode de traitement standard de ces données, afin que les résultats aient une meilleure visibilité. Les fichiers de paramètres sont fournis à l'utilisateur afin de leur permettre facilement de modifier éventuellement ces paramètres. Une routine d'interfaçage a également été développée par l'équipe afin de traiter des journées complètes et de trouver automatiquement les fichiers de calibration correspondant à une observation donnée. A l'heure actuelle 3 ans de données ont été dépouillés par l'équipe, des campagnes 2002 à 2004. Les principaux problèmes recontrés sont les suivants :

- Run non standard (balayages exotiques, observations hors disque de protubérance)
- Mauvais noms de fichiers
- Mauvaises données (niveau proche du dark-current entre autres)
- Problème de calibration ou de géometrie

5.3.2 Le dépouillement de données MTR-THEMIS

Dans le cas du mode MTR, la situation était assez différente, car de nombreux codes, développés indépendamment par différentes équipes, existaient. Par ailleurs, les données présentent une variabilité beaucoup plus grande (plus de 100 domaines spectraux observés, 3 modes, objets). Associé à un très gros volume (plusieurs To), le code choisi doit donc être robuste et rapide. Nous avons utilisé plusieurs logiciels externes :

- Le code permettant d'obtenir les profils de Stokes a été fourni par A. Sainz Dalda de l'équipe THEMIS (Sainz Dalda & López Ariste 2007). Le traitement est optimisé pour une raie donnée, en particulier pour l'alignement des spectres des deux voies.
- Un code permettant de fournir le vecteur champ magnétique à partir d'une méthode de type PCA, dans le domaine 630 nm, a été fourni par A. López Ariste de l'équipe THEMIS (voir Rees et al. 2000 pour plus d'informations). Des paramètres supplémentaires (thermodynamiques en particulier) sont également fournis, ainsi que les incertitudes sur les résultats.
- Un logiciel d'inversion des profils de Stokes, fournissant également le vecteur champ magnétique, a été fourni par V. Bommier du LERMA-Observatoire de Meudon (Bommier et al. 2007; Landolfi, Arena, & Deglinnocenti 1984). Ce logiciel est fondé sur une solution analytique de Unno-Rachkowski, qui fournit la polarisation émergeant d'une atmosphère de Milne-Eddington pour un champ magnétique donné. Le code peut être utilisé pour n'importe quelle raie spectrale. Cependant, étant donné les temps de calculs assez longs, nous nous sommes limités au calcul pour les raies du fer à 6302.5 Å et 5250.2 Å.

Le travail de l'équipe a ensuite consisté à tester ces codes, et à développer un logiciel comprenant l'ensemble de la réduction en incluant ces logiciels. Les différentes étapes de l'analyse sont les suivantes :

- Organisation des fichiers d'un "run" (typiquement de l'ordre d'une semaine).
- Elimination de mauvais fichiers (non standard ou très courts).
- Préparation des paramètres d'entrée pour les codes de réduction, incluant une comparaison avec un spectre de référence pour calibrer les spectres en longueur d'onde et pour identifier automatiquement les raies intéressantes.
- Appel des routines.
- Calcul des cartes d'intensité, Dopplergrammes et magnétogrammes.
- Calcul de paramètres supplémentaires pour aider l'utilisateur à faire son choix.
- Finalisation du formatage des fichiers et préparation des fichier JPEG en ligne.
- Validation à l'aide d'une base de données de test.
- Sauvegarde des résultats et introduction dans la base en ligne.

La réduction des données en suivant cette méthode est en cours et des données réduites sont déjà dans la base de données.

5.4 L'organisation d'ateliers de dépouillement

J'ai initié et organisé plusieurs ateliers sur le dépouillement de données THEMIS. L'objectif était double. Dans le cas du DPSM, il s'agissait d'aider des observateurs ou utilisateurs de données à traiter leurs données en utilisant le code de P. Mein. Ces 2 ateliers ont été organisés avec succès en 2003 et 2006. Dans le cas du MTR, il s'agissait plutôt de rassembler les membres de la communauté THEMIS ayant développé des routines de manière indépendante. L'objectif était d'échanger sur les difficultés rencontrées, et d'avoir aussi d'obtenir des inputs de la communauté pour la mise en place du dépouillement de données MTR à BASS2000. Deux ateliers ont également été organisés. A noter qu'avec la mise en place du dépouillement de données MTR en 2006, il faudrait organiser à l'horizon 2008 une réunion pour apprendre à des utilisateurs à dépouiller ces données, soit dans le cadre d'un atelier comme cela a été fait pour le DPSM, soit dans le cadre d'une école avec un contenu plus étoffé sur la spectro-polarimétrie si suffisamment de participants sont attendus.

5.5 La vulgarisation de la physique solaire et le site web de BASS2000

J'ai activement participé à la refonte et mise à jour du site web de BASS2000, dont le webmaster est F. Grimaud. J'ai en particulier mis en place un site de réponse aux questions posées en ligne sur la physique solaire. J'ai répondu à une grande partie des $\sim$ 140 questions posées sur ce site, essentiellement par des scolaires. J'ai aussi pris l'initiative de mettre de nombreux documents en ligne, soit concernant directement BASS2000 (compte-rendu de réunions et d'ateliers, etc.) soit concernant les données (THEMIS en particulier) ou bien d'interêt plus général pour les observateurs en physique solaire (profondeurs de formation de raies par exemple).

5.6 L'implication dans les Observatoires Virtuels

Au sein de BASS2000, J. Aboudarham, responsable du site de Meudon, est le plus actif dans le cadre des Observatoires Virtuels, du fait de son implication dans le projet européen EGSO. Ce projet n'a malheureusement pas pu être pérennisé, et l'inclusion d'un lien vers l'archive de BASS2000-Tarbes n'a pu être réalisée à temps. Depuis fin 2005, je participe cependant à un groupe de travail formé par l'Action Spécifique OV, le groupe “OV système solaire”. Ce groupe est actuellement placé sous la responsabilité de C. Jacquey. Des sous-groupes ont été définis, et j'ai été en charge d'un sous-groupe dont l'objectif est d'identifier les données solaires pouvant intéresser nos collègues étudiant la magnétosphère terrestre. Dans ce cadre, nous avons établi des listes de données “Soleil entier”, soit obtenues au sol, soit dans l'espace. Dans cette liste, nous avons privilégié les instruments fournissant une cadence temporelle élevée et une bonne couverture temporelle. Ceci est en effet un paramètre essentiel pour essayer de remonter des événements observés à la Terre vers les éruptions solaires ou les éjections de masse coronale ayant été à l’origine de l’événement. Les catalogues d’événements sont probablement les données les plus importantes, et en tout cas celles qui seront utilisées en premier. Nous avons cependant commencé à établir une liste de produits dérivés qui pourraient être utiles et adaptées pour des collègues n’ayant pas forcément l’habitude de regarder et d’interpréter des images du Soleil. Ce projet devra se poursuivre en fonction de l’évolution des bases de données plasma au niveau international (qui cherchent actuellement à standardiser leurs approches), et en fonction de l’implication de la communauté. Il serait en particulier souhaitable de parvenir à réaliser, à notre échelle, un prototype fonctionnant sur les bases de données solaires (BASS2000 et MEDOC) et sur la base de données plasma (CDPP), comme le met en place actuellement C. Jacquey.

Chapitre 6

Conclusion et perspectives

La montagne et l'eau finiront par
se rencontrer un jour.
(Shanshui shangyou xiangfeng zhiri.)

6.1 Bilan de mon approche

La principale caractéristique de la plupart des travaux présentés dans ce document est la volonté de caractérisation la plus complète possible d'un certain nombre de processus liés à la dynamique du plasma photosphérique, aux structures magnétiques et aux relations entre les deux. Par exemple, la caractérisation très complète des propriétés du réseau magnétique au cours du cycle et du point de vue de sa dynamique globale ont montré des liens très forts entre ces structures et la dynamique tant globale qu'à l'échelle de la supergranulation. Réciproquement, la caractérisation de la supergranulation a montré, outre la nécessaire prise en compte du champ magnétique pour cette étude, une interconnection entre champ magnétique local et propriétés dynamiques. Le lien entre les propriétés "statiques" et la dynamique a montré la nécessité d'étudier les deux conjointement, ce qui a été fait. Une certaine continuité entre les propriétés des grandes structures (régions actives) et des petites structures (réseau magnétique) a été mise en évidence.

L'approche suivie a nécessité l'analyse de volumes importants de données, en particulier du fait de la volonté d'étudier des détails fins dans les relations dynamique / champ magnétique ainsi que leur variations au cours du cycle. Le traitement de gros volumes de données est un élément de plus en plus présent dans les projets instrumentaux. Ceci renforce d'ailleurs la nécessité de mettre en place des bases de données permettant non seulement la pérénisation de ces données et l'accès au plus grand nombre d'utilisateurs pour rentabiliser les instruments, mais offrant aussi la possibilité pour une équipe d'utiliser un très gros volume de données qui auraient été inaccessibles à un observateur individuel.

6.2 Comment aller plus loin ?

6.2.1 Nouveaux instruments et analyses

L'instrument CALAS commence à porter ses fruits, et bien sûr il reste beaucoup à faire, tant du point de vue instrumental que du point de vue des observations et de l'analyse des données, même si la plupart des actions sont actuellement engagées voire en bonne voie (voir chapitre 4).

Le lancement d'Hinode fin 2006 est un concurrent très sérieux pour la Lunette Jean Rösch, car il s'agit d'un instrument de même diamètre mais situé dans l'espace. Sur des petits champs, la LJR ne peut bien sûr pas faire mieux. Le créneau de CALAS reste cependant libre car Hinode ne pourra pas effectuer les observations grands champs comme CALAS. Néanmoins, du fait de la possibilité d'obtenir des images proches de la diffraction de l'instrument avec la LJR, un certain nombre de programmes coordonnés CALAS-Hinode pourront être effectués. Par exemple, l'observation durant la même prériode, sur Soleil calme, d'une séquence de quelques heure de CALAS (grand champ) et d'une série plus longue avec Hinode (petit champ) devrait permettre d'étudier à quel point la granulation solaire est ergodique. De plus, l'observation exactement simultanée (à l'échelle de la seconde), sur une même (petit) champ avec les deux instruments devrait permettre de valider de manière directe la technique de déconvolution des images développée par G. Molodij, et qui présente un très grand intérêt pour CALAS.

A moyen terme, un certain nombre des travaux effectués avec les données MDI/SOHO pourront être repris avec une plus grande précision avec les données de HMI/SDO. Le champ disque entier unique permettra d'avoir accès à une meilleure résolution spatiale pour une plus grande quantité de données, ce qui permettra de réduire les incertitudes d'une part, et d'aborder des champs nouveaux (par exemple la prise en compte du champ inter-réseau dans l'étude statistique des propriétés des structures magnétiques) d'autre part ; la mesure du vecteur champ magnétique permettra d'aborder l'étude des champs inter-réseau de manière très intéressante : certes le signal est moins complet qu'avec une analyse spectropolarimétrique, mais la quantité de données sera énorme et certains travaux pourront être abordés en incluant toutes les composantes du champ magnétique.

6.2.2 Modélisation et simulations numériques

Un certain nombre de besoins en simulations numériques et en modélisations sont apparus au cours de mes travaux. Du côté des simulations, il faudrait pouvoir simuler plusieurs supergranules et regarder si on retrouve les variations d'intensité à l'intérieur des supergranules. Ces variations sont assez complexes, et l'analyse de davantage de données permettra de mieux les caractériser. Il faudra ensuite voir si ces variations sont plutôt compatibles avec une origine convective de la supergranulation, ou bien avec une instabilité à grande échelle. De manière plus simple, des simulations de type “bouchon passif” dans la lignée de celles qui ont été effectuées par Krijger & Roudier (2003) devraient être refaites afin de voir dans quelles conditions il est possible de retrouver la distribution de champ magnétique dans les cellules de diverses tailles.

6.3 Le magnétisme stellaire

Le magnétisme solaire se présente sous des formes très variées en terme d'échelles temporelles (événements ponctuels, durée de vie des structures ; cycle solaire, évolution des propriétés des structures au cours du cycle) et spatiales (au niveau photosphérique par exemple : grandes régions actives / taches solaire ; réseau magnétique constitué de petites structures distribuées à la surface ; champs inter-réseau). J'ai abordé certains de ces aspects, comme décrit en détail dans ce document, et en particulier les aspects dynamique photosphérique, distribution du champ magnétique la surface, lien entre dynamique et champ magnétique, et les variations de ces propriétés au cours du cycle solaire. Par ailleurs, le magnétisme des étoiles de divers types est maintenant étudié très en détail (à l'aide de plusieurs instruments dédiés : CFHT/Espadons, TBL/Narval) et on commence à avoir accès à diverses échelles spatiales et temporelles comme pour le Soleil. Des variations de rotation en fonction de la phase du cycle stellaire ou du type de structure ont par exemple été observées (Donati, Collier Cameron, & Petit 2003). Le magnétisme stellaire se manifeste aussi indirectement dans d'autres types d'observations (certaines raies comme CaII K et H montrant probablement des variations d'éclairement au cours de cycle comme pour le Soleil, influence du champ magnétique en spectroscopie même sans polarimètre), comme c'est le cas pour le Soleil. Enfn, les observations à très haute résolution spatiale, en particulier par interférométrie, permettent également de commencer à avoir accès à des informations sur la dynamique globale des structures, par exemple la rotation. Je compte poursuivre mes travaux dans cette direction, en y apportant mon expérience de la dynamique solaire et du magnétisme solaire, qui présentent une très grande variabilité à diverses échelles.

Annexe I

Tâches au service de la communauté

I.1 Responsabilités locales

- Membre de la commission de spécialistes section 34 Université Paul Sabatier depuis 2001.
- Correspondante de la direction de l'UMR 5572 à Tarbes 2003–2006.
- PI du projet CALAS ("CAmera for the LArge Scales of the solar surface", ACI jeune chercheur) depuis 2002.
- Co-direction de 2 thèses (dans le cadre du projet CALAS, responsable de thèse M. Rieutord) : Ruben Tkaczuk (2002-2006) et Sylvain Rondi (2002-2006, soutenue le 14/12/2006).

I.2 Responsabilités nationales

- Responsable de la base de données BASS2000 (Service d'Observation labellisé de l'INSU) depuis 2001.
- Membre nommé de la section 17 depuis 2004.
- Membre du conseil scientifique de MEDOC depuis 2001.
- Membre du groupe de travail "OV plasma système solaire" depuis 2005.

I.3 Responsabilités internationales

- Membre du CA de THEMIS Avril 2003 – début 2007.
- Membre du conseil de JOSO (Joint Organization for Solar Observations) depuis 2004.
- Referee d'articles (A & A, Astrophys. J., Sol. Phys.), demandes de financement (agences de pays européens), évaluation de personnel (Inde).

I.4 Organisation de conférences et d'ateliers.

- Participation active à l'organisation de 2 conférences internationales à Toulouse en 2002 (et co-éditrice avec J. Arnaud) : ”Atelier THEMIS” ($\sim$50 participants) et ”Magnetism and activity of the Sun and Stars” en l'honneur de Jean-Louis Leroy ($\sim$60 participants).
- Organisation de 4 ateliers sur le dépouillement de données THEMIS depuis 2003.

Annexe II

Liste de publications

II.1 Publications à comité de lecture

- Tkaczuk, R., Rieutord, M., Meunier, N., Roudier, T., Tracking granules at the Sun's surface and reconstructing velocity fields. II. Error analysis, 2007, A & A, sous presse
- Rondi S., Roudier T., Molodij, G., Bommier V., Sütterlin P., Malherbe J.-M., Keil S., Meunier N., Mein P., Mein N., Schmieder B., Maloney P., Photospheric general context around dark filament, 2007, A & A 467, 1289
- Meunier N., Roudier, T., Tkaczuk R., Are supergranule sizes anti-correlated with magnetic activity ?, 2007, A & A 466, 1123
- Meunier N., Roudier T., The superrotation of supergranules, 2007, A & A 466, 691
- Meunier N., Tkaczuk R., Roudier T., Rieutord M., Intensity variations accross supergranules, 2007, A & A 463, 745
- Romeuf D., Meunier N., Noëns J.-C., Koutchmy S., Jimenez R., Wurmser O., Rochain S., et al., Analysis of broad-band Hα coronagraphic observations, 2006, 2007, A & A 462, 731
- Meunier N., Tkaczuk R., Roudier T., Rieutord M., Velocities and divergences as a function of supergranule size, 2007, A & A 461, 1141
- Meunier N., Large-scale photospheric dynamics below coronal holes, 2005, A & A 443, 309
- Meunier N., Temporal variations in the magnetic network large-scale dynamics, 2005, A & A 442, 693
- Meunier N., Large-scale dynamics and polarities of magnetic structures, 2005, A & A 437, 303
- Meunier N., Magnetic network dynamics: activity level, feature size and anchoring depth, 2005, A & A 436, 1075

- Meunier N., Complexity of active regions: flares and cycle phase dependence, 2004, A & A 420, 333
- Meunier N. & Kosovichev A., Fast photospheric flows and magnetic field in a flaring active region, 2003, A & A 412, 541
- Meunier N., Statistical properties of magnetic structures: their dependence on scale and solar activity, 2003, A & A 405, 1107
- Meunier N. & Jefferies S.M., Two-Dimensional Modeling of the Solar Oscillation l-ν Power Spectrum, 2000, Astrophys. J., 530, 1016
- Meunier N., Large scale dynamics of active regions and small photospheric magnetic features, 1999, Astrophys. J., 527, 967
- Meunier N., Fractal analysis of MDI magnetograms: a contribution to the study of the formation of solar active regions, 1999, Astrophys. J., 515, 801
- Meunier N., Solanki S.K. & Livingston W.C., Infared lines as probes of solar magnetic features. XIII. The magnetic flux in weak and strong quiet-sun fields, 1998, A & A 331, 771
- Meunier N., Nesme-Ribes E. & Collin B., Cycle 19 facula dynamics II. Meridional circulation, rms velocity and Reynolds stresses, 1997, A & A 319, 683
- Meunier N., Nesme-Ribes E. & Grosso N., Cycle 19 facula dynamics I. Angular rotation, 1997, A & A 319, 673
- Nesme-Ribes E., Meunier N., & Vince I., 1997, Solar dynamics over cycle 19 using sunspots as tracers, 1997, A & A 321, 323
- Meunier N., Proctor M.R.E., Sokoloff D.D., Soward A.M. & Tobias S.M., Asymptotic properties of a non-linear alpha-omega dynamo wave: period, amplitude and latitude dependence, 1997, Geophys. Astrophys. Fluid Dynamics, 86, 249
- Meunier N., Nesme-Ribes E. & Sokoloff D.D., 1996, A dynamo wave in the alpha^2-omega dynamo, Astron. Zh. 73, 460 (version anglaise : Astronomy reports 40, 415)
- Nesme-Ribes E., Meunier N. & Collin B., 1996, Fractal analysis of magnetic patterns from Meudon spectroheliograms, A & A 308, 213
- Collin B., Nesme-Ribes E., Leroy B., Meunier N., Sokoloff D., La dynamique interne du Soleil à partir des traceurs magnétiques, 1995, C. R. Acad. Sci. Paris 321, Serie IIb, 111

II.2 Contributions à des conférences ayant donné lieu à publication

- Jacquey C., Bocchialini K., Aboudarham J., Meunier N., André N., Génot V., Harvey C., Budnik E., Hitier R., Gangloff M., Bouchemit M., European Planetary Science Congress 2006. Berlin, Germany, 18 - 22 September 2006., p 714
- Meunier N., Lafon M., Maeght P., Grimaud F., & Roudier T., BASS2000-Tarbes : current status and THEMIS data processing, 2007, Conférence THEMIS Octobre 2006, eds. V. Bommier & S. Sahal-Bréchot, Mem. S.A.It. 78, p 172
- Rondi R., Roudier T., Molodij G., Bommier V., Malherbe J.M., Schmieder B., Meunier N., Rieutord M., Beigbeder F., Photospheric flows around a quiescent filament and CALAS first results, 2007, Conférence THEMIS Octobre 206, eds. V. Bommier & S. Sahal-Bréchot, Mem. S.A.It. 78, p 114
- Meunier N., Lafon M., Maeght P., Grimaud F., & Roudier T., BASS2000 : on-going projects and results, 2006, Journées SF2A 2006, Paris, eds. D. Barret, F. Casoli, G. Lagache, A. Lecavelier, L. Pagani, p 553
- Noëns J.-C., Romeuf D., Meunier N., Koutchmy S., Vilinga J., Jimenez R., Wurmser O., Rochain S., and the ” O.A. ” team, Analysis of broad-band Hα coronagraphic observations, 2006, Journées SF2A 2006, Paris, eds. D. Barret, F. Casoli, G. Lagache, A. Lecavelier, L. Pagani, p 557
- Turck-Chieze, S. et al., The magnetism of the solar interior for a complete MHD solar vision, Proceedings of 2005 ESLAB symposium 19-21 April 2005
- Meunier N. & équipe BASS2000, BASS2000: status, services and projects, Journées SF2A 2005, Strasbourg, eds. F. Casoli, T. Contini, J.M. Hameury, L. Pagani, p 169
- Meunier N., Rondi S., Tkaczuk R., Rieutord M. & Beigbeder F., CALAS: CAmera for the Large Scales of the solar surface, 2005, 22th Solar Sacramento Peak Workshop, Octobre 2004, ASP Conf. Series 346, p 169
- Meunier N., Rondi S., Tkaczuk R., Rieutord M. & Beigbeder F., CALAS: CAmera for the Large Scales of the solar surface, 2003, Journées SF2A 2003, p 93
- Lòpez Ariste A., Paletou F., & Meunier N., The technology Advanced Solar Telescope, 2003, Journées SF2A 2003, p 97
- Meunier N., Photospheric magnetic field structures derived from THEMIS spectroscopic observations, 2nd Franco-Chinese meeting, Meudon 2002 (**invité**)
- Meunier N., Observations of solar photospheric magnetic fields and differential rotation, Solar and Stellar Magnetism, Toulouse 2002 (**invité**), p 159
- Meunier N. & Kosovichev A., Velocity fields in a flaring active region, 2003, in ”THEMIS workshop”, Toulouse, 2002, p 79

- Meunier N. & Lopez-Ariste A., Solar co-spatiality in the THEMIS-MTR mode, 2003, in ”THEMIS workshop”, Toulouse, 2002, p 121
- Meunier N. & the BASS2000 team, BASS2000: status and prospectives, 2003, in ”THEMIS workshop”, Toulouse, 2002, p 137
- Meunier N. & Kosovichev A., Fast photospheric flows in a flaring active region, 2002, in ”Magnetic Coupling of the Solar Atmosphere” Euroconference and IAU Colloquium 188, p 505
- Meunier N., Arnaud J. & Vigneau J., Observations of intranetwork magnetic fields with THEMIS, 2002, Il Nuovo Cimento 25C (5-6), in ”THEMIS and the new frontiers of solar atmosphere dynamics”, Rome, March 19-21, 2001, p 659
- Fligge M., Solanki S., Meunier N. & Unruh Y., Solar surface magnetism and the increase of solar irradiance between activity minimum and maximum, 2001, in : ”The Solar Cycle and Terrestrial Climate”, Santa Cruz de Tenerife, September 2001, Proc. 1st Solar & Space Weather Euroconference, p 117
- Meunier N. & S.M. Jefferies, Modeling the solar oscillation l-ν power spectrum, SOHO6/GONG 98 Meeting (Boston), Structure and Dynamics of the Interior of the Sun and Sun-like Stars, ESA SP-418, p 267 (poster)
- Meunier N., Nesme-Ribes E. & Collin B., Observational study of turbulence in magnetic regions, Colloque ASPE 96 (Tenerife) 2-6 Octobre 1996, poster publié dans le rapport annuel JOSO 1996
- Livingston W., Wallace L., Gray D., Huang Y., Meunier N., Solanki S., White D. & Wang Y., Long-term Trends in Solar indices, Hermosilla, April 1996

II.3 Contributions à des conférences sans publication

- Meunier N. & équipe BASS2000, Le dépouillement de données spectropolarimétriques à BASS2000, 2005, Atelier Polarisation Nice, Mai 2005
- Meunier N., Rondi S., Tkaczuk R., Rieutord M. & Beigbeder F., CALAS : CAmera for the Large Scales of the solar surface, 2005, Atelier Polarisation Nice, Mai 2005
- Meunier N., Rondi S., Tkaczuk R., Rieutord M. & Beigbeder F., CALAS: CAmera for the Large Scales of the solar surface, 2004, Journées PNST Autrans, Janvier 2004
- Meunier N., Fractal analysis of MDI magnetograms, Spring AGU meeting (Boston), Juin 1998 (poster)
- Meunier N. & S.M. Jefferies, 2-D fitting of the m-averaged power spectrum, GONG-SOI Joint meeting, Stanford, 3-5 decembre 1997

- Bassom. A.P., Kuzanyan, K.M., Meunier, N., Proctor, M.R.E., Sokoloff, D.D., Soward, A.M. & Tobias, S.M., Asymptotic Properties of a Nonlinear alpha-omega-Dynamo Wave on a spatially varying background, Prague, 1997
- Meunier N. & Nesme-Ribes E., Analyse fractale des facules photospheriques, Journees scientifiques de la SFSA (Meudon), 1-3 April 1997
- Serre T., Meunier N., Nesme-Ribes E., Hoyt D. & Schatten K., Prediction of forthcoming activity solar cycles, Fall AGU meeting (San Francisco) 15-19 Dcembre 1996 (présentation par N. Meunier), Suppl. to Eos, Transactions, AGU 77 No. 46, 1996
- Meunier N., Sokoloff D. & Soward A., Asymptotic properties of non linear dynamo waves, Forum Themis (Meudon) 14-15 Novembre 1996
- Meunier N., Nesme-Ribes E. & Collin B., Fractal analysis of magnetic patterns, Forum Themis 14-15 Novembre 1996
- Meunier N., Propriétés asymptotiques d'une onde dynamo alpha-omega non linéaire, Lille, Workshop "Modélisation en dynamique des fluides géophysiques", 20-21 Février 1996

II.4 Publications de cours et vulgarisation

- Cours à l'Ecole d'Aussois (Dynamique des fluides stellaires, 2004) : Observations de la dynamique de la surface solaire, "Observations of the solar surface dynamics", dans "Stellar Fluid Dybamics and Numerical Simulations: From the Sun to Neutron Stars", eds. M. Rieutord and B. Dubrulle, p 221 (**invité**)
- Article de vulgarisation : N. Meunier, Le mystère des cycles solaires, La Recherche Hors Série Le Soleil N°15, 2004, p 16

II.5 Mémoires

- Mémoire de Thèse de doctorat : *Diagnostics observationnels du champ magnétique solaire : distribution spatiale, dynamique et processus de génération*, Université Denis Diderot, Thèse soutenue le 18/06/1997 (directrice de thèse : Elizabeth Nesme-Ribes)
- Mémoire de DEA : *Observations récentes des sondes Voyager à 40 et 50 UA : modélisation du fond diffus (900-1400 Å) et détection du lyman-alpha galactique*, Université Denis Diderot, Juin 1994 (directrice de stage : Rosine Lallement)

Annexe III

Enseignement, encadrements et vulgarisation

III.1 Cours

- Cours à l'International School of Space Science (The physics of the Sun : the active Sun on your desktop, Italie, 2006) : Active region analysis using scaling laws (cours et travaux pratiques)
- Cours Licence Université Paul Sabatier, 4h en 2004-2006 : Le Soleil
- Cours à l'Ecole d'Aussois (Dynamique des fluides stellaires, 2004) : Observations de la dynamique de la surface solaire, "Observations of the solar surface dynamics", dans "Stellar Fluid Dybamics and Numerical Simulations: From the Sun to Neutron Stars", eds. M. Rieutord and B. Dubrulle, p 221
- Cours à l'Ecole Doctorale Science de l'Univers de Strasbourg (2004) : Les relations Soleil-Terre

III.2 Encadrements

- Co-direction de la thèse de Ruben Tkaczuk (directeur M. Rieutord) 2002-2006, 4 articles à comité de lecture en commun
  - Tkaczuk, R., Rieutord, M., Meunier, N., Roudier, T., Tracking granules at the Sun's surface and reconstructing velocity fields. II. Error analysis, 2007, A & A, sous presse
  - Meunier N., Roudier, T., Tkaczuk R., Are supergranule sizes anti-correlated with magnetic activity ?, 2007, A & A 466, 1123
  - Meunier N., Tkaczuk R., Roudier T., Rieutord M., Intensity variations accross supergranules, 2007, A & A 463, 745
  - Meunier N., Tkaczuk R., Roudier T., Rieutord M., Velocities and divergences as a function of supergranule size, 2007, A & A 461, 1141

  - Meunier N., Rondi S., Tkaczuk R., Rieutord M. & Beigbeder F., CALAS: CAmera for the Large Scales of the solar surface, 2005, 22th Solar Sacramento Peak Workshop, Octobre 2004, ASP Conf. Series 346, p 169
  - Meunier N., Rondi S., Tkaczuk R., Rieutord M. & Beigbeder F., CALAS: CAmera for the Large Scales of the solar surface, 2003, Journées SF2A 2003, p 93

- Co-direction de la thèse de Sylvain Rondi (directeur M. Rieutord) 2002-2006, soutenue le 14/12/2006, 1 article à comité de lecture en commun
  - Rondi S., Roudier T., Molodij, G., Bommier V., Sütterlin P., Malherbe J.-M., Keil S., Meunier N., Mein P., Mein N., Schmieder B., Maloney P., Photospheric general context around dark filament, 2007, A & A 467, 1289
  - Rondi R., Roudier T., Molodij G., Bommier V., Malherbe J.M., Schmieder B., Meunier N., Rieutord M., Beigbeder F., Photospheric flows around a quiescent filament and CALAS first results, 2006, Conférence THEMIS Octobre 2006, ed. V. Bommier, sous presse
  - Meunier N., Rondi S., Tkaczuk R., Rieutord M. & Beigbeder F., CALAS: CAmera for the Large Scales of the solar surface, 2005, 22th Solar Sacramento Peak Workshop, Octobre 2004, ASP Conf. Series 346, p 169
  - Meunier N., Rondi S., Tkaczuk R., Rieutord M. & Beigbeder F., CALAS: CAmera for the Large Scales of the solar surface, 2003, Journées SF2A 2003, p 93

III.3 Vulgarisation

- Article de vulgarisation : N. Meunier, Le mystère des cycles solaires, La Recherche Hors Série *Le Soleil* N°15, 2004, p 16
- 4 Cours aux Université du Temps Libre à Toulouse et à Tarbes
- Plusieurs conférences dans des clubs d'astronomie et associations

Annexe IV

Collaborations

Mes collaborations passées (depuis la thèse), en cours et futures sont les suivantes :

- Etude de la supergranulation et projet CALAS (2000-) : T. Roudier, M. Rieutord, F. Beigbeder, S. Rondi, R. Tkaczuk (LATT)
- Dynamique dans les régions actives et le réseau magnétique, étude conjointe à l'aide de THEMIS et MDI/SOHO (2000–2003) : A. Kosovichev (Université de Stanford)
- Analyse des données spectropolarimétriques de THEMIS (2000–2003) : J. Arnaud, J. Vigneau (LATT)
- Etude de la dynamique photosphérique sous les filaments dans le cadre du JOP 178 (2004-) : T. Roudier (PI), S. Rondi, G. Molodij, V. Bommier, P. Sütterlin, J.-M. Malherbe, S. Keil, P. Mein, N. Mein, B. Schmieder (LATT, LESIA, LERMA, Utrecht, NSA/Sacramento Peak)
- Héliosismologie, analyse 2-D des spectres de puissance solaires (1995–2000) : S. Jefferies (NSO/Tucson)
- Traitement de données spectropolarimétriques THEMIS à BASS2000 (2003–2007) : M. Lafon, P. Maeght, P. Mein, A. Sainz Dalda, A. Lòpez Ariste, V. Bommier (LATT, THEMIS, LERMA)
- Analyse des donnés Hα du coronographe du Pic du Midi (2005–2007) : D. Romeuf, J.-C. Noëns, S. Koutchmy, R. Jimenez, O. Wurmser, S. Rochain, M. Lafon (LATT, IAP, Observateurs associés)
- Magnétisme des étoiles M et exoplanètes (2007-) : X. Delfosse, T. Forveille (LAOG)

Annexe V

Articles

Les articles suivants, correspondant à mes travaux après la thèse, sont inclus ci-après dans cet ordre :

- Meunier N., Fractal analysis of MDI magnetograms: a contribution to the study of the formation of solar active regions, 1999, Astrophys. J., 515, 801
- Meunier N., Large scale dynamics of active regions and small photospheric magnetic features, 1999, Astrophys. J., 527, 967
- Meunier N. & Jefferies S.M., Two-Dimensional Modeling of the Solar Oscillation l-ν Power Spectrum, 2000, Astrophys. J., 530, 1016
- Meunier N., Statistical properties of magnetic structures: their dependence on scale and solar activity, 2003, A & A 405, 1107
- Meunier N. & Kosovichev A., Fast photospheric flows and magnetic field in a flaring active region, 2003, A & A 412, 541
- Meunier N., Complexity of active regions: flares and cycle phase dependence, 2004, A & A 420, 333
- Meunier N., Magnetic network dynamics: activity level, feature size and anchoring depth, 2005, A & A 436, 1075
- Meunier N., Large-scale dynamics and polarities of magnetic structures, 2005, A & A 437, 303
- Meunier N., Temporal variations in the magnetic network large-scale dynamics, 2005, A & A 442, 693
- Meunier N., Large-scale photospheric dynamics below coronal holes, 2005, A & A 443, 309
- Meunier N., Tkaczuk R., Roudier T., Rieutord M., Velocities and divergences as a function of supergranule size, 2007, A & A 461, 1141
- Meunier N., Tkaczuk R., Roudier T., Rieutord M., Intensity variations accross supergranules, 2007, A & A 463, 745
- Meunier N., Roudier T., The superrotation of supergranules, 2007, A & A 466, 691

- Meunier N., Roudier, T., Tkaczuk R., Are supergranule sizes anti-correlated with magnetic activity ?, 2007, A & A 466, 1123

The Astrophysical Journal, 515:801–811, 1999 April 20

FRACTAL ANALYSIS OF MICHELSON DOPPLER IMAGER MAGNETOGRAMS: A CONTRIBUTION TO THE STUDY OF THE FORMATION OF SOLAR ACTIVE REGIONS

N. Meunier

W. W. Hansen Experimental Physics Laboratory, Annex A207, Stanford University, Stanford, CA 94305-4085; nadege@quake.stanford.edu

Received 1998 July 13; accepted 1998 November 24

ABSTRACT

In this paper a fractal analysis of active regions observed by the Michelson Doppler Imager (MDI) instrument on the *SOHO* spacecraft is performed. The purpose of such an analysis is to study the shape of these magnetic regions via their fractal dimension, which characterizes their complexity, and to deduce some information on the processes that led to their formation. Both full disk and high-resolution MDI magnetograms are used and the fractal dimensions using the perimeter/area relation (d_1) and the linear size/area relation (d_2) are calculated. A statistical analysis of the estimate of a fractal dimension is performed, as well as that of the influence of noise on it. The fractal dimension for a range of sizes is calculated. The fractal dimension d_1 is found to increase with the area of the active regions (from 1.48 for supergranular size structures to 1.68 for the largest structures). The fractal dimension d_2 also increases with the area of the active regions (from 1.78 to 1.94). The fractal dimension d_1 decreases with the magnetic threshold for moderate sizes and increases for the largest structures. The high-resolution results match those of full disk magnetograms when the images are degraded. This fractal analysis is performed in relation to the size distribution properties: the two analyses provide complementary information. Then some models of active regions very similar to those of Wentzel & Seiden are introduced to interpret the observations in terms of a percolation process at the bottom of the convective zone and diffusion at the surface. These models lead to structures that are more complex than the observed structures.

Subject headings: Sun: activity — Sun: faculae, plages — Sun: magnetic fields — Sun: photosphere

1. INTRODUCTION

The distribution of the solar surface magnetic fields is very complex, and its study provides information about the generation processes leading to solar active regions. However, a direct comparison between observed images and modeled images would be difficult, so one must find parameters to describe the structures in a simple way. The fractal dimension, which allows the characterization of their complexity, is thus a useful tool to test models of formation of active regions. A certain number of observations lead to such a fractal analysis of active regions. First, observations show the self-similarities of these magnetic structures, particularly in the photosphere. Self-similarity means the same degree of complexity regardless of the scale at which the structures are observed. Second, the size distribution of active regions (Harvey 1993; Harvey & Zwaan 1993) exhibits a power law, which is characteristic of an underlying fractal pattern. Third, measurements of diffusion coefficients of magnetic flux elements show large discrepancies. This could be due to anomalous diffusion, which is different from the classical diffusion for which $\langle r^2 \rangle$ is proportional to t (see Lawrence & Schrijver 1993, and references therein).

In this paper, the prime motivation is to study the fractal dimension of active regions, both observationally and theoretically. Fractal analysis allows one to quantify the degree of complexity of these structures. Once a geometrical description is performed (which provides the fractal dimension of the observed structures), the next step is to model this description in term of physical processes. The only published models of active regions that are suitable to a fractal analysis (i.e., which produce *maps* of magnetic fields at the solar surface) are those of Wentzel & Seiden (1992) and Seiden & Wentzel (1996). Note that another approach of this problem is provided by Schrijver et al. (1997), who study the histogram of magnetic fluxes in active regions. The interpretation of the fractal appearance of solar active regions is related to the spatial distribution of magnetic flux tubes. This distribution of the magnetic field at the surface is probably strongly connected to the mechanisms for the generation of magnetic field deep at the bottom of the solar convective zone or in the overshoot layer, to the rise of magnetic flux from the generation zone to the surface, and to surface phenomena such as the diffusion of flux tubes and their interaction with the convective pattern. Fractal analysis then provides clues to help us understand these complex mechanisms because the fractal dimension can be used to test models.

The main results concerning the fractal dimension of solar active regions that have been obtained up to now are the following: Ruzmaikin, Sokoloff, & Tarbell (1991) studied magnetograms with both high spatial resolution (0$''$.6 per pixel) and moderate resolution (2$''$.5 per pixel). They defined the fractal dimension as the slope of the curve representing the area covered by the active regions versus the pixel size (in a log/log plot). For the first type of observations they obtained a fractal dimension decreasing from 1.71 to 1.49 for magnetic thresholds between 200 and 800 G, and decreasing from 1.42 to 1.19 for magnetic thresholds between 12 and 48 G in the second case. The study of the relation between the fractal dimension and the threshold is important because the choice of a given threshold is necessary but arbitrary. It allows different parts of active regions to be studied. Balke et al. (1993) analyzed a few high-resolution magnetograms (1/3$''$ per pixel). They determined the fractal dimension of small structures (areas between 4 and 20 pixels only) by using the relation between the area and the linear size of the structures (see § 3.1.2). They did not detect any systematic variation of the fractal dimension with the magnetic threshold between 200 and 900 G and obtained an average fractal dimension of 1.54. More recently, Nesme-Ribes, Meunier, & Collin (1996) estimated the fractal dimension from a data set of 1000 faculae larger than the supergranular scale determined from Meudon spectroheliograms (with a pixel size of $1\farcs8$). They found a fractal dimension of 1.72 by using the area/linear size relation, 1.60 by using the area/pixel size relation, and 1.64 by using the relation between perimeter and area (see § 3). Their results were not in good agreement with the ones obtained by Balke et al. (1993). However, different samples and spatial resolutions might explain these differences. So the analysis of a very large data set remained to be performed, which is the purpose of this paper.

The outline of this paper is as follows. In § 2 the data sets used to perform the fractal analysis are described: the full disk and high-resolution Michelson Doppler Imager (MDI) magnetograms (denoted hereafter, respectively, as FD and HR magnetograms). The necessity of studying a very large number of structures to perform a reliable measurement of the fractal dimension is then emphasized. In § 3 the fractal dimension using two methods that will prove to be complementary is calculated. The main difficulties that arise when one tries to measure the fractal dimensions of observed structures are discussed. The results obtained from the analysis of FD magnetograms are presented in § 4, whereas in § 5 the results obtained from HR magnetograms are presented. The importance of the spatial resolution is explored; this question is crucial because the magnetic flux tubes are not resolved. Models that provide fractal dimension estimates and size distributions are presented in § 6. These characteristics can be compared with the results obtained in §§ 4 and 5. Finally, the results are discussed in § 7 and some perspectives are presented.

2. THE DATA SETS

2.1. *Full Disk MDI Magnetograms*

The active regions are observed on FD magnetograms obtained by MDI on the *SOHO* spacecraft (Scherrer et al. 1995). These magnetograms constitute maps of the line-of-sight component of the magnetic field, averaged over the resolution element. They are obtained from observations made in the Ni λ6768 spectral line and represent magnetic structures at a height of approximately 200 km above the $\tau_{5000} = 1$ level (Jones 1989). These data are unaffected by seeing, so they are particularly appropriate for this research, which is very sensitive to any variations in spatial resolution. The pixel size is $2''$ (with a spatial resolution of $4''$). The telescope is slightly defocused to match the spatial resolution with the pixel size in order to avoid aliasing. An example of such a magnetogram is shown in Figure 1.

One image is available every 96 minutes. However, some gaps are present due to defects in image processing on the spacecraft, especially at the beginning of the time series. Images from 1996 April 30 to 1998 February 4 are used, which comprise a data set of 7929 FD magnetograms. The data set contains two types of magnetograms. Some images are individual 1 minute magnetograms, whereas others are averaged over 5 minutes. This leads to different noise levels: 8 G in the averaged magnetograms and 15 G in the single magnetograms. Note that this noise level includes both actual noise from the observations and a solar contribution due to small-scale weak magnetic fields. The histogram of the whole time series is shown in Figure 2 for the two types of images. The central peak (up to a few tens of Gauss) mainly represents the noise. The long tails correspond to pixels in active regions. The small number of pixels with very large magnetic fields makes the difference between the different types of magnetograms not very significant. The calibration of the MDI magnetograms may differ from those for other instruments, which means that a value of, for example, 50 G in the MDI images does not necessarily correspond to a value of 50 G in magnetograms from other data sets.

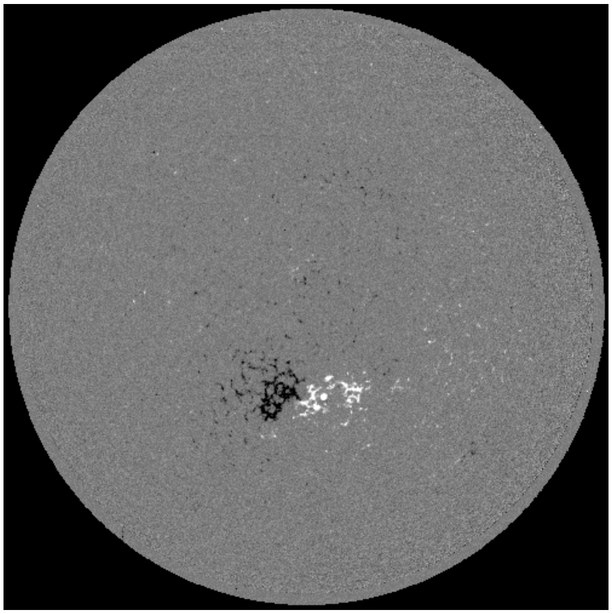

FIG. 1.—Full disk Magnetogram of 1996 August 30

The magnetic threshold issue will be discussed in the following sections. However, a rough estimate of the size distribution of magnetic structures can be made from the following sample: for a threshold of 40 G, it is possible to recognize 221,507 structures with areas larger than 30

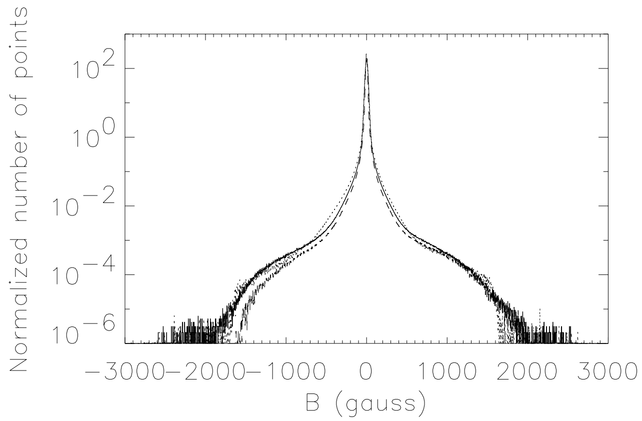

FIG. 2.—Histograms of the three types of magnetograms. *Solid lines:* Single FD magnetograms (4013 images). *Dashed lines:* Averaged FD magnetograms (3916 images). *Dotted lines:* HR magnetograms (783 images). They have been normalized to the same number of pixels: respectively, 1,920,320, 1,767,730, and 3,795,910 pixels have been used to calculate these histograms.

pixels,[1] 17,529 with areas larger than 300 pixels, and 4108 with areas larger than 1000 pixels.

2.2. *High-Resolution MDI magnetograms*

The pixel separation of the HR magnetograms obtained by MDI is 3 times better than that for the FD magnetograms: 0″.625 for the former, which provides a spatial resolution of 1″.25. This resolution corresponds to the diffraction limit of the instrument. Images have a size of 1024 × 1024 pixels and are centered on a position approximately 160″ north of the disk center. One image per hour is examined, but there are many gaps in the data set. A data set containing 783 images between 1996 May 1 and 1997 November 9 is used. At a threshold of 40 G, it is possible to recognize 676 structures with an area larger than 1000 high-resolution pixels (note that the areas must be divided by 9 to be compared with results from the FD magnetograms) and 131 with an area larger than 9000 high-resolution pixels. The noise level is 15 G, which is similar to that for the single FD magnetograms.

3. METHOD AND LIMITATIONS

3.1. *Calculation of Fractal Dimensions*

3.1.1. *Recognition of Active Regions*

The first step for calculating the fractal dimension of active regions is to determine their contours. The absolute value of the magnetic fields is taken. Then the contours are determined on these new maps for a given magnetic threshold. From these contours the areas and perimeters of the active regions are determined. Different thresholds allow study of the behavior of active regions close to the center of the regions or far from it (see § 4.2).

The contours are corrected for projection effects. The structures that are too close to the limb (farther than 53° from disk center) are also eliminated from the analysis because they present large distortions.

3.1.2. *Methods of Calculating a Fractal Dimension*

Once the contours of the structures are determined, the fractal dimension can be calculated. Two different methods are used:

1. *The relation between the area and perimeter of active regions.*—A first fractal dimension d_1 is defined by

$$d_1 = 2\,\frac{\Delta \log P}{\Delta \log A}\,, \tag{1}$$

which corresponds to twice the slope of the variation of perimeter P with area A on a log/log scale. The fractal dimension d_1 is called the Hausdorff dimension. If the active regions were perfect circles, or squares, then d_1 would be unity. The more denticulate the structure, the closer d_1 is to 2. This definition is very convenient and has been widely used (see, for example, Mandelbrot 1983). An example of the perimeter versus the area is shown in Figure 3.

2. *The relation between area and linear size.*—In this second method, the fractal dimension is deduced from the relation between the area A and the linear size L where L is defined as the perimeter of the smallest square box containing the structure. The box sides lie parallel to the longitudes and meridians. The fractal dimension d_2 is then defined by

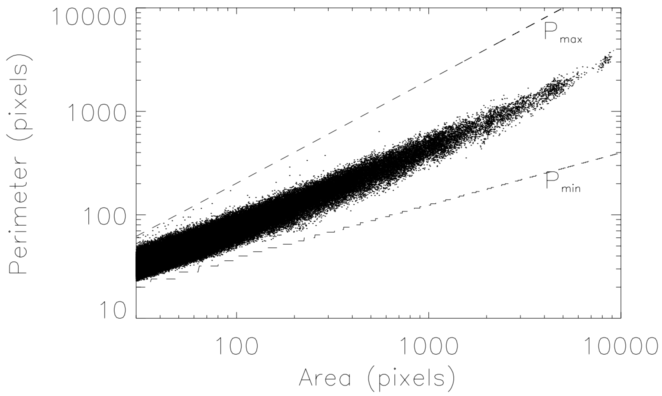

FIG. 3.—P versus A for the whole data set of FD magnetograms for a threshold of 40 G and area larger than 30 pixels. The dashed curves represent the minimum value $P_{\rm min}$ and the maximum value $P_{\rm max}$ that can be taken by the perimeter for a given area (see text).

$$d_2 = \frac{\Delta \log A}{\Delta \log L}\,. \tag{2}$$

In this case, the more denticulate the structure the smaller d_2, with d_2 equal to two for nonfractal structures. This method has been used to study solar magnetic regions by Balke et al. (1993).

It is appropriate to use the two methods simultaneously because they provide complementary information. However, the most useful one will be the first method because it is more sensitive to the complexity of the structures. For example, some fractal curves that exhibit a fractal dimension $d_1 > 1$ have $d_2 = 2$, which would suggest that these structures are not fractal. On the other hand, fractal structures with large d_1 generally appear more complex than those with d_1 close to 1. Therefore, from this point d_1 will be regarded as synonymous with the "complexity" of the structure, i.e., a greater d_1 will be regarded as characterizing a more complex structure. I chose these two methods instead of others because it is then possible to separate the regions easily into different data sets. This would allow us to recognize local effects such as may enter into the relation between the fractal dimension and the occurrence of flares.

3.1.3. *The Prefactor*

Fractal analysis usually consists of the calculation of a fractal dimension, i.e., on the exponent in the relation between perimeter P and area A, as in my first method, for example. This relation can be written as

$$P(\delta) = k(\delta)A(\delta)^{d_1/2}\,, \tag{3}$$

where δ is the scale (i.e., the spatial resolution) used to make the measurement. The factor k is not constant and obeys the expression:

$$k(\delta) = C\delta^{d_1 - 1}\,, \tag{4}$$

where C is a constant for a given type of structure and is called the prefactor. The values of $\delta = 2$ for the FD magnetograms and $\delta = 0.625$ for the HR magnetograms will be used, according to their spatial resolution in arcseconds.

The prefactor can provide information on the gaps present in the structures, or on their shape. For example, C

---

[1] Since structures are corrected for projection effects, one pixel in the rest of this paper corresponds to the size of one pixel of 2″ at the disk center, unless stated otherwise.

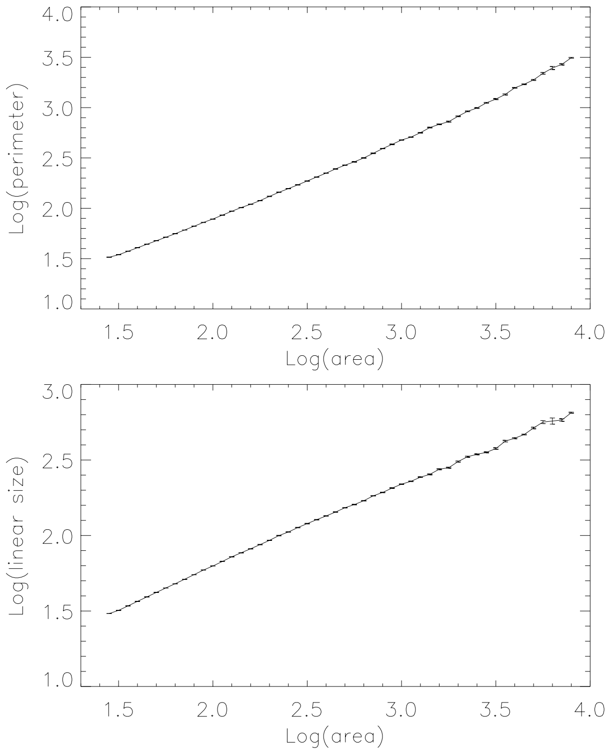

FIG. 4.—*Top:* Average perimeter P versus the area A for the whole data set of FD magnetograms for a threshold of 40 G and area larger than 30 pixels. The interval in area is $\Delta \log A = 0.05$. *Bottom:* Similar relation between L and A. A, P, and L are in pixels.

is larger when the structures are more elongated. In the following, this prefactor C will also be studied to check whether it can provide complementary information. In the case of the second method (d_2), the prefactor does not depend on δ, but is also related to the texture and shapes of the structures. Note that Hetem & Lepine (1993) performed tests on simulated data and showed that the fractal dimension and the prefactor C are not completely independent, thus concluding that C does not provide additional information on the structures.

3.2. *Limitations*

There are a number of difficulties in measuring the fractal dimension of observed solar structures:

1. *Statistical self-similarity.*—Because the self-similarity of the solar structures is only statistical, there is an intrinsic dispersion in the estimate of the fractal dimension.

2. *Limited scale.*—The self-similarity is not valid for all scales from 0 to infinity. The highest scale corresponds to the largest observed structure. The smallest scale is the size of magnetic elements. Furthermore, even in the observed range, the mechanisms responsible for the observed fractal dimension can vary depending on the structure size, which could lead to a variation of the fractal dimension.

3. *Finite spatial resolution.*—All solar data are obtained with limited spatial resolution. Different methods can be used to determine the fractal dimension from the observed structures, for example, the two methods described in § 3.1.2. However, these methods will give the same result only in the limit of perfect spatial resolution. Furthermore, because of the limited resolution for a given area A the perimeter P must always lie between two extreme values, $P_{\min}$ and $P_{\max}$, defined as

$$P_{\max}(A) = 2A + 2 \tag{5}$$

and

$$P_{\min}(A) \approx 4 \text{ Int } (\sqrt{A}) \ , \tag{6}$$

where Int represents the integer part (Brandt, Greimel, & Guenther 1991). These two limits are shown in Figure 3. For small structures, no determination of the slope (and thus of d) is possible. The problem with the second definition of the fractal dimension is similar. The question that arises then is "Above what size is it possible to measure a reliable fractal dimension?" Vogelaar & Wakker (1994) conducted some experiments measuring the fractal dimension of molecular clouds. They showed that measurements were generally reliable above 30 pixels, which is the value that will be used in the next sections.

4. *Effects of noise.*—Because of the noise in the images, the magnetic threshold must be chosen significantly above the noise level. Indeed, for a threshold close to the noise level, the perimeters are artificially lengthened and the estimated fractal dimension increased. Vogelaar & Wakker (1994) have made some tests to quantify the influence of noise on the fractal dimension estimate. They showed that the fractal dimension was much more sensitive to the noise when the structures were not very complex, and on the other hand it was not very sensitive for very complex structures. The effect was larger for low signal to noise ratio, and they deduced that the noise had a negligible effect for structures 3 σ above the noise level. Because MDI magnetograms have different noise levels, it is crucial to quantify this effect on these magnetograms. Some tests have been performed by adding Gaussian noise of various rms values to the original images. There is a variation in the estimate of the fractal dimension for magnetic thresholds up to 5 σ above the noise level in the case of HR magnetograms. The effect is significant for the smallest structures and is negligible for structures larger than 1000 pixels. For example, for areas around 100 pixels, d_1 must be decreased by ~ 0.1 at $B = 40$ G and by ~ 0.03 at $B = 80$ G. The influence of the noise on the estimate of the fractal dimension from FD magnetograms is qualitatively the same as for the HR magnetograms. However, the amplitude of the variations due to the noise is then slightly smaller. A similar analysis of the fractal dimension d_2 shows that its estimate also increases as the noise level increases. The prefactor C and the size distribution of active regions seem to be less sensitive to the noise than the fractal dimension.

5. *Projection effects.*—Some projection effects could influence the fractal dimension estimate. (1) The spatial resolution is better close to the disk center. (2) Close to the limb, the measured magnetic field is averaged over a larger surface and thus the measurement might vary. (3) The magnetic field in active regions is predominantly vertical, so the measured magnetic field (which is the line-of-sight component) decreases as the distance to disk center increases. Thus the magnetic threshold corresponds to different intrinsic values of magnetic field with the distance to the disk center. (4) The noise level seems to be slightly higher far from disk center.

The fit on the curve P/A is made as follows. An average value of the perimeter for each area interval is calculated (the width of the intervals is constant in log A). Such curves are shown in Figure 4 for $\Delta \log A = 0.05$, which is the value used in this paper. Then, the slope on this new curve in a certain range in A is calculated: this provides the fractal dimension on overlapping running windows of various sizes $\Delta \log A$ to study more precisely the dependence of the fractal dimension estimate on the size of the structure. Because the problem is symmetric in A and P, a good estimate of the slope is obtained by using the bisector (Isobe et al. 1990). The results presented in the following sections are obtained from a least-square minimization providing the bisector slope. The method is similar for the second calculation method, which is based on the relationship between the linear size and the area L/A.

4. FRACTAL DIMENSION FROM THE FULL DISK MAGNETOGRAMS

4.1. *Variation in the Fractal Dimension with Area*

Figure 5 shows the variation of the fractal dimensions d_1 and d_2 with the region size for the whole data set of FD magnetograms and regions larger than 30 pixels. A magnetic threshold of 40 G has been used for this plot, which corresponds to 3 times the sensitivity level for the single magnetograms and 5 times that for the averaged magnetograms. The slope has been calculated over a range slightly greater than 1 order of magnitude in area ($\Delta \log A = 1.5$) from the plots of Figure 4 (bin size in area of $\Delta \log A = 0.05$). Figure 5 also shows the variation in the prefactor C (calculated under the same conditions) and the size distribution for a bin size of $\Delta \log A = 0.05$.

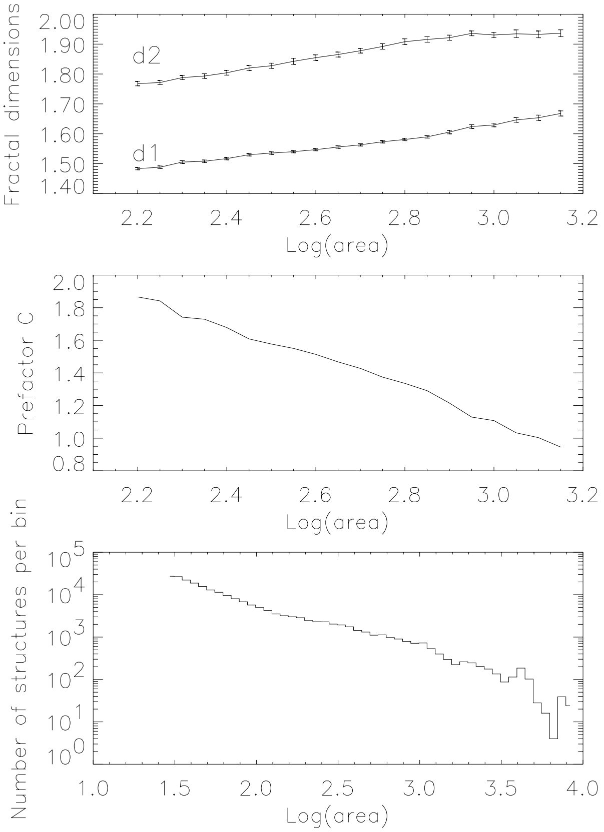

FIG. 5.—*From top to bottom:* d_1 and d_2 vs. A for the whole FD magnetogram data set, a magnetic threshold of 40 G, and $\Delta \log A = 1.5$; C vs. A and N vs. A calculated in boxes of size $\Delta \log A = 0.05$. The areas are in pixels and larger than 30 pixels.

The fractal dimension d_1 increases with increasing domain in area, so that the structures seem to be less complex at lower sizes. The variation of the prefactor is consistent with this result. Different factors could lead to such a variation: spatial resolution effects, noise, or intrinsic properties. Another important characteristic is that d_1 and d_2 appear to be *correlated*. However, from their respective definitions, we would expect them to be anticorrelated because d_1 is the fractal dimension of the contour and d_2 is the fractal dimension of the surface (see § 3.1.2). The general trend exhibits a correlation that is not easy to explain. As noted in § 3.1.2, d_2 is less sensitive than d_1. It is also less sensitive to gaps inside the structures, for example. If the two types of FD magnetograms (single and averaged over 5 minutes) are considered separately, the results are not significantly different.

The calculation of the statistical errors, which are based on the dispersion of the perimeters and areas, assumes that all points are independent. However, within the 96 minutes separating consecutive magnetograms, structures are distorted but not completely independent. This means that the statistical errors on the fractal dimension have probably been slightly underestimated.

Another interesting property is the size distribution of active regions (which has been studied by other authors, for example, Harvey 1993). The size distribution appears to be close to a power law, i.e., constant slope in a log-log plot. The power law for a threshold of 40 G over the entire time series is shown in Figure 5. A slope of -1.20 ± 0.04 for all structures larger than 30 pixels is found. Harvey & Zwaan (1993) observed a power law for the distribution of smaller active regions and an exponential distribution for the largest ones. However, the latter is hardly seen on MDI images, probably because the epoch of our study was one of low activity. It is possible to separate the distribution into two power laws, with structures smaller than about 1000 pixels having a slope of -1.03 ± 0.03, and those larger than 1000 pixels a slope of -1.8 ± 0.26. Furthermore, Harvey & Zwaan (1993) obtained a slope of -1.91, which is much steeper than the one found in the present work. This is probably due to a difference in the selection of the structures: a given structure is counted in each image, whereas they count a given structure only once in its lifetime, at the time of its maximum size.

Our results are close to those obtained by Nesme-Ribes et al. (1996) studying calcium plages at the photospheric level, particularly for d_1. They observed a variation in d_1 with A below 300 pixels[2] (see Fig. 4 of their paper) that is close to what is found here, and for A larger, they found a value of 1.64, close to ours. However, the comparison with other results such as those of Ruzmaikin et al. (1991) and Balke et al. (1993) is difficult because they studied a very small sample. However, Balke et al.'s results are in good agreement with an extrapolation of the d_2 curve from Figure 5 to the small size they consider.

4.2. *Variation in the Fractal Dimension with the Magnetic Field Threshold*

Figure 6 displays an active region (NOAA 7986) at different magnetic thresholds. We can see the effects of noise on

---

[2] This is equivalent to 370 pixels from full disk MDI magnetograms and corresponds to the supergranular scale.

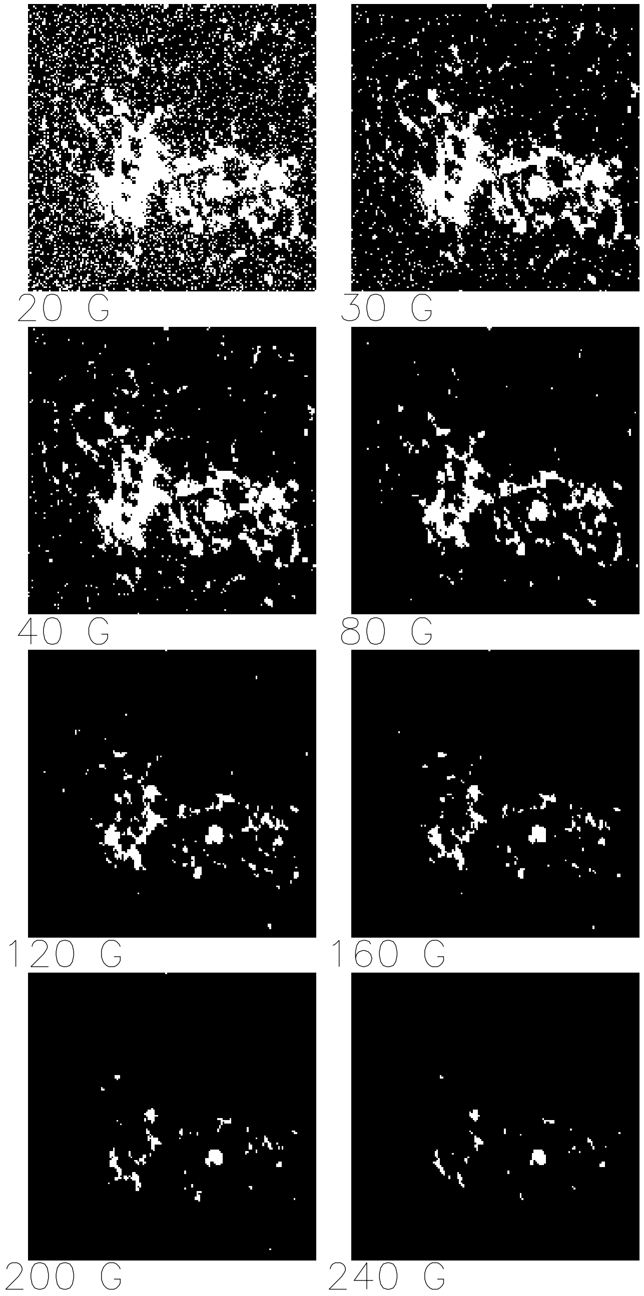

FIG. 6.—NOAA active region 7986 (1996 August 27) shown using different magnetic threshold (absolute value of the magnetic field): 20, 30, 40, 80, 120, 160, 200, and 240 G. From a single full disk magnetogram. The size of the region is 400″.

the images at the lowest thresholds. In Figure 7, d_1 is plotted versus the area (the slope is calculated over the range $\Delta \log A = 1.5$) for different thresholds (from 40 to 240 G) for sizes larger than 30 pixels. Above 240 G there are very few structures, so it was not possible to study higher thresholds.

The fractal dimension d_1 decreases as the magnetic threshold increases for areas lower than 400 pixels. Larger structures are observed only for thresholds up to 120 G and exhibit an increasing d_1 with increasing magnetic threshold. The other fractal dimension, d_2, exhibits an anticorrelated behavior. This means that magnetic structures of moderate size are less complex at higher magnetic thresholds, i.e., closer to the core of the region. The larger structures could have an opposite behavior, although it is less significant because of the lack of very large structures. The pivot point between the moderate sizes and the large sizes appearing on the curves in Figure 7 defines a characteristic size that is close to the supergranular scale. The effects of noise decrease as the threshold increases, so that d_1 is overestimated for the lowest magnetic thresholds. However the observed trend is still significant. Note a difficulty in the direct comparison of the curves: a given structure corresponds to a smaller area when the magnetic threshold increases. Furthermore, the structure could be cut in several parts so that it would correspond to even smaller areas.

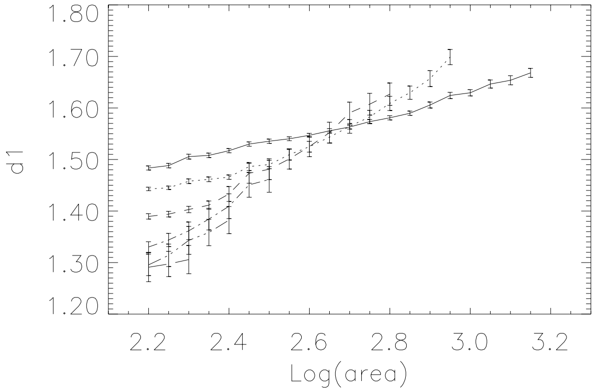

FIG. 7.—d_1 versus A for various magnetic thresholds for the whole set of FD magnetograms. The areas are in pixels and larger than 30 pixels. The slope has been calculated over a range $\Delta \log A = 1.5$. Separate curves correspond to various magnetic thresholds: *solid line*, 40 G; *dotted line*, 80 G; *dashed line*, 120 G; *dot-dashed line*, 160 G; *triple-dot–dashed line*, 200 G; *long-dashed line*, 240 G.

The following interpretation can be proposed: it is well known that the magnetic pattern in the quiet Sun is comprised largely of flux tubes that move along the intergranular lanes. However, inside plages, the granules are smaller or absent (Title et al. 1992), and thus the structures should be less complex (in that case with fewer gaps) close to the core of the regions where the field is the strongest. A small number of sunspots could also be responsible for part of the small d_1 of small structures at large magnetic thresholds. Note that Ruzmaikin et al. (1991) observed a trend that is opposite to the one we find for most of our structures (of moderate size), and Balke et al. (1993) did not observe any systematic effect.

The variation of the prefactor, C, with the magnetic threshold is anticorrelated with that of d_1, so it does not provide any additional information. The size distribution does not exhibit any strong variation as the magnetic threshold is increased.

4.3. *Variation in the Fractal Dimension with Time*

The structures in the data set have been separated into six successive periods of 106 days each. The corresponding fractal dimension d_1 versus the area A is shown for each of these periods in Figure 8 for a threshold of 40 G. The corresponding curves for d_2 exhibit a strong anticorrelation. The curves exhibit large differences that are very likely to be real. They do not exhibit any particular trend with time, and there is no significant correlation with the activity level determined by the Wolf numbers during these periods. They

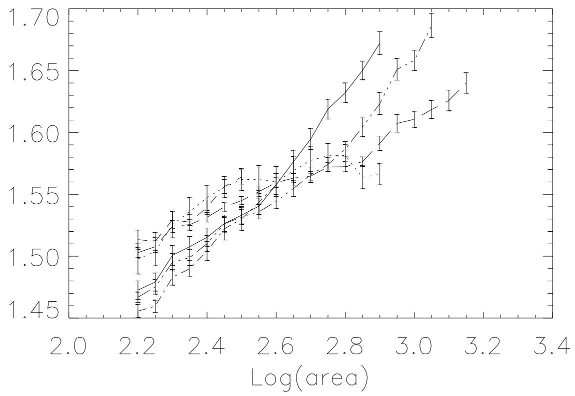

FIG. 8.—d_1 vs. area calculated over range $\Delta \log A = 1.5$ on curves P versus A (bins of $\Delta \log A = 0.05$) for different subsamples (threshold of 40 G on FD magnetograms). The areas are in pixels and larger than 30 pixels: *solid line*, period 1; *dotted line*, period 2; *dashed line*, period 3; *dot-dashed line*, period 4; *triple-dot–dashed line*, period 5; *long-dashed line*, period 6.

probably represent the dispersion of the fractal dimension from one structure to another.

4.4. *Variation in the Fractal Dimension with Polarity*

The results described above have been obtained by studying the absolute value of the magnetic field. However, the two polarities present in active regions are also part of their complexity. A simple way to study the effect of polarity is to perform a similar study on the different polarities separately. The results are as follows. For large magnetic thresholds (above 120 G), d_1 is smaller for positive magnetic fields than d_1 for the absolute magnetic fields by approximately 0.04. For negative magnetic fields, d_1 is larger by a similar amount. For 40 G, both curves are smaller than for the absolute value by 0.04, whereas for 80 G the results are intermediate. Separation of the structures in the northern and southern hemispheres leads to similar results for a given polarity, so the observed difference does not seem to be related to the leading/following properties.

5. FRACTAL DIMENSION FROM THE HIGH-RESOLUTION MAGNETOGRAMS

In this section a similar analysis of the HR magnetograms provided by MDI is performed. This is a very good opportunity to observe the magnetic structures under the same conditions except for the spatial resolution, since this is a very sensitive parameter in the estimate of the fractal dimension. Recall that the spatial resolution of the HR magnetograms is 3 times better than for the FD magnetograms. The time series is more homogeneous, since these are all single magnetograms, so they all exhibit a similar noise level. However, the sample is reduced compared to the FD magnetogram time series (less than half of the largest active regions observed on the FD images appear in the HR magnetograms). Even when images are taken at the same time, the field of view is smaller in the case of the HR magnetograms, so that some regions cannot be analyzed. Thus there is a lack of large regions.

At low magnetic thresholds (40 or 80 G), the estimated fractal dimension exhibits a variation with A similar to that obtained from FD magnetograms for the same days, although d_1 is higher for the HR magnetograms (Fig. 9). An interesting point is that if those HR magnetograms are degraded by factors of 2 and 4, fractal dimensions closer to the ones obtained from the FD magnetograms are obtained.

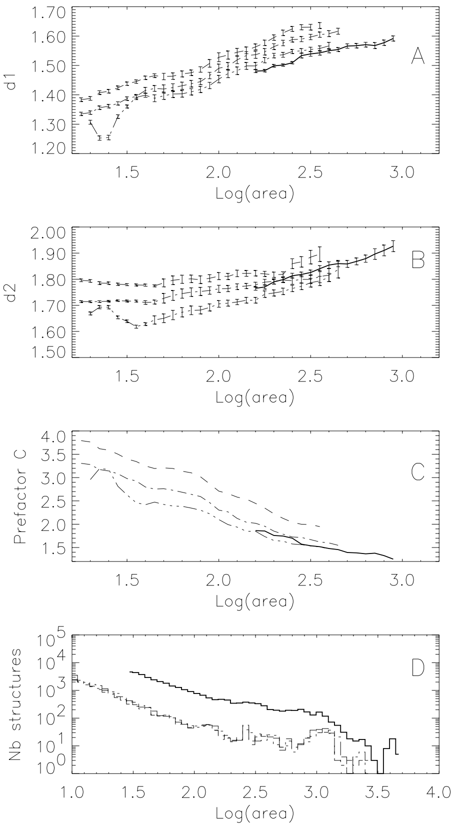

FIG. 9.—(*a*) d_1 versus the area for a threshold of 40 G: *solid line*, FD magnetograms; *dashed line*, HR magnetograms (original); *dot-dashed line*, HR magnetograms (degraded by a factor of 2); *triple-dot–dashed line*, HR magnetograms (degraded by a factor of 4). The curves for HR magnetograms have been shifted toward smaller areas by 0.95 (i.e., log 9, scaling factor between pixel sizes). The area is in "FD" pixels. (*b*) Same for d_2. (*c*) Same for the prefactor C. (*d*) Same for the size distribution, calculated for $\Delta \log A = 0.05$.

The variation of the fractal dimension d_1 with the magnetic threshold is shown in Figure 10. For magnetic threshold up to 240 G, d_1 is increasing slightly: curves are then similar to the curves obtained for the large structures on FD

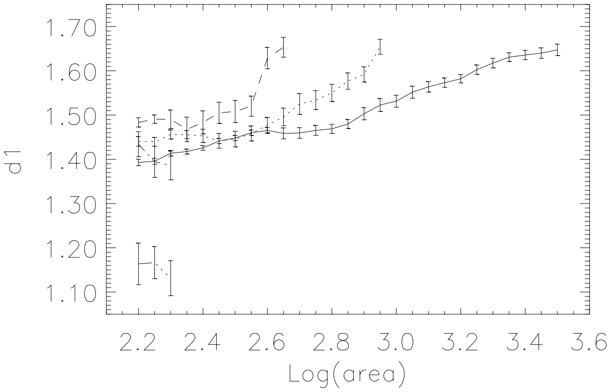

FIG. 10.—Fractal dimension d_1 versus the area for HR magnetograms for different thresholds: *solid line*, 40 G; *dotted line*, 120 G; *dashed line*, 200 G; *dot-dashed line*, 300 G; *triple-dot–dashed line*, 400 G. A is in "HR" pixels.

magnetograms at thresholds up to 120 G. Between 200 and 240 G there is a drop in d_1 similar to that obtained from the FD magnetograms above 120 G. This could be partly related to the different "magnetic level" in the two time series (see Fig. 2): a given threshold on the HR magnetogram corresponds to a lower threshold on the FD ones.

The variation of d_2 with magnetic field is anticorrelated with that of d_1. The prefactor C is very close to that obtained from the FD magnetograms. The behavior of C as the magnetic threshold increases is anticorrelated with that of d_1, as observed for the FD magnetograms.

The slope of the size distribution of the structures at a threshold of 40 G is -1.20 ± 0.05 for all structures larger than 30 pixels. At higher thresholds it is close to unity, as for the part of the FD distribution corresponding to structures of moderate sizes.

6. MODELS OF PHOTOSPHERIC ACTIVE REGIONS

6.1. *Objectives and Principles*

In the present section models of active regions are described in order to compare the fractal dimension estimated for these models with the observations presented in the two previous sections.

These models affect the distribution of flux tubes, the smallest structures that are considered here. The interactions between these flux tubes are described in a very simple way, using a discrete approach to the flux tube representation. It would be very difficult to model the distribution of the detailed magnetic field profile within the flux tubes (including its physical properties) at the same time as the stochastic distribution of these flux tubes on a large scale. In the following the distribution of pixels occupied by one or several flux tubes is thus addressed. The models described here are very close to the ones of Wentzel & Seiden (1992) and Seiden & Wentzel (1996). They have described models of active regions based on this approach in order to study the size distribution of active regions. They scaled their pixel size to 4000^2 km^2. Note that the pixel (or cell) size is in fact related to the distance scale for which the "stimulation" of new emerging flux tubes by existing flux tubes in terms of percolation (see § 6.2) is efficient. The appropriate scale for characterizing photospheric flux tubes this way is not known. If the scale is small, then one must degrade the resolution of model images to match the spatial resolution of the observations. For the sake of simplicity, the convective motions, those of supergranules in particular, are not included in these models. Therefore, the possible link between the variation of the fractal dimension, the magnetic threshold, and the supergranular scale are not addressed in this work.

6.2. *Descriptions of the Models*

The following variants have been considered.

1. *Variant 0.*—This model is described in Wentzel & Seiden (1992) and does not take into account the polarities of the flux tubes.
2. *Variant 1.*—The polarity of the flux tubes as in Seiden & Wentzel (1996) are taken into account. When a new flux tube is created, the corresponding counterpart of opposite polarity is also added to the map. Diffusion at the surface is thus more realistic, since the disappearance of flux is due to cancellation of flux tubes with opposite polarity. One site at the surface can be occupied by several flux units: this corresponds to different magnetic field levels. An example of such a map is shown on Figure 11.
3. *Variant 2.*—An interpretation of the magnetic field distribution is proposed by Schrijver et al. (1992), although they do not describe any models: the thin magnetic flux tubes that constitute the active region can move only in intergranular lanes and then form a fractal pattern. It would be interesting to take the granulation pattern into account in the diffusion process at the surface, as well as the supergranulation. As a first attempt to model this process, the flux tubes at the surface have been constrained to move only on a square lattice, with sides of several pixels to match the ratio between the flux tube diameter and the granule diameter. The polarity of the flux tubes is treated as in variant 1.

Since variants 0 and 1 are very close to the models described by Wentzel & Seiden (1992) and Seiden & Wentzel (1996), respectively, I refer to these papers for more details. However, I summarize the main characteristics here:

1. *Percolation from the convection zone where the flux tubes are formed.*—The percolation interpretation is motivated by the fact that we observe a continuous emergence of magnetic flux in active regions, on a timescale much longer (several months) than the flux tube lifetimes (less than a day at the surface). They propose that when a flux tube emerges toward the surface, this leads to a modification of the magnetic configuration around the emerging flux tube, inducing the formation of other flux tubes in the same region (see Wentzel & Seiden 1992, Appendix, for more details). The probability of the stimulated formation of a new flux tube at an adjacent pixel will be denoted as P_{st}. Variant 0 makes no attempt to account for magnetic polarity.
2. *Rising toward the surface.*—In these simple models, there is no distortion of any sort between the configuration

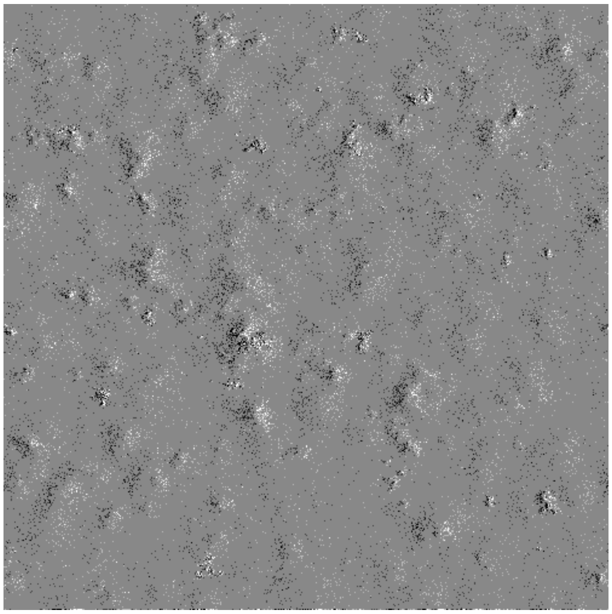

FIG. 11.—Example of modeled structures made with variant 1, with parameters $P_{\mathrm{st}} = 0.092$, $D = 0.01$, $P_{\mathrm{init}} = 0.001$, $P_{\mathrm{sp}} = 10^{-6}$, at $t = 1000$. Dark areas correspond to negative polarity, and bright ones to positive polarity.

below the convection zone and that at the surface, so that an excited pixel at position (*i*, *j*) will be transferred to the same position on the surface map.

3. *Diffusion at the surface.*—The parameter D is the probability that a flux tube will diffuse to a given adjacent pixel at a given time step.

This model provides a two-dimensional description of the flux tube distribution in two layers. A third dimension is provided by the temporal evolution of the structures. In addition to the percolation process, a small number of sites are stimulated spontaneously, with a probability $P_{\rm sp}$, to maintain a given level of activity after a long time.

At $t = 0$, a certain number of sites are randomly excited, with a probability $P_{\rm init}$. At each time step the percolation process is calculated for each excited site. The old excited sites are then canceled at this level and transferred to the surface, where diffusion occurs. Both the percolation and diffusion occur on the spatial scale of one pixel. The maps are usually in a stable state after 1000 time steps. One image every 300 time steps after time step 1000 is selected. The main difference between this work and that of Wentzel & Seiden (1992) is that here a square lattice is used instead of a triangular one, so that the percolation and diffusion can act on four neighbors of the excited pixel, or eight if the corners are considered. Wentzel & Seiden (1992) did not detect any strong influence of differential rotation on their results, so it has not been included in this work. Maps of 1024 × 1024 pixels are generated, and projection effects are neglected.

Another issue concerns the temporal and spatial scales. The size of one time step can be related to the time it takes an active region to attain its maximum size, for example (i.e., to the rate of emerging flux). Wentzel & Seiden give a crude estimate of 0.1 day per time step in their model. As for the spatial scale, already mentioned at the beginning of this section, the pixel size could be strongly related to the flux tube diameter, probably in the range 100–200 km. It would then be independent of D (which is another difference between my model and that of Wentzel & Seiden). Degradation of the simulated images is then necessary to match the observations. A reasonable degradation is of 1 order of magnitude to match the FD magnetogram observations, less if the cells are larger than the flux tubes.

From these various models, the fractal dimension of the structures can be measured, its variation with area and magnetic threshold, as well as the prefactor C and the size distribution with area. These can be calculated for different parameter choices that determine the models ($P_{\rm init}$, $P_{\rm st}$, $P_{\rm sp}$, and D), different degradations, and different thresholds.

6.3. *Results*

Modification of the various parameters (particularly $P_{\rm sp}$ and D) has a relatively small influence on the fractal dimensions, which remain in a restricted range. They mainly influence the filling of the surface and the maximum size that the structures can attain. This last point is strongly related to the degradation applied to the model, if any.

In general, the structures before degradation appear to be fractal, i.e., the estimate of the fractal dimension is almost independent of the area. When the structures are degraded, d_1 for the lowest areas starts to decrease, whereas it remains constant above a certain value. When the degradation is increased, the occurrence of large structures is more frequent. If the degradation is strong (as it is for the observations), then the area range in which the fractal dimension is constant is considerably reduced. This is what is observed here: the minimum size we can resolve far exceeds the size of the flux tubes that represent the magnetic pattern.

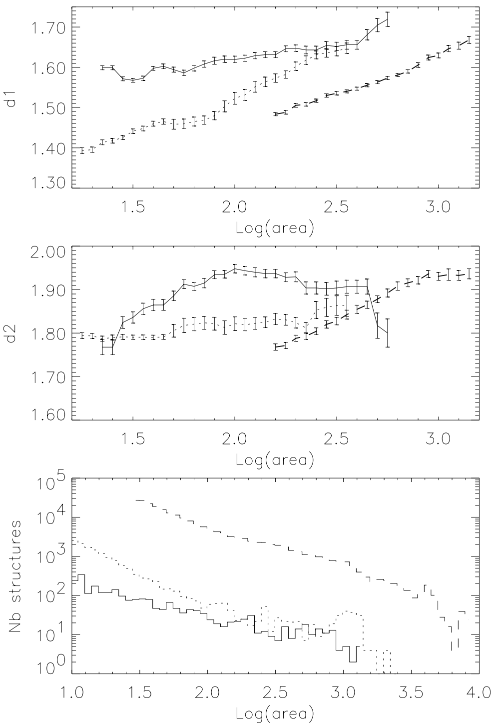

FIG. 12.—Comparison between observations and model (variant 1). *Top:* d_1 versus A (calculated over $\Delta \log A = 1.5$) for FD magnetograms, threshold: 40 G (*dashed line*), HR magnetograms, threshold: 40 G (*dotted line*), and model, degraded by a factor of 4 (*solid line*). *Middle:* Same for d_2 versus A. *Bottom:* Same for the size distribution. The parameters for the model are $P_{\rm st} = 0.092$, $D = 0.01$, $P_{\rm init} = 0.001$, $P_{\rm sp} = 10^{-6}$. The curves for HR magnetograms and models have been shifted toward smaller areas by 0.95 and 1.20, respectively.

Many parameters are needed to describe the results: the maximum area, the shape of the size distribution and its slope, the range in which d_1 and d_2 are varying and whether they are decreasing or increasing with area, and the dispersion of the perimeter (and linear size) for a given area and magnetic threshold. The best models for the fractal dimension d_1, for example, are not necessarily the best for the size distribution. Figure 12 shows an example of one of these models. The slope of the size distribution is in better agreement with the observations when the model is not degraded. In some cases d_1 fits the observations concerning the variation with A well (although it is too large), but then d_2 is anticorrelated with d_1, instead of being correlated as the observations require. The perimeter for a given area is always higher than in the observations, although its dispersion is of the same order of magnitude. One great difficulty is to obtain maximum sizes similar to the observed ones: the generated structures are too small. So none of the models leads to good agreement with observations.

The results for variants 0 and 1 are very similar, although variant 1 is more interesting because it takes the polarities into account. The inclusion of the corner pixels as neighbors provides slightly different results, but the results depend on the choice of parameters, and it is not obvious which choice is the best.

The application of variant 2, which takes into account a granulation pattern at the surface to provide a more realistic constraint on the position of the flux tubes, increases d_1 as expected (the structures are more complex). This reinforces the discrepancy with the observations. This result might provide an explanation for the variation of the fractal dimension with the magnetic threshold, as suggested in § 4.2.

Some tests on the variation in the fractal dimension with the magnetic threshold have been conducted. The fractal dimension for two different thresholds is calculated in several models: d_1 decreases as the magnetic threshold increases, in agreement with the observations of structures of moderate size.

The various models described above generate structures that are too complex compared with the observations. One possibility would be that the percolation might not be as efficient as described above and that the flux tubes are coming from a more restricted region, like a "hot point." However, it is then more difficult to generate large active regions as in the observations.

7. DISCUSSION AND CONCLUSION

In this paper I have presented a fractal analysis of magnetic regions observed by MDI on *SOHO*. One first conclusion is that two conditions are crucial when one wants to perform such an analysis. First, one has to be very careful with the calculation method, in particular the quality of the sampling, the influence of the noise, and the spatial resolution effects. Second, for that reason, the analysis of the models must be performed under the same conditions as far as possible, particularly with respect to the degradation of the simulated structures to match the spatial resolution of the observations. This means that a comparison with a very general model of percolation that does not express important solar properties is not very reliable.

The efforts to characterize solar magnetic structures in terms of fractals have given the following results:

1. *A variation of d_1 and d_2 with the area is found.* On a large scale, there seems to be a correlation between the estimates d_1 and d_2, instead of an anticorrelation as expected. This could be related to a variation in the range of shapes available to structures as a function of size. If the small structures are more elongated, such a pattern may emerge. Note also that the linear size does not take into account the cavities inside the structures, which could also be a source of discrepancy when analyzing d_2. The complex behavior of d_2 needs further investigation. Recall that some choices of model parameters yield a correlation between d_1 and d_2, others an anticorrelation. These two estimates thus provide complementary information. The fractal dimensions and prefactor obtained from FD and HR magnetograms are in good agreement.

2. The variation of the fractal dimension with the magnetic threshold used to determine the active region boundaries shows that *structures of moderate sizes are more complex at lower magnetic thresholds. Large structures seem to exhibit the opposite trend*, as observed on both FD and HR magnetograms. The scale at the junction between these two trends may be related to the supergranulation. These last results will have to be confirmed when larger structures become available. The difference in granulation size in the outer parts of the regions and close to the core could be responsible for that effect.

3. A comparison with some models of active regions similar to those described by Wentzel & Seiden (1992) and Seiden & Wentzel (1996) is performed. The general variation of d_1 with area (i.e., an increase) is in good agreement with the observations when the modeled images are degraded by a reasonable factor. However, the *models render structures that are more complex than the observed structures*, which can be seen by an offset in d_1. An important result is that even if the model exhibits fractal behavior, after a strong degradation the fractal dimension can remain constant only for the largest structures, as observed. Because this spatial resolution effect can be taken into account in the comparison between models and observations (Fig. 12), this fractal analysis is very useful: even if the structures do not appear as exactly fractal (i.e., if the observed fractal dimension varies with size), this approach can still provide very useful information on the mechanisms that lead to the formation of active regions. Furthermore, the understanding of the effect of degradation due to the limited spatial resolution is also crucial to the understanding of the observations obtained from ground-based observations.

4. *The simultaneous analysis of the fractal dimension and of the size distribution provides complementary information.* This work showed that it is necessary to consider a number of different aspects for a good comparison with models. For example, the observed and modeled size distributions are in good agreement when the images are not degraded (which was also the main result of Wentzel & Seiden 1992), but this is not the case of the fractal dimension. When the images are degraded, the fractal dimension improves to some degree but the size distribution begins to show discrepancies.

Most similar studies of active regions (except Nesme-Ribes et al. 1996, in which 1000 structures larger than the supergranular scale over 6 months were studied) have been performed on a much smaller number of structures, often on the same region observed several times within one day. This means that our present study provides a huge improvement from the statistical point of view. This is important for a reliable comparison with general models of active regions. The observational part of this study needs to be extended into the future because the period 1996–1997 exhibited a low activity level. Many more active regions are expected within the next years. Many questions will be resolved by studying the maximum of the solar cycle, such as the variation of the fractal dimension with the activity level. It will also be interesting to establish some comparison with other types of data. The MDI Dopplergrams, for example, may offer some clues that could lead to more realistic models.

The main improvement that remains to be made concerns the models: the main result of this work is that the current models are not realistic enough to provide structures with fractal dimensions in agreement with the observations. It will thus be *necessary to improve the models*, particularly in the following respects. (1) First, the percolation process needs to incorporate more physical parameters, particularly the velocity field. (2) Second, the description of flux tube rising to the surface should also be improved; tests that combined flux tubes rising to the surface did not lead to any difference in the results. (3) The supergranulation plays a role in the distortion of magnetic regions at the surface. Other effects could also be important and may lead to less complex structure than the ones suggested by the current models. Such a realistic model was beyond the scope of this paper and needs to be investigated in the future. Another contribution to the variation in the fractal dimension with area could be that the large regions and the very small structures might not be related to the same depth inside the Sun. The magnetic field constituting the large active regions probably comes from the base of the convection zone, in the overshoot layer. On the other hand, small structures like ephemeral regions may be generated much closer to the surface, where processes such as percolation could be completely absent, leading to less complex structures. However, diffusion mechanisms at the surface are probably similar for both, unless there are differences in the granulation patterns due to different magnetic field strengths.

I am grateful to C. Lindsey, T. Duvall, A. G. Kosovichev, T. Hoeksema, and R. Bogart for many helpful comments on the manuscript. This research is supported by the SOI-MDI NASA grant NAS 5-3077 at Stanford University. *SOHO* is a mission of international cooperation between the European Space Agency (ESA) and NASA.

REFERENCES

Balke, A. C., Schrijver, C. J., Zwaan, C., & Tarbell, T. D. 1993, Sol. Phys., 143, 215

Brandt, P. N., Greimel, R., & Guenther, E. W. M. 1991, in Applying Fractals in Astronomy, ed. A. Heck & J. M. Perdang (Berlin: Springer), 77

Harvey, K. 1993, Ph.D. thesis, Univ. Utrecht

Harvey, K., & Zwaan, C. 1993, Sol. Phys., 148, 85

Hetem, A., Jr., & Lepine, J. R. D. 1993, A&A, 270, 451

Isobe, T., Feigelson, E. D., Akritas, M. G., & Babu, G. J. 1990, ApJ, 364, 104

Jones, H. 1989, Sol. Phys., 120, 211

Lawrence, J. K., & Schrijver, C. J. 1993, ApJ, 411, 402

Mandelbrot, B. B. 1983, The Fractal Geometry of Nature (New York: Freeman)

Nesme-Ribes, E., Meunier, N., & Collin, B. 1996, A&A, 308, 213

Ruzmaikin, A., Sokoloff, D., & Tarbell, T. 1991, in The Sun and Cool Stars: Activity, Magnetism, Dynamos, eds. I. Tuominen, D. Moss, & G. Rüdiger (Berlin: Springer), 140

Scherrer, P. H., et al. 1995, Sol. Phys., 162, 129

Schrijver, C. J., Title, A. M., Hagenaar, H. J., & Shine, R. A. 1997, Sol. Phys., 175, 329

Schrijver, C. J., Zwaan, C., Balke, A. C., Tarbell, T. D., & Lawrence, J. K. 1992, A&A, 253, L1

Seiden, P. E., & Wentzel, D. G. 1996, ApJ, 460, 522

Title, A. M., Topka, K. P., Tarbell, T. D., Schmidt, W., Balke, C., & Scharmer, G. 1992, ApJ, 393, 782

Vogelaar, M. G. R., & Wakker, B. P. 1994, A&A, 291, 557

Wentzel, D. G., & Seiden, P. E. 1992, ApJ, 390, 280

THE ASTROPHYSICAL JOURNAL, 527:967–976, 1999 December 20

LARGE-SCALE DYNAMICS OF ACTIVE REGIONS AND SMALL PHOTOSPHERIC MAGNETIC FEATURES

N. MEUNIER
W. W. Hansen Experimental Physics Laboratory Annex A207, Stanford University, Stanford, CA 94305-4085; nadege@quake.stanford.edu
Received 1999 March 11; accepted 1999 August 5

ABSTRACT

This paper presents an analysis of the dynamics of magnetic features within and outside active regions using full-disk magnetograms obtained by the MDI (Michelson Doppler Imager) instrument on the *SOHO* spacecraft. The absence of distortion and the short time interval (96 minutes) between images allow us to calculate high-quality cross-correlations between regions on each magnetogram. Therefore, each cross-correlation can be studied individually, which provides information with resolution in longitude as well as good temporal resolution. Rotation rates and meridional motions are simultaneously derived from an analysis of the cross-correlation functions. This analysis shows that the meridional motions are very different during the quiet period and the active period. In the former case, a poleward meridional circulation is observed, which increases with latitude. In the latter case, the meridional motions of magnetic features in active regions are smaller by a factor of 2 than those exhibited by small magnetic structures outside active regions. The rotation rate seems slightly larger in active regions, while the rotation rate decreases as the activity level rises. Some differences in the meridional circulation of different polarities are found.

Subject headings: Sun: activity — Sun: faculae, plages — Sun: magnetic fields — Sun: photosphere — Sun: rotation

1. INTRODUCTION

Knowledge of solar flows at different temporal and spatial scales constitutes a key element of the dynamo theories attempting to explain the behavior of the solar cycle. There are currently three main techniques for measuring the solar dynamics: (1) Dopplergrams provide the velocity of the nonmagnetized plasma at the solar surface (see Hathaway 1992 for rotation rate results and Hathaway 1996 for the meridional circulation, for example); (2) helioseismology provides the dynamics of the plasma at different depths inside the Sun (for a recent paper on a global analysis see Schou et al. 1998; for recent time-distance analysis results see Giles, Duvall, & Scherrer 1998 and Duvall 1998); and (3) the tracking of various magnetic features (sunspots, plages, and network elements) with many different techniques has also been used (see Howard 1996a for a review). All provide results that are quantitatively different, because they probe different depths or represent structures with different intrinsic properties. In general, these differences should not be interpreted as incompatibilities or biases but rather as complementary information on different phenomena. Thus, it is very important to use and compare different approaches.

In this work, cross-correlation of magnetograms is used to detect motions. Analyses of the dynamics of magnetic features using cross-correlations between magnetograms separated by 1 day or more have been performed in the past (Howard, Harvey, & Forgach 1990; Komm, Howard, & Harvey 1993a, 1993b; Komm 1994). However, distortions of the magnetic features are large over the course of 24 hr, and so cross-correlations had to be averaged over a long period (several months) to provide a significant signal. MDI magnetograms are typically separated by only 96 minutes, which provides a great opportunity to complement this work using shorter time intervals. The purpose of this paper is to study the rotation rate and the meridional circulation derived from magnetic features using the first 2 yr of MDI data available. These data allow us to improve both the temporal resolution and the spatial resolution in longitude. (Because of the rotation, the use of averaging over an extended period of time primarily influences the longitudinal direction.)

The data and cross-correlation calculations are presented in § 2. The rotation rate and the meridional circulation of the magnetic features averaged over periods of different activity levels are presented in § 3, and possible biases in the analysis are described. Section 4 presents the variation of the dynamics with time, while § 5 shows the dependence of the dynamics on the magnetic field. The dependence on the magnetic polarities is presented in § 6. In § 7 the new results are compared with previous works.

2. DATA AND ANALYSIS

2.1. *MDI Magnetograms*

Full-disk magnetograms obtained by MDI on the *SOHO* spacecraft (Scherrer et al. 1995) constitute maps of the line-of-sight component of the magnetic field averaged over the resolution element. These magnetograms allow us to study both active regions and small-scale magnetic fields in the quiet regions (Fig. 1). They are obtained from observations made in the Ni 6768 spectral line and represent magnetic structure at a height of approximately 200 km above the $\tau_{5000} = 1$ level (Jones 1989). The pixel size is 2″ (with a subsequent spatial resolution of 4″). The data set comprises both 1 minute individual magnetograms and averaged 5 minute magnetograms. In this work, images from 1996 June 22 (mission day 1268) to 1998 June 21 (mission day 1997), i.e., 730 days, are used. During the first half of this period the activity level was very low, with only small active regions close to the equator corresponding to the end of cycle 22. The activity level started to increase around mission day 1650 (1997 July) in the north and around mission day 1700 (1997 September) in the south, in the latitude range 20°–40°. This corresponds to the beginning of cycle 23.

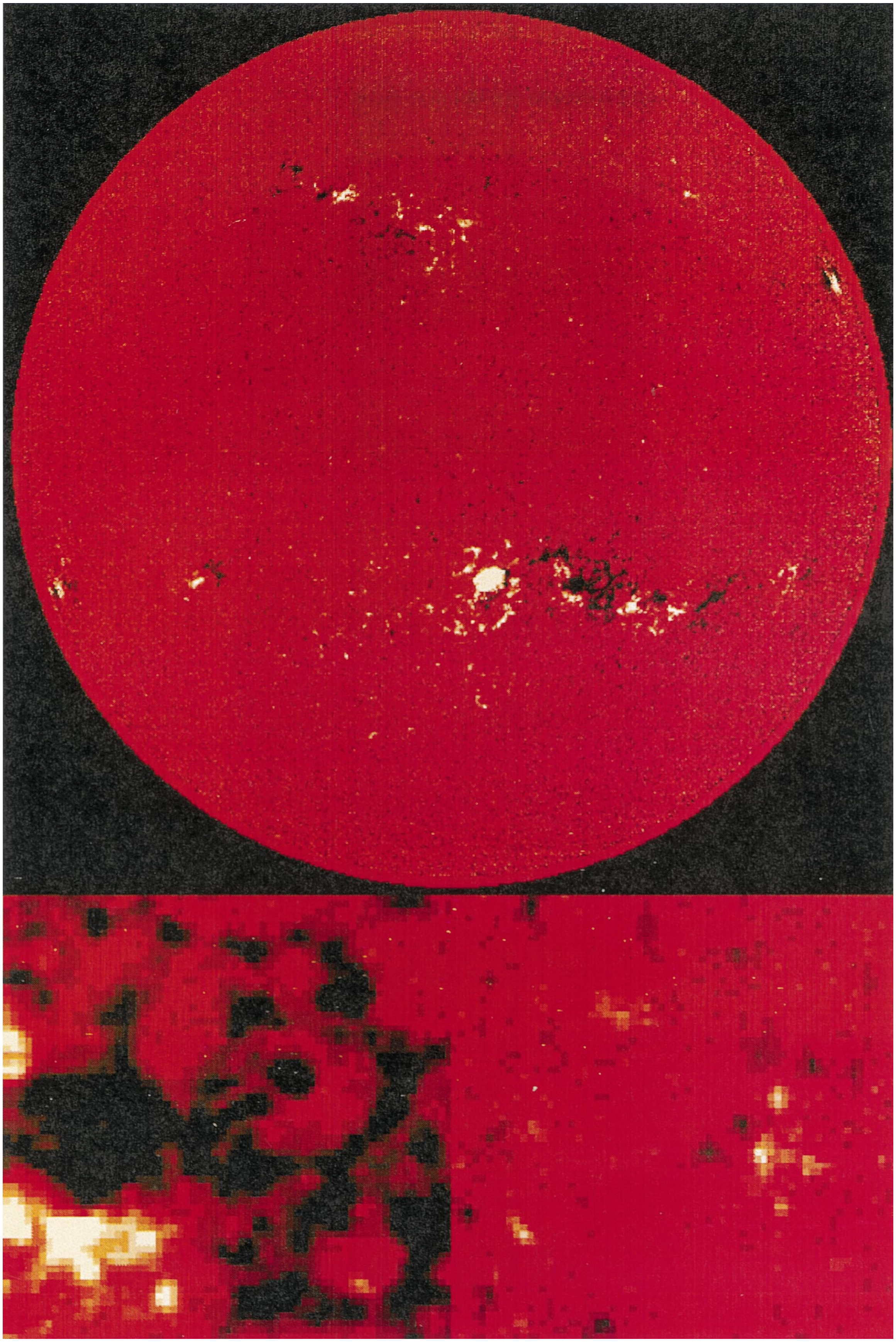

FIG. 1.—*Top*: Full-disk MDI magnetogram of 1998 March 29. *Bottom*: Example of a 64 × 64 pixel region on the flat map, in an active region (*left*) and in a quiet region (*right*).

One image is generally available every 96 minutes, and the data set provides 9249 full-disk magnetogram pairs. This is a great improvement over previous work, because the structures that we attempt to cross-correlate did not undergo large distortions between images. The cross-correlations are therefore more significant. Furthermore, images are not distorted by the atmosphere, as were magnetograms in previous analyses. We are thus able to analyze individual cross-correlations so that the relation between the magnetic field and the dynamics can be studied in more detail. On the other hand, the displacements to measure are very small, 1° per day, which corresponds to half a pixel only (at disk center), instead of 8 pixels within a 24 hr interval. Therefore, it is necessary to be more cautious about certain biases that can occur.

2.2. *Cross-correlation Calculations*

Magnetograms are corrected for the B_0 angle and projection effects by remapping them using a bilinear interpolation with a pixel size of 0°.12 (corresponding to the pixel size at disk center on the original magnetograms). We study 64×64 pixel square regions (i.e., 7.68×7.68 deg^2) on these flat maps (19 in each direction, i.e., latitudes and longitudes $-69°.12$–$69°.12$). Figure 1 shows two examples of such square regions. For each flat map (subscript 1 in the following discussion) we consider similar regions on the magnetogram observed 96 minutes later (subscript 2), shifted in longitude by a certain number of pixels according to a preliminary rotation rate (between 5 and 7 pixels, depending on the latitude). This method is thus very similar to that described by Howard et al. (1990). The 64×64 pixel region on the second image is shifted by i and j pixels to calculate the cross-correlation,

$$C_{i,j} = \frac{\sum_{k,l=1}^{64} B_1(k, l) B_2(k+i, l+j)}{\sqrt{\sum_{k,l=1}^{64} B_1(k, l)^2 \sum_{k,l=1}^{64} B_2(k+i, l+j)^2}} ,$$

where B_1 and B_2 correspond to the magnetic field on the first and second flat maps, respectively. The subscripts i and j vary in the range $[-10, 10]$, which corresponds to an available range of motion of $\pm 8°.9$ per day around the central position. This range is large enough to ensure that most of the distribution is taken into account. The size of 64 pixels results from a compromise between the spatial resolution achieved in latitude and longitude, and the signal-to-noise ratio of the cross-correlation function. A fit using a two-dimensional Gaussian is then performed on $C_{i,j}$ over an 11×11 pixel region surrounding the position of maximum cross-correlation. From this fit the rotation rate and the meridional motions are deduced for the corresponding position on the solar disk for each individual image pair.

Points with a maximum cross-correlation below 0.2 are eliminated because the signal-to-noise ratio of the cross-correlation is too small. Note that the maximum cross-correlations often reach values very close to 1 in active regions. Points with both large latitudes and large longitudes are also eliminated. For each position of the 64×64 pixel region, averages of rotation rate and meridional circulation are calculated.

2.3. *Additional Calculations*

Additional calculations are performed on each of the 64×64 pixel regions: (1) the average $|B|$ (denoted by $\overline{|B|}$) gives the activity level at the current position in latitude and longitude, (2) the average B (denoted as $\bar{B}$) provides the sign of the magnetic field in that region, and (3) the maximum $|B|$ (denoted as $|B|_{\max}$) is also related to the activity level. This information is useful in studying the relationship between the dynamics and the magnetic field.

3. ROTATION RATE AND MERIDIONAL MOTIONS

3.1. *Variation of Dynamics with Latitude*

Figure 2 shows the rotation rate and the meridional circulation versus latitude obtained during two periods of 300 days: one of low activity from mission days 1278–1577 (1996 July 2 to 1997 April 27) and one of high activity from mission days 1698–1997 (1997 August 26 to 1998 June 21). The error bars are derived from the scatter. Because of side effects in active regions, the cross-correlation function is slightly asymmetric, leading to a biased estimate of the displacement. A correction is made by subtracting the "displacement" measured for a time interval $\Delta t = 0$, i.e., using an autocorrelation, for the same features.

The rotation rate close to the equator is slightly larger during the low-activity period, by ~0°.07 per day, but this is significant only at the 1 σ level. At larger latitudes there are no significant differences. Fits performed using a polynomial of degree 5 in sin(latitude) show that there is no significant asymmetry between the northern and southern

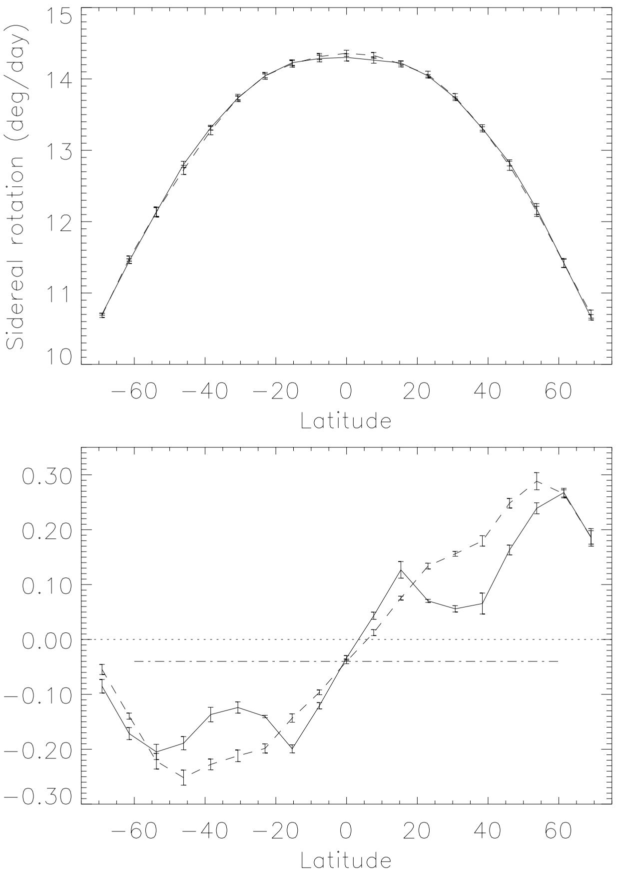

FIG. 2.—*Top*: Sidereal rotation rate in degrees per day for the mission days 1278–1577 (*dashed line*, quiet period) and 1698–1997 (*solid line*, active period). *Bottom*: Same for the meridional motions. Positive meridional flows are northward. A meridional flow of 0°.3 per day corresponds to 42 m s^{-1}. The horizontal dot-dashed line shows the level of the disk-averaged meridional motions.

hemispheres, such as the one observed by Meunier, Nesme-Ribes, & Grosso (1997a), obtained by tracking plages on spectroheliograms. These fits provide a sidereal rotation rate at the equator of 14°.34 ± 0°.02 per day during the low-activity period and 14°.31 ± 0°.02 per day during the high-activity period.

The meridional circulation during the quiet period is poleward, with an increasing flow as latitude increases, reaching 0°.3 per day around latitude 50° (i.e., 42 m s^{-1}). Results obtained during the same quiet period using a time-distance analysis of MDI Dopplergrams (Giles et al. 1998) showed a meridional circulation that is very similar in amplitude. On the other hand, during the active period the meridional motions first increase with latitude, then decrease slightly, and then increase again. These lower meridional motions in the latitude range 20°–40° are similar in both hemispheres. However, at high latitudes, the meridional circulation is similar for the two periods. In the two following sections we establish the relationship between active regions and the difference between the two periods more precisely. Note an apparent southward motion at the equator of −0°.04 per day; this is discussed in § 3.3. The meridional circulation seems to decrease at high latitudes (above 60°), with a slightly larger meridional circulation in the northern hemisphere.

3.2. *Difference between Individual and 5 Minute Magnetograms*

A study of two periods (mission days 1308–1487 and 1698–1817) during which the distribution of individual and 5 minute averaged magnetograms is relatively homogeneous shows that pairs of single magnetograms only and pairs of 5 minute magnetograms only give similar rotation rates. However, during the quiet period, the meridional circulation derived from 5 minute magnetograms is larger by approximately 20% than the one derived from individual magnetograms. During the active period the large poleward motions are reduced in the 5 minute magnetograms, while the small poleward motions are increased compared to the results obtained using only individual magnetograms; the pattern observed in Figure 2 has a larger amplitude when using single magnetograms. This could be due to a difference in sampling for the two data sets; when single magnetograms are used, the noise is larger and so a smaller proportion of weak magnetic field structures are studied. We will see in § 5 that the pattern is mainly due to active regions, and this is consistent with what we observe here. Results for pairs of single/5 minute magnetograms and 5 minute/single magnetograms show a behavior intermediate between the two previous results.

3.3. *Possible Biases*

3.3.1. *Bias on the Rotation Rate*

Figure 3 shows the variation of the rotation rate residuals versus disk longitude. The residuals are calculated by subtracting the polynomial fit mentioned in § 3.1 from the rotation rate. We find that the rotation rate appears to be larger on the western part of the disk, with a peak-to-peak amplitude of ∼0°.5 per day between longitudes −50° and 50°. The residuals vary approximately linearly with longitude in the range ±40°, reaching a maximum around 50°–60°. Recall that 0°.2 per day corresponds to 0.11 pixel in 96 minutes. A plausible error of the coordinate system, in the radius or in the disk center position, cannot explain such an amplitude and such a shape (the slope close to disk center is very large). An analysis of the limb shape of images shows that the solar disk might be elongated by a fraction of a pixel. However, such a distortion would be equivalent to a radius error and would lead to a bias symmetric with respect to the central meridian, and not to an antisymmetric one as observed. The following observations provide some information on this bias.

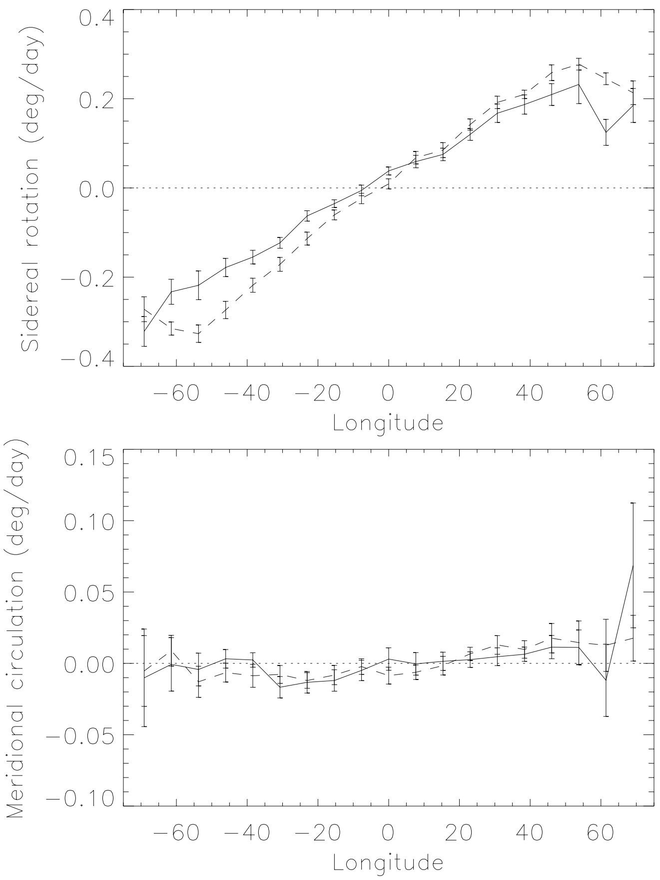

FIG. 3.—*Top*: Residuals of the rotation rate (rotation rate minus fit) in degrees per day for the mission days 1278–1577 (*dashed line*, quiet period) and 1698–1997 (*solid line*, active period). *Bottom*: Residuals of the meridional motions (meridional motions minus the average in the corresponding latitude range). Positive meridional flows are northward. A rate of 0°.2 per day corresponds to approximately 28 m s^{-1}.

1. The bias amplitude is reduced by a factor 1.9 when the dynamics are derived from individual magnetograms rather than from 5 minute magnetograms. Since the bias is smaller for single magnetograms, the noise is not likely to produce this bias. The averaging process leading to the 5 minute magnetograms, which does not take into account the rotation rate, might lead to this additional bias. However, it is not clear at this point whether the larger bias for 5 minute magnetograms is due to an amplification of the bias already present in single magnetograms, or if it has a different origin. This difference between single and 5 minute magnetograms is probably responsible for the difference between the residuals of Figure 3 for the two periods, since the relative numbers of the two types of magnetograms is changing with time.

2. The use of larger time intervals Δt between images for a 1 month period shows that the bias decreases when Δt increases. The slope reaches zero for $\Delta t = 5 \times 96$ minutes

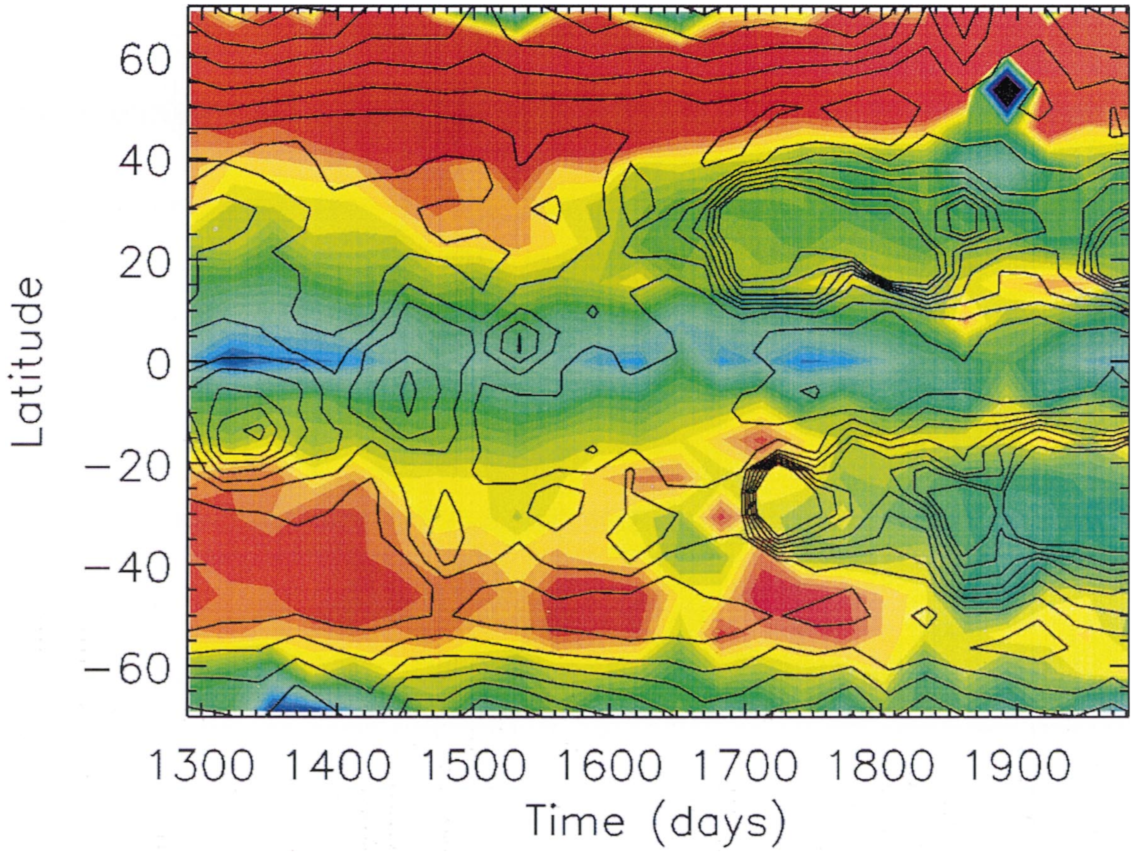

FIG. 4.—Color levels display the meridional motions vs. time (in days, from 1996 July 2 to 1998 June 21) and latitude (in degrees). The pixel sizes are 30 days and 7°.68, respectively. Red corresponds to a poleward motion larger than 0°.2 per day and blue to a slightly equatorward motion, while green corresponds to no meridional flow or moderate positive values of the flow. For each time period of 30 days, the disk-averaged meridional flow has been subtracted (see § 3.2). Level of uncertainties are 0°.025 per day on average, with the largest values at high latitudes. The black contours represent the absolute value of the magnetic field deduced from synoptic maps obtained at the Wilcox Solar Observatory. The contours are separated by 0.15 G between 0 and 1.5 G.

and becomes negative and stable at a value 4 times smaller for larger values of Δt (i.e., a bias with a peak-to-peak amplitude of 0°.05 per day). Therefore, the bias does not seem to be proportional to the displacement amplitude (in pixels), and is thus more likely to be due to the shape of the cross-correlation function rather than a simple shift of these correlations.

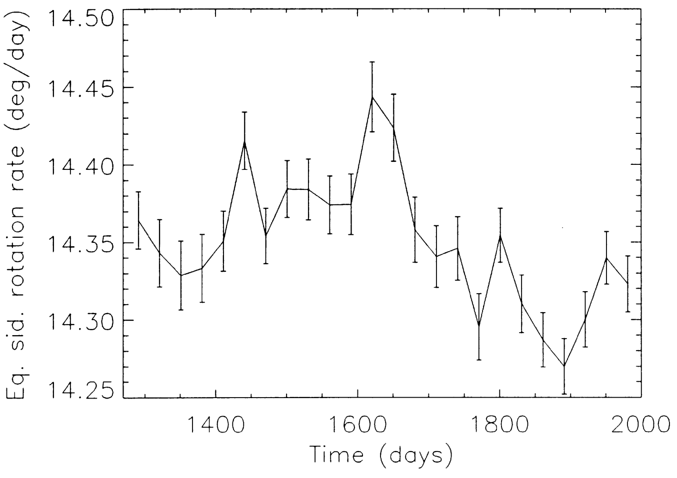

FIG. 5.—Equatorial sidereal rotation rate vs. time (in days, from 1996 July 2 to 1998 June 21) for points close to the disk center (longitudes smaller than 16°).

3. No significant difference between the two polarities is observed.

4. Such a bias has also been observed using other types of MDI data with other processing techniques: time-distance analysis of Dopplergrams (P. M. Giles 1998, private communication), ring-diagram analysis (J. Schou 1998, private communication), and granulation tracking on continuum images (N. E. Hurlburt 1998, private communication).

5. Image distortions due to the optical system could cause this type of bias. However, tests made prior to launch did not show any significant distortions (P. M. Giles & T. L. Duvall 1998, private communication).

Note also that the observed variations of this bias with time are small and are probably due mainly to the variation of the relative numbers of single and 5 minute magnetograms during the 2 yr period.

3.3.2. *Bias on the Meridional Motions*

Since the origin of this bias on the rotation rate is not yet understood, its influence on the average level of the rotation rate (we cannot know if the value at disk center is the true one) and on the meridional motions is not known. The difference of meridional motions between 5 minute and single magnetograms (a factor of 1.2) could be due to the same bias. If true, the actual amplitude of the meridional circulation could be smaller by almost a factor of 2.

Figure 3 also shows the variation of the meridional motion residuals (the average value at the corresponding latitude has been subtracted) versus disk longitude. A slight increase is observed but is not significant. However, the residuals for individual latitude ranges are larger, and they are anticorrelated between the two hemispheres. This behavior may be related to the bias described in the previous subsection.

A southward motion at the equator was observed in Figure 2. The disk-averaged meridional circulation is indeed negative on average, and shows a variation of peak-to-peak amplitude of 0°.04 per day with a period of 1 yr (two periods are observed). This variation is correlated with the velocity of the spacecraft. The average is close to zero in 1996 May, 1997 April, and 1998 May, and has a maximum amplitude in 1997 November and 1998 December. The amplitude of this variation is larger when calculated close to disk center only (0°.08 per day). It also depends on latitude (larger close to the equator), but does not seem to depend on longitude. An error of 0°.08 per day in the meridional motions at disk center could be caused by an orientation error of the polar axis of 21′, which is relatively large. However, the variation of the average meridional motions with latitude and longitude, as well as the variation of the residuals of the meridional motions with latitude and longitude, do not correspond to those expected from an error on the P angle of that magnitude.

4. TEMPORAL VARIATIONS

In order to study more precisely the relation between active regions and the pattern in meridional flows observed in Figure 2, the data set between mission days 1278 and 1997 is separated into 24 periods of 30 days each. Figure 4 shows the evolution of the meridional circulation versus time and latitude. The magnetic activity deduced from the synoptic maps provided by the Wilcox Solar Observatory is also displayed for comparison. The disk-averaged meridional motions for each 30 day period have been subtracted (this bias was discussed in § 3.3.2). However, this correction is small compared to the signal we observe. Note that in Figure 4 the sign convention is different from that in Figures 2 and 3; here a positive flow is poleward and a negative flow is equatorward. It is very clear from this figure that the smaller meridional motions during the second period are closely related to the magnetic activity. This pattern is strongly correlated with the presence of active regions, in both latitude and time. This property is studied in more detail in the next section and will be discussed in § 7. This figure also shows an asymmetry between hemispheres, especially at high latitudes: the poleward motion seems stronger in the northern hemisphere.

After mission day ~1650, the equatorial rotation rate (Fig. 5) decreases by almost 0°.2 per day. Note that the main instrument problem that could create an important variation in the rotation rate is the change of focus in 1997 November (mission day 1767), which caused the apparent solar radius to decrease by ~0.5 pixel. However, this would lead to a much smaller variation of the rotation rate than the observed one. On the other hand, the correlation between the equatorial rotation rate and $\overline{|B|}$ is −0.65, and between the rotation rate and $|B|_{\max}$ is −0.69, which is significantly different from zero. A rotation rate during the solar minimum that is typically 0°.1–0°.2 per day larger than during the solar maximum has been observed by various authors in the past using sunspots (Balthasar & Wöhl 1980; Arevalo et al. 1982; Lustig 1983; Gilman & Howard 1984; Hathaway & Wilson 1990; Kambry & Nishikawa 1990). In the present study, a variation in the same direction and of a similar order of magnitude is observed, although it is not yet very significant; a longer time series would be necessary to confirm such a relationship between the rotation rate of magnetic features and the activity level for plages. Note that the analysis of Kitt Peak magnetograms by Komm et al. (1993a) did not show any variations of that magnitude. No pattern similar to the torsional oscillations seen by other authors (Labonte & Howard 1981; Snodgrass 1983, 1991) has been observed.

5. DEPENDENCE ON THE LEVEL OF ACTIVITY

The previous section showed that the smaller meridional circulation is present only during the active period. In this section we concentrate our study on this active period (1997 September to 1998 June) to determine if this pattern is global (present at all longitudes) or local (concentrated in active regions only).

5.1. *Synoptic Maps*

Active regions are present only at certain longitudes on the disk. This is particularly true during the epoch of our study because the activity level was still low and activity was not yet present everywhere in longitude. A plot of the dynamics versus Carrington longitude, i.e., within a frame of period 27.2753 days, and latitude should thus exhibit regions with activity and others without activity.

Figure 6 shows the meridional motions for mission days 1698–1877 (from 1997 August 26 to 1998 February 21) versus Carrington longitude and latitude. It is important to study a time interval that is long enough to obtain a good signal-to-noise ratio, but if the time interval is too short, the activity would be present in a larger range in longitude. We observe that the small meridional motions are present only in active regions, especially in the southern hemisphere.

Figure 7 shows a similar map for the rotation-rate residuals. They are corrected for the bias in longitude described in § 3.3.1 using a polynomial fit on the curve similar to that of Figure 2, but for the period 1698–1877. The rotation rate seems to be slightly larger in some active regions compared to the quiet regions, but the signal is not as significant as for the meridional circulation.

Similar maps from magnetograms obtained during a quiet period do not show any evidence of large-scale patterns such as giant cells (e.g., Beck, Duvall, & Scherrer 1998). Reducing the size of the latitude bins does not provide any additional information because the signal becomes very noisy.

5.2. *Dynamics versus* $\overline{|B|}$

It is also possible to separate the data set (mission days 1698–1997) into two subsamples: one with weaker magnetic fields and one with stronger magnetic fields. The choice of a threshold between small and large fields is delicate and arbitrary. If the threshold is too large, then the effect we want to estimate might be large, but the uncertainties from the

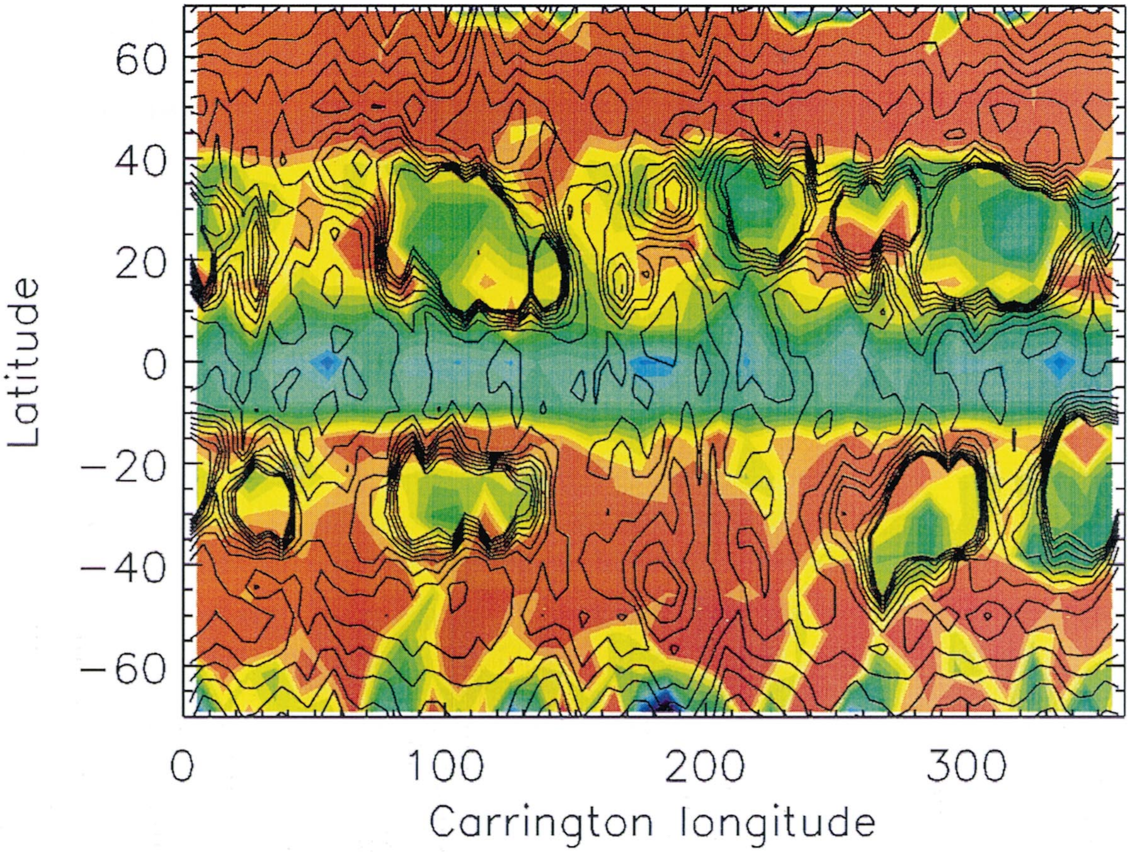

FIG. 6.—Color levels display the meridional motions vs. Carrington longitude and latitude (in degrees), for the period 1698–1877 (6 months). Red corresponds to a poleward motion larger than 0°.2 per day and blue to a slightly equatorward motion, while green corresponds to no meridional flow or moderate positive values of the flow. For each time period of 30 days, the disk-averaged meridional flow has been subtracted. Level of uncertainties are 0°.04 per day on average, with values from 0°.01 per day in active regions to values as high as 0°.18 per day at high latitudes. The black contours represent the absolute value of the magnetic field deduced from synoptic maps obtained at the Wilcox Solar Observatory (see Fig. 4).

scatter will also be very large, because there are few points. Furthermore, it will be more influenced by sunspots, which might have a different behavior (see, among others, Nesme-Ribes et al. 1993a, 1993b, 1997). The opposite is true if the threshold is too low. The choice of the threshold must also take into account the different signal-to-noise ratios (which lead to different $\overline{|B|}$ values) in single and 5 minute magnetograms, as well as the varying noise level across the solar disk.

Different thresholds for $\overline{|B|}$ and $|B|_{\max}$ (deduced from particular points in the distribution, for example) do not lead to any significant difference in rotation rate between regions with a strong magnetic field and those with a weak magnetic field. However, the meridional circulation has a smaller amplitude in regions with a strong magnetic field. This confirms the results obtained in § 5.1, but the error bars are larger. A longer time series would be necessary to study this effect more precisely.

6. MAGNETIC POLARITY DEPENDENCE

The data set from mission days 1698–1997 (1997 August 26 to 1998 June 21) is separated into two subsamples with positive and negative $\bar{B}$ in both magnetograms. The purpose is to study the difference between the leading part and the following part of active regions (the leading part had a positive polarity in the northern hemisphere during that period). The rotation rates are corrected for the bias described in § 3.3.1. No difference is found between the rotation rates of the two polarities, which diverges from what has been observed for sunspots in some previous works; Howard (1985), Gilman & Howard (1985), and Nesme-Ribes et al. (1993a) observed that the leading sunspots were rotating ~0°.1 per day faster than the following sunspots. However, in the northern hemisphere the meridional motions of the negative polarity features are slightly larger than that of the positive-polarity features (Fig. 8); the opposite is observed in the southern hemisphere. This corresponds to a slightly more poleward meridional circulation of the following features compared to that of the leading features. The result is similar for the period 1278–1577. However, for the quiet Sun, the interpretation of the polarities in terms of following and leading features may not be valid, so it is surprising that a similar difference is observed.

7. DISCUSSION AND CONCLUSION

The main new result obtained during this work concerns the meridional motions. The importance of the meridional circulation in the dynamo process has been shown in several works (see, e.g., Wang, Sheeley, & Nash 1991; Choudhuri, Schussler, & Dikpati 1995). For example, it may have an influence on the direction of propagation of the dynamo wave (observed to be equatorward). It could also be related to the reversal of polar magnetic fields (Leighton 1964; Durney 1996). The present work shows that in active regions, the meridional motions are smaller than that derived from the motions of small magnetic fea-

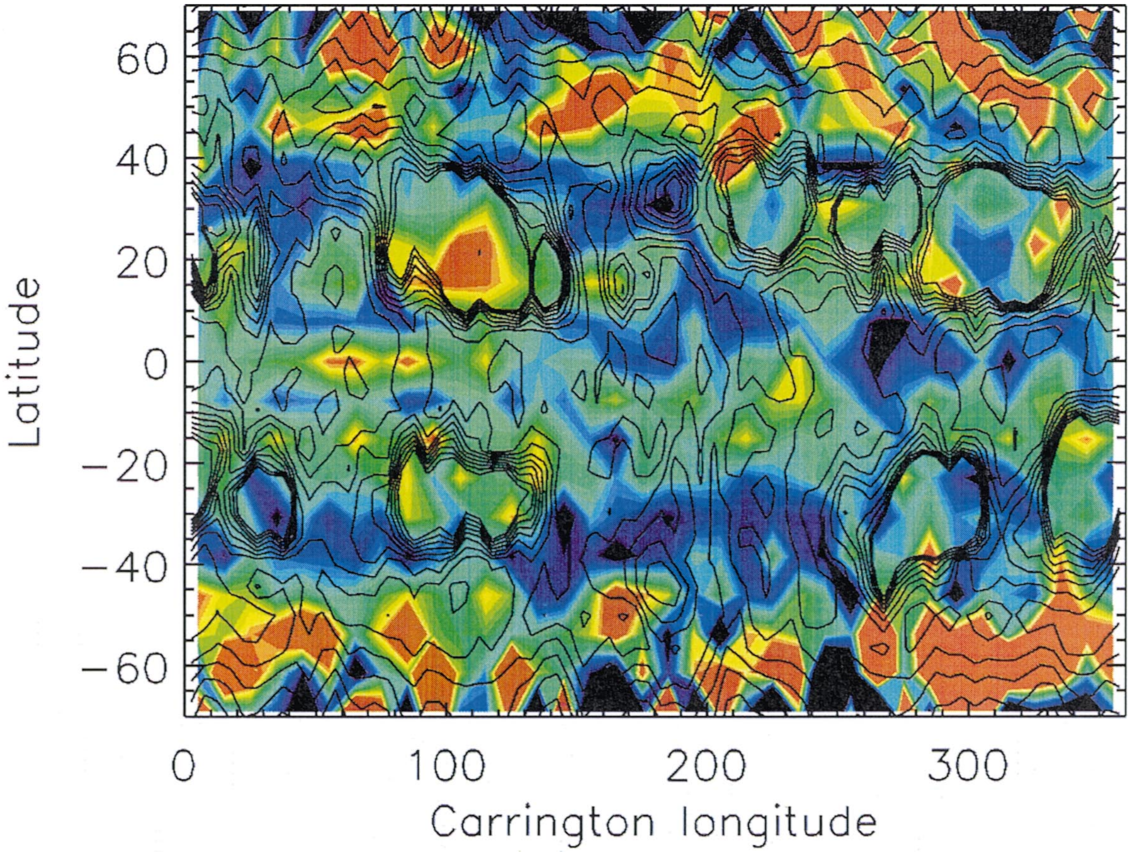

FIG. 7.—Color levels display the residuals of the rotation rate vs. Carrington longitude and latitude (in degrees) for the period 1698–1877 (6 months). Red corresponds to a faster than average motion (+0°.1 per day) and blue to a slower than average motion (−0°.1 per day). Green corresponds to average motion. The rotation rates have been corrected for the bias observed in longitude and described in § 3.3.1. Level of uncertainties are 0°.06 per day on average, with values from 0°.01 per day in active regions to values as high as 0°.34 per day at high latitudes. The black contours represent the absolute value of the magnetic field deduced from synoptic maps obtained at the Wilcox Solar Observatory (see Fig. 4).

tures in quiet regions, by a factor of ∼2. Analysis of the variation of the meridional motions with time and with Carrington longitude both lead to a strong dependence of the meridional motions on the activity level. In quiet regions, small-scale magnetic features exhibit a poleward motion of amplitude 0°.2–0°.3 per day (28–42 m s^{-1}) at latitude 60°, with an asymmetry between the two hemispheres. This amplitude is slightly larger than most previous results obtained with other data sets. The meridional circulation also seems to decrease at high latitudes.

The leading and following parts of active regions seem to rotate similarly, which differs from sunspot observations. However, the poleward motion of the following part seems slightly larger than that of the leading part by a few m s^{-1}. This could be related to the following property. The "tilt" of an active region is defined as the angle between the magnetic axis of the region on the solar surface (joining the positive- and negative-polarity parts) and the local circle of latitude (Howard 1996a). The average tilt has been observed to be ∼5° on average, with a very large dispersion around that value. Two geometrical effects due to the tilt angle could lead to a different meridional motion between the leading part and the following part of an active region. First, because the two extremities of a region are at different latitudes, the increasing meridional circulation with increasing latitude would lead to a difference in meridional motions. For a typical region with a tilt of 8° (average tilt for a plage at medium latitudes; Howard 1996a), the difference would be of the order of 1 m s^{-1}. However, because of the large dispersion of the tilt angles, the small number of active regions we observe may exhibit a different mean tilt. Second, if the tilt is increasing with time (with the leading part moving equatorward while the following part is moving poleward in a local frame of reference), then this motion would appear as a difference of meridional motions between the two regions. An increase of the tilt angle of 0°.5 per day would lead to the observed difference for a region of a typical size. However, observations of plages made by Howard (1996b) show that such a change is possible, but mainly for a region with a negative tilt (here again with a large dispersion), so if the tilt is negative the previous effect would go in the wrong direction. A larger sample of active regions would be needed to obtain more informations on that effect.

Two main types of meridional circulation have been obtained in the past, depending on tracers and processing techniques: (1) an equatorward motion at small latitudes and a poleward motion at larger latitudes (i.e., a divergence from the latitude of activity), and (2) a poleward motion.

1. A divergence has been observed using sunspots (Nesme-Ribes et al. 1993b, 1997; see also the review by Howard 1996a) and cross-correlations of magnetograms separated by one solar rotation (Snodgrass & Dailey 1996). The difference between these last results and the result presented in this paper could be due to the fact that the use of a

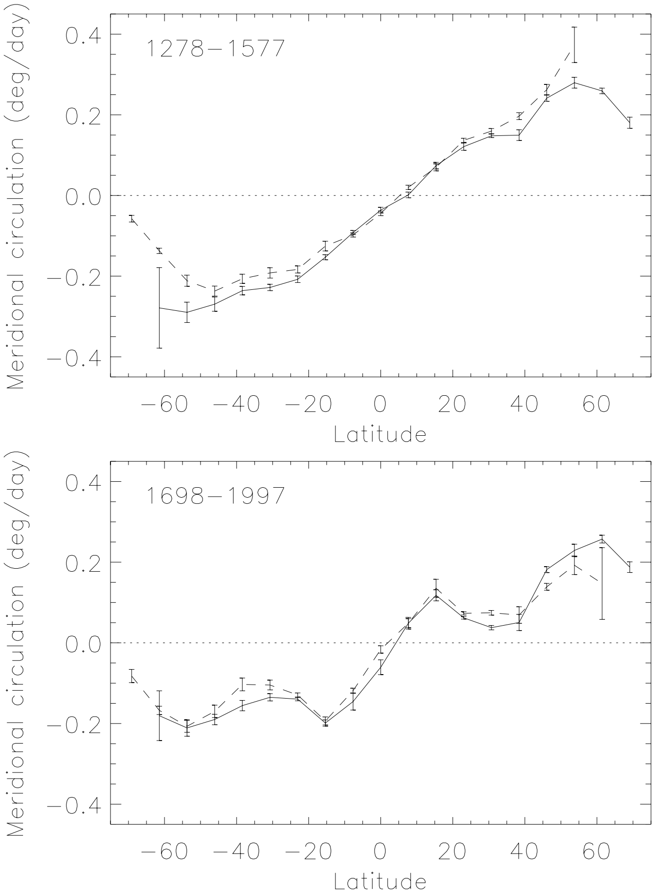

FIG. 8.—Meridional motions in degrees per day for positive magnetic fields (*solid line*) and negative magnetic field (*dashed line*), for the mission days 1278–1577 (*top*) and 1698–1997 (*bottom*). The positive polarity is leading in the north and following in the south. Positive meridional flows are northward. A rate of 0°.3 per day corresponds to approximately 42 m s^{-1}.

time interval of one solar rotation is more likely to characterize some processes deeper within the solar convection zone that controls the emergence of the magnetic flux, while a short time interval is more sensitive to diffusion processes at the surface. However, Strous et al. (1996) analyzed an active region with high resolution and tracked the small magnetic features (flux tubes or groups of flux tubes) individually; for a growing region, they found an expansion of the region. The spatial resolution used in the cross-correlation calculations may be of importance in detecting that type of divergence.

2. Poleward motions have been observed by Howard et al. (1990) and Komm et al. (1993b) while cross-correlating magnetograms separated by one day and selecting weak field regions. Similar results have been observed by Meunier et al. (1997b) while tracking bright features in plages using spectroheliograms obtained close to the photospheric level, and by Cameron & Hopkins (1998) using synoptic maps of magnetic fields averaged in longitude. Doppler measurements also show a poleward meridional circulation (see, e.g., Hathaway 1996).

Komm (1994) also observed a small equatorward motion at medium latitudes using only active regions from magnetograms separated by 1 day, but this motion was not very significant. The meridional circulation obtained in the present work is much more significant and very different from most other results. Such a difference is not yet understood. Why are the meridional motions of magnetic features inside active regions smaller than those of features in quiet regions? One explanation could be that these features are anchored at a different depth (for example, deeper than the quiet-Sun magnetic features), so that they would probe a different layer and therefore could exhibit a different meridional circulation. In that case, these motions would also correspond to a meridional flow (i.e., this would be due to a global circulation). On the other hand, the observation could also be due to local motions inside the active region, where they would be related either only to the motions of the magnetic flux tubes or to the dynamics of the flux tubes plus the entire plasma. Note that helioseismic measurements performed by Braun & Fan (1998) showed a small decrease of the meridional circulation with depth, while time-distance measurements (Giles et al. 1998) and ring-diagram analysis (González Hernández et al. 1998) of MDI data showed that the meridional circulation was increasing slightly from the surface and then decreasing again, although the results are still noisy. Future work using local helioseismology will probably provide more informations that will help to clarify whether the behavior of active regions observed in the present work has a local or global origin.

A number of other questions remain unanswered. Are these smaller meridional motions in active regions observed during the whole cycle? Is the small decrease of rotation rate with time real? In addition, the long-term variation of the meridional circulation is not yet well established; Komm et al. (1993b) found a larger meridional circulation during the minimum of activity, while Meunier et al. (1997b) and Cameron & Hopkins (1998) found the opposite. It is still too early to provide an answer to this question using the MDI data set. New analyses of the MDI magnetograms during the coming solar maximum should allow us to answer some of the questions arising from these new results.

I am grateful to T. L. Duvall and R. W. Komm for their many constructive comments on this work and the manuscript. I would also like to thank P. Giles for helpful discussions regarding the analysis of biases. This research is supported by the SOI-MDI NASA grant NAS 5-3077 at Stanford University. *SOHO* is a mission of international cooperation between the European Space Agency (ESA) and NASA. Wilcox Solar Observatory data used in this study were obtained courtesy of J. T. Hoeksema. The Wilcox Solar Observatory is supported by NASA, NSF, and ONR.

REFERENCES

Arevalo, M. J., Gomez, R., Vazquez, M., Balthasar, H., & Wöhl, H. 1982, A&A, 111, 266

Balthasar, H., & Wöhl, H. 1980, A&A, 92, 111

Beck, J. G., Duvall, T. L., Jr., & Scherrer, P. H. 1998, Nature, 394, 683

Braun, D. C., & Fan, Y. 1998, ApJ, 508, L105

Cameron, R., & Hopkins, A. 1998, Sol. Phys., 183, 263

Choudhuri, A. R., Schussler, M., & Dikpati, M. 1995, A&A, 303, L29

Durney, B. R. 1996, Sol. Phys., 166, 231

Duvall, T. L., Jr. 1998, in Proc. SOHO 6/GONG 98 Workshop, ed. S. Korzennik & A. Wilson (ESA SP-418; Nordwijk: ESA), 581

Giles, P. M., Duvall, T. L., Jr., & Scherrer, P. H. 1998, in Proc. SOHO 6/GONG 98 Workshop, ed. S. Korzennik & A. Wilson (ESA SP-418; Nordwijk: ESA), 775

Gilman, P. A., & Howard, R. 1984, ApJ, 283, 890

———. 1985, ApJ, 295, 233

González Hernández, I., Patrón, J., Bogart, R. S., & SOI Ring Diagrams Team. 1998, in Proc. SOHO 6/GONG 98 Workshop, ed. S. Korzennik & A. Wilson (ESA SP-418; Nordwijk: ESA), 781

Hathaway, D. H. 1992, Sol. Phys., 137, 15

———. 1996, ApJ, 460, 1027

Hathaway, D. H., & Wilson, R. M. 1990, ApJ, 357, 271

Howard, R. 1985, ApJ, 295, 233

———. 1996a, ARA&A, 34, 75

Howard, R. 1996b, Sol. Phys., 167, 95

Howard, R., Harvey, J. W., & Forgach, S. 1990, Sol. Phys., 130, 295

Jones, H. 1989, Sol. Phys., 120, 211

Kambry, M. A., & Nishikawa, J. 1990, Sol. Phys., 126, 89

Komm, R. W. 1994, Sol. Phys., 149, 417

Komm, R. W., Howard, R. F., & Harvey, J. W. 1993a, Sol. Phys., 145, 1

———. 1993b, Sol. Phys., 147, 207

Labonte, B. J., & Howard, R. 1981, Sol. Phys., 73, 3

Leighton, R. B. 1964, ApJ, 140, 1547

Lustig, G. 1983, A&A, 125, 355

Meunier, N., Nesme-Ribes, E., & Grosso, N. 1997a, A&A, 319, 673

Meunier, N., Nesme-Ribes, E., & Collin, B. 1997b, A&A, 319, 683

Nesme-Ribes, E., Ferreira, E. N., & Mein P. 1993a, A&A, 274, 563

Nesme-Ribes, E., Ferreira, E. N., & Vince, L. 1993b, A&A, 276, 211

Nesme-Ribes, E., Meunier, N., & Vince, L. 1997, A&A, 321, 323

Scherrer, P., et al. 1995, Sol. Phys., 162, 129

Schou, et al. 1998, ApJ, 505, 390

Snodgrass, H. B. 1983, ApJ, 270, 288

———. 1991, ApJ, 383, L85

Snodgrass, H. B., & Dailey, S. B. 1996, Sol. Phys., 163, 21

Strous, L. H., Scharmer, G., Tarbell, T. D., Title, A. M., & Zwaan, C. 1996, A&A, 306, 947

Wang, Y. M., Sheeley, N. R., Jr., & Nash, A. G. 1991, ApJ, 383, 431

THE ASTROPHYSICAL JOURNAL, 530:1016–1025, 2000 February 20

TWO-DIMENSIONAL MODELING OF THE SOLAR OSCILLATION l-ν POWER SPECTRUM

NADÈGE MEUNIER
W. W. Hansen Experimental Physics Laboratory, Annex A207, Stanford University, Stanford, CA 94305-4085; nadege@quake.stanford.edu

AND

STUART M. JEFFERIES
National Solar Observatory, Tucson, AZ 85726; stuartj@mallard.bbso.njit.edu

Received 1999 July 6; accepted 1999 October 1

ABSTRACT

We describe an algorithm which can accurately model the spatial-temporal l-ν solar oscillation power spectrum over large ranges in frequency (ν) and degree (l). We show how modeling in two dimensions provides a better representation of the observed spectrum than can be obtained with traditional one-dimensional approaches. The gain comes from using more of the observed signal to constrain the model and improved descriptions of the solar background spectrum and the signal leakage between different spatial scales. We discuss the level of systematic error that can be expected in the solar oscillation mode frequency data published to date.

Subject headings: methods: data analysis — Sun: interior — Sun: oscillations

1. INTRODUCTION

The high-quality solar oscillation spectra currently being generated from data acquired with the Michelson Doppler Imager (MDI) on board the *Solar and Heliospheric Observatory* (*SOHO*) satellite and the Global Oscillation Network Group (GONG) are enabling helioseismologists to study some of the more subtle characteristics of the oscillation spectrum. Indeed, it has become apparent that current models for the spectrum are too simple and that the observed data are being analyzed in a less-than-optimal manner. This statement is based on two facts: (i) to date, no credible fits have been obtained for the high-l region ($l \gtrsim 170$) of the spectrum, and (ii) different fitting algorithms yield different model parameter estimates from the same data set (e.g., Schou et al. 2000). To produce accurate and precise mode frequencies, amplitudes, and line widths requires not only realistic models for the line profile, the background, and the observational response function, but also the use of all available observational information to constrain the models. Broadly speaking, use of only a subset of the available information reduces the precision of the measurements, while incorrect models reduce the accuracy. The latter is far more treacherous as systematic errors in the measurements of the mode parameters lead to incorrect inferences on the solar interior. A loss of precision, on the other hand, just hides some of the detail of the solar structure. Having said this, needlessly throwing away measurement precision is folly.

To correctly model the solar oscillation spectrum requires working in a complicated three-dimensional model space (i.e., l-m-ν). By sacrificing information about the latitudinal variation of the properties of the solar interior (including rotation), the modeling space can be reduced to two dimensions (by averaging the different m spectra at each l-value to produce an l-ν or "m-averaged" spectrum: Pohl & Anderson 1998). Even so, the observed spectrum is still complicated. Because of the computational difficulty involved with modeling large regions of the data space at one time, current fitting algorithms confine their modeling to a data space that has one or more fewer dimensions than the observed data; i.e., they fit "slices" of the observed spectrum. For example, when fitting an l-m-ν spectrum, either single m-ν slices or even just simple ν slices of the spectrum are modeled at any one time. In addition, some algorithms also restrict the fitting regions within these slices to small frequency intervals around each target peak. This "limited region" approach has two drawbacks: (i) the leakage signal in the fitting domain is not well constrained, and (ii) there is insufficient data to allow a reliable determination of the background signal. Both of these effects lead to inaccurate model parameter estimates.

In this paper we investigate the problem of how to accurately model the oscillation spectrum simultaneously in all the observed dimensions; in particular, we address the problem of modeling the l-ν power spectrum.

2. A TWO-DIMENSIONAL MODEL FOR THE l-ν POWER SPECTRUM

Assuming the solar oscillations are randomly excited (Goldreich & Kumar 1988), an observation of a finite time realization of the l-ν power spectrum, $O(l, \nu)$, is given by

$$O(l, \nu) = FM(l, \nu) , \tag{1}$$

where F is a random function with statistics that follow a χ^2 distribution with $2(2l + 1)$ degrees of freedom (Anderson, Duvall, & Jefferies 1990) and $M(l, \nu)$ is the limit spectrum that would be obtained by averaging an infinite number of realizations. The limit spectrum can be modeled by

$$M(l, \nu, \boldsymbol{a}) = \sum_{\nu'} \sum_{l'} [L(l', \nu', \boldsymbol{a}_L) + B(l', \nu', \boldsymbol{a}_B)] W(l, l'; \nu, \nu') . \tag{2}$$

Here $L(l, \nu, \boldsymbol{a}_L)$ is the oscillation line profile, $B(l, \nu, \boldsymbol{a}_B)$ is the background spectrum, $\{\boldsymbol{a}\} = \{\boldsymbol{a}_L, \boldsymbol{a}_B\}$ is the set of model parameters, and $W(l, l'; \nu, \nu')$ is the response function which describes how the signal from spectral location (l', ν') leaks into (l, ν). In order to extract the maximum amount of information from the spectrum it is important to use realistic, physically based models for *all* components of M. This is the approach we have taken.

For the oscillation line profile we use the simple two-wave interference model of Duvall et al. (1993), modified to take into account the component of the background signal that is correlated with the p-mode signal (Roxburgh &

Vorontsov 1998; Nigam et al. 1998), i.e.,

$$L(\nu, l, \boldsymbol{a}) = \left| A(l, \nu)\left(1 + \frac{De^{-i2(\theta - \delta\theta)}}{1 - Re^{-i2\theta}}\right) + B_c e^{-i\phi} \right|^2 . \qquad (3)$$

In this model the oscillation source is assumed to lie outside the subphotospheric acoustic cavity. Following the notation of Duvall et al. (1993), A is the amplitude of the upward-emitted wave from the acoustic source, R is the wave reflection coefficient at the solar surface, D is the amplitude of the downward-emitted wave (with respect to the upward-emitted wave), θ is the phase delay of a wave incurred in traveling from the top of the acoustic cavity to the bottom, $\delta\theta$ is the phase delay between the acoustic source and the top of the acoustic cavity, B_c is the amplitude of the correlated component of the background signal, and ϕ is the phase difference between B_c and the p-mode signal. The parameter θ is related to the mode frequency, ν_0, through the expression

$$\theta \equiv \frac{\pi(\nu - \nu_0)}{\Delta\nu} , \qquad (4)$$

where $\Delta\nu$ is the separation between radial orders at constant degree l.

For the background component of M, we follow the approach of Harvey et al. (1992) and assume the background spectrum can be decomposed into periodic and nonperiodic components and white instrumental noise, i.e.,

$$B(l, \nu, \boldsymbol{a}_B) = \sum_{i=1}^{k} \frac{C_i}{\{1 + [2\pi\tau_i(\nu - \nu_i)]^{\eta_i}\}^{\beta_i}} + N . \qquad (5)$$

Here C_i, τ_i, ν_i, η_i, and β_i are the amplitude, characteristic lifetime, central frequency, and two decay parameters, respectively, for the periodic and nonperiodic components, k is the number of components required for the data (see Harvey et al. 1992 and Straus et al. 1999 for details), and N is the instrumental noise.

The response function can be separated into spatial and temporal components. The spatial component is normally modeled (e.g., Schou & Brown 1994; Hill & Howe 1998) and the temporal component is measured (although sometimes it is even ignored). Unfortunately, the spatial component of the response function has the property that it varies with ν and l which makes modeling the l-ν spectrum computationally expensive. However, for modes with radial orders $n > 3$ (see Fig. 3 of Schou 1996) and $l \gtrsim 20$, the response changes slowly with spectral location and can thus be treated as invariant over moderate ranges of ν and l. That is, $W(l, l'; \nu, \nu') \simeq W(l - l', \nu - \nu')$, and equation (2) reduces to a convolution that can be efficiently computed in the Fourier domain. The convolution approximation also makes it straightforward to allow the spatial components of W to be free parameters in the fit (i.e., $\{\boldsymbol{a}\} = \{\boldsymbol{a}_L, \boldsymbol{a}_B, \boldsymbol{a}_W\}$). This is important, as not all of the sources of signal leakage are fully understood, and thus W is never exactly known (Korzennik 1990). The amplitudes of all of the δ-functions in the spatial component of W should be made free parameters whenever the signal-to-noise ratio of the data enables the individual m leaks to be detected, i.e., at low frequencies in high-resolution spectra. Otherwise the amplitude ratios of the δ-functions at each δl-value are fixed to their calculated values (J. Schou 1998, private communication), but the sum of the amplitudes is allowed to vary with δl (δl is measured relative to the center of the response). The positions of the leaks in frequency are given by $\nu_{\rm leak} = \nu_0 + L \sum_{i=0}^{i_{\rm max}} a_i P_i(m/L)$, where $L = [l(l+1)]^{1/2}$ and P_i are Legendre polynomials. The values for the a_i coefficients we used in this work are taken from Brown & Morrow (1987), i.e., $a_1 = 435$ nHz, $a_3 = 21$ nHz, $a_5 = -4$ nHz, and $a_{\rm even} = 0$.

3. FITTING THE TWO-DIMENSIONAL MODEL TO THE OBSERVED SPECTRUM

For $l \gtrsim 5$, the noise distribution in the logarithm of the l-ν spectrum is well approximated by a Gaussian distribution (Walden, McCoy, & Percival 1995). Thus, maximum likelihood estimates for the model parameters, $\{\boldsymbol{a}\}$, can be obtained by minimizing the error metric

$$\epsilon = \sum_{l} \sum_{\nu} \frac{[\ln O(l,\nu) - \ln M(l, \nu, \boldsymbol{a})]^2}{(n_{\rm dat} - n_{\rm par})[(2l + 1)/(2l_0 + 1)]\sigma^2} , \qquad (6)$$

where l_0 is the central l-value of the fitting region, σ^2 is the variance of the signal in the $\ln[O(l_0, \nu)]$ data, $n_{\rm dat}$ is the number of data points, and $n_{\rm par}$ is the number of free parameters. The quantity $(n_{\rm dat} - n_{\rm par})\sigma^2$ is a constant for each fitting region and does not affect the minimization. This definition of ϵ allows it to be used as a goodness-of-fit measure (Bevington & Robinson 1992).

The spectral region required for two-dimensional fitting is shown schematically in Figure 1. To accurately model the region $(l_1{:}l_2, \nu_1{:}\nu_2)$ requires $M(l, \nu, \boldsymbol{a})$ to be estimated over the interval $(l_1 - 2\Delta l_W{:}l_2 + 2\Delta l_W, \nu_1 - 2\Delta\nu_W{:}\nu_2 + 2\Delta\nu_W)$ and compared with the observed spectrum over the region $(l_1 - \Delta l_W{:}l_2 + \Delta l_W, \nu_1 - \Delta\nu_W{:}\nu_2 + \Delta\nu_W)$. Here Δl_W and $\Delta\nu_W$ are one-half the spatial and temporal extent of the response. In practice, because W varies with spectral location more quickly with ν than with l, we normally restrict the frequency range $(\nu_1{:}\nu_2)$ to encompass only three adjacent radial orders. We typically use $\Delta l_W = 8$–10 (which generates a spectral multiplet with 17–21 peaks, respectively), while $\Delta\nu_W$ is determined by the size of the temporal window and the number of m leaks with significant amplitudes. We note that the parameters for the model in the region outside $(l_1{:}l_2, \nu_1{:}\nu_2)$ become less and less constrained by the data as one moves to the extremes of the region $(l_1 - 2\Delta l_W{:}l_2 + 2\Delta l_W, \nu_1 - 2\Delta\nu_W{:}\nu_2 + 2\Delta\nu_W)$. When Δl_W is large, many of the modes in the ranges $(l_1 - 2\Delta l_W{:}l_1 - \Delta l_W)$ and $(l_2 + \Delta l_W{:}l_2 + 2\Delta l_W)$ appear in the region of comparison with the observations only as very small leaks (never through their target peak). Thus, they are a source of instability. For this reason, the parameters of the modes corresponding to the smallest leaks in these domains are frozen to their initial values. Any small inaccuracies incurred by this practice are removed by iterating the fitting procedure for the full l-ν spectrum.

Because we model the spectrum over several ridges, the transition region between modes (i.e., near $\nu = [\nu_0(n-1, l) + \nu_0(n, l)]/2$ and $\nu = [\nu_0(n+1, l) + \nu_0(n, l)]/2$) is problematic. If one switches from one set of mode parameters to another, then the model exhibits unrealistic discontinuities at the crossover points. We solve this problem by treating the parameters as continuous functions of frequency. In practice, we still define a set of parameters R, D, A, B_c, and $\delta\theta$, as well as Δ_ν, for each mode, but we use a linear interpolation between the parameters that correspond to the two closest target peaks. This provides a significant improvement to the fit.

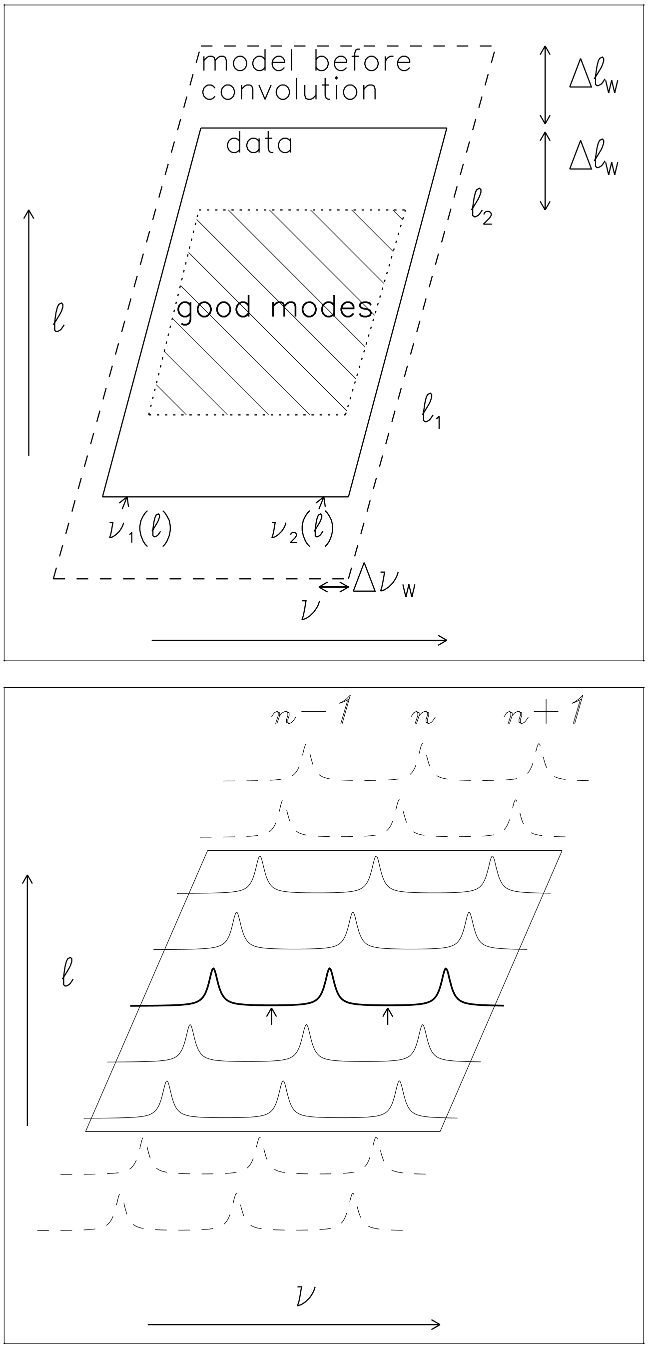

FIG. 1.—*Top*: Schematic representation of the spectral region required for two-dimensional fitting (see text). *Bottom*: Illustration of the spectral region required for three n-values and $\Delta l_W = 2$ (note that in practice we use $\Delta l_W = 8$–10), with one "good mode" (*thick line*). The dashed curves correspond to the modes outside of the domain that are necessary for the calculation of the convolution, while the solid curves correspond to the modes inside the domain where the model is compared to the data. The modes are shown as they appear before the convolution (i.e., without leakage). The two arrows show the limits of the fits represented in Figs. 2 and 4.

We obtain initial estimates for the line profile parameters ν_0, R, D, A, and $\delta\theta$ by first fitting the data using a modified version of the algorithm of Duvall et al. (1993). In the modified version of the Duvall et al. algorithm, the nature of the background has been changed from multiplicative to additive (using a linear representation of B). The initial estimate for B_c is set to zero, while ϕ is currently set to zero and is not allowed to vary. Attempts to fit the phase provided very noisy values and did not improve the goodness-of-fit values; it is possible that a simultaneous fit of velocity and intensity spectra (if available) would provide a reliable estimate of the phase. The parameters R and D are constrained to lie in the range [0, 1]. Initial estimates for the background parameters are determined by separately fitting the observed signal below $\sim$1.5 mHz and the signal in the minima between the peaks above this frequency using equation (5) (see Meunier & Jefferies 1998). Only the background components which have a significant amplitude in the fitting domain are allowed to vary during full spectral fitting.

Equation (6) is minimized using the Levenberg-Marquardt method (Press et al. 1986). This method calculates the Hessian matrix using the first derivatives of equation (6). The diagonal terms in the Hessian are multiplied by the factor $(1 + \lambda)$ and at each step of the minimization λ is decreased (or increased) by a factor of 10 if ϵ has decreased (or increased, respectively). That is, if the fit is successful, the off-diagonal terms are given more weight and vice versa. This strategy makes the minimization more efficient. We start with values of λ between 0.1 and 10 depending on the domain in the spectrum.

4. TWO-DIMENSIONAL ALGORITHM PERFORMANCE

To test the ability of the model described in § 2 to replicate the true solar limit spectrum, we need to be able to see the fine details of the observed l-ν spectrum. Therefore, to get a high signal-to-noise spectrum of real data, we took an l-ν spectrum generated from 360 days of MDI velocity data (J. Schou 1998, private communication), which has a duty cycle close to 100%. The frequency resolution is reduced to 0.64 μHz by frequency smoothing and subsampling (Gardner 1988), and then the resultant spectrum is wavelet denoised (Komm et al. 1999).

The first tests of the two-dimensional algorithm showed that it is computationally expensive compared to one-dimensional algorithms (approximately 200 times slower). Because of this we have restricted our initial evaluation of two-dimensional model fitting to selected regions of the spectrum. Figure 2 shows the fit to the multiplet centered on ($n = 12$, $l = 38$). This region of the spectrum is contaminated by a particularly insidious manifestation of the signal leakage: "n leaks" (Howe & Thompson 1998). These leaks pass through a target mode as one moves along a ridge (see Fig. 3) and, if not properly modeled, lead to systematic errors in the parameter estimates. Since these errors change with ν and l, they can mimic random errors when looking at averages of the parameter estimates made over small ranges in ν and l, a common practice. The fit to the multiplet ($n = 20$, $l = 38$) represents the beginning of the high-ν region where the peaks are strongly overlapped and the shape of the line profile is significantly different from that at 3.5 mHz and below (due to the transition from trapped waves to traveling waves). Figure 2 also shows the fit to the multiplet centered on ($n = 5$, $l = 150$). This is an example of a case where the individual peaks in a multiplet are strongly overlapped but still sufficiently separated to remain resolved. It also represents the high-l edge of the spectral region that can currently be modeled with any reliability for p-modes. Note that this fit, as well as the fit to the multiplet centered on ($n = 5$, $l = 100$), shows that the residuals around the target peak are not flat: the fitted width seems to

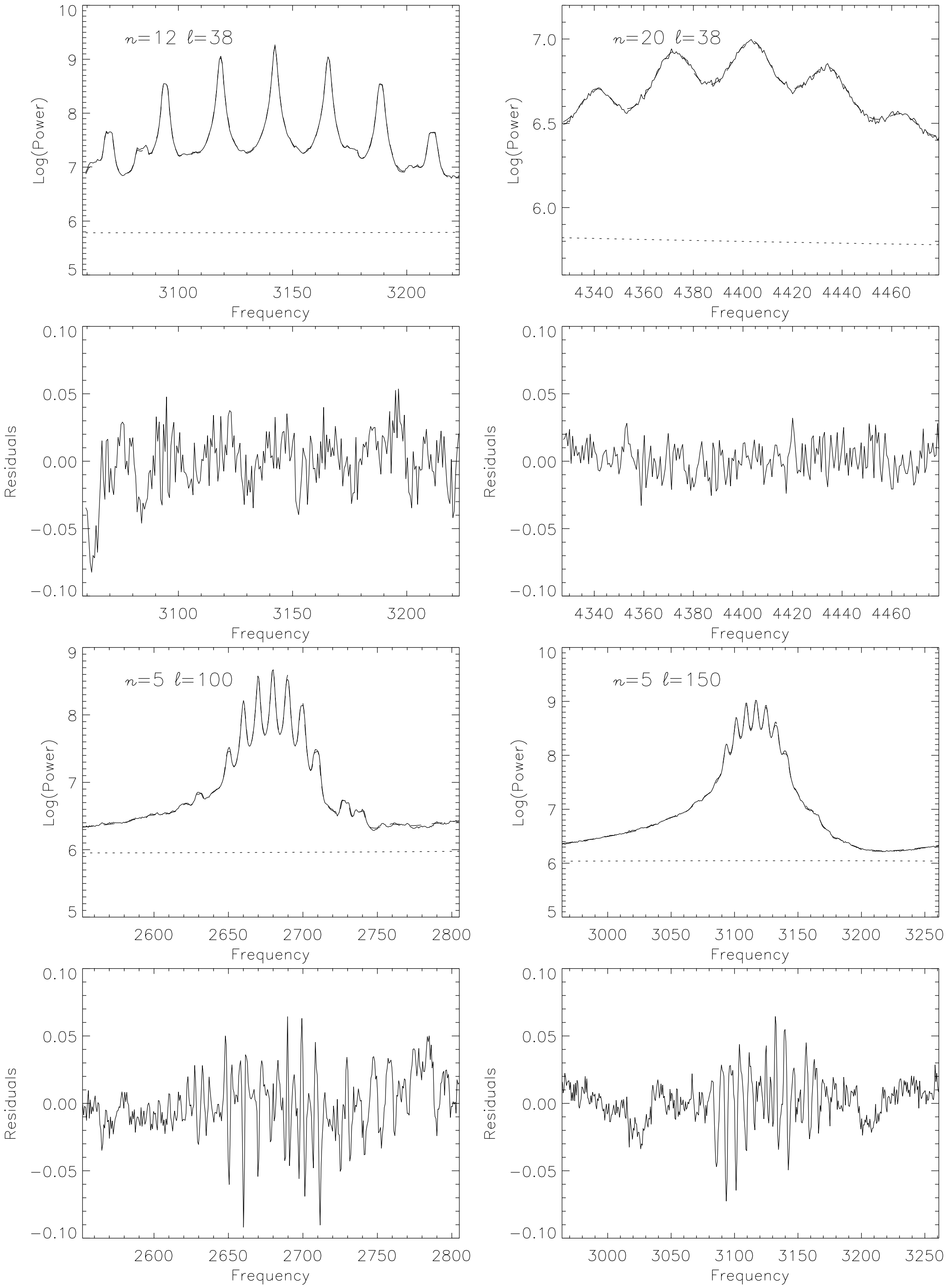

FIG. 2.—Two-dimensional fits (*dashed lines*) to four multiplets in the low-resolution, wavelet-denoised, MDI velocity *l*-*ν* power spectrum (*solid lines*). The dotted lines represent the fitted background *B*. The residuals are equal to log (model) − log (data).

be slightly too large. This could be due either to a problem with the background estimate (an accurate determination may require fitting over a larger frequency range in this domain) or to slightly incorrect *m*-leak amplitudes. Even so, the residuals from two-dimensional fitting are still superior to those from one-dimensional fitting (see Table 3). Figure 2 shows that our two-dimensional model provides a good representation of the data at some of the more difficult locations in the intermediate-*l* range ($20 \lesssim l \lesssim 170$).

As a further demonstration of our two-dimensional model, we show the fits to the multiplet at ($n = 5$, $l = 220$) (Fig. 4). This example represents the beginning of the high-*l* region where the individual peaks in a multiplet are no longer resolved and blend into a single smooth ridge. As can

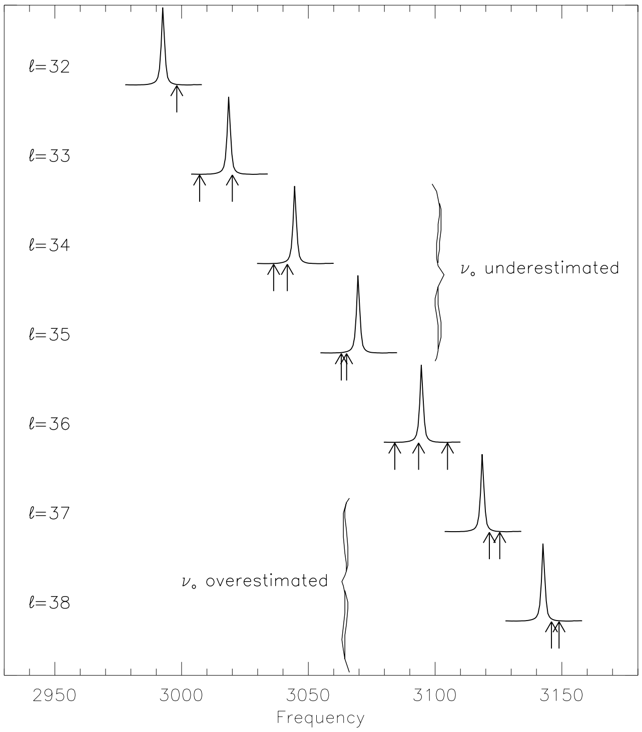

FIG. 3.—Schematic representation of n leakage. The profiles represent the target peak for different modes along the ridge $n = 12$; the arrows denote the position of leaks from the adjacent ridges and show how the leaks "cross" the target peak as l increases.

be seen from Figure 4, the data are well modeled even in this notoriously difficult-to-model area.

Contrary to the theoretical expectation that $B_c \simeq 0$ for velocity data (Kumar & Basu 1999a), our fitting of the MDI velocity spectrum produced values for B_c which, although small in comparison to the values for A, had a significant impact on the quality of the fits (as a result of the term proportional to $B_c A$ in the power spectrum derived from eq. [3]). Furthermore, we found that the fit made at ($n = 5$, $l = 220$) (for which the improvement due to the inclusion of B_c is the largest) showed a large correlation (0.98) between B_c and A.[1] This result is in agreement with Kumar & Basu's (1999a) suggestion that A and B_c should be highly correlated (see eq. [2] of their paper). However, for our fits to the lower l–modes we found very small correlations (close to 0). The issue of to what extent B_c and A are correlated will have to await a more extensive fitting of the spectrum. However, if B_c and A are highly correlated (the lack of correlation for low-l–modes could be due to a less accurate determination of B_c in these regions because of the smaller signal-to-noise ratio), then this behavior could be incorporated into the model. This would reduce the number of parameters. We note that Skartlien & Rast (2000) have recently shown that to successfully model the qualitative shape of the observed intensity-velocity phase difference and power spectra requires a correlated noise component in both the intensity and velocity signal (i.e., $B_c \neq 0$ for velocity).

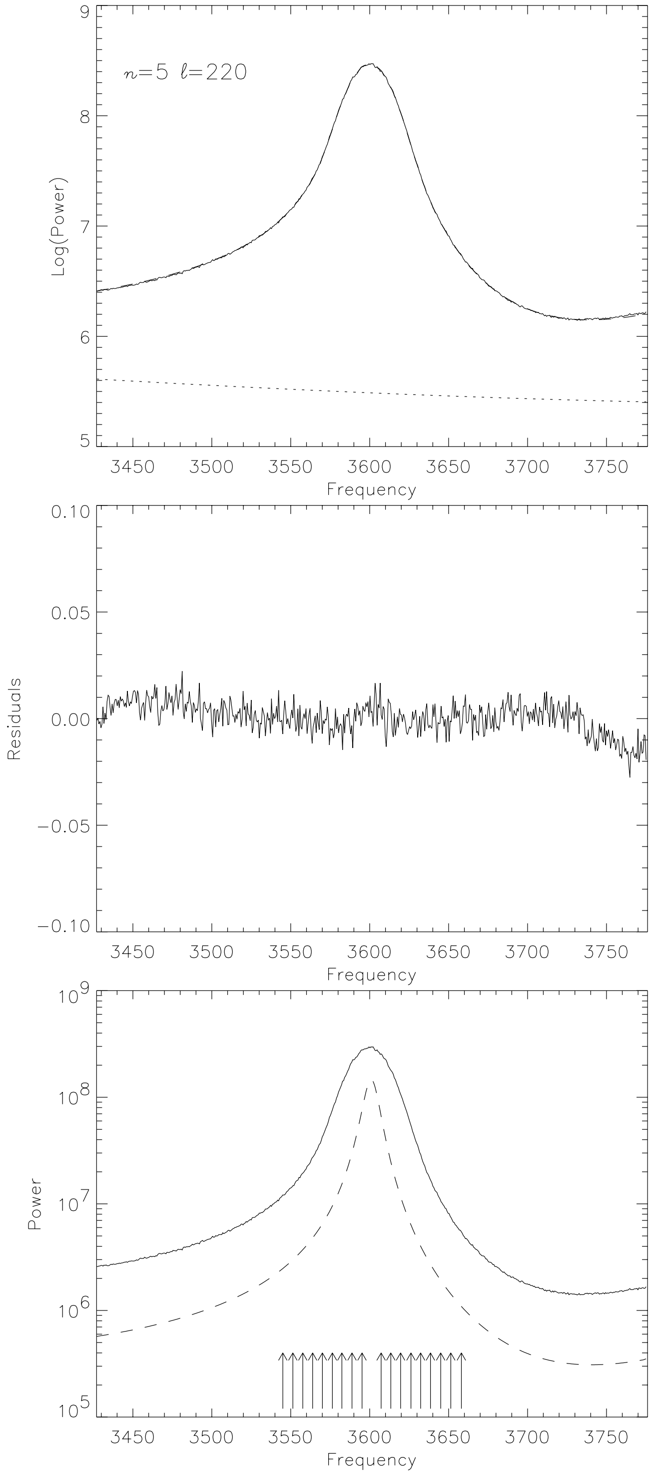

FIG. 4.—*Top*: Two-dimensional fit (*dashed lines*) to the $n = 5$, $l = 220$ multiplet in the low-resolution, wavelet-denoised, MDI velocity l-v power spectrum (*solid lines*). The dotted line represents the fitted background B. *Middle*: Residuals, equal to log (model) − log (data). *Bottom*: The component due to the target peak only (*dashed line*) is shown compared to the observed profile (*solid line*). The arrows show the position of the leaks that were used to perform the fit.

Figure 5 shows the difference between the calculated l leaks and the ones estimated from fitting the data. The differences are small at low Δl but increase as Δl increases (i.e., for the small-amplitude leaks). Note that the residuals for the responses are very similar for all the three fits at large l (100, 150, and 220), which probably indicates a systematic error in the theoretical response. The very large

---

[1] The correlation was calculated over the modes $n = 4$–6, $l = 211$–229, i.e., all the modes in the "data domain" for the fit. We also observed a sign reversal of B_c across the domain corresponding to this fit.

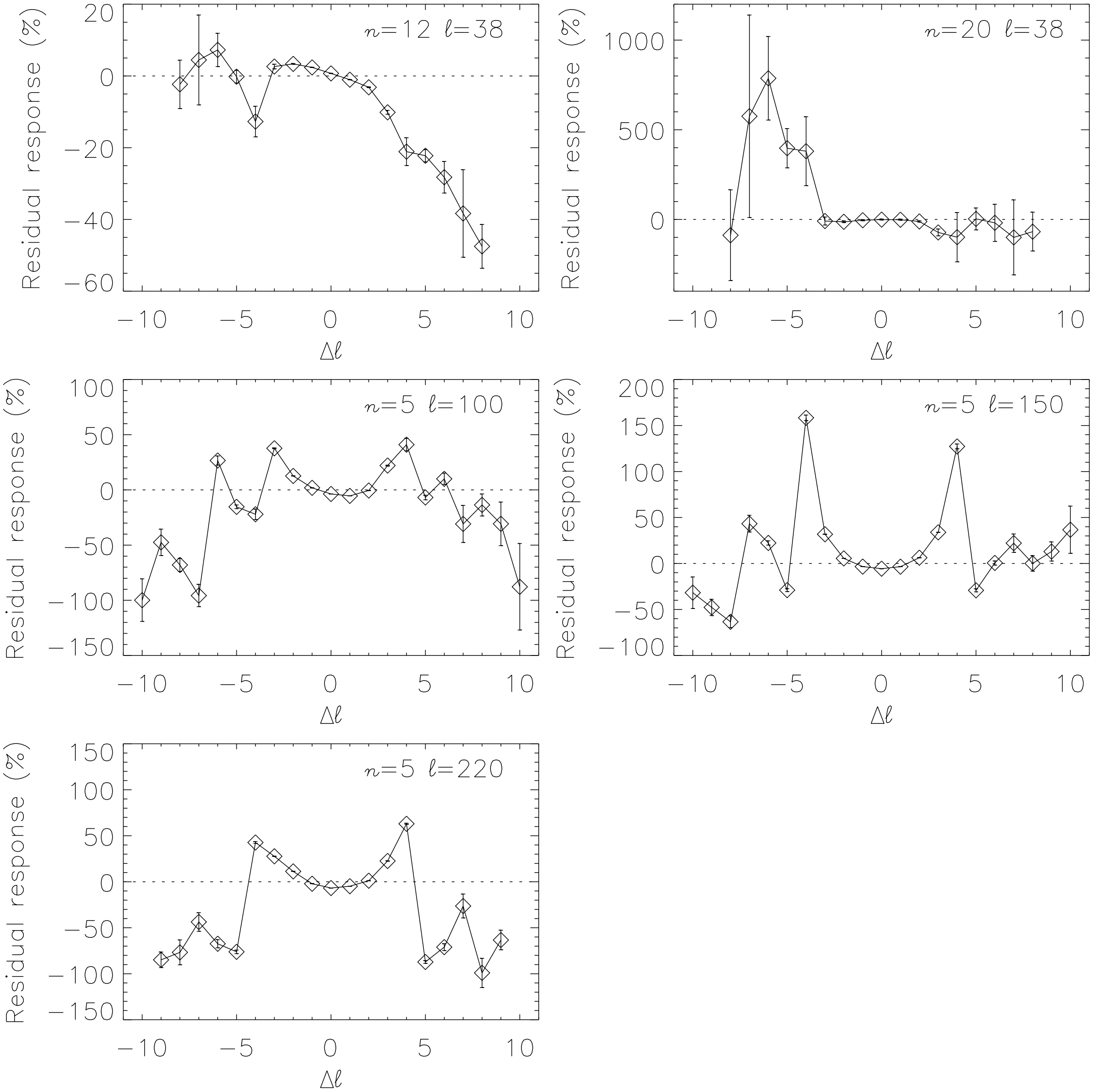

FIG. 5.—Residuals of the l-response (fitted response values minus the calculated ones divided by the calculated ones), in percentage

response residuals for the multiplet ($n = 20$, $l = 38$) correspond to very small leaks that are not very well constrained because of both the strong overlapping and the small signal-to-noise ratio. Fits made with the response function parameters fixed at the calculated values yield goodness-of-fit parameters, ϵ, that are up to 4 times worse than those obtained when the response function parameters are variables in the minimization. The effect on the line profile parameters of not allowing the response to vary is illustrated in Table 1. The differences in ν_0 and R increase with l, while the influence on D and $\delta\theta$ is large mainly at large frequencies.

TABLE 1

FIT PARAMETERS OBTAINED FOR DIFFERENT l-RESPONSES (FIXED AND VARIABLE)[a]

Mode	ν_0 (mHz)	σ_{ν_0} (nHz)	$\epsilon_{\rm fit}/\epsilon_{\rm froz}$	$\Delta\nu_0$[b] (nHz)	$R_{\rm fit}$	ΔR[b]	$D_{\rm fit}$	ΔD[b]	$\delta\theta_{\rm fit}$	$\Delta\delta\theta$[b]
$n = 12$, $l = 38$......	3.14	1	0.81	3	0.975	-6×10^{-4}	0.608	−0.002	−0.105	0.022
$n = 20$, $l = 38$......	4.40	2900	0.80	−4	0.676	−0.024	0.724	0.081	0.032	−0.046
$n = 5$, $l = 100$......	2.68	2	0.33	37	0.972	-2×10^{-4}	0.569	0.011	−0.242	−0.019
$n = 5$, $l = 150$......	3.11	2	0.26	57	0.967	−0.002	0.884	−0.006	−0.210	−0.014
$n = 5$, $l = 220$......	3.60	50	0.22	89	0.901	0.006	0.930	−0.018	−0.127	−0.005

[a] Fit denotes the parameters obtained when the l response is fitted.

[b] The parameter differences Δ correspond to (fixed l-response − variable l-response). The uncertainties on the frequencies are determined from the diagonal elements of the Hessian matrix.

TABLE 2

Fit Parameters Obtained for Two Different Line Profiles

Mode	$\epsilon_{\rm os}/\epsilon_{\rm nk}$[a]	$\Delta\nu_0$[b] (nHz)	Γ[c] (μHz)	$\Delta\Gamma$[b] (μHz)
$n = 12, l = 38$......	0.29	−29	1.35	−0.01
$n = 20, l = 38$......	0.50	886	19.20	−1.66
$n = 5, l = 100$......	0.34	−18	2.24	0.12
$n = 5, l = 150$......	0.20	−48	3.18	−0.28
$n = 5, l = 220$......	0.03	1102	11.64	−4.28

[a] os = eq. (3); nk = Nigam & Kosovichev profile.

[b] The differences Δ are for (nk − os).

[c] The widths Γ for the profile of eq. (3) are obtained using eq. (A3).

We note that several other physically based line profile models have been proposed in the literature (Gabriel 1995; Rosenthal 1998; Nigam & Kosovichev 1998). Because a number of groups are using the polynomial version of the Nigam & Kosovichev profile (e.g., Toutain et al. 1998; Bertello et al. 1999),

$$L(\nu, l, \boldsymbol{a}) = A(l, \nu)\,\frac{(1 + Bx)^2 + B^2}{1 + x^2}\,, \tag{7}$$

where $x = 2(\nu - \nu_0)/\Gamma$ and B is an asymmetry parameter related to the correlated background, we also performed some fits using this profile. We found that two-dimensional fits made with equation (7) produce significantly worse goodness-of-fit values than those obtained with equation (3) (see Table 2). The worse performance of the Nigam & Kosovichev profile is most likely due to it having been derived from a truncated Taylor series expansion of the full expression for the profile. We note that in the limit of high reflectivity ($R \simeq 1$), a Taylor series expansion of equation (3) reduces it to a form which will yield the same fit to the data as is obtained by using equation (7) (see the Appendix). This means that the shape of the profiles is similar, although the physical interpretation of the parameters is different. We note that since equation (7) is not a periodic function, interpolation of the parameters to get a continuous function versus frequency still results in discontinuities in the model (this would not be a problem with the full version of the Nigam & Kosovichev profile). Equation (7) is therefore not suitable for fitting the spectrum over a large range in frequency. The frequency estimates obtained using equation (7) are systematically smaller than those obtained using equation (3) by 20–40 nHz (except at high frequencies and high l where the difference is positive and much larger, up to 1 μHz), while the widths are different by 1%–40% (however, the width difference could be biased due to our use of eq. [A3] to convert the reflection coefficient R into a line width).

5. COMPARISON WITH ONE-DIMENSIONAL MODELING

In principle, two-dimensional modeling of the data should provide better parameter estimates than one-dimensional modeling as the model is better constrained by the data. In particular, the frequency, width, and asymmetry of the low signal-to-noise leakage peaks are strongly constrained by the target peak and the high signal-to-noise leakage peaks through the response function. However, a determination of the accuracy of the model parameter estimates obtained from two-dimensional and one-dimensional modeling of the l-ν spectrum is difficult: real data cannot be used as the "true" parameters are not known; simulated data are not useful as they are limited by our incomplete knowledge of the true parent function and are thus biased toward models similar to that used to generate the data.[2] An intuitive solution to this problem is to determine which model best represents the parent function using the F-test (Bevington & Robinson 1992) and then, by inference, assume that the better model provides the most accurate parameters. However, even this solution has a problem if one wants to compare one-dimensional (1D) and two-dimensional (2D) models. The problem is "What should we use for the two-dimensional goodness-of-fit value when computing the ratio $\epsilon_{\rm 2D}/\epsilon_{\rm 1D}$?" Although it is lacking in "statistical rigor," we propose that the goodness-of-fit ratio

$$\frac{\epsilon_{\rm 2D}(l)}{\epsilon_{\rm 1D}(l)} \equiv \sum_{\nu} \frac{[\ln O(l, \nu) - \ln M(l, \nu)]^2_{\rm 2D}[n_{\rm dat}({\rm 1D}) - n_{\rm par}({\rm 1D})]}{[\ln O(l, \nu) - \ln M(l, \nu)]^2_{\rm 1D} \times [n_{\rm dat}({\rm 1D}) - [n_{\rm dat}({\rm 1D})/n_{\rm dat}({\rm 2D})]n_{\rm par}({\rm 2D})]}\,, \tag{8}$$

which is designed to mimic the ratio required for the F-test, should be a reliable measure of which model best represents the true parent model. (The summation in eq. [8] is over the frequency interval used for the one-dimensional modeling.)

The one-dimensional algorithms we used for the one-dimensional/two-dimensional comparison were the GONG peakfind algorithm (Hill et al. 1996), the Duvall et al. ofitpow algorithm (Duvall et al. 1993), and the modified version of the ofitpow algorithm. In practice, the best one-dimensional fits for all the modes except ($n = 5$, $l = 220$) were obtained using the original version of the ofitpow algorithm with the multiplicative background. This shows that the one-dimensional results are sensitive to the choice of background, which is not very well constrained, and are therefore not very robust. Note also that the ofitpow algorithm makes the assumption that the leaks have the same parameters (D, R, and $\delta\theta$) as the target peak; this is not valid if these parameters change quickly with frequency or degree. As can be seen from the values of $\epsilon_{\rm 2D}/\epsilon_{\rm 1D}$ in Table 3, two-dimensional modeling provides a superior representation of the data. The ratio $\epsilon_{\rm 2D}/\epsilon_{\rm 1D} = 1$ for the mode ($n = 20$, $l = 38$) can probably be explained by the fact that different models can more easily represent data which have a low signal-to-noise ratio (which shows that in this domain the use of an accurate model to describe the data is very important). The main reason for the poorer performance of the peakfind algorithm, in comparison to the ofitpow algorithm, is that the former uses an incorrect line profile (a Lorentzian).[3] The differences between the parameter estimates obtained using the modified ofitpow algorithm and those obtained using our two-dimensional algorithm are the result of the coupling that takes place between the model parameters. Some couplings are weak (e.g., B and ν_0), others are strong (e.g., B and D, B and $\delta\theta$, ν_0 and $\delta\theta$). This

---

[2] Generating simulated data with a given model (e.g., eq. [3]) and then fitting the data using the same model—but with initial parameter estimates that differ from the true parameter values—tells us nothing about the accuracy of the model parameters when fitting real data; it only tells us if the fitting algorithm is working correctly.

[3] Using simulated data, we found that the correction proposed by Abrams & Kumar (1996) for the frequency offset produced by fitting the observed asymmetric line profile with a symmetric Lorentzian profile is not valid when there is overlapping of the spectral peaks.

TABLE 3

COMPARISON OF THE PARAMETERS OBTAINED WITH THE ONE-DIMENSIONAL AND TWO-DIMENSIONAL ALGORITHMS

Mode	$\epsilon_{2D}/\epsilon_{1D}$	$\Delta\nu_0$[a] (nHz)	ΔR[a]	$\Delta\Gamma$[a,b] (μHz)	ΔD[a]	$\Delta\delta\theta$[a]
$n = 12, l = 38$[c]......	0.21	5	−0.006	0.33	0.069	0.004
$n = 12, l = 38$[d]......	0.07	−33	...	0.04	...	...
$n = 20, l = 38$[c]......	1.01	−1390	−0.043	8.78	0.099	0.139
$n = 5, l = 100$[c]......	0.35	−13	−0.002	0.24	−0.026	0.099
$n = 5, l = 100$[d]......	0.19	−89	...	−0.06	...	...
$n = 5, l = 150$[c]......	0.63	−1	0.003	0.06	−0.042	0.058
$n = 5, l = 150$[d]......	0.07	−66	...	−0.57	...	...
$n = 5, l = 220$[c]......	0.72	704	−0.002	0.83	−0.025	10^{-4}
$n = 5, l = 220$[d]......	0.03	716	...	−7.20	...	...

[a] The differences Δ correspond to (one-dimensional − two-dimensional).

[b] The widths Γ are obtained using eq. (A3).

[c] The one-dimensional fit was made using the modified ofitpow algorithm.

[d] The one-dimensional fit was made using the peakfind algorithm.

interdependence of the parameters emphasizes the importance of correctly modeling all the components of M, especially if one wants to extract the physics behind the mode parameters outside of ν_0.

We note that because of the diversity in one-dimensional algorithms currently in use in helioseismology, both in the models used and in their application to the data, the results from the peakfind and ofitpow algorithms may not necessarily represent the performance of other one-dimensional algorithms. Even so, we believe that Table 3 provides good estimates of the sizes of the systematic errors that may be present in the mode frequency and line width estimates published to date.

6. DISCUSSION

We have shown the importance of using an accurate model for the spectrum and how a shortcoming in any aspect of the model (line profile, background, or response function) can lead to systematic errors in the measured model parameters. As would be expected, the more shortcomings there are, the more the model parameters are affected by systematic errors. Although two-dimensional modeling is computationally expensive compared to one-dimensional methods, the inherent inability of one-dimensional modeling to correctly reproduce the background component of the spectrum means that one-dimensional techniques cannot produce unbiased model parameters. For example, Kumar & Basu (1999b) tried to estimate the depth of the oscillation source (which is directly related to the asymmetry of the modes). They performed some fits around target peaks over a very small range in frequency (14 μHz). However, as they point out, the parameters are influenced by the background level. The reason for this is well demonstrated by the ($n = 12$, $l = 38$) multiplet in Figure 2. Here the level of the background is approximately 1 order of magnitude smaller than the spectrum at the minimum next to the target peak. This shows that the use of a linear background fitted to the spectrum minima, without taking the leaks into account, will strongly bias the measurement of the mode parameters. The asymmetry, in particular, is strongly dependent on the frequency dependence of the background and the asymmetries introduced by the presence of leaks. We note that in addition to an accurate determination of the background level, a good estimation of the source depth requires the use of spectral information in both the low- and high-frequency domains (Nigam & Kosovichev 1999).

Although the two-dimensional approach outlined in this paper is an improvement over any one-dimensional approach, by limiting the fitting region to three radial orders we are still using too little of the observed signal to accurately determine the background. To improve the determination of the background requires larger areas of the spectrum to be modeled at one time, ideally the whole spectrum. From a practical standpoint this is not feasible because of the large number of free parameters used (especially if W is allowed to vary with ν and l). However, for modeling of the l-ν power spectrum, a dramatic reduction in the number of free parameters could be obtained by modeling θ using second-order asymptotic theory, i.e.,

$$\theta \equiv \omega F(w) + \frac{\Phi(w)}{\omega} - \pi\alpha(\omega) , \quad (9)$$

where the various quantities are as defined in Gough & Vorontsov (1995). By modeling the functions $F(w)$, $\Phi(w)$, $\alpha(\omega)$, $R(l, \nu)$, $D(l, \nu)$, $\delta\theta(\nu)$, and $A(l, \nu)$ in terms of back-to-back cubic splines, the entire l-ν spectrum could be modeled by many fewer parameters than by determining ν_0, R, D, $\delta\theta$, and A for every mode in the spectrum. This is keeping with the principle of Occam's razor and should lead to more accurate and precise parameter estimates. By obtaining an accurate representation of the background spectrum, it may be possible to study the interaction of the acoustic waves with the solar convection (Rast 1999).

In addition to better modeling of the background spectrum, a major improvement of our two-dimensional model over one-dimensional models is the ability to measure the response function directly from the data. Inaccuracies in the response function produce frequency errors from a few nHz to several tens of nHz depending on the domain in the spectrum. The other parameters are also significantly affected. Errors of this size become important when studying small effects in the frequencies (such as the oscillatory signal due to the sound speed discontinuity at the base of the convection zone). Constraining the line profile parameter values for the leakage peaks through the response function is especially important for modeling the spectral region around $l \sim 40$, $\nu \sim 3$ mHz, where n leaks are a problem. Modes in this region of the spectrum have lower turning points near 0.7 $R_\odot$. This is the location of the "tachocline," where solar differential rotation vanishes. It is also the location where the solar dynamo is believed to reside (i.e., the source of solar magnetic activity). Accurate knowledge of both the response function and the background spectrum will also allow a better determination of the oscillation source depth (Kumar & Basu 1999b).

The ability of our two-dimensional model to fit the ($n = 5$, $l = 220$) and ($n = 20$, $l = 38$) multiplets in a credible way demonstrates that it is possible to accurately model the high-l and high-ν regions of the spectrum. These regions represent the vast majority of the observed spectrum and have been little explored. However, as noted above, further work needs to be done on modeling the background spectrum before the problem of modeling these regions can be fully addressed.

Throughout this paper we have stressed the importance of using a good physical model for the spectrum. However, we have omitted one aspect of the spectrum that becomes important at frequencies close to the spatial and temporal Nyquist frequencies: aliased signal. The modeling of the aliased signal is the subject for further research.

Lastly, there has been an undercurrent of belief among some helioseismologists that the l-ν spectrum is of limited scientific use. This is because different oscillation modes require different frequency corrections—due to the effects of the Sun's differential rotation—when making the l-ν spectrum. If one takes this standpoint then it might seem that our results only confirm what is intuitively obvious, i.e., the better the model and the more signal that is used in the analysis, the better the result. However, one would be missing an important point: our results show that accurate modeling of large regions of the oscillation spectrum *is* feasible (contrary to popular belief). This work therefore provides an important "proof of concept" step for three-dimensional modeling of the oscillation spectrum. Having said this, we believe that if care is taken in generating the spectrum (e.g., Pohl & Anderson 1998), then fits to this spectrum should yield credible mode parameters. Determining the sensitivity of the mode parameter estimates on small errors in the rotation coefficients, however, is a subject for further research.

We thank T. Duvall, F. Hill, R. Howe, R. Komm, R. Larsen, J. Leibacher, Y. Osaki, J. Schou, H. Shibahashi, P. Stark, and C. Toner for helpful discussions about various aspects of this work. We also thank J. Schou for providing the calculated values of the m leaks for the MDI observations as well as the l-ν MDI velocity spectrum used in this work. The National Solar Observatory is a division of the National Optical Astronomy Observatories, operated by the Association for Research in Astronomy Inc., under a cooperative agreement with the National Science Foundation. *SOHO* is a project of international cooperation between ESA and NASA. This work was supported in part by the National Science Foundation under the grant OPP9219515 and by NASA grants NAS 5-3077, NRA-98-03-SEC-003, and S-92698-F.

APPENDIX

TAYLOR EXPANSION OF EQUATION (3)

Equation (3) takes large values only when θ is very near $n\pi$ in the denominator. If we denote the eigenfrequency of the nth mode by ν_n, then we may write

$$\theta = \theta_n + (\theta - \theta_n) , \tag{A1}$$

where $\theta_n = n\pi$, $\theta - \theta_n = \pi(\nu - \nu_n)/\Delta\nu$. By using the Taylor expansion of cos 2θ about $\theta = \theta_n = n\pi$, we get

$$\cos 2\theta = \cos 2(\theta - \theta_n) \simeq 1 - \frac{1}{2}\left[\frac{2\pi(\nu - \nu_n)}{\Delta\nu}\right]^2 + \cdots = 1 - \delta . \tag{A2}$$

If we now substitute this expression, along with the expression for the wave reflectivity when $R \simeq 1$ (Duvall et al. 1993), i.e.,

$$R = 1 - (2\pi\Gamma S)\sqrt{R} \simeq 1 - \frac{2\pi}{\Delta\nu}\frac{\Gamma}{2} = 1 - \epsilon , \tag{A3}$$

into equation (3), we find in the limit of small ϵ and δ

$$\text{denominator} \simeq 2\delta + \epsilon^2 \tag{A4}$$

and similarly for the numerator of equation (3). Expanding the term cos $2(\theta - \delta\theta)$ gives a term in sin 2θ. Using a Taylor expansion gives $\sin 2\theta \simeq \sqrt{2\delta}$. Substituting this expression along with equations (A3) and (A2) into the numerator of equation (3), neglecting the term in $\epsilon\delta$, and dividing by equation (A4) produces

$$P \simeq A_0 \frac{1 + \alpha^2 x^2 + 2\beta x + \gamma^2}{1 + x^2} , \tag{A5}$$

where

$$x = 2\pi \frac{\nu - \nu_n}{\Gamma/2} , \tag{A6a}$$

$$A_0 = A^2 + 2AB_c\,, \tag{A6b}$$

$$\alpha^2 = \{A^2(1 - D\cos 2\delta\theta) + AB_c[2\cos\phi - D\cos(\phi - 2\delta\theta)]\}A_0^{-1}\,, \tag{A6c}$$

$$\beta = \frac{A^2 D\sin 2\delta\theta + AB_c D\cos(\phi + 2\delta\theta)}{A_0}\,, \tag{A6d}$$

$$\gamma^2 = \frac{1}{\epsilon A_0}\left\{\frac{A^2D^2 + 2AB_c[1 - \cos\phi - D\cos(2\delta\theta - \phi)] + B_c^2}{\epsilon} + 4AB_c[\cos\phi - 1 + D\cos(2\delta\theta - \phi) + 2A^2D\cos 2\delta\theta]\right\}. \tag{A6e}$$

REFERENCES

Abrams, D., & Kumar, P. 1996, ApJ, 472, 882

Anderson, E. R., Duvall, T. L., Jr., & Jefferies, S. M. 1990, ApJ, 364, 699

Bertello, L., Henney, C. J., Ulrich, R. K., Varadi, F., Kosovichev, A. G., Roca Cortes, T., Garcia, R. A., & Scherrer, P. H. 1999, BAAS, 194, 108.05

Bevington, P. R., & Robinson, D. K. 1992, Data Reduction and Error Analysis for the Physical Sciences (2d. ed; New York: McGraw-Hill)

Brown, T. M., & Morrow, C. A. 1987, ApJ, 314, L21

Duvall, T. L., Jr., Jefferies, S. M., Harvey, J. W., & Pomerantz, M. A. 1993, ApJ, 410, 829

Gabriel, M. 1995, A&A, 299, 245

Gardner, W. A. 1988, Statistical Spectral Analysis: A Non-Probabilistic Theory (New York: Prentice Hall)

Goldreich, P., & Kumar, P. 1988, ApJ, 326, 462

Gough, D. O., & Vorontsov, S. V. 1995, MNRAS, 273, 573

Harvey, J. W., Duvall, T. L., Jr., Jefferies, S. M., & Pomerantz, M. A. 1992, in ASP Conf. Ser. 42, GONG 1992: Seismic Investigation of the Sun and Stars, ed. T. Brown (San Francisco: ASP), 111

Hill, F., et al. 1996, Science, 272, 1292

Hill, F., & Howe, R. 1998, in Structure and Dynamics of the Interior of the Sun and Sun-like Stars, ed. S. Korzennik & A. Wilson (ESA SP-418; Noordwijk: ESA), 1, 225

Howe, R., & Thompson, M. J. 1998, A&AS, 131, 539

Komm, R., Gu, Y., Hill, F., Stark, P. B., & Fodor, I. K. 1999, ApJ, 519, 407

Korzennik, S. G. 1990, Ph.D. thesis, Univ. California, Los Angeles, 78

Kumar, P., & Basu, S. 1999a, ApJ, 519, 389

———. 1999b, ApJ, 519, 396

Meunier, N., & Jefferies, S. M. 1998, in Structure and Dynamics of the Interior of the Sun and Sun-like Stars, ed. S. Korzennik & A. Wilson (ESA SP-418; Noordwijk: ESA), 1, 267

Nigam, R., & Kosovichev, A. G. 1998, ApJ, 505, L51

———. 1999, ApJ, 514, L53

Nigam, R., Kosovichev, A. G., Scherrer, P. H., & Schou, J. 1998, ApJ, 495, L115

Pohl, B., & Anderson, E. A. 1998, in Structure and Dynamics of the Interior of the Sun and Sun-like Stars, ed. S. Korzennik & A. Wilson (ESA SP-418; Noordwijk: ESA), 1, 297

Press, W. H., Flannery, B. P., Teukolsky, S. A., & Vetterling, W. T. 1986, Numerical Recipes (Cambridge: Cambridge Univ. Press)

Rast, M. P. 1999, ApJ, 524, 462

Rosenthal, C. S. 1998, ApJ, 508, 864

Roxburgh, I. W., & Vorontsov, S. V. 1998, MNRAS, 292, L33

Schou, J. 1996, BAAS, 188, 69.06

Schou, J., & Brown, T. M. 1994, A&AS, 107, 541

Schou, J., et al. 2000, in preparation

Skartlien, R. & Rast, M. P. 2000, ApJ, in press

Straus, Th., Severino, G., Deubner, F.-L., Fleck, B., Jefferies, S. M., & Tarbell, T. 1999, ApJ, 516, 939

Toutain, T., Appourchaux, T., Frohlich, C., Kosovichev, A. G., Nigam, R., & Scherrer, P. H. 1998, ApJ, 506, L147

Walden, A. T., McCoy, E. J., & Percival, D. B. 1995, Technical Report (Dept. Math., Imperial College of Science, Technology and Medicine), 28

A&A 405, 1107–1120 (2003)
DOI: 10.1051/0004-6361:20030713

Astronomy & Astrophysics

Statistical properties of magnetic structures: Their dependence on scale and solar activity

N. Meunier[*]

Observatoire Midi-Pyrénées, 57 Avenue d'Azereix, BP 826, 65008 Tarbes Cedex, France

Received 27 November 2002 / Accepted 24 April 2003

Abstract. A long data set of MDI/SOHO full-disk magnetograms is analyzed in order to provide a large sample of network features as well as active regions associated with their magnetic properties (magnetic flux and magnetic flux density for example). The main objective of the paper is to study the variations of these properties along the solar cycle, and to compare the behavior of the magnetic features at various scales (covering three orders of magnitude in size). I also investigate the dependence of these properties on the activity level in their neighborhood and in the context of their global configuration on the solar disk. This study is important for a better understanding of the emergence and decay of active regions, as well as of the role of the network in the removal of the magnetic flux and in solar irradiance variations. The main results are as follows. *(i)* I observe a characteristic scale in the range 400–800 Mm^2 (close to the supergranular scale) below which the size and magnetic flux distributions are power laws down to 40 Mm^2 (corresponding to the range 3×10^{19}–10^{21} Mx). This scale increases from solar minimum to solar maximum. The shape of the distributions also suggests a strong similarity between small active regions (below the supergranular scale) and network patches. *(ii)* The North-South asymmetry in the number of structures, compatible with easier-to-detect leading structures in most cases, surprisingly exhibits a sign reversal for the weakest structures, suggesting a different origin, while the East-West asymmetry is compatible with a predominantly eastward inclination of magnetic flux tubes, including network structures and not only for emerging active regions as suggested by models. *(iii)* The dependence of the magnetic characterictics on the size of the structures is found to be variable with the activity level, the magnetic flux beeing more concentrated at solar maximum (especially for small features). Small-scale properties are also dependent on the proximity of an active region. *(iv)* Latitudinal distributions and flux variations along the solar cycle suggests a significant role of the meridional flows in the properties of the very small network features as well as an influence of supergranulation properties. *(v)* The variations of the magnetic properties of network elements and active regions with time are strongly size-dependent. The results also show a correlation between the number (or magnetic flux) of network structures and the sunspot cycle, with an amplitude larger than expected from previous results.

Key words. Sun: magnetic fields – Sun: photosphere – Sun: activity – Sun: faculae, plages

1. Introduction

Most of the magnetic network flux emerges as ephemeral regions and covers the whole surface of the Sun outside active regions. However, these small flux concentrations are organized in a large-scale pattern resulting from the decay of active regions: The patches of small flux tubes constituting the network are mostly present at the edge of supergranular cells (~30 000 km in diameter), also observed as velocity patterns in dopplergrams and from granule dynamics. At first order, the individual flux tubes are similar to the flux tubes in plages. With a diameter smaller than 300 km, they are mostly vertical, with magnetic fields larger than 1 kG and are observed as bright structures warmer than their surrounding.

The understanding of the small and large scale properties of the network allows to comprehend better the processes leading to the diffusion of magnetic flux away from active regions and to the removal of the magnetic flux from the surface of the Sun. Such an analysis is therefore of great interest in the context of the study of the emergence and decay of active regions as well as ephemeral regions. It should supply information on the processes at the origin of the concentration of the magnetic flux in network flux tubes and its interaction with the dynamics of the photosphere at various scales. On the small scale end of magnetic strutures, it should also provide some clues about the origin of intranetwork magnetic fields, weak field structures that are not well understood yet. Furthermore, the contribution of the network to solar irradiance variations has long been a controversial subject.

Network properties have often been studied through the diffusion coefficient (see for example Schrijver et al. 1996 and references therein), but no work on its variation along the solar cycle has been done. On the other hand, the work of

---

[*] e-mail: meunier@bagn.obs-mip.fr

Harvey (1993) on bipolar regions (from ephemeral regions to large active regions) considers properties such as lifetime or tilt (among others) but most magnetic characteristics such as the flux density are not analyzed (only the flux content of the regions have been studied, and not in detail). Structures not involved in a bipolar configuration (such as network features) are not included in this study. Therefore the intrinsic properties of the magnetic network are mostly known through a few spectropolarimetric studies (for example Sànchez Almeida & Lites 2000; Sigwarth 2001; Socas-Navarro & Sànchez Almeida 2002) of a small number of structures without any simultaneous large-scale analysis. On the other hand, several studies of the network contribution to solar irradiance variations have been performed over the last two decades. White & Livingston (1981) found the Ca II K emission in quiet regions at the equator to be constant during the solar cycle. Labonte & Howard (1982) studying magnetic fluxes found no cycle dependence of the network magnetic flux either. On the other hand, Muller & Roudier (1984, 1994) found the number of network bright points (hereafter NBP) in very quiet regions to be anticorrelated with the solar cycle. Later however, Foukal & Lean (1988) showed that the network contribution is necessary to explain the general downturn of the solar irradiance during the declining phase of the solar cycle. Foukal et al. (1991) showed that the quiet sun network covers 15% and 21% of the solar surface at solar minimum and solar maximum (ratio of 1.5) respectively, and the network properties are consistent with the solar irradiance variations. Nishikawa (1994) and more recently Lean et al. (1998) confirmed the contribution of the network to solar irradiance variations.

There is therefore a need for more detailed studies of possible cyclic variation of the magnetic properties of the network, as well as the dependence of their properties on their magnetic environment (activity level and relationship with active regions). Such approaches should include a very large sample of network features for a good statistical study. Also, the puzzling anticorrelation with the solar cycle obtained by Muller & Roudier (1984, 1994) requires an explanation in view of the more recent results about the network contribution to solar irradiance variations. These studies about irradiance variations have been made considering constant properties of the network features throughout the solar cycle, which may not be correct.

The objective of this paper is to study the properties of network features as well as their variation along the solar cycle, and to compare them with active regions. I also investigate the variation of network properties in the context of their global configuration on the solar disk. For this purpose, a long data set of MDI full disk magnetograms (Sect. 2) is analyzed in order to study the characteristics of magnetic structures over more than three orders of magnitude in size from network to active regions (Sect. 3). The evolution of these characteristics along the solar cycle (6 years from minimum to maximum) is studied in Sect. 4. Section 5 presents a summary of the results, which are discussed in Sect. 6. Very recently, a study focusing on bipolar regions using the same data set but a slightly different approach has been published by Hagenaar et al. (2003).

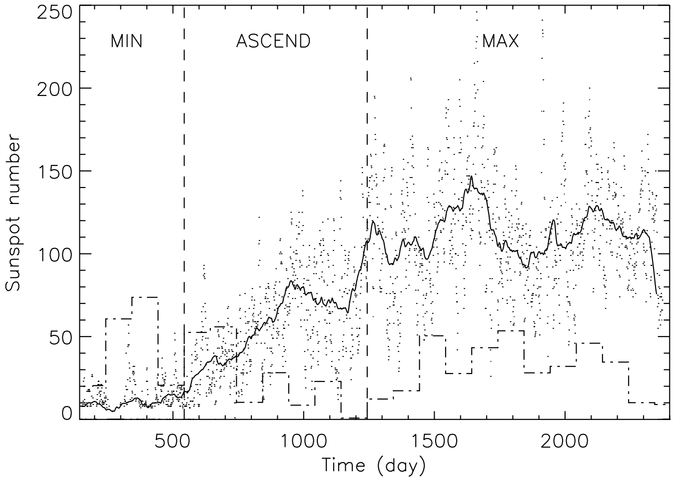

Fig. 1. Daily sunspot number (dots) versus time (day 1 is Jan. 1996, 1). The solid line represents the sunspot number smoothed over 100 days. The dashed-dotted line is the number of processed magnetograms divided by 10 for each 100 day period (starting on May 1996, 23).

2. Observations and data processing

2.1. MDI/SOHO: Full-disk magnetograms

MDI/SOHO observations (Scherrer et al. 1995) provide maps of the line-of-sight component of the magnetic field averaged over the resolution element (2 arcsec). The observations are made in the Ni I 6768 Å spectral line. I select 5-min full-disk magnetograms only, because they are less noisy (noise level of ~8 G, see for example Meunier 1999a). This led to a data set of 7184 images between May 1996, 23 and June 2002, 19, covering 6 years. These magnetograms are separated by a multiple of 96 min.

Figure 1 shows the Wolf number and data availability (number of magnetograms per 100 day period) during that period. The data availability is poor at the end of the ascending phase. In order to study solar cycle variations, I define the three following periods, illustrated in Fig. 1: The cycle minimum from day 143 (May 23, 1996) until day 543 (June 1997, 27), an ascending phase from day 543 until day 1243 (May 1999, 28) and the cycle maximum after that date until the end of the data set. Solar variations will be subsequently studied either over these three periods or over the 23 100-day period constituting the data set.

I also study 15 series of one-hour data sets (60 magnetograms each with a temporal cadence of 1 min) in order to analyze the variation of the noise level with time in Sect. 2.3.

2.2. Data processing

Magnetograms are analyzed using a method similar to that described in Meunier (1999a), except that we consider B/μ (where $\mu = \cos\theta$, θ being the angle from disk center and B is the line-of-sight magnetic field provided by MDI) instead of B, as is done in Hagenaar (2001) for ephemeral regions, because the magnetic field lines in both active regions and network regions are believed to be close to the vertical, within 10° (the only exception is the penumbra of sunspots but this

Table 1. Number of structures of all sizes for the different magnetic thresholds.

Magnetic threshold	Number	< *Number* > per image
25 G	6967532	970
40 G	4291752	597

concerns only a very small proportion of the studied features). Computations using B instead of B/μ do not differ significantly from the results presented in this paper however. Each structure above a given magnetic threshold (discussed below) is determined within 53° from disk center ($r < 0.8\ R_\odot$). Areas A and perimeters P are corrected for projection effects. They are converted to Mm^2 and to Mm respectively. Structures of different polarities are counted separately (the threshold is applied to the signed magnetograms). In addition, I compute the following parameters in order to characterize the magnetic properties of the structures: *(i)* The magnetic flux per structure, Φ (in Mx) (the unsigned value is often used in the paper); *(ii)* The maximum unsigned magnetic field in the structure, $|B_m|$ (this is also a flux density averaged over the MDI pixel, not an intrinsic field strength); *(iii)* The ratio between the maximum magnetic field B_m and the average magnetic field in the structure $\bar{B}$; *(iv)* And finally $|\Phi|$ divided by the area, which provides the unsigned magnetic flux per "pixel" in the structure, where the pixel size corresponds to that of disk center (this is the mean magnetic field density in the structure), or flux density. In order to characterize the activity level in the close neighborhood of a structure, I also compute the number of pixels over the magnetic threshold in the range of $[R + 20, R + 40]$ pixels (where R is defined as $\sqrt{A/\pi}$).

The number of structures per image for the two thresholds (25 G and 40 G) is shown in Table 1. These thresholds correspond to 3 and 5 times the noise level in these magnetograms, respectively (see Sect. 2.3). An example of a magnetogram after the application of these thresholds is shown in Fig. 2 for $r < 0.8\ R_\odot$. The threshold of 25 G is a minimum considering the noise level. The choice of a second threshold allows to get more informations. A low threshold allows to look at weaker flux features compared to a larger threshold, although it could be more sensitive to the noise. We will see that most of the results are not strongly dependent on this choice.

2.3. Limitations

2.3.1. Sensitivity limitations

In this study, structures with a size below 4 pixels are eliminated because of the limited spatial resolution. Note that the small features observed in the south-western quadrant of the 25 G thresholded magnetogram in Fig. 2 (due to a higher noise level) are removed when selecting these sizes only. In addition to the limit on the size of the structures, the magnetic thresholds impose a limit on the magnetic flux density, which could correspond to different types of structures (for example structures larger than 4 pixels but with a weak magnetic flux everywhere).

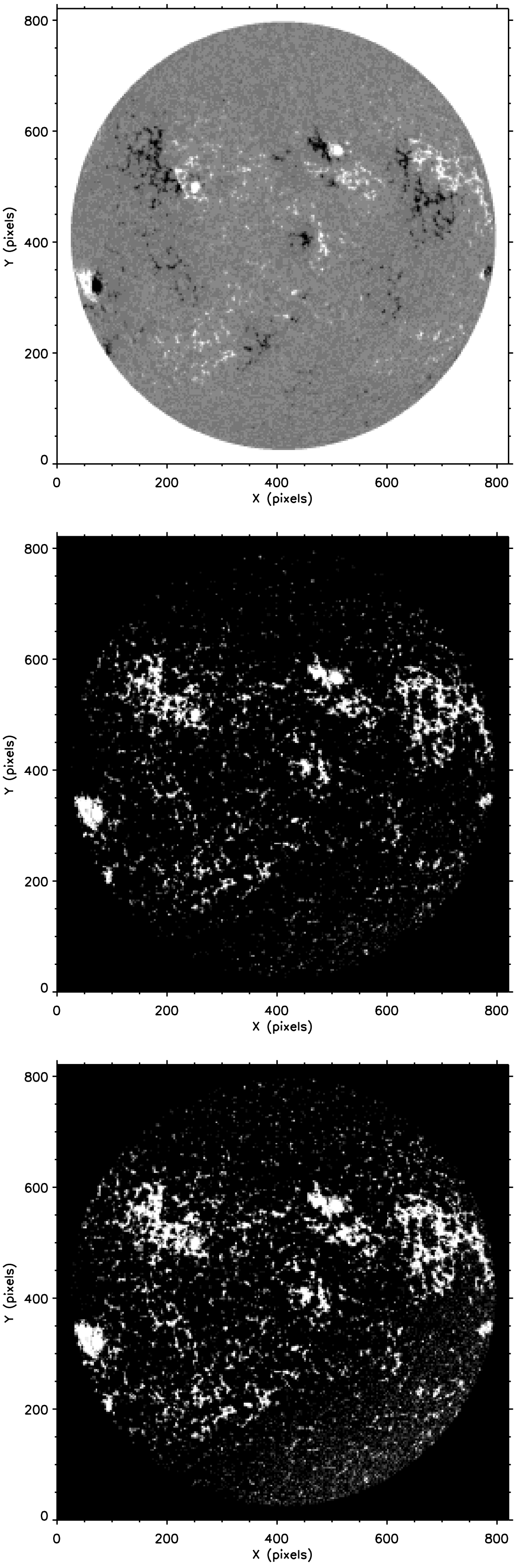

Fig. 2. Top: a magnetogram for $r < 0.8\ R_\odot$. Middle: after a 40 G threshold. Bottom: after a 25 G threshold.

One should also remember that the magnetograms provide only the line-of-sight magnetic flux over the resolution element.

2.3.2. Influence of the noise

In order to check the noise level and its variation with time, I study 15 one-hour data sets of full-disk magnetograms spread over the 6 years. We process each data set according to the following steps: *(i)* Pairs of 5-min magnetograms are computed using 10 images separated by 1 min; *(ii)* Pixels with magnetic fields larger than 25 G in the 5-min magnetograms are removed in order to consider quiet regions only; *(iii)* The difference between magnetograms of each pair is computed; *(iv)* The percentage of pixels above the magnetic threshold for $r < 0.8\ R_\odot$ as well as the width of the corresponding distribution of magnetic fields are computed.

The results confirm the 8 G noise level (the average over the whole data set is 8.7 G). On average, the percentage of pixels in the magnetogram differences above the 40 G threshold is 0.03%, and 0.9% above the 25 G threshold. The noise level seems to increase slightly over the 6 years of the study: from a linear fit on the noise versus time, the noise level is around 8.2 G at the beginning of the period and around 9.1 G at the end of the period. A similar variation is observed in all hemispheres although the average level is different: 8.4 G in the North, 9.1 G in the South, 8.2 G in the East and 9.3 G in the West. Simulations made by adding noise of different amplitudes (typical of the 4 hemispheres) are made in order to study their influence on the results. The only significant influence concerns the number of structures and size distribution (Sect. 3.1) and will be discussed later. The other characteristics (such as the dependence of the magnetic flux on the size) exhibits variations due to different noise levels that are insignificant. It is also important to note that the noise measured here contains not only instrumental noise but also some “noise” of solar origin which is due to weak fields or even strong fields with a significant evolution over a few minutes: therefore the actual variation of the instrumental noise is likely to be smaller.

2.3.3. Non-linearity of MDI magnetic field measurements

Berger & Lites (2003) showed that the MDI response concerning magnetic field measurements was starting to be nonlinear above 1600 G, with a strong saturation around 2200 G. This problem will mostly affect the maximum magnetic field computed in very large regions and, to a lesser extent, the magnetic flux and flux density. Furthermore, even in large structures, the pixels with a magnetic field larger than 1600 G represent the tail of the magnetic field distribution in the structure. It will not affect the thresholding. Small scale feature properties, such as network patches and small active regions, for which no pixel shows a magnetic field above 1600 G are not influenced. Therefore most of the structures we will be interested in are not affected. Note that the values of the measured magnetic field (for example the threshold of 40 G) is also instrument-dependent, as emphasized by Berger & Lites (2003). They show for example that MDI magnetic fields are underestimated by at least 30%.

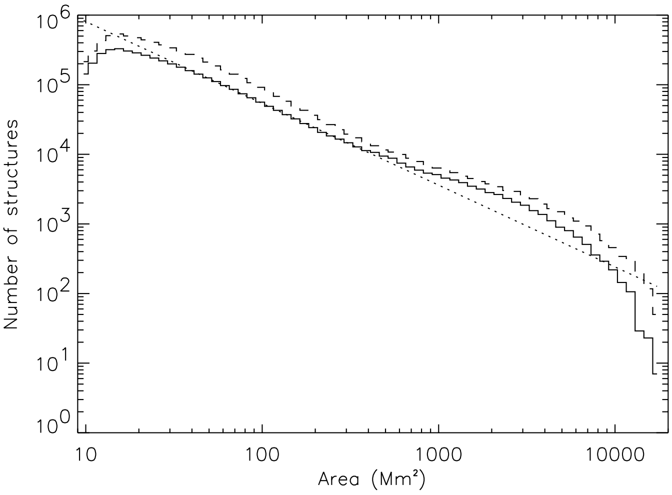

Fig. 3. Size distribution for all structures (solid: 40 G threshold, dashed: 25 G threshold). The dotted line is a linear fit to the 40 G distribution in the 40–400 Mm^2 range on a log-log plot (power law).

3. Magnetic feature characteristics

3.1. Size and asymmetries

3.1.1. Size distribution

Figure 3 shows the size distribution on a log/log plot. It is important to point out that a direct comparison with size distributions obtained for active regions by other authors (Harvey & Zwaan 1993, for example) is difficult because they have counted each active region region once, taking into account their lifetime. This is not the case here: when dealing with small magnetic features (such as in this study), this is a lot more complex to perform and would request a better temporal cadence. This is beyond the scope of this paper and therefore a feature or region is counted each time it is present on the disk. As a consequence, the distributions shown in this paper are not directly related to the emergence rate of regions but correspond to the proportion of features of different sizes present on the disk at a given time. The lifetime being dependent on the size, we expect a slope smaller than the one found by Harvey & Zwaan for example.

The size distribution exhibits a maximum around 15 Mm^2, for both thresholds (25 G and 40 G). This may be due to the fact that the smaller features may not be visible at that magnetic threshold. This has also been observed by Schrijver et al. (1997) for small bipoles (ephemeral regions). The distribution is then a power law in the range 40 Mm^2 (linear size of 7100 km) to 400 Mm^2 (linear size of 25 000 km), although the departure from the power law is mostly observed above 800 Mm^2 (linear size of 31 900 km, close to the supergranulation scale). Note that this supergranular cell size is much larger than network features: Wang (1988), using cross-correlation of magnetograms, finds a typical size of the network of 5700 km (33 Mm^2) with a maximum size of ~80 Mm^2. Above 800 Mm^2, the distribution is slightly increasing and then dropping. This suggests that properties are similar from network to small active regions, while large active regions show a different behavior. This is in agreement with Garcia de la Rosa (1983), who observed that small active regions below 10^{21} Mx were related to the decay of larger active regions: We will see in the next section that this flux corresponds to the supergranular size regions seen here. A shift along the A axis of the 25 G threshold curve to match the 40 G threshold curve shows a very good agreement for A larger than ~100 Mm^2. Below this scale, the 25 G distribution is starting to show some structures that are not seen on the 40 G distribution. The three domains observed here will often be used in the paper to compare the behavior of structures of different sizes.

3.1.2. North-South asymmetry

North-South asymmetries are listed in Table 2. At the 40 G threshold, there are more structures in the northern hemisphere for regions of all sizes, although the amplitude of the asymmetry is larger for sizes in the range 40–800 Mm^2. At the 25 G threshold, the situation is surprisingly reversed when considering all sizes: This is due to a larger number of small structures (below 40 Mm^2) in the southern hemisphere when using this threshold. One should remember that the sample of structures when going from a 40 G threshold to a 25 G threshold is different: Many structures in the range 10–40 Mm^2 at the 40 G threshold will be above 40 Mm^2 at the 25 G threshold, while the range 10–40 Mm^2 at 25 G threshold will contain many new structures corresponding to weaker fluxes that were excluded from the 40 G sample. So this result suggests that the asymmetry is actually reversing for weak flux structures which are not seen at the 40 G threshold, as if they were due to a different process.

The amplitude of the asymmetry must be compared to the noise influence in the different hemispheres. Simulations show that the different noise levels in the northern and southern hemispheres (Sect. 2.3.2) should lead to 0.4% more structures in the South, with a more pronounced effect for small structures (0.8% for sizes below 25 Mm^2). Therefore the positive asymmetry observed here (more structures in the North) are likely to be underestimated and the sign reversal is probably true.

3.1.3. Polarity asymmetry

The two polarities also exhibit different behaviors. At the 40 G threshold, there are more structures of negative polarity. However this is true for small structures only (below 40 Mm^2) while the asymmetry seems to be reversed for larger structures. On the other hand, the North-South asymmetry is quite large when one considers the polarities separately: there is a much larger number of positive polarity structures in the northern hemisphere and of negative polarity structures in the southern hemisphere, i.e. the leading polarity is dominating in each hemisphere[1]. The magnetic flux is known to be more concentrated in the leading polarity so this would change the detection level for each of them and could explain the result. The asymmetry is also observed for the total fluxes. At the 25 G threshold, there are more negative polarity structures for all sizes, and the asymmetry is of larger amplitude than at the 40 G threshold. The origin of such a difference (especially for large regions) and of this global imbalance is not understood: for most structures, the observed North-South asymmetry and the easier detection of leading polarity should lead to more positive polarity structures, which is not what is observed at the 25 G threshold. The North-South asymmetry is however similar to the one found for the 40 G threshold when separating the polarities.

Table 2. North-South, East-West and polarity asymmetry in the number of structures (%) for various selections in term of size, polarity and hemisphere (defined as the difference in numbers N of structures – first criterion minus the second one – divided by their sum). The uncertainties correspond to $1/\sqrt{N}$. The area A is in Mm^2.

Selection	25 G (%)	40 G (%)
North, *South*	-0.43 ± 0.05	0.98 ± 0.07
North, *South* ($A > 800$)	2.07 ± 0.52	0.61 ± 0.61
North, *South* ($40 < A < 800$)	2.07 ± 0.10	3.03 ± 0.13
North, *South* ($A < 40$)	-1.48 ± 0.06	0.15 ± 0.08
$B > 0$, $B < 0$	-2.96 ± 0.05	-0.61 ± 0.07
$B > 0$, $B < 0$ ($A > 800$)	-0.95 ± 0.53	0.20 ± 0.61
$B > 0$, $B < 0$ ($40 < A < 800$)	-1.83 ± 0.10	0.27 ± 0.13
$B > 0$, $B < 0$ ($A < 40$)	-3.44 ± 0.06	-0.99 ± 0.08
North, *South* ($B > 0$)	3.99 ± 0.07	5.63 ± 0.09
North, *South* ($B < 0$)	-4.60 ± 0.08	-3.61 ± 0.10
East, *West*	-3.23 ± 0.05	-2.28 ± 0.07
East, *West* ($B > 0$, *North*)	-3.67 ± 0.10	-3.28 ± 0.13
East, *West* ($B < 0$, *North*)	-1.55 ± 0.11	-1.84 ± 0.14

3.1.4. East-West asymmetry

East-West asymmetries for a few selections of parameters are also shown in Table 2. There are always more structures on the western side, even for large structures and this is independent of the polarity: The asymmetry is in the range of 1.8–3.3% with the 40 G threshold (1.5–4.0% with the 25 G threshold) for various selections. The amplitude of the asymmetry is larger for the leading polarity (positive in the north for example) than for the following polarity (negative in the north for example). Therefore the behavior is very different from the North-South asymmetry.

The East-West asymmetry could have been due to the noise level, which is known to be larger in the south-western quadrant of MDI magnetograms, especially close to the limb. However this should not influence significantly the larger structures. A simulation shows that we expect 0.6% more structures in the western hemisphere due to the different noise level, and 1.3% more structures for small sizes below 25 Mm^2. Therefore the asymmetry observed here seems significant although slightly overestimated. It is therefore more likely to be due to another effect, for example a different projection effect if leading and following polarities have different typical inclinations with

---

[1] For this cycle, the leading polarity in the northern hemisphere is positive.

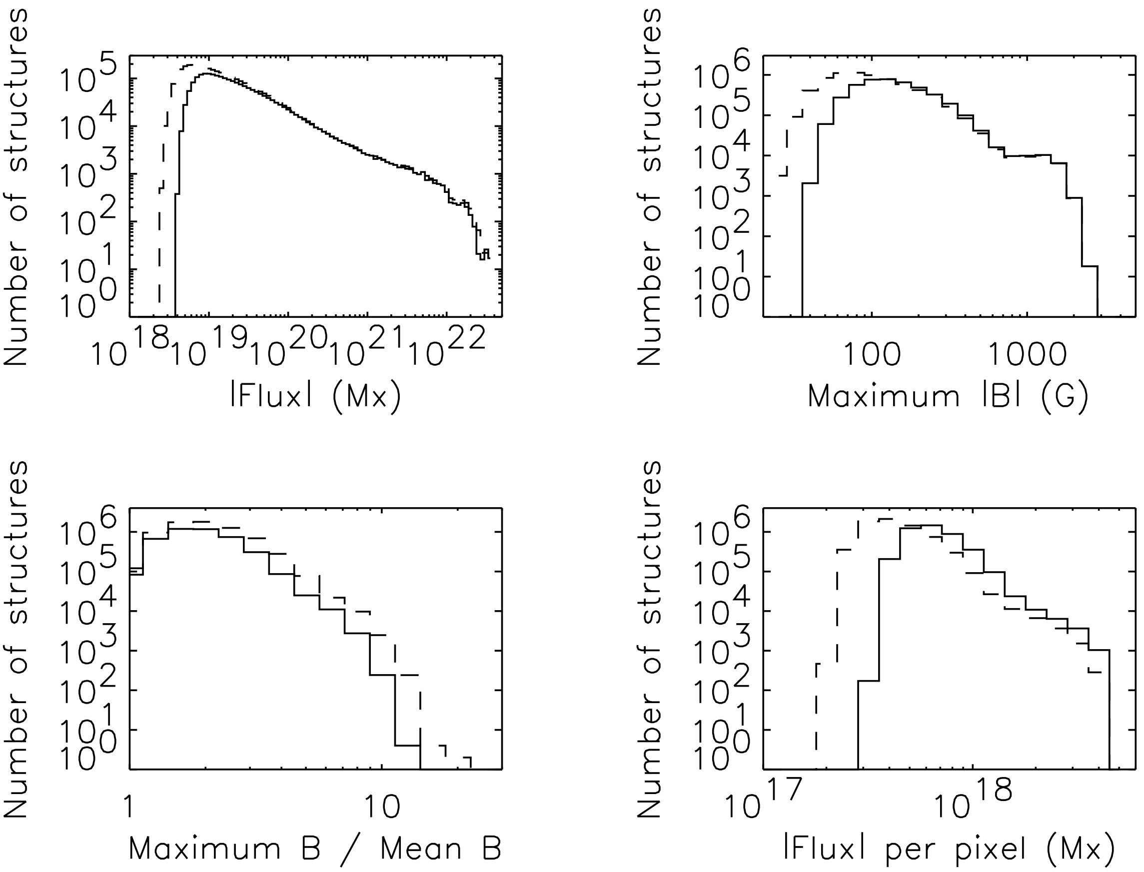

Fig. 4. Distribution of $|\Phi|$ (top left), $|B_m|$ (top right), $B_m/\overline{B}$ (bottom left) and $|\Phi|/A$ (bottom right) in all structures (Solid: 40 G threshold, dashed: 25 G threshold).

respect to the vertical for example: the larger number of structures in the West is compatible with a preferentially eastward inclination of the flux tubes that would lead to a different detection level in the two hemispheres. This subject is still controversial. An eastward inclination of the emerging flux tubes has been proposed by van Driel-Gesztelyi & Petrovay (1990) in order to explain the asymmetry in the proper motions of bipoles. Howard (1991) found an average eastward inclination of 1.9° of flux tubes in young active regions (inclination that became westward for growing regions) while Harvey (1993) found an westward inclination of ephemeral region flux tubes (using a counting method similar to ours). On the other hand, models predict an eastward inclination (Caligari et al. 1995; Abbett et al. 2001) in agreement with van Driel-Gesztelyi & Petrovay's predictions and Howard's results for emerging active regions. So our results are compatible with the observations of bipolar active region proper motions and from models, but it is extended to structures of all sizes, including network features.

3.2. Magnetic field characteristics

3.2.1. Magnetic fields of the structures

In this section I study the magnetic field characteristics of the structures, using the four parameters defined in Sect. 2.2: $|\Phi|$, $|B_m|$, $B_m/\overline{B}$ and $|\Phi|/A$. Figure 4 shows the distribution of these four parameters for both magnetic thresholds (25 and 40 G). They are quite similar, although it is of course possible to access smaller values of $|\Phi|$ and $|B_m|$ at 25 G, while the ratio between maximum and average magnetic field can reach larger values. Figure 5 shows these four parameters versus the size of the structures. They are all correlated with the size. Linear fits to the parameters versus size (on a log/log scale) after averaging over small ranges of size ($\Delta \mathrm{Log} A = 0.1$) are also computed. The slopes are indicated in Table 3: This tool will be usefull when looking at solar cycle variations.

The shape of the flux distribution is very similar to that of the size distribution shown in Fig. 3. I observe a modification in behavior of the flux distribution around 10^{21} Mx, as expected given the observed dependence of the flux with the size and the size distribution. Note that the 40 Mm^2 size corresponds to the 3×10^{19} Mx flux.

I find that the magnetic flux $|\Phi|$ in each structure is very dependent on the size of the structures with a slope larger than one. This is to be compared to the results obtained by Harvey (1993) for large active regions (A above 373 Mm^2), who found a slope of 1 (i.e. $|\Phi|$ is proportionnal to A). The general behavior is not very different, especially for large active regions: For example she found a flux of 1.2×10^{21} Mx for a size of 800 Mm^2, which is close to the results presented here. However, an extrapolation at $A = 1$ of Harvey's results gives 1.5×10^{18} Mx while we find smaller fluxes (4×10^{17} Mx). Schrijver et al. (1996) also observed that the active region size is correlated

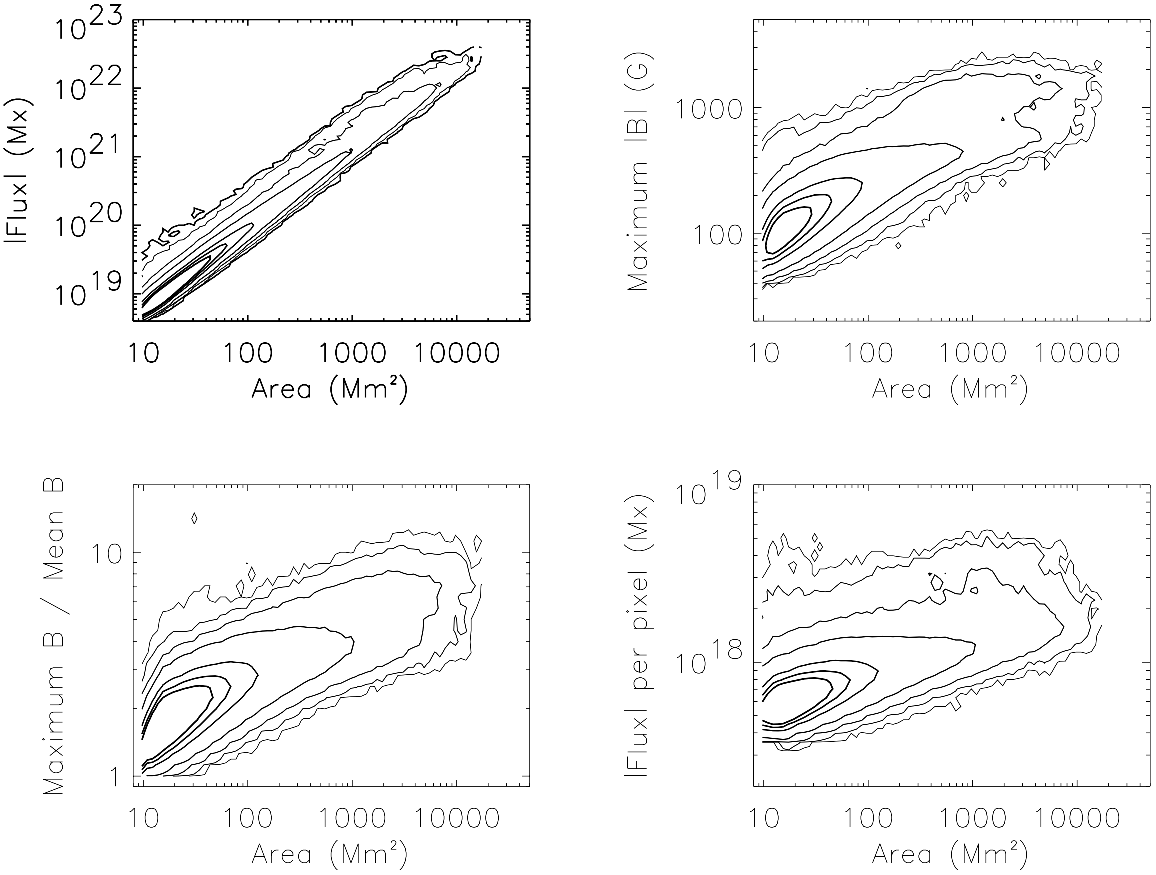

Fig. 5. Distribution of magnetic flux in all structures (resp. maximum magnetic field, ratio between maximum magnetic field and the average magnetic field over the structure and the magnetic flux density in the the structures) versus the size of the structures, for the 40 G threshold. The lines correspond to 1, 10, 100, 10^3, 10^4, 2×10^4 and 3×10^4 structures (from the outside to the center of each distribution).

with the mean magnetic flux in a region over a small field-of-view, but it concerns only a small range of sizes as well. The present study extends this result down to network structures and does not show any sharp transition between active regions and network structures (the same is true for the size distribution): although the properties are changing through the scales it is a gradual process over the three orders of magnitude in size.

Furthermore, the slope larger than 1 implies that the flux density $|\Phi|/A$ is also scale-dependent. The other parameters ($|B_m|$ and $B_m/\bar{B}$) are also clearly dependent on the size but the slopes are much smaller than for the flux (see Table 3). The flux density in particular increases with the size but not by a large factor, as shown by the slope much smaller than 1 (0.16–0.18). We know that this parameter is either related to the filling factor or to the magnetic field strength in individual flux tubes constituting the region. From studies of contrast differences between network and faculae, Ortiz et al. (2002) found that faculae were constituted of larger flux tubes than the network. It is too early to make a direct comparison with the present results, especially because definitions of the network and faculae are different: They use the pixel magnetic field value to decided whether this is a network or facula pixel, while I do consider the size of the structures. More work need to be done to improve the comparison. However, the increase of flux density as a function of the size (factor of 2.8 between 10 Mm^2 and 10 000 Mm^2 structures) may indeed be related to this contrast variabilities. The flux density also exhibits a large dispersion for a given size however, between 2×10^{17} and 5×10^{18} Mx (more than one order of magnitude), and this large dispersion is observed from small network features to active regions. There is a small departure from the power law (at small and large scales). The departure from the power law at very large scales for $|B_m|$ and $|\Phi|/A$ could be due to the non-linearity in MDI magnetic fields described in Sect. 2.3.3.

Table 3. Slope of the Log(parameter) versus Log(A) after averaging over small ranges of size ($\Delta \mathrm{Log} A = 0.1$).

Parameter	25 G	40 G
$\lvert\Phi\rvert$	1.210 ± 0.007	1.175 ± 0.006
$\lvert B_m\rvert$	0.429 ± 0.009	0.384 ± 0.007
$B_m/\bar{B}$	0.222 ± 0.005	0.209 ± 0.004
$\lvert\Phi\rvert/A$	0.184 ± 0.006	0.161 ± 0.005

3.3. Latitudinal and longitudinal distributions

Synoptic maps for structures of different sizes show that small size structures (even below 40 Mm^2) are preferentially located around or at the location of active regions. This has already been observed for bipolar regions by Harvey (1993).

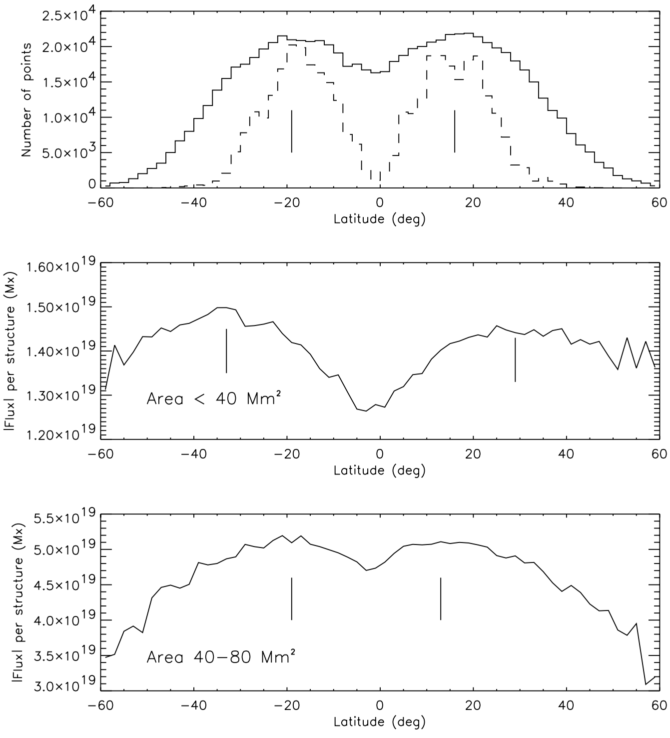

Fig. 6. Top: number of structures in a longitude range [−10°:10°] for area below 40 Mm^2 (solid line) and above 800 Mm^2 (dashed line, curve multiplied by 7) as a function of latitude. Middle: Average flux per structure (area below 40 Mm^2) as a function of latitude. Bottom: same but for structures in the range 40–80 Mm^2. The small vertical lines indicate the approximate position of the curve maxima.

Surprisingly, it appears to be true for network features as well: latitudinal distributions are shown in Fig. 6 (for the 40 G threshold). Results are similar for the 25 G threshold. The number of small structures (below 40 Mm^2) peaks at the same latitude within 2° than active region number (as in Harvey 1993, for bipoles), around latitudes −19° and 15° for the whole time period studied here.

On the other hand, the latitudinal variation of the average flux in these small structures have a maximum around latitudes −33° and 29° as shown in Fig. 6. Only structures in the longitude range [−10°:10°] are selected, i.e. close to the central meridian (however, results are similar when all longitudes are considered). The average flux per structures is the largest in the northern hemisphere (respectively the southern hemisphere) is 11% (respectively 9.5%) larger than at the equator, with a value close to 1.5×10^{19} Mx. At high latitudes (60°) the flux is decreasing again toward values similar to those at the equator. This means that the small structures have their largest magnetic flux at a latitude larger (by ~10°) than the latitude where their number is maximum. At these positions the number of detected structures has decreased by 18% in the North (27% in the South) compared to the maximum number. However, the exact values could be slightly biased by projection effects.

The stronger concentration of flux at higher latitudes in small structures may be due to a combination of two processes: (i) the poleward meridional circulation in surface observed by many authors (see for example Meunier 1999b, and references therein), should transport preferentially the flux toward high latitudes; (ii) supergranulation may concentrate the flux in smaller structures compared to larger size structures at high latitude. Note that the the size distributions in different latitude ranges show an excess of small structures (below 40 Mm^2) compared to larger structures in the latitude range 30°–40° compared to the 20°–30° range.

The distribution of the small structures extends further toward large latitudes from the active region belt limit in the North (~14°) than in the South (~9°) at solar maximum. The smaller maximum $< |\Phi| >$ in the northern hemisphere (for $A <$ 40 Mm^2), could be due to a smaller concentration of flux per unit area in this hemisphere. On the other hand, one should remember that the northern hemisphere was more active during that period (Table 2). Therefore the effect at the origin of this North-South asymmetry must be strong. The North-South asymmetries could be due an asymmetry of any of the process involved (supergranular diffusion, meridional circulation). However, results obtained by Meunier (1999b) suggests a weaker meridional circulation in the northern hemisphere though, while no study of asymmetry in the diffusion coefficient has been done. Instrumental effects, such as the larger noise in the South, may also play a role however. A detailed modeling of the different effects should therefore be done in order to understand better the observed asymmetries.

3.4. Magnetic field environnement dependence

3.4.1. Immediate surrounding

In a first approach I study the variation of the magnetic field characteristics when the activity level in a ring surrounding the structure is changing. I characterize this activity level in the neighborhood of the structure by the parameter α, defined as the proportion of pixels above the magnetic threshold (i.e. 25 G or 40 G) in the region $[R + 20, R + 40]$ pixels (see Sect. 2.2). A distance of 30 pixels at disk center corresponds to 42 Mm. α takes values between 0 and 97% and is linear in the range 5–65% on a linear-log scale. Results above 70% are not significant due to the smaller number of points.

When considering a sample of small magnetic features only (with a size below 20 Mm^2), the average size is decreasing by 2% when α is increasing (i.e. when the activity surrounding the feature is increasing) from 5% to 65%: therefore the size distribution does not change very much. For structures with $A <$ 40 Mm^2, the average size is quite constant also. However the average flux is meanwhile increasing by 28% and the flux density by 26%, for the 40 G threshold and $A <$ 20 Mm^2 (respectively 37% and 35% for $A <$ 40 Mm^2). Results are similar for the 25 G threshold. Given the dependence of Φ versus A and the small decrease in A, the flux is expected to decrease slightly if the properties of the network structures were constant. Therefore small features of a given size seems to have significantly stronger magnetic fluxes when their immediate surrounding is more active. This is likely to be related to the diffusion of magnetic flux from active regions to the network and the decay into network patches such as those observed here.

Considering features of all sizes, I compute the slope of the magnetic flux Φ versus A (log/log scale) as in Sect. 3.2, as well as the slope of the magnetic flux density versus A. For Φ versus A, the slope is increasing from 1.08 to 1.28 for α increasing from 5% to 65%. Given the values obtained at $A = 1$ from this fit, this means that the larger the size is, the larger the increase in flux is when α is increasing. The same is true for the flux density.

3.4.2. Proximity of active regions

Another approach consists in computing the minimum distance δ to regions larger than 800 Mm^2 in order to look at larger scales. Projection effects are taken into account when computing this distance. To avoid biases when a structure is far from disk center (meaning that its whole surrounding is not visible), only features in a box of 200×200 pixels at disk center are considered (latitudes and longitudes are then in the range ±24°). For 11% of them there is no large structure on the disk (this happens mostly during cycle minimum). δ takes values between 0.1° and 72°. The distribution of δ shows a maximum around 5° and then decreases sharply, especially above 55°. The shape of the distribution is however slightly different depending on the cycle phase (flatter at cycle minimum, sharper decrease at cycle maximum). A value of δ of 10° corresponds to 121 Mm.

When looking at small magnetic structures (below 20 Mm^2), I find that although the average size is remaining constant, the average flux is decreasing linearly by 11% when δ increases from 2.5° to 42.5°. The flux density is also decreasing, by 10%. For $A < 40$ Mm^2, results are similar although of larger amplitude, with percentages of 22% and 13% respectively. The results are similar for the 25 G threshold. When differentiating for the 3 phases of the cycle defined in Sect. 2.1, it is found that the variation is mostly observed at cycle minimum and during the ascending phase: there is a sharp decrease up to $\delta = 10°$, then the decrease is much slower. The decrease is of 13% during the minimum and of 8% during the ascending phase. During cycle maximum, there is almost no variation.

Therefore, results are qualitatively similar to the previous analysis but at a larger scale: The flux in small magnetic structures of a given size is decreasing when the structure is further from an activity center. The results for the 11% with no structures larger than 800 Mm^2 on the disk confirm this. These network properties are consistent with the argument of Schrijver et al. (1997) that each time there is cancellation of network structures (of opposite polarities), only the residual (because of a non-zero flux imbalance) will reappear again. Therefore we expect less flux to concentrate far from active region location for availability reasons. A given quiet or enhanced network region could also be related to a strong activity happening at the same location a long time before (several rotations for example).

On the other hand the slope of the flux versus the size (for structure of all sizes) does not show any clear behavior. The same is true for the flux density. This mean that the flux variation is similar for all scales.

3.5. Bipolar structures

I extract a subset of structures by selecting bipoles using the rules defined by Hagenaar (2001): the maximum distance between structures is set to 10 Mm^2 and the difference in flux is smaller than 33%. This analysis provides a subset of 29 337 bipolar structures. Although this subsample does not correspond exactly to small ephemeral regions (because of possible chance encounters between network features of opposite polarity), the proportion of ephemeral regions in this subsample is likely to be much larger than in the general sample, allowing to compare qualitatively network and ephemeral region properties. An exhaustive analysis of ephemeral regions is outside the scope of this paper (see Hagenaar et al. 2003, for such a study). The slopes of the parameters defined in Table 3 for the whole data set are larger for this selection of bipoles. When considering a subsample of structures with sizes below 40 Mm^2 only, Φ is larger by 3.7% in bipolar structures compared to features which are not involved in a bipolar structure, $|B_m|$ is larger by 6.7%, $B_m/\overline{B}$ is smaller by 1.3% while Φ/A is larger by 7.4% (for the 40 G threshold). Note that the average size is also smaller (by 3.5%). Results are similar for the 25 G threshold. Therefore small features not involved in bipoles do not have the same magnetic characteristics than bipoles of similar size.

4. Solar cycle variations

4.1. Size distribution

The average number of structures of all sizes per image is increasing from 237 at cycle minimum to 864 at cycle maximum (for the 40 G threshold). Figure 7 shows the size distribution for the three periods of the cycle defined in Fig. 1. It was, of course, expected to have a much larger number of large structures during cycle maximum. This is true for all sizes, confirming the recent results about the correlation between network variations and the solar cycle. The shape of the distribution is quite similar although the slope is different in the size range of the distribution where a power law is observed (smaller at cycle maximum) and this power law regime seems to extend toward larger sizes at cycle maximum. This result is therefore different from that of Harvey (1993), who found that the shape of the size distribution is an invariant with time. The difference could have been due to the fact that, in this work, more weight is given to structures with a longer lifetime: a longer lifetime of large active regions at cycle maximum could explain the result. However, she found the opposite (faster decay rate at cycle maximum).

4.1.1. Number of structures of various sizes and fluxes

The variation of the number of structures versus time for different ranges in magnetic flux $|\Phi|$ is shown in Fig. 8 for the 40 G threshold. Results are similar for the 25 G threshold and for different ranges in size. I find that, at first order, structures of all types exhibit a similar increase with the solar activity level, with mostly a difference in amplitude.

I also observe that the increase at the beginning of the ascending phase seems to happen first for large active

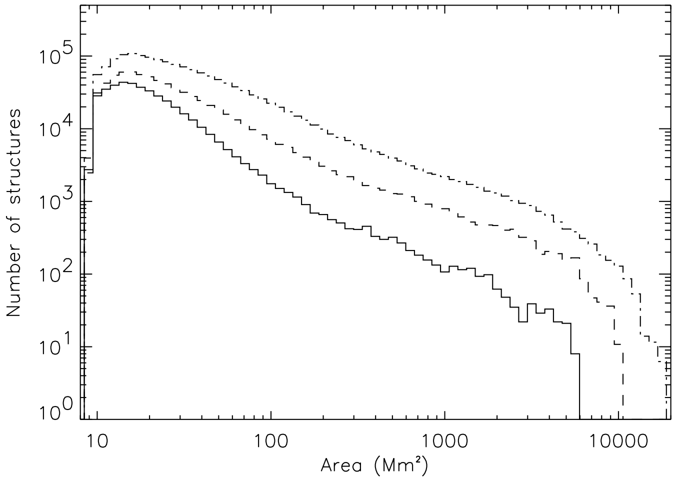

Fig. 7. Size distribution during the three phases of the cycle: cycle minimum (solid), ascending phase (dashed) and cycle maximum (dotted-dashed), for the 40 G threshold.

regions (flux above 10^{21} Mx, corresponding to areas larger than 800 Mm^2) and medium size regions (in correlation with the Wolf number), and then later for the smaller structures (below 40 Mm^2). The difference is of the order of one of our 100-day period; this corresponds to our sampling, therefore it would be useful to use a smaller time step to check this result. This is a difficult task, however, because of the data gaps and this should be investigated further using another data set. This result seems in contradiction with the observations made by Harvey (1993) that the minimum of the cycle occurs one year before for small bipolar structures compared to large ones. Our sample is dominated by non-bipolar structures however, which may explain the discrepancy if much of the network – which is dominating the sample – is fed by decaying active regions. Later during the cycle, the variation for these three types of structures seems similar although again not in phase.

The amplitude of the variation (illustrated in Fig. 8, bottom) is of course very large for large structures (factor of 15.2 in number for example for flux above 10^{21} Mx, and factor of 19.6 in integrated flux), and much smaller for small structures (factor of 2.9 in number for flux below 3×10^{19} Mx, and factor of 3.5 in integrated flux). The ratio between the number of structures at maximum and minimum is therefore increasing with increasing size or magnetic flux in the structure. During solar maximum the Sun is more largely covered by strong (and large) magnetic structures, which leaves less "free area" for the small magnetic structures. However, if we correct the variations for small features by dividing the numbers by the "free area", the results are not modified significantly. Foukal et al. (1991) found a ratio of 1.5 between maximum and minimum for network features. Typical network patches corresponding to fluxes below $\sim 5 \times 10^{19}$ Mx approximately, and Fig. 8 shows that the variation may be of larger amplitude for the network compared to what have been found by Foukal et al. (1991), close to a factor 7 instead of 1.5. We also find a larger factor (7.9 for bipolar regions smaller than 373 Mm^2) than Harvey's (1993) results for ephemeral regions, who found a ratio of 2–2.5. Surprisingly, while results of the past decade tended to show that the network variations were anti-correlated with the solar cycle, a very recent study by Hagenaar et al. (2003) using an approach close to the present one found a weak anti-correlation of the number density of emerging ephemeral resgions, also observed for the network. This discrepancy is not yet understood.

An extrapolation shows that this ratio would reach 1 (below which the variation with time would be anti-correlated with the solar cycle) very close to the lower boundary of the range studied here (between 1 and 10 Mm^2 and close to 10^{18} Mx). The departure from the linear fit (in the log-linear plot) is only at the 1-σ level. This extrapolation suggests that there could be a reversal of the variation of the flux in small structures with solar activity compared to larger structures such as studied in this paper. This could be related to the observations made by Muller & Roudier (1984, 1994) that the number of NBP observed at very high spatial resolution (in the *G*-band) in the quietest zones available is anti-correlated with the solar cycle.

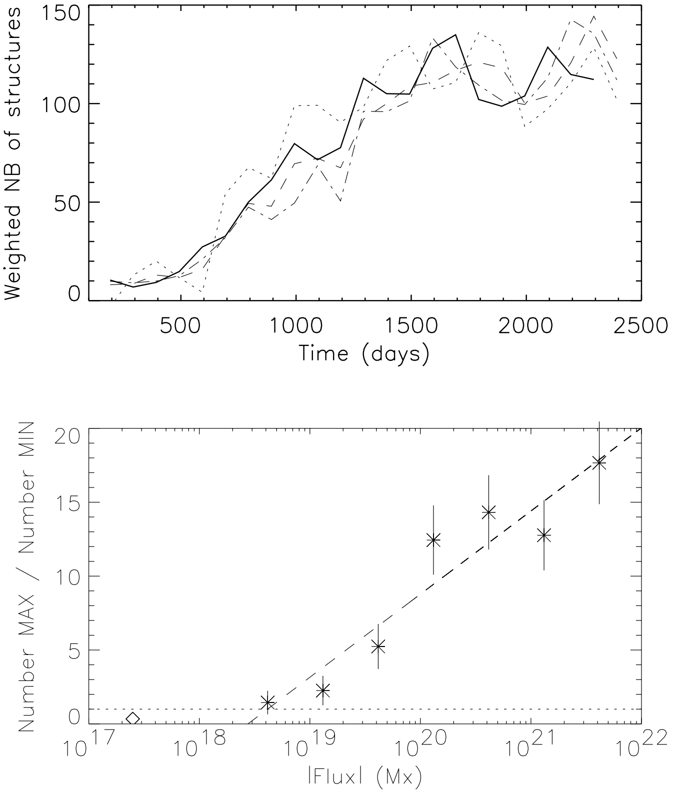

Fig. 8. Top: variation of the weighted number of structures for fluxes smaller than 3×10^{19} Mx (dotted), between 3×10^{19} and 10^{21} Mx (dashed) and above 10^{21} Mx (dotted-dashed); the thick solid line is the Wolf number. Curves are normalized to have the same average number during cycle minimum and during cycle maximum. Numbers are also normalized to the number of images in the period. Bottom: The stars represent the ratio between the number of structures at activity maximum and minimum for different ranges of flux (range of Log $\Phi = 0.5$), and the dashed line is a linear fit over these points (in the log-linear plot. The horizontal dotted line shows the ratio = 1 level (reversal of the variation during the solar cycle) and the diamond point represent the result of Muller & Roudier (1984) assuming a flux of 2.5×10^{17} Mx per individual NBP.

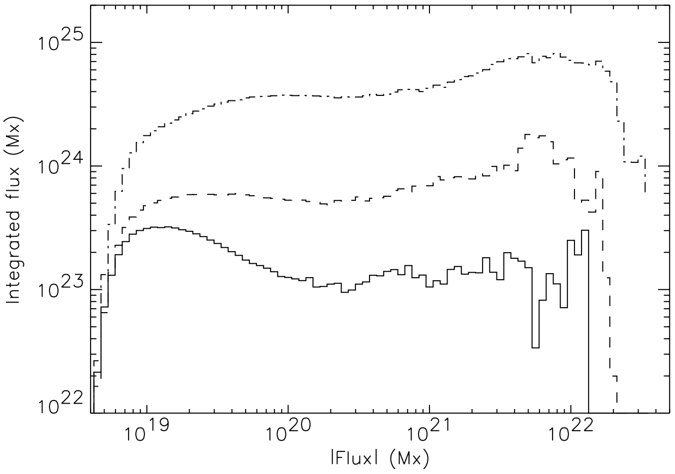

Fig. 9. Magnetic flux distribution during the three phases of the cycle: cycle minimum (solid), ascending phase (dashed) and cycle maximum (dotted-dashed), for the 40 G threshold.

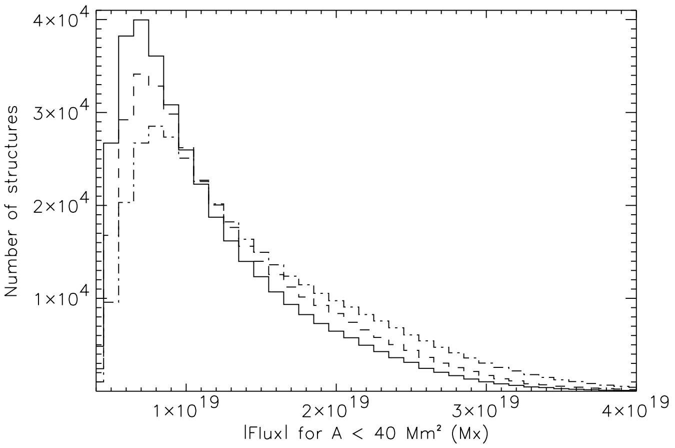

Fig. 10. Flux distribution for small magnetic features (below 40 Mm^2), during the three phases of the cycle: cycle minimum (solid), ascending phase (dashed) and cycle maximum (dotted-dashed), for the 40 G threshold.

4.1.2. Magnetic flux distribution

Another interesting parameter is the integrated magnetic flux for a given range in size or magnetic flux. As expected from Fig. 8, we find an increase of the total flux for the three ranges of flux (below 3×10^{19} Mx, above 10^{21} Mx and in between). At the 40 G threshold, the ratio is 0.96 at solar minimum (meaning that there is as much flux in structures with flux below 3×10^{19} Mx and above 10^{21} Mx) and 5.21 at solar maximum. The distribution of integrated flux versus the flux in the structures is shown in Fig. 9 for the three periods (cycle minimum, ascending phase and maximum): The flux in network structures is predominant during solar minimum and the increase in flux in network structures is quite large along the cycle.

4.2. Magnetic field characteristics

The variation of the flux distribution during the solar cycle is similar to that of the size distribution shown in the previous section. Figure 10 shows the flux distribution variation for small structures only (below 40 Mm^2). I find that the distribution is extending toward larger fluxes from cycle minimum to cycle maximum (longer tail) and the maximum of the distribution is also shifted toward larger fluxes: The average magnetic flux $|\Phi|$ for A lower than 40 Mm^2 increases by 26% from minimum to maximum. This is consistent with the larger variation found previously for the flux than for the number of structures (20% expected). The other magnetic characteristics are also increasing: 33% for $|B_m|$, 16% for $B_m/\overline{B}$, and 14% for the $|\Phi|/A$ (for the 40 G threshold). The increase for $A < 20$ Mm^2 is slightly smaller as in the range 40–80 Mm^2. Values are similar or slightly larger in the range 40–400 Mm^2. In Sect. 3.4.2, I found that the average magnetic flux $|\Phi|$ was decreasing when the distance to an active region was increasing. One should note that curves for the different periods reflected the larger concentration of flux during cycle maximum, and that this is true for all distance to active region: in other words, at a given distance from an active region and for a given size, the average magnetic flux is larger at cycle maximum, the effect being stronger far from active region. For very small structures (below 20 Mm^2), the variations for the subset of bipoles defined in Sect. 3.4 are much smaller than the variations for non-bipolar structures.

The slopes defined in Sect. 3.2 and Table 3 (magnetic characteristics versus size) are found to decrease along the solar cycle, while the values extrapolated for $A = 1$ (from power law fits) are increasing. This is true for both magnetic thresholds. As a consequence, all parameters increase with the activity level for a given size, but the variation is more pronounced for small structures. The variation of the slope for the bipole selection is not as large however. This suggests that the processes leading to magnetic flux concentration in network patches is more efficient during solar maximum, but the dynamo process at the origin of the ephemeral regions of similar size (Schrijver et al. 1997) is not modified by a large factor. The observed variations for network features could also be due to the fact that more flux is available during solar maximum; however the link is not direct because more flux means also more cancellations since opposite polarity features meet more easily (see Harvey 1993, showing that magnetic flux from active region was removed in 4 months at solar cycle maximum and 10 months at solar cycle minimum for this reason).

The observed variation along the solar cycle could be due to a larger availability of magnetic flux, but it could also be related to the relationship between network components and granulation or supergranulation. Several processes could lead to such a variation: *(i)* Size of intersupergranule. However Singh & Bappu (1981) found no variation with the solar cycle. *(ii)* Horizontal velocities in granules and supergranules. *(iii)* Number of explosive granules during the cycle. They are an important factor if they are at the origin of supergranular flows (Rieutord et al. 2000). *(iv)* Diffusion coefficient. *(v)* Supergranular cell sizes. Münzer et al. (1989) found an increase of cell size with the activity level, while Singh & Bappu (1981) found the opposite using data obtained at several maximum and minima. More recently, Berrilli et al. (1999) also found an increase of supergranular cell sizes with the solar activity level using 1 year of data. We know that magnetic elements are confined along the edges of supergranules, and those which emerge inside the cells are quickly advected toward the edges (Lisle et al. 2000). If the cells are smaller at cycle maximum, there will be less space available at the borders of supergranules (perimeters of the cells) and therefore we could expect a given amount of flux to be more concentrated. On the other hand, if the cells are smaller we could expect a larger cancellation rate. I am not aware of studies about points *(ii)*, *(iii)*, and *(iv)*. Concerning point *(iv)*, we know however that an increased amount of flux during the solar maximum is diffusing into the network. A modeling of these processes could be useful to determine whether the larger flux concentrations is only due to the increase of available flux at cycle maximum or to additionnal processes. Such a modelisation is beyond the scope of this paper. Models by Schrijver (2001) and Parnell (2002) would be adequate to study the influence of these parameters.

The more concentrated magnetic flux in structures of small sizes such as network patches during solar maximum may explain the observation of Muller & Roudier (1984) mentionned in the previous section: There may be less flux in the quietest regions selected in these observations due to a larger concentration in others. A complementary result has been obtained by Dermendjev et al. (1994), studying the clusters of NBP using high resolution observations in the *G*-band. They used the same data set than Muller & Roudier (1984), i.e. there may be a bias in the selection of the quietest region on the Sun at a given time. They found a predominence for smaller clusters (5.2 arcsec) with more NBP (typically 4 NBP per clusters) during minimum, while at maximum they found a predominence for larger clusters (6.5 arcsec) with less NBP per clusters (two): This result seems to be in contradiction with the observations presented in this paper showing that magnetic flux seems to be more concentrated at solar maximum. This could be due to a selection effect, because the quietest regions are not necessarily representative of the whole surface. Note also that the anti-correlation of NBP numbers with the solar cycle has often been related to the anti-correlation between X bright points and the solar cycle. However this latter variation may be an artifact of the analysis as shown by Sattarov et al. (2002).

5. Summary

The study of the properties of magnetic features over more than 3 orders of magnitude in size (ranging from the network to active regions) during the first half of solar cycle 23 using an extensive data set of low-noise full disk magnetograms led to the main following new results.

1. The size and flux distributions exhibit 3 main domains: The range below 40 Mm^2 (3×10^{19} Mx), the range 40–400 Mm^2 (3×10^{19}–10^{21} Mx) where the distributions are power laws, and the range above 400–700 Mm^2 ($\sim10^{21}$ Mx). This latter typical scale, close to the supergranular scale, is found to increase from cycle minimum to solar maximum. The shape of the size distribution is not exactly an invariant along the solar cycle.

2. A strong power law dependence of the magnetic flux of the structures on their size (from small network patches to active regions) suggests continuity from small scales to large scales. The slope larger than 1 means that the flux density is also size-dependent. The size-dependence of the magnetic flux is less pronounced during solar maximum however: Differences between solar minimum and maximum are more pronounced for small structures. The magnetic flux of small structures is increasing from solar minimum to solar maximum (for a given area), suggesting that there are more flux tubes concentrated in the same area or the intrinsic magnetic field in the flux tubes is larger at cycle maximum. Small structures involved in a bipolar configuration present larger magnetic fluxes (as well as larger maximum magnetic fields and flux densities) for very small sizes, but their variation along the solar cycle is less pronounced than for other features of similar size.

3. The maximum magnetic field, the ratio between maximum and average magnetic field and the flux density exhibit a behavior similar to the magnetic flux although the dependence on the size is less pronounced. In addition I observe a very large dispersion of the flux density for structures of a given size. The average values of these parameters for a given size are also increasing with increasing solar activity.

4. The North-South asymmetry of the number of structure is reversing at small sizes for the 25 G threshold only (below 40 Mm^2), suggesting a different origin of these weakest flux structures. The North-South asymmetries for the two polarities is compatible with the fact that features of leading polarity are easier to detect (as is expected for active regions) for structures of all sizes including the network structures. The global flux imbalance is not understood.

5. The East-West asymmetry is compatible with an eastward inclination of flux tubes, including for network features although they result from the decay of active region and do not correspond to newly emergent magnetic flux. The East-West asymmetry is slightly different for leading and following polarities (although of the same sign), which could be due to a relative inclination between the two polarities with respect to each other in addition to the global eastward inclination.

6. There is a strong dependence of the magnetic flux of small structures with the activity of their surrounding, both at small scale (immediate surrounding) and large scale (distance from a large active region): Their flux, as well as their flux density, are decreasing when they are further from an active region. At small scales, the effect is of larger amplitude for active regions compared to smaller structures.

7. The latitudinal distribution of structures of various sizes as well as the butterfly diagrams confirm that small structures appear in larger number in the region of high activity level. However the flux per structure in small features (below 40 Mm^2) is maximal at higher latitudes. A North-South asymmetry is also observed.

8. I observe a similar variation of the integrated flux for various size or flux ranges with time, except for the amplitude which is smaller for small and weak flux structures, i.e. the number of structures is correlated with the solar cycle for all sizes. The amplitude of network variations appears to be larger than what have been found previously however (factor 7). A time lag of the order of 100 days (between regions with size above 40 Mm^2 and below) is observed but must be investigated further.

9. The amount of flux at cycle minimum is of the same order of magnitude in large active regions and in network structures.

6. Conclusion

Our results suggest that the properties of structures from active regions down to network features are varying continuously. However we have identified a typical scale corresponding to the supergranular scale using different approaches, which is increasing from cycle minimum to cycle maximum. Structures above this size tend to behave differently than smaller structures, no transition being observed between network structures and small regions. This suggests a modification of the properties between small and large active regions – at the supergranular scale – and not only between active regions and network structures. The variation of that scale along the solar cycle is compatible with recent results showing that the supergranular cells are increasing from solar minimum to solar maximum, which would suggest that this typical scale may indeed by related to supergranulation cells or to the processes at the origin of supergranulation.

It is interesting to consider the different behavior of small and large scales structures concerning the slope of $|\Phi|$ (or the other magnetic properties characteristics) depending on the approach: The slope of the magnetic flux versus size is decreasing when the activity level is increasing along the solar cycle while it is increasing when the local activity level is increasing. On the other hand, no significant variation is observed when looking at these slopes for different distances to a large active region. This shows that although the flux is always larger (at a given size) when it is “more active”, this variation is different for the various sizes. Variations observed for network structures may be due to a variation of granulation or supergranulation properties, while the variation for active regions and ephemeral regions is more likely to be due to the emergence of magnetic field due to the dynamo processes, including a possible variation at the bottom of the convective zone and a strong relation between the involvement of the region in a nest and its characteristics.

For the largest structures, the main result is that active regions have different properties when they are close to another one: Not only active regions seem to emerge preferentially in regions previously occupied by other active regions as observed by other authors (the presence of active longitudes or nests has been observed by many authors, for example Gaizauskas et al. 1983; Harvey & Zwaan 1993; Harvey 1993; Schrijver & Zwaan 2000), but the flux is more concentated in these structures than for isolated ones: we do not identify strictly the nests, however active regions close to another one are more likely to be part of a nest. Harvey (1993) has suggested from a small sample that the properties of active regions emerging in a preexisting spot region is related to the already emerged flux, by observing the orientation of bipoles. We confirm this by using a different approach: The flux characteristics of a structure seems influenced by the involvement in a nest or not. The larger flux at cycle maximum could be related to this, because she observed that the emergence rate in nests was larger during solar maximum (50%) than during solar minimum (30%). When looking at small-scale behavior (close environment), the large regions are more sensitive to their close environment compared to small features.

The small bipolar structures however, related to ephemeral regions, have properties different from network features of the same size. Although for all structures the magnetic flux (as well as other magnetic characteristics) is larger when the environment is more active or during cycle maximum, the detailed variation of the concentration of the magnetic field in network structures is different from that of small bipolar structures. This difference is also likely to be due the difference in origin: Creation by the dynamo process (similar to large active regions) and decay from active regions. Results suggest that surface motions (such as in granules and supergranules) are less efficient to concentrate the flux than the dynamo process but exhibits larger variations along the solar cycle. However part of the bipolar association are probably due to network patches resulting from the decay of some active region just before they merge to participate in the flux removal processes, so the differences are probably underestimated.

The fact that the average magnetic flux of small structures is not the largest at latitudes where activity occurs is not necessarily inconsistent with the observation that the flux is decreasing when the structures are further from an active region. The latter approach averages the dependence in all directions. This suggests that the diffusion of magnetic flux is not isotropic, possibly due to the meridional flows that are predominantly poleward. A possible interpretation for the observed latitudinal variation could be the following: At latitude of strong activity, supergranular diffusion may not be very efficient so that the concentration of small patches of flux are weaker; at high latitude, the supergranulation may be more effective in concentrating the flux, available in larger quantity than close to the equator due to the meridional circulation. However it is surprising that this is not true for structures in the range 40–80 Mm^2 also, which are also network structures resulting from the flux dispersal at the surface. The small number of features close to the equator is indeed surprising because this is also where the detection is the easiest.

We suggest that the anti-correlation of NPB with the solar cycle found by Muller & Roudier (1984) may be due to both a selection effect (the quiestest regions at a given time) and the largest concentration of the flux in network patches during solar maximum. The variation of the magnetic properties of the network structures may also be related to the different contrasts of network and plages found by Ortiz et al. (2002). These results are therefore very important in the context of the solar irradiance variations. Furthermore, the contribution of the magnetic network is probably larger than what have been previously observed.

In the future it would be very useful to perform simulations such as the ones performed by Simon et al. (2001) and Krijger & Roudier (2003) by including solar cycle variations of parameters such as the supergranulation size (see Sect. 4.2) in order to help to interpret these new results. It would also be interesting to compare whether global models such as those made by Schrijver (2001) and Schrijver et al. (2002) can reproduce such results. The model of the magnetic carpet elaborated by Parnell (2002) could also be used. These models reproduced with success the histogram of flux densities. They would also be useful to check the difference in efficiency between supergranular diffusion and meridional circulation in transporting the flux, as well as their solar cycle dependence, and their influence on the flux contents of structures of a given sizes.

More observationnal work will also be needed to confirm the new results obtained in this work, in particular by performing large field-of-view network observations (*G*-band, magnetograms and dopplergrams) and spectropolarimetric measurements at very high spatial resolution. Both types of observations should be performed regularly during at least a solar cycle.

Acknowledgements. I am very grateful to L. van Driel for her careful reading of a preliminary version of the manuscript and many useful comments that helped to improve it. I also thank the anonymous referee for his/her comments on this paper. SOHO is a mission of international cooperation between the European Space Agency (ESA) and NASA. Sunspot numbers have been provided by the National Geophysical Data Center (National Oceanic and Atmospheric Administration).

References

Abbett, W. P., & Fisher, G. H. 2001, ApJ, 546, 1194
Berger, T., & Lites, A. 2003, Sol. Phys., 213, 213
Berrilli, F., Ermolli, I., Florio, A., & Pietropaolo, E. 1999, A&A, 344, 965
Caligari, P., Moreno-Insertis, F., & Schüssler, M. 1995, ApJ, 441, 886
Dermendjev, V. N., Muller, R., & Madjarska, M. S. 1994, Sol. Phys., 155, 45
Foukal, P., & Lean, J. 1988, ApJ, 328, 347
Foukal, P., Harvey, K., & Hill, F. 1991, ApJ, 383, L89
Gaizauskas, V., Harvey, K. L., Harvey, J. W., & Zwaan, C. 1983, ApJ, 265, 1056
Garcia de la Rosa, J. I. 1983, Sol. Phys., 89, 51
Hagenaar, H. J. 2001, ApJ, 555, 448
Hagenaar, H. J., Schrijver C. J., & Title, A. M. 2003, ApJ, 584, 1107
Harvey, K., & Zwaan, C. 1993, Sol. Phys., 148, 85
Harvey, K. L. 1993, Ph.D. Thesis, Astronomical Institute, Utrecht University
Howard, R. 1991, Sol. Phys., 134, 233
Krijger, J. M., & Roudier, T. 2003, A&A, 403, 715
Labonte, B. J., & Howard, R. 1982, Sol. Phys. 80, 15
Lean, J. L., Cook, J., Marquette, W., & Johannesson, A. 1998, ApJ, 492, 390
Lisle, J., De Rosa, M., & Toomre, J. 2000, Sol. Phys., 197, 21
Meunier, N. 1999a, ApJ, 515, 801
Meunier, N. 1999b, ApJ, 527, 967
Muller, R., & Roudier, T. 1984, Sol. Phys., 94, 33
Muller, R., & Roudier, T. 1994, Sol. Phys., 152, 131
Münzer, H., Hanslmeier, A., Schröter, E. H., & Wöhl, H. 1989, A&A, 213, 431
Nishikawa, J. 1994, Sol. Phys., 152, 125
Ortiz, A., Solanki, S. K., Domingo, V., Fligge, M., & Sanahuja, B. 2002, A&A, 388, 1036
Parnell, C. E. 2002, MNRAS, 335, 389
Sattarov, I., Pevtsov, A. A., Hojaev, A. S., Sherdonov, C. T. 2002, ApJ, 564, 1042
Rieutord, M., Roudier, T., Malherbe, J.-M., & Rincon, F. 2000, A&A, 357, 1063
Sànchez Almeida, J., & Lites, B. W. 2000, ApJ, 532, 1215
Scherrer, P., Bogart, R. S., Bush R. I., et al. 1995, Sol. Phys., 162, 129
Schrijver, C. J., Shine, R. A., Hagenaar, H. J., et al., 1996, ApJ, 468, 921
Schrijver, C. J., Title, A. M., van Ballegooijen, A. A., Hagenaar, H. J., & Shine, R. A. 1997, ApJ, 487, 424
Schrijver, C. J. 2001, ApJ, 547, 475
Schrijver, C. J., & Zwaan, C. 2000, Solar and Stellar Magnetic Activity, Cambridge Astrophysics Ser. 34 (Cambridge Univ. Press)
Schrijver, C. J., De Rosa, M. L., & Title, A. M. 2002, ApJ, 577, 1006
Sigwarth, M. 2001, ApJ, 563, 1031
Singh, J., & Bappu, M. K. V. 1981, Sol. Phys., 71, 161
Simon, G. W., Title, A. M., & Weiss, N. O. 2001, ApJ, 561, 427
Socas-Navarro, H., & Sànchez Almeida, J. 2002, ApJ, 565, 1323
van Driel-Gesztelyi, L., & Petrovay, K. 1990, Sol. Phys., 126, 285
Wang, H. 1988, Sol. Phys., 116, 1
White, O. R., & Livingston, W. C. 1981, ApJ, 249, 798

A&A 412, 541–553 (2003)
DOI: 10.1051/0004-6361:20031435

Astronomy
&
Astrophysics

Fast photospheric flows and magnetic fields in a flaring active region

N. Meunier[1] and A. Kosovichev[2]

[1] Observatoire Midi-Pyrénées, 57 avenue d'Azereix, BP 826, 65008 Tarbes Cedex, France
[2] Hansen Experimental Physics Laboratory, Stanford University, Stanford, CA 94305, USA
e-mail: `sasha@khors.stanford.edu`

Received 25 June 2003 / Accepted 3 September 2003

Abstract. We present new results from the coordinated observations between the THEMIS telescope (in the multi-line spectropolarimetric mode) and Michelson Doppler Imager (MDI) on SOHO obtained in November 2000 for active region NOAA 9236 which was the source of several X-class flares. The goal of these observations was twofold: to verify MDI measurements of the line-of-sight components of flow velocity and magnetic field, and to obtain more information about the photospheric flows and magnetic fields in flaring regions. Using the simultaneous observational data in several lines we have analyzed the structure and dynamics of this active region at the photospheric level before and after a X4.0 flare of November 26, the last major flare produced by this very active region. Vector magnetic field maps are computed from the THEMIS data by full inversion of the Stokes line profiles. In the Doppler velocity maps from THEMIS and MDI, we observe fast photospheric flows which appear to be supersonic in two regions located close to the region where the flare occurred. These flows seem to be long-lived (several hours at least). In one position, we observe a supersonic downflow strongly inclined with respect to the vertical (by 51°), while in another position, a flow suggesting a strong shear with a supersonic component as well, although almost horizontal upflows and downflows cannot be ruled out in that case. These flows seem to be present at least 8 hours before the flare, and the amplitude in the second case appeared to be modified during the flare, especially, during the first minutes. In the MDI data, we observed strong permanent changes of the longitudinal magnetic flux, associated with the flare. The role of the strong flows and their interaction with the magnetic field in the development of the active region and the flare is not understood yet.

Key words. Sun: magnetic fields – Sun: flares – Sun: photosphere – Sun: activity

1. Introduction

Observations of photospheric magnetic fields and flows as well as plasma thermodynamic properties in flaring active regions are important for understanding the mechanisms of energy storage and release. Despite the long history, these observations have not produced a clear picture of the flare processes in the photosphere. Severny (1958) first discovered that solar flares tend to occur in the vicinity of neutral lines separating regions with opposite polarities of the line-of-sight (LOS) magnetic field components, and where the field gradient is particularly strong (of the order of 1 G/km). Martres & Soru-Escaut (1977) argued that flares were often associated with the neutral line of the line-of-sight velocity. Several observers found significant upflows in the photosphere prior some flares (e.g. Yoshimura et al. 1971; Harvey & Harvey 1976). More recent observations (Keil et al. 1994) revealed strong horizontal and shearing flows near flare kernels. However, the role of the photospheric flows and magnetic fields in the mechanism of solar flares is still not understood.

The space observations from Michelson Doppler Imager (MDI) on SOHO (Scherrer et al. 1995) provide an unique opportunity to study the structure and variations of the LOS magnetic field and flows in flare regions. However, the LOS information from a single line is insufficient for physical interpretation of these observations (Kosovichev & Zharkova 2001). Also, the MDI measurements, obtained from a sequence of filtergrams taken in four positions across the spectral line, suffer from saturation in the case of strong flow velocity and field strength, and also may be not sufficiently accurate when rapid changes, on the a few minute scale, occur. Therefore, it is highly desirable to combine the MDI data with spectral ground-based observations of solar flare. In this paper, we report about one of the first attempts of such coordinated observations which were carried as a part of the SOHO Joint Observing Programs.

We have performed spectropolarimetric observations of a flaring active region at the photospheric level using the THEMIS telescope. Our objective is to describe the complex

---

Send offprint requests to: N. Meunier,
e-mail: `meunier@bagn.obs-mip.fr`

topology of this active region by using vector magnetic field measurements, investigate mass flows, and study the variations of magnetic field and flows, associated with a strong flare. We also study the spectral characteristics in the flare region, and, particularly, unusual V and Q Stokes spectra. The outline of this paper is the following. In Sect. 2 we describe the coordinated THEMIS and MDI observations on SOHO, as well as also additional Hα observations obtained at the CU Cesco Station in Argentina. The processing of THEMIS data is described in Sect. 3. In this paper we use the multi-line capabilities of THEMIS mostly to confirm that the strong flows we observe are not an observational bias. The precise comparison between the different wavelengths will be the subject of a future paper. Analysis of the results is made in Sect. 4: We describe the general evolution of the region and then emphasize the strong flows which are observed in both THEMIS and MDI data. These new results are summarized and discussed in Sect. 5.

2. Observations

2.1. THEMIS: Multi-line spectropolarimetry

Observations were performed using the multi-line spectropolarimetric mode (MTR) of THEMIS telescope. This mode, described by Paletou & Molodij (2000), allows simultaneous I+Stokes and $I-$Stokes observations. The field of view was ~110 arcsec in the direction along the 0.5 arcsec wide slit. We observed sequences of Stokes parameters $[Q, -Q, U, V]$ to allow for a beam exchange analysis. It took ~6 s to record such a sequence on 6 cameras (3 spectral domains). In this paper, we focus on three observations of active region NOAA 9236, that are summarized in Table 1.

The two scans of this region were performed with a step of 0.8 arcsec and the time exposure of 800 ms. The first scan was made during a better seeing period (in the range of 1–2 arcsec). The angle between the normal to the solar surface and the line-of-sight was ~41° at the center of the region (on Nov. 26). In addition, spectropolarimetric observations at a fixed position were carried out near the end of the Hα emission of the X4.0 flare occurring between 16:38 and 17:32 on Nov. 26 (see Fig. 1). The exposure time was 600 ms. During these observations, the Sun was rather low, about 9° above the horizon, and the seeing was poorer (several arcseconds).

In all cases, the flat-field measurements were made using an elliptical motion of the telescope in a quiet region around disk center. The slit was oriented toward the celestial North. The spectral resolution was between 18.5 and 22.8 mÅ per pixel depending on the wavelength.

The line characteristics are described in Table 2. The Fe I 6301.5 and 6302.5 Å lines have characteristics only slightly different from the Ni line, but the 5635.8 and 5634.0 Å lines are formed much deeper in the photosphere. One should note that other values for the line formation height have been published, for example the value of ~200 km for the Ni I 6767.8 Å line by Jones (1989). The difference between this last computation and the results of Table 2 could be due to slightly different computation method, in particular the physical quantity for which the response functions are computed. Therefore it is important to compare line formation heights with computations made in similar conditions, as in Table 2. One should also keep in mind that these line formation heights are averaged over a larger distribution and therefore provide only an approximation.

Table 1. Characteristics of THEMIS observations: Set 1 is [Fe I 6302.1 Å and 6302.5 Å, Fe I 5576.1 Å, Ni I 6767.8 Å], set 2 is [Fe I 6302.1 Å and 6302.5 Å, Ni I 6767.8 Å, Fe I 5635.8 and 5634.0 Å]. The indicated time corresponds to the starting time of the observation. A *scan* means that the whole region has been observed. The *fixed* position corresponds to the slit positioned as indicated in Fig. 2.

Date	Time	Length	Type	Wavelength
25 Nov. 2000	8:34	29 min	scan	set 1
26 Nov. 2000	8:24	29 min	scan	set 1
26 Nov. 2000	17:20	12 min	fixed	set 2

Table 2. Spectral line characteristics for the wavelength used in this paper. Lande factors are courtesy of J.-F. Donati. The line formation heights above the photospheric level are computed from the LTE response functions at the disk center for the atmosphere model VAL-C (K. Puschmann, private communication).

Wavelength (Å)	Landé factor	Formation height
6302.5	2.487	281 km
6301.5	1.669	400 km
6767.8	1.426	374 km
5635.8	0.677	153 km
5634.0	1.425	22 km

2.2. MDI/SOHO: Full-disk magnetograms and Dopplergrams

The THEMIS observations were coordinated with MDI/SOHO observations, which provide maps of the line-of-sight component of the magnetic and velocity fields (Scherrer et al. 1995). The MDI observations are made in the Ni I 6767.8 Å spectral line, which was also used for THEMIS observations (see Table 2). We used MDI in the full-disk mode (FD) from Nov. 26 (8:00) to Nov. 26 (24:00), with a temporal cadence of 1 min (the pixel size is 2 arcsec). The observed active region has been tracked to remove the displacement caused by solar rotation.

2.3. OAFA: Full disk Hα images

We have analyzed Hα full-disk images obtained with the Hα telescope from the CU Cesco Station at the Observatorio Astronómico Félix Aguilar (OAFA) in Argentina between 16:00 and 18:00 UT on Nov. 26, 2000. The data are available with a temporal cadence of approximately 12 s and a relatively low spatial resolution, significantly lower than 2.1 arcsec defined by the pixel size. The intensity level reached a saturation level in the flare region. Unfortunately

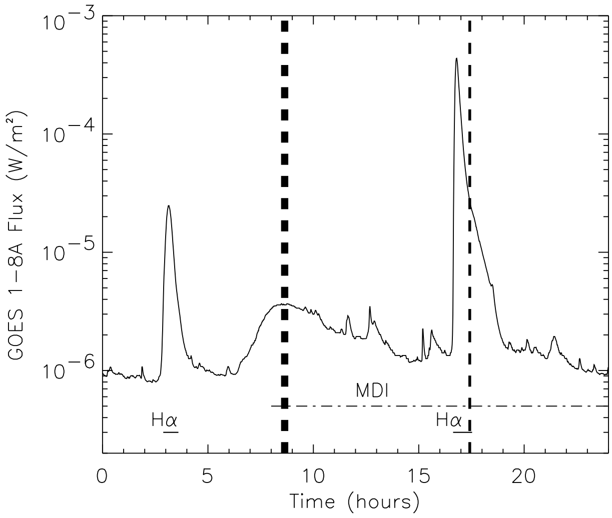

Fig. 1. GOES X-ray flux in the range 1–8 Å for Nov. 26, 2000. The first flare (from 2:47 to 3:20 UT) is an M2.2 flare with a total energy of 4 × 10^{21} J and is located around latitude 19° and longitude 30° while the second one (from 16:34 to 16:56) is a X4.0 class flare with a total energy 10 times larger and is located around latitude 18° and longitude 38°. The thick vertical dashed line indicates the time of the THEMIS scan (Nov. 26, 8:24) and the thin dashed line shows the time of the fixed position THEMIS observation (Nov. 26, 17:20). The thickness of these lines is proportional to the duration of the observation. The duration of Hα flares are indicated by 2 small horizontal lines. The long horizontal dotted-dashed line corresponds to the MDI observations used in this paper.

10 min of the Hα data simultaneous with our THEMIS observations were lost because of clouds (Nov. 26, 17:20).

3. THEMIS data processing

3.1. Stokes parameter computation

The main steps of the THEMIS data analysis are the following:

(i) *Flat-field and line curvature correction*. For each Stokes parameter of the averaged flat-field, we compute the spectral line curvature. After a correction of the curvature, a mean spectral profile is computed. The flat-field images are normalized by this profile to remove the spectral signatures and shifted back to the initial line curvature. The scan spectra are corrected for the flat-field before the curvature correction, which is then performed using the curvature values computed for the flat-field.

(ii) *Shift in x (wavelength) and y (spatial)*. The shift in wavelength (x coordinate) is computed using a profile averaged over each spectrum. A cut in the slit direction averaged over the continuum is used to compute the spatial shift (y coordinate). For these calculations we use a cross-correlation of the granulation signal.

(iii) *Beam exchange computation*. We compute the Stokes parameters using the beam exchange technique: Stokes Q is computed separately for each optical path using two spectra taken at a different time, and, then, the two resulting Q spectra are averaged. For Stokes U and V, the technique is similar except that the Q measurements are also used, i.e. we need 3 spectra for each optical path (during our observations the beam exchange was possible for one Stokes parameter only, see Sect. 2.1).

Table 3. Polarization phase versus wavelength for the analyzer plates (Characteristics and code kindly provided by F. Paletou).

Wavelength (Å)	Phase (degrees)
5576	93.18
5636	92.95
6302	89.71
6768	86.99

(iv) *Crosstalk corrections*. Although THEMIS is a polarization free instrument, the quarter wave plates are not perfect for all wavelengths, and the polarization phase can be off by several degrees (see Table 3). The amplitude of the crosstalks reaches a few percents for some of our wavelengths.

(v) *Zero corrections*. Due to the problem of "co-spatiality" between the two slits described in more detail in the next section, the simultaneous spectra of I+Stokes and I−Stokes (see Sect. 2.1) do not correspond to the same position on the Sun. As a consequence there are residuals in the continuum of the Stokes spectra, especially in the U profiles. This represents a problem for inversions. Therefore, we have subtracted the observed zero from the data, modulated by the I profile.

(vi) *Line-of-sight components computation*. Maps of LOS magnetic and velocity fields are obtained using the center-of-gravity method (Rees & Rayrole 1979) applied to the $I \pm V$ spectra. Results are shown in Fig. 2 for the two scans of the region.

(vii) *Vector magnetic field computation*. This is performed over the whole field of view using a computer code kindly provided by T. Metcalf. This code, described by Jefferies et al. (1989), is routinely used at the Mees Observatory (University of Hawaii) for preliminary data reduction of the Haleakala Stokes Polarimeter data. It is based on the weak-field approximation and does not perform a full inversion. The 180°-ambiguity of the azimuth is solved using the same code (see, e.g. Canfield et al. 1993), as well as the projection effects. The maps are very similar for the Ni and Fe lines. A full inversion of the interesting profiles has also been performed using the inversion code described in Fruttiger (2000). This code allows to consider models with any number of structural components (magnetic or not) and takes into account variation of the model parameters with height.

3.2. Main limitations

We summarize here some limitations of our THEMIS observations in addition to the crosstalks and zero corrections mentioned above (some of them are discussed by López Ariste et al. 2000):

(i) *Cospatiality*. The polarimeter is followed by a calcite beam splitter and two slits to allow the simultaneous analysis of I+Stokes and I−Stokes (see Sect. 2.1). As a consequence, the two slits must be adjusted with great precision to allow observations of the same position on the Sun. Unfortunately, this did not work well during these observations; there was a difference of 0.23 arcsec between the two beams, because the

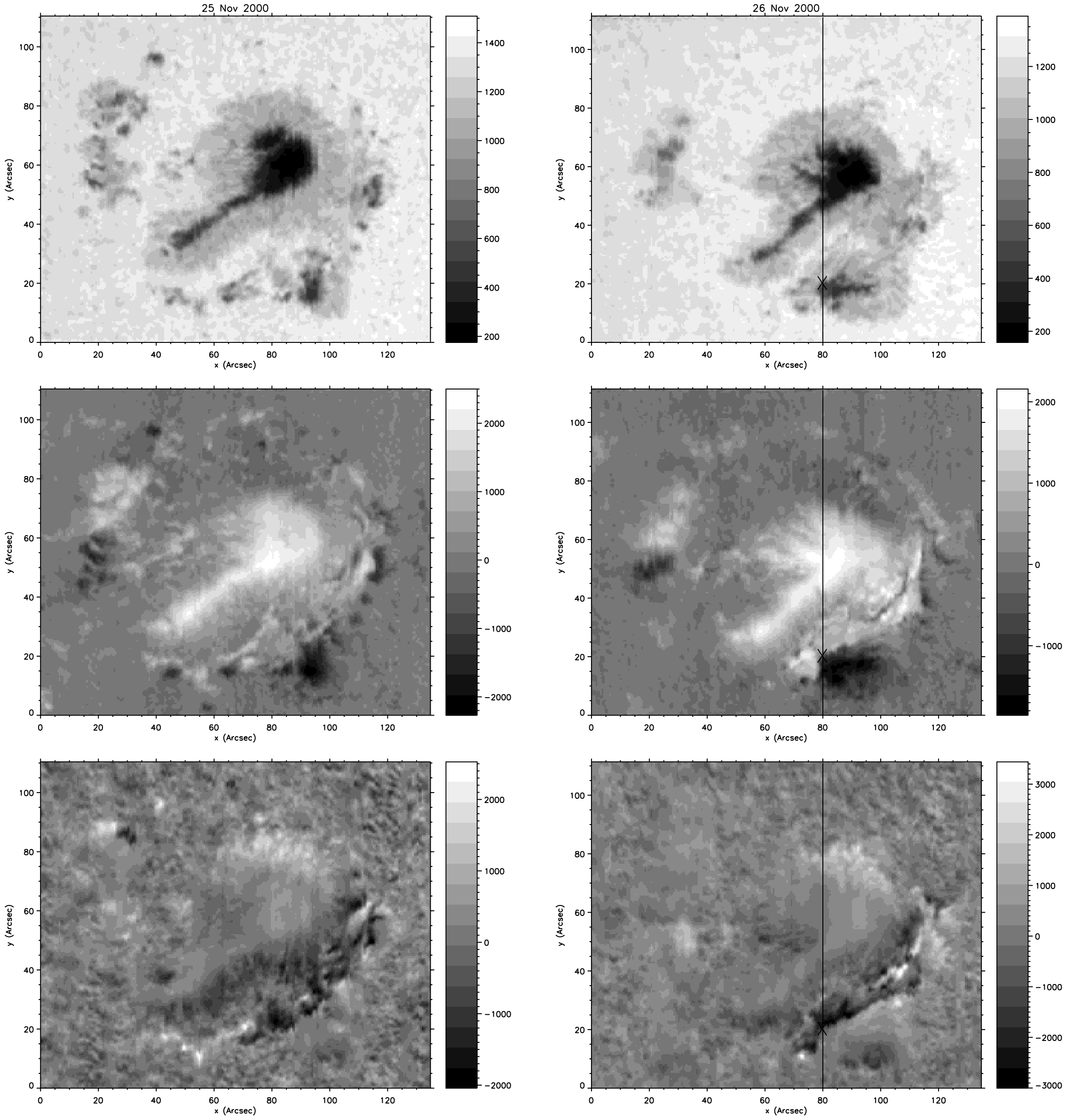

Fig. 2. Maps of continuum intensity (*top*), line-of-sight magnetic field (*middle*) and velocity (*bottom*) observed with THEMIS using the Ni line, for Nov. 25 (8:34 UT) and Nov. 26 (8:24 UT) scans. The vertical line shows the approximate position of the slit during the fixed position at the time of the flare. The cross corresponds to the plot in Fig. 10 (left). The top corresponds to the celestial North.

instrument configuration did not allow a good precision for this adjustment. This problem and its influence on spectropolarimetric precision are discussed by Meunier et al. (2002).

(ii) *Image motion and seeing*. There is no image stabilization in the telescope. The actual spatial resolution for the fixed position spectra after averaging is of the order of 1.5 to 2 arcsec. The scan spectra have a better spatial resolution, but stronger contaminated by Doppler residuals (no averaging is done).

(v) *Absolute wavelength*. There is no absolute wavelength calibration. Therefore, the zero level of the longitudinal velocity is not known precisely (an uncertainty of 100 to 200 m s^{-1} is likely). Furthermore, the spectra between the two paths have to be shifted as well as each image of a series for a given path because a trend with time is observed. The presence of magnetic field introduces some noise in this computation, and this is taken into account in the data reduction.

(vii) *Atmospheric refraction*. The various wavelengths are observed simultaneously with THEMIS. However, because of the atmospheric refraction, the observations are not at the same position on the solar surface. If the slit is perpendicular to the horizon, a shift along the slit is sufficient to correct for this problem, with only a small loss in the field-of-view. However, if the slit is not perpendicular to the horizon (and this was the case for these observations, especially for the flare data obtained at 17:20), then the interpretation becomes more difficult. For example, for our flare observations, the 5635.8/5634.0 Å lines correspond to a position more than 1 arcsec away from the 6767.8 Å line, with the 6301.5/6302.5 Å lines in between.

Other limitations are due to magnification and focus differences (the adjustments are made with a precision of 0.5% for the magnification for example) and to uncertainties in pixel size calibrations. They can limit the precise comparison between wavelengths.

4. Results

4.1. General description of the evolution of AR 9236

The observed region, illustrated in Fig. 2 (THEMIS) and Fig. 3 (MDI) contained a roundish spot with an extension in the approximate direction towards the disk center. It had magnetic type $\beta\gamma$. The spot was of the positive (leading) polarity. The opposite polarity region (following polarity) constituted of plages only and is not visible on these maps (it is located East to the observed region). On Nov. 22, some small spots of opposite polarity appeared West of the large spot. The location of emerging magnetic flux of the opposite polarity moved later toward South: on Nov. 25 and Nov. 26, the opposite polarity spots were located mainly South to the main spot. This region has been very active over 3 days, Nov. 24–26, producing big flares on the last day of this run. Most of these large flares produced CMEs.

In this paper, we concentrate on the evolution of the region on Nov. 26 during 16 hours starting at 8:00 UT, and on the flare which started at 16:38 UT in Hα intensity (see Fig. 1). Figure 4 shows contours of the Hα intensity shortly after the beginning of the flare superimposed on the maps of magnetic and velocity fields from MDI (the South part of the active region). The Hα emission covered a wide region with the angular size of more than 1 arcmin and was located close to the small spot of the opposite polarity and to the neutral line. It overlapped with the region where strong velocity flows of both signs are found. In particular, the brightest part of the flare was close to the strong positive velocity flows. The variations of the magnetic and velocity fields occurred mostly in these regions, as can be seen from the rms value of the magnetic field and velocity signals for the 16 hours of the MDI data for each CCD pixel (Fig. 4). Figure 2 displays maps of the LOS components for the scans made on Nov. 25 and Nov. 26, revealing completely different magnetic and velocity patterns South of the main spot, between the two observations separated by 24 hours.

More details of the evolution of the line-of-sight magnetic flux are shown in Fig. 5 separately for positive and negative polarities for selected regions. For the whole active region shown in Fig. 3 (which includes the main spot with surrounding opposite polarity small spots), the positive magnetic flux was decreasing steadily starting at least 8 hours before the flare, while the negative magnetic flux was slowly increasing.

At the time of the flare, a sharp increase of the positive magnetic flux by 10^{21} Mx is observed during at least 1 hour. The flux continued to vary after the end of the flare. The negative flux, however, decreased abruptly at the beginning of the flare by 0.5×10^{21} Mx, and then continued to decrease more slowly. In region 1, we observe a similar evolution at the time of the flare, which is consistent with the fact that most of the evolution related to the flare occurred in this region. However most of the variation observed before the flare in the whole active region occurred somewhere else because the flux was quite constant in region 1 before the flare. A third of the positive flux increase was observed in region 2, and another third in region 3, although the increase was more gradual in the latter. On the other hand, the negative flux was decreasing mostly in region 3.

We note that a strong variation of the magnetic field in one pixel could correspond to flux emergence, flux cancellation, or motions of magnetic structures (or of the neutral line). Because MDI measures only the line-of-sight component of the magnetic field, the observed variation could also be caused by changes of the inclination of the magnetic field lines. In some cases, the slow change of the line-of-sight flux could be caused by solar rotation. For instance, the relative changes of the whole-region flux, shown in top panels of Fig. 5, before the flare, $|\mathrm{d}\log|B|/\mathrm{d}t| \simeq 2 \times 10^{-6}\ \mathrm{s}^{-1}$, are comparable with the maximum change of $2.7 \times 10^{-6}\ \mathrm{s}^{-1}$, due to the projection effect. However, in the case of region 2 (middle left panel in Fig. 5), the flux decrease rate before the flare was much stronger, $\simeq 1.2 \times 10^{-5}\ \mathrm{s}^{-1}$, and must be related to changes in the magnetic field structure in the flaring region.

In addition, MDI observations of the line-of-sight magnetic fields, which are obtained from nine filtergrams taken with 3-s cadence, can be affected by rapid variations of the line profile and intensity due to the photospheric heating in the region of the flare. However, these effects can be significant only for rapid transient variations in the MDI signals. Clearly, the permanent changes that have been observed during the flares and never restored after the flares for the whole period of observations lasting hours and days, cannot be explained by flare heating which does not last that long. Also, unlike traditional magnetographs, MDI accounts for the variations of the line intensity that are slower than the 30-s measurement time. Therefore, the permanent changes of the line-of-sight magnetic signal detected by MDI certainly result from the structural changes of magnetic field related to solar flares. However, the transient impulsive variations in the MDI magnetic signal may be affected by the line-profile variations. These impulsive magnetic signals correlate spatially and temporally with hard X-ray impulses and, therefore, are likely be caused by direct hits of the photosphere by high-energy particles (Kosovichev & Zharkova 2001). Whether these effects are mostly of the thermal or electromagnetic nature is not known yet. Simulations of the MDI measurements for some of the impulsive events published by Kosovichev & Zharkova (2001) showed that the thermal effects can be responsible only for a relatively small portion of the observed variations. We note that a detailed discussion of these effects is beyond the scope of our paper; a complete interpretation requires high-cadence observations of the Stokes profiles of the Ni I 6767.8 Å line for such events, which are not yet available.

In the next section, we will investigate in detail two small regions of interest defined in Fig. 4, as regions 2 and 3. These regions are characterized by strongest variations of magnetic fields and the largest velocity flows, and also showed the most unusual Stokes profiles in the THEMIS data. Region 2 exhibits a strong stationary downflow (positive) velocity flow (corresponding to redshift of the spectral line), while strong flows, directed both up and down, are observed in region 3, especially at the time of the flare.

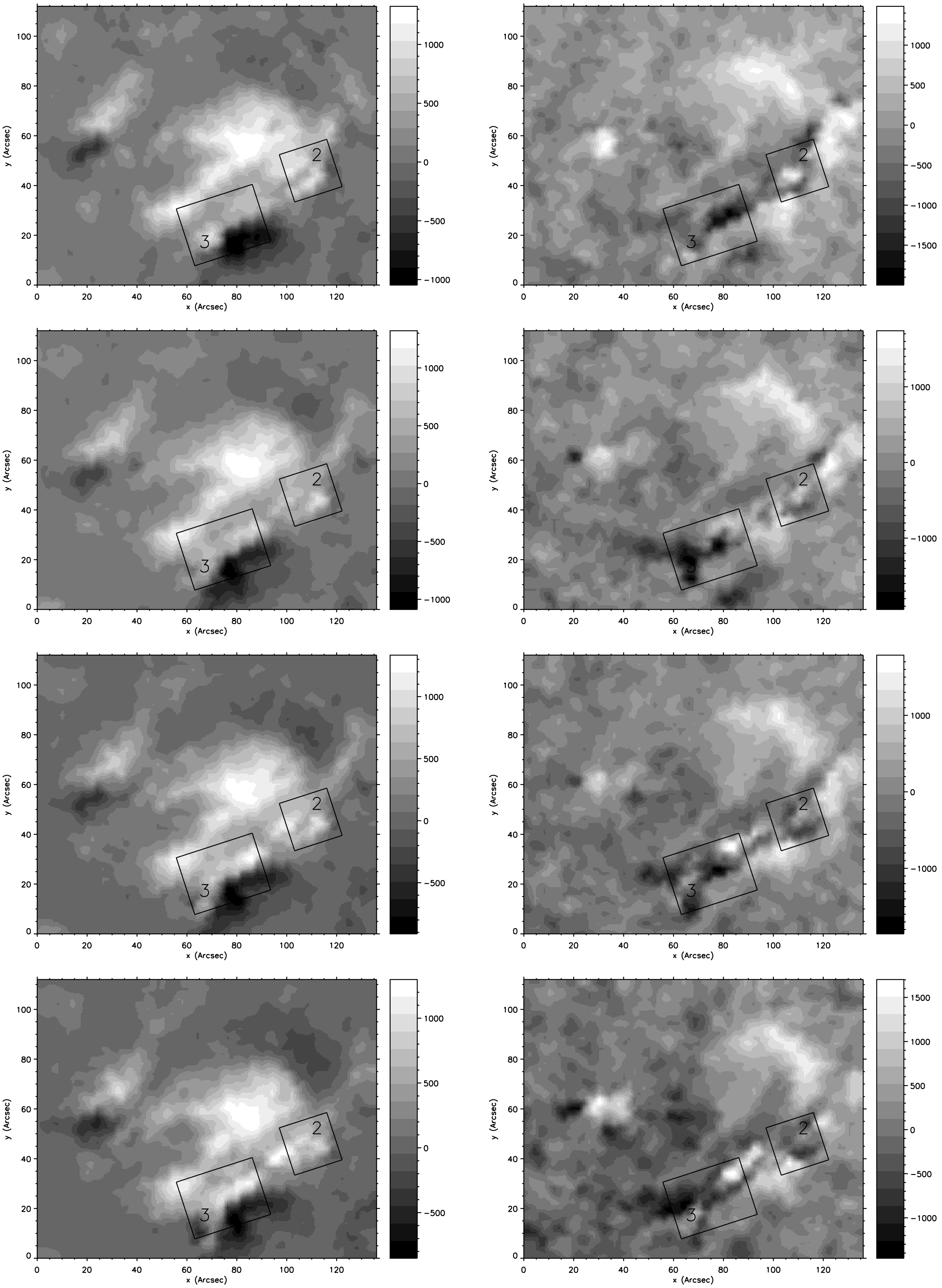

Fig. 3. MDI line-of-sight magnetic field (*left*, in G) and velocity field (*right*, in m s^{-1}) at four different times (*from top to bottom*): 10:00, 15:38 (one hour before the beginning of the Hα flare), 19:02 (~1.5 hour after the end of the Hα flare), and 24:00 UT (Nov. 26, 2000).

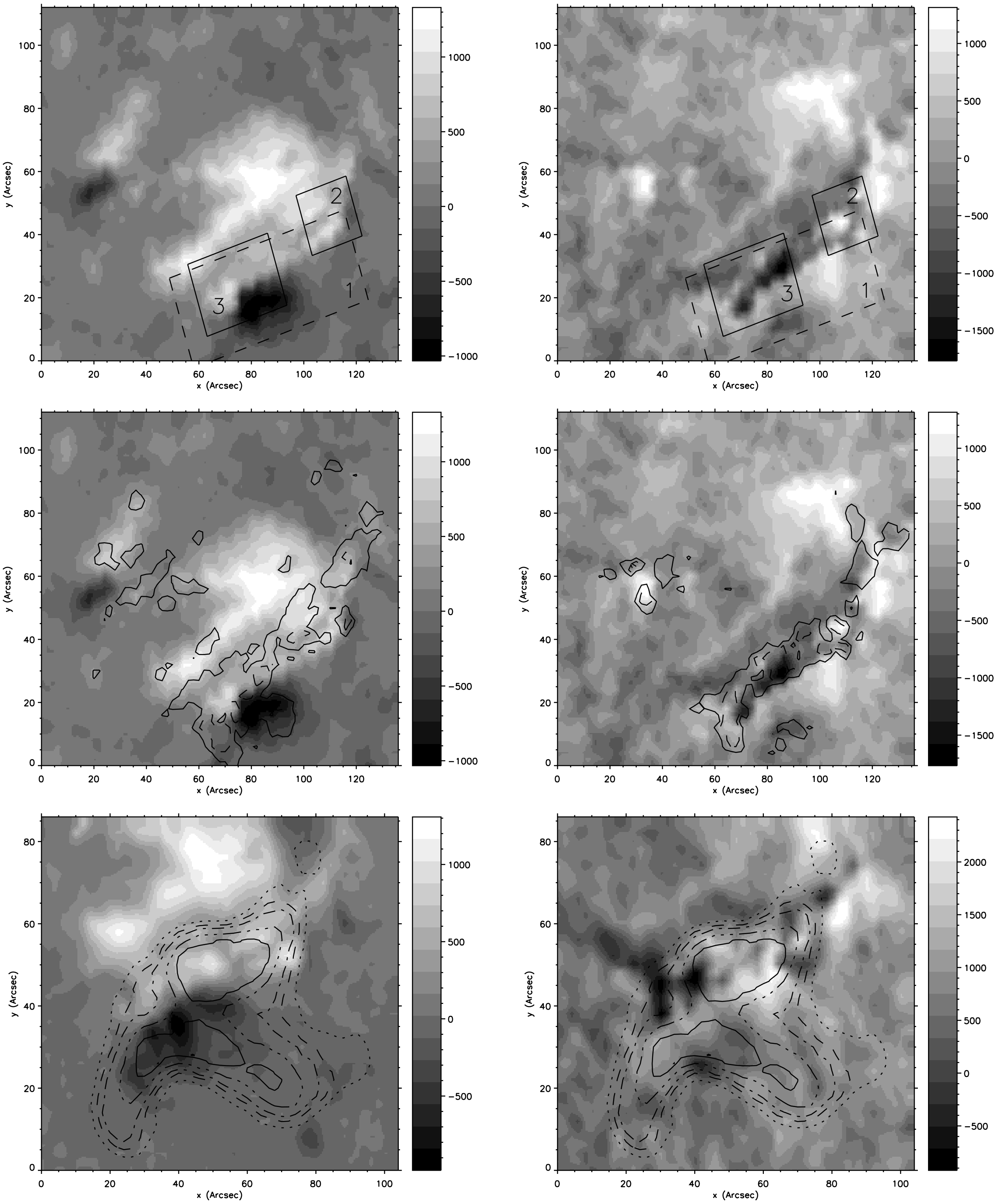

Fig. 4. *Top*: Map of the line-of-sight magnetic field component (*left*, in G) and Doppler velocity field (*right*, in m s^{-1}) observed by MDI (Nov. 26, 2000, 8:00 UT). Boxes indicate regions that are investigated in detail in the paper. Positive velocity is redshifted (shown in light color). The images have been rotated to match the orientation of THEMIS data. *Middle*: Same maps, with contours of the rms magnetic field (*left*, solid line 100 G, dashed line 200 G) and velocity field (*right*, solid line 300 m s^{-1}, dashed line 500 m s^{-1}) in each pixel. *Bottom*: Map of the line-of-sight components of magnetic field (*left*, in G) and velocity field (*right*, in m s^{-1}) observed with MDI at 16:46 UT (i.e. close to the beginning of the flare) on a smaller field of view, on which are superimposed several Hα intensity contours from 3500 to 6700 ADU (Analog Digit Unit).

4.2. Analysis of region 2

4.2.1. Observation of a supersonic flow

A very interesting feature in the Nov. 26 scan of the region made by THEMIS (Fig. 2) is a very strong downflow (redshifted), clearly visible in the Stokes *V* spectrum shown in Fig. 6. This figure also shows the location of this region, which corresponds to the relatively large flows observed in MDI region 2 in Fig. 7 at the same time (around 1400 m s^{-1}). However, the signal observed in the THEMIS data correspond

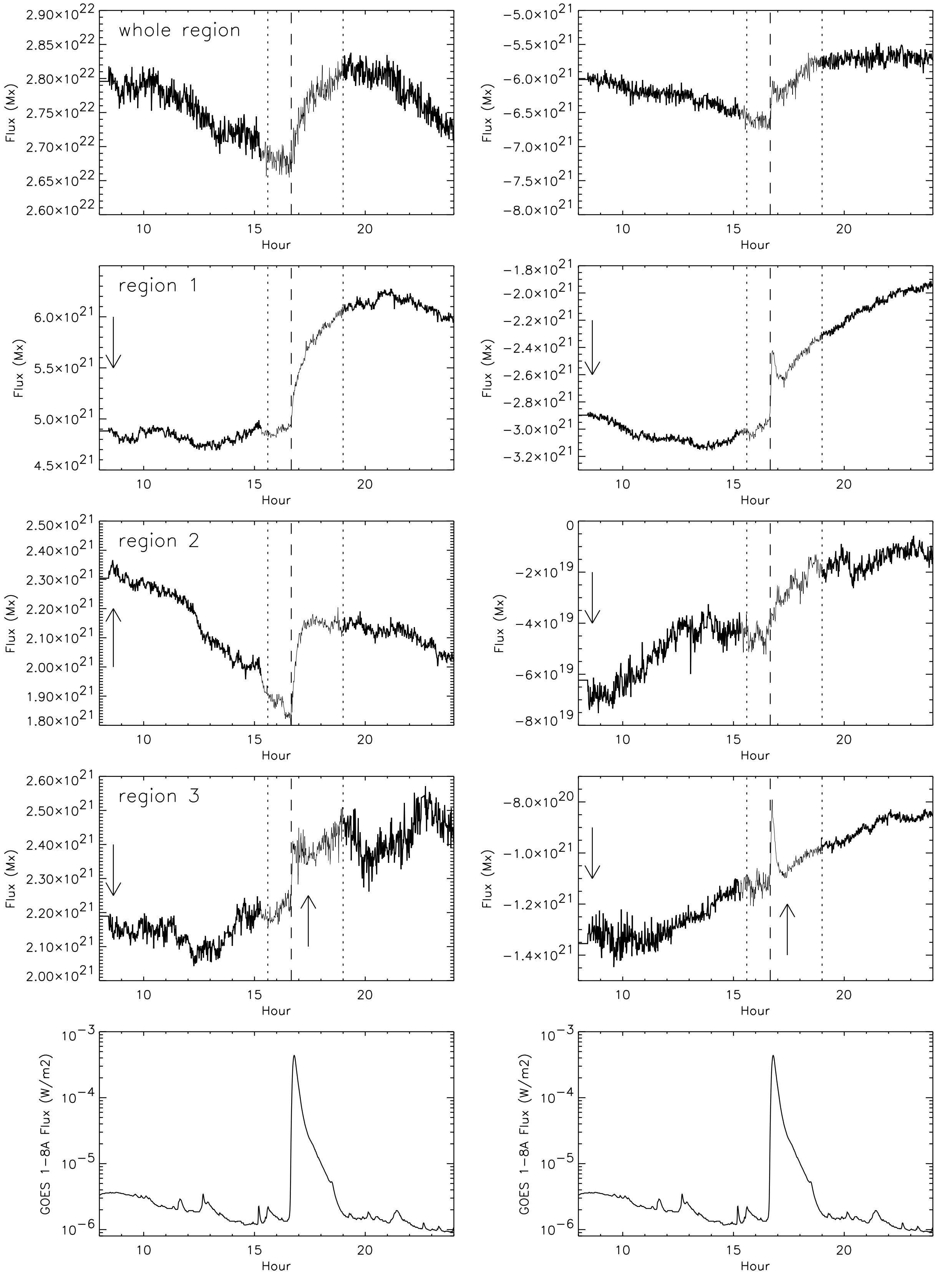

Fig. 5. *Top plots* (four rows): Positive (*left*) and negative (*right*) magnetic flux in different regions of the field of view (numbers refer to regions defined in Fig. 4). The vertical dashed line marks the beginning of the Hα flare. The dotted line correspond to one hour before the beginning of the Hα flare and to 1.5 hour after its end. The arrows indicate that the region has been observed with THEMIS at that time. The projection effects are small. *Bottom*: GOES X-ray flux in the range 1–8 Å for comparison (same as Fig. 1).

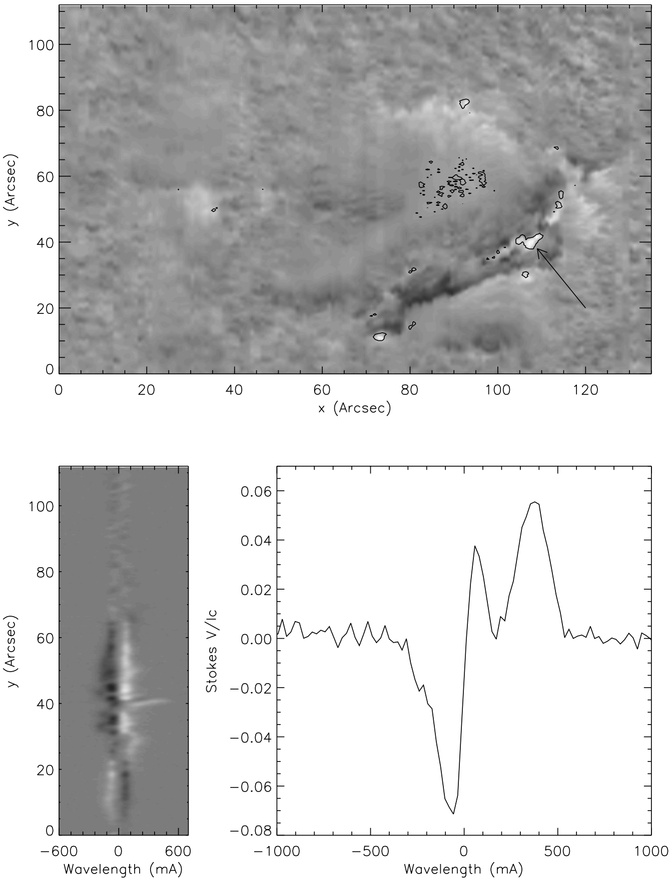

Fig. 6. Contours (*top*) show regions where the amplitude of Stokes *V* is large at ∼300 mÅ from the line center (at zero LOS velocity), superimposed on a map of LOS velocity field (Ni line) made at THEMIS on Nov. 26 (8:24 UT). Note that in the center of the spot, the structures correspond to some Zeeman signal due to some weak lines. We are mainly interested in the region pointed by the arrow. An example of *V* spectra (position $x = 105$ arcsec) across this region is shown at the *bottom left*. A cut through *V* around position $y = 40$ arcsec shows an abnormal profile (*bottom right*). Heliographic North is ∼18° CCW from the top.

to a signal much further from the line center than could be measured by MDI. We can fit such a profile with an unshifted "normal" *V* profile added to a strongly redshifted (10 km s^{-1}) "normal" *V* profile of the same polarity. The resulting LOS flow is therefore supersonic: the sound speed in the photospheric layers is about 6–7 km s^{-1} (Kentischer & Mattig 1995). This flow occupies a 5×2 arcsec^2 region, and is resolved in our data. It is also mostly observed in Stokes *V*, while almost no signal is visible in Stokes *Q* and *U*. The center-of-gravity method applied to the same THEMIS data shows a flow of only 3 km s^{-1}, close to what is provided by MDI observations (it is larger by a factor two, probably due to the better spatial resolution in THEMIS observations). This feature is visible at all wavelengths. A strongly redshifted signal is also seen in Stokes *I*, including for the 5576.1 Å line. Since this line is not sensitive to the magnetic field, we can rule out abnormal behavior of the magnetic field to explain these observations. Thus, this is very likely to be due to a real strong Doppler redshift.

4.2.2. Inversion and magnetic topology of region 2

From the THEMIS Stokes spectra, we compute vector magnetic fields using the weak-field method described in Sect. 3.1. The results are shown in Fig. 8. The average inclination (in the local frame of reference) in the strong flow zone is 51°, and, therefore, the field lines are significantly inclined with respect to the vertical (0°) in this zone. If the flow is following the magnetic field then these supersonic flows are also inclined with respect to the vertical. Note that even without the knowledge of the inclination, we can conclude that these flows are supersonic. The azimuth is in the range $[40°, 60°]$ (i.e. the field line are approximately in the North direction). We have also performed full inversion of Stokes profiles in that region, using two magnetic components (in addition to one non-magnetic component). We did not include any depth-dependence except for the temperature as it did not improve our fits significantly. The polarity of the shifted component has the sign of the main polarity in the region. We find differences in the inclination for the two magnetic components in the range $[-30°, 30°]$ and differences in azimuths between 0 and ∼30°. This means that the region exhibits a complex magnetic topology.

4.2.3. Temporal evolution of the flow

We were able to obtain only one spectropolarimetric observation of this strong flow with THEMIS. The scan made the day before did not show any similar behavior. Therefore, the THEMIS observations alone do not tell us anything about the temporal characteristic of this supersonic flow. However, the strong redshifted flow observed by MDI at the same location (Fig. 7) and at the same time corresponds to the same flow (although, of course, it is underestimated due to the MDI magnetograph-type technique). This flow, of the order of 1400 m s^{-1}, is remaining until the beginning of the flare as shown in Fig. 7 (top-right of the figure). The strong flow observed after the flare may correspond to a different structure since this flow slowly decayed throughout the day, as follows from Fig. 3. This observation suggests that the strong supersonic downflow observed with THEMIS is long-lived (at least 8 hours), and that we observed its decaying phase. Note that there were also strong blueshifted flows in that region 1.5 hour before the flare the maximum amplitude of the negative velocity (blue shift), which reached a peak of almost 2 km s^{-1}. This means that there was a very strong shear flow before the flare.

4.3. Analysis of region 3

4.3.1. Line-of-sight magnetic and velocity fields

Region 3 (shown in Fig. 4) also exhibits strong plasma flows observed in the MDI data. This region was observed twice with THEMIS on Nov. 26: first, on a scan of the region made on the morning of Nov. 26, and, then, at the end of Hα flare. In this latter observation, the slit was at a fixed position (shown in Fig. 2) during 12 min. THEMIS LOS magnetic and velocity fields as well as the continuum intensity during the last 12 min of the flare are shown in Fig. 9 for the Ni line. The other wavelengths

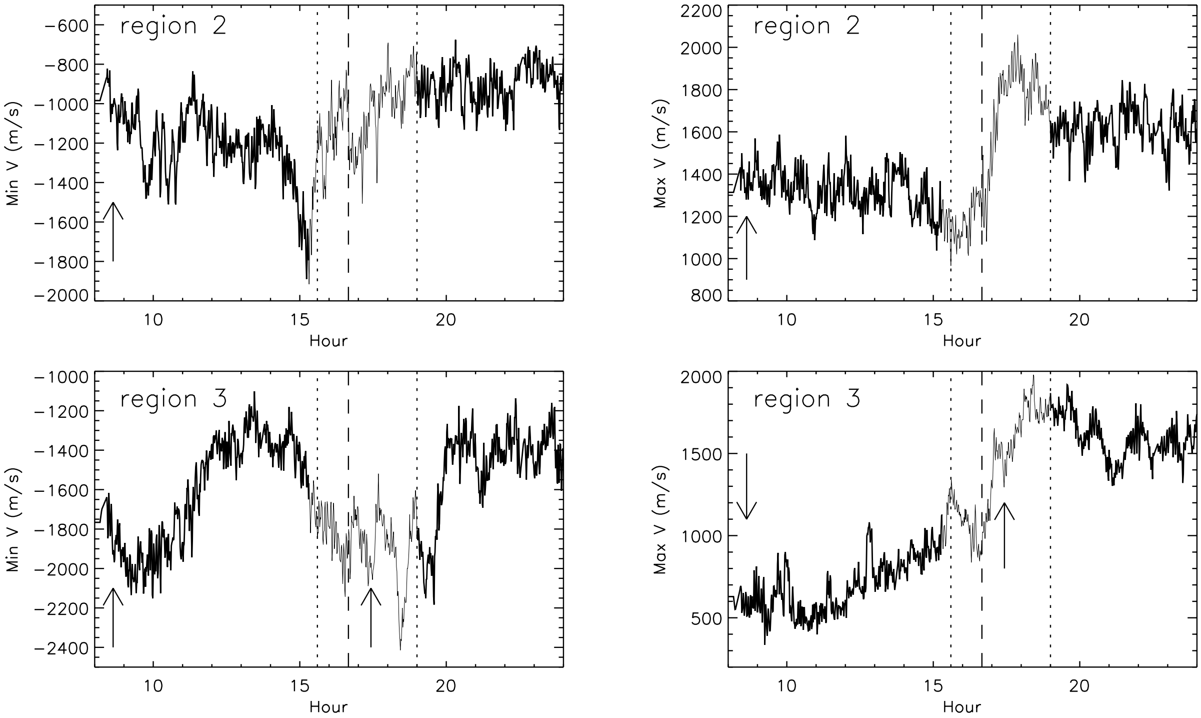

Fig. 7. Minimum (*left*) and maximum (*right*) velocity in regions 2 and 3 (numbers refers to regions defined in Fig. 4) from MDI data. The vertical dashed line marks the beginning of the Hα flare. The dotted line correspond to one hour before the beginning of the Hα flare and to 1.5 hour after its end. The arrows indicate that the region has been observed with THEMIS at that time. The projection effects are small.

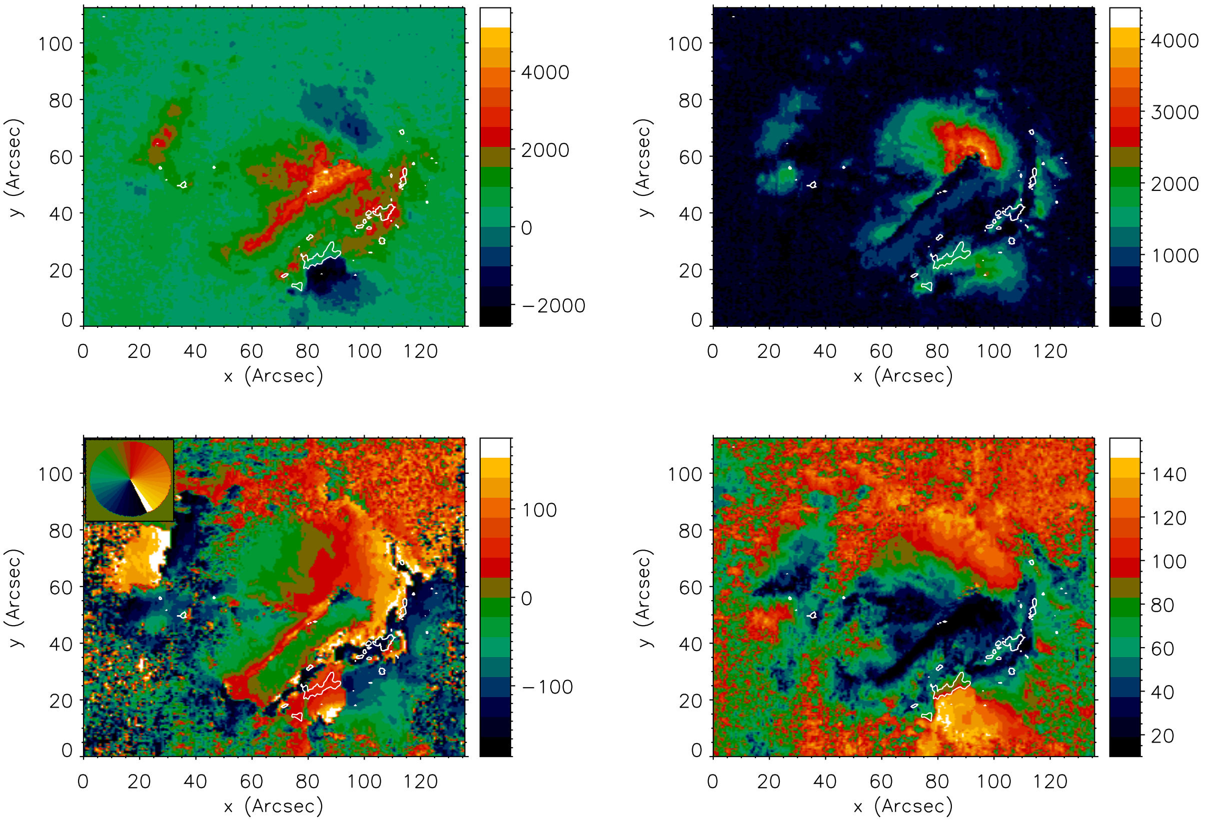

Fig. 8. Vertical magnetic field strength (*top left*, in G), horizontal magnetic field strength (*top right*, in G), azimuth (*bottom left*, in degrees), and inclination with respect to the vertical (*bottom right*, in degrees) for the Nov. 26 scan made at THEMIS (8:24), after correction of the 180° ambiguity (see text, Sect. 3.1) and projection effects, using the Mees Observatory code (see text). The reference for the azimuth is shown at the top of the plot. Thin white lines show the location of strong velocity flows (-2 km s^{-1}) corresponding to the blueshifted part of region 3. Thick white lines show the location of a strong Stokes *V* amplitude at ~300 mÅ from the line center (same as Fig. 6 top with umbra signal removed), corresponding to the strong flow in region 2.

have a similar behavior. These data are less noisy than the data obtained by scans, because we were able to average 125 spectra together. We observe a strong negative velocity of ∼3 km s^{-1} (blueshift, corresponding to upflow), which was already visible on the Nov. 26 scan (i.e. 9 hours before). This suggests that this is a long lived structure despite the occurrence of the flare in that region. However we also observe a strong positive velocity of ∼1.3 km s^{-1} which was not clearly visible on the morning scan. So, the region has significantly evolved over that time period, as can be seen in Fig. 3, which shows MDI maps at different times. These two velocity features are located North of the neutral line (next to the small spot of opposite polarity). The peaks of these two flows are separated by 11 arcsec and are quite stable during the 12 min of observations. The amplitudes of the peaks are also stable. However, some variations (1 km s^{-1} over 12 min) are seen in Fig. 9 at coordinates [40″, 47″] along the slit. Such variations could be related to the occurrence of the flare, and to changes observed in the MDI data after the flare on the scale of 1 hour in region 3.

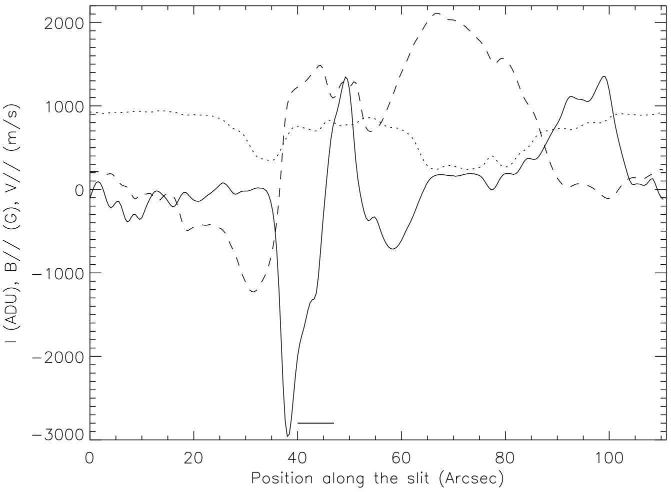

Fig. 9. LOS velocity field (solid line) from which the average has been subtracted, magnetic field (dashed line) and continuum intensity (dotted line) along the slit from THEMIS observation made at a fixed position on Nov. 26 (17:20 UT), using the Ni line. The small horizontal line correspond to the position where a variation over time is observed (see Sect. 4.3.1).

4.3.2. Fine structure of the flows

The line-of-sight magnetic and velocity fields shown in Fig. 9 are similar for all wavelengths of the data set. The 5635.8 and 5634.0 Å lines also show a double structure in the negative velocity flow region, which is clearly seen on several individual spectra. They are separated by a distance of 5 arcsec. There is probably a double structure in the positive velocity flow as well, visible on some individual spectra, with a separation of 1.5 to 3 arcsec. Given the relatively poor spatial resolution of these data, the difference in pointing due to the atmospheric refraction probably has a small effect. Therefore, it is likely that the more complex structure (with smaller features) is due to the low formation height of these lines.

The peak-to-peak amplitude of the velocity signal (which is independent of the chosen zero) varies with the wavelength: it is larger for the 5635.8 and 5634.0 Å lines (resp. 4.79 km s^{-1} and 4.58 km s^{-1}) and smaller for the other wavelengths (4.31 km s^{-1} for the Ni line and 4.00 km s^{-1} for the 6301.5 line). We exclude the 6302.5Å line from this comparison because the computation of the line-of-sight velocity is less reliable due to the presence of a telluric line across the shifted line. The maximum amplitude for the negative velocity field is also larger for the 5635.8 line (3.08 km s^{-1}), and smaller for the 6301.5 line. Again, this difference is probably due to the different height formation of these lines.

4.3.3. Stokes profile analysis and inversion results

The Stokes spectra for the Ni line in the region around the flare (after averaging over 125 frames, at 17:20) are shown in Fig. 10. Just above the LOS magnetic field reversal (position 8″), one can clearly see the strong negative velocity flows, previously seen in region 3. We also observe peculiar *Q* profiles, in particular for the Ni line, as shown in Fig. 10. A closer inspection of the *Q* profiles shows two components: one that would be blueshifted corresponding to LOS velocity of ∼5 km s^{-1}, and another to zero velocity. This feature is visible over several pixels along the slit and seems to form a coherent structure. These abnormal *Q* profiles were also observed in the morning scan 9 hours before, and, therefore, probably correspond to long-lived features. It is also very clearly visible in the 5634.0 and 5635.8 Å lines, which are formed deeper, but almost not visible in the 6301.5 line, and not visible at all in the 6302.5 line. The structure of the downflow region seems to be more simple, although the Stokes *U* profiles are quite complex.

From the computation of the vector magnetic field (using the first method with a single component only, see Sect. 4.2.2 and Fig. 8) for the morning scan, we find an average inclination of the negative velocity zone of about 84°, that is almost horizontal (90°). We also obtain a similar azimuth over the whole zone, in the range [60°, 70°]. If the flows are aligned with the magnetic field, this would correspond to a strong shear since the adjacent velocity components (of opposite sign) would be close to horizontal and in the same direction. The inclination with respect to the LOS is ∼58° in the region of large negative velocity flow, which gives amplitude of 9.4 km s^{-1} for a 5 km s^{-1} LOS component of flows. This is also supersonic. A MDI movie of the LOS magnetic field in the region does not show any motion of small magnetic features that would correspond to such an horizontal flow, but this could be due to the insufficient spatial resolution. The amplitude of this flow, integrated over the whole time period corresponds to a large distance, which may look surprising; if these observations correspond to downflows and upflows, for example, they would be more or less perpendicular to the magnetic field lines, which is also puzzling. However, the observations of such flows could mean that the magnetic field has unresolved filamentary structure allowing plasma to flow throw without disturbing the field lines.

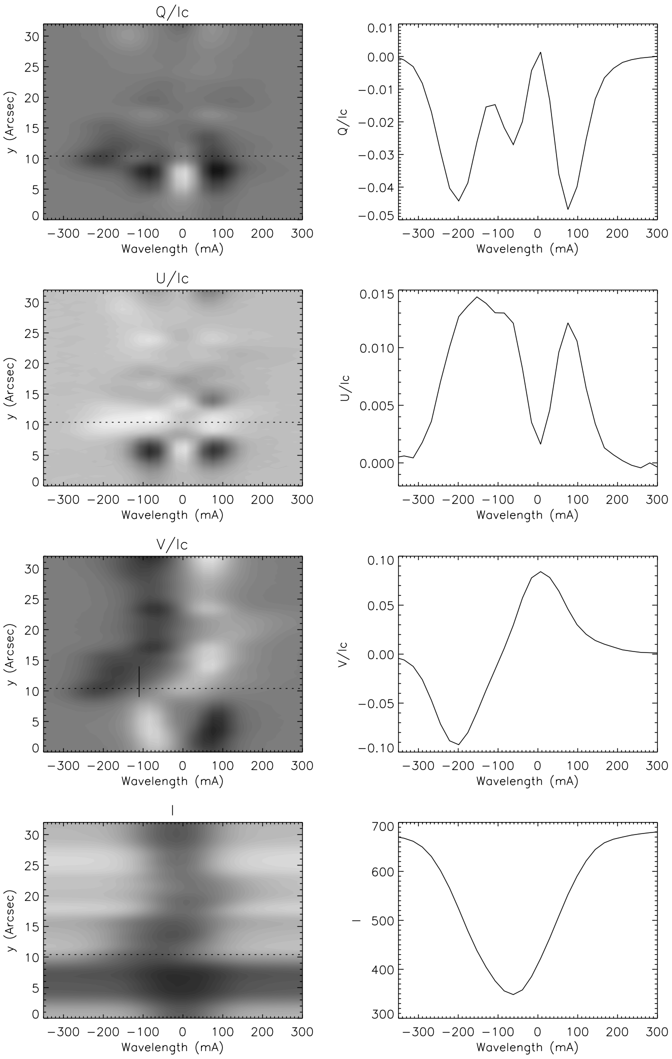

Fig. 10. *Left*: Stokes spectra for the Ni line in the flare region (the neutral line is at the bottom of that field-of-view) on Nov. 26 (17:20 UT). The y-axis is along the slit. I_c is the continuum intensity. The small vertical line on Stokes V indicates the position of the strong blueshifted flow. *Right*: Stokes spectra at the position indicated by the dotted line on the spectra on the left, where some unusual Q profiles are observed. The location of this cut is also shown in Fig. 2.

The full inversion using two magnetic components (in addition to the non-magnetic component) has been performed simultaneously for separate wavelengths, using the Ni line and the 6302.5/6301.5 Å lines and assuming that there is no depth dependence (except for the temperature). These lines give similar results. After correction for the projection effects (inclination) we find flows that are supersonic over the distance of 2–3 arcsec, the maximum flow being 7.7 km s^{-1}. The polarity of both magnetic components is the same than the main polarity. There is no difference in azimuth between the two magnetic components (although the azimuths differ from the previous computation by ~30°). However the inclinations for the two magnetic components are quite different and differ by ~36° from each other. The errorbars for the inclinations and azimuths are of the order of 1–2 degrees. They have similar filling factors (0.4) and similar magnetic fields. The microturbulence velocity seems to be larger for the blueshifted component, but this is more uncertain.

5. Summary and discussion

This paper presents new results from the first coordinated campaign between THEMIS (providing multiline spectropolarimetric data) and MDI (providing a high temporal cadence over a long period). We have observed two peculiar flows in AR 9236:

(i) *A supersonic downflow (10 km s^{-1}) mostly visible in Stokes V, inclined by 51° from the vertical*. The redshift is also visible in Stokes I, including the spectral line not sensitive to the magnetic field. The azimuth and inclination of this component differ from the non-shifted magnetic component and show a complex topology. This flow was observed only in the morning data of Nov. 26, 2000, in spectropolarimetric mode of THEMIS, and, unfortunately, no other THEMIS measurements are available. However, MDI observed this flow with reduced amplitude of 1.5–2 km s^{-1} (in region 2). Since this flow is visible in MDI data for at least 8 hours, we suggest that this flow is a long-lived downflow which is observed during its decaying phase. We do not have any explanation concerning the origin of this flow. It could originates in the previous Hα flare, which ended 5 hours before, or it could be related to the strong X-ray emission observed at that time (Fig. 1). Unfortunately we have not been able to establish with certainty that this strong X-ray flux is associated to this active region: H-α images from Learmonth Observatory do not show any enhancement at that time in this region nor in the other large active region present on the disk that day (AR 9240), while the radio flux from Nancay Observatory shows enhancements in both region. Therefore, the origin of this flow is still an open question. We note that the decreasing magnetic fluxes, both positive and negative, from 8:00 UT up to the beginning of the Hα flare are surprising because one would expect an increase in magnetic flux from a strong downflow (however, no converging pattern is visible either).

(ii) *A strong blueshifted flow adjacent to a strong redshifted flow, next to the neutral line.* For the same reasons than for the flow above, MDI data (region 3) suggest that this is a rather long-lived structures. Furthermore, THEMIS provided two observations of this flow, 9 hours apart, which also suggest that this was long-lived, although the global configuration of the LOS velocity field changed significantly over the day. If we make the assumption that these flows follow magnetic field lines, the magnetic topology of the region deduced from the inversion of the Stokes parameters observed with THEMIS suggests that these flows are close to horizontal and in the same direction, which can be interpreted as a horizontal shear, with one of the component (the blueshifted one) being supersonic over 2–3 arcsec. A shear of such amplitude has not been observed before in the photosphere. We cannot rule out a downflow (adjacent to an upflow) that would be almost horizontal instead of a shear, since the field lines are not strictly horizontal. The initial existence of this strong flow may be unrelated to the flare. However, the redshifted component increased by 800 m s^{-1} after the flare on the long time scale.

Therefore, this flow was influenced by the flare occurring in the region, and might play important role in the MHD process of restructuring of the magnetic configuration during the flare. The kinetic energy density of the flows was comparable with the magnetic energy density. Also, the changes of these quantities during the flare are also of the same order of magnitude. Preliminary Stokes profile inversions show that the supersonic component has an azimuth similar to the non-shifted component but a different LOS inclination, suggesting a complex topology as well. THEMIS observations also show that this flow presents some fine structures with scales in the range of 1–3 arcsec.

Supersonic flows in the photosphere have been observed by very few observers so far. Martinez Pillet et al. (1994) observed supersonic downflows in a δ-type spot at the location of polarity inversion, which they claim has nothing to do with a reconnection process because it is long-lived (more than 3 hours); the polarity of the shifted component is the same than the polarity of the non shifted component or opposite depending on the pixel. del Toro Iniesta et al. (2001) also observed a supersonic downflow in the penumbra of a simple sunspot using high resolution observations and a full inversion method, the downflow corresponding to a polarity opposite to that of the unshifted components. Our features are also different from mustaches which are very short-lived structures (5–10 min) as well as from Ellerman bombs (1–2 arcsec features). Our observations were made in different conditions and the features have different characteristics (very inclined flows one case, and different polarity properties). The supersonic flows are probably long-lived (8 hours at least), and the second one is modified at (or around) the time of the flare. Strong downflows and upflows have also been observed by Sigwarth (2001), with Stokes V profiles similar to ours with strongly shifted components (implying supersonic velocities) of either the same polarity or opposite polarities. His observations are associated with flux emergence and are interpreted as redshifted preshock and blueshifted postshock profiles.

It could seem surprising that flows of such amplitude have been rarely observed before at the photospheric level, but spectropolarimetric observations of solar flares using spectral lines formed in the photosphere are not very common, which make these new results very important. The origin of these strong flows is not clear at this stage, and would request more observations in similar conditions with a better coordination with chromospheric observations to see if they are affected by the flare or if they are related to the triggering of the flare.

For another improvement to this analysis, it is the necessity to make robust inversions of Stokes profiles. This is critical for the interpretation. The results presented in this paper confirm the existence of a 10 $\mathrm{km\,s^{-1}}$ LOS flow for example, and show that the strong downflow probably exhibits a complex fine structure over the field of 2×5 arcsec^2. However more work needs to be done on these data to compare the Stokes parameters at all wavelengths to be able to derive the variation of these strong flows with height in the photosphere: this is a work in progress. Note that the line profile inversions with a depth dependence did not improve the fit; therefore, it is difficult at this point to conclude if the differences for the different wavelengths are due to strong vertical or horizontal gradients. We would also like to point out that we observed very interesting features in Stokes spectra provided by the Ni line as well as with lines with a small Lande factor, and that the inversion using the Fe lines and the Ni line gave similar results.

Acknowledgements. We thank F. Paletou, our resident astronomer during the THEMIS observations, J. Arnaud for his help with the data processing and fruitful discussions, T. Metcalf for providing some codes to compute the vector magnetic fields. We also thank S. Solanki and A. Lagg for providing their inversion code and for taking some time to explain to us how to use it. We thank K. Puschmann who kindly provided the line formation depths of Table 2. The THEMIS telescope is operated on the Tenerife island by CNRS-CNR in the Spanish Observatorio del teide of the Instituto de Astrofísica de Canarias. SOHO is a mission of international cooperation between the European Space Agency (ESA) and NASA. This study is also based on Hα data obtained at OAFA (El Leoncito, San Juan, Argentina) in the framework of the German-Argentinean HASTA/MICA Project, a collaboration of MPE, IAFE, OAFA and MPAe. GOES data have been provided by the Space Environment Center (National Oceanic and Atmospheric Administration). Trips to Stanford were financed by the PNST (Programme National Soleil-Terre).

References

Canfield, C., de La Beaujardière, J.-F., Fan, Y., et al. 1993, ApJ, 411, 363
del Toro Iniesta, J. C., Bellot Rubio, L. R., & Collados, M. 2001, ApJ, 549, L139
Fruttiger, C. 2000, Inversion of Zeeman Split Stokes Profiles, Ph.D. Thesis
Harvey, K. L., & Harvey, J. W. 1976, Sol. Phys., 47, 233
Jefferies, J., Lites, B. W., & Skumanich, A. 1989, ApJ, 343, 920
Jones, H. 1989, Sol. Phys., 120, 211
Keil, S. L., Balasubramaniam, K. S., Bernasconi, P., Smaldone, L. A., & Cauzzi, G. 1994, 14th NSO/Sacramento Peak Summer Workshop, ASP Conf. Ser., 68, 265
Kentischer, T. J., & Mattig, W. 1995, A&A, 300, 539
Kosovichev, A. G., & Zharkova, V. V. 2001, ApJ, 550, L105
López Ariste, A., Rayrole, J., & Semel, M. 2000, A&AS, 142, 137
Martinez Pillet, V., Lites, B. W., Skumanich, A., & Degenhardt, D. 1994, ApJ, 425, L113
Martres, M. J., & Soru-Escaut, I. 1977, Sol. Phys., 53, 225
Meunier, N., Arnaud, J., & Vigneau, J. 2002, Il Nuevo Cimento C, 25C(5-6), 659
Paletou, F., & Molodij, G. 2000, 20th NSO/Sacramento Peak Summer Workshop, ASP Conf. Ser., 236, 9
Rees, D., & Rayrole, J. 1979, A&A, 74, 1
Severny, A. B. 1958, Izv. Krym. Astr. Obs., 20, 22
Scherrer, P. H., Bogart, R. S., Bush, R. I., et al. 1995, Sol. Phys., 162, 129
Sigwarth, M. 2001, ApJ, 563, 1031
Yoshimura, H., Tanaka, K., Skimizu, M., & Hiei, E. 1971, Publ. Astr. Soc. Japan, 23, 443

A&A 420, 333–342 (2004)
DOI: 10.1051/0004-6361:20034044

Astronomy & Astrophysics

Complexity of magnetic structures: Flares and cycle phase dependence

N. Meunier[*]

Observatoire Midi-Pyrénées, 57 avenue d'Azereix, BP 826, 65008 Tarbes Cedex, France

Received 2 July 2003 / Accepted 17 February 2004

Abstract. A long data set of MDI/SOHO full-disk magnetograms is analyzed to provide a large sample of active regions. The objective is to study the variations of the fractal dimension of these structures on different time scales: in relation to their activity level (spots, flares) and during the solar cycle. First, the variations of the fractal dimension of the structure during solar flares are studied using a very large sample. Variations are found to be of very small amplitude. The complexity of the structures is slightly larger after the flare when considering regions close to the flare (2–3°), while a decrease seems to be observed at larger scales (up to 10°), although this should be confirmed using other approaches. The results obtained by Meunier (1999a) concerning the fractal dimension versus the size of the structures for various magnetic thresholds are confirmed on a much larger sample, with a peculiar behavior seen around 550–800 Mm^2. This scale is observed to increase from cycle minimum to cycle maximum. In addition, I observe that the fractal dimension of active regions reaches a plateau above 3000 Mm^2 and that structures of a given size are more complex when they have spots. The fractal dimension is strongly variable during the solar cycle, with the sign of the variation depending on their size and on their flux content (spot or no spot) and with an amplitude up to 0.17 between the ascending phase and cycle maximum.

Key words. Sun: magnetic fields – Sun: photosphere – Sun: activity – Sun: faculae, plages

1. Introduction

The variation of the magnetic topology before, during and after solar flares has been the subject of many studies, because the evolution of the region topology before the flare and the mechanisms for triggering the flare are not well understood yet. Many detailed studies of a given region have been performed using vector magnetograms and extrapolations of photospheric magnetic fields to look at the evolution of the 3D topology (see among others the recent papers by Bleybel et al. 2002; Zhang & Wang 2002; Fletcher et al. 2001; Zhang & Wang 2000; Aulanier et al. 2000; Mathew & Ambastha 2000, and references therein). Some statistical studies of small data sets (no more than a few regions) have also been performed by several authors to study the variation of the complexity of active region during solar flares. A first approach consisted of comparing the complexity of quiet region with flaring region. For example, Patty & Hagyard (1986) observed that the maximum line-of-sight (hereafter LOS) magnetic field and its gradient were much larger in flaring regions than in quiet regions. Abramenko et al. (2002) studied the structure function exponent on 8 active regions of different flaring activity levels and found a larger degree of intermittency in regions that were more active. Recently, a second approach consisted of studying the variation of the complexity during the evolution of the region before and after flares. This was done by Adams et al. (1997) for example, who applied the Hurst analysis to 10 vector magnetograms of an active region and did not observe any variation due to flares, except for the shear of the region: they obtained an increase of the complexity of the region before the flare, and a decrease during the 5 min preceeding the flare. Stark et al. (1997) tested two other methods with the same purpose and showed that they were not very sensitive. On the other hand, Hagyard et al. (1999) studied the vector magnetic field of an active region during 6 h and found the azimuth to be very variable. Yurchyshyn et al. (2000) and more recently Sorriso-Valvo et al. (2003) computed the cancellation exponent on the helicity for 5 regions. The cancellation exponenent is anti-correlated with the fractal dimension (see Sorriso-Valvo et al. 2003) and it shows a strong increase in complexity at the time of the flare (or during the 3 h preceeding the flare).

Vector magnetic fields are very useful because the LOS magnetic field is not necessarily the component that is expected to change the most during flares (see Adams 1997 for example). Nothing conclusive concerning LOS fields has been obtained, while recent observations of vector magnetic fields suggest larger variations of physical parameters other than the LOS magnetic field. However, time series of vector magnetograms are scarce. On the other hand, no study of a very large sample of LOS magnetograms has been performed, so it will be interesting to check the variations of the fractal dimension of regions observed that way when a large sample becomes available. This investigation is the first objective of this paper.

---

[*] e-mail: `meunier@bagn.obs-mip.fr`

The second objective is to determine the variation of the complexity of active regions on a much longer time scale. The distribution of solar magnetic fields in the photosphere is controled by the generation processes, including the solar dynamo. Statistical analyses such as studies of the size distribution of active regions or of the fractal dimension are necessary to compare the very complex observed regions and models. No realistic models of active regions have been developed to my knowledge so far, although the approach followed by Wentzel & Seiden (1994), Seiden & Wentzel (1996) and Vlahos et al. (2002) should provide some clues about the various processes at play in their formation and disappearance. Hopefully they will become more realistic in the near future. Up to now, only very small series of high resolution magnetograms have been analyzed (Ruzmaikin et al. 1991; Balke et al. 1993) or larger sets of full disk images covering a small period (Nesme-Ribes et al. 1996, studying spectroheliograms, Meunier 1999a, studying MDI full-disk magnetograms). Although these studies are obviously related to the solar dynamo, no studies have been performed to study the cycle dependence of the fractal dimension of active regions. I am not aware of analyses of the fractal dimension as a function of flux content either. Therefore, in this Paper I continue the work of Meunier (1999a) on a much longer data set. The study of a long series of LOS MDI magnetograms is possible covering a period from the cycle minimum to the end of the cycle maximum. The main advantage is the huge quantity of data of constant quality, allowing a very good statistical study.

The complexity of magnetic structures, studied using fractal dimension techniques, is primarily related to the complexity of their morphology. However, this complexity must tell us something about the physics underlying the active region and the flares: the turbulent character of the convection means that the magnetic fields generated by the dynamo are intermittent, with a complex structure, and the analysis of their self-similarity using fractal dimensions is therefore relevant (see for example Tao et al. 1995 and Vainshtein et al. 1996). This has also been studied for example by Zelenyi & Milovanov (1991), who have developed a fractal model of sunspots. The study of how this complexity depends on the activity level on various scales should therefore provide clues about the influence of this activity level on the formation processes (for example how the clustering of flux tubes can form large coherent regions) or about the later stages of evolution of the region (processes at play during flares or during the dilution of the active region and spreading of its flux across the solar surface, for example through a percolation process such as the one studied by Balke et al. 1993).

Therefore my objective is two-fold: 1) study of the variation of the fractal dimension from LOS magnetograms during solar flares as well as a detailed analysis of the fractal dimension with magnetic properties of the regions; 2) study of the solar cycle dependence. After describing the observations in Sect. 2 and the data processing in Sect. 3, I present the results in Sects. 4 and 5. First I address the question of the variation of the fractal dimension for two populations of active regions with different maximum magnetic fields obtained by Meunier (2003) and the variation of the fractal dimension during solar flares. Then I consider the solar cycle variations in Sect. 5. The results are discussed in Sect. 6.

Table 1. Average Wolf number for the 3 periods defined in the text.

Period	Average Wolf number
Cycle minimum	10.3
Ascending phase	57.1
Cycle maximum	113.4

2. Observations

2.1. MDI/SOHO: Full-disk magnetograms

MDI/SOHO observations (Scherrer et al. 1995) provide maps of the LOS component of the magnetic field averaged over the resolution element (2 arcsec in the full disk mode). The observations are made in the Ni I 6768 Å spectral line. I select 5-min full-disk magnetograms only, because they are less noisy (noise level of ~8 G, see for example Meunier 1999a). This led to a data set of 7184 images between 23 May 1996 and 19 June 2002, covering 6 years. These magnetograms are separated by multiples of 96 min. This data set is the one used in Meunier (2003).

To study solar cycle variations, I define the three following periods: the cycle minimum from day 143 (23 May 1996) until day 543 (27 June 1997), an ascending phase from day 543 until day 1243 (28 May 1999) and the cycle maximum after that date until the end of the data set. The corresponding average Wolf numbers are shown in Table 1 (see Meunier 2003, Fig. 1 for a plot of the Wolf number versus time for this period).

2.2. The flare data set

Flare data are obtained from the National Geophysical Data Center archive. Each Hα flare is counted once, and I extract from the data set the time, position and area of the flare. The number of Hα flares in the data set available during the period is 16 140. There are a few gaps in the flare data set, due to the reduced number of stations operating the flare patrol. However, in our analysis, the starting point is this flare data set, and for each flare we search for magnetograms observed around the same time: therefore, the relevant temporal coverage to consider is that of the magnetogram data set with respect to these flares. It was possible to select 7629 flares for which at least one magnetogram within 6 h of the flare exists. For a quarter of them, there is only one magnetogram available, while there are at least 2 (and up to 8) magnetograms for the other flares. Their average lifetime is 19 min, and 83% of the flares have a lifetime shorter than 30 min.

3. Data processing

3.1. Magnetogram processing

3.1.1. Region identification

Magnetograms are analyzed using a method similar to that described in Meunier (2003). This is close to what was done in Meunier (1999a), except that we consider B/μ (where $\mu = \cos\theta$, θ being the angle from disk center and B is the LOS magnetic field provided by MDI) instead of B, because the magnetic field lines in both active regions and network regions are believed to be close to the vertical, within 10°[1]. As in Meunier (2003), each structure above a given magnetic threshold (applied to the signed magnetograms) is determined within 53° from disk center ($r < 0.8\ R_\odot$). The area A is defined by the number of pixels in the structure. The perimeter P is derived from the pixel sides for which there is no neighbor. Areas and perimeters are corrected for projection effects and are converted to Mm^2 and to Mm respectively. For each structure we also consider the average magnetic field $\bar{B}$ in that region as well as the maximum magnetic field $|B_\mathrm{m}|$ (both are fluxes averaged over the resolution element) and the flux Φ in the structure. Magnetic fields in this paper always mean magnetic fluxes (averaged over the resolution element) and not the actual field strength.

In this paper we mostly use a magnetic threshold of 40 G, which corresponds to 5 times the noise level on these magnetograms. The other thresholds (from 80 G to 240 G) allow some comparisons with the results obtained earlier by Meunier (1999a) on a much smaller data set. The size distributions for the 3 periods of the solar cycle are shown and discussed in Meunier (2003, Fig. 7).

This method allows us to select magnetic structures corresponding to a given polarity, i.e. rather smaller scale individual structures of all sizes. Therefore they do not provide full active regions with both polarities. This allows us to make comparisons with previous results. However, when looking at the variation of the complexity of the structures with solar flares, this means that the complexity at this small scale is considered and not at the scale of the full region. This will be discussed in more detail in Sect. 4.2.

3.1.2. Computation of the fractal dimension: Perimeter-Area method

From the data set of structures defined in Sect 3.1.1, we define the fractal dimension d from the relation between area and perimeter as:

$$d = 2\frac{\Delta \log P}{\Delta \log A},$$

which corresponds to twice the slope of the curve P versus A on a Log/Log scale. If regions were perfect circles, or squares, then d would be equal to unity. The more denticulate the structure, the closer d is to 2. This definition is very convenient and has been widely used. It is described in more detail in Meunier (1999a). In the following, the fractal dimension is computed either from average P versus average A (where the average P is computed over a size range of $\Delta \log A = 0.1$) over size ranges of $\Delta \log A = 1.5$ or, when indicated, over all data points (or a subset) in a given size range.

The first method had proved to be useful in the past (Meunier 1999a) because the fractal dimension is observed to vary with size (i.e. the structures are not strictly self-similar) and therefore one should consider the fractal dimension computed over smaller ranges of size. This method is used in Sect. 5 to allow some comparisons with the previous results. However, when few data points are available or when one wants to compute the fractal dimension for small subsets (in particular in size) I have computed the slope over all the points of the subset and this method is used in most of the paper. Note that both methods are used in Sect. 5.2.1 and they give similar results.

It has already been pointed out that one should be careful about the influence of spatial resolution on fractal dimension computations. For example, Meunier (1999a) found different behaviors for the full-disk and high-resolution MDI magnetograms and pointed out that it is necessary to establish comparisons between observations and simulations in similar conditions. This has also been discussed in detail by Janssen et al. (2003). However, when studying data obtained in similar conditions, the observed variations are still significant even though the comparison with other results (either observations or simulations) remains sometimes difficult.

3.2. Association of the flares with a magnetic structure

From the list of 85 605 magnetic structures larger than 500 Mm^2 every 96 min or multiple of 96 min and the list of Hα flares, we need to associate each flare with an MDI structure observed close enough in time (before and after the flare). The parameters in this study are the following:

1. magnetic threshold on the magnetogram: 40 G;
2. minimum size for a magnetic structure: 500 Mm^2;
3. maximum distance D_max between the flare position and structure center of gravity: dependent on the size of the structure or fixed. Different values are studied. D is computed after correction of the rotation rate for the different time of the flare and of the magnetogram;
4. maximum time lag between the MDI observation and the flare: 6 h;
5. maximum variation of the size of the structure over the 12 h time lag: no limit or 40%. The purpose of this parameter is to provide a constraint for a better identification of the same structure over time.

The two first parameters are related to the way the list of magnetic structures is built. Parameters 3 to 5 are related to the way the association flare-structure is performed. The limitations of this approach will be discussed in Sect. 4.2.2.

---

[1] This is not strictly the case in the penumbra. However, a similar analysis in which B is used instead of B/μ leads to very similar results.

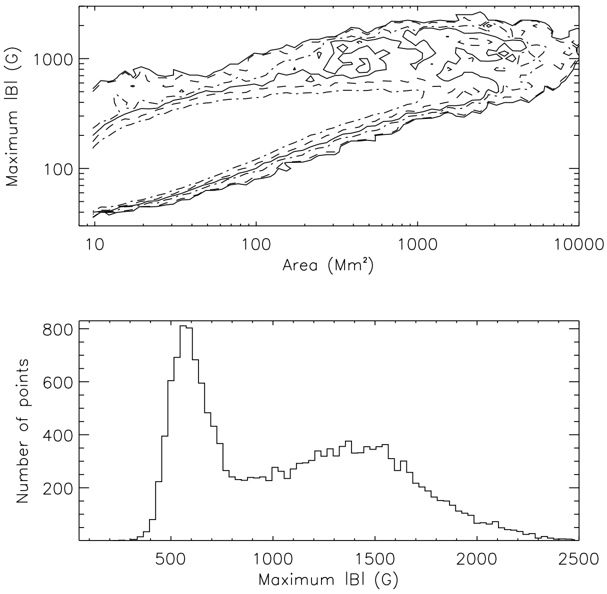

Fig. 1. *Top*: number of structures for each size and $|B_{\rm m}|$ ranges, for the whole period. The thickest lines correspond to thresholds of 100, 40, and 20 structures (respectively dotted-dashed, dashed, and solid). The thin lines correspond to thresholds of 10, 2, and 1 structures (respectively dotted-dashed, dashed, and solid). *Bottom*: number of structures versus $|B_{\rm m}|$, in the size range 2000−7000 Mm^2.

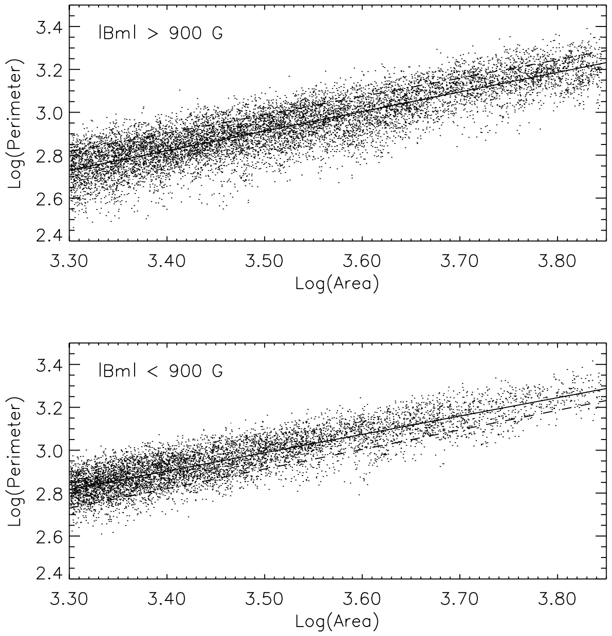

Fig. 2. *Top*: Log of the perimeter (Mm) versus log of the area (Mm^2) in the size range 2000−7000 Mm^2, for $|B_{\rm m}| > 900$ G. The solid line is a linear fit to the points, while the dashed line is a linear fit to the points for $|B_{\rm m}| < 900$ G for comparison. *Bottom*: Log of the perimeter (Mm) versus log of the area (Mm^2) in the size range 2000−7000 Mm^2, for $|B_{\rm m}| < 900$ G. The solid line is a linear fit to the points, while the dashed line is a linear fit to the points for $|B_{\rm m}| > 900$ G for comparison.

4. Fractal dimension and activity of the region

4.1. Complexity and magnetic flux

The 2-D distribution of the unsigned maximum magnetic field, $|B_{\rm m}|$, versus the size of the structures was shown by Meunier (2003) to exhibit a strong correlation between $|B_{\rm m}|$ and the size (Fig. 1, upper panel, for a threshold of 40 G). The distribution of $|B_{\rm m}|$ is however slightly more complex than that of $\bar{B}$ for example, because it exhibits a tail toward large values of $|B_{\rm m}|$ (especially for large sizes) corresponding to a second distribution (see lower panel in Fig. 1). In the range 2000−7000 Mm^2 for example, where the phenomenon is the most visible, a narrow distribution peaks at ~600 G while the second one, broader, peaks at ~1500 G. This 2-component distribution is mostly present during the ascending phase and at solar maximum. In the range 2000−7000 Mm^2, structures with $|B_{\rm m}|$ larger than 900 G (distribution peaking at 1500 G) have larger magnetic fluxes (by 35%), larger flux density (by 27%) and a larger ratio $B_{\rm m}/\bar{B}$ (by 22%) than structures with a maximum magnetic field below 900 G. A given region is in the same category during all its lifetime. Although there are sunspots in both categories, most of the regions with spots are in the large $|B_{\rm m}|$ category while very few structures of the small $|B_{\rm m}|$ category have spots, as we checked visually from a subset of the data: it is plausible that larger $|B_{\rm m}|$ structures correspond to spots. Therefore the 2-component distribution is probably due to the presence or absence of spots in structures of a given size.

It is possible that the peak around 1500 G could be an artifact due to the non-linearity in MDI LOS magnetic fields studied by Berger & Lites (2003): this could lead to an excess of structures around the saturation magnetic field. This does not seem to be the case however, for two reasons: first, on the original values of B (i.e. before the division of B by μ, which are the values to consider to compare with the Berger & Lites results), the peak is visible around 1000 G, i.e. below the saturation level described by Berger & Lites, i.e. 1300 G. Second, this peak is less pronounced on these data than on the B/μ data: this probably means that the peak is not due to an observational bias such as magnetic field saturation but is an intrinsic property of magnetic structures.

The fractal dimension in the range 2000−7000 Mm^2 is computed separately for the two categories (using a linear fit over all points of the selection). The fits are shown in Fig. 2. In this size range, structures with $|B_{\rm m}|$ larger than 900 G have a fractal dimension of 1.82 ± 0.01, while structures with $|B_{\rm m}|$ smaller than 900 G have a fractal dimension of 1.71 ± 0.01, which is significantly lower. The errorbars corresponds to the formal uncertainties on the fit and not the standard deviation of the fractal dimension of the individual structures, because with this method the fractal dimension can be computed only on a sample of structures, not on individual structures. This shows that structures of a given size with spots are more complex than structures of the same size with no spots. When looking at a larger domain, I find a similar result: structures with a larger $|B_{\rm m}|$ still seem to be more complex.

Because the structures are studied via their contours at low magnetic thresholds, the presence of sunspots inside the structures cannot bias the computations of their fractal dimension. Therefore, the difference in complexity must be due to the processes associated with the presence of spots, either during their

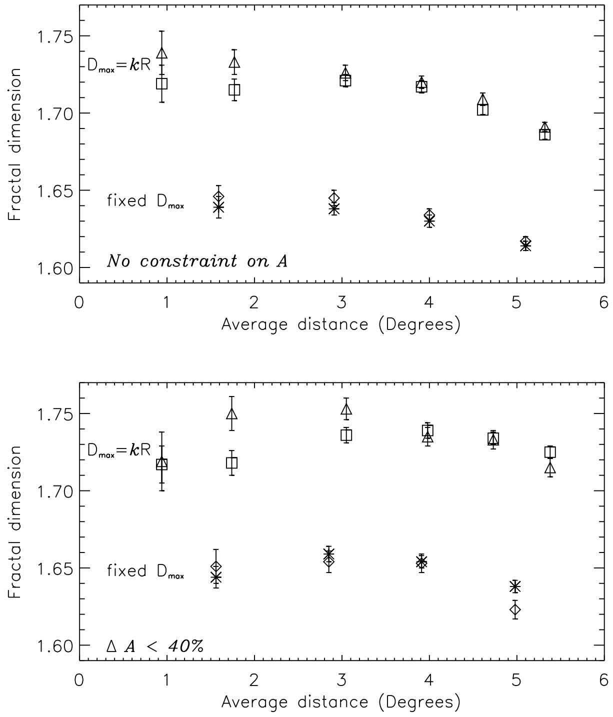

Fig. 3. Fractal dimension before (star) and after (diamond) the flares for fixed $D_{\rm max}$, as a function of the average distance $\langle D \rangle$ between the flare and the region. The squares and triangles represents the same fractal dimensions, but for $D_{\rm max} = kR$ (see text). *Top*: for no constraint on the size variation before and after the flares. *Bottom*: maximum variation of 40% of the size (see parameter #5 in Sect. 3.2).

formation and emergence from the convective zone up to the photosphere, or during their evolution at the solar surface, in particular their dilution.

4.2. Flare dependence

4.2.1. Results

The comparison of the fractal dimension, averaged over 6 h, before and after the flares is summarized in Fig. 3 for various average distances D between the flare and the center of gravity of the magnetic structure. The maximum distance $D_{\rm max}$ between the flare location and the center of gravity of the structure (parameter #3 in Sect. 3.2) is either constant or size-dependent ($D_{\rm max} = kR$, with $R = \sqrt{A/\pi}$) and both possibilities are shown on each panel. The influence of a constraint on A (parameter #5 in Sect. 3.2) is also shown: no constraint for the top panel and a constraint on the bottom panel.

For most selections (i.e. when searching for structures at various distances from the flares and for various constraints on A), the fractal dimension is not significantly different before and after the flare. However, we observe a larger fractal dimension after the flare (significant at the 1-σ level) in 3 cases, all for medium size $D_{\rm max}$ ($\langle D \rangle$ in the range 1.5−3°): $D_{\rm max} = 1R$ and all ΔA, $D_{\rm max} = 1R$ and $\Delta A < 40\%$, $D_{\rm max} = 2R$ and $\Delta A < 40\%$. We conclude than on average, the magnetic structure seems more complex after the flare when considering structures in the range 1.5−3° from the flare, but only when the maximum distance is dependent on the size of the structure. Above a distance of 3°, and although the error bars are decreasing, no variation is observed except for one point ($D_{\rm max} = 10°$, $\langle D \rangle = 5.0°$, $\Delta A < 40\%$): this may be an indication that magnetic structures are less complex after the flare when including structures much further from the flare in the data set.

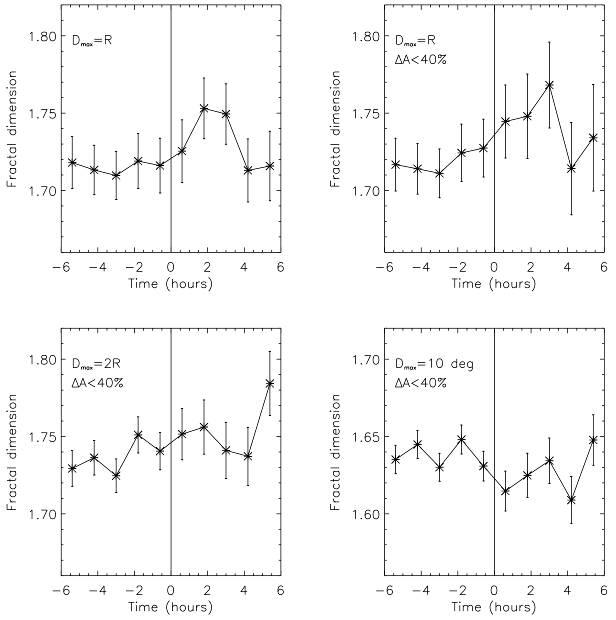

Fig. 4. Fractal dimension versus time for various values of $D_{\rm max}$. The vertical lines indicate the time of the flare: negative time correspond to the time before the *beginning* of the Hα flare, and positive correspond to the time after the *end* of the Hα flare.

The same data set allowed us to look at the variation of the flux content of the structure before and after the flare. No significant variations of $|B_{\rm m}|$, $\bar{B}$ nor Φ are observed.

Figure 3 also shows that the fractal dimension is significantly larger (~0.1) when considering a variable $D_{\rm max}$. A detailed comparison of the set of structures selected for $D_{\rm max} = 7.5°$ and $3R$ (both have the same $\langle D \rangle$) shows that: 1) there is a small deficit of large structures and an excess of small structures in the 7.5° subset, which would lead to smaller fractal dimension (see Sect. 5.1); 2) all sizes considered, the low $|B_{\rm m}|$ population (below 900 G) is twice the size for $D_{\rm max} = 7.5°$, and we have seen that this population is associated with a much smaller fractal dimension (see Sect. 4.1). These two effects are likely to explain the smaller fractal dimension obtained for fixed $D_{\rm max}$.

Figure 4 shows the variation of the fractal dimension with time, for the 4 cases mentioned above exhibiting a significant variation before and after the flares when averaged over 6 h. The errorbars correspond to the formal errors of the linear fits for each subset of selected structures. With this better temporal resolution, no clear fluctuations are observed to occur within the error bars on short time scales. Furthermore, a subset of the flare data set (representing 35% of the whole data set) is constructed by selecting only flares with no other flare occuring in the same region within 6 hours (defined from the NOAA number associated to the flare in the Hα flare list), to investigate the limitation pointed out in Sect. 3.2: with this selection, the results are noisier (due to the smaller number of points) and no obvious trend is observed.

As noted in Sect. 3.1.1, the structure identification is made using a threshold applied to structures of a given polarity. The study of the association of magnetic structures inside active regions is beyond the scope of this paper and will constitute a future work. However it was interesting to check whether the above results were confirmed and not biased by the fact that only sub-structures in the active regions were considered. An attempt was made to consider full active regions by associating the various magnetic structures of the data set using a closest neighbor analysis. With a definition of clusters representing active regions based on a maximum distance of 3° between structures above 200 Mm^2, one can use the approach described above to associate a flare with these newly defined active regions. In that case, the size R of the region used to defined $D_{\text{max}} = kR$ is not based on the area but on the extension of the magnetic structures constituting the regions, and the limitation using D_{max} means that the flare occurs closer to the center of the active region or further away. With that definition of an active region, the results show that the fractal dimension decreases for a fixed D_{max} and the constraint of 40% on the size variation, either for small distance to the center of gravity of the region (lower than 2°) or much further (larger than 5°), but not in between. At large distances this is consistant with the previous result. At small distances, this is quite different, and it may imply that the active region as a whole has a behavior different from that of the individual magnetic structures close to a flare inside the active region.

Finally, we have attempted to consider subsets of the whole data set to check whether the amplitude of the variation was larger when only bright flares were involved. Unfortunately, although the large data set covers almost a full cycle, it is impossible to detect any variation because the error bars are several times larger than the observed variations for the whole data set.

4.2.2. Limitations

The limitations of this analysis are the following:

(i) Consider the variation of the fractal dimension with time before and after a given flare, i.e. the variations with $t = t_{\text{flare}} - t_{\text{magnetogram}}$; all the variations are then then averaged together. Several flares can occur in the same area (parameter #3) within 6 h (parameter #4) ; for example, consider 2 flares (#1 then #2) separated by 2 h. If there is an actual variation of the fractal dimension at the time of the flare, then this variation will appear not only at $t = 0$ but also at $t = -2h$ (due to flare #1 when making the computation for flare #2) and at $t = 2h$ (due to flare #2 when making the computation for flare #1). I have estimated that 65% of the flares of the whole data set corresponds to the same magnetic structure as at least another flare within 6 h. Therefore the variation of the fractal dimension with time before and after flares may be smoothed, and this is probably the most serious limitation of the approach. It may explain partially the behavior of the curves of Fig. 4.

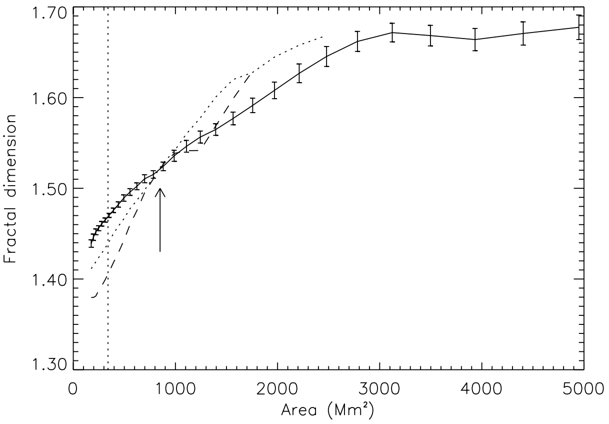

Fig. 5. Fractal dimension versus size for the whole periods. Solid line corresponds to 40 G, dotted to 80 G, dashed to 120 G on all plots. For clarity, error bars are shown for the 40 G threshold only. The arrows indicate the critical sizes discussed in the text. The vertical dotted line indicates the minimum size above which the fractal dimension computation does not include feature below 30 pixels.

(ii) Since we are looking at the magnetic structures within a certain distance of the flare, there may be several structures corresponding to the above criteria, therefore there may be a contribution from structures not directly involved in the flare despite their proximity to the flare; the actual structure at the origin of the flare could also be a small structure below the 500 Mm^2 threshold for example despite the presence of a larger region in the vicinity. This uncertainty will increase with increasing D_{max} and this should also smooth the signal. Studies of different values of D_{max} should help to bypass this problem, as studied from Fig. 3.

(iii) For a given flare, there may be magnetograms available before the flare but not after it, however these data will still be used. If the data sample is large enough, the result should not be biased although it will increase the noise.

5. Fractal dimension over the solar cycle

5.1. Average fractal dimension

Meunier (1999a) performed the fractal analysis of magnetic structures using MDI magnetograms (both 1 and 5 min images) until day 765 (4 February 1998), which corresponds to the solar minimum and the beginning of the ascending phase as defined here. The results for the whole period are shown in Fig. 5 for a magnetic threshold up to 120 G, for 5-min magnetograms only. For larger thresholds up to 240 G I find results similar to that of Meunier (1999a) and they are not displayed here.

With the much longer data set studied here, I also find that the fractal dimension, although varying with the size of the structure (as in Meunier 1999a), reaches a plateau above 3000 Mm^2 (linear size of 55 000 km) with an average value of 1.67.

Meunier (1999a) also found a critical size around 600 Mm^2: this size corresponded to a “pivot point” between large structures, for which the fractal dimension was increasing for increasing magnetic thresholds, and smaller structures,

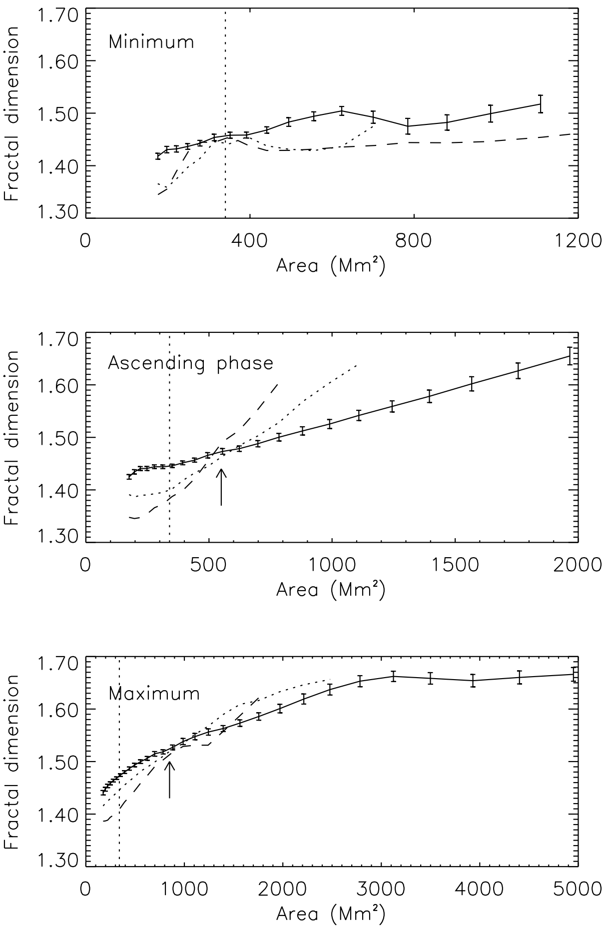

Fig. 6. Fractal dimension versus size for the 3 periods of the solar cycle, on the same vertical scale. Solid line corresponds to 40 G, dotted to 80 G, dashed to 120 G on all plots. For clarity, error bars are shown for the 40 G threshold only. The arrows indicate the critical sizes discussed in the text. The vertical dotted line indicates the minimum size above which the fractal dimension computation does not include feature below 30 pixels and is therefore reliable.

for which the fractal dimension was decreasing. Here I confirm this on a much larger data set: the position of this critical point is shown by an arrow in Fig. 5. One should remember that a given structure detected at a different magnetic threshold corresponds to a different size in these plots. The origin of such a "pivot point" is not well understood: The "pivot point" is not only due to the fact that for increasing threshold (i.e. field closer to the core of the region), the structures are less and less "fractal" (dimension varies more strongly with size), but also that they happen to cross at the same scale. Models should be able to reproduce this type of results to be realistic.

5.2. Cycle phase dependence

5.2.1. Influence of the size

Figure 6 shows the variation of the fractal dimension with size for the 3 phases of the cycle defined in Sect. 2. The critical size has a value of ~550 Mm^2 during the ascending phase (which is similar to the result of Meunier 1999a) and of ~850 Mm^2 during cycle maximum.

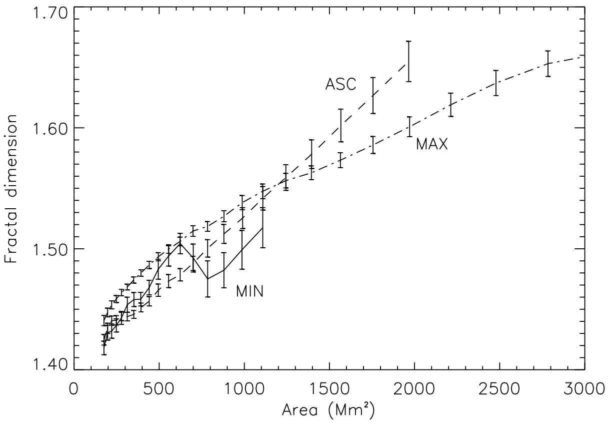

Fig. 7. Fractal dimension versus size for the 3 periods at the 40 G threshold. Solid line corresponds to cycle minimum, dashed line to the ascending phase and the dotted-dashed line to cycle maximum.

A comparison of the variations during the solar cycle for the 40 G threshold is shown in Fig. 7. The complex pattern is similar when observed at the 80 G threshold (although shifted toward smaller sizes of course). At the 40 G threshold, structures larger than 1200 Mm^2 are more complex during the ascending phase than during the cycle maximum (there are very few such structures during cycle minimum). Between the ascending phase and cycle maximum, the variation reaches 0.06 when considering the largest structures. Below this size down to $A \sim 700$ Mm^2 (i.e. close to the "pivot point" mentioned above), I observe the opposite, with structures less complex during solar minimum: in this range, structures are more complex when the activity level is larger. For even smaller structures, the fractal dimension at cycle minimum is intermediate between the other curves. In the range where the fit is significant (i.e. including size above 30 pixels only as shown in Meunier 1999a, or 60 Mm^2), the difference of fractal dimension between cycle maximum and minimum is of the order of 0.02 only (this is for small structures since there are almost no large structures during solar minimum), the structures at cycle maximum beeing only slightly more complex than at cycle minimum (this is marginally significant).

Another way to look at this is to compute directly the slope of Log (P) versus Log (A) for all points in a given size range. For example, for A in the range 800−1200 Mm^2, the fractal dimension is 1.19 ± 0.17 at cycle minimum, 1.38 ± 0.07 during the ascending phase and 1.47 ± 0.03 during the maximum, showing a significant increase from cycle minimum to cycle maximum. On the other hand, for $A > 1200$ Mm^2, the fractal dimension is 1.59 ± 0.04 at cycle minimum, 1.78 ± 0.01 during the ascending phase and 1.669 ± 0.004 during the maximum, exhibiting the largest value during the ascending phase, the fractal dimension remaining the smallest during cycle minimum. This confirms the results shown in Fig. 7.

Table 2. Fractal dimension and number of points (in italic) in the size range 2000–7000 Mm^2.

Period	$\lvert B_\mathrm{m}\rvert < 900$G	$\lvert B_\mathrm{m}\rvert > 900$G
Total	1.71 ± 0.01 *(10 147)*	1.89 ± 0.01 *(7273)*
Cycle minimum	1.09 ± 0.11 *(2432)*	1.53 ± 0.06 *(143)*
Ascending phase	1.64 ± 0.03 *(1047)*	1.97 ± 0.03 *(1385)*
Cycle maximum	1.73 ± 0.01 *(6097)*	1.80 ± 0.01 *(8619)*

5.2.2. Influence of B_m

When one separates the 2 populations described in Sect. 4.1 (with low $|B_\mathrm{m}|$ and large $|B_\mathrm{m}|$), one obtains the results shown in Table 2 for the size range 2000–7000 Mm^2: from the ascending phase to cycle maximum, a strong increase (+0.09) is observed for low $|B_\mathrm{m}|$ structures, while a strong decrease (−0.17) is observed for strong $|B_\mathrm{m}|$ structures. This also means that the difference between the fractal dimensions of the 2 populations is larger during the ascending phase compared to cycle maximum. Note that although the proportion of strong $|B_\mathrm{m}|$ structures is slightly larger at cycle maximum, the effect on the fractal dimension is expected to be very small (0.001).

During cycle minimum, some of the largest regions are likely to be due to the end of the previous cycle, i.e. some of them may correspond to the end of a maximum phase rather than to the beginning of the studied cycle. Indeed, at cycle minimum, the latitude distribution is made up of two components, one centered on 7.5° (68% of the points, corresponding to the end of the previous cycle) and the other on 26.7° (32% of the points, corresponding to the beginning of the current cycle). This suggests that from the beginning of the ascending phase until the very end of maximum period, the very large active regions may be less and less complex. However there are few points during cycle minimum (1094 structures larger than 800 Mm^2 only).

The variations during the solar cycle for the different components is also shown in Fig. 8 with better temporal resolution. On this plot, the values for low latitudes at cycle minimum are shown *at the end* of the time series (see caption of Fig. 8). One can clearly see the very different behavior of larger and small structures and of different $|B_\mathrm{m}|$ structures for the largest sizes. Large structures with high $|B_\mathrm{m}|$ have their maximum fractal dimension during the middle of the ascending phase (2 years after the beginning of the activity raise), then they decrease to reach an approximately constant level during cycle maximum. A small increase is also observed at the end of cycle maximum. The structures of the same size with low $|B_\mathrm{m}|$ exhibits an increase of the fractal dimension during the ascending phase, a maximum during solar maximum and then a decrease and finally a small increase as for the large $|B_\mathrm{m}|$ structures. Small structures shows a behavior like the latter structures, also the detailed variations during cycle maximum may be slightly different. At the end of the cycle we expect to observe much smaller fractal dimensions for all structures.

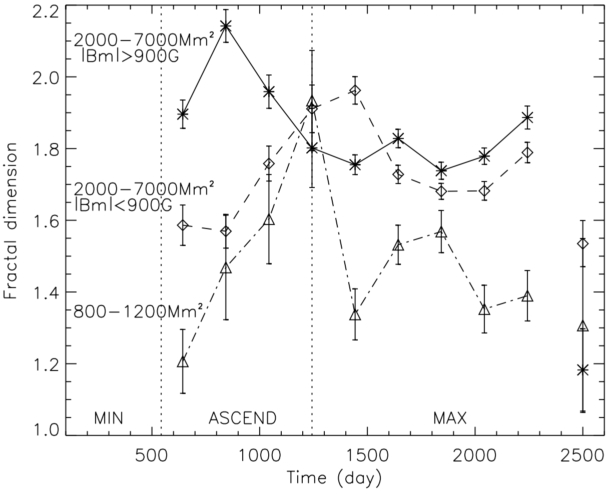

Fig. 8. Fractal dimension versus time for various selections: A in the range 800–1200 Mm^2 (dotted-dashed line and triangles), A in the range 2000–7000 Mm^2 and $B_\mathrm{m} > 900$ G (solid line and stars), and A in the range 2000–7000 Mm^2 and $B_\mathrm{m} < 900$ G (dashed line and diamonds). The points at $t = 2500$ days correspond to the structures of cycle minimum ($t < 543$ days) with latitude smaller than 17°, i.e. to the end of the previous cycle, and are shown arbitrarily at this time. The same structures for latitude larger than 17° (i.e. beginning of the studied cycle) are not shown because of the very large errorbars (there are very few large structures during cycle minimum).

5.2.3. Influence of latitude

It is also useful to check whether the observed variations with time are due to latitude or to temporal variations. It is not easy to do since most structures are at different latitudes during the ascending phase and the cycle maximum. I have considered the latitude range 17–22° in which there are many structures in both cases. When considering the size range 2000–7000 Mm^2 studied above, a small increase of the fractal dimension is observed from the ascending phase to cycle maximum, but this is mostly due to the large increase for the $|B_\mathrm{m}| < 900$ G structures, while there is still a decrease for the $|B_\mathrm{m}| > 900$ G structures. When considering the range $A > 1200$ Mm^2, I still observe a decrease of half the size of that for all points (from 1.77 ± 0.02 to 1.72 ± 0.01) while I observe an increase for the size range 800–1200 Mm^2 (from 1.25 ± 0.13 to 1.33 ± 0.06), although this is not significant due to the small number of points in that latitude range.

I deduce from these computations that the time variation is real, as are the different properties between the two populations observed in Sect. 4.1. Furthermore, this is reinforced by the complex evolution through the cycle observed in Fig. 8, which is not correlated at all with the also complex latitude variation and the variation that could be expected from it due to the butterfly diagram.

Finally, when considering the latitude distribution for $|B_\mathrm{m}| < 900$ G and $|B_\mathrm{m}| > 900$ G in the size range 2000–7000 Mm^2, a small deficit of the latter is observed in the latitude range 20–30°. However the difference of fractal dimensions between the range 0–20° and 20–30° is too small to explain the behavior of these two populations observed in Sect. 4.1.

6. Discussion

I have performed several analyses to study the dependence of the fractal dimension of magnetic structures on the activity level at different time scales. The following results have been obtained:

(i) The variation of the fractal dimension of magnetic structures computed on LOS magnetograms due to flares is observed to be very small, and in most cases hardly significant, despite the very large sample compared to previous studies. Close to the flares (2–3°), an increase towards larger complexity of individual magnetic structures is observed. On the other hand, when considering large structures further from the flares (with distance up to 10°), there is a tendancy to get smaller fractal dimensions after the flare, i.e. less complex structures, suggesting large-scale modifications as pointed out by Yurchyshyn et al. (2000). The very small variations could be due to the fact that there are other flares in the active region within the studied time interval, but a subset of flares that does not have this limitation does not show any significant trend with time either. Because the variations that are observed are very small and not very significant despite the large sample, it does not seem realistic to use the variation of the LOS magnetic fields to predict solar flares. This confirms previous results obtained by Adams et al. (1997) for example, but on a much larger sample. It could indeed be expected that most of the topology modifications should happen in that layer and not in the photosphere, as studied with the MDI magnetograms, since the energy release during a flare takes place mostly in the chromosphere.

(ii) Structures with spots (strong $|B_\mathrm{m}|$) are significantly more complex than structures with no spots (low $|B_\mathrm{m}|$), for a given size. This is surprising because we could expect that many large structures with no spots are decayed structures with an apparently complex structure (more diluted structure). The effect is more pronounced for large structures.

(iii) The general behavior of the fractal dimension (in particular the dependence on the size of the structures) obtained by Meunier (1999a) is confirmed on a much larger data sample, especially for large scales. The “pivot point”, also observed by Meunier (1999a) and close to the supergranular size, is observed to increase from solar minimum to solar maximum. A plateau above 3000 Mm^2 is also observed, with an average fractal dimension of 1.67.

(iv) Variations of the order of 0.02 to 0.06 (depending on the size) of the fractal dimension are observed during the cycle. The sign of the variation depends on the size range and on $|B_\mathrm{m}|$. The results are complicated by the different behavior of the strong $|B_\mathrm{m}|$ structures (which, on average, exhibit a decrease of the fractal dimension from the ascending phase to cycle maximum) and the low $|B_\mathrm{m}|$ structures (which shows an increase, as observed for medium size structures above 800 Mm^2). When one separates these populations, the amplitude of variations is of the order of 0.1–0.2. Therefore structures with spots seem more complex at the beginning of the cycle compared to cycle maximum and the structures with no spots seem less complex. The detailed temporal variations are also quite complex, with the fractal dimension peaking at different times for the structures of different sizes or different $|B_\mathrm{m}|$ (ranging from the middle of the ascending phase to the beginning of cycle maximum). We showed that these variations are mostly due to a temporal variation and not to a latitudinal dependence.

The linear size derived from the square root of the structure areas shows that the “pivot point” at ~800 Mm^2, which corresponds to 28 300 km, happens to be close to the supergranular scale. A scale of similar amplitude was also identified by Meunier (2003) from the size distribution of active regions. They could be related, since in both cases they seem to increase during the solar cycle. This particular pattern should be taken into account by models. The different complexity behavior for different sizes may be due to a different formation process for small and large active regions: I suggest that models looking at the formation of active regions such as those of Wentzel & Seiden (1994), Seiden & Wentzel (1996) and more recently of Vlahos et al. (2002) should try to reproduce this result.

The variation of the fractal dimension with the solar cycle is one of the most important results and models should also be able to reproduce this. Whether they are due to a variation of the dynamo process during the cycle (including a variation with depth) or to surface effects affecting the decay of active regions is still an open question. The magnetic field must play an important role given the large variation of the fractal dimension with the size of the structures and with $|B_\mathrm{m}|$. This should favor a dynamo origin. The non-monotonous variation, with a peak during the ascending phase or cycle maximum, could be associated with the influence of two processes that would be out of phase. On the other hand, surface flows may influence in different manners structures of different sizes. Harvey (1993) showed that during cycle maximum, structures have a longer lifetime than at cycle minimum, with a factor ~1.3 which is independent of the size for $A > 1500\ \mathrm{Mm}^2$ but this factor seems to be slightly smaller for smaller sizes. This could lead to a longer decay phase at cycle maximum that would lead to diluted structures a larger proportion of the time and therefore a larger fractal dimension at cycle maximum. This could not be the only factor however since the observed variations are much more complex than this. Divergent and convergent flows around active regions could also play a role. On a large scale, convergent flows are observed (Meunier 1999b; Chou & Dai 2001; Beck et al. 2002) although on smaller scales the moat flow is divergent. The latter is likely to contribute to the erosion of active regions and to their dilution in a more complex pattern. The moat flows around sunspots may also be part of the reason why the structures with spots are more complex. A study allowing one to follow and separate young and old regions would also be useful to sort out the different contributions.

Finally, the observed timescale of a few years (peak of fractal dimension after the activity level has started to rise) leads to the question of whether this behavior is purely transient or related to some oscillatory behavior such as the 1.3 year period observed in the rotation rate at the bottom of the tachochline (Howe et al. 2000) or to the multipeaked structures observed in the Wolf number during the ascending phase and cycle maximum. More observations during future cycles will be necessary to investigate this in more detail.

Acknowledgements. SOHO is a mission of international cooperation between the European Space Agency (ESA) and NASA. Sunspot numbers and flare data have been provided by the National Geophysical Data Center (National Oceanic and Atmospheric Administration). I gratefully ackowledge the referee for his remarks which have helped to improve the paper.

References

Abramenko, V. I., Yurchyshyn, V. B., Wang, H., Spirock, T. J., & Goode, P. R. 2002, ApJ, 577, 487
Adams, M., Hathaway, D. H., Stark, B. A., & Musielak, Z. E. 1997, Sol. Phys., 174, 341
Aulanier, G., DeLuca, E. E., Antiochos, S. K., McMullen, R. A., & Golub, L. 2000, ApJ, 540, 1126
Balke, A. C., Schrijver, C. J., Zwaan, C., & Tarbell, T. D. 1993, Sol. Phys., 143, 215
Beck, J. G., Gizon, L., & Duvall, T. L. 2002, ApJ, 575, L47
Bleybel, A., Amari, T., van Driel-Gesztelyi, L., & Leka, K. D. 2002, A&A, 395, 685
Chou, D. Y., & Dai, D. C. 2001, ApJ, 559, 175
Fletcher, L., Metcalf, T. R., Alexander, D., Brown, D. S., & Ryder, L. A. 2001, ApJ, 554, 451
Hagyard, M. J., Stark, B. A., & Venkatakrishnan, P. 1999, Sol. Phys., 184, 133
Harvey, K. L. 1993, Ph.D. Thesis, Astronomical Institute, Utrecht University
Howe, R., Christensen-Dalsgaard, J., Hill, F., et al. 2000, Science, 287(5462), 2456
Janssen, K., Vögler, A., & Kneer, F. 2003, A&A, 409, 1127
Nesme-Ribes, E., Meunier, N., & Collin, B. 1996, A&A, 308, 213
Mathew, S. K., & Ambastha, A. 2000, Sol. Phys., 197, 75
Meunier, N. 1999a, ApJ, 515, 801
Meunier, N. 1999b, ApJ, 527, 967
Meunier, N. 2003, A&A, 405, 1107
Patty, S. R., & Hagyard, M. J. 1986, Sol. Phys., 103, 111
Ruzmaikin, A., Sokoloff, D., & Tarbell, T. 1991, in The Sun and Cool Stars: Activity, Magnetism, Dynamos, ed. I. Tuominen, D. Moss, & G. Rüdiger (Berlin: Springer), 140
Scherrer, P. H., Bogart, R. S., Bush, R. I., et al. 1995, Sol. Phys., 162, 129
Seiden, P. E., & Wentzel, D. G. 1996, ApJ, 460, 522
Sorriso-Valvo, L., Carbone, V., Veltri, P., et al. 2003, Planet. Space Sci., in press
Stark, B., Adams, M., Hathaway, D. H., & Hagyard, M. J. 1997, Sol. Phys., 174, 297
Tao, L., Du, Y., Rosner, R., & Cattaneo, F. 1995, ApJ, 443, 434
Vainshtein, S. I., Sagdeev, R. Z., Rosner, R., & Kim, E.-J. 1996, Phys. Rev. E, 53(5), 4729
Vlahos, L., Fragos, T., Isliker, H., & Georgoulis, M. 2002, ApJ, 575, L87
Wentzel, D. G., & Seiden, P. E. 1992, ApJ, 390, 280
Yurchyshyn, V. B., Abramenko, V. I., & Carbone, V. 2000, ApJ, 538, 968
Zelenyi, L. M., & Milovanov, A. V. 1991, Soviet Astron. Lett., 17(6), 425
Zhang, C., & Wang, J. 2000, Sol. Phys., 196, 377
Zhang, C., & Wang, J. 2002, Sol. Phys., 205, 303

A&A 436, 1075–1086 (2005)
DOI: 10.1051/0004-6361:20042414

Astronomy
&
Astrophysics

Magnetic network dynamics: Activity level, feature size and anchoring depth

N. Meunier

Laboratoire d'Astrophysique de l'Observatoire Midi-Pyrénées, 57 avenue d'Azereix, BP 826, 65008 Tarbes Cedex, France
e-mail: `meunier@bagn.obs-mip.fr`

Received 23 November 2004 / Accepted 16 February 2005

Abstract. A large data set of MDI magnetograms is studied in order to analyze the global dynamics of magnetic structures from network to active regions. Two complementary techniques are used: feature tracking and correlation tracking. The very large data set allows the variation of their dynamics (angular rotation velocity and meridional circulation) to be studied in detail. Variation both in the dynamics as a function of size and distance to active regions (for feature tracking) and as a function of activity level in the correlation box are studied. These new results allow the possible anchoring depth of these magnetic features to be constrained. The observations of the magnetic network dynamics are not consistent with the dynamics deduced from helioseismology. So, some additional processes must be acting on the magnetic network in order to explain their global dynamics.

Key words. Sun: magnetic fields – Sun: photosphere – Sun: faculae, plages

1. Introduction

The differential rotation of the most active solar features (spots and plages) have been studied extensively over the past decades. The various methods and data selection have led to angular rotation velocity (hereafter rotation rates) of various amplitudes (see for example Howard 1996; Beck 2000, for reviews). These differences have long been interpreted in terms of anchoring depth of these features, since structures anchored in layers rotating differently should rotate at different rates as well. Before the advent of helioseismology this interpretation was used to obtain some clues about the internal rotation rate. The opposite approach can now be used, such that it is possible to try to determine the anchoring depth of magnetic features from their rotation rate. Javaraiah & Gokhale (1997), Hiremath (2002), and Sivaraman & Gokhale (2004) have thus used the internal rotation inferred by helioseismology to determine the anchoring depth of spots during their lifetimes. However, this interpretation of the different rotation rates of magnetic structures by their anchoring in the convection zone has never been completely analyzed, especially using large data sets and several dynamical variables. One should also remember that the faster rotation rate of sunspots, compared to the photospheric plasma, has also been explained by D'Silva & Howard (1994) as the interaction between magnetic buoyancy and drag and the Coriolis force acting on the rising flux tubes. Therefore there is a need for analysis of global dynamics data in order to check the consistency of the interpretation.

In this paper, the angular rotation velocity (in heliographic degrees per day) of magnetic structures from network to large regions is studied using two complementary methods, where measurement of the meridional circulation is used as an additional constraint. We focus mainly on magnetic network analysis since fewer work has been done for these less active structures. The works of Snodgrass & Ulrich (1990), Komm et al. (1993a,b), Meunier et al. (1997a,b), and Meunier (1999) did not study the variation of the dynamics of the magnetic network in detail and did not address the issue of anchoring depth. Variation in the rotation rate and meridional circulation provides additional constraints. In Sect. 2, the methods and limitations are described. Section 3 shows the time-averaged results, with the dependence of the dynamics on latitude, on the type of features, and on their location with respect to active regions. Finally a discussion in terms of anchoring depth is presented in Sect. 4.

2. Data and processing

2.1. MDI data

A data set of full-disk magnetograms obtained by MDI on SOHO (Scherrer et al. 1995) between June 22, 1996 and April 1, 2004 is used, covers 8 years, i.e. most of cycle 23 from cycle minimum to the end of cycle maximum. For this study, I have selected only 5-min averaged magnetograms as in Meunier (2003), in order to have a homogeneous data set. These magnetograms, all at level 1.8, are separated by 96 min or a multiple of 96 min. The distribution of image pairs with time is shown in Fig. 1 and is exactly the same for both methods described below. There are a few gaps because during some

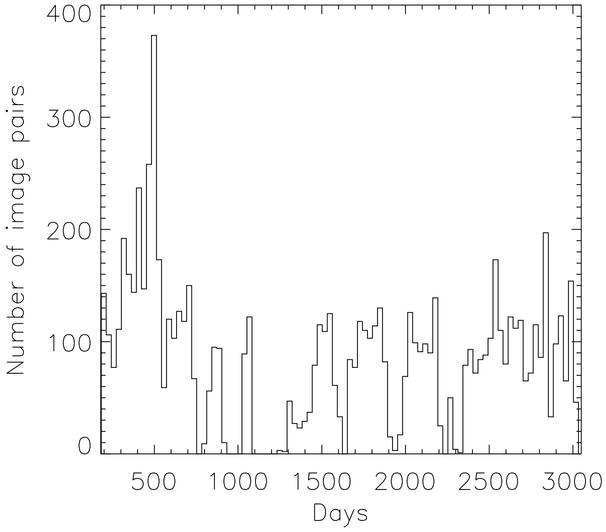

Fig. 1. Distribution of image pairs versus time. Day 1 corresponds to January 1, 1996.

periods only 1-min magnetograms are available. One important gap is also due to the interruption of SOHO activities in 1998. For a separation of 96 min, 8117 image pairs are thus available.

2.2. Feature tracking

Feature identification is performed as in Meunier (2003), using a 40 G threshold on $B/$ maps, where B is the measured line-of-sight magnetic field (i.e. a magnetic flux averaged over the pixel size) and the cosinus of the angle between the line-of-sight direction and the normal to the solar surface. Note that this threshold of 40 G is quite conservative and is well above noise level in these data (below 10 G). Following this identification on each image, an association between features observed on two consecutive images separated by 96 min is performed. For each feature on the first image, the closest feature is identified once shifted by a reference synodic rotation rate of $13.5{-}3.5\sin^2$ deg/day (latitude). Only feature pairs are selected such that this distance d is below 4.5 Mm (which corresponds to a diffusion coefficient of 1000 km^2 s^{-1}) and such that the size is not modified by more than 5%. The threshold of 4.5 Mm derives from the distribution of d, which shows a peak around 1.2 Mm, then a minimum (much smaller than the maximum) around 4.5 Mm and increases slightly again. The second distribution above 4.5 Mm, visible mostly for small structures, corresponds to cases where the structure has either disappeared or split on the second magnetograms and is therefore identified with a random structure anywhere on the disk. The 2 distributions are distinct, and therefore it is quite safe to consider that below 4.5 Mm the tracking is correct. The distribution of d up to 4.5 Mm is shown in Fig. 2. The maximum of 1.2 Mm would correspond to a diffusion coefficient of 250 km^2 s^{-1}. One should note that for the smallest structures (10 Mm^2), 4.5 Mm corresponds to 2.5 times the radius of this structure and only 3 pixels. A distance of 4.5 Mm corresponds to the radius of structures with a size of 63 Mm^2. We have checked that the results are not affected significantly by this selection. In addition, the use of a different reference rotation rate (for example an equatorial rate of 13.3 or 13.7 deg/day instead of 13.5 deg/day, or a coefficient very different from −3.5 deg/day) does not change the results, i.e. the tracking appears to be very robust.

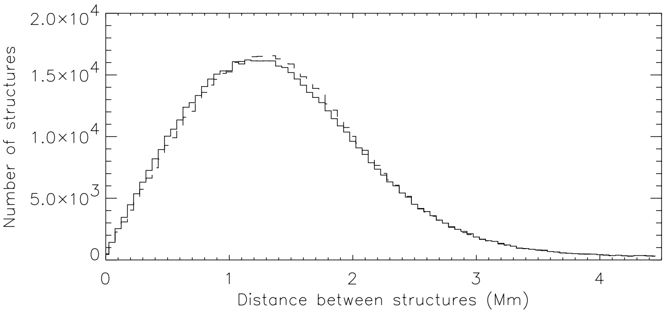

Fig. 2. Distribution of distances between two associated magnetic features in the FT method for sizes below 80 Mm^2 (solid line) and all structures (dashed line).

This feature tracking method is hereafter denoted as FT. In order to look at the dependence of the dynamics on the type of structure, additional variables are computed:

- The size A_t of the structure, defined by the 40 G threshold on $B/$, in Mm^2.
- The perimeter P_t of the structure, defined by the 40 G threshold on $B/$, in Mm.
- The flux in that structure, $_t$, in Mx (unsigned).
- The maximum absolute magnetic field in that structure, Bm_t, in G.

2.3. Correlation tracking

The correlation tracking (hereafter denoted as CT) is performed as in Meunier (1999). I recall here the main characteristics: the cross-correlations are computed over boxes of 7.68×7.68 deg^2 (64×64 pixels^2) on remapped magnetograms (1 pixel corresponds to 0.12 degrees, i.e. 1.45 Mm at disk center). Individual cross-correlation functions are then fitted with 2D Gaussians, which provides the rotation rate and the meridional circulation. Only boxes with maximum correlation above 0.2 are considered in this analysis.

In order to look at the dependence of the dynamics on the type of regions, additional variables are computed:

- The average of the absolute magnetic field in the box $|B_c|$ in G.
- The maximum absolute magnetic field in that structure Bm_c in G.
- The number of pixels above the 40 G threshold in the box $N\mathrm{pix}_c$.

2.4. Additional computation

Corrections from synodic rotation rates to sidereal rotation rates are performed. The residuals of the rotation rate and meridional circulation are computed with respect to the average value in the corresponding latitude range (5° bin) averaged over the full time period and all points. The sign convention is as follows for the meridional circulation: a positive circulation means motion toward the north, i.e. it is poleward in the Northern hemisphere and equatorward in the Southern hemisphere. The convention is changed for the residual circulation to make it easier to average values over both hemispheres: a positive residual is positive when it is more poleward than the average, and negative otherwise. Note that for the equator, the notion of poleward and equatorward motions does not make sense and only the notion of southward or northward motions is usefull.

2.5. Possible biases

2.5.1. Variation of the rotation rate with longitude

In Meunier (1999), a bias in longitude has been observed and studied. The rotation rate was observed to be larger on the west side than on the east side. We refer to that paper for the main characteristics. This bias is shown in Fig. 3 for various feature sizes (FT method) and various magnetic field levels (CT method). These plots show that the strong variation in rotation with longitude is mostly visible for CT and only for quiet regions. It has been suggested (Giles 1999) that variation of the plate scale across the disk in MDI data could lead to such a result. However, if this were true, the effect would probably be visible for all features and both methods.

That this is seen only for weak field regions suggests that the noise level, which is also strongly varying on the solar disk in MDI data, could play a part in the problem. However, as the noise is larger far from disk center, one expects a small rotation residual on the east and west sides (with a stronger effect on the west side where the noise gradient is larger) and a larger rotation residual at disk center, which is not what is observed. Also, Meunier (1999) observed that the amplitude of the bias was larger for 5-min magnetograms compared to single ones, although the former are less noisy.

As a consequence, the origin of this bias remains unclear. It does not correspond to any of the possible biases studied extensively by Strous (2000), and is almost certainly of instrumental origin though. Therefore the CT results presented in this paper have been corrected for this bias as observed in Fig. 3: the bias for the rotation rate is computed for different ranges in magnetic field for the whole period and then subtracted from the original rotation rate. However the results are not significantly affected by this correction. Furthermore, we checked that a subset of structures located close to disk center led to similar results.

2.5.2. Non-zero disk-center meridional circulation

A non-zero meridional circulation at the equator has already been observed with MDI data using various techniques (Meunier 1999; Giles 2000, for example). Here, for the FT method, the average meridional circulation at the equator is -0.051 ± 0.003 deg/day (-0.047 ± 0.002 deg/day for 0.95). For the CT method, the average meridional circulation at the equator is -0.034 ± 0.002 deg/day (-0.012 ± 0.001 deg/day for 0.95). In addition to an average offset of a few m/s (toward the South Pole), this offset is observed to vary with a period of approximately 1 year, suggesting influence from the SOHO orbit. It has been suggested that this could in part be due to a misalignment of the MDI CCD. Giles (1999) has also suggested that the B and P angles should be corrected in order to suppress this equatorial flow; but so far they are uncertain, and there is no way at this time to be sure that this apparent flow across the equator is not real. The different amplitudes for the 2 methods show that it cannot be due to an instrumental problem alone; otherwise they would be similar. Therefore the results presented in the following sections are not corrected for it. This uncertainty makes the comparison with helioseismic results a little more difficult because it introduces a north-south asymmetry that may or may not be real.

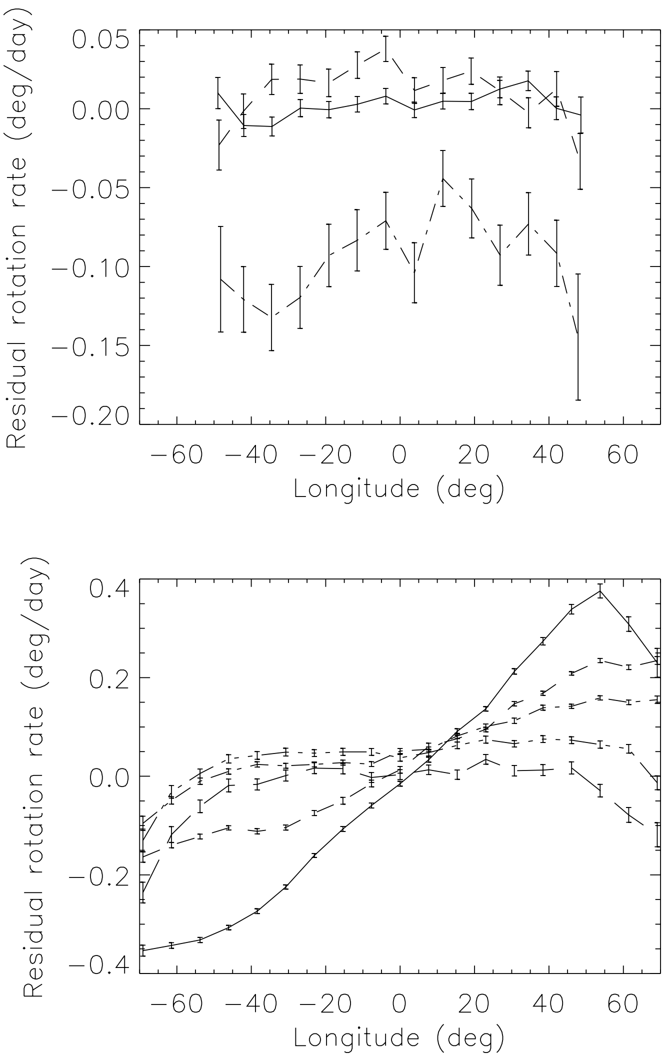

Fig. 3. *Top*: FT residual rotation rates versus longitude for A_t 80 Mm^2 (solid), A_t in the range 80–500 Mm^2 (dashed), and A_t 500 Mm^2 (dotted-dashed). *Bottom*: CT residual rotation rate versus longitude for $|B_c|$ below 6 G (solid), in the range 6–9 G (dashed), in the range 9–15 G (dotted-dashed), in the range 15–30 G (dot-dot-dot-dashed), and above 30 G (long dashed).

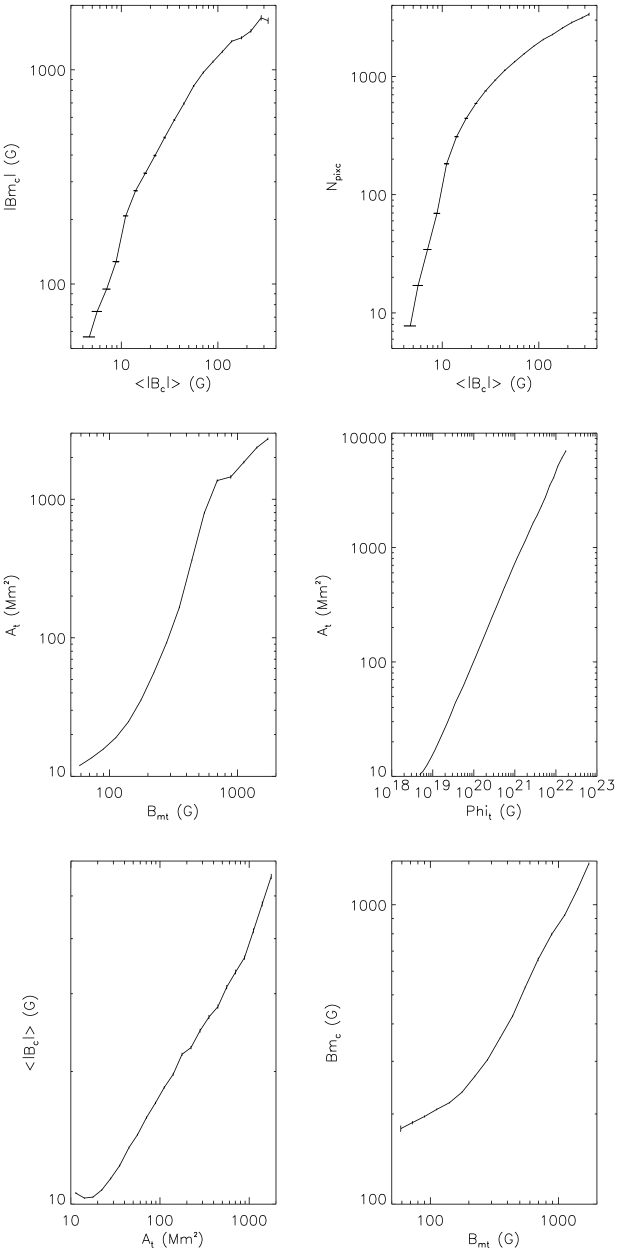

Fig. 4. *Top*: CT correspondences, showing $Bm_{\rm c}$ versus $|B_{\rm c}|$ (*left*) and $N{\rm pix}_{\rm c}$ versus $|B_{\rm c}|$ (*right*). *Middle*: FT correspondences showing $A_{\rm t}$ versus $Bm_{\rm t}$ (*left*) and $A_{\rm t}$ versus $_{\rm t}$. *Bottom*: FT-CT correspondences showing $|B_{\rm c}|$ versus $A_{\rm t}$ (*left*) and $Bm_{\rm c}$ versus $Bm_{\rm t}$ (*right*).

2.6. Correspondence between the two methods

In order to help in interpreting the results, it is useful to build a correspondence between the characteristics of a given box used for correlation tracking, such as the average magnetic field or the number of pixels above 40 G and the properties of individual features in that box, such as the average size of the features in that box or their average magnetic field. Note that in some cases, the correlation tracking method provides a result in very weak field regions where no feature above the magnetic threshold of 40 G has been tracked. For the other cases, the results are shown in Fig. 4. Magnetic fields and sizes are naturally well correlated (Meunier 2003).

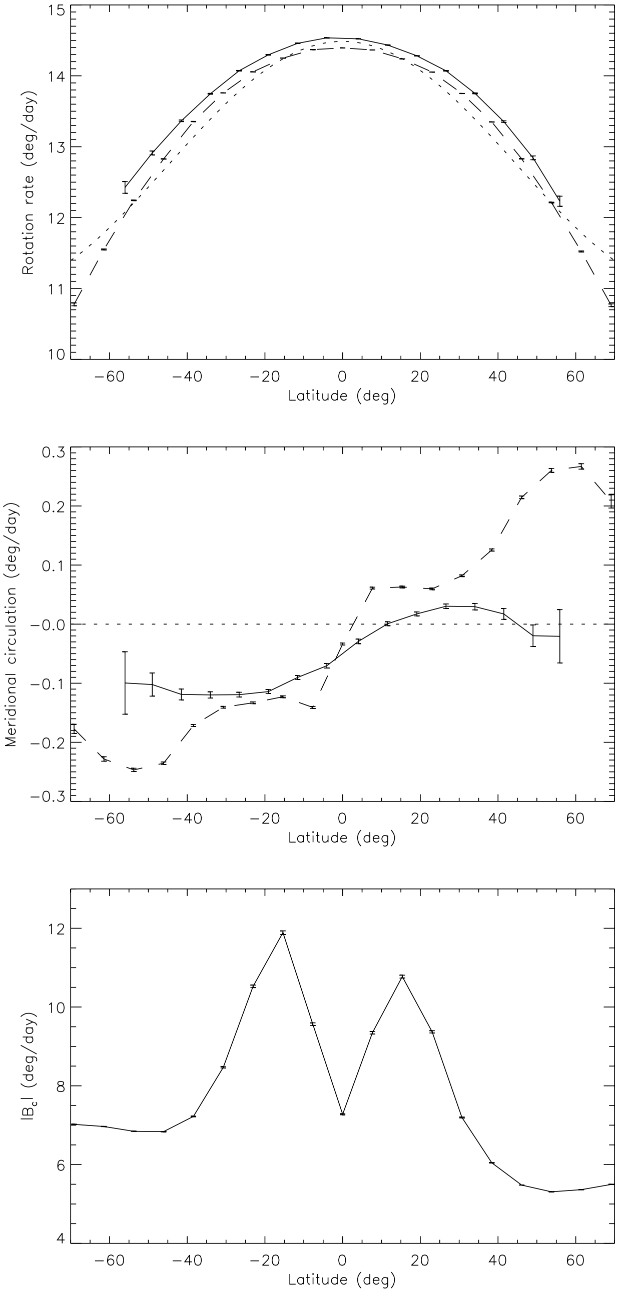

Fig. 5. *Top*: sidereal rotation rate for FT (solid line) and CT (dashed line); the dotted line represents the reference rotation rate around which the correct value is searched. *Middle*: same for the meridional circulation. *Bottom*: averaged $|B_{\rm c}|$ showing active latitude regions. 0.1 deg/day corresponds to 14 m/s.

3. Time-averaged results

3.1. Rotation rate and meridional circulation versus latitude

Figure 5 shows the rotation rates obtained for all regions for the 2 methods. Note that both are very different from the "reference" rotation rate. The CT provides a rotation rate which is smaller than the FT rotation rate at all latitudes by about 0.17 deg/day. In the first case the results are compatible with

Table 1. Equatorial rotation rate (in deg/day) from different works: photospheric magnetic features using CT or FT, except for: the work of Brajša et al. (2004), which concerns coronal bright points (Method 1 is interactive and selects less features in latitude range 10–40° than the automatic Method 2); The work of Meunier et al. (1997) is from CaII photospheric images. Supergranulation (denoted as SG) is from autocorrelation of dopplergrams. Coefficients A_2 and A_4 are Legendre coefficients from the fit on the rotation versus latitude.

Reference	Period	Rotation rate	*B*	*C*
CT present work	1996–2004	14.390 ± 0.001	−2.568 ± 0.003	−0.552 ± 0.003
CT Meunier (1999)	1996–1998	14.33 ± 0.02	−2.671 ± 0.005	−0.630 ± 0.005
CT Komm et al. (1993a)	1975–1991	14.43 ± 0.02	−2.53 ± 0.12	−0.48 ± 0.03
CT Snodgrass & Ulrich (1990)	1967–1987	14.25 ± 0.01	−2.49 ± 0.07	−0.55 ± 0.02
SG Duvall (1980)	1979	14.72 ± 0.07	–	–
SG Snodgrass & Ulrich (1990)	1967–1987	14.71 ± 0.05	−2.62 ± 0.19	−0.41 ± 0.06
FT present work	1996–2004	14.562 ± 0.002	−2.21 ± 0.03	−0.34 ± 0.02
FT Meunier et al. (1997)	1957–1964	14.42 ± 0.02	−1.85 ± 0.51	0.16 ± 0.20
Cor. BP Brajša et al. (2004)[1]	1998–1999	14.454 ± 0.027	−2.65 ± 0.36	−0.32 ± 0.11
Cor. BP Brajša et al. (2004)[2]	1998–1999	14.677 ± 0.033	−2.52 ± 0.42	−0.63 ± 0.13

previous results using a similar method (Snodgrass & Ulrich 1990; Komm et al. 1993a; Meunier 1999), with an equatorial rotation rate of 14.39 deg/day (see Table 1). In the FT case, no work for photospheric network features has been performed, except Meunier et al. (1997a) using a manual tracking of facula features observed on calcium images, including network magnetic fields: the equatorial rotation rate of 14.56 deg/day is larger than their results. However, the results are quite close to coronal bright point rotation rates (Brajša et al. 2004). Their automatic method provides a large equatorial rotation rate closer to FT than to CT results, and the interactive method is closer to the CT results. Note that the rotation rate obtained with their automatic method is also very close to that observed by Antonucci et al. (1979) for small-scale features in the corona.

Table 1 also shows a comparison of the Legendre coefficients A_2 and A_4, corresponding to the differentiality of the rotation (at low and high latitudes respectively). There is a tendency for the CT method to provide a more differential rotation than for the FT method. The large errorbars of the FT method in the literature prevents a detailed comparison, however. The CT coefficients seem significantly different, though quite close, but part of these differences could be due to a temporal variation. This is true in particular for the comparison of the present result with that of Meunier (1999), which shows a more differential rotation at cycle minimum.

The meridional circulation is also quite different for the 2 methods, as the FT provides a meridional circulation of much smaller amplitude (7 m/s instead of 35 m/s) than CT. The CT results are significantly larger than those obtained by Komm et al. (1993b) for example (10–15 m/s), but these differences could be due to a time variation. The peculiar pattern observed with the CT in active latitudes (and already observed by Meunier 1999, who found that it corresponded to active regions) is not observed. The CT flow is observed to peak around latitudes 50−60°, while the FT peaks around 30°.

The pattern in the meridional circulation observed for CT is highly correlated with active latitudes. When looking at similar plots for various periods through the cycle, the location of this pattern is moving toward the equator similarly to the activity belt. Therefore the complex pattern is not due to superimposition of various components resulting from different periods. However, no clear pattern is observed for the FT analysis. Following the work of Howard (1991), we recomputed the FT meridional circulation with respect to the average meridional circulation found for the latitude that corresponds to the mean activity belt. For each time period of 30 days, the average latitude of structures larger than 200 Mm^2 in each hemisphere is computed, as well as the average meridional circulation within 3° of that latitude. The meridional circulation in each hemisphere is then recomputed with respect to this average meridional circulation.

Results in both hemispheres are averaged together, with the following convention: a positive meridional circulation corresponds to a more poleward motion than the reference. Results are shown in Fig. 6. For small structures, a divergent pattern is observed with a stronger flow closer to the hemisphere than to the poles. The amplitude is quite low at a few m/s, as has been observed for other features such as recurrent sunspots using the same techniques (Wöhl & Brajša 2001; Wöhl 2002). This signal is observed mainly for structures close to active regions (see Sect. 3.3.1) but becomes very small farther than 30° from large structures. Note that we do not find the convergent pattern observed for faculae by Howard (1996). Large structures also exhibit a diverging pattern; however, poleward of the activity belt, the meridional circulation is constant within the errorbars.

The FT and CT methods are probably affected by the presence of active regions in different ways and in different proportions. Is this effect enough to explain the difference in results? To answer this question, the next section examines the variation in dynamics for various magnetic field regimes for both

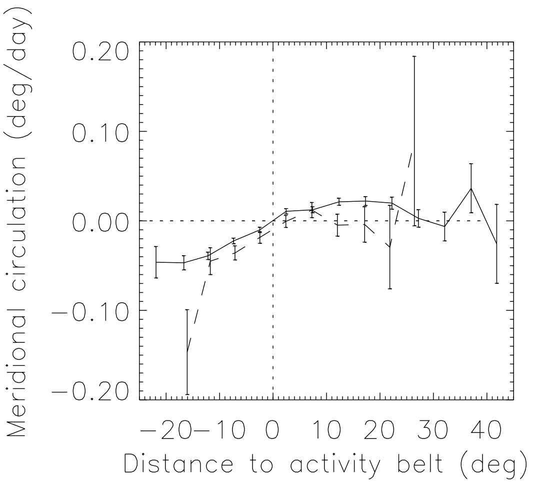

Fig. 6. FT meridional circulation with respect to the activity belt averaged over the two hemispheres. A positive signal means a more poleward motion than the reference. The solid line corresponds to all structures (dominated by small structures) and the dashed line to structures larger than 200 Mm^2.

methods independently, and then looks at the correspondence between the 2 methods using the results of Sect. 2.6.

3.2. Dynamics versus structure size and magnetic field

3.2.1. Feature tracking

Figure 7 shows the variation in residual rotation rates and residual meridional circulation with feature size A_t, flux $_\mathrm{t}$, and maximum magnetic field in the structures Bm_t. We observe that the rotation rate of larger structures is smaller than for small features down to 40 Mm^2, i.e. network features. Such a trend has already been observed many times (see e.g. Howard 1990, 1992) for active regions, but this is the first time that this has been observed for network features down to 40 Mm^2. The slope is more pronounced for A_t above ~700 Mm^2 ($_\mathrm{t} \sim 8\times10^{20}$ Mx and $Bm_\mathrm{t} \sim$ 500 G), and these 3 values correspond reasonably well (Fig. 4). Between 40 and 700 Mm^2, there is also a decrease in rotation rate with increasing size, but the slope is less pronounced; the curve even becomes a plateau for $_\mathrm{t}$ and Bm_t. For very small features below 40 Mm^2, as well as for low $_\mathrm{t}$ and low Bm_t, the rotation rate is again significantly smaller. Note that even when using a different reference rotation rate when performing the tracking, this result remains the same.

The meridional circulation residuals, on the other hand, are found to decrease from 10 Mm^2 to large active regions; i.e. large structures have a less poleward motion. Note that values around the equator were suppressed for this computation. The amplitude of the variation is much smaller than for the rotation rate.

It is important to keep in mind that a given size range may cover very different types of magnetic structures. For example, in Meunier (2003), it was found that in the range 2000−7000 Mm^2, 2 populations were present with distinct distributions of Bm_t, some with Bm_t above 900 G corresponding to structures including spots while the others did not. The population with large Bm_t also had a much larger fractal dimension than the other one. Table 2 shows the dynamics for these two populations; the structures with spots rotate slower and exhibit less poleward motion than the other structures of similar size.

Structures of different sizes also represent a different evolutionary state. Emerging active regions, for example, are growing regions. Later they decay into smaller structures down to network features below 80 Mm^2. Therefore the largest structures are probably relatively old active regions, while very small structures like network features are older remnants. Structure of intermediary sizes probably cover a large range in age, however.

3.2.2. Correlation tracking

Figure 8 shows variation in the rotation rate and residual meridional circulation with average magnetic field $|B_\mathrm{c}|$, with the number of pixels $N\mathrm{pix}_\mathrm{c}$ above 40 G in the box, as well as with Bm_c. We observe a strong decrease of the residual rotation rate for $N\mathrm{pix}_\mathrm{c}$ above 1000 pix, $|B_\mathrm{c}|$ above 35 G and Bm_c above 700 G. These 3 levels correspond well to each other in Fig. 4. Starting from this level and going down to weaker magnetic field regions, we observe a decrease in the rotation rate residual, followed again by an increase up to $N\mathrm{pix}_\mathrm{c} \sim$ 20 pix, $|B_\mathrm{c}| \sim$ 9 G and $Bm_\mathrm{c} \sim$ 80 G, and then again a decrease.

The meridional circulation residuals are decreasing for increasing $N\mathrm{pix}_\mathrm{c}$, $|B_\mathrm{c}|$, and Bm_c, which means that weak field areas have a more poleward motion. The decrease is monotonous for $N\mathrm{pix}_\mathrm{c}$, but there is a tendency to increase again for $|B_\mathrm{c}|$ above 100 G. A peak is also superimposed for $Bm_\mathrm{c} \sim$ 400 G, due to the converging pattern observed in Fig. 5. Furthermore, when looking in detail at the meridional circulation, it is found that the decrease with increasing $|B_\mathrm{c}|$ is observed everywhere except close to the equator (at latitudes ± 7.68°), where the gradient is reversed for $|B_\mathrm{c}|$ lower than 10 G. This is consistent with the negative gradient observed by Komm et al. (2004) in a shallow layer (down to 1 Mm) close to the equator in the Northern hemisphere. However they did not observe it in the Southern hemisphere.

Figure 9 also shows the meridional circulation versus latitude for various magnetic field domains. It confirms the results of Meunier (1999), where the pattern of converging flows (with respect to the average) is observed only for strong field regions, i.e. active regions with $|B_\mathrm{c}|$ in the range 10−50 G. Also, the variation with magnetic field is very strong at high latitude, with a much stronger poleward motion for weak field areas.

3.2.3. Comparison of FT and CT

For active regions, the most striking difference is for the meridional circulation, which exhibits very different patterns. However, one should keep in mind that with the CT, one box may see only a part of the active region, while the FT sees the whole structure. Therefore, the CT can probe more local flows in the case of very active regions compared to the CT; if there

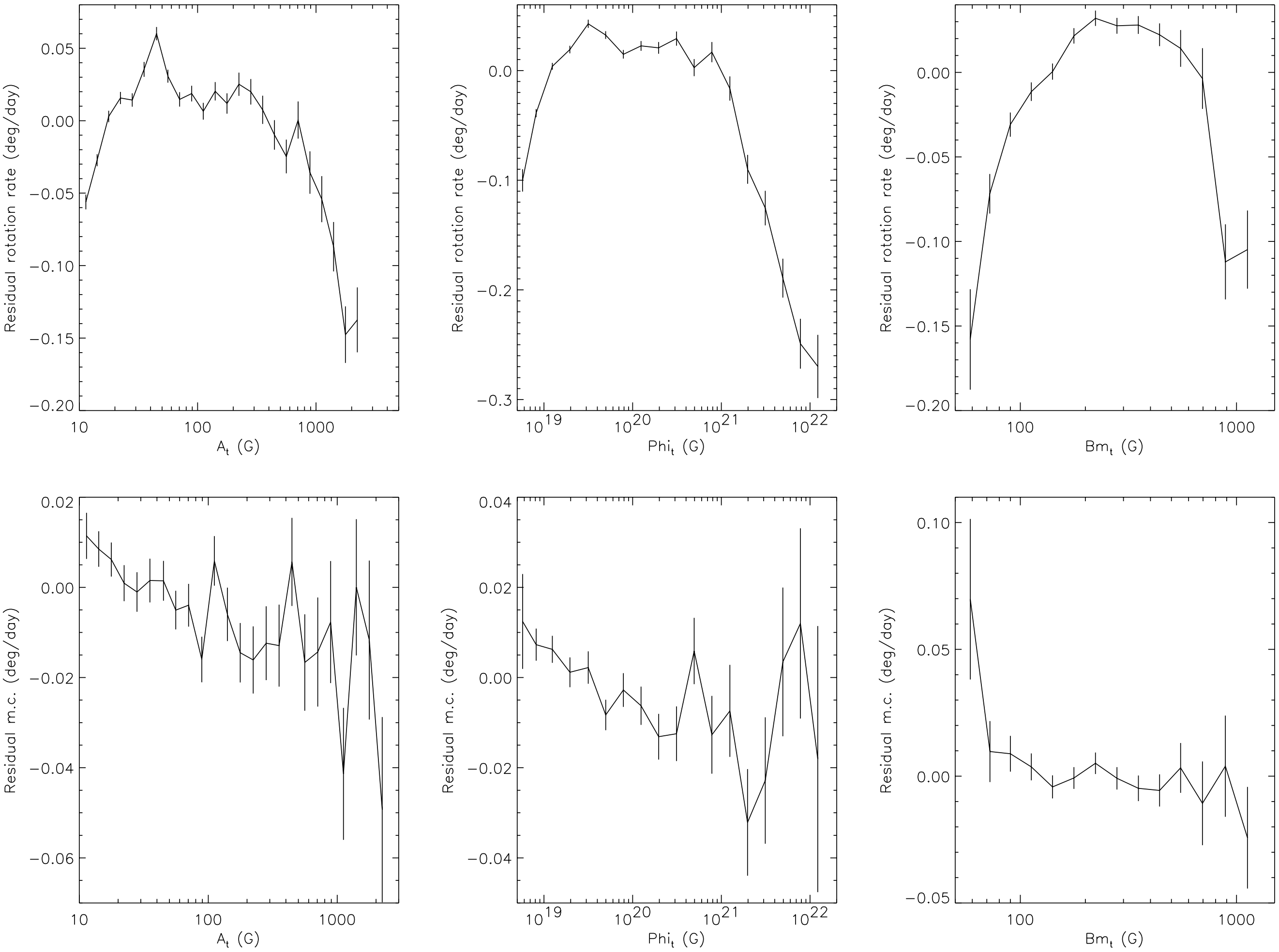

Fig. 7. *Top*: FT rotation residuals; *Bottom*: FT meridional circulation residuals. *Left*: versus A_{t}. *Middle*: versus $_{\mathrm{t}}$. *Right*: versus Bm_{t}.

Table 2. FT residuals in deg/day for A in the range 2000–7000 Mm^2.

Dynamics	B 900 G	B 900 G
Rotation rate	−0.153 ± 0.023	−0.232 ± 0.015
Meridional circulation	0.018 ± 0.021	−0.002 ± 0.014

are convergent flows inside a region, the CT will see them but not the FT. Also, CT is more sensitive to the strongest fields in the box, while the FT defines the region using only its contour, so CT will be more influenced by spot behavior for example.

The much smaller meridional circulation in quiet regions for FT compared to CT is probably real as well. In fact, if the FT method were biased toward lower values (the “reference” meridional circulation for the tracking is 0), it would also underestimate the equatorial meridional circulation of ∼−0.05 deg/day, which is not the case. Therefore it must represent a difference in meridional circulation for the individual magnetic structures and for the large scale pattern they constitute (such as supergranulation or organization on a larger scale).

Correspondence between the two methods can be established both ways. First, for a given correlation box, one can look at the average dynamics of the features inside that box. When a certain type of correlation box is selected, for example with $|B_{\mathrm{c}}|$ in a certain range, the list of FT features corresponding to these boxes can be selected and the variation with size, for example, can be compared to the average one (not very different). Second, to each feature one can attribute the characteristic of the CT box in which this feature is present, including the dynamics and the magnetic field level. Such an analysis shows that FT and CT results are actually different: they are shifted despite the similarity between the curves in Figs. 7 and 8. This analysis confirms that the differences are real and not due to a simple selection effect for example; individual magnetic structures have different dynamics from their collective behavior organized in the magnetic network.

Finally, Table 3 shows the coefficients from a Legendre polynomial fit on the rotation rates versus latitude for various selections. Rotation is more differential for CT than for FT (both at low and high latitudes), and it is also more differential for weak field areas and small features. The asymmetry between the 2 hemispheres is very small and, in fact, almost insignificant for FT. For CT, a smaller rotation in the Northern hemisphere is found (mostly for low latitudes), which seems to be present mostly for weak field regions.

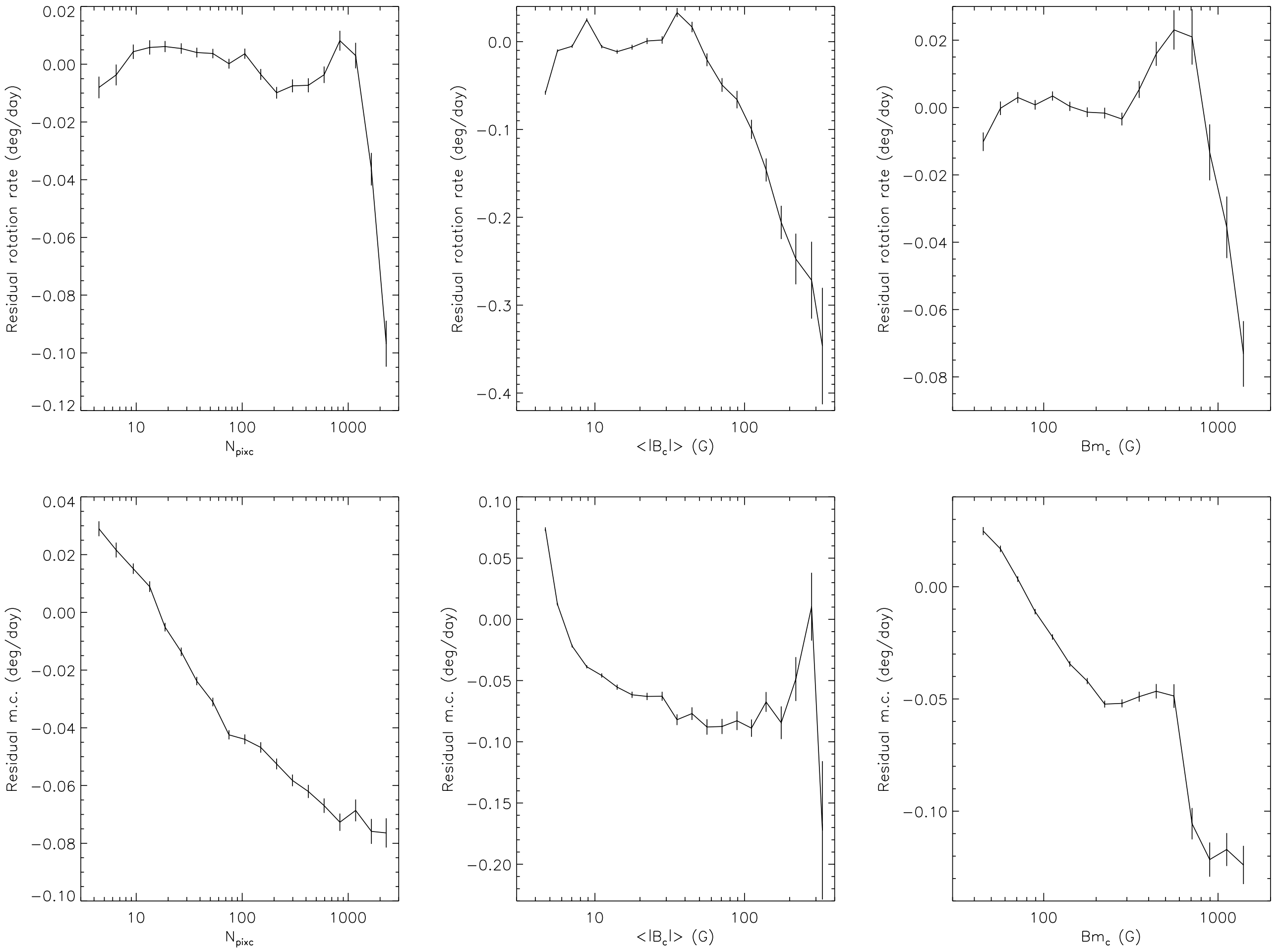

Fig. 8. *Top*: CT rotation residuals. *Bottom*: meridional circulation residuals. *Left*: versus $N\mathrm{pix}_\mathrm{c}$. *Middle*: versus $|B_\mathrm{c}|$. *Right*: versus Bm_c.

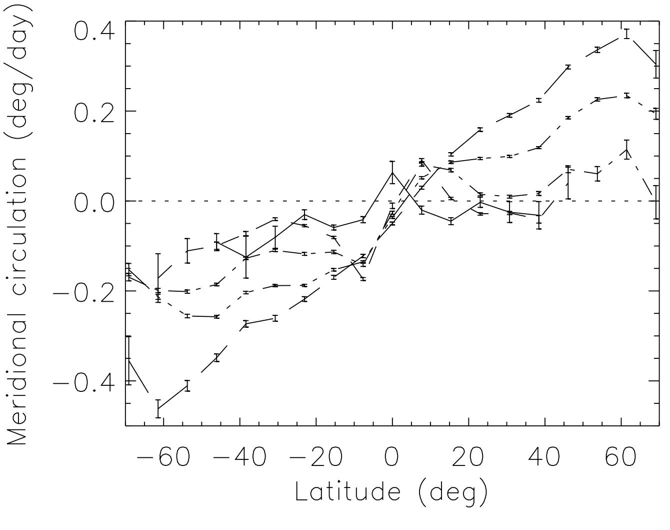

Fig. 9. CT meridional circulation residuals versus latitude for $|B_\mathrm{c}|$ below 5 G (long dashed), in the range 5–7 G (dot-dot-dot-dashed line), in the range 7–10 G (dot-dashed line), in the range 10–50 G (dashed line), and above 50 G (solid line).

3.3. Weak field dynamics and proximity to active regions

It is interesting to check whether the small magnetic structures behave differently depending on their position with respect to active regions. For example, do small structures inside an active region have a meridional circulation such as that obtaind by the CT in these regions? To study this aspect, the dynamics of these structures is examined depending on their distance to large structures, as well as the dynamics for structures inside or outside a cluster of large structures.

3.3.1. Dynamics and distance to large structures

For each small structure, its distance to the closest large structure (with A_t 500 Mm^2) is computed. The dynamics of these small structures versus this distance can then be studied for various size ranges. The results are shown in Figs. 10 and 11.

Figure 10 shows the residual rotation rate and meridional circulation versus latitude for A_t 40 Mm^2 in two cases: structures very close to a large structure or far away from them. It shows that in active latitude areas, network features farther from active regions are rotating faster than similar features close to active regions (or inside it). Their meridional circulations are hardly different, however. For small structures close to active regions, no motion is observed like that of active regions with CT. The meridional circulation for structures far from active regions is more poleward above 20° and less poleward close to the equator, compared to structure close to active

Table 3. FT and CT coefficients from the Legendre polynomial fit performed on rotation rates versus latitude (such as in Fig. 4): A_1 and A_3 corresponds to the North-South asymmetry (respectively at low and high latitudes), and A_2 and A_4 corresponds to the differentiality of the rotation (at low and high latitudes respectively).

Selection	A_1	A_3
FT	0.013 ± 0.012	0.028 ± 0.012
FT (A 80 Mm^2)	−0.001 ± 0.02	0.01 ± 0.01
FT (A 500 Mm^2)	0.16 ± 0.11	0.14 ± 0.09
CT	−0.008 ± 0.002	−0.001 ± 0.002
CT ($\|B_c\|$ 10 G)	−0.007 ± 0.002	0.002 ± 0.003
CT ($\|B_c\|$ 10 G)	0.007 ± 0.012	0.009 ± 0.012
Selection	**A_2**	**A_4**
FT	−2.21 ± 0.03	−0.34 ± 0.02
FT (A 80 Mm^2)	−2.24 ± 0.03	−0.37 ± 0.02
FT (A 500 Mm^2)	−1.93 ± 0.34	−0.17 ± 0.19
CT	−2.568 ± 0.003	−0.552 ± 0.003
CT ($\|B_c\|$ 10 G)	−2.573 ± 0.003	−0.560 ± 0.003
CT ($\|B_c\|$ 10 G)	−2.289 ± 0.025	−0.360 ± 0.016

regions. These structures far from active regions also tend to exhibit a convergence pattern as for active regions.

Figure 11 shows the variation of the residual rotation rate versus the distance for different sizes. The difference is mostly seen for features smaller than 40 Mm^2 and only up to a few degrees from the large structures, which confirms the previous result, with increasing rotation rates as the distance from the region increases. The influence of the active region remains closeby; note that 3° corresponds to 36 Mm, i.e. like a large supergranule.

3.3.2. Cluster analysis

Large structures with A_t above 200 Mm^2 are grouped inside clusters by using a cluster analysis technique. The number of neighbors is computed within a given distance (taken as 19°, typical of the largest seperation in a bipolar region, from Howard 1992). If there are more than 2 neighbors, they are associated with the same cluster. This analysis over the whole data set, which concerns 81 306 larger structures, leads to 6843 clusters, with an average of 8.5 large structures per cluster, and to 71% of the large structures inside this structure. This percentage increases slightly with size, up to 80% for the largest ones. Note that Pojoga & Cudrik (2002) found that 40 to 50% of the active regions are inside clusters, when taking into account only those that would live more than 4 rotations. We find a slightly larger percentage here, but this is not surprising because we consider all structures. Using a distance criterion of 5° (derived from Fig. 11), smaller structures can be associated to these clusters as well. We find 11.6 small structures inside these clusters. This percentage also increases from ~10% (A_t ~ 10 Mm^2) to 24% (A_t ~ 200 Mm^2).

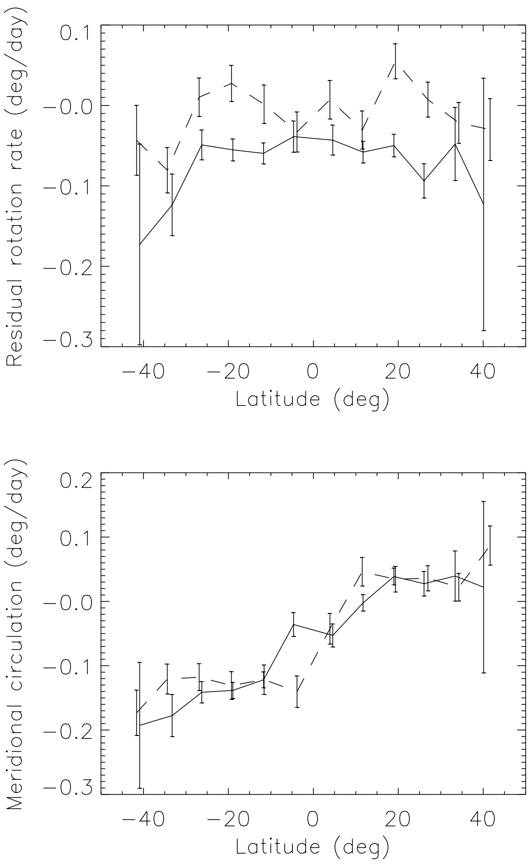

Fig. 10. FT residual rotation rates versus latitude for small distance to active region (below 5°, solid) and large distances (above 40°, dashed), for A_t below 40 Mm^2.

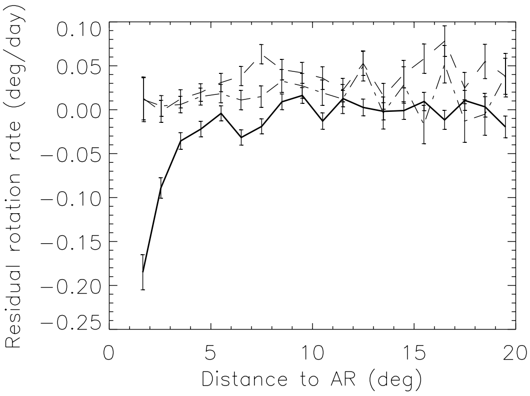

Fig. 11. FT residual rotation rate versus the distance to active regions, for A_t below 40 Mm^2 (solid thick line), in the range 40–80 Mm^2 (dashed line) and in the range 80–200 Mm^2 (dotted-dashed line).

Figure 12 confirms the faster rotation of small structures outside active regions defined here as clusters. This is seen only for small features (still significant when considering A_t 200 Mm^2), not for larger ones. There may be a tendency to a less poleward meridional circulation of small structures outside clusters, but this is observed only in the southern hemisphere.

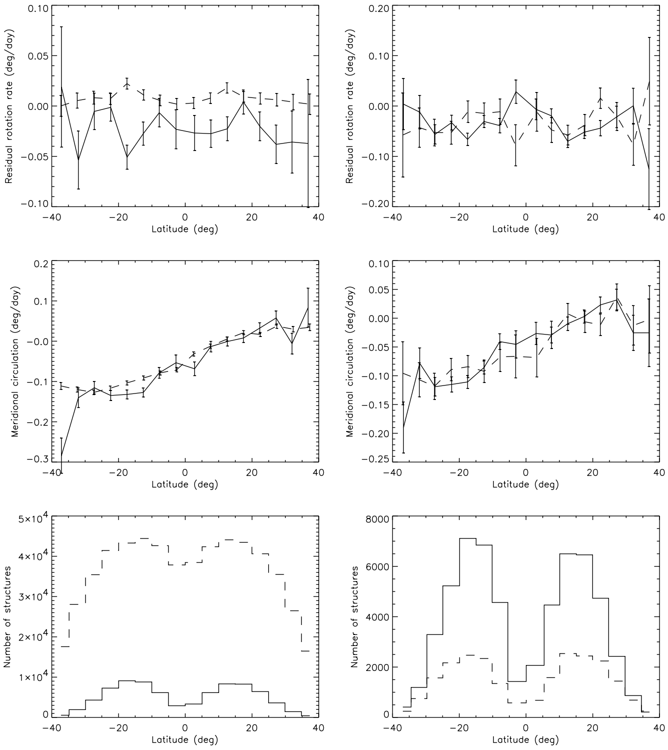

Fig. 12. FT residual rotation rates (*top*), FT meridional circulation (*middle*), and number of structures (*bottom*) versus latitude for structures inside a cluster (solid line) and outside (dashed line). *Left*: A_t 200 Mm^2; *Right*: A_t 200 Mm^2.

4. Discussion and conclusion

In this Paper I have studied the large scale dynamics of magnetic structures down to the network using a homogeneous data set covering most of a solar cycle. The two complentary methods (CT over a 93 Mm scale and FT) should allow the anchoring depths of these features to be constrained.

The first new result is that CT provides a smaller rotation rate and larger meridional circulation than FT at all latitudes and almost all sizes. The rotation of structures observed with CT is likely to be related to supergranulation, but it is puzzling to see that the supergranular rotation rate is much larger (Duvall 1980; Snodgrass & Ulrich 1990; Beck & Schou 2000) and is in fact closer to the FT results than to the CT results (see Table 1). The meridional circulation in active areas using CT also exhibits a convergent pattern already observed previously (e.g. Meunier 1999; Haber et al. 2003; Zhao & Kosovichev 2004). However, the small features associated with these active regions do not exhibit the converging pattern, but do exhibit a smaller rotation rate, as for large features. Furthermore, FT structures exhibit a small divergent pattern with respect to the latitude of the mean activity belt around active regions.

Given the increase in rotation rate observed by helioseismology as one goes inward (e.g. Schou et al. 1998, for example) down to ~35−50 Mm, it is tempting to attribute a deeper anchoring to individual network features than to the pattern formed by these features. The decreasing meridional circulation usually observed by time-distance analysis (Zhao & Kosovichev 2004) or ring-diagram techniques (Haber et al. 2002; Komm et al. 2004) as one goes inward is consistent with this preliminary interpretation.

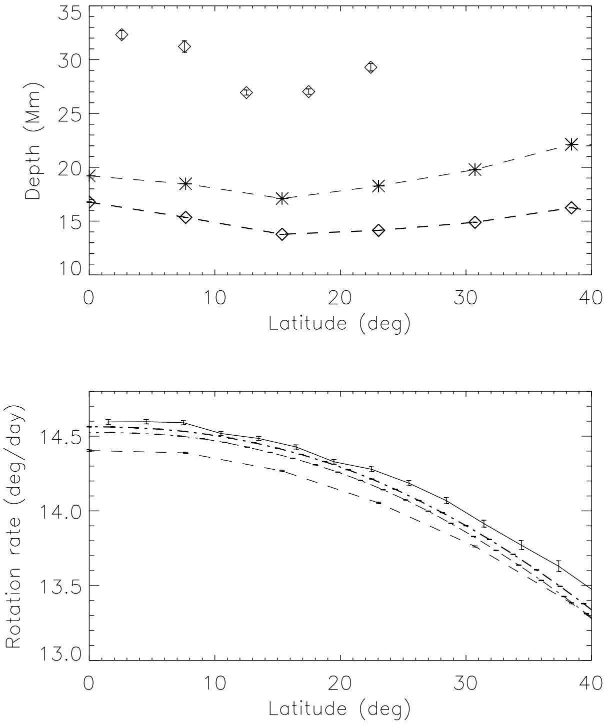

Fig. 13. *Top*: depth corresponding to FT rotation rate (diamonds with no line: GONG) and to the CT rotation rate (diamonds with thick dashed line: GONG; stars with thin dashed line: MDI) versus latitude. The depths correspond to the first intersection with the internal rotation rate from the surface. Internal rotation rates from helioseismology (MDI and GONG) are courtesy of R. Howe. Note that above ~25°, no FT points for GONG are available since the FT rotation rate is larger than any internal rotation rate at that latitude. No FT point for MDI is available either, for the same reason. *Bottom*: rotation rate versus latitude for FT (solid line, A in the range 40–50 Mm^2), for CT (dashed line, $|B_c|$ in the range 8–9 G), MDI (thin dotted-dashed line, maximum rate in the bulk of the convection zone), and GONG (thick dotted-dashed line, maximum rate in the bulk of the convection zone).

An attempt to attribute an anchoring depth to these structures is shown in Fig. 13. Internal rotation rates have been provided by R. Howe for MDI (OLA inversion) and GONG (RLS inversion). We concentrate on the results obtained below latitude 40°, because both data sets provide very different internal rotation rates at high latitudes (Schou et al. 2002). The FT and CT results are symmetrized with respect to the equator for this discussion. When using the MDI rotation rate, no anchoring depth can be attributed to the FT structures because the observed FT rate is too low; it is possible to attribute one for GONG, but only for the lowest latitudes (27−33 Mm). The CT rates beeing smaller, the attribution is easier to make, with depth in the range 13−17 Mm for MDI and 18−22 Mm for GONG. However, the impossibility of making the association for the FT rotation rates casts some doubt on the interpretation in term of anchoring. Figure 13 also shows the maximum rotation rate in the convection zone as a function of latitude. This rate is compared to the rate for FT structures that are rotating the fastest from (Fig. 7) and for the corresponding CT boxes from Fig. 8, and it also shows that most small FT structures rotate faster than any layer in the convection zone.

Another problem arises from the further constraint that can be derived from the observation of meridional circulation. Some features rotating with the same rate have a different meridonal circulation, for example with $|B_c|$ around 4 G and 90 G, or features with $A \sim 10$ Mm^2 and $\sim$1000 Mm^2. So this problem also concerns CT, despite the fact that Fig. 13 does not show any problem for that method. This is illustrated in Fig. 14, where a variation of the meridional circulation with depth can be deduced from the variation of meridional circulation with $|B_c|$, the variation of rotation rate with $|B_c|$, and the correspondence between our rotation rate and the internal rotation rate from helioseismology. This figure (bottom) shows clearly that the interpretation in terms of anchoring is not reasonable. If a structure is anchored at a certain depth so that its rotation rate is that of the layer in which it is anchored, we expect it to have the meridional circulation of that layer as well. Of course, a possibility would be that these two groups of structures are anchored in two different layers with a similar rotation rate (but a different meridional circulation). Helioseismology indeed shows that below 35−50 Mm the internal rotation rate is decreasing again, so some of these features could be anchored above that layer, and the other below. However, it is quite unlikely that they could be anchored that deep. Indeed, recent results by Hiremath (2004) and Javaraiah & Gokhale (1997) show that old spots always rotates in such a way that they are likely to be anchored above that turning point. Furthermore, it is likely that the rotation rates observed in this paper are related to supergranular flows, since the formation of network structures is associated with strong downflows on the edges of supergranules. However, it has been observed that the supergranulation pattern was probably present in a shallow layer only; for example, November (1994) found horizontal velocities in supergranules down to 2 Mm only, with plumes associated with the strong downflows (therefore with the magnetic network) reaching 7 Mm. There is currently no evidence from helioseismology that a strong increase is present, followed by a decrease in the rotation rate close to the surface. Such a result has been observed by González Hernández & Patron (2000), but they have not been observed in more recent works and are probably an artefact of the method (González Hernández, private communication).

The similarities in the curves of the rotation rate versus A (FT) and versus $|B|$ (CT) led us to think that they are correlated, however. Note that the increase for the weakest regions may be related to the recent results of Zhao et al. (2004), who have recently found that the surface rotation rate was higher for location with larger magnetic field up to 600 G. The amplitude is on the order of 70 m/s over these 600 G. However, this does not necessarily represent the velocities of the magnetic features because of the filling factor smaller than 1. Here we do observe this increase (15 m/s) for features with size up to 40 Mm^2, corresponding to a flux of 3×10^{19} Mx, which corresponds to an average magnetic field of 75 G, and maximum magnetic field of 200 G. For such an average magnetic field, Zhao et al. (2004) find a residual rotation rate around 17−18 m/s; therefore our results are quite consistent with their rotation rate increase up to 200 G. Between 200 and 600 G, we would expect to see an increase above 40 Mm^2 (or 10 G for CT), if this was due to a horizontal motion of the magnetic structures, which we do not see. Their errorbars above 200 G are quite large, however.

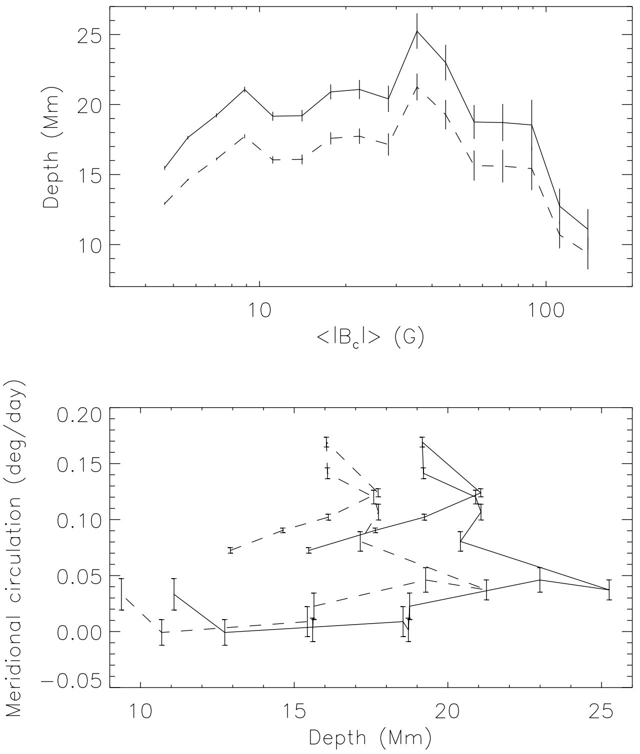

Fig. 14. *Top*: depth versus $|B_c|$ deduced from the CT rotation rate versus $|B_c|$, at latitude ±7.68° (first intersection with internal rotation rate from the surface), for MDI (solid line) and GONG (dashed line). Internal rotation rates from helioseismology (MDI and GONG) are courtesy of R. Howe. *Bottom*: meridional circulation versus depth deduced from the top curve and from the meridional circulation versus nedit $|B_c|$, at latitude ±7.68°.

Understanding these variations with magnetic level and their inconsistency with helioseismology should provide some clues about the origin of the magnetic network. An additional constraint is provided by the cluster analysis performed in this paper, which allows the dynamics of small features inside active regions to be compared with those of large structures in these regions, and with similar features far from active regions. I find that the smallest network features (below 40 Mm^2) tend to rotate slower than the others when they are located within 5° of a large structure, but their rotation rate is not, however, as small as that of large structures. Their meridional circulation is independent of their location, as they do not exhibit this converging pattern when close to active regions. This shows that the smallest features belonging to active regions may be slightly influenced by the large structure behavior, as they would if they were resulting from their decay, but they do not behave in the same way. It is, however, too early to establish the anchoring depth of the FT and CT structures, either in absolute value or with respect to each other.

It is difficult to establish a complete comparison with all helioseismic results. First, the different analyses (time distance, ring diagrams) exhibit different results for various reasons: sensitivity to different layers for example, see also Hindman et al. (2004). However it is already possible to conclude that the anchoring of network structures at various depths cannot explain all characteristics, as their rotation rates and meridional circulation are not compatible with results from helioseismology. This does not mean that they cannot be anchored at a certain depth, but it is very likely that additional processes play a role in their dynamics and probably accelerate them. The excess of velocity would be in the range 30−60 m/s if they were anchored in the range 2−7 Mm (75−90 m/s for supergranules). Second, it has been shown (see e.g. Haber et al. 2002; Zhao & Kosovichev 2004) that the meridional circulation seems highly variable; therefore it will be necessary to study its temporal variation in order to go further, an analysis to be presented in a separate paper (Meunier 2005b). The study of the dynamics versus polarities will also provide additional clues (Meunier 2005a).

Acknowledgements. I am very grateful to R. Howe who has provided the internal rotation rates from helioseismic observations (GONG and MDI). I also thank the referee for suggesting the analysis of the flows with respect to the activity belt. SOHO is a mission of international cooperation between the European Space Agency (ESA) and NASA.

References

Antonucci, E., Azzarelli, L., Casalini, P., Cerri, S., & Denoth, F. 1979, Sol. Phys., 63, 17
Brajša, R., Wöhl, H., Vršnak, B., et al. 2004, A&A, 414, 707
Beck, J. G. 2000, Sol. Phys., 191, 47
Beck, J. G., & Schou, J. 2000, Sol. Phys., 193, 333
D'Silva, & Howard, R. 1994, Sol. Phys., 151, 213
Duvall, T. L., Jr. 1980, Sol. Phys., 66, 213
Giles, P. 1999, Ph.D. Thesis, Stanford University
González Hernández, I., & Patron, J. 2000, Sol. Phys., 191, 37
Haber, D. A., Hindman, B. W., & Toomre, J. 2003, in Proc. SOHO 12/GONG+ 2002, Local and Global Helioseismology: The Present and Future, ed. H. Sawaya-Lacoste, 103
Haber, D. A., Hindman, B. W., Toomre, J., et al. 2002, ApJ, 570, 855
Hindman, W. B., Gizon, L., Duvall, T. L., Jr., Haber, D. A., & Toomre, J. 2004, ApJ, 613, 1253
Hiremath, K. M. 2002, A&A, 386, 674
Howard, R. 1990, Sol. Phys., 126, 299
Howard, R. 1991, Sol. Phys., 135, 327
Howard, R. 1992, Sol. Phys., 142, 233
Howard, R. 1996, ARA&A, 34, 75
Javaraiah, J., & Gokhale, M. H. 1997, A&A, 327, 795
Komm, R. W., Howard, R. F., & Harvey, J. W. 1993a, Sol. Phys., 145, 1
Komm, R. W., Howard, R. F., & Harvey, J. W. 1993b, Sol. Phys., 147, 203
Komm, R. W., Corbard, T., Durney, B. R., et al. 2004, ApJ, 605, 554
Meunier, N. 1999, ApJ, 527, 967
Meunier, N. 2003, A&A, 405, 1107
Meunier, N. 2005a, A&A, in press
Meunier, N. 2005b, submitted
Meunier, N., Nesme-Ribes, E., & Grosso, N. 1997a, A&A, 319, 673
Meunier, N., Nesme-Ribes, E., & Collin, B. 1997b, A&A, 319, 683
November, L. J. 1994, Sol. Phys., 154, 1
Pojoda, S., & Cudrik, B. 2002, Sol. Phys., 208, 17
Sivaraman, K. R., & Gokhale, M. H. 2004, Sol. Phys., 220, 209
Snodgrass, H. B., & Ulrich, R. K. 1990, ApJ, 351, 309
Scherrer, P. H., Bogart, R. S., Bush, R. I., et al. 1995, Sol. Phys., 162, 129
Schou, J., Howe, R., Basu, S., et al. 2002, ApJ, 567, 1234
Strous, L. H. 2000, Sol. Phys., 195, 219
Wöhl, H. 2002, Astr. Notes, 323, 329
Wöhl, H., & Brajša, R. 2001, Sol. Phys., 198, 57
Zhao, J., & Kosovichev, A. G. 2004, ApJ, 603, 776
Zhao, J., Kosovichev, A. G., & Duvall, T. L., Jr. 2004, ApJ, 607, L135

A&A 437, 303–310 (2005)
DOI: 10.1051/0004-6361:20042415

Astronomy
&
Astrophysics

Large-scale dynamics and polarities of magnetic structures

N. Meunier

Laboratoire d'Astrophysique de l'Observatoire Midi-Pyrénées, 57 avenue d'Azereix, BP 826, 65008 Tarbes Cedex, France
e-mail: `meunier@bagn.obs-mip.fr`

Received 23 November 2004 / Accepted 16 February 2005

Abstract. A large data set of MDI magnetograms is studied in order to analyse the dependence of the global dynamics of magnetic structures on their polarity. Two complementary techniques (feature tracking and correlation tracking) are used to determine the differential rotation and meridional circulation. A faster rotation of leading polarity structures is found for active areas, while a faster rotation of following polarity structures is found for weak field areas. However the latter is found only when using correlation tracking: individual small features do not seem to exhibit any difference between leading and following polarities. From correlation tracking, the mixed polarity areas (with a low activity level) do rotate as the following polarity areas. Furthermore, the latter have a more poleward motion when the correlation tracking is used.

Key words. Sun: magnetic fields – Sun: photosphere – Sun: faculae, plages

1. Introduction

A variation of the angular rotation velocity (hereafter rotation rates, in heliographic degrees per day) of plages and sunspots have been previously observed by several authors (see Howard 1996, for a review). However, such a variation with polarity for the magnetic network has not been obtained up to now, probably due to the limited amount of data (Komm et al. 1993a,b; Meunier 1999) or due to the lack of information about the polarities (Meunier et al. 1997). In fact, Meunier (1999) attempted that study, but the errorbars were too large to allow any significant result. Furthermore, the variation of the meridional circulation with polarity has not been studied as well, since this motion is of a much smaller amplitude (two orders of magnitude) and therefore requires an even better data set. The main work is that of Ward (1973), who studied the latitudinal motion of sunspots and its dependence on various characteristics, including polarities. He found a more poleward motion of spots with the following polarity.

This type of analysis is very important in order to understand the emergence of active regions and their decay. Analysis of the magnetic network dynamics in that context should also provide some clues about the decay of active regions into network structures.

The global dynamics (differential rotation and meridional circulation) over a very large data set of MDI magnetograms were studied by Meunier (2005a, hereafter Paper I). Here, I use this data set in order to study the variation of the dynamics with polarity. The data processing and analysis are briefly described in Sect. 2. Section 3 presents the results for differential rotation and Sect. 4 the results for the meridional circulation. The results are discussed in Sect. 5.

2. Data and processing

2.1. MDI data

The data set is a subset of the one used in Paper I for the study of the rotation rate and meridional circulation: I use a data set of 5-min averaged full-disk magnetograms obtained by MDI on SOHO (Scherrer et al. 1995) between June 1997 and April 2004, processed at the 1.8 level. These magnetograms are separated by 96 min or a multiple of 96 min. The polarities of structures or regions (leading or following) will be determined considering that at a given time, all structures obey Hale's law, which is why the data set is slightly reduced compared to Paper I, and it ensures that no structure from the previous cycle is present. The butterfly diagram for these structures is shown in Fig. 1. For Cycle 23, the leading polarity was positive in the Northern hemisphere and negative in the Southern hemisphere.

The noise level in 5-min magnetograms is reduced compared to that of 1-min magnetograms and is of the order of 8 G. An additional source of error comes from the shutter noise, which induces a small random shift of the zero level in the magnetograms. This error has been studied in detail by Liu et al. (2003). One way to estimate this noise level is to compute the distribution of magnetic field values in the image and then to use a gaussian fit on this distribution to compute the offset. This determination will, however, be strongly influenced by the presence of activity, but because filtering this time series with many gaps is not straightforward, it is beyond the scope of this paper. We compared the results when no offset is performed or when a raw offset is applied for the first part of the series (560 days, with low activity level). The influence on the results

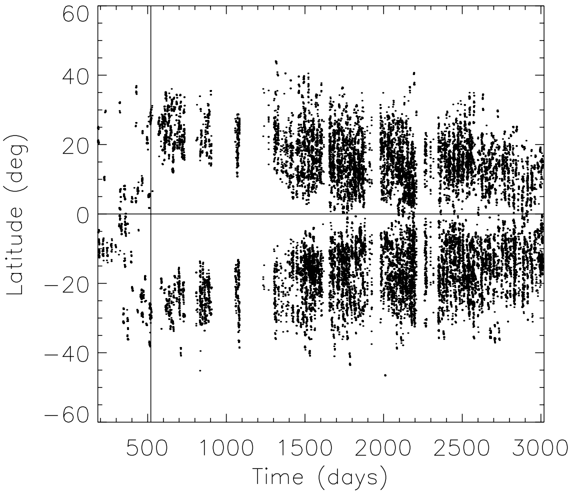

Fig. 1. Butterfly diagram of the structures larger than 500 Mm^2 for the whole data set. Day 1 corresponds to January 1, 1996. The vertical solid line at day 520 (June 1997) corresponds to the limit considered in this paper.

is much smaller than the errorbars, so that we consider that the effect can be neglected and the results presented in this paper are obtained with no offset correction.

2.2. Data processing

The data processing here is identical to that of Paper I. Both feature tracking (hereafter FT) and correlation tracking (hereafter CT) are used. I refer to Paper I for all details and here indicate only the most important points (see also Meunier 1999). Feature tracking is done by identifying magnetic structures above a threshold of 40 G (separately for the 2 polarities), which is well above the noise, and then by following them on pairs of magnetograms (separated by 96 minutes). Correlation tracking is done by cross-correlating boxes of size 7.68×7.68 deg^2 (93×93 Mm^2) on these same pairs of magnetograms after remapping. Various quantities such as the magnetic field, maximum magnetic field, flux, and size of the structures are computed. Some relevant correspondences between variables are discussed in Sect. 2.3 (see also Paper I).

Note that there are more negative polarity boxes/structures than positive polarity. Because this is seen in both hemispheres (already noted in Meunier 2003) it will not change the results reported here qualitatively; however, if that is an instrumental bias, it could in theory create artificial asymmetries between hemispheres, such as a difference between polarities larger in one hemisphere compared to the other.

2.3. Correspondence between sizes and magnetic fields

The polarity of FT structures is easily defined since for one structure the polarity of all pixels is the same. The correspondences between the size A_t, magnetic flux $_t$, and the maximum of the absolute magnetic field Bm_t are shown in Paper I. It is important to keep in mind that Bm_t in structures larger than 500 Mm^2 may be saturating due to a bias in MDI data. Except for this limitation, the non-linearity studied by Berger & Lites (2003) does not affect the results presented here.

Polarity in CT boxes is less straightforward, because in mixed polarity regions there are magnetic features of both polarities inside a given box. To determine the polarity in a given box, I compute the average (signed) magnetic field B_c in that box. Roughly, $B_\mathrm{c} \sim 0$ means a mixed polarity area, and B_c close to $|B_\mathrm{c}|$ means a unipolar area with polarity of one sign or the other. As a consequence, the significance of B_c depends on the activity level as well, and it will be useful in the following to use the variable $B_\mathrm{c} / |B_\mathrm{c}|$. This is illustrated in Fig. 2. The variation in behavior of B_c for various $|B_\mathrm{c}|$ domains is also illustrated in Fig. 3. In the range 9–12 G, for example, the 3 components are clearly visible with the mixed polarity component centered on 0, and the 2 unipolar components centered on ±6 G.

Because of the noise level, $|B_\mathrm{c}|$ is slightly overestimated, and the effect is larger for weak magnetic regions; B_c is not affected significantly however. As a consequence, the ratios $B_\mathrm{c} / |B_\mathrm{c}|$ are also slightly underestimated. Note that $B_\mathrm{c} / |B_\mathrm{c}|$ close to ±1 are usually for very active areas.

3. Rotation rates

3.1. Correlation tracking

Figure 4 shows the variation of the CT residual rotation rates versus B_c separately for the two hemispheres. It shows that for $| B_\mathrm{c} |$ larger than 20 G, the areas of following polarity are rotating slower than that of leading polarity. Below that threshold, the opposite is observed, as the areas of following polarity are rotating faster. Note that here small B_c zones correspond either to areas of mixed polarity with a large active level or to all kinds of weak field regions.

The plot of these residuals versus $B_\mathrm{c} / |B_\mathrm{c}|$ (Fig. 5) confirms that for weak fields the following polarity is rotating faster. In fact, on that plot, the strong activity levels are present for all ratios, and because there are many more weak field areas, they are dominating the data set. This is why this plot does not show the fastest rotation of leading polarities for strong field regions. One should also note that the plots are not symmetrical with respect to $B_\mathrm{c} = 0$. For example in the Northern hemisphere, the curve is quite flat for all small positive ratios, but much steeper for a negative ratio. Another way to see it is that the leading polarity areas exhibit a quite constant rotation rate residual over the whole range of ratios, while the following polarity areas exhibit strong variation, with a slower rotation rate for mixed polarity areas as well as unipolar regions. Intermediate areas rotate faster by 0.05 deg/day (7 m/s at the equator).

To better understand the mixing of $|B_\mathrm{c}|$ and $B_\mathrm{c} / |B_\mathrm{c}|$, Fig. 5 also shows the variation of $|B_\mathrm{c}|$ with $B_\mathrm{c} / |B_\mathrm{c}|$. The pattern seen at the top of Fig. 5 is mostly present up to $Npix_\mathrm{c}$ around 600, that is, a 15% coverage of the boxes by fields above 40 G. This corresponds well to the 20 G level (see Paper I, Fig. 3). Note that the following polarity residuals are maximum

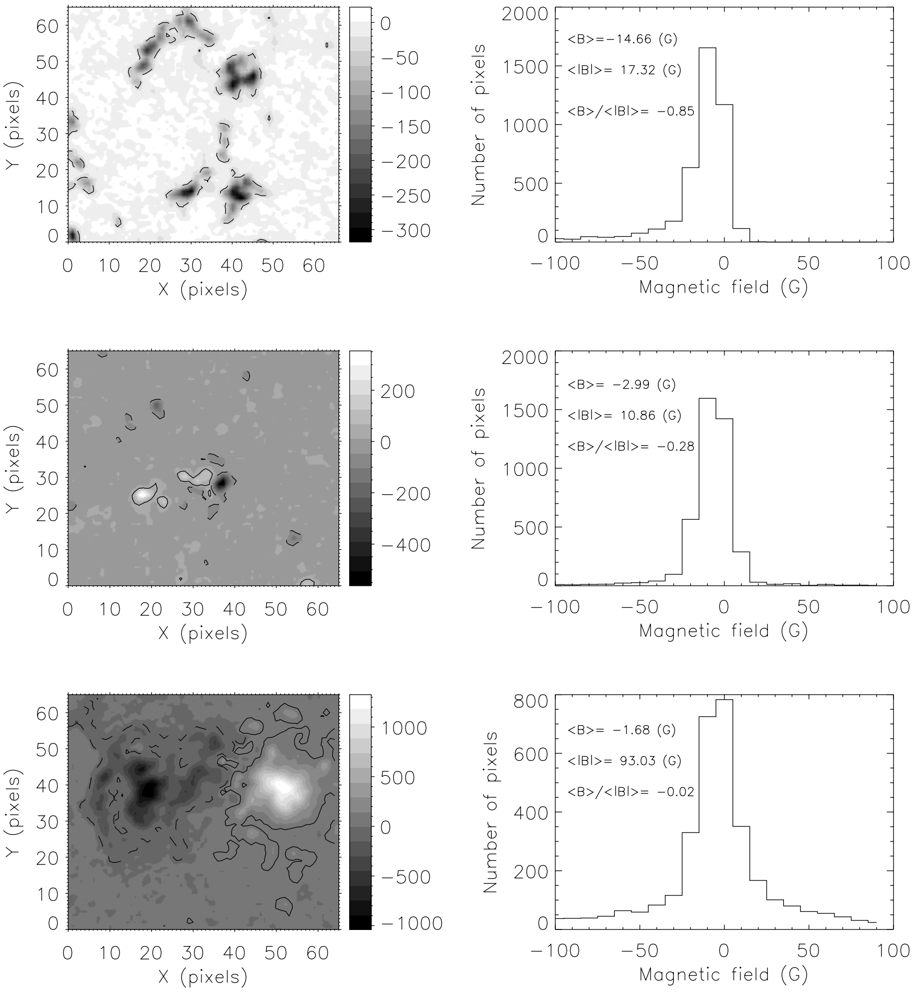

Fig. 2. *Left*: 3 examples of CT boxes, with the 40 G level outlined (threshold used in the FT analysis), in solid lines for positive magnetic fields, and dashed lines for negative magnetic fields. *Right*: distribution of the corresponding magnetic field values in these areas, with an indication of B_c , $|B_c|$, B_c / $|B_c|$.

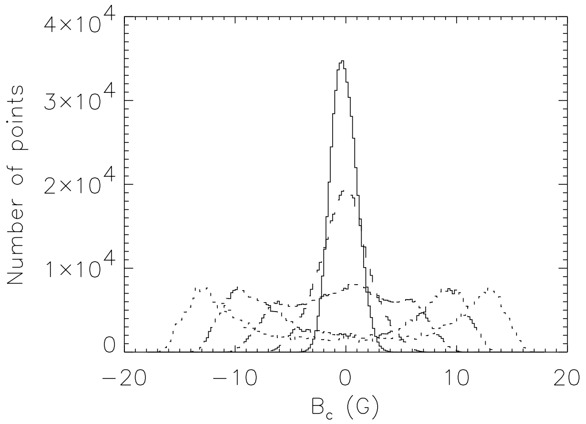

Fig. 3. Distribution of B_c for $|B_c|$ in the range 3–6 G (solid), 6–9 G (dashed), 9–12 G (dotted-dashed), 12–15 G (dotted).

for | B_c / $|B_c|$ | ~ 0.5, which is also where the distribution of the number of points is changing its slope (bottom of Fig. 5).

Figure 6 shows the variation of residual rotation rates for the two polarities and the two hemispheres separately, as a function of $|B_c|$ and Bm_c. For $|B_c|$ above ~20 G and Bm_c above ~500 G, areas of leading polarity are again rotating faster than areas of following polarity as in Fig. 4. Below, it is the opposite again and is quite significant over a wide range of activity levels. For very small $|B_c|$, the difference may disappear, however. In order to make a better link with Fig. 4, Fig. 7 shows the residual rotation rates versus latitude for one of the domains displayed in Fig. 3, i.e. 9–12 G. Each curve represents one of the 3 components. It confirms previous results concerning the rotation of areas of following and leading polarity in weak field regions. It also shows that areas of mixed polarity are rotating at a rate similar to that of the following polarity. There is, however, a strong asymmetry between hemispheres at high latitudes.

3.2. Feature tracking

Figure 8 shows variation in the residual rotation rates versus feature size, magnetic flux, and maximum magnetic fields, and does so separately for the two polarities and the two hemispheres for the FT method. At large scales, features with the leading polarity are rotating faster than those with the

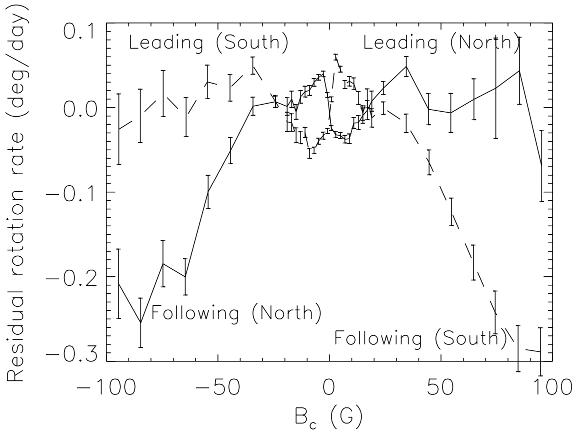

Fig. 4. CT residual rotation rates versus B_c for the Northern hemisphere (solid line) and Southern hemisphere (dashed line).

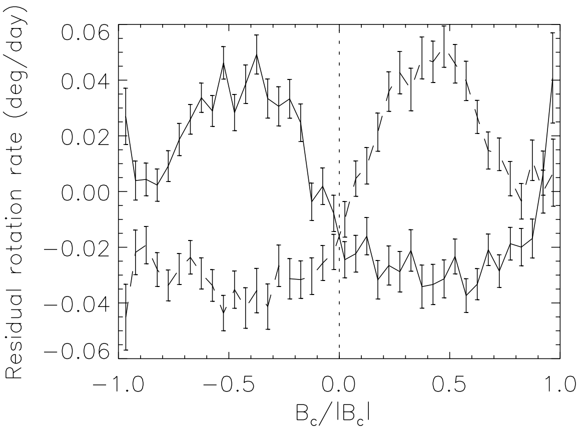

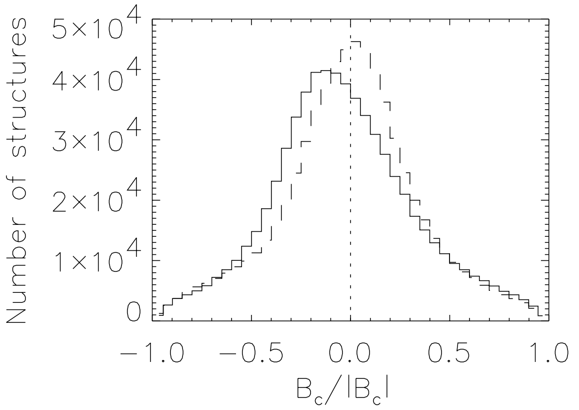

Fig. 5. *Top*: CT residual rotation rates versus B_c / $|B_\mathrm{c}|$ for the Northern hemisphere (solid line) and Southern hemisphere (dashed line). *Bottom*: same for the number of boxes versus B_c / $|B_\mathrm{c}|$.

following polarity, similar to what is observed with the CT method in Fig. 6.

However, below this threshold of a few hundred Mm^2 (as well as a flux of ~2×10^{20} Mx, and a maximum field of ~400 G), no difference between structures of following and leading polarities is observed, at the level of our errorbars (down to 1 m/s in Table 1), as is seen with the CT method. Furthermore, if one selects boxes in the range 9–12 G for example (for which the difference was quite large), and then studies the dynamics of the FT structures present inside these boxes, no reversal is seen either, as shown in Table 1. An attempt was made to identify small bipoles, which led to very few structures; and they did not exhibit a different behavior between leading and following polarities either.

4. Meridional circulation

4.1. Correlation tracking

As for Figs. 4 and 5, Fig. 9 exhibits the residual meridional circulation versus B_c and B_c / $|B_\mathrm{c}|$ separately for the two hemispheres. Remember that a positive residual means a more poleward motion than the average in that latitude band. These two plots show several important characteristics. On the first plot, in both hemispheres areas with following polarity have a more poleward motion than areas with leading polarity. This is mostly seen on the plot versus B_c . The plot versus B_c / $|B_\mathrm{c}|$ shows that mixed polarity regions move more poleward than the unipolar areas, which is probably mostly the case for weak field areas only, because the corresponding peak on the plot versus B_c is very narrow (a few Gauss). This is also consistent with the larger poleward meridional circulation observed for weaker fields in Paper I. As for the rotation rate plot in the previous section, we observe on the plot versus B_c / $|B_\mathrm{c}|$ an asymmetry close to mixed polarity areas (ratio in the range –0.2 to 0.2) again with the following polarity area moving more poleward, but only for the Southern hemisphere.

In Fig. 10, the residual meridional circulation versus $|B_\mathrm{c}|$ and Bm_c shows that for strong field regions, the area of following polarity are moving more poleward, which is true in both hemispheres down to $|B_\mathrm{c}|$ ~ 20 G and Bm_c ~ 600 G. Below that it is more complex, as the following part also seems to be moving more poleward for weak field areas (as in Fig. 9, bottom), but only in the Southern hemisphere. It is the opposite in the Northern hemisphere.

Figure 11 shows the residual meridional circulation versus latitude for one of the domains displayed in Fig. 3, i.e. 9–12 G. Each curve represents one of the 3 components, as in Fig. 7 for the residual rotation rate. For latitudes smaller than 20°, the mixed polarity areas tend to move more poleward than the others, and areas of leading polarity move more poleward than areas of following polarity. At latitude larger than 20°, the mixed polarity areas move less poleward than the others, while the areas of following polarity move more poleward. This dependence on latitude may explain why we do observe some differences between Figs. 9 and 10. There are also some differences between the two hemispheres, showing that the meridional circulation is far from symmetric between them.

4.2. Feature tracking

Similar plots for the FT residual meridional circulation are not shown here, and no difference between the polarities is seen for any size range. Here again the CT and FT behavior is very different, even for large structures.

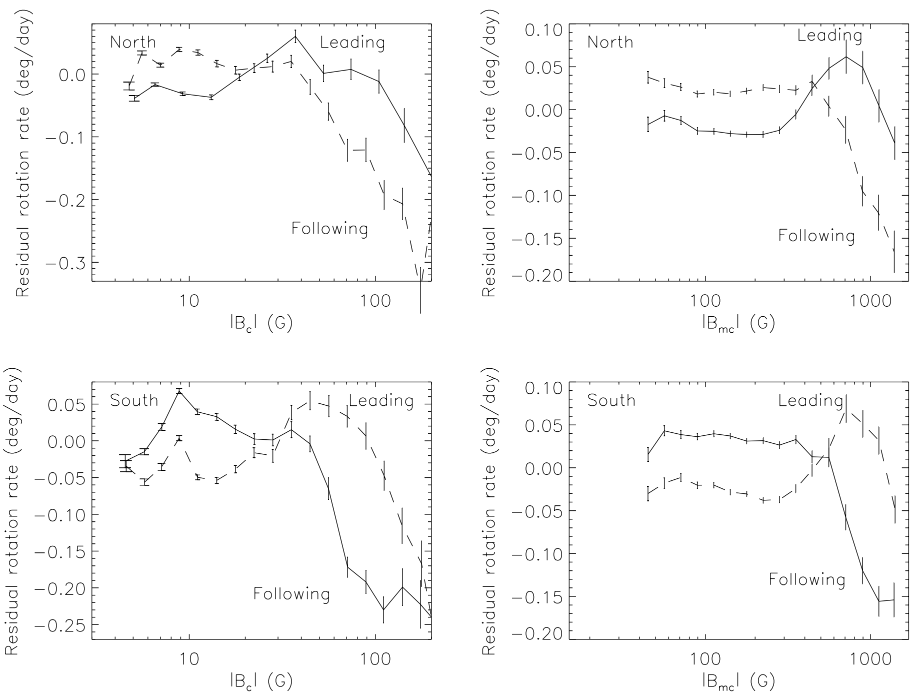

Fig. 6. CT residual rotation rates versus $|B_c|$ (*Left*) and versus Bm_c (*Right*) for the positive polarity (solid line, leading in the Northern hemisphere) and negative polarity (dashed line, following in the Northern hemisphere). *Top*: Northern hemisphere. *Bottom*: Southern hemisphere.

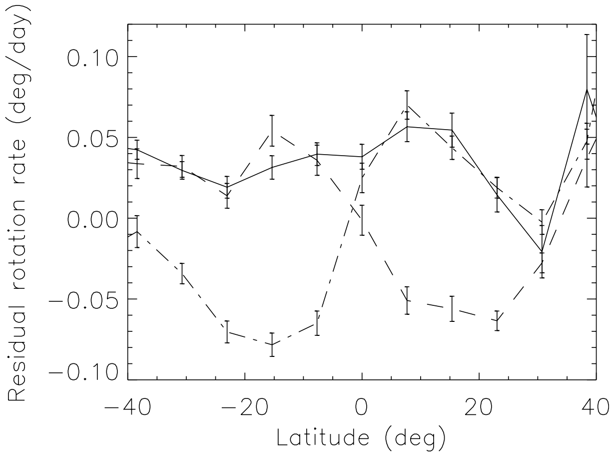

Fig. 7. CT residual rotation rates for $|B_c|$ in the range 9–12 G. The solid curve represents mixed polarity areas (B_c between −4 and 4 G), the dotted-dashed line represents B_c smaller than −4 G and the dashed line represents B_c larger than 4 G.

5. Discussion and conclusion

In this Paper I have studied the dynamics of magnetic features down to network-size structures depending on their polarity in each hemisphere. Two complementary methods (CT and FT) have been used. The most significant result is that for $|Bc|$ below 20–30 G (Bm_c below 400–500 G), areas (defined with CT) of the following polarity are rotating faster than those of leading polarity, which is the opposite of what is observed in active regions. We also find that the positive gradient of the residual rotation rate versus $|B_c|$ or Bm_c observed in Paper I for $|B_c|$ below 10 G is in fact occuring at different values of $|B_c|$ for the two polarities, which contributes strongly to the observed reversal. It is in the range $|B_c|$ below 10 G for areas of following polarity, but in the range 15–40 G for areas of leading polarity. For Bm_c, we mostly see a positive gradient for leading polarities in the range 300–700 G. I observe that this reversal, observed for weak field regions, is present even for small B_c / $|B_c|$ ones (i.e. regions with a small degree of unipolarity), while mixed polarity areas are rotating like areas of following polarity, although this reversal is not observed with FT.

Zhao et al. (2004) have observed a faster surface plasma rotation rate (deduced from a time-distance analysis) where following polarity was present, which is interpreted as a preferential location of these following polarity magnetic features in the following edge of supergranules. However, it is likely that magnetic features observed at the solar surface do not move following this supergranular flow because I do not observe it with FT despite the fact that the errorbars are smaller than their signal. Because it is observed only for CT, it is likely that whole pattern of a given polarity moves with this characteristic. We find a maximum difference of approximately 7 m/s while Zhao et al. (2004) find a difference reaching 10 to 40 m/s around 300 G, which is significantly larger. Therefore it could have the same origin (following polarities preferentially at the leading edge of supergranules) but with smaller amplitude due to a deeper anchoring, where we expect the horizontal flow to be smaller. It may also be related to how coronal holes are preferentially present in unipolar areas of following polarity (they may be rotating more rigidly, Timothy et al. 1975), but it is unlikely to be due to this only because the faster rotation rate of following polarity areas is also seen for boxes with a low degree of unipolarity.

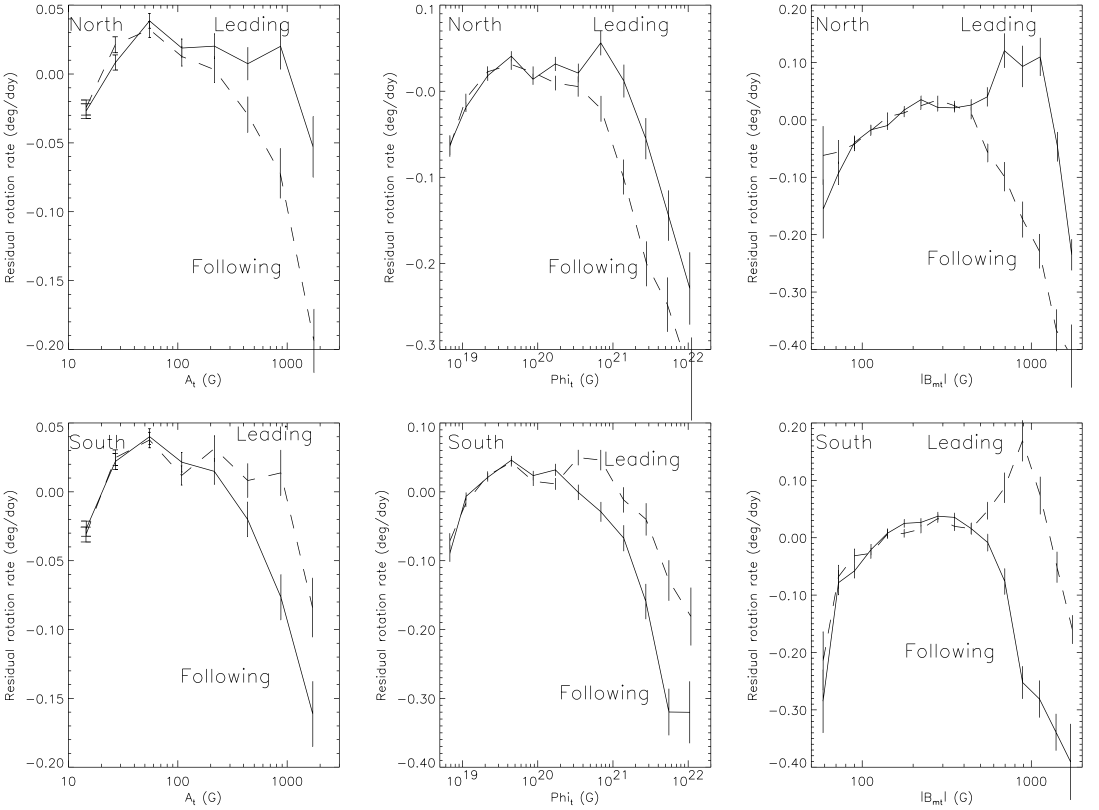

Fig. 8. FT residual rotation rates versus A (*left*), versus $_t$ (*middle*), and versus Bm_t (*left*) for the positive polarity (solid line, leading in the Northern hemisphere) and negative polarity (dashed line, following in the Northern hemisphere). *Top*: Northern hemisphere. *Bottom*: Southern hemisphere.

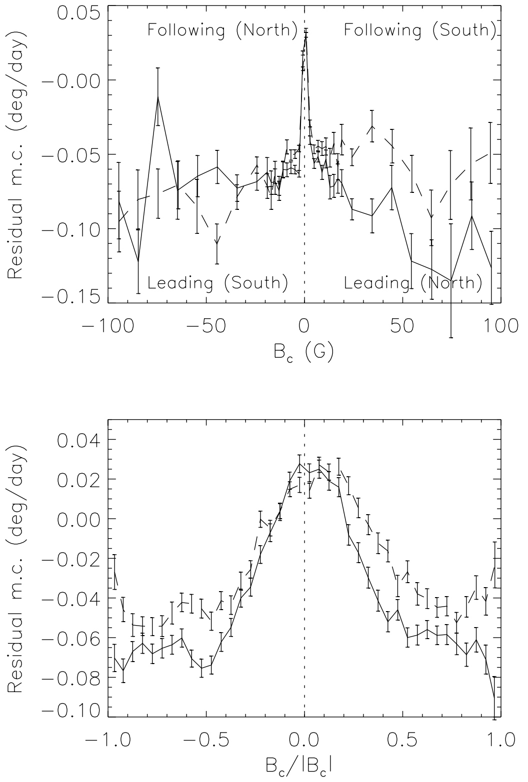

Fig. 9. *Top*: CT residual meridional circulation versus B_c for the Northern hemisphere (solid line) and Southern hemisphere (dashed line). *Bottom*: same versus B_c / $|B_c|$.

Table 1. Residual rotation rates for the CT method (for $|B_c|$ in the range 9–12 G, when some FT structures are present) and for the FT method (for structures present in CT boxes), in deg/day.

Polarity	CT	FT
Leading N	–0.013 ± 0.003	0.015 ± 0.008
Following N	0.046 ± 0.003	0.015 ± 0.008
Leading S	–0.017 ± 0.003	0.016 ± 0.008
Following S	0.038 ± 0.003	0.026 ± 0.008

Furthermore, a larger poleward meridional circulation is observed for areas of following polarities mostly for large structures, which is a new result, observed with CT only. It is similar to the result of Ward (1973) for sunspots, however, who found a more poleward motion of sunspots reaching 0.05 deg/day in the latitude range 15–20°. For weak field regions, we do observe a more poleward meridional circulation for areas of following polarities, but only in the Southern hemisphere (when averaged over all latitudes) and above 20° in the Northern hemisphere. Following polarity areas with latitude in the range 0–20° are moving less poleward. A more poleward meridional circulation for following polarities may reinforce the reversal of polar magnetic fields due to a diffusion towards the poles of these following polarities. However, the polar magnetic field reversal occurred first for the Northern hemisphere and only 1 year later in the Southern hemisphere

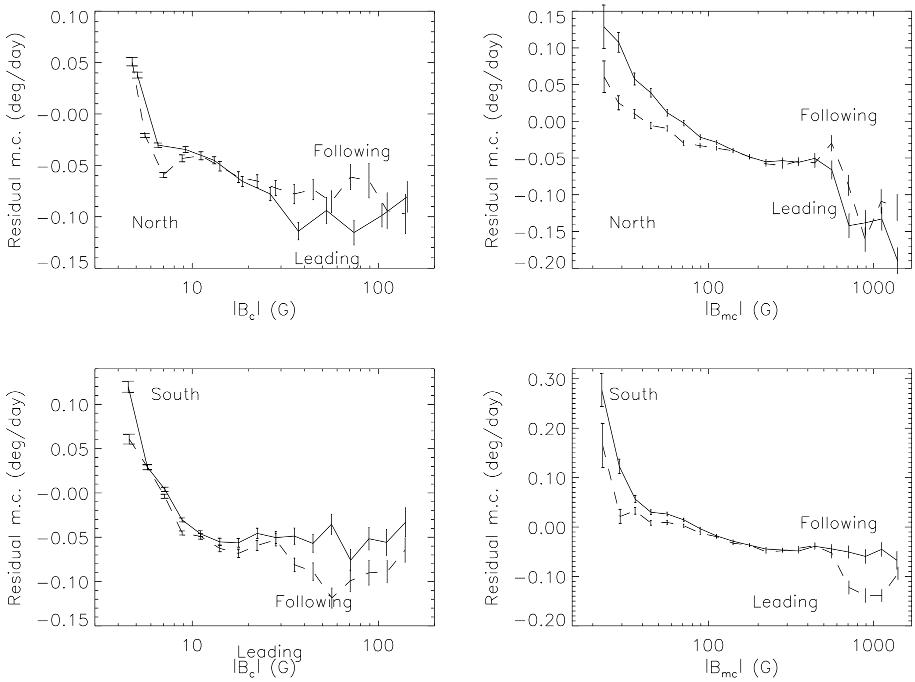

Fig. 10. CT residual meridional circulation versus $|B_c|$ (*left*) and versus $|Bm_c|$ (*right*) for the positive polarity (solid line, leading in the Northern hemisphere) and negative polarity (dashed line, following in the Northern hemisphere). *Top*: Northern hemisphere. *Bottom*: Southern hemisphere.

(Harvey & Recely 2002; Wang et al. 2002), as was explained by Dikpati et al. (2004) by the reversed cell in meridional flow in the Northern hemisphere. One should note that a difference of 0.02 deg/day out of a meridional circulation of 0.2 deg/day over 60 degrees in latitude (from latitude 40° to the poles) corresponds to a time-scale of 1 month only, i.e. much smaller than 1 year, so this factor is probably neglegible compared to other effects. Areas of mixed polarity with a weak field are also moving more poleward below 20° latitude in both hemispheres and less poleward above. As has been shown using other approaches (Haber et al. 2002; Zhao & Kosovichev 2004; Komm et al. 2004), the meridional circulation exhibits strong asymmetry between hemispheres.

The way the flux disappears in mixed polarity areas is not completely understood (Zwaan 1987). If the mixed polarities areas corresponded to regions at the interface between unipolar areas, we might expect the rotation rate of mixed polarity areas to be close to the average of following and leading polarity area rotation rates, which is not what we observe. This is also true for the meridional circulation. This does not lead to a direct conclusion about the way the flux evolves in the various contexts (unipolar, mixed) and disappear, but it provides a clue.

A faster rotation of sunspots with leading polarity has been observed before (see for example Gilman & Howard 1985; Howard 1992a,c). However, Howard (1992c) finds that this is observed for growing spot groups only, while a reversal is observed for decaying regions. Howard (1996) also finds that plages with leading and following polarities are rotating at the same rate close to the equator, but that following polarity plages are rotating faster than the leading part at higher latitudes (the difference reaches 0.3 deg/day at 40° latitude). His interpretation is as follows: during the growing phase, the emerging loop intersects the surface in two locations, leading to two regions of opposite polarities that are moving apart, providing a faster rotation rate for the leading polarity than for the following polarity. They suggest that during the decay phase, the two parts of the loop become closer again, leading to the reversal. It is not yet clear whether this is what is happening, but it would not apply directly to network features. Howard (1996) argues that the asymmetries between the leading and following parts of plages associated to the differential rotation elongating the features could create the faster observed rotation rate of following plages. However, if the faster rotation rate of the network region with the following polarity is the remnant of what is observed for plages, it is likely that the results obtained for plages are real.

A possibility for the faster rotation rate of following polarity areas could be a different orientation of the corresponding flux tubes (between leading and following). Indeed several authors have published some variations in the characteristics of these features (van Driel-Gesztelyi & Petrovay 1990; Howard 1991, 1992b; and Meunier 2003, for network features), which could lead to some biases in the position of the features (we measure the line-of-sight magnetic field only). However, such a bias would lead to a variation of the rotation rate using FT as well, and not only for CT. It is still possible however that a different inclination would lead to a different interaction with supergranulation.

Another possibility could be that following polarity flux tubes are anchored deeper in the convection zone (in the shear layer, 7 m/s represent 2 Mm). This interpretation has to be taken with caution, however, because Paper I shows that the rotation

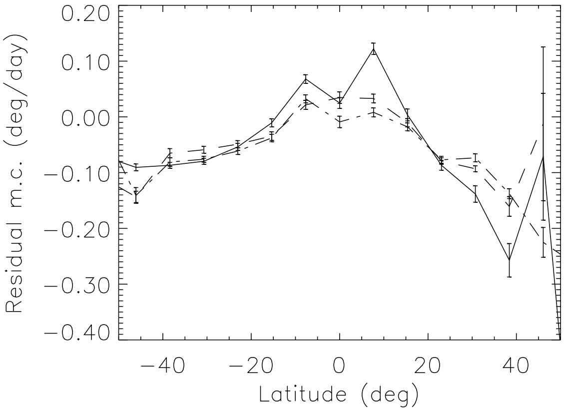

Fig. 11. CT residual meridional circulation for $|B_c|$ in the range 9–12 G. The solid curve represents mixed polarity areas (B_c between −4 and 4 G); the dotted-dashed line represents B_c smaller than −4 G; and the dashed line represents B_c larger than 4 G.

rates of magnetic features cannot be interpreted only by their anchoring in certain layers. For example, because the following part of active region usually decays faster than the leading part, and following flux tubes may have more time to be swept deeper. This would also be consistent with the results found in Paper I where small features rotate faster when they are far from a large structure. Since they probably result from the decay of these regions, their faster rotation rate may result from submergence of these fields to a deeper region before appearing again as network features with faster rotation rates. On the other hand, this is not completely consistent with a more poleward motion since the meridional circulation seems to decrease inward (Haber et al. 2002; Komm et al. 2004; Zhao & Kosovichev 2004). It is also possible that the action of the supergranular flow on the flux tubes of either the following or the leading polarity is different if they have a different inclination. However, here again the supergranular flow should act on the pattern formed by the network features, and not the features themselves, since FT does not show any difference between following and leading polarities.

The reason for the faster rotation rate and more poleward motion of following polarity areas with weak field is therefore not clear yet. Future work on the temporal variations may help to understand it better. In a future work, we will study these temporal variations (Meunier 2005b) and compare them to the results of Zhao et al. (2004). Their relation with possible large-scale patterns in longitude and with coronal holes will also be the subject of future work: these patterns could be associated to large-scale zonal flows.

Acknowledgements. SOHO is a mission of international cooperation between the European Space Agency (ESA) and NASA. I thank Y. Liu, R. Bogart, H. Carfantan and the referee for useful comments on MDI data and this work.

References

Berger, T., & Lites, A. 2003, Sol. Phys., 213, 213
Dikpati, M., de Toma, G., Gilman, P. A., Arge, C. N., & White, O. R. 2004, ApJ, 601, 1136
Gilman, P. A., & Howard, R. 1985, ApJ, 295, 233
Haber, D. A., Hindman, B. W., Toomre, J., et al. 2002, ApJ, 570, 855
Harvey, K. L., & Recely, F. 2002, Sol. Phys., 211, 31
Howard, R. F. 1991, Sol. Phys., 134, 233
Howard, R. F. 1996, ARA&A, 34, 75
Howard, R. F. 1992a, Sol. Phys., 142, 47
Howard, R. F. 1992b, Sol. Phys., 137, 205
Howard, R. F. 1992c, Sol. Phys., 137, 51
Howard, R. F., & Stanchfield, D. H. II 1995, Sol. Phys., 156, 29
Komm, R. W., Howard, R. F., & Harvey, J. W. 1993a, Sol. Phys., 145, 1
Komm, R. W., Howard, R. F., & Harvey, J. W. 1993b, Sol. Phys., 147, 203
Komm, R. W., Corbard, T., Durney, B. R., et al. 2004, ApJ, 605, 554
Liu, Y., Xuepu, Z., & Hoeksema, J. T. 2003, Sol. Phys., 219, 39
Meunier, N. 1999, ApJ, 527, 967
Meunier, N. 2003, A&A, 405, 1107
Meunier, N. 2005a, A&A, 436, 1075 (Paper I)
Meunier, N. 2005b, A&A, submitted
Meunier, N., Nesme-Ribes, E., & Grosso, N. 1997, A&A, 319, 673
Scherrer, P., Bogart, R. S., Bush, R. I., et al. 1995, Sol. Phys., 162, 129
Timothy, A. F., Krieger, A. S., & Vaiana, G. S. 1975, Sol. Phys., 42, 135
van Driel-Gesztelyi, L., & Petrovay, K. 1990, Sol. Phys., 126, 285
Wang, Y.-M., Sheeley, N. R. Jr., & Andrews, M. D. 2002, J. Geophys. Res., 107, 1465
Ward, F. 1973, Sol. Phys., 527
Zhao, J., Kosovichev, A. G., & Duvall, T. L. Jr. 2004, ApJ, 607, L135
Zhao, J., & Kosovichev, A. G. 2004, ApJ, 603, 776
Zwaan, C. 1987, ARA&A, 25, 83

A&A 442, 693–702 (2005)
DOI: 10.1051/0004-6361:20053250

Astronomy & Astrophysics

Temporal variations in the magnetic network large-scale dynamics

N. Meunier[1]

Laboratoire d'Astrophysique de l'Observatoire Midi-Pyrénées, 57 avenue d'Azereix, BP 826, 65008 Tarbes Cedex, France
e-mail: `meunier@bagn.obs-mip.fr`

Received 15 April 2005 / Accepted 26 July 2005

ABSTRACT

The variation in the magnetic network large-scale dynamics is investigated using MDI magnetograms from 1996 to 2004. Cross-correlation and feature tracking techniques are used on pairs of magnetograms in order to derive the dynamics at the solar surface, including magnetic network regions. The variations for both methods are very different, the feature tracking technique leading to generally much less variable dynamics over the cycle, except for the rotation versus latitude. At cycle minimum, the increased differential rotation at high latitude combined with a more rigid rotation at low latitude is indeed more pronounced with the feature tracking. The rotation variations put a strong constraint on the origin of these variations, as some strong correlations between coefficients deduced from fits with Legendre polynomials are observed. When using the cross-correlation technique, the meridional circulation also tends to exhibit a more complex behavior compared to rotation. This study provides the temporal variations in the dependence of the dynamics on the magnetic field and feature size as well as on polarities. The dispersions in velocity for the following and leading polarities are studied over the cycle.

Key words. Sun: magnetic fields – Sun: photosphere – Sun: activity – Sun: faculae, plages

1. Introduction

The large-scale dynamics of the solar surface plays an important role in the solar cycle processes. The angular rotation velocity (hereafter rotation rate), the meridional circulation and the supergranular diffusion at the solar surface have a strong impact on the solar dynamo and on the spatial distribution of the magnetic field on the surface of the Sun. As a consequence, the variation in this dynamic with time is important to constrain the dynamo models, and in particular the possible retroaction of the dynamo on the flows.

For that purpose, many works have been done in the past concerning the variation in sunspot rotation (e.g. Balthasar & Wöhl 1980; Arévalo et al. 1982; Lustig 1983; Gilman & Howard 1984; Balthasar et al. 1986; Vazquez & Wöhl 1986; Hathaway & Wilson 1990; Kambry & Nishikawa 1990; Nesme-Ribes et al. 1993; 1997). The variations in sunspot meridional circulation have been more difficult to detect (Balthasar & Wöhl 1980; Arévalo et al. 1982; Hanslmeier & Lustig 1986; Howard & Gilman 1986; Lustig & Hanslmeier 1987; Javaraiah 1999). Some work has also been done to use local helioseismology to determine the variation in large-scale flows just below the surface of the Sun (Chou & Dai 2001; Haber et al. 2002; Basu & Antia 2003; Zhao & Kosovichev 2004). A complementary approach is the study of the magnetic network dynamics. Komm et al. (1993a,b) attempted this study but the uncertainties were still quite large. Meunier et al. (1997a,b) also studied the variation in rotation and meridional circulation with time, using a manual feature tracking. Using a more extensive data set, Meunier (1999, 2005a) used cross-correlation and feature tracking between pairs of MDI full-disk magnetograms. Meunier (2005a) was able to use this large data set to study the variation in the dynamics with various physical parameters such as magnetic field or structure size. Meunier (2005b) used the same large data set to study the dependence on polarities.

In this work we investigate the variation in the magnetic network dynamics over almost a complete solar cycle using the same techniques on this large data set. This allows the stability of the new results obtained by Meunier (2005a) to be tested, such as the variation in dynamics with the local magnetic field, and by Meunier (2005b), such as the difference in dynamics between the leading and following polarity areas in weak field regions. This approach should also provide some clues to better understand these results. The data processing is briefly described in Sect. 2. The variations in angular velocity are described in Sect. 3 and those in meridional circulation in Sect. 4. The new results are discussed in Sect. 5.

2. Data and processing

The time series used in Meunier (2005a,b) is used here to study the temporal variation in the dynamics of the magnetic network. Pairs of full-disk MDI magnetograms covering 8 years are analyzed, from June 1996 to April 2004. Only 5-min magnetograms[1] at the 1.8 level, i.e. the latest level provided by the MDI/SOHO team, are considered in this study. Their temporal distribution is shown in Meunier (2005b). Pairs of magnetograms are separated by 96 minutes. The dynamics were derived using two complementary techniques. First, a cross-correlation technique over large boxes (7.68 ×7.68 deg^2), hereafter CT, was used. The output consists of maps of horizontal velocities in both directions (rotation and meridional circulation). The average unsigned magnetic field $|B_c|$ is computed over each box, as well as the unsigned maximum magnetic field $|B_{mc}|$ averaged over the box. Second, a feature tracking analysis, hereafter FT, is used. Magnetic structures are defined by adjacent pixels with magnetic field above a threshold of 40 G (or below –40 G for negative magnetic fields). These structures are then tracked between pairs of magnetograms separated by 96 min as for CT. The output of FT is a list of structures associated with their properties (such as size or average magnetic field) and velocities (rotation and meridional circulation as for CT). We refer to Meunier (2005a) for more details, as the analysis is exactly the same. The dynamics is then computed for each year separately, or as a function of time with a small time step. In this paper, we are mostly interested in the network dynamics. As a consequence, only the CT boxes with $|B_c|$ lower than 20 G are considered, as well as FT structures with a size lower than 100 Mm^2 for FT (Wang 1988; Meunier 2003). These 2 thresholds correspond well to each other (Meunier 2005a). Note that the results are dominated by the weaker field regions.

3. Variation in the angular velocity

3.1. Variations in latitude

Fits using Legendre polynomial in sin^i( ) (the latitude) up to the 4th degree are performed on the rotation rates versus latitude. The variations in these coefficients with time are shown in Fig. 1 for the CT and FT methods. The variation in the average magnetic field (for all CT boxes) is also shown for comparison and allows the identification of typical phases of the solar cycle, such as cycle minimum, the rising phase, cycle maximum and the declining phase. The values for cycle minimum and cycle maximum are also shown in Table 1. The equatorial rotation rate, deduced from A_0, A_2 and A_4, is shown in Fig. 2 for CT. The FT rate is not shown because the large errorbars on A_2 and A_4 with that technique lead to large errorbars on the equatorial rate as well. However, the variation deduced from a fit directly using polynomials in sin^i( ) is also shown. In the CT case, they give a variation similar to that deduced from the Legendre polynomials.

The CT equatorial rotation rate is larger at cycle maximum than at cycle minimum. However, the variation is far from monotonous from minimum to maximum, as it starts to decrease from cycle minimum to the middle of the rising phase (this was already seen by Meunier 1999), and then increases toward larger values at cycle maximum. The FT equatorial rate shows a similar variation at the beginning of the cycle, but the subsequent increase is smaller than for CT as shown in Fig. 2. This is confirmed by the equatorial rate values in Table 1.

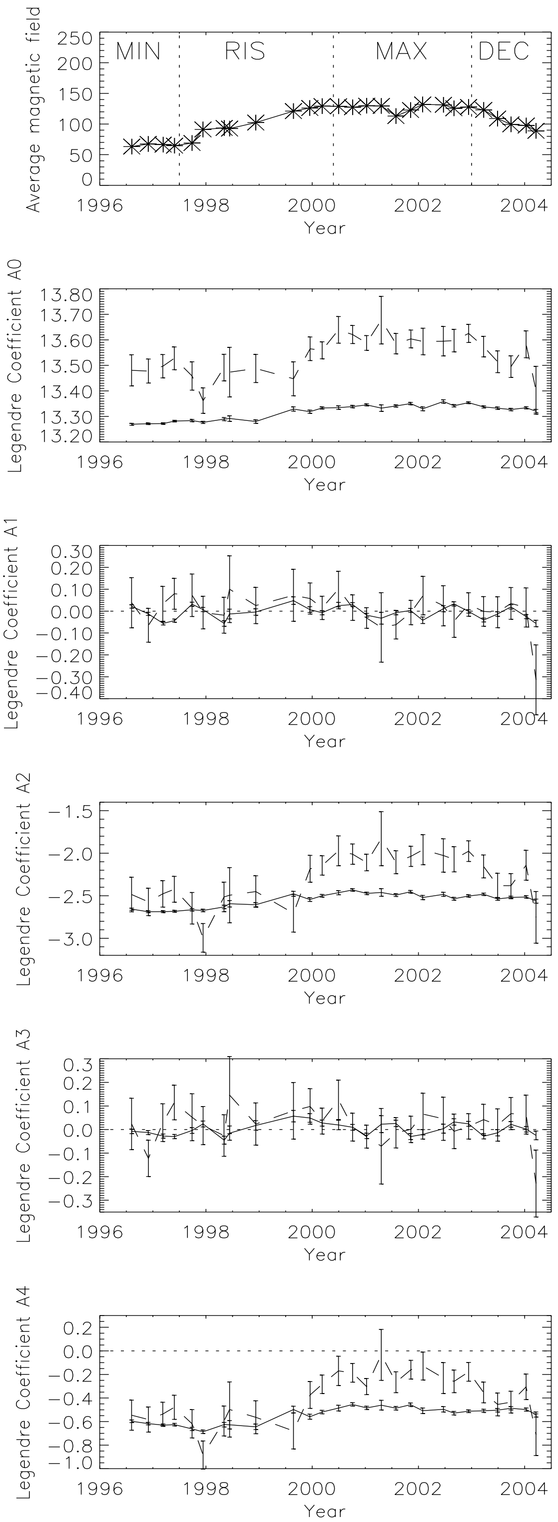

Fig. 1. *Top*: average CT unsigned magnetic field versus time. Following plots: temporal variation in the coefficients from Legendre polynomial fits on the rotation rates versus latitude (in deg/day) for CT (solid lines) and FT (dashed lines).

---

[1] The averaged magnetogram is derived from 5 single magnetograms covering 5 min.

t1

Table 1. Coefficients A_0 to A_4 from fits with Legendre polynomials in sin^i( ) on rotation rates versus latitude (in deg/day) and equatorial rate, A_{eq}, from a polynomial fit in sin^i( ), for CT and FT at cycle minimum and cycle maximum.

Mode	A_0	A_1	A_2	A_3	A_4	A_{eq}
CT min	13.274 ± 0.002	−0.027 ± 0.004	−2.678 ± 0.006	−0.019 ± 0.005	−0.617 ± 0.006	14.381 ± 0.002
CT max	13.339 ± 0.001	−0.0005 ± 0.0026	−2.493 ± 0.004	0.006 ± 0.003	−0.497 ± 0.004	14.400 ± 0.001
FT min	13.48 ± 0.02	0.02 ± 0.03	−2.53 ± 0.07	0.02 ± 0.04	−0.57 ± 0.05	14.535 ± 0.006
FT max	13.58 ± 0.01	0.01 ± 0.01	−2.13 ± 0.03	0.03 ± 0.01	−0.28 ± 0.02	14.535 ± 0.003

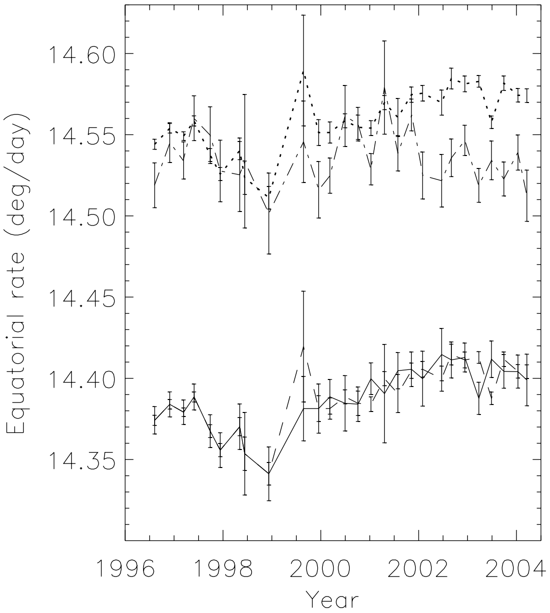

Fig. 2. Equatorial rotation rate versus time (in deg/day), for CT derived from the Legendre polynomial fit (solid line), for CT derived from the sin^i( ) fit (dashed line), for FT derived from the sin^i( ) fit (dotted-dashed line). The dotted curve is the same as the dashed line shifted by 0.17 deg/day so as to match approximately the FT curve around solar minimum.

The variation until 1999 is however very well correlated between the two techniques.

Furthermore, for both CT and FT, the absolute values of A_2 and A_4 are decreasing, which means that the rotation is also more rigid at cycle maximum compared to cycle minimum and to the rising phase. The correlations of A_2 and A_4 with the activity level are quite good. However, the amplitude of the variation is much larger for FT than for CT as shown in Fig. 1 and in Table 1. Figure 3 also shows the difference between the polynomials fits at cycle minimum and cycle maximum for both techniques. The more differential rotation at cycle minimum is mostly present at high latitude above 40°. At low latitude, the rotation is less differential at cycle minimum, although it is less significant.

An interesting feature in Fig. 1 is that A_2 and A_4 variations are strongly correlated. This is true for both CT (correlation coefficient 0.94 and 0.67 respectively) and FT (correlation coefficient 0.99 and 0.94 respectively). This is surprising because the Legendre polynomial are orthogonal to each other which means that there is no correlation between coefficients due to the fitting technique. The only reason for such a correlation is that various domains in latitude must have an actual correlated behavior. The effect of the negative A_4 term is to provide a more rigid rotation at low latitudes (in the range ±20°) compared to what it would be with A_2 only, and a more differential rotation at high latitudes. So the more rigid rotation at cycle maximum at high latitude is physically correlated with a less rigid rotation at low latitude. This constrains a lot the processes at the origin of this variability. On the other hand, a plot of all polynomials for each period shows that the variations in rotation around latitudes 35–40°, i.e. the activity belt limit, in both hemispheres is very small, especially for FT.

On the other hand, Fig. 1 shows that the antisymmetry between hemispheres remains very small during the whole period. Coefficients A_1 and A_3 are also strongly correlated although very small in amplitude. However, when averaging over a longer period, it is possible to detect some antisymmetry. Table 1 shows that there is a significant antisymmetry with CT at cycle minimum, as the Southern hemisphere rotates faster (see also Fig. 3). This is not the case at cycle maximum. This antisymmetry could be related to the similar antisymmetry, although of larger amplitude, detected by Meunier (2005c) in coronal holes at high latitude. For FT, coefficients A_1 and A_3 are more uncertain and therefore it is more difficult to conclude. There may be an antisymmetry in the other direction (the Northern hemisphere rotating faster than the Southern hemisphere) with FT at cycle maximum, however.

3.2. Size and magnetic field dependence

In each latitude bin, the average rotation rate is computed and subtracted from the individual rotation rates, providing a residual rotation rate. Meunier (2005a) found that the residual rotation rates increased with increasing size of the magnetic features when using FT (up to 40 Mm^2) and with increasing magnetic field when using CT (for $|B_c|$ up to ~8–9 G). The residuals then decreased strongly down to smaller rotation rates for active regions. Here the emphasis is put on weak field regions. Figure 4 shows the variation in rotation residuals for each year and for both methods. It shows that the variation in rotation with size observed by Meunier (2005a) for the FT method exhibits the same pattern at all time. However, the curves for the CT method are much more variable with time. The pattern averaged over the whole period observed by Meunier (2005a) is indeed observed in 1997 and 1998 for example and is in agreement with the previous result, but it is absent in 2003 and even reversed in 2004.

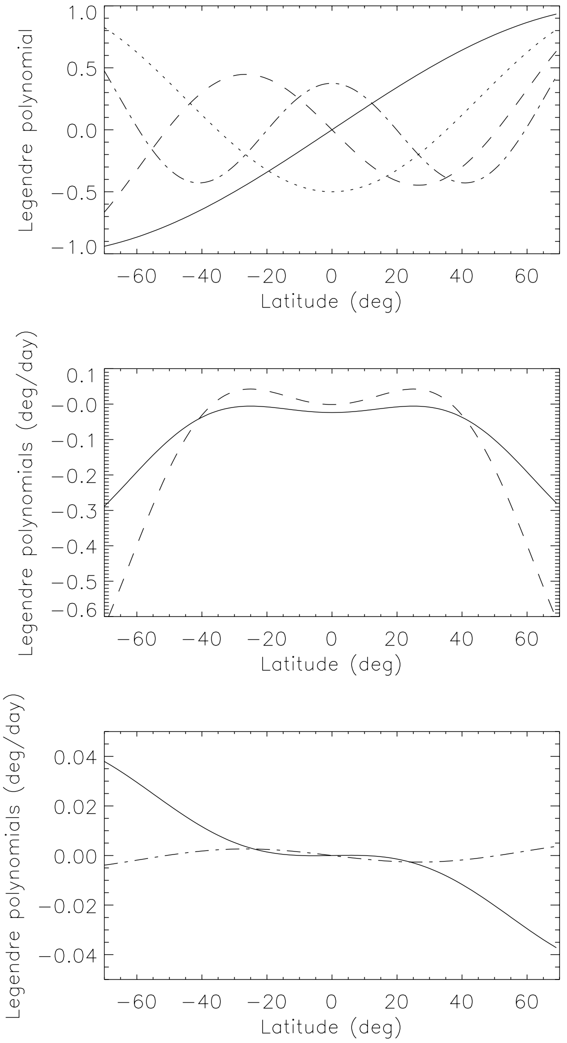

Fig. 3. *Top*: Legendre polynomial versus latitude, for degree 1 (solid line), degree 2 (dotted line), degree 3 (dashed line), and degree 4 (dotted-dashed line). *Middle*: symmetrical part of the Legendre polynomial fit difference $_{\rm min} -\ _{\rm max}$ between cycle minimum and cycle maximum for CT (solid line) and FT (dashed line), with the symmetrical part of the Legendre polynomial fit of the rotation rate versus latitude. *Bottom*: antisymmetrical part of the Legendre polynomial fit for CT at cycle minimum (solid line) and cycle maximum (dotted-dashed line).

3.3. Polarities

Meunier (2005b) found that weak-field regions of following polarity were rotating faster than regions of leading polarity when using the CT method. This was not observed with the FT method. Independently, a faster rotation at the location of following polarity magnetic fields has been observed by Zhao et al. (2004) when using a helioseismologic time-distance analysis to derive the large-scale flows, with a larger amplitude than in Meunier (2005b). They also observed a temporal variation in amplitude of this effect. It is therefore interesting to compare both temporal variations to see whether they correspond to the same phenomenon.

Figure 5 shows the amplitude of the difference between following and leading residual rotation rates for CT, in both hemispheres. A first plot shows the average of residuals for | $B_{\rm c}$ |/ $|B_{\rm c}|$ in the range 0.2–0.7, where the effect is the largest. This is similar to the computation made in Meunier (2005b) except that the variation is computed for each year separately and averaged over | $B_{\rm c}$ |/ $|B_{\rm c}|$. The second plot shows

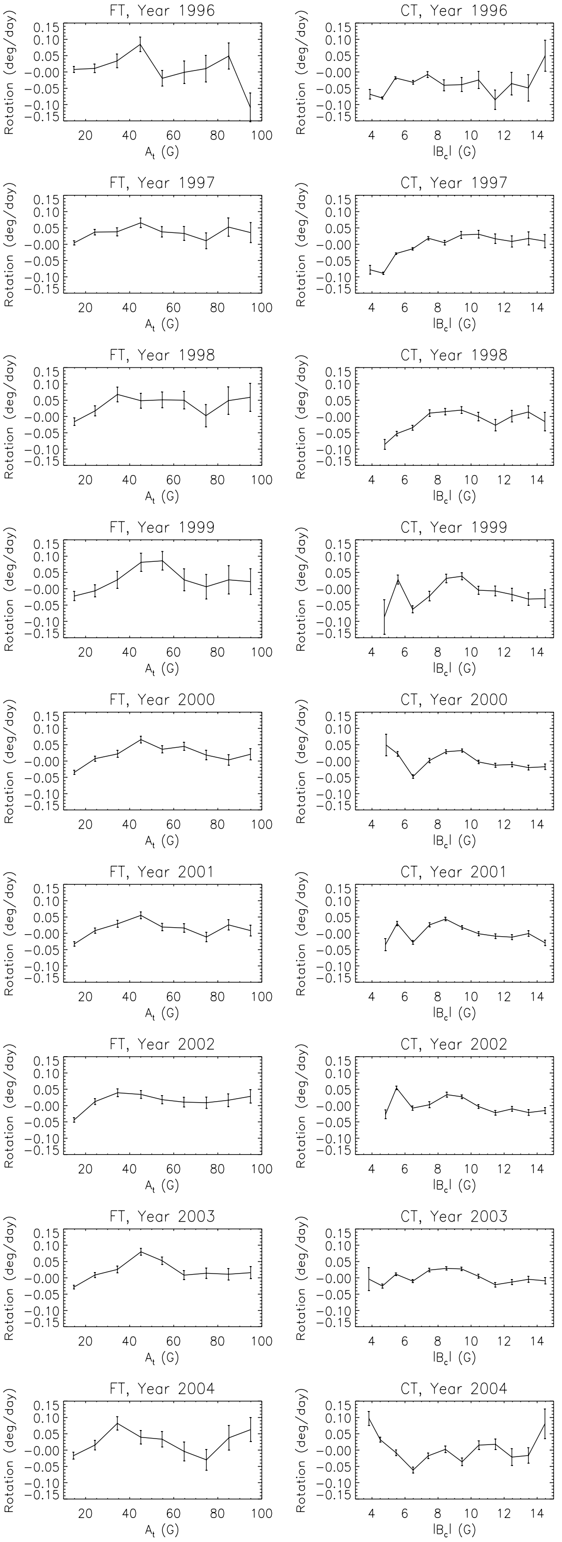

Fig. 4. *Left*: FT residual rotation rates versus feature size A_t from 1996 (*top*) to 2004 (*bottom*). *Right*: same for CT residual rotation rates versus the average unsigned magnetic field $|B_{\rm c}|$.

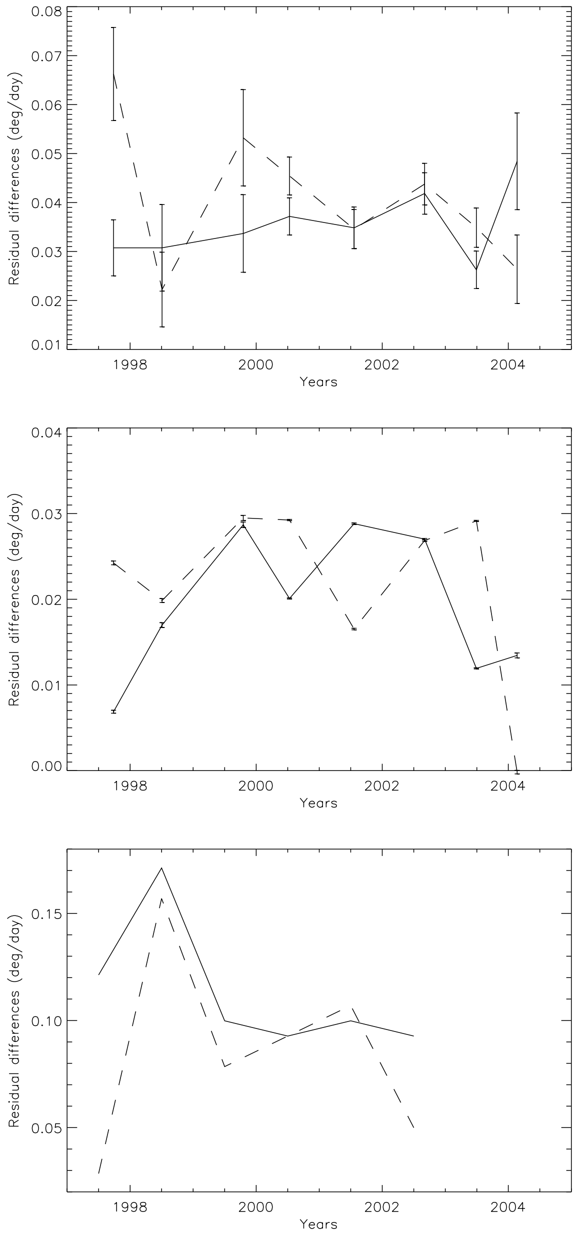

Fig. 5. Difference between the rotation residual for following and leading polarity in the Northern hemisphere (solid lines) and Southern hemisphere (dashed lines), versus time. *Top*: averages computed for $|\ B_c\ |/\ |B_c|$ in the range 0.2–0.7. *Middle*: position of the Gaussian fit on the distribution of residuals, in the same conditions. *Bottom*: residual differences from Zhao et al. (2004) for a magnetic field of 100 G.

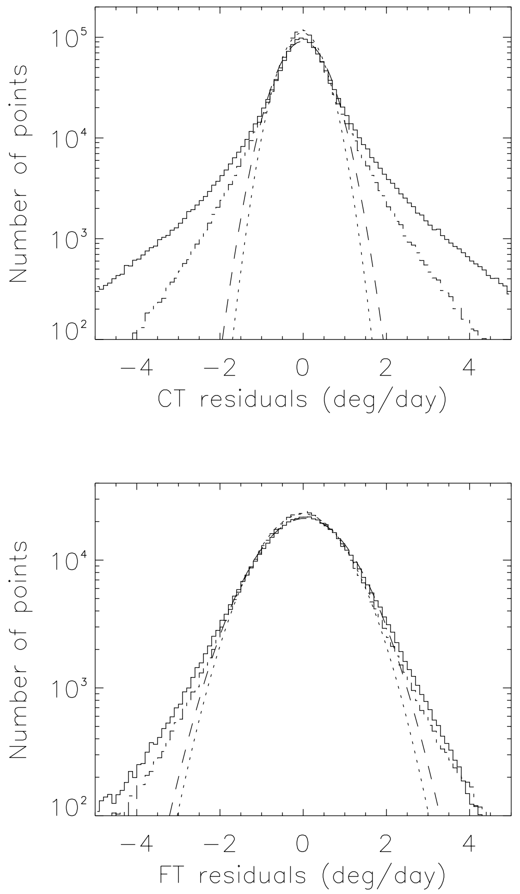

Fig. 6. *Top*: distribution of CT rotation residual (solid line) and CT meridional circulation (dotted-dashed line). Gaussian fits on these distribution are shown as dashed and dotted lines respectively. *Bottom*: same for FT.

the location of a Gaussian fit on the distribution of the residual rotation rates, instead of the average. This is justified by the fact that these distributions exhibit large tails, as shown in Fig. 6, and it is interesting to see which part of the distribution contributes the most to the following-leading difference. On average, the points corresponding to the Gaussian distribution (90% of the whole set) contribute to approximately 60% of the following-leading difference. Therefore the points in the tails of the distribution contribute more than expected from the percentage of points they represent (10%). The errorbars in the first panels of Fig. 5 correspond to the statistical errors at the 1- confidence level. In the second panel, they correspond to the uncertainty on the Gaussian fit at the 1- confidence level.

Figure 5 also shows a comparison with the Zhao et al. (2004) results. The values are deduced from their plots for a 100 G magnetic field. For this value, the errorbars on the residual velocity for each polarity are of the order of 2.8 m/s, leading to a typical uncertainty on the differences plotted in Fig. 5 of the order of 0.03 deg/day. At lower magnetic fields, the difference between following and leading residual rotation rates is not very different because the slope on the following polarity side is steep. The variations are very different for the various approaches, as none of the results obtained with the average or the Gaussian fit on the distribution have a good correlation with the results of Zhao et al. (2004). However, the errorbars on the Zhao et al. (2004) results are quite large; it is therefore difficult to compare the variations. Only between 1997 and 1998 does there seem to be a significantly different trend.

No significant difference between following and leading regions could be observed for small structures in Meunier (2005b) when using the FT technique. When looking at the temporal variation, the result remains the same and I do not identify any period with a significant signal.

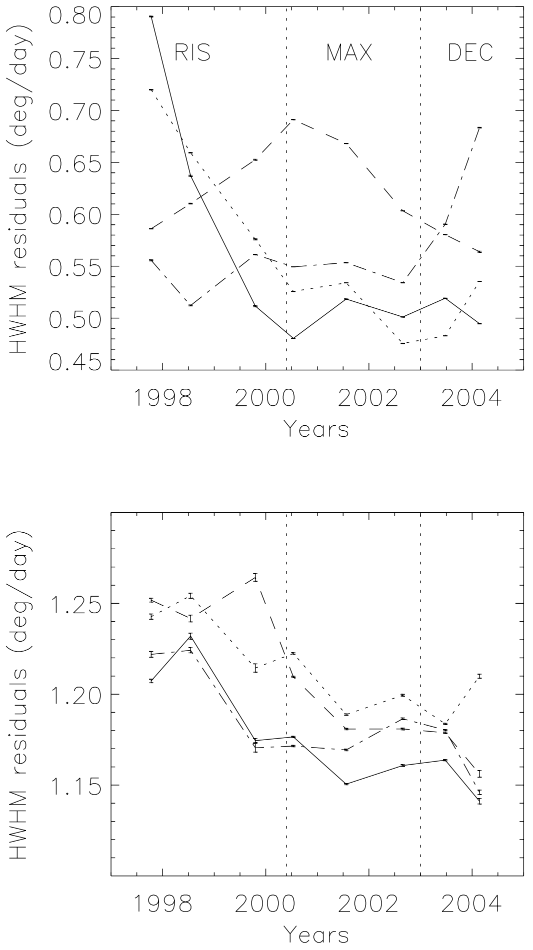

Fig. 7. *Top*: HWHM on CT rotation residual distributions versus time, for the leading polarity in the Northern hemisphere (solid line), following polarity in the Northern hemisphere (dashed line), leading polarity in the Southern hemisphere (dotted line) and following polarity in the Southern hemisphere (dotted-dashed line). *Bottom*: same for the FT method.

3.4. Velocity dispersions

The tails of the distribution as shown in Fig. 6 extend further for the rotation than the meridional circulation. The effect is more pronounced for CT. Such a difference between rotation and meridional circulation could be due to the differential rotation inside each bin. For this reason we expect a stronger effect for FT. As FT concerns individual features and CT results from a weighted average over a larger box which may include several features, we expect CT velocities to exhibit smaller dispersions. The results are not compatible with this. We also find that on average, the width of the Gaussian fit is larger for FT than for CT, despite the fact that the tails have a smaller extent. It is likely that the larger width in FT is related to the diffusion of magnetic features at the surface. The CT residuals are related to large-scale flows (such as those studied by Ambrŏz 2001), and the results suggest that CT provides stronger large-scale flows.

Figure 7 shows the HWHM of the residuals for both polarities in both hemispheres. For the CT method, leading polarity regions exhibit large HWHM at cycle minimum. The HWHM then decreases towards lower values by a factor of 2 during the maximum and declining phase. On the other hand, the following polarity starts with low values, which then increase during cycle maximum and the declining phase of the cycle. As a consequence the 2 categories of curves (leading and following) cross each other, just before the solar maximum. The Northern hemisphere is in advance by about 1 year compared to the Southern hemisphere. The rms values over the whole series of residuals show the same behavior although shifted in time by about 6 months to 1 year. The percentage of points in the tails compared to the core is well correlated with these curves. Therefore, large-scale flows exhibit large variations over the solar cycle, a large North-South asymmetry and large differences between polarities. At the end of the cycle the following polarity will become the leading polarity and vice-versa. So a cyclic behavior must be observed and this will have to be checked with a longer data set.

For the FT method, there is a large North-South asymmetry as well. However, there is no clear difference between leading and following polarities. From the beginning of the rising phase to the declining phase, a decrease in HWHM is observed.

4. Variation in the meridional circulation

4.1. Variations in latitude

Figure 8 shows the meridional circulation versus latitude for two years, in 1997 (at the end of solar minimum) and in 2004 (just after solar maximum). The FT meridional circulation is not very different in the two plots. On the other hand, the CT meridional circulation, larger in amplitude, is very different, especially at high latitudes. Another way to visualize these variations is to look at the temporal variation separately for each latitude bin, as shown in Fig. 9. At low latitudes (roughly in the activity belt), there is a correlation showing that the CT meridional circulation is evolving similarly in both hemispheres. Most of the signal is due to the propagation of the strong converging flows observed by Meunier (1999, 2005a) toward the equator. The FT meridional circulation remains very small, except around 15°, with a more poleward motion at cycle minimum.

At high latitude, i.e. above 60°, it is completely different. In the Northern hemisphere, the large poleward circulation decreases toward much smaller values at the end of cycle maximum. On the other hand, in the Southern hemisphere, the small poleward circulation increases during the whole period.

4.2. Polarities

Meunier (2005b) has detected some differences in meridional circulation between following and leading polarity weak field regions. For the weakest fields there was a strong asymmetry between hemispheres, with a more poleward motion of following polarity in the Southern hemisphere, while the opposite was observed in the Northern hemisphere. Some variations with latitudes were also observed. Figure 10 shows the variation in the following-leading difference with time, for $|\ B_{\rm c}\ |/\ |B_{\rm c}|$ in the range 0.2–0.7. The variations in average and Gaussian fit position are well correlated in the Northern hemisphere

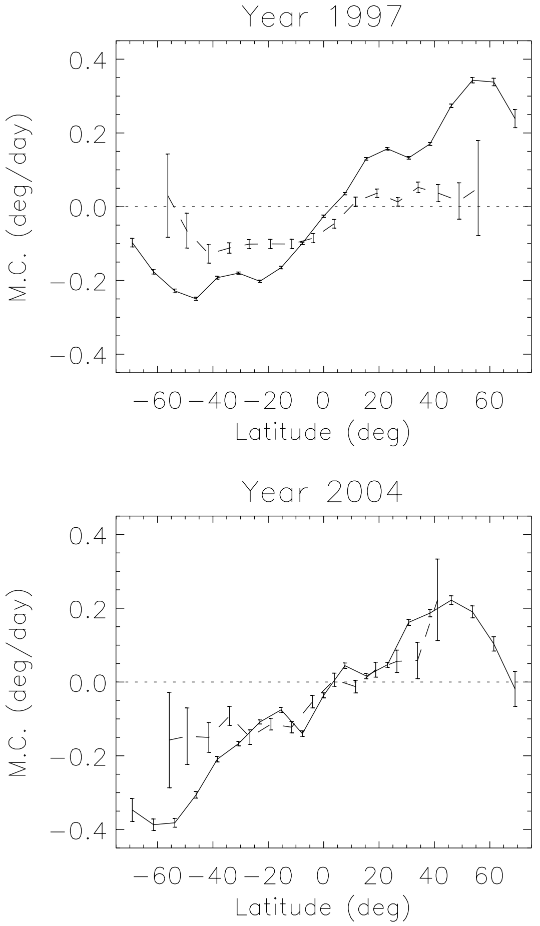

Fig. 8. CT (solid line) and FT (dashed line) meridional circulations versus latitude, for 1997 and 2004. Positive meridional circulation is towards the North pole.

(correlation of 0.84) but they are not as well correlated in the Southern hemisphere (correlation of 0.44). The Gaussian fit tends to provide a smaller difference than the average, as for rotation. On the other hand, there is a strong North-South asymmetry, as the following polarity tends to have a more poleward motion in the Southern and a less poleward motion in the Northern hemisphere, as detected by Meunier (2005b). However, this is not true at all time, as there are periods with a more poleward motion for the following polarity in the Northern hemisphere, and a tendency for a less poleward motion in the Southern hemisphere as deduced from the Gaussian fit in 1998 and 2003. The correlation between the 2 hemispheres is significant for the average (correlation of 0.56) but smaller for the fit position (correlation of 0.28).

4.3. Velocity dispersions

As for rotation, Fig. 11 shows the HWHM on the residual distribution for the CT techniques and FT techniques. The results are qualitatively similar to those obtained for rotation in the previous section.

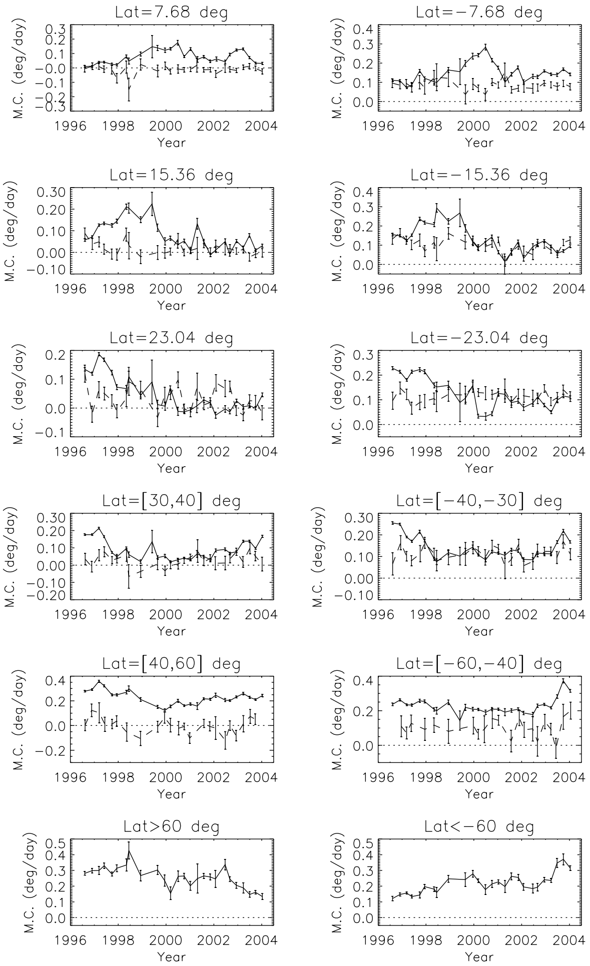

Fig. 9. CT (solid line) and FT (dashed line) meridional circulations versus time for various latitude ranges, represented on the same scale. The latitude values in the latitude belt correspond to the central values of the bin used to compute the CT boxes. *Left*: northern hemisphere. *Right*: southern hemisphere. Positive meridional circulation is towards the poles.

5. Discussion and conclusion

It is interesting to compare the magnetic network dynamics with sunspots and plage dynamics. The variations in sunspot rotation have been studied by many authors, and there is a good agreement for a more rigid rotation during cycle maximum (Balthasar & Wöhl 1980; Lustig 1983; Nesme-Ribes et al. 1993), especially at the end of the cycle (Balthasar & Wöhl 1980). This is consistent with the result obtained here for the magnetic network. Many works on sunspots rotation have found more equatorial rotation at cycle minimum (Balthasar & Wöhl 1980; Lustig 1983; Gilman & Howard 1984; Balthasar et al. 1986; Vazquez & Wöhl 1986; Hathaway & Wilson 1990; Kambry & Nishikawa 1990). Furthermore, most of them have found a second peak in the equatorial rotation during cycle maximum, the lowest rotation rate occuring between cycle minimum and cycle maximum. In that case again, there is a qualitative agreement with the results for the magnetic network obtained here. However, the high equatorial rotation during cycle maximum is spread over a longer period and is observed

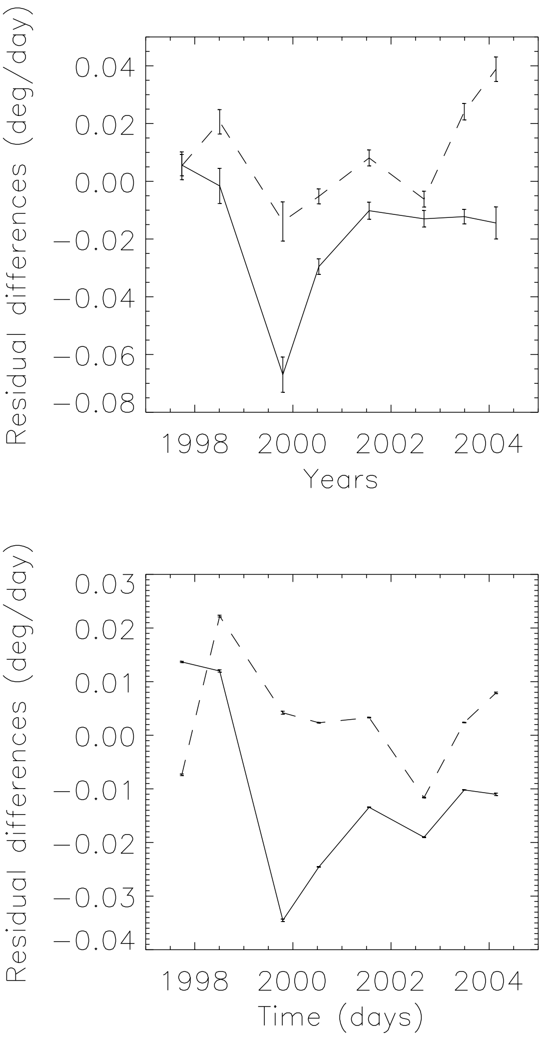

Fig. 10. Difference between the meridional circulation residual for following and leading polarity in the Northern hemisphere (solid line) and Southern hemisphere (dashed line), versus time. *Top*: averages computed for $|B_c|/|B_c|$ in the range 0.2–0.7. *Bottom*: position of the Gaussian fit on the distribution of residuals, in the same conditions.

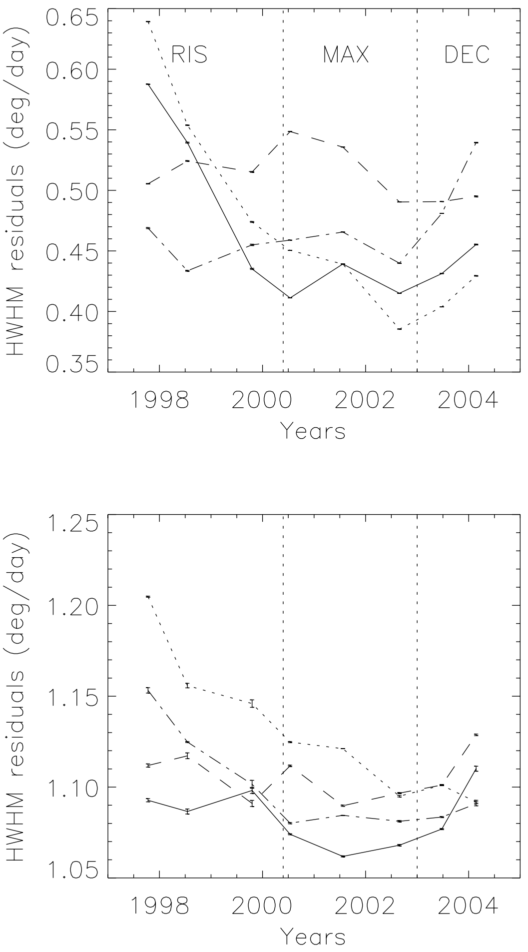

Fig. 11. *Top*: HWHM on CT meridional circulation residuals distributions versus time, for the leading polarity in the Northern hemisphere (solid line), following polarity in the Northern hemisphere (dashed line), leading polarity in the Southern hemisphere (dotted line) and following polarity in the Southern hemisphere (dotted-dashed line). *Bottom*: same for the FT method.

mostly for CT. It also has a larger amplitude at cycle maximum than at cycle maximum (for CT), which is not the case for sunspots. Howard (1990) found plage rotations similar to that of sunspots, with two sharp peaks in the rotation as well. One should note that Meunier et al. (1997a) found a larger rotation of plage and network structures at cycle maximum, while Komm et al. (1993a) found a constant equatorial rotation.

Komm et al. (1993b) found that the meridional circulation maximum amplitude was larger at cycle maximum compared to cycle minimum by about 30%. On the other hand, Meunier (1997b) found that the meridional circulation of plages and network features was larger at cycle maximum compared to cycle minimum (but more or less constant in the Southern hemisphere). They do not compare easily with the results presented in this paper. However both these studies concerned previous cycles, so the comparison may not be valid and it is possible that meridional circulation do not show a systematic behavior from one cycle to the other.

On the other hand, the variations in sunspot meridional circulation have been difficult to study. Many works did not find any variation with the phase of the solar cycle or any variation at all (e.g. Balthasar & Wöhl 1980; Howard & Gilman 1986). Several authors (Arévalo et al. 1982; Hanslmeier & Lustig 1983; Lustig & Hanslmeier 1986) found only variations from one cycle to the other. This was confirmed by Javaraiah (1999) who also found some variation during the solar cycle, with a meridional circulation close to zero during the rising phase of the cycle, and a small equatorward motion during the declining phase. Furthermore, he has detected a anticorrelation of these variations from one cycle to the other. This means that the comparison of various results from different cycles may not be valid. The results obtained here for the magnetic network confirm that the meridional circulation is very complex and may not exhibit a systematic behavior, but the general behavior is different.

The magnetic network dynamics is therefore in agreement with certain results obtained with sunspots previously, such as the more rigid rotation during cycle maximum and two peaks in the equatorial rotation rate. This agreement is mostly qualitative, however, since the more rigid rotation and higher equatorial rotation rates during maximum seems to cover a larger period when using the magnetic network. With the magnetic network, it has also been possible to investigate higher latitudes. The new detection of a strong correlation between the Legendre polynomial coefficients should strongly constrain the interpretation of these variations.

The magnetic network analysis also provides new results concerning the variations in the dynamics. Not only has the dynamics versus latitude been studied, but also the dependence on feature size, on magnetic field and on polarity. The distribution in velocity also exhibits some interesting variations with time. A common property of these approaches is that the dynamics are much more variable with time when using cross-correlation than when using feature tracking, except for the differential rotation. Despite the difficulty in attributing an anchoring depth to each type of approach (Meunier 2005a), it is possible that the dynamics derived from FT may be anchored deeper than CT dynamics: this was derived from the rotation versus depth derived from helioseismology and the larger rotation of FT structures compared to CT. Note that both CT and FT correspond to the same magnetograms formed at the same height (in the range 200–400 km above the photospheric level, Jones 1989; Meunier & Kosovichev 2003). This would mean that most of the temporal variations may be present in a very shallow layer close to the surface. It is also puzzling to see that the differential rotation is more variable with FT, while the other characteristics, such as the rotation residuals as a function of the structure size, are very stable. The opposite is observed for CT.

For that reason, it was very interesting to compare our data to recent results using time-distance helioseismology for various depths (Chou & Dai 2001; Haber et al. 2002; Basu & Antia 2003; Zhao & Kosovichev 2004). The North-South asymmetry of the meridional circulation at high latitude significantly decreases over the cycle, and this is in good agreement with the result of Basu & Antia (2003). However, they observed a decrease in the meridional circulation with time in both hemispheres, as is the case here. Their asymmetry variation comes from the fact that the decrease is stronger in the Northern hemisphere, so the agreement is not complete. Their variation in amplitude of meridional circulation is visible down to 0.985 R (10.5 Mm) and the meridional circulation variations are more complex below this value. On the other hand, Zhao & Kosovichev (2004) have studied the period 1996–2002 using a time-distance analysis for two ranges of depths, 3–4.5 Mm and 6–9 Mm. Close to the surface and at latitude 50° they found an increase followed by a decrease towards zero, while they found a very small decrease in the Southern hemisphere. Deeper in the convective zone, only decreases are seen. Therefore, their results may match our result in the Northern hemisphere to some extent but not in the Southern hemisphere. At lower latitude, in the range 30–40°, they observed a significant decrease that we do not observe. Haber et al. (2002) have also used a time-distance analysis for data between 1996 and 2001. They have extracted the meridional circulation in two ranges of depths as well, around 0.9 Mm and 7.1 Mm deep. Close to the surface and around latitude 50°, an increase in meridional circulation with time is not compatible with our observation in the Northern hemisphere, while a constant meridional circulation in the Southern hemisphere does not fit with our results either. Deeper, they found a cell reversal in the Northern hemisphere which we do not observe. Chou & Di (2001) have determined the meridional circulation between 1994 and 2000 for depths in the ranges 9–26 Mm and 26–43 Mm. For the second half of the period they found a tendency for an increase in meridional circulation at high latitude in both hemispheres, so here again this does not fit our results.

This comparison with helioseismology shows that the meridional circulation derived from this technique leads to different temporal variations than the FT and CT measurements. Several limitations may be at the origin of this discrepancy. First, the anchoring depth may be different, and Basu & Antia (2003) showed how the variation in meridional circulation was variable with depth. Furthermore, the processes at the origin of the difference between the dynamics close to the surface and the CT and FT dynamics (Meunier 2005a) are not known, and they may vary with time. Also, the temporal coverage for a given year may be different. Here most of the year is covered (except for a large gap in 1998), while helioseismological studies have often used shorter time intervals, down to 30% coverage only.

The variations in leading-following differences (discovered in Meunier 2005b) are quite different from that deduced from the Zhao et al. (2004) analysis using time-distance analysis to derive the flows. Because such a difference was observed with CT but not with FT, Meunier (2005b) concluded that this may be a different phenomenon. The larger amplitude observed by Zhao et al. (2004) suggests that their leading-following differences may contain a contribution related to our CT differences. Note that FT, CT and time-distance analysis correspond to different sensitivities to the layers below the surface. This is relatively well-known for the time-distance but it is not the case for CT and FT (Meunier 2005a). It is therefore difficult to conclude about a common physical process at the origin of the two observations. Our present observation is in good agreement with this conclusion. The following-leading difference in meridional circulation also exhibits some temporal variations, which are relatively well correlated between the hemispheres despite the strong North-South asymmetry. These variations could be related to the polar reversal in the magnetic field.

In general, the meridional circulation tends to exhibit a more complex behavior than the rotation. The strong North-South asymmetry of the meridional circulation variation shows that it is very difficult to derive a simple cyclic behavior (with an 11 year period) for the meridional circulation as opposed to the rotation. However, the width of the distribution in both velocities also exhibits a complex behavior, especially when considering the different polarities with CT, while the variations are simpler when using FT. The CT variations indicate a shift between the two hemispheres of about a year, as the Northern hemisphere is in advance. We know that the polar magnetic field reversal occurred first for the Northern hemisphere and one year later in the Southern hemisphere (Harvey & Recely 2002; Wang et al. 2002) and at approximately the same epoch than the typical period derived in this study. Therefore, this distribution in velocity could be related to the polar magnetic field reversal. What we do observe is that large-scale flows associated with the following polarity regions (which play an important role in the magnetic field reversal) increase faster with time in the hemisphere where the reversal occurs first. It is quite likely that the large-scale circulation associated with the following polarity regions plays a role in this reversal.

Acknowledgements. SOHO is a mission of international cooperation between the European Space Agency (ESA) and NASA.

References

Ambrož, P. 2001, Sol. Phys., 198, 253
Arévalo, M. J., Gomez, R., Vázquez, M., Balthasar, M., & Wöhl., H. 1982, A&A, 111, 266
Balthasar, H., & Wöhl., H. 1980, A&A, 92, 111
Balthasar, H., Vazquez, M., & Wöhl, H. 1986, A&A, 155, 87
Basu, S., & Antia, H. M. 2003, ApJ, 585, 553
Chou, D.-Y., & Dai, D.-C. 2001, ApJ, 559, L175
Gilman, P. A., & Howard, R. F. 1984, ApJ, 283, 385
Haber, D. A., Hindman, B. W., Toomre, J., et al. 2002, ApJ, 570, 855
Hanslmeier, A., & Lustig, G. 1986, A&A, 154, 227
Harvey, K. L., & Recely, F. 2002, Sol. Phys., 211, 31
Hathaway, D. H., & Wilson, R. M. 1990, ApJ, 357, 271
Howard, R., & Gilman, P. A. 1986, ApJ, 307, 389
Javaraiah, J. 1999, Sol. Phys., 189, 289
Jones, H. 1989, Sol. Phys., 120, 211
Kambry, M., & Nishikawa, J. 1990, Sol. Phys., 126, 89
Komm, R. W., Howard, R. F., & Harvey, J. W. 1993a, Sol. Phys., 145, 1
Komm, R. W., Howard, R. F., & Harvey, J. W. 1993b, Sol. Phys., 147, 203
Lustig, G. 1983, A&A, 125, 355
Lustig, G., & Hanslmeier, A. 1987, A&A, 172, 332
Meunier, N., Nesme-Ribes, E., & Grosso, N. 1997a, A&A, 319, 673
Meunier, N., Nesme-Ribes, E., & Collin, B. 1997b, A&A, 319, 683
Meunier, N. 1999, ApJ, 527, 967
Meunier, N. 2003, A&A, 405, 1107
Meunier, N., & Kosovichev, A. 2003, A&A, 412, 541
Meunier, N. 2005a, A&A, 436, 1075
Meunier, N. 2005b, A&A, 437, 303
Meunier, N. 2005c, A&A, in press
Nesme-Ribes, E., Ferreira, E. N., & Mein, P. 1993, A&A, 274, 563
Nesme-Ribes, E., Meunier, N., & Vince, I. 1997, A&A, 321, 323
Scherrer, P., Bogart, R. S., Bush, R. I., et al. 1995, Sol. Phys., 162, 129
Snodgrass, H. B., & Ulrich, R. K. 1990, ApJ, 351, 309
Vazquez, M., & Wöhl, H. 1986, A&A, 155, 87
Wang, H. 1988, Sol. Phys., 116, 1
Wang, Y.-M., Sheeley, N. R.Jr., & Andrews, M. D. 2002, J. Geophys. Res., 107, 1465
Zhao, J., Kosovichev, A. G., & Duvall, T. L.Jr. 2004, ApJ, 607, L135
Zhao, J., & Kosovichev, A. G. 2004, ApJ, 603, 776

A&A 443, 309–317 (2005)
DOI: 10.1051/0004-6361:20053249

Astronomy & Astrophysics

Large-scale photospheric dynamics below coronal holes

N. Meunier

Laboratoire d'Astrophysique de l'Observatoire Midi-Pyrénées, 57 avenue d'Azereix, BP 826, 65008 Tarbes Cedex, France
e-mail: `meunier@bagn.obs-mip.fr`

Received 15 April 2005 / Accepted 11 July 2005

ABSTRACT

A large data set of MDI magnetograms is studied to analyze the global dynamics of magnetic structures from network to active regions inside and outside coronal holes. We find a weaker meridional circulation at almost all latitudes, as well as a more differential rotation of the photospheric magnetic structures below high-latitude coronal holes. Stronger asymmetries in the dynamics are observed in coronal holes at high latitude compared to outside coronal holes. The variation in the dynamics is also studied as a function of the coronal hole size as well as its variation with time and with magnetic field. The smaller velocity dispersion obtained in coronal holes when using a cross-correlation technique shows that the large-scale circulation may be inhibited inside coronal holes compared to outside. However, there is an indication of a larger diffusion of magnetic features within coronal holes than outside.

Key words. Sun: magnetic fields – Sun: photosphere – Sun: activity – Sun: corona

1. Introduction

Coronal holes (herefafter CHs) are defined as regions of open magnetic field lines (Wang et al. 1996), as opposed to closed loops mostly associated with active regions. They are observed as dark areas in X-ray and EUV, and as bright regions in spectroheliograms made in the He I λ10830 Å line. They are also associated with regions that are almost unipolar in the photosphere. Identification procedures for CHs have been elaborated using complementary data sets, for example by Harvey & Recely (2002) who used a combination of He I spectroheliograms and photospheric magnetograms. There are three types of CHs: polar CHs, low latitude extension of polar CHs and transient CHs more closely associated with active regions. Their respective typical lifetimes are very variable, as is their distribution in time over the solar cycle (e.g. Harvey & Recely 2002).

However, all properties of CHs are not known nor understood. For example, not all unipolar regions are associated with a CH, and the differences between similarly quiet photospheric regions in and outside CHs are not well known (De Toma & Arge 2005), despite studies of the magnetic properties inside and outside CHs (Harvey et al. 1982; Harvey & Recely 2002). Also, polar CHs with extensions towards low latitudes exhibit a rigid rotation, despite the differential rotation of the magnetic structures in the photosphere (Snodgrass & Ulrich 1990; Komm et al. 1993a; Meunier 1999, 2005a) and of the coronal bright points (Antonucci et al. 1979; Brajša et al. 2004). There have been several theoretical works (e.g. Wang & Sheeley 1990, 2004; Fisk et al. 1999) to explain this rigid rotation, which is likely due to processes occuring at the boundary of CHs. The study of the boundaries of CHs is therefore very important. Kahler & Hudson (2002) have studied in detail the morphology of the boundary of long-lived coronal holes. However, we are still lacking observations of the dynamics in the photosphere in relation to CHs.

In this paper, the large-scale photospheric dynamics of small magnetic features is determined for the first time inside and outside CHs. The observations and data analysis are described in Sect. 2. The resulting meridional circulation and angular rotation velocity, hereafter rotation rate, are presented in Sect. 3. Additional information can be derived from the dispersion in these velocities. The results are discussed in Sect. 4.

2. Observations and data analysis

2.1. MDI magnetograms

Full-disk magnetograms obtained by MDI/SOHO (Scherrer et al. 1995) cover most of cycle 23. In this study, 5-min averaged magnetograms[1] at level 1.8, i.e. the latest data level provided by the MDI/SOHO team, are used between June 1996 and September 2003. The averaged magnetograms are separated by 96 min or a multiple of 96 min, with a few gaps (see Meunier 2005b, for the temporal distribution of pairs of magnetograms). Only pairs of magnetograms separated by 96 min are considered in this study.

Large-scale dynamics using correlation tracking (hereafter CT) are derived from these pairs of magnetograms separated by 96 min as described in Meunier (2005a), with a method

---

[1] An averaged magnetogram is computed from 5 single magnetograms covering 5 min.

similar to that of Komm et al. (1993a,b). The correlation tracking is done by cross-correlating boxes of size 7.68 × 7.68 deg^2 (93×93 Mm^2) on pairs of magnetograms after remapping on a grid with constant steps in latitude and longitude, as in Meunier (1999). The average unsigned magnetic field $\langle|B_c|\rangle$ is computed over each box, as well as the unsigned maximum magnetic field $\langle|B_{mc}|\rangle$. The output of CT consists of maps of horizontal velocities (rotation and meridional circulation). The comparison with the large-scale dynamics of individual features obtained by feature tracking (hereafter FT), also described in Meunier (2005a), has also been attempted. Magnetic structures are defined by adjacent pixels with a magnetic field above a threshold of 40 G (or below –40 G for negative magnetic fields). These structures are then tracked between pairs of magnetograms separated by 96 min as for CT. The output of FT is a list of structures associated with their properties (such as size or average magnetic field) and velocities (rotation and meridional circulation as for CT).

2.2. The coronal hole data set

Coronal hole boundaries over a long period have been determined using Kitt Peak full-disk photospheric magnetograms and He I spectroheliograms (Harvey & Recely 2002). Figure 1 shows an example of such boundaries. The coordinates of the boundaries have been retrieved from the archive at `ftp://solarch.tuc.noao.edu/kpvt/coronal_holes/`. They are available with a 1° spatial resolution in latitude and longitude.

Due to possible gaps in the CH contours, the original resolution of 1° has been degraded by a factor of 2 to avoid losing too many CH data points. Low resolution maps (2°) are therefore derived from these boundaries (see an example in Fig. 1). The areas occupied by the CHs are determined from these boundaries. This analysis provides 3 types of pixels:

- pixels outside CHs have 0 values;
- pixels inside CHs have positive values;
- boundary pixels have negative values.

Because of the low resolution, small CHs or thin extensions of CHs have negative values only, i.e. as if they were only constituted of boundaries. Therefore boundary CH pixels correspond either to an actual boundary pixel of a large CH or to a small CH including the core of the CH. In the following, three categories of CH regions will be studied: *inside CHs* (positive values), *CH boundary* (negative values), *all CHs* (both positive and negative values). For each CT box (or each structure defined by FT), the location on the low resolution map is identified after correction of their rotation (CH maps are available once per day or less often and MDI data are available a few time per day at most). The number of boxes or features for each category is shown in Table 1. CT results for which CH data are not available are of course eliminated from the analysis.

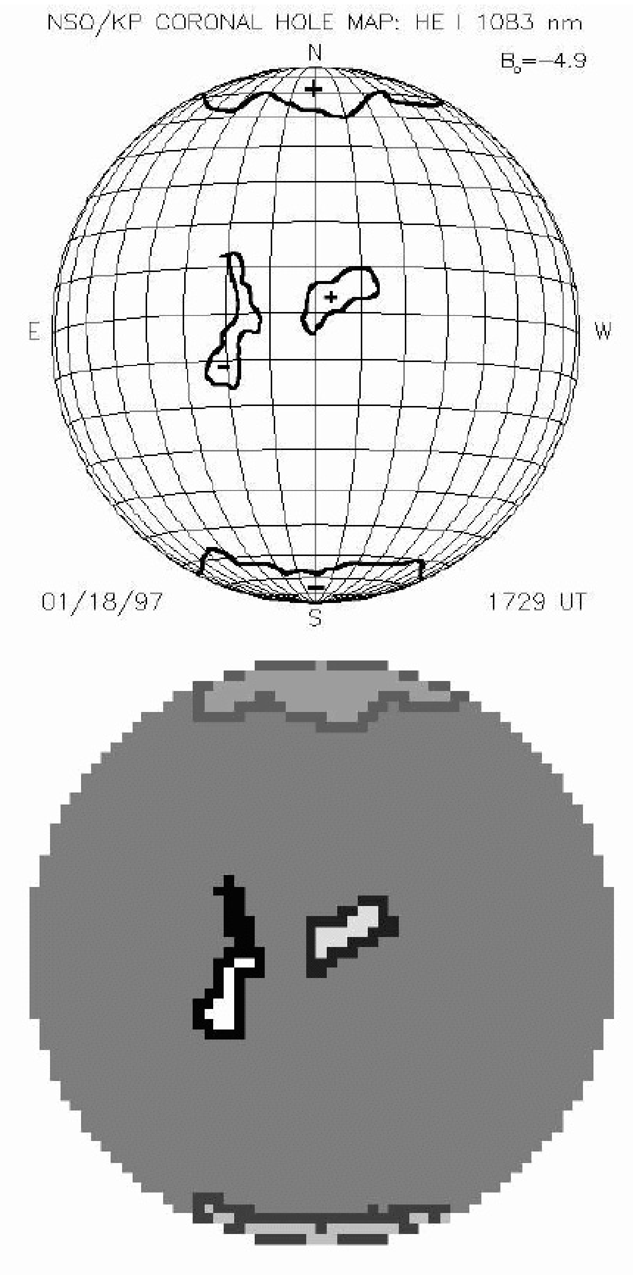

Fig. 1. *Top*: coronal hole contour for 1997 January 18 (plot from the Kitt Peak archive). *Bottom*: low resolution map derived from the list of coordinates of the coronal hole boundaries. CH boundary pixels are the darker ones, and inside CH pixels are the brighter ones.

Table 1. Number of data points for each category, before selection (all) and after selection (sel), as described in Sect. 2.3.

	all CT	sel CT	all FT	sel FT
Outside CHs	1 284 090	442 231	593 084	181 325
Inside CHs	38 167	19 131	16 440	5749
CH boundary	379 247	87 929	29 857	9956

2.3. Selection biases

Because CHs are unevenly distributed over the solar surface, great care must be taken to possible selection effects when comparing the dynamics inside and outside CHs. Similarly, the number of CHs varies during the solar cycle and selection biases are possible. Furthermore, the magnetic level inside and outside coronal holes is different, as active regions are not present inside CHs. Figure 2 shows the distribution of

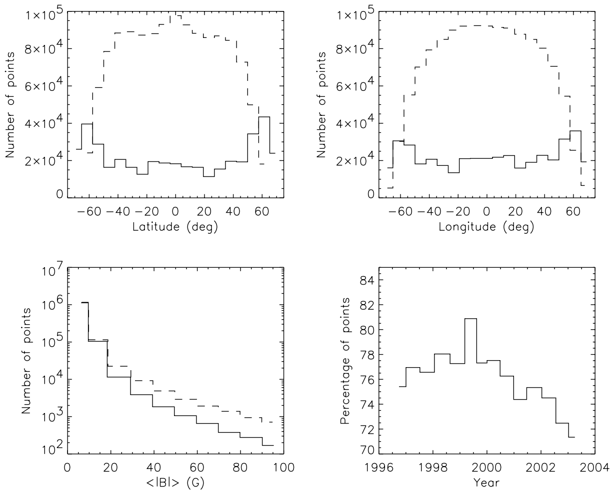

Fig. 2. *Top left*: number of CT points outside CHs (dashed line) and for all CHs (solid line) versus latitude. *Top right*: same plot versus longitude. *Bottom right*: same plot versus $\langle|B_\mathrm{c}|\rangle$ inside the CT boxes. *Bottom left*: percentage of points outside CHs.

the number of CT boxes outside CHs and for all CH data versus latitude, longitude, time and $\langle|B_\mathrm{c}|\rangle$. Because the latitudinal and temporal variations are large, the variation in the dynamics with time and latitude will be studied in the following. Furthermore, the distribution versus longitude is very different for points outside and in CHs. Therefore, in the following, points within ±16° of the central meridian only are selected. For the same reason, only weak field regions will be considered, namely with $\langle|B_\mathrm{c}|\rangle$ lower than 20 G for CT, and sizes below 100 Mm^2 for FT (i.e. network structures, see Wang 1988; and Meunier 2003). When using slightly different thresholds, the results presented in Sect. 3 are not significantly affected, because they are dominated by the weakest field regions. The number of boxes or features for each category after this selection is shown in Table 1.

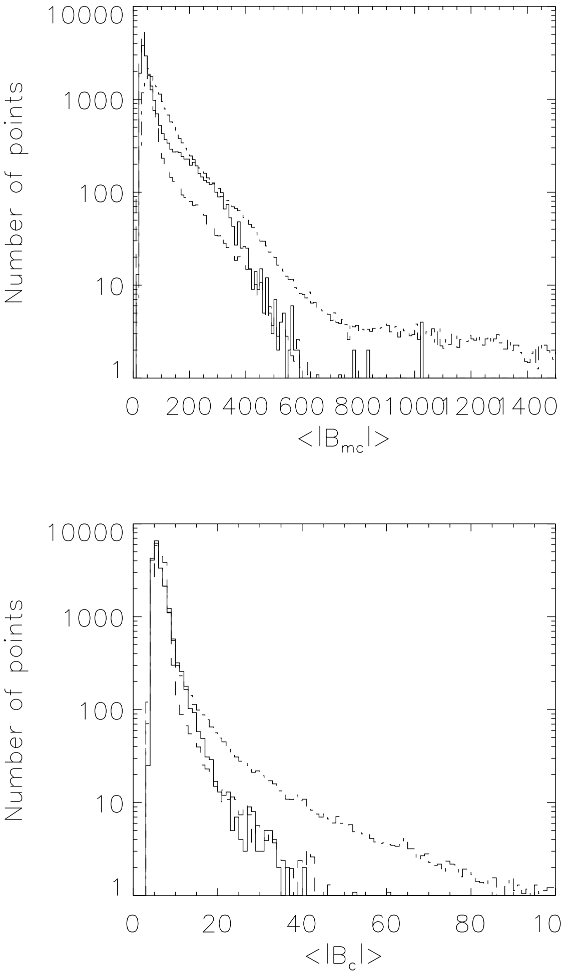

Fig. 3. *Top*: distribution of the maximum unsigned magnetic field $\langle|B_\mathrm{mc}|\rangle$ for regions outside CHs (dotted-dashed line), inside CHs (solid line) and at the CH boundary (dashed line). Histograms are normalized to the same number of points. *Bottom*: same for the average unsigned magnetic field $\langle|B_\mathrm{c}|\rangle$. All plots are for CT boxes within ±16° of the central meridian.

2.4. A few CH properties

Figure 3 shows that the distributions of the average unsigned magnetic field $\langle|B_\mathrm{c}|\rangle$ and maximum unsigned magnetic field $\langle|B_\mathrm{mc}|\rangle$ in CT boxes are quite similar inside CHs and at the CH boundary. The only exception is an excess of points for $\langle|B_\mathrm{mc}|\rangle$ in the range 50–400 G inside CHs compared to the distribution in $\langle|B_\mathrm{c}|\rangle$ and to what is observed for the CH boundary. Figure 3 shows that the distributions outside CHs extend toward much larger magnetic fields due to the presence of active regions.

Figure 4 shows the variation with time in average unsigned magnetic field outside CHs, inside CHs and at CH boundary before and after the $\langle|B_\mathrm{c}|\rangle$ selection described in Sect. 2.3. In the following, cycle minimum corresponds to the period until June 1997 and cycle maximum cover the period from May 1999 to December 2003. In the first case, the ratio between the average $\langle|B_\mathrm{c}|\rangle$ at cycle maximum and at cycle minimum is respectively 1.80, 1.43 and 1.20. After the selection $\langle|B_\mathrm{c}|\rangle <$ 20 G, they are 1.41, 1.38 and 1.14. On the other hand, the flux inside CHs is known to be variable during the solar cycle. Harvey et al. (1982) found a flux 3 times larger at cycle maximum than at cycle minimum inside low latitude CHs (for a similar area), which means that the average magnetic field is increasing by the same factor. In our case, we find a smaller variation in the average magnetic field inside CHs compared to outside (top of Fig. 4). This could be due to a selection effect when computing the dynamics. The dynamics are indeed not computed everywhere on the disk but only when the signal is large enough. In practice, the cross-correlation with amplitude lower than 0.2 are eliminated in the analysis. As a consequence, the weakest field regions are not counted, which has two effects. The first is that the average magnetic field is overestimated. This could be different inside CHs and outside CHs if the proportion of very weak field regions is different, as well as between cycle minimum and cycle maximum for the same reason. Therefore it is quite likely that the ratio is underestimated in both cases, especially in the case of CHs where we expect more weak field regions. Second, the proportion of the surface occupied by CHs is also different from what is usually observed. G. de Toma (private communication) has estimated

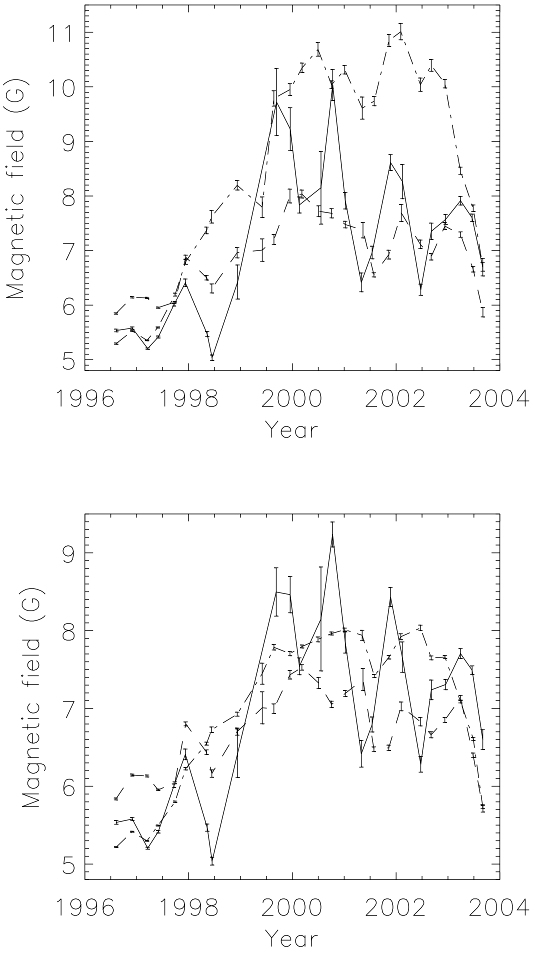

Fig. 4. *Top*: variation in $\langle|B_c|\rangle$ outside CHs (dotted-dashed line), inside CHs (solid line) and at CH boundary (line) with time for all CT boxes. *Bottom*: same for CT boxes with $\langle|B_c|\rangle$ lower than 20 G. All plots are for CT boxes within ±16° of the central meridian.

a coverage of about 20–30% of the surface by CHs at cycle minimum (from the same CH data base) and a coverage lower than 5% at cycle maximum. Here the number of points inside CHs and at the CH boundary is about 22% at cycle minimum (after selection) and still 18% at cycle maximum. The proportions are very similar before the selection described in Sect. 2.3, so the sampling effect related to the discarding of regions with low cross-correlation could explain this difference.

Figure 5 shows the CH size distribution for various latitude ranges in our CT sample. There is an asymmetry between hemispheres at high latitudes. The size distributions at high latitude show a peak around 5–6% of the visible hemisphere. On the other hand, at low latitude, there is a strong peak for small size (below 3% of the visible hemisphere), as well as a significant contribution in the range 5–6% as well, which may be due to the fact that a large fraction of high latitude CHs have an extension toward low latitudes. There is also an asymmetry between hemispheres at low latitudes.

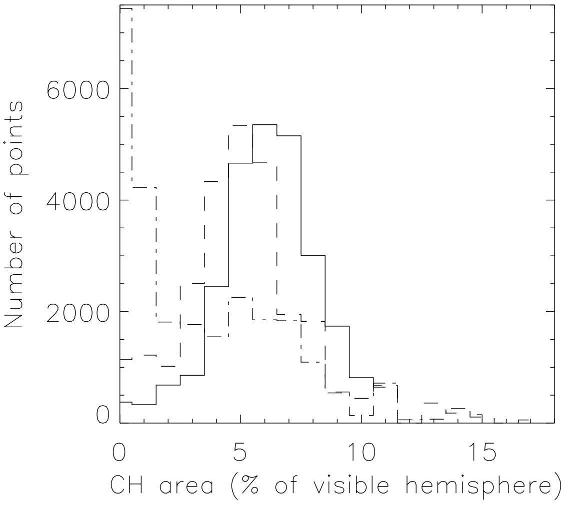

Fig. 5. CH area distribution above latitude 40° (solid line), below latitude –40° (dashed line), and between latitudes –40° and 40° (dotted-dashed line). Plots are for CT boxes within ±16° of the central meridian and for CT boxes with $\langle|B_c|\rangle$ lower than 20 G.

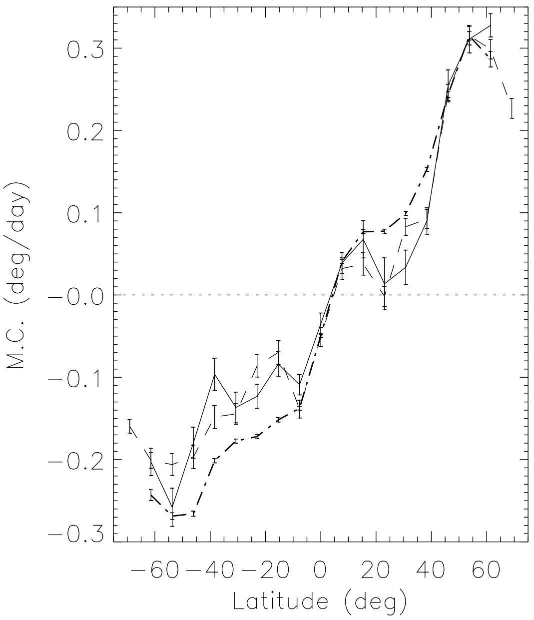

Fig. 6. Meridional circulation versus latitude outside CHs (thick dotted-dashed line), inside CHs (solid line), and at the CH boundary (dashed line). Positive meridional circulation is toward the North pole. Plots are for CT boxes within ±16° of the central meridian and for CT boxes with $\langle|B_c|\rangle$ lower than 20 G.

3. Results

3.1. Meridional circulation

Figure 6 shows the meridional circulation versus latitude for the various categories. In the range 10–40°, i.e. in the activity belt, the meridional circulation is less poleward inside CHs and at the CH boundary than outside CHs in both hemispheres. Meunier (1999, 2005a) for example observed a converging pattern (higher poleward motion at low latitude compared to the adjacent poleward latitude band) in the activity belt superimposed on the traditional poleward meridional circulation

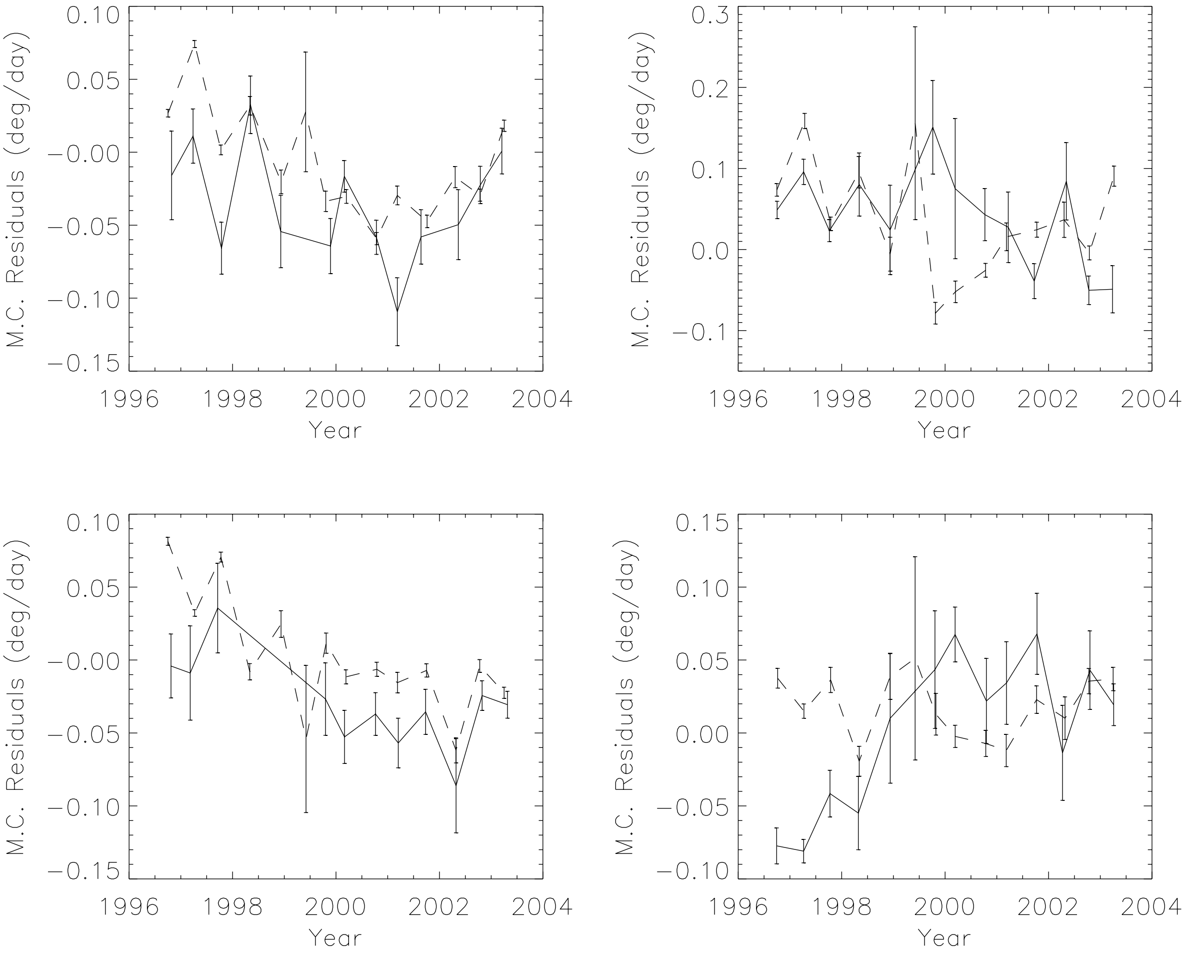

Fig. 7. Meridional circulation residuals versus time outside CHs (dashed line) and for all CHs (solid line). *Top*: northern hemisphere. *Bottom*: southern hemisphere. *Left*: latitudes lower than 40°. *Right*: latitudes larger than 40°. Positive residuals correspond to a more poleward motion than average. Plots are for CT boxes within ±16° of the central meridian and for CT boxes with $\langle|B_c|\rangle$ lower than 20 G.

which increases monotonously as a function of latitude (see also Haber et al. 2003; Zhao & Kosovichev 2004). Meunier (1999) found that this pattern was mainly seen in active regions. The more precise study of Meunier (2005a) showed that this pattern was more pronounced for larger values of $\langle|B_c|\rangle$ while it disappeared for very small values of $\langle|B_c|\rangle$. Here, the converging pattern is clearly seen in CH in the weak field regime, but it is almost absent outside the CH for similar values of $\langle|B_c|\rangle$. It also shows that this pattern is not associated with active regions only. At high latitude, i.e. above 40°, CH points have a smaller meridional circulation than outside CH in the Southern hemisphere. However, in the Northern hemisphere, the meridional circulation is very similar outside and inside CHs, with a tendency for a slightly larger meridional circulation in CHs. Therefore, the high-latitude asymmetry between hemispheres is larger in CHs than outside CHs.

The meridional circulation residuals are computed as in Meunier (2005a) as follows. The average meridional circulation in a latitude bin is subtracted from all values corresponding to that range. The sign is changed in the Southern hemisphere, so that a positive residuals means a more poleward motion than average, for that latitude range. Furthermore, Fig. 7 shows the meridional circulation residuals separately at high and low latitudes, and in the two hemispheres. At low latitude, the residuals in CHs are smaller than outside CHs at all time, which shows that the characteristics seen in Fig. 6 are quite stable. At high latitude on the other hand, the residuals are similar in and outside CHs at all time, with a tendency to have smaller residuals in CHs until 1999, larger ones from 2000 to 2001, and smaller ones afterwards. In the Southern hemisphere the tendency is the same with smaller errorbars, as the residuals are significantly smaller in CHs during the first years.

Figure 8 shows the average meridional circulation inside CHs versus the size of CHs in two cases, at high latitude and in the activity belt. At high latitude, there is a tendency for a smaller meridional circulation associated with small CHs in the Northern hemisphere but this is not seen in the Southern hemisphere. On the other hand, the weaker meridional circulation in CHs compared to outside is quite clear in the Southern hemisphere for almost all size ranges, except perhaps the very large ones. However, this is not the case in the Northern hemisphere, as the weaker meridional circulation seems only present for small CHs. Therefore, there is a strong asymmetry between hemispheres as already seen in Fig. 6. In the activity belt, the weaker meridional circulation in CHs is clearly seen for areas up to 7% of visible hemisphere. Above this value, it may not

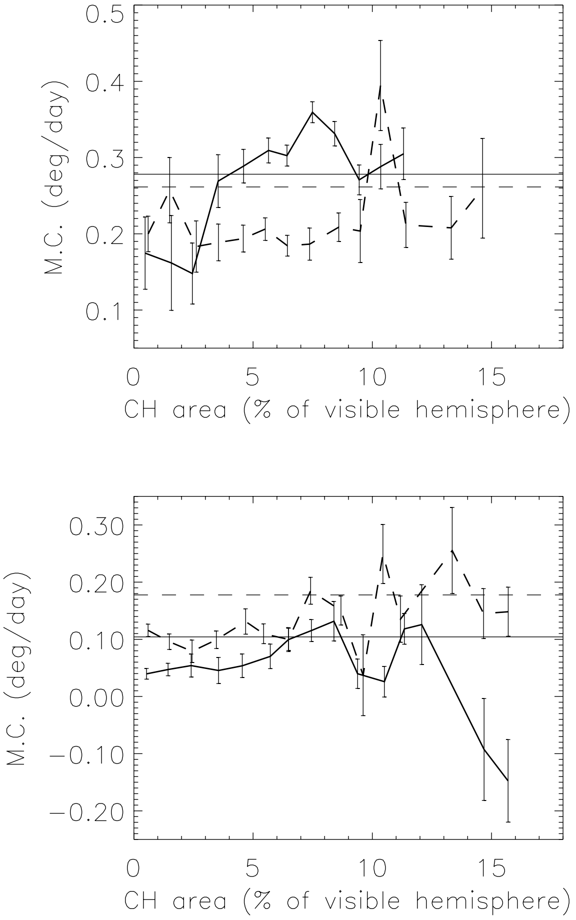

Fig. 8. *Top*: meridional circulation versus the CH size (extracted from the CH data base) at latitudes larger than 40° in the Northern hemisphere (thick solid line) and in the Southern hemisphere (thick dashed line), for all CH categories. The horizontal thin lines correspond to the meridional circulation outside CHs. *Bottom*: same for the latitude range 10–40°. Positive meridional circulation is toward the poles. CH areas are in % of the visible hemisphere. Plots are for CT boxes within ±16° of the central meridian and for CT boxes with $\langle|B_c|\rangle$ lower than 20 G.

be present, but the very large CHs in the Northern hemisphere may have a much smaller meridional circulation as well.

The variation in meridional circulation with increasing $\langle|B_c|\rangle$ observed by Meunier (2005a) is computed separately for the different categories. The resulting decrease is shown in Fig. 9. For the weakest fields the slope is steeper inside CHs and at CH boundary than outside CHs, up to $\langle|B_c|\rangle \sim 6$ G. For $\langle|B_c|\rangle$ above 5 G, the meridional circulation become less poleward in CHs. Above 7 G, there is no significant difference as the uncertainties become larger.

The errorbars, larger in the FT method, prevented the detection of any difference of the order of those detected with CT when looking at the latitude variation with this technique.

3.2. Rotation

Table 2 shows the coefficients obtained from fits made with Legendre polynomials in $\sin^i(\theta)$ (θ the latitude) on the CT angular velocity versus latitude (as in Meunier 2005a). The equatorial rate A_{eq} is also shown and is slightly larger inside CHs than outside CHs and at the CH boundary. More interesting is the fact that the photospheric rotation in CHs is consistently more differential than outside CHs, with significantly more differential rotation at the boundaries compared to inside CHs. The differences between the various categories are shown in Fig. 10 (bottom). At low latitudes, the differences are hardly significant. At latitudes greater than 40° however, the differential rotation is not as strong inside CHs and outside CHs as at CH boundaries, as could already be suspected from the A_2 and A_4 coefficients in Table 2.

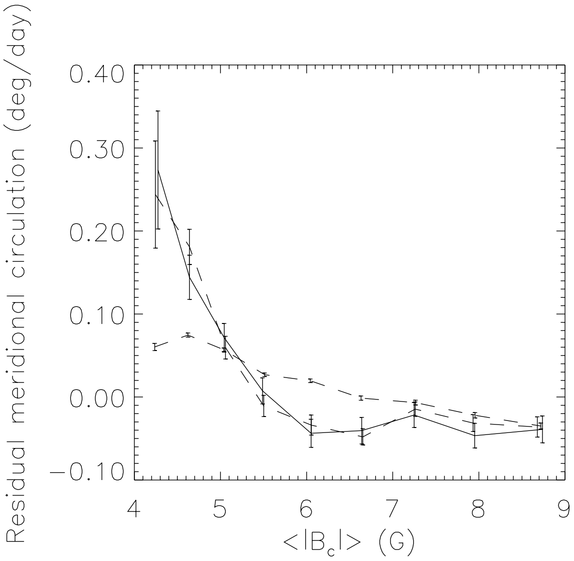

Fig. 9. Meridional circulation residuals versus $\langle|B_c|\rangle$ outside CH (dotted-dashed line), inside CHs (solid line) and at the CH boundary (dashed line). Positive residuals correspond to a more poleward motion than average. Plots are for CT boxes within ±16° of the central meridian and for CT boxes with $\langle|B_c|\rangle$ lower than 20 G.

The antisymmetry between hemisphere, characterized by the A_1 and A_3 coefficients is also shown in Fig. 10 (top). In Meunier (2005a), it was found to be very small. Here it remains small outside CHs but it is significantly different from zero inside CHs, as the Southern hemisphere rotates faster than the Northern hemisphere inside CHs. This is true at high latitude only (i.e. above 40°).

As for meridional circulation, the temporal variation in rotation residuals is computed separately at high and low latitudes, and in the two hemispheres. It is difficult to extract any systematic pattern. At low latitude, the rotation seems lower in CHs than outside CHs in 2001–2002 in the Northern hemisphere, and at the beginning of the cycle in the Southern hemisphere but the errorbars are quite large. At high latitude, no systematic pattern is seen either.

Figure 11 shows the variation in the CT rotation residuals versus CH area. For small CHs, which correspond mostly to low latitudes, the residuals may be larger in CHs compared to outside, and similar in both hemispheres, but this is not significant. On the other hand, for CH sizes in the range of 6–9% of the visible hemisphere, the residuals are much larger in the Southern hemisphere than in the Northern hemisphere, which reproduces the asymmetry at high latitude obtained from the

Table 2. Coefficients A_i with $i = [0, ..., 4]$ from fits with Legendre polynomials in $\sin^i(\theta)$ on rotation rates versus latitude (in deg/day) and equatorial rate, $A_{\rm eq}$, from a polynomial fit in $\sin^i(\theta)$.

Location	A_0	A_1	A_2	A_3	A_4	$A_{\rm eq}$
Outside CHs	13.309 ± 0.002	–0.004 ± 0.003	–2.559 ± 0.006	0.003 ± 0.004	–0.540 ± 0.005	14.386 ± 0.001
Inside CHs	13.317 ± 0.006	–0.060 ± 0.013	–2.589 ± 0.019	–0.067 ± 0.019	–0.553 ± 0.023	14.404 ± 0.008
CH boundary	13.281 ± 0.004	–0.010±0.007	–2.682 ± 0.009	0.010 ± 0.011	–0.642 ± 0.013	14.381 ± 0.008

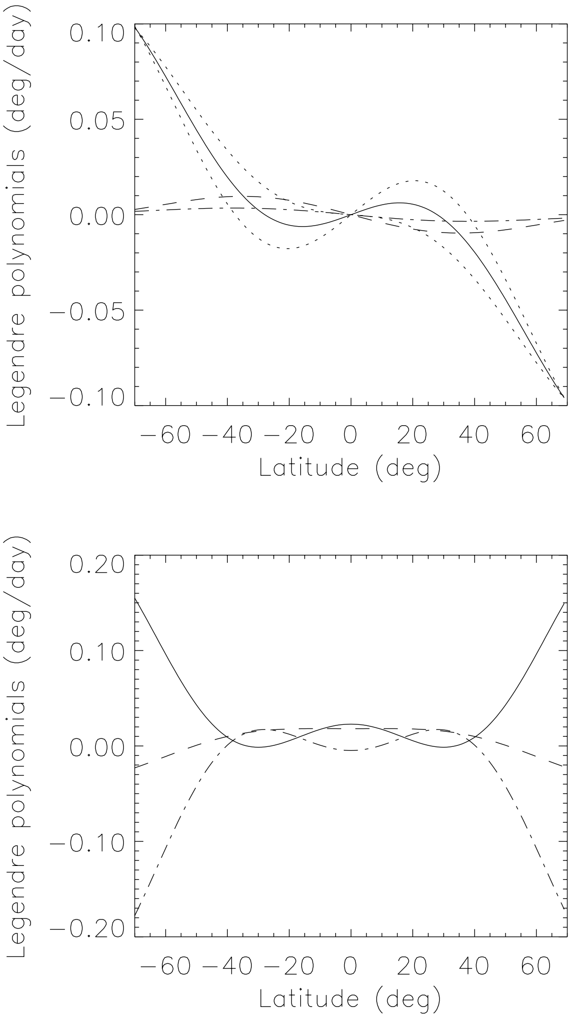

Fig. 10. *Top*: antisymmetrical part of the Legendre polynomial fit outside CHs (dotted-dashed line), inside CHs (solid line) and at CH boundary (dashed line), as deduced from the A_1 and A_3 coefficients in Table 2. The two dotted lines give an estimation of the uncertainty on the dashed line. *Bottom*: difference between the symmetrical part of the Legendre polynomial fit from the A_0, A_2, and A_4 coefficients in Table 2, in three cases, inside CHs minus outside CHs (dashed line), CH boundary minus outside CHs (dotted-dashed line), and inside CHs minus CH boundary (solid line). The errorbars are not shown for clarity, but are of the order of the signal at low latitude.

polynomial fits. This effect may still be present for the largest CHs. This is also consistent with the fact that CHs in that size range are predominantly present at high latitude.

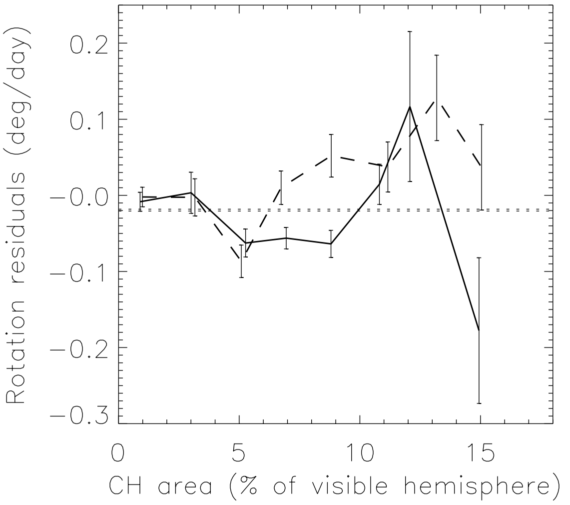

Fig. 11. *Top*: rotation residuals versus CH size (in percentage of visible hemisphere) in the Northern hemisphere (solid line) and Southern hemisphere (dashed line). The horizontal dotted line shows the average residual values outside CHs. Plots are for CT boxes within ±16° of the central meridian and for CT boxes with $\langle|B_{\rm c}|\rangle$ lower than 20 G.

When separating the leading and following polarity regions as in Meunier (2005b), we find a similar result, with the following regions rotating faster than the leading regions for weak fields. On the other hand, the variation in rotation with increasing $\langle|B_{\rm c}|\rangle$ observed by Meunier (2005a) is computed separately for the different categories. The difference between the various categories is not very significant.

3.3. Velocity dispersions

A Gaussian fit to the residual velocity distribution is performed in each latitude bin for the various categories. The latitude bins are 7.68° wide, which is derived from the size of the CT boxes (see Sect. 3.1). The resulting HWHM are shown in Fig. 12 for CHs in the activity belt. For CT, the HWHM is smaller in CHs than outside CHs for both rotation and meridional circulation. The latitude dependence for both velocities is however different, with a peak around the equator for the rotation. The amplitude of this peak is twice as large in CHs than outside CHs. On the other hand, the HWHM for the FT residuals tends to be larger in CHs than outside CHs. It is not as significant at the CH boundary, however. The latitude dependence is also different between rotation and meridional circulation, and is different to the CT variation.

4. Discussion and conclusion

Comparison of the large-scale dynamics deduced from cross-correlation between pairs of photospheric magnetograms and

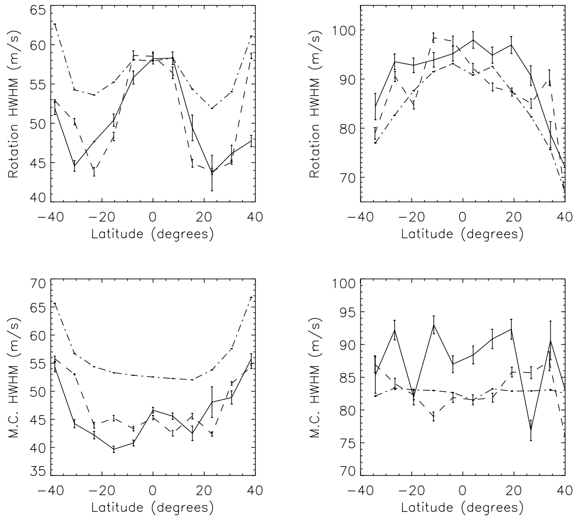

Fig. 12. *Top*: HWHM computed from gaussian fits over the CT (*left*) and FT (*right*) rotation residuals versus latitude, for boxes outside CHs (dotted-dashed lines), inside CHs (solid lines) and at the boundary (dashed lines). Bottom: same for meridional circulation. Plots are for CT boxes within ±16° of the central meridian and for $\langle|B_c|\rangle$ lower than 20 G and for FT structures smaller than 100 Mm^2 within ±16° of the central meridian.

CH data shows some significant differences between the behavior of the photosphere outside and inside CHs. However, the FT technique did not lead to many significant differences between CHs and outside CHs, due to larger uncertainties. The new results can be summarized as follows:

- A weaker CT meridional circulation inside CHs, with a stronger converging pattern in CHs in the activity belt.
- A more differential CT rotation inside CHs at high latitude.
- More asymmetrical dynamics between the hemispheres for high latitude CHs.
- A dependence of the dynamics on the CH size related to the latitude distribution of CHs and to the size distributions of CHs.
- A different temporal variability of the meridional circulation at high latitude.
- A smaller CT dispersion in velocity inside CHs in the activity belt than outside CHs, and a larger FT dispersion.
- A different CT rotation in the core of the CHs compared to the boundaries, at high latitude.
- A different dependence of the meridional circulation on magnetic field, with steeper variations in CHs than outside for the weakest magnetic fields.

With supergranular diffusion, the differential rotation and meridional circulation are crucial ingredients in the distribution of the magnetic flux at the solar surface (Wang & Sheeley 1990, for example). The more differential rotation in particular may appear in apparent contradiction to the relatively rigid rotation of CHs themselves. On the other hand, a weaker meridional circulation is compatible with a more differential rotation, which may explain the observed dynamics at high latitude. The variability of the dynamics inside CHs is as large as outside CHs, while the average magnetic field level is less variable in our sample. The North-South asymmetry is already well known, as shown by the asymmetric distribution in size with latitude, but it also shows up in the dynamics inside CHs, as the rotation is larger and the meridional circulation smaller in the Southern hemisphere at high latitude. These properties remain to be explained.

The dispersion in CT meridional circulation and rotation are mostly related to large-scale flows such as those derived by Ambrož (2001). They have rms amplitudes around 40–60 m/s while the flows derived by Ambrož (2001) have a rms amplitude around 40 m/s, so the orders of magnitudes are in very good agreement. This large-scale circulation seems therefore partially inhibited inside CHs and at the CH boundary. On the other hand, FT dispersions are related to the large-scale circulation as well, possibly at a different depth and therefore of different amplitude, but also to the diffusion of individual magnetic features. The FT dispersion is indeed larger than the CT ones, and is also larger inside CHs than outside CHs. This suggests that the diffusion inside CHs and at CH boundary is larger than outside CHs. However, the FT dispersion is smaller than expected from typical diffusion coefficients obtained in the literature. For example, Berger et al. (1998) and Hagenaar et al. (1999) measured diffusion coefficients of about 50–70 km^2/s. Over 96 min, this corresponds to an average displacement of the order of 180–220 m/s, which is larger than the FT dispersion obtained here, of the order of 130 m/s at the equator. A value of 130 m/s corresponds to a diffusion coefficient of about 25 km^2/s. This may be due to the fact that the FT tracking is biased toward larger network structures than in the work of Berger et al. (1998) and Hagenaar et al. (1999), as only structures with an unsigned magnetic field above 40 G on MDI full-disk magnetograms and sizes larger than 10 Mm^2 are considered with FT. Therefore a more detailed analysis with high spatial resolution observations would be necessary.

Wang & Sheeley (2002) explain the rigid rotation of CHs by some reconnection between small magnetic structures at the boundary of CHs. The field lines associated with these structures change their status between open and closed loops in the process and, therefore, cross the boundary, allowing for a rigid rotation of CHs despite the differential rotation of these magnetic structures. On the other hand, Fisk et al. (1999) explain the rigid rotation by large excursions of the field lines in latitude, due to the differential rotation and the non radial expansion of the solar wind from the Sun. The model of Wang & Sheeley (2002) is already favored by the work of Madjarska et al. (2004), who found some evidence of reconnection along CH boundaries for the first time (these reconnections have been detected as bidirectional jets observed with SUMER on SOHO). Raju et al. (2005) also found some evidence of reconnection from the study of correlations between CHs and quiet Sun intensities. The results obtained here are compatible with a larger diffusion at the CH boundary compared to outside, but it is not larger than inside CHs for example. This larger diffusion may contribute to the larger excursion of the field lines as in the Fisk et al. (1999) model. On the other hand, this larger diffusion may be due to the open field-line of these structures, or to different properties of supergranules in CHs compared to outside CHs. This should be taken into account when studying the behavior of the open magnetic field, as in the model of Fisk & Schwadron (2001). The main specific behavior of the CH boundary found here is the larger differential rotation at the CH boundary at high latitude. This may also play a role in the reconnection processes occuring at these boundaries.

These new results show that large-scale flows inside CHs are smaller than outside CHs. Despite the more differential rotation of the photosphere inside CHs, these weaker flows may play a role in the processes leading to the rigid rotation of CHs, while the small-scale dynamics may be consistent with reconnection processes. There is a possibility that the rigid boundary of CHs may prevent the largest scale flows from developing. This should be investigated further, as should the depth dependence of these characteristics. The temporal variability in the dynamics inside CHs must also be compared to the results obtained in Meunier (2005c). The large variation in meridional circulation of high-latitude CHs in the Southern hemisphere may be responsible for most of the variation in the Southern hemisphere observed by Meunier et al. (2005c), but that does not seem to be the case in the Northern hemisphere. In future works, it will be necessary to increase the temporal coverage (by using several cycles), as with one cycle the uncertainties are still large when trying to study the dependence on the various physical parameters.

Acknowledgements. SOHO is a mission of international cooperation between the European Space Agency (ESA) and NASA. The coronal hole data used in this work were compiled by K. Harvey and F. Recely using NSO KPVT observations under an NSF grant. I am very grateful to C. Henney for his help with these data and to G. de Toma for her estimations of the magnetic contents of coronal holes.

References

Ambrož, P. 2001, Sol. Phys., 198, 253
Antonucci, E., Azzarelli, L., Casalini, P., Cerri, S., & Denoth, F. 1979, Sol. Phys., 63, 17
Berger, T. E., Löfdahl, M. G., Shine, R. A., & Title, A. M. 1998, ApJ, 506, 439
Brajša, R., Wöhl, H., Vršnak, B., et al. 2004, A&A, 414, 707
de Toma, G., & Arge, N. 2005, 22th Sacramento Peak Solar Workshop, October 2004, in press
Fisk, L. A., Zurbuchen, T. H., & Schwadron, N. A. 1999, ApJ, 521, 868
Fisk, L. A., & Schwadron, N. A. 2001, ApJ, 560, 425
Haber, D. A., Hindman, B. W., & Toomre, J. 2003, in Proc. SOHO 12/GONG+ 2002, Local and Global Helioseismology: The Present and Future, ed. H. Sawaya-Lacoste, 103
Hagenaar, H. J., Schrijver, C. J., Title, A. M., & Shine, R. A. 1999, ApJ, 511, 932
Harvey, K. L., & Recely, F. 2002, Sol. Phys., 211, 31
Harvey, K. L., Sheeley, N. R. Jr., & Harvey, J. W. 1982, Sol. Phys., 79, 149
Kahler, S. W., & Hudson, H. S. 2002, ApJ, 574, 467
Komm, R. W., Howard, R. F., & Harvey, J. W. 1993a, Sol. Phys., 145, 1
Komm, R. W., Howard, R. F., & Harvey, J. W. 1993b, Sol. Phys., 147, 203
Madjarska, M. S., Doyle, J. G., & van Driel-Gesztelyi, L. 2004, ApJ, 603, L57
Meunier, N. 1999, ApJ, 527, 967
Meunier, N. 2003, A&A, 405, 1107
Meunier, N. 2005a, A&A, 436, 1075
Meunier, N. 2005b, A&A, 437, 303
Meunier, N. 2005c, A&A, 442, 693
Raju, K. P., Bromage, B. J. I., Chapman, S. A., & Del Zanna, G. 2005, A&A, 432, 341
Scherrer, P., Bogart, R. S., Bush, R. I., et al. 1995, Sol. Phys., 162, 129
Snodgrass, H. B., & Ulrich, R. K. 1990, ApJ, 351, 309
Wang, H. 1988, Sol. Phys., 116, 1
Wang, Y.-M., & Sheeley, N. R. Jr. 1990, ApJ, 365, 372
Wang, Y.-M., & Sheeley, N. R. Jr. 2004, ApJ, 612, 1196
Wang, Y.-M., Hawley, S. H., & Sheeley, N. R. Jr. 1996, Science, 271, 464
Zhao, J., & Kosovichev, A. G. 2004, ApJ, 603, 776

A&A 461, 1141–1147 (2007)
DOI: 10.1051/0004-6361:20065625

Astronomy & Astrophysics

Velocities and divergences as a function of supergranule size

N. Meunier[1], R. Tkaczuk[2], Th. Roudier[1], and M. Rieutord[2]

[1] Laboratoire d'Astrophysique de l'Observatoire Midi-Pyrénées, Université Paul Sabatier Toulouse III, CNRS, 57 avenue d'Azereix, BP 826, 65008 Tarbes Cedex, France
e-mail: `[nadege.meunier;thierry.roudier]@ast.obs-mip.fr`
[2] Laboratoire d'Astrophysique de l'Observatoire Midi-Pyrénées, Université Paul Sabatier Toulouse III, CNRS, 14 avenue Édouard Belin, 31400 Toulouse, France
e-mail: `[ruben.tkaczuk;michel.rieutord]@ast.obs-mip.fr`

Received 17 May 2006 / Accepted 23 September 2006

ABSTRACT

Context. The origin of supergranulation is not understood yet and many scenarios, which range from large-scale deep convection to large-scale instabilities of surface granular flows, are possible.
Aims. We characterize the velocities and divergences in supergranulation cells as a function of their size.
Methods. Using local correlation tracking, we determine the horizontal flow fields from MDI intensity maps and derive the divergences. The smoothed divergences are used to determine the cells for various spatial smoothings, in particular at the supergranular scale.
Results. We find evidence of intermittency in the supergranular range and a correlation between the size of supergranules and the strength of the diverging flow. We also show that the relation between rms velocities and scale (the supergranule radius R) can be represented by a law $V_{\rm rms} \sim R^{0.66}$.
Conclusions. The results issued from our data point towards a scenario where supergranulation is a surface phenomenon of the sun, probably the consequence of a large-scale instability triggered by strong positive correlated rising flows.

Key words. Sun: granulation – Sun: photosphere – Sun: general

1. Introduction

Since its discovery by Hart (1954), the origin of supergranulation has not been determined. It has long been thought to be due to convection related to the He^{++}–He^{+} transition (Simon & Leighton 1964; van der Borght 1979) but recent work shows that this may not be the case. Another suggestion has been made by Rieutord et al. (2000) that the supergranulation could be the result of a large-scale instability triggered by exploding granules. Rast (2003b) has also explored that possibility. However, this scenarios need to be refined and call for more observations.

Unfortunately only a few attempts have been made to discriminate between these scenarios. Most studies of the intensity variation accross supergranules found an enhancement at the boundary due to the presence of the network (Beckers 1968; Frazier 1970; Foukal & Fowler 1984; Lin & Kuhn 1992) but recently a decrease of the intensity from the center to the boundary of supergranules has been observed (Rast 2003a; Meunier et al. 2006a). Following another approach, Krishan et al. (2002) studied the variation of maximum velocities in supergranule cells as a function of their size. They found a slope on a log-log scale of 1/3 surprisingly compatible with an interpretation of supergranulation as a turbulent feature in the Kolmogorov model of turbulence. However, these authors worked with a small number of cells, hence with large errorbars. Moreover, their velocity fields were deduced from Dopplergrams thus needing additional assumptions to remove projection effects and adding more uncertainties to the results.

Krishan et al. (2002) pointed out the importance of the relation between velocity and scale in order to constrain the dynamics of supergranulation. Here, we present new and more precise determinations of scaling laws for the velocity field in the supergranulation range. We also investigate the statistics of supergranulation, looking for intermittency and examine the gross features of the flow inside a supergranule, especially their relation with size.

We use a data set from the MDI instrument onboard the SOHO observatory. With the local correlation tracking technique applied to a set of intensity maps, we derive horizontal velocities (Sect. 2) and study the dependence of a typical velocity versus cell size as a function of the spatial smoothing (Sect. 3). In Sect. 4, we investigate the variations of the divergence moments over the cells as a function of cell size and spatial smoothing. In Sect. 5, we examine the velocity and divergence radial profiles as a function of the cell size as well as the locations of the pixel with maximum velocity inside the cells. Discussion and conclusions follow.

2. Data processing

2.1. The MDI data set

Our data set is constituted of 15 h of MDI-SOHO intensity maps obtained in the high resolution mode (Scherrer et al. 1995) in March 1997. The pixel size is 0.605 arcsec (0.43 Mm) and the image size is 1024×500 pixels (i.e. ~620″×303″). The cadence is one image per minute. The field-of-view is centered on disk center and contains only quiet network magnetic fields.

2.2. Velocity fields

As large-scale intensity gradients are present in MDI intensity maps due to the center-to-limb darkening and to residuals from flat-field corrections, a correction is applied to the maps in order to make them suitable to compute the horizontal velocity fields. For this purpose, a third degree polynomial 2D fit is performed over an intensity map averaged over the whole period. Over each 1-h period, the 60 corrected intensity maps are then shifted to match a reference (the central image of each 1-h data set). Due to the loss of a few columns because of the solar rotation over one hour, the final maps contain 1002×500 pixels (i.e. $607''\times303''$). Each 1-h time series is then filtered using a $k-\omega$ filter with a velocity cut at 6 km s^{-1}, as is usually done to remove 5-min solar oscillations.

The horizontal flow fields are then computed using a classic Local Correlation Tracking (hereafter LCT) method between 2 consecutive images. They are averaged over each 1-h period. The LCT computations are made using 3×3 pixel boxes, and the velocities are smoothed with a Gaussian with a 6 pixels *FWHM*, i.e. $3.63''$ (a few granules). This leads to 15 individual velocity maps. We refer to Roudier et al. (1999), to DeRosa & Toomre (2004) and to references therein for discussions about the LCT.

2.3. Divergence and velocity maps

A divergence map is computed for each velocity field map as well as a smoothed divergence map showing only the large-scale variations, as our purpose is to identify supergranules. The smoothed map is obtained by convolving in Fourier space the original map by a 2D Gaussian function with a *FWHM* "Γ". Supergranules have been determined using a smoothing of $\Gamma = 10.2$ Mm. This smoothing will be justified in the next section by the resulting cell radius distribution, which has an average of $\sim$15 Mm, as being adapted to the typical size of supergranules. We also observe that at this scale the magnetic network is located in the regions of strong converging flows and at the cell boundary as expected (Meunier et al. 2006a,b). Our purpose is not to determine *exactly* the supergranular size (to compare with other estimates for example, as this is indeed very sensitive to the choice of the spatial smoothing), but to consider maps at the supergranular scale and then determine various properties at this scale. The parameter Γ will also be used to study the dependence of the results on the spatial smoothing.

Velocity maps showing the modulus of the horizontal velocity are also computed. They are smoothed using the same method as the divergence maps. Velocities are in m/s and divergences in s^{-1}. A correction is applied to take into account the projection effects over the field of view. These effects are small however, with a maximum of 1% distortion in the corners of the images, and the residuals are much smaller. Furthermore, as the velocity and cell radius suffer from the same projection effects, the dependence of the radius on the velocity is not significantly affected. The divergences, in s^{-1}, are not significantly affected either.

2.4. Supergranule cell determination

The cells are determined using the smoothed divergence maps. A steepest gradient algorithm is used to determine the cell to which a given pixel belongs (see Hagenaar et al. 1997, for an application of this method to smoothed CaIIK images for supergranule cells determination). Thus for each pixel of the smoothed divergence map, the direction of the steepest gradient is computed. If this gradient is positive, we iterate the computation for the corresponding pixel until it converges to a fixed position. For each starting pixel, the iteration ends when a local maximum is reached. Pixels associated with the same local maximum are considered to belong to the same cell. Cells joined by a high amplitude of divergence are associated. Because of the spatial smoothing done in Fourier space, sides effects appear. To remove them, we do not use divergences close to the edges of the field of view. We also eliminate incomplete cells. This algorithm can be used for any smoothing Γ.

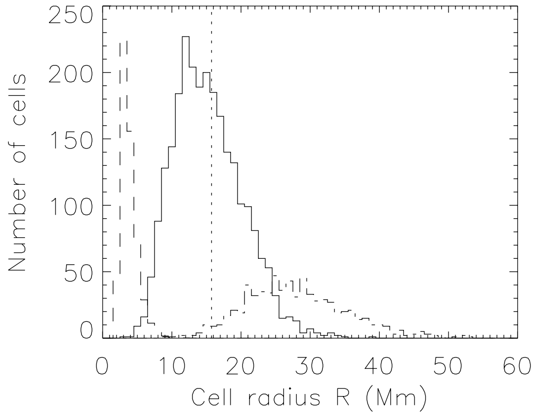

Fig. 1. Distribution of the cell radius R (Mm) for $\Gamma = 10.2$ Mm (solid line), for $\Gamma = 20.4$ Mm (dotted-dashed line) and for no smoothing (dashed line, number of cells divided by 60). The vertical dotted line indicates the average R for $\Gamma = 10.2$ Mm.

The center of gravity computed over the surface of a cell is then considered to be its center. The maximum distance R between this center of gravity and the edge of the cell is considered as a radius estimate. Figure 1 shows the distribution of R for the 2268 identified cells for $\Gamma = 10.2$ Mm. The average cell size is 15.7 ± 0.1 Mm. The distribution is slightly asymmetric and peaks at values smaller than the average, i.e. around 13−14 Mm. Hagenaar et al. (1997) found a peak around 12−13 Mm, which is very similar. The maximal extent of this distribution is also close to that of Krishan et al. (2002), who used the linear size $L = \pi R$, as it covers a similar range of sizes, but our cell sample is much larger. Figure 1 shows for comparison the distributions for no smoothing and for a large smoothing. As expected, Γ and R are strongly correlated (Fig. 2). Small values of Γ correspond to the mesogranulation scale, and Γ around 10 Mm to the supergranulation one. We will see in the following that a specific signal is associated with these typical scales. Figure 2 also shows the number of cells for each spatial smoothing. There are of course more cells at smaller scales. On the linear-log plot, the slope slightly changes at $\Gamma \sim 10$ Mm.

In each cell and for a given pixel, we also define the relative distance $d_{\rm rel}$ to the cell center as follows. The distance of each pixel P located at position (i, j) of the cell to the center of gravity O is called d. We then consider the pixel B belonging to the cell boundary with the following properties: B, P and O must be aligned, and B is as close as possible to P. The distance between the cell center O and this boundary pixel B is d'. $d_{\rm rel}$ is then derived as d/d'. $d_{\rm rel}$ takes the value of 0 at the center of gravity of the cells and 1 on the boundary. This will be used in Sect. 5 to study the radial profiles.

With this definition of supergranules, we find a good coincidence between the cell boundary and the magnetic network, which shows that our cells represent a fairly good definition of supergranules. Moreover, we obtain typical horizontal velocity fields of the order of a few 100 m/s, in very good agreement

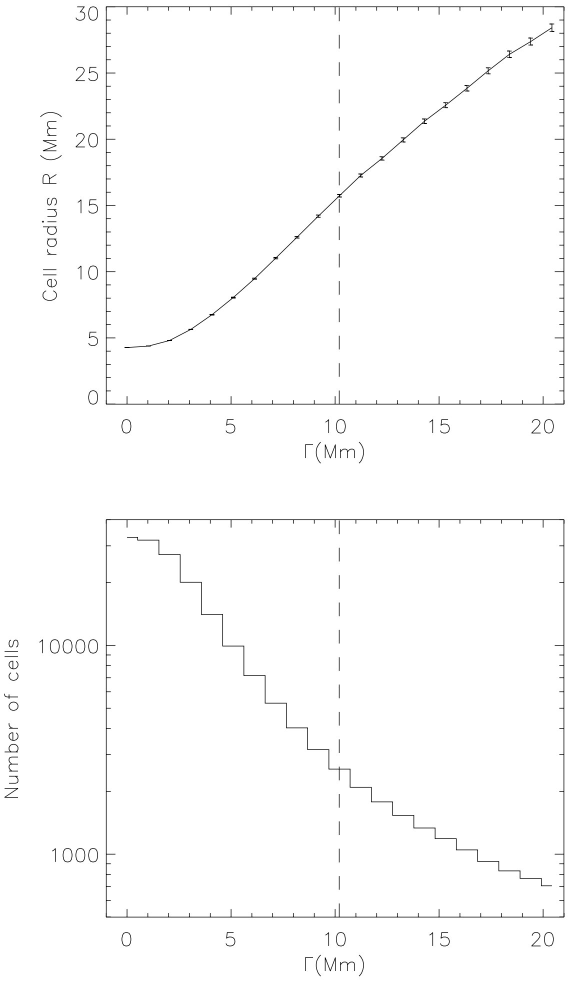

Fig. 2. *Upper panel*: mean cell radius versus the spatial smoothing Γ. The smoothing of 10.2 Mm indicated by a dashed line corresponds to an average cell radius R of 15.7 Mm and is used in this work to characterize supergranulation. *Lower panel*: number of cells versus the spatial smoothing Γ.

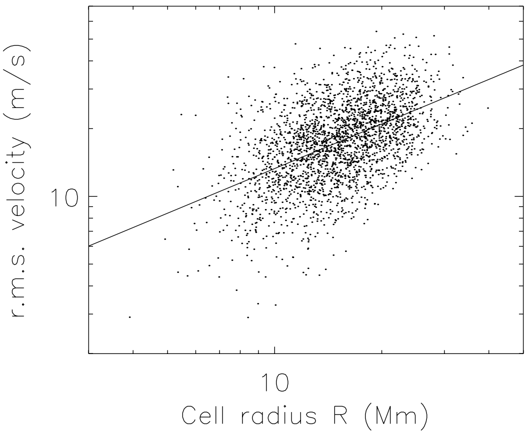

Fig. 3. Rms velocity versus the radius of supergranules using smoothing parameter $\Gamma = 10.2$ Mm. The x-axis goes from 3 to 50 Mm and the y-axis from 2 to 70 m/s. The straight line is a linear fit on the points.

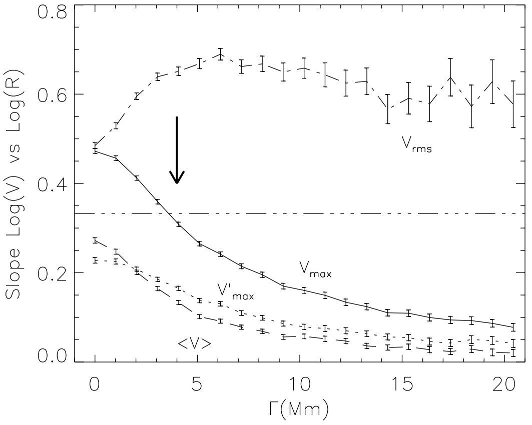

Fig. 4. Slope of Log (V) versus log (R) versus the smoothing Γ in the velocity maps, for $V_{\rm max}$ (solid line), $\langle V\rangle$ (dashed line), $V_{\rm rms}$ (dotted-dashed line) and $V'_{\rm max}$ (dotted line). The horizontal dot-dot-dot-dashed line corresponds to 1/3. The errorbars correspond to the 1σ uncertainty on each linear fit.

with previous results on supergranulation (Leighton et al. 1962; Simon & Leighton 1964; Deubner 1971; Giovanelli 1980; Kueveler 1983).

3. Characteristic velocities versus cell size

3.1. Scaling laws

One way to constrain the dynamics of turbulent flows is to determine the dependence of the velocity field on the scales. Ideally, we would like to know the spectral quantity $\tilde{v}(\boldsymbol{k})$, i.e. the Fourier transform of the velocity field. This quantity being difficult to measure with available data, we determine a proxy of it, namely the relation between typical velocities inside a supergranule and the size of the supergranule. This is a first step which follows the work of Krishan et al. (2002).

In Fig. 3, we show the relation between the rms velocity and the corresponding size for all the supergranules appearing on a map with a given smoothing Γ. The slope of this log-log plot gives an exponent of the best power law adjusting the data. For instance, using $\Gamma = 10.2$ Mm, the exponent is $\sim 0.66 \pm 0.02$ meaning that $V_{\rm rms}$ scales like $R^{0.66}$ in the range of sizes covered by supergranulation. The error bar is the 1σ uncertainty on the parameter derived from a linear fit. Does this law depend on Γ? We repeated the operation for various values of Γ. We determined this exponent for different velocity proxys such as $V_{\rm max}$ (the maximum velocity in a cell), $\langle V\rangle$ (the mean velocity in a cell) and $V'_{\rm max}$ (the maximum velocity in an average radial profile). The results displayed in Fig. 4 show that this exponent, for $V_{\rm rms}$, is independent of Γ provided $\Gamma \gtrsim 5$ Mm. It thus confirms that a law $V_{\rm rms} \propto R^{0.66}$ in the supergranular range emerges from the data. On the other hand, all other quantities seem to be dependent on the smoothing.

The scale dependence found above is different to the one derived by Krishan et al. (2002) who suggested a much weaker exponent, namely $1/3$. A closer look at the results of Krishan et al. (2002) shows that their method for the determination of the scaling law is not the same as ours. They use $V_{\rm max}$ as the proxy for the velocity field. Our results (see Fig. 4) show that this quantity depends very much on the smoothing used. Although they did not use any spatial smoothing, Krishan et al. (2002) used Dopplergrams averaged over 10 mn. This averaging inevitably leads to some spatial smoothing.

To understand the results of Krishan et al. (2002), we examine the scale dependence of the velocity fields using various smoothing Γ_v but keeping a fixed $\Gamma = 10.2$ Mm for the smoothing of the divergence maps used for the determination

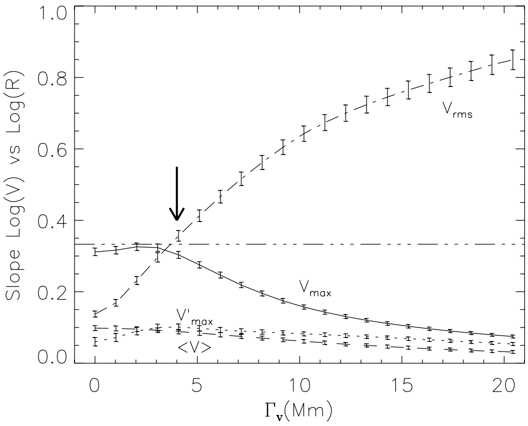

Fig. 5. Same as Fig. 4 but the velocity fields are smoothed with a variable Γ_v while the size of supergranule is determined using a fixed smoothing parameter $\Gamma = 10.2$ Mm.

of the cell sizes; with this procedure we hope to reproduce the smoothing effect on velocities due to time averaging. We use different smoothing values for the velocity fields and for the divergence maps in this section only, to establish this comparison. Results are shown in Fig. 5 where the exponent 1/3 found by Krishan et al. (2002) has been marked with an arrow. The 1/3-exponent emerges when little or no smoothing is imposed, i.e. when $\Gamma \leq 5$ Mm. We thus understand the result of Krishan et al. (2002) as the consequence of the choice of the velocity proxy ($V_{\max}$), combined with the dominant role of small scales when they are not filtered out. We show below that $V_{\max}$ should be rejected as a proxy because it does not trace the velocity field.

3.2. Relevance of the velocities observed after the spatial smoothing

It could be argued that the rms velocities obtained after the spatial smoothing for a given Γ include a significant contribution from the small-scale rms velocities. In order to quantify the amplitude of this effect, we consider the rms velocities before and after smoothing in the original data. The latter, which we call v_{obs}, can be considered as being constituted of two contributions, a rms velocity due to the large-scale fluctuations, v_{ls}, and a contribution from the small-scale fluctuations, v_{ss}, with

$$v_{\mathrm{obs}}^2 = v_{\mathrm{ls}}^2 + v_{\mathrm{ss}}^2.$$

v_{ss} can be estimated as follows. We filter the original velocity field in order to remove all large-scale fluctuations above ~10 Mm. Then, we smooth the filtered velocity field with Γ and compute the rms velocity v_{ss}. This procedure gives a realistic velocity field containing only small-scale variations. We observe that v_{ss} is significantly smaller than v_{obs} and that the difference between v_{ls} and v_{obs} is smaller than 0.1%.

4. Divergence moments versus cell size and spatial smoothing

In the previous section we studied in detail the relation between typical velocities in supergranules and cell size. We concluded that this relationship is not compatible with a power law with a 1/3 exponent as suggested by Krishan et al. (2002). We now complement this study by examining the properties of the divergence field at various scales. More specifically, we study the distribution of the divergences in order to detect intermittency, which is a signature of turbulence at different scales.

For this purpose, we determine the rms of the divergence computed over all the pixels, as well as its skewness and kurtosis. The skewness is the third moment of the divergence normalized by the rms. A negative skewness means that the distribution presents a longer tail toward negative values and a larger amount of pixels with small positive divergences, compared to a Gaussian distribution. The kurtosis is the fourth order moment of the divergence normalized by the rms and from which 3 (i.e. the fourth order moment for a Gaussian distribution) is subtracted. On the one hand, a negative kurtosis means that the tails of the distribution are not as long as for a Gaussian distribution, with a larger number of pixels with a small divergence (in absolute value). A positive kurtosis, on the other hand, reveals the presence of intermittency: strong fluctuations more frequent than in Gaussian noise.

To appreciate the effects of smoothing we compute these moments for various values of Γ. We consider the moments computed over the maps independently of the cell determination. The results are shown in Fig. 6. As expected the divergence rms decreases as the spatial smoothing increases. The skewness is also positive. This was observed by Duvall & Gizon (2000) at the supergranular scale. Here we observe two domains, one below the supergranular scale in which the skewness increases from small values to large values, and one above the supergranular scale in which the skewness remains strong but decreases due to the smoothing. The maximum occurs for $\Gamma \sim 14$ Mm. The kurtosis is also positive at all scales and is minimum for $\Gamma \sim 5$–6 Mm. It is maximum at small scales presumably because of the strong turbulent fluctuations at small scales but the curve also reveals, after the elimination of small scales by smoothing, an increasingly fluctuating divergence at increasing scale.

This can be understood with the distributions of the divergences shown in Fig. 7. The divergences are normalized by the maximum value. We fit a Gaussian curve to these distributions to visualize the differences with a Gaussian distribution. Without smoothing, the distribution are almost symmetric (as already seen by the small skewness), but the tails are longer than the Gaussian distribution (positive kurtosis). This plot demonstrates the presence of intermittency. On the other hand, the distribution for a smoothing of 10.2 Mm shows a very strong asymmetry, explaining the increasing skewness with Γ (Fig. 6). However, we observe that the tail is longer than a Gaussian distribution for positive divergences but smaller for negative divergences. This last observation explains why the kurtosis decreases as the smoothing increases, but remains large. We observe a strong skewness when smoothing the divergence maps because areas of strong positive divergences (cell center) are larger than areas of strong negative divergence by up to 30%. When smoothing the maps, we first remove the values in converging areas, while the diverging areas are not much affected. For an even larger smoothing, the difference between the observed distribution and the Gaussian curve for positive divergences is similar, but the difference decreases again for negative divergences, in agreement with the increasing kurtosis for $\Gamma > 5$ Mm (see Fig. 6).

We conclude from this study of the divergence distribution that intermittency is present in the data. It is strong at small scales (as expected in turbulent flows) but, surprisingly, seems to increase again in the supergranulation range.

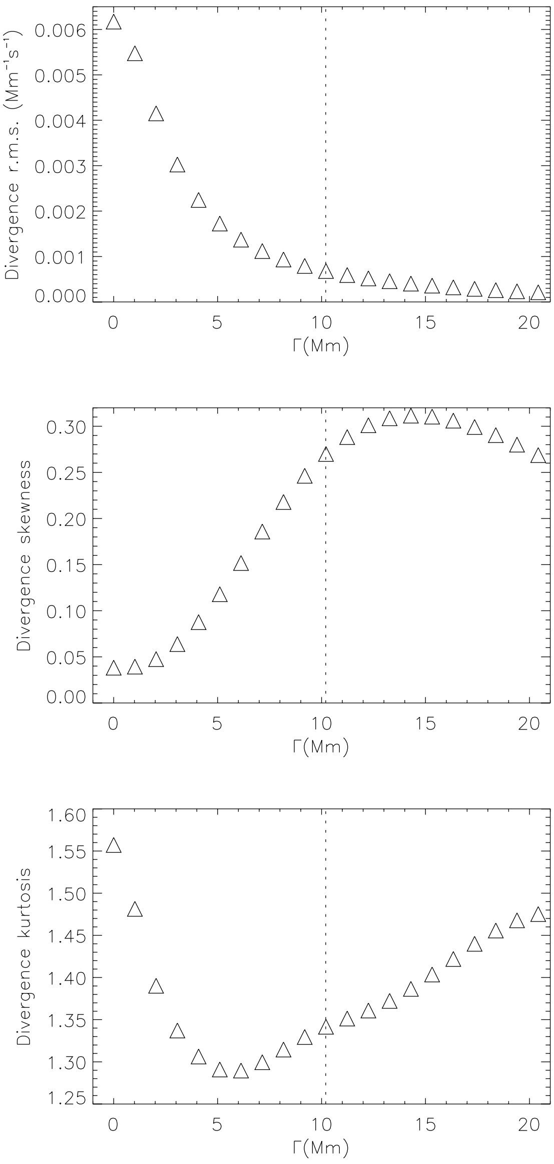

Fig. 6. Divergence moments computed over the whole map versus the smoothing Γ. The vertical dotted line indicates the $\Gamma = 10.2$ Mm spatial smoothing.

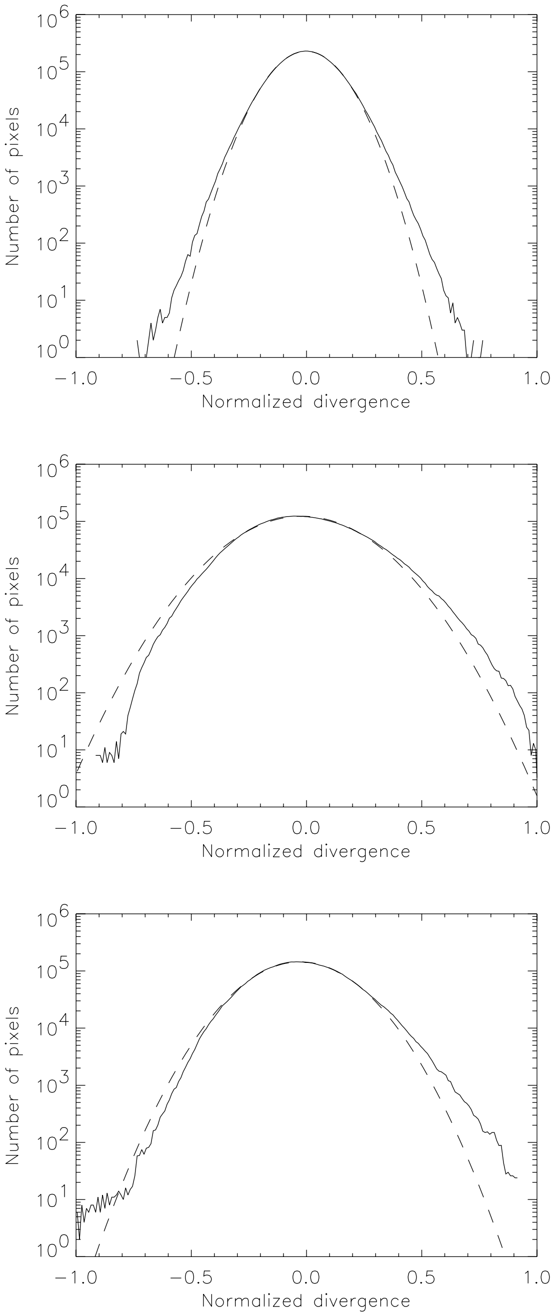

Fig. 7. *Upper panel*: distribution of the normalized unsmoothed divergences (solid line) and Gaussian fit (dashed line). *Middle panel*: same for $\Gamma = 10.2$ Mm. *Lower panel*: same for $\Gamma = 20.4$ Mm.

5. Inside supergranules: velocity and divergence profiles versus cell sizes

5.1. Profiles inside a supergranule

In the foregoing sections we presented a global view of the set of supergranules and its associated velocity and divergence fields. We now focus our attention on the flow inside a supergranule.

As we have seen before, supergranular flows strongly fluctuate from one cell to the other and only a statistical approach is appropriate. In this section, a constant value of Γ (10.2 Mm) has been been used to determine the cells. We then divide the set of supergranules in four subsets following the radii: the four ranges are defined a) 6–10 Mm, b) 10–16 Mm, c) 16–20 Mm and d) above 20 Mm. Cells smaller than 6 Mm are discarded[1]. For each subset we determine the mean profile of velocity, divergence and examine the correlation of these quantities.

Results are shown in Fig. 8. Divergence profiles clearly show that small cells are dominated by converging flows. This is consistent with the fact that, for such cells, the maximum velocity occurs at the boundary (see Fig. 8 top). Such cells are thus mildly diverging in their center and converging at their periphery. If we now consider larger cells, we clearly see that positive divergences occupy most of the radius leaving some convergences on the side. Maximum velocity now occurs near the center although in the largest cells the true maximum is around $d_{\rm rel} = 0.45$.

These data show that there is a relation between the size of a supergranule and the strength of the divergence field, supporting the idea that correlated small-scale positive divergences may be at the origin of supergranulation.

---

[1] They are too small to allow measurements and are out of the supergranulation range.

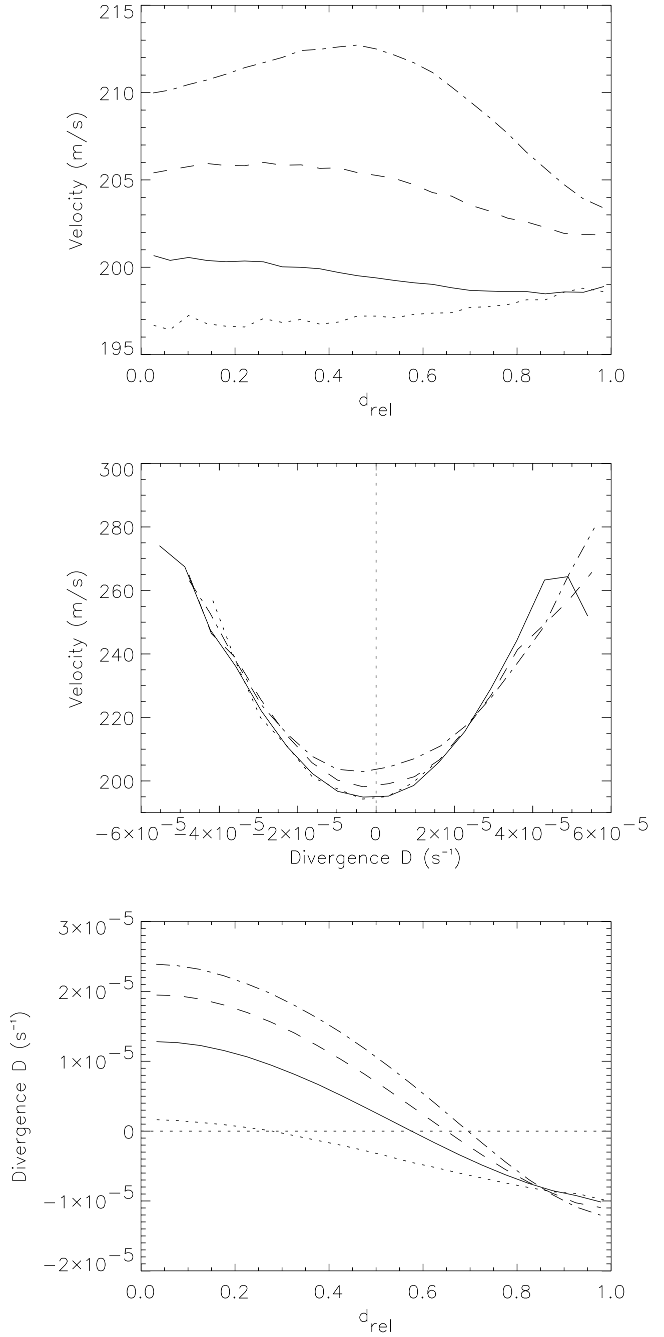

Fig. 8. Profiles for sizes in the range 6−10 Mm (dotted line), 10−16 Mm (solid line), 16−20 Mm (dashed line), and sizes larger than 20 Mm (dotted-dashed line). Velocities and divergences are smoothed with $\Gamma = 10.2$ Mm. *Upper panel*: velocity versus the relative distance to cell center $d_{\rm rel}$. *Middle panel*: velocity versus divergence D. *Lower panel*: divergence D versus the relative distance to cell center $d_{\rm rel}$. The error-bars are not shown for clarity. They are between a small fraction of 1 m/s and 1 m/s for the velocities (*lower panel*), and of the order of the line thickness for the divergences (*upper and middle panel*).

Divergence being a gradient of the velocity field, high values of this quantity may be obtained by either high velocities or rapid variations of velocity. The correlation of these quantities, as shown in Fig. 8 (middle), indicates that divergence values are strongly correlated with velocities and depend little on the scale of the flow. For the four ranges of scale defined above, divergences thus appear as another view of the velocity field. The velocity profiles as a function of divergence show some similarity with those used in the models of Rast (2003b).

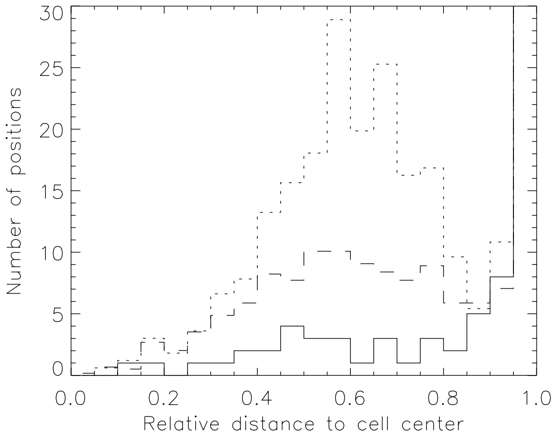

Fig. 9. Distribution of the relative distance to cell center of the position of $V_{\rm max}$ inside the cells. Plots are for cells with R smaller than 10 Mm (solid line), R between 10 and 20 Mm (dashed line) and R larger than 20 Mm (dotted line). Values for $d_{\rm rel}$ above 0.95 are offscale (see text) for the 3 curves.

5.2. The position of maximum velocity

These results may also be used to understand the quantity $V_{\rm max}$ used by Krishan et al. (2002) to determine scaling laws. The maximum velocity inside a cell is easily obtained and its distribution in the different subsets can be determined. It is shown in Fig. 9 as a function of the relative distance to the cell center. For most of the cells, $V_{\rm max}$ is observed very close to the boundary. As the cell size increases, there is however a second component of increasing amplitude, with a maximum around 0.6. Hence, as could be expected from the results of the preceding section, two populations of $V_{\rm max}$ appear: one associated with large cells that represents divergent flows within the central region and the other associated with small cells that represents converging flows near the boundary. The choice of $V_{\rm max}$ as a proxy for the velocity is unreliable since it does not always refer to the same dynamical feature.

6. Discussion and conclusion

We have performed a detailed analysis of divergence and velocity maps from mesogranulation scales to scales larger than supergranulation, with an emphasis on the dynamics at the supergranular scale.

Using the maximum velocity inside a cell as a proxy of the velocity field, as done in Krishan et al. (2002), should be avoided. We have shown that it does not always refer to the same dynamical feature, sometimes being a diverging flow and sometimes a converging flow.

Our study of the probability density functions of the velocity and divergences and the associated moments, showed a clear signature of intermittency at all scales but with local maxima at the largest and smallest ones. Although expected in the small scale, it is the first time that this has been shown in the supergranular range; this is evidence of its turbulent nature.

Focusing on the mean divergence and velocity profiles inside a supergranule, we have established a clear correlation between the size of the cells and the strength of the divergences: the larger the supergranule, the stronger the divergence. This correlation suggests that supergranulation may originate in the correlation of many small-scale positive divergences "synchronized" by a large-scale instability, as proposed by Rieutord et al. (2000). These velocity and divergence profiles can be used in kinematic models such as those tested by Simon et al. (1991).

Our study of the scale dependence of the velocities, namely the relation between velocity and the radius of cells, suggests a powerlaw dependence with an exponent around 0.66, i.e. the data suggest a scaling $V_{\rm rms} \sim R^{0.66}$. We thus do not confirm the result of Krishan et al. (2002) and explain the disagreement as due to the different choice of the velocity proxy. The present scaling law is reminiscent of the Bolgiano-Obukhov scaling $V_\ell \sim \ell^{3/5}$. Such a scaling, if confirmed, is a signature of the effect of stratification on turbulence in the surface layers. Combined with the abovementioned large-scale instability, it points to a scenario where supergranulation would result from a redistribution of the kinetic energy on a large scale at the surface of the sun. This appealing scenario for the origin of supergranulation needs to be confirmed by an independent set of data. A set of images of the solar surface with higher angular resolution, allowing for a computation of the (horizontal) velocity field at smaller scale and with different methods, will complement this first study.

Acknowledgements. SOHO is a mission of international cooperation between the European Space Agency (ESA) and NASA.

References

Beckers, J. M. 1968, Sol. Phys., 5, 309
DeRosa, M. L., & Toomre, J. 2004, ApJ, 616, 1242
Deubner, F.-L. 1971, Sol. Phys., 17, 6
Duvall, T. L., & Gizon, L. 2000, Solar Phys., 192, 177
Foukal, P., & Fowler, L. 1984, ApJ, 281, 442
Frazier, E. N. 1970, Sol. Phys., 14, 89
Giovanelli, R. G. 1980, Sol. Phys., 67, 211
Hagenaar, H. J., Schrijver, C. J., & Title, A. M. 1997, ApJ, 481, 988
Hart, A. B. 1954, MNRAS, 114, 17
Krishan, V., Paniveni, U., Singh, J., & Srikanth, R. 2002, MNRAS, 334, 230
Kueveler, G. 1983, Sol. Phys., 88, 13
Leighton, R. B., Noyes, R. W., & Simon, G. W. 1962, ApJ, 135, 474
Lin, H., & Kuhn, J. R. 1992, Sol. Phys., 141, 1
Meunier, N., Tkaczuk, R., & Roudier, T. 2006a, A&A, in press
Meunier, N., Tkaczuk, R., & Roudier, T. 2006b, A&A, submitted
Rast, M. P. 2003a, in Local and Global Helioseismology: the Present and Future, ed. H. Sawaya-Lacoste, ESA SP-517: GONG+ 2002, 163
Rast, M. P. 2003b, ApJ, 597, 1200
Rieutord, M., Roudier, T., Malherbe, J. M., & Rincon, F. 2000, A&A, 357, 1063
Roudier, T., Rieutord, M., Malherbe, J., & Vigneau, J. 1999, A&A, 349, 301
Scherrer, P. H., Bogart, R. S., Bush, R. I., et al. 1995, Sol. Phys., 162, 129
Simon, G., & Leighton, R. 1964, ApJ, 140, 1120
Simon, G., Title, A., & Weiss, N. 1991, ApJ, 375, 775
van der Borght, R. 1979, MNRAS, 188, 615

A&A 463, 745–753 (2007)
DOI: 10.1051/0004-6361:20066314

Astronomy & Astrophysics

Intensity variations inside supergranules

N. Meunier[1], R. Tkaczuk[2], and Th. Roudier[1]

[1] Laboratoire d'Astrophysique de l'Observatoire Midi-Pyrénées, Université Paul Sabatier Toulouse III, CNRS, 57 avenue d'Azereix, BP 826, 65008 Tarbes Cedex, France
e-mail: `[nadege.meunier;thierry.roudier]@ast.obs-mip.fr`
[2] Laboratoire d'Astrophysique de l'Observatoire Midi-Pyrénées, Université Paul Sabatier Toulouse III, CNRS, 14 avenue Edouard Belin, 31000 Toulouse, France
e-mail: `ruben.tkaczuk@ast.obs-mip.fr`

Received 29 August 2006 / Accepted 24 October 2006

ABSTRACT

Context. The convective origin of supergranulation is highly controversial. Past measurements of intensity variations inside supergranules have often been influenced by the brightness enhancement at the cell boundaries due to the magnetic network.

Aims. We conduct a precise determination of intensity variations inside supergranules.

Methods. We determine the supergranule cell boundary from smoothed divergence maps derived from horizontal flow maps. We derive these flow maps from intensity maps obtained by MDI/SOHO in high resolution mode. We discuss the different possible approaches to take into account the influence of the magnetic field which can be used to determine the intensity variations inside supergranules.

Results. We observe a significant decrease of the intensity from the center to the boundary of supergranules. We also obtain additional clues from the behavior of the maximum intensities and minimum intensities around each pixel, which are related to granules and intergranules: the maximum intensity decreases from center to boundary, while the minimum intensity is constant or increases depending how restrictive the selection is. The difference between intensity profiles versus divergence and relative distance to cell center also provides complementary information. The corresponding temperature differences between cell center and boundary are in the range 0.8–2.8 K. The intensity enhancement (for the magnetic network) or deficit (for intranetwork fields) depends on the localisation inside the cell.

Conclusions. It is the first time that such a detailed analysis of intensity variations inside supergranulation is performed. Our results are compatible with a convective origin of supergranulation, as the intensity decreases toward the boundary of the cells. However, new simulations of supergranulation are necessary to verify whether the compared behavior of granule and intergranule intensity variations is in close agreement with convection.

Key words. Sun: granulation – Sun: photosphere – Sun: general

1. Introduction

Supergranulation was discovered by Hart (1954). It has long been thought to be due to convection (Simon & Leighton 1964; van der Borght 1979). Such an interpretation has however been questioned, in particular by Rieutord et al. (2000) and Rast (2003b). One clue to understand the origin of supergranulation would be the determination of intensity variations inside supergranules, as it is expected that a convective cell will exhibit a lower temperature at the boundary of the cell compared to the cell center. Most studies of intensity variations across supergranules found an enhancement at the boundary due to the presence of the magnetic network (Beckers 1968; Frazier 1970; Foukal & Fowler 1984; Lin & Kuhn 1992). More recently however, Rast (2003a) found a small decrease in intensity from cell center to the boundary when keeping pixels associated with very low magnetic field only (keeping less than 2.5% of the pixels and down to 0.1%).

In this work, we study the variation of intensities inside supergranules in detail. We determine the intensity variations as a function of the smoothed divergence and as a function of the position inside the cell. We study not only the intensity at a given pixel in the images, but also its magnetic environment, in order to make a better diagnosis. The data processing is described in Sect. 2. We also discuss the different possible approaches to take into account the influence of the magnetic field on intensity variations. The results obtained with different pixel selections are described in Sect. 3 and discussed in Sect. 4.

2. Data processing

2.1. The MDI data set

We use two time series of high resolution MDI/SOHO observations (Scherrer et al. 1995) obtained with a 1 min temporal cadence: 46 h in January 1997 and 15 h in March 1997. We use intensity maps (continuum of the Ni 6768 Å line) and magnetograms. These maps cover $\sim 620'' \times 303''$ and the pixel size is 0.6054 arcsec. The observed regions are very quiet, except for the presence of a pore with active network surrounding it in the January time series. The area around the pore is eliminated from the analysis.

The rest of this section describes the data analysis. The steps described in Sect. 2.2 are similar to those described in detail in Meunier et al. (2007), except for the additionnal intensity maps.

2.2. Map computation

2.2.1. Intensity maps

We consider 1-h long sets of intensity maps. In each set, the time cadence is 1 min. Large-scale intensity gradients are present in MDI intensity maps, due to the center-to-limb darkening and to residuals from the flat-field correction. A first correction is therefore applied to the maps (see Meunier et al. 2007, for more details). Over each 1-h period, the 60 corrected intensity maps are then carefully aligned with the image at the center of the 1-h set.

In the following, we will present results obtained using 5 successive intensity maps (therefore covering 4 min) averaged together. The resulting map is denoted I hereafter. Most of the solar oscillation signal is then removed. However, similar computations can be done with the filtered intensity maps (see Sect. 2.2.2), and they lead to similar results, which shows their robustness. For clarity, these results are therefore not presented here. There is a very large intensity dispersion in the intensity maps, much larger than the effect we wish to detect. The dispersion is however intrinsic to the solar photosphere as it is due to solar granulation. One could smooth them out before the analysis, for example using a spatial smoothing. However, this approach is not adequate because it would mix the contributions from the magnetic field coming from different pixels with no way to sort them out afterward.

For a better diagnosis of the intensity variations, we compute additional intensity maps to clarify the results obtained with the intensity I. For each pixel of the intensity map, we compute the minimum intensity I_{min} and the maximum intensity I_{max} over a 7×7 pixel box around the original pixel. The size of the box has been chosen so that it covers a typical granule. These intensities give some information on the intensity inside the granules themselves and in the corresponding intergranules. Of course, due to the limited spatial resolution of the instrument, the information is not complete as the intensities are smoothed in the original maps.

2.2.2. Velocity maps

The horizontal flow fields are computed using a Local Correlation Tracking method between two consecutive images in each 1-h intensity data set, after a k-ω filtering with a cut-off at 6 km s^{-1}. These velocity maps are then averaged over each 1-h period. This leads to 61 velocity maps aligned with the intensity maps.

2.2.3. Divergence maps

A divergence map is then computed for each velocity field map and moothed in the Fourier space using a 2D Gaussian with a *FWHM* of 10.2 Mm. We refer to Meunier et al. (2007) for the choice of this spatial smoothing. It provides a supergranule cell size distribution in agreement with expected results (see Sect. 2.2.4).

2.2.4. Cell determination

In this paper, we use two ways of spatially characterizing the supergranular cells. First, we define the cells using the smoothed divergence maps, and then derive a normalized distance to the center of gravity of the cell. Second, we directly use the smoothed divergence defined in Sect. 2.2.3.

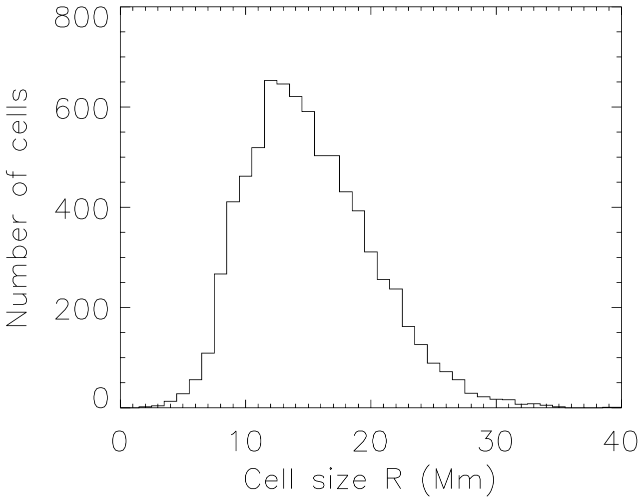

Fig. 1. Size distribution of the cell size R in Mm. R represents the maximum distance between the center of gravity of the cell and the boundary of the cell.

First, we define the boundary of the cells using a steepest descent method (see Hagenaar et al. 1997; Meunier et al. 2007). Then, for each pixel of the cell we compute the relative distance to the center of gravity of the cell. This relative distance to the cell center, hereafter d_{rel}, takes the value 0 at the center of gravity, and 1 for the pixels located at the boundary of the cell. The normalisation by cell size is very convenient when averaging the results from all cells. Figure 1 shows the distribution of the cell sizes R for the 7629 cells, where R is the maximum distance between the center of gravity and the cell boundary. The average value of R is 15.6 ± 0.1 Mm. It extends up to 40 Mm, but there are in fact only a few cells above 30 Mm.

A given divergence value does not correspond to the same location in the cell for different sizes (Meunier et al. 2007): for example, an intermediate value will correspond to the cell center in a small cell and to a position further from the cell center in a large cell, where the maximum divergence is much larger. As a consequence, we have also normalized the smoothed divergence using the following method. In each cell, the positive divergences are normalized by the maximum positive divergence in the cell. The same is done for the negative divergences (converging flows). This correction leads to a divergence D'. We then consider D_{norm} using the following formula :

$$D_{\mathrm{norm}} = (-D' + 1) \times 0.5.$$

This normalized smoothed divergence D_{norm} takes the value of 0 at the location of maximum positive divergence in the cell (diverging flows), 1 at the location of maximum negative divergence (converging flows) and 0.5 when the divergence is equal to zero. The results obtained can be easily averaged and compared to those obtained with d_{rel}. Furthermore, the maximum of D_{norm} now corresponds to the maximum of d_{rel}, which also makes the comparison with d_{rel} much easier to visualize.

Note that there is not a one to one comparison between the two methods (the correlation factor is 0.70), as there is a large dispersion. This is primarily due to the fact that the strongest positive divergences do not necessarily coincide with the center of gravity of the cell. Second, even if the strong convergences are located on the edge of the cell, many pixels of the boundary do not exhibit strong convergence as shown in Fig. 2. In all cases, 20 pixel-wide bands are removed at the egdes of the images to

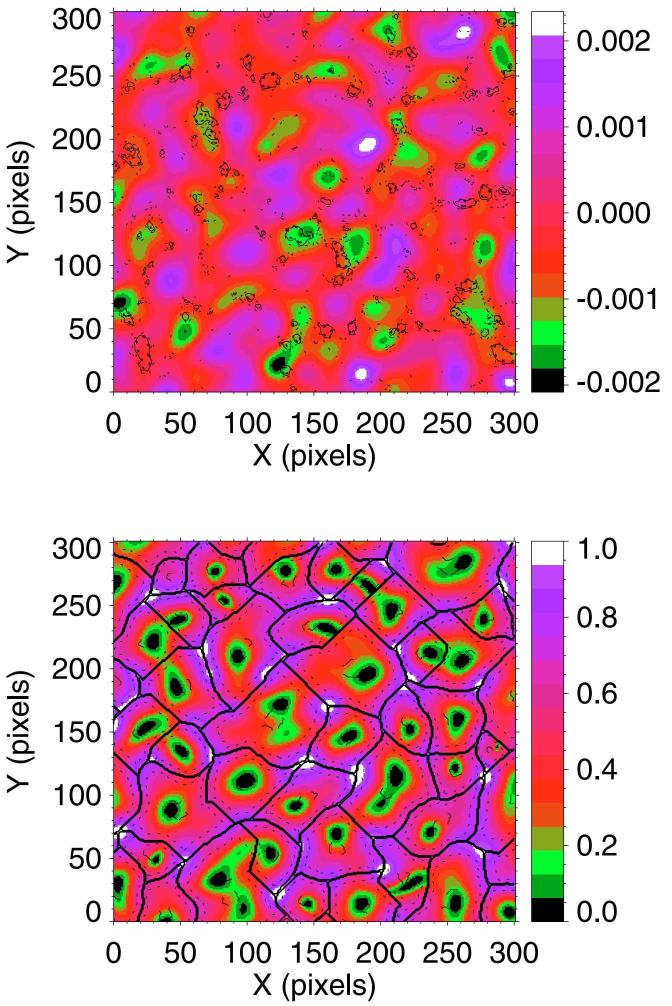

Fig. 2. *Upper panel*: smoothed divergence map (in s^{-1}) for a 300 × 300 pixels square. The line contours represent the magnetic field derived from the 1-hour averaged magnetogram at the levels of 10, 20 and 40 G (i.e. the magnetic network). *Lower panel*: normalized divergence map D_{norm} as color level. The solid line contours represent the cell boundaries. The dashed lines represent the contour of d_{rel} at the 0.2 level, and the dotted line at the 0.8 level.

take into account the spatial smoothing. Cells overlapping these boundaries are also eliminated. Note that the results presented in this paper are very similar when considering the divergence before the normalization, or when considering another geometrical approach such as the distance to the center of gravity divided by the maximum size R: the exact values are different but are of the same order of magnitude and as significant.

2.3. How to determine the influence of the magnetic fields

For each 1-h set, magnetograms are aligned with the image at the center of the set, and then averaged. Figure 2 also shows a subset from a smoothed divergence image. The magnetic network is superimposed on the divergence map, as well as cell boundaries and contours of d_{rel}. It shows that strong converging flows coincide well with the boundary, but there are many pixels of the boundary with almost absent converging flows. This magnetic field is actually magnetic flux in each pixel.

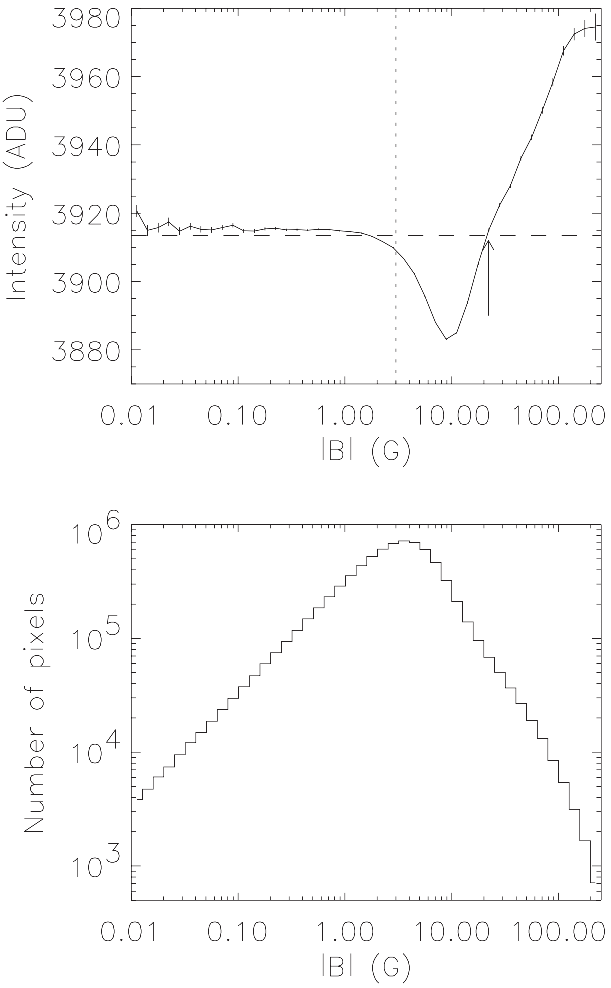

Fig. 3. *Upper panel*: intensity variations versus the absolute value of the magnetic field $|B|$, for the March 1997 time series. The horizontal dashed line represents the average intensity level for $|B| < 3$ G. The vertical dotted line, at $|B| = 3$ G, corresponds to the noise level. The arrow indicates the magnetic field value for which the intensity variation changes sign with respect to the low magnetic field intensity level. *Lower panel*: number of pixels versus the absolute value of the magnetic field $|B|$.

The presence of a magnetic field can contribute to intensity variations, in particular through unresolved bright points (Koutchmy & Lebecq 1986; Title et al. 1987; Wang 1988; Title et al. 1992; Montagne et al. 1996). Figure 3 shows the variation of the intensity versus the magnetic field for the March 1997 time series. Below the noise level of 3 G (defined at the 1σ level in the 1-h averaged magnetograms), a constant intensity level, I_0, is observed. Above that threshold, two domains of magnetic fields are observed. In the range 3–20 G, the intensity is less than I_0, with a maximum difference to I_0 of 0.8% for $|B| \sim 10$ G. This domain corresponds to weak field structures spread over the cells and is likely to be a component of the intranetwork magnetic field. For $|B|$ larger than ~20 G, the intensity increases with $|B|$ and is larger than I_0, reaching values greater than I_0 by 1.5%. This domain corresponds to magnetic network structures.

Several approaches are possible to eliminate the effects of $|B|$. We could correct the intensities, study the variations of the intensity with the magnetic field for several domains in the cells or select pixels for which the influence of the magnetic field is very small. These approaches are described and discussed below.

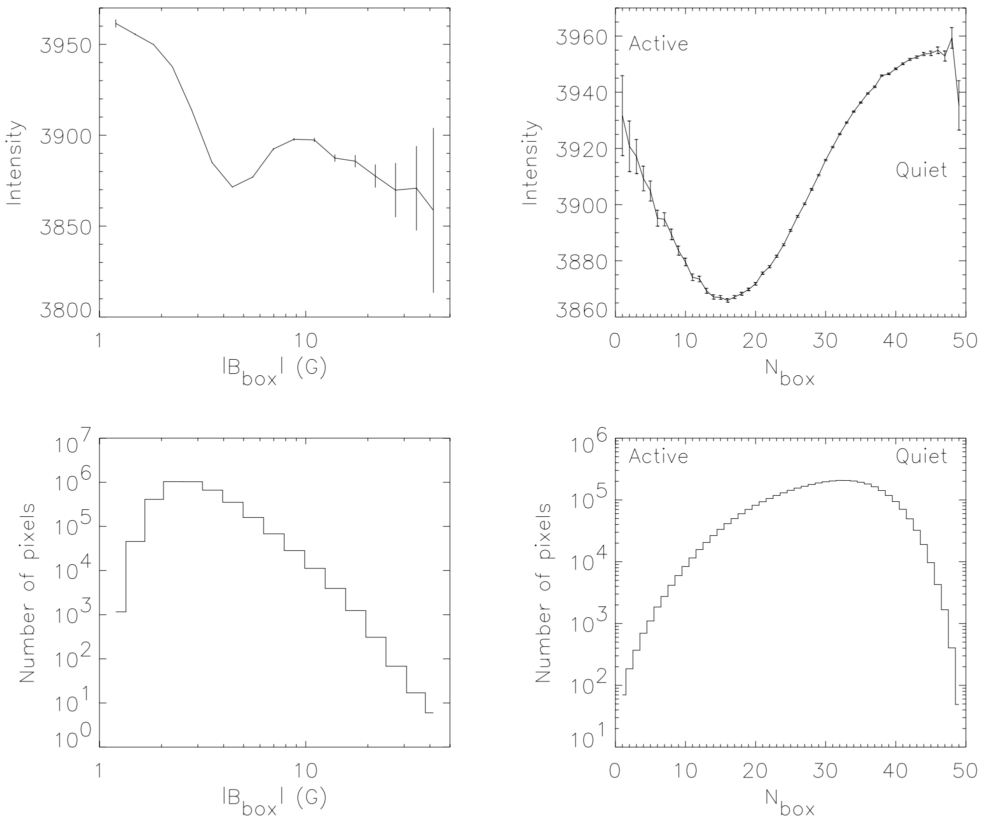

Fig. 4. *Left panel*: Intensity variations versus the absolute value of the magnetic field $|B_{\rm box}|$ for $|B| < 3$ G (*upper panel*) and number of pixels (*lower panel*), for the March 1997 time series. $|B_{\rm box}|$ is the average magnetic field in a 7 × 7 pixels box around the current pixel. *Left panel*: same versus $N_{\rm box}$, where $N_{\rm box}$ is the number of pixels below 3 G in a 7×7 pixels box around the current pixel.

2.3.1. Intensity correction

It should be possible to use the observation of the dependence of the intensity on the magnetic field to correct the original intensity and then to look at the spatial variations of the corrected intensities. The observed magnetic field dependence of the intensity is shown in Fig. 3. For example, if we note I_b, the intensity, as a function of $|B|$ as shown in Fig. 3, the intensity I could be corrected by computing $I+I_0-I_b$. The corrected intensity variations versus $d_{\rm rel}$ or $D_{\rm norm}$ for three domains of magnetic fields (namely $|B| < 3$ G, in the range 3–20 G and > 20 G) approach each other but they are not the same yet. For $|B| > 20$ G in particular, they remain very different despite the correction.

This may be due to the fact that the intensity-magnetic field relationship does not depend only on $|B|$. We therefore define $N_{\rm box}$ as the number of pixels with $|B|$ below the 3 G threshold in a 7 × 7 pixel box around the current pixel. This size of the box was chosen to cover a typical granule as in Sect. 2.2.1. This variable will be used throughout the paper to characterize the influence of the magnetic environment on the intensity of a given pixel: pixels with a low $N_{\rm box}$ value, despite corresponding to a very weak magnetic field ($|B| < 3$ G), may be surrounded by an active environment, while pixels with $N_{\rm box}$ close to 49 are in very quiet regions. The average absolute magnetic field over the same box, hereafter $|B_{\rm box}|$, is also computed and will be used to check the amplitude of the influence of the magnetic field in the environment of the current pixel. For small values of $N_{\rm box}$, the average magnetic field $|B|$ is large, with an average $|B|$ and $|B_{\rm box}|$ around 25 G for $N_{\rm box}$ close to 0 and around 8 G for $N_{\rm box}$ around 10. For large values of $N_{\rm box}$, these values are lower than 2 G. The size of the magnetic structures defined by a 10 G threshold can also help to interpret the significance of $|B_{\rm box}|$ and $N_{\rm box}$. We find that above 40, there is no overlap between the location of these pixels and the magnetic network.

We observe a large intensity variation versus $|B_{\rm box}|$ and $N_{\rm box}$ mostly due to the surroundings, even when we consider only pixels with a very low magnetic field, in this example $|B| < 3$ G, as shown in Fig. 4. For $|B| < 3$ G, the intensity is indeed higher for small values of $|B_{\rm box}|$ and smaller for large values. On the other hand, the smaller intensities are observed for intermediate $N_{\rm box}$, around 15 pixels. Intensity corrections taking into account this new complex dependence still lead to different dependences on the localisation for various $|B|$ domains. This should further complicate the correction to be performed on the intensity maps and we conclude that such a correction is too uncertain to allow the use of all pixels of the maps.

2.3.2. Intensity dependence on the magnetic field across the cells

A second possible approach is to compute the intensity variations versus $|B|$ for various locations in the cells. If there is an offset between the curves, then this may be a good indication of intensity variations across supergranules, and such a plot would also allow us to directly take into account the influence of the magnetic field. The result is shown in Fig. 5, where the intensity as a function of the magnetic field is shown separately for selections of pixels in strong divergences and convergences. The result is similar for pixels at cell center and at the cell boundary. The intensity deficit for $|B|$ in the range 3–20 G has a smaller amplitude close to the cell boundary (or to regions of convergence), which suggests that weak field structures, likely to correspond to intranetwork magnetic fields, are associated with lower intensities than the surroundings, but that the intensities are higher closer to the cell boundary. It is the opposite for the high intensities observed for $|B|$ greater than 20 G, corresponding to the magnetic network: the network features are brighter close to the cell center than at the boundary, for a given magnetic field. This

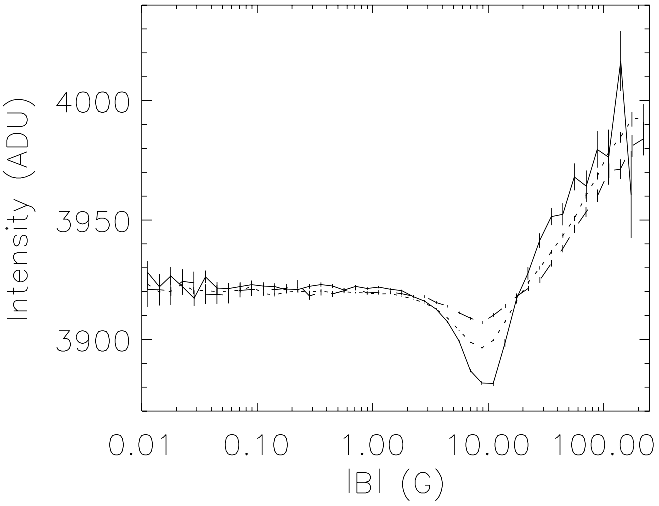

Fig. 5. Intensity variations versus the absolute value of the magnetic field $|B|$ for 3 ranges of $D_{\rm norm}$: $D_{\rm norm}$ lower than 0.2 (solid line), in the range 0.2–0.8 (dotted line) and larger than 0.8 (dashed line).

is an important result, showing again that it is difficult to directly apply a correction to the intensity maps, as it is likely that the intensity properties for a given magnetic field vary with the localisation inside the cell.

When considering $|B|$ lower than 3 G, the variations are much smaller and we obtain a smaller intensity in convergences (compared to divergences) and at the cell boundary (compared to cell center), with a variation of the order of 1 ADU (Analog Digit Unit). This observation leads naturally to the approach described in the next section, which consists of selecting the pixels in the quietest regions.

2.3.3. Pixel selection

A third approach, which will be followed in the rest of this paper, is to select pixels for which the intrinsic intensity variations are very small. We consider pixels with $|B|$ below a threshold of 3 G only, as most pixels above that threshold have a significant magnetic field and we are interested in extrapolating the intensity variations for $B = 0$. To discriminate further, we also use the criterion $N_{\rm box}$ defined in Sect. 2.3.1. Only pixels with $N_{\rm box}$ above 7 are retained. Pixels with $N_{\rm box}$ close to 49 are in very quiet regions and will be the most suitable for our analysis. We will study the dependence of the intensity variations on $N_{\rm box}$ in order to identify the influence of the magnetic field on these intensity variations.

The noise level in the magnetograms varies over the field of view. In particular, there is a region located in the bottom-right corner of the images with a significantly higher noise level. In practice, in this region, $N_{\rm box}$ is always very low due to this noise, and almost all pixels in this region are eliminated from the analysis.

2.4. Final parameters and errorbars

We obtain a number of variables defined in each pixel of the maps where $|B|$ is below 3 G and $N_{\rm box}$ larger than 7 pixels:

- Intensity informations: I, $I_{\rm min}$, $I_{\rm max}$
- Cell property informations: R, $d_{\rm rel}$, $D_{\rm norm}$
- Magnetic field informations: $|B|$, $N_{\rm box}$, $|B_{\rm box}|$.

They are defined for slightly more than 10^7 pixels, which covers 34% of the surface. The other pixels have a magnetic field above 3 G or are too close to the edges of the images. All intensities are in ADU, i.e. the original CCD counts.

The correlation factor between 2 successive divergence maps is of the order of 0.6. It falls to ~0 in ~22 hours. This means that the maps are not entirely independent from one hour to the next. In the following, the errorbars will be given by the standard deviations at the 1σ level. This is not entirely correct due to this correlation and they could be overestimated by a factor of less than 2. On the other hand, the intensity maps are uncorrelated as over one hour the granulation pattern is completely different.

3. Results

Before studying the intensity variations over the selected pixels, we examine the influence of the magnetic field around the current pixel on the results. We apply a more severe selection in order to eliminate the influence of the magnetic field. The possible biases will be discussed.

3.1. Influence of the magnetic environement

We first study the intensity variations as a function of $N_{\rm box}$, which characterizes the activity level in a granule-size region around the current pixel. The number of pixels as a function of $N_{\rm box}$ was shown in Fig. 4 (lower-right panel) and peaks for $N_{\rm box} \sim 33$. To characterize the intensity variations with $d_{\rm rel}$ and $D_{\rm norm}$, we compute the slope of the intensity as a function of $d_{\rm rel}$ or $D_{\rm norm}$. A negative slope means than the intensity is lower at the cell boundary. These slopes can be obtained for various pixel selections. Figure 6 shows the variation of the slope for the intensity I as a function of $N_{\rm box}$. The plot for $D_{\rm norm}$ (upper panel) shows that the slope is close to 0 for small values of $N_{\rm box}$, i.e. when the environment of the pixels associated with low magnetic fields is more active. However, the slope becomes negative at larger values ($N_{\rm box}$ above ~37). The result is similar for the variation with $d_{\rm rel}$ (lower panel), although the change in sign appears at smaller values ($N_{\rm box}$ above ~23). Therefore there is a strong indication that when looking at the quietest regions, we observe a significantly lower intensity at the cell boundary.

The influence of the network magnetic field is expected to lead to an increase of the intensity at the cell boundary, i.e. where these strong magnetic fields are predominantly located. When considering the minimum and maximum intensities around each current pixel, defined by $I_{\rm min}$ and $I_{\rm max}$, it is possible to study the influence of the environment. The variations of $I_{\rm min}$ and $I_{\rm max}$, which are less dependant on the 3 G threshold (as they can have larger values), show an even larger variation for intermediate values of $N_{\rm box}$. In particular, the slope for $I_{\rm min}$ is positive, which may be due to an intensity increase in the intergranules due to the presence of activity there.

3.2. Intensity variations in very quiet regions

3.2.1. Pixel selection

In this section we study in more detail the intensity variations as a function of $D_{\rm norm}$ and $d_{\rm rel}$ for the quietest regions. We first consider the pixels where $N_{\rm box}$ is larger than 40. In that case, we are well in the range where the intensity variations are significant, with a negative slope. This leads to a selection of 755934 pixels, which represent 2.5% of the surface.

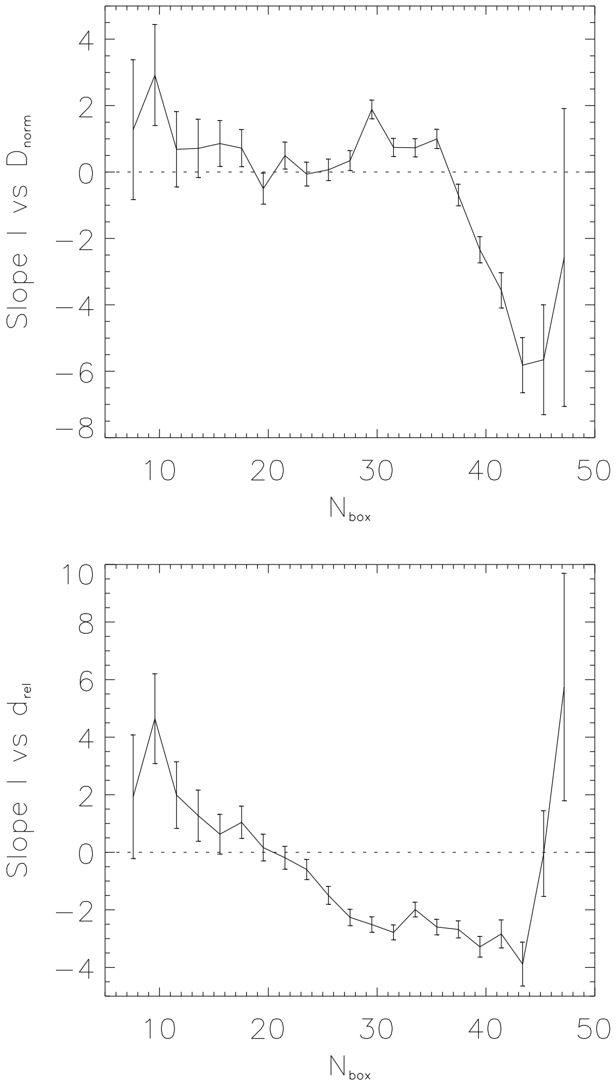

Fig. 6. *Upper panel*: slope of the intensity I versus the normalized divergence $D_{\rm norm}$, as a function of $N_{\rm box}$, for $|B| < 3$ G. $N_{\rm box}$ is the number of pixels below 3 G in a 7×7 pixels box around the current pixel. *Lower panel*: same for the slope versus the relative distance to cell center $d_{\rm rel}$.

Figure 7 shows the number of pixels versus $D_{\rm norm}$ and $d_{\rm rel}$. In the case of $D_{\rm norm}$, there are more pixels for values smaller than 0.5, i.e. the slopes will be more strongly influenced by this part of the cell. This is due to the fact that most pixels associated with strong magnetic fields are located in convergence regions. In the case of $d_{\rm rel}$, it is the opposite and there are more pixels for values larger than 0.5, so the slope will be more sensitive to the outer region of the cells. This is simply due to the definition of $d_{\rm rel}$: in a circular cell for example there will be many more pixels with $d_{\rm rel}$ larger than 0.9 than smaller than 0.1. Despite the low percentage of pixels kept for the analysis, they are widely distributed over the cells. Furthermore, pixels are not distributed randomly but tends to cover significant part of granules, with 80% of the pixels in structures larger than 10 pixels (about 2.5 × 2.5 arcsec). This will limit possible biases due to the preferential location with respect to granules and intergranules (see also Sect. 3.2.5). This low percentage also shows that there is a significant magnetic field almost everywhere on the surface. The decrease in number of pixels versus $d_{\rm rel}$ and $D_{\rm norm}$ at the boundary is also due to the presence of more magnetic flux there.

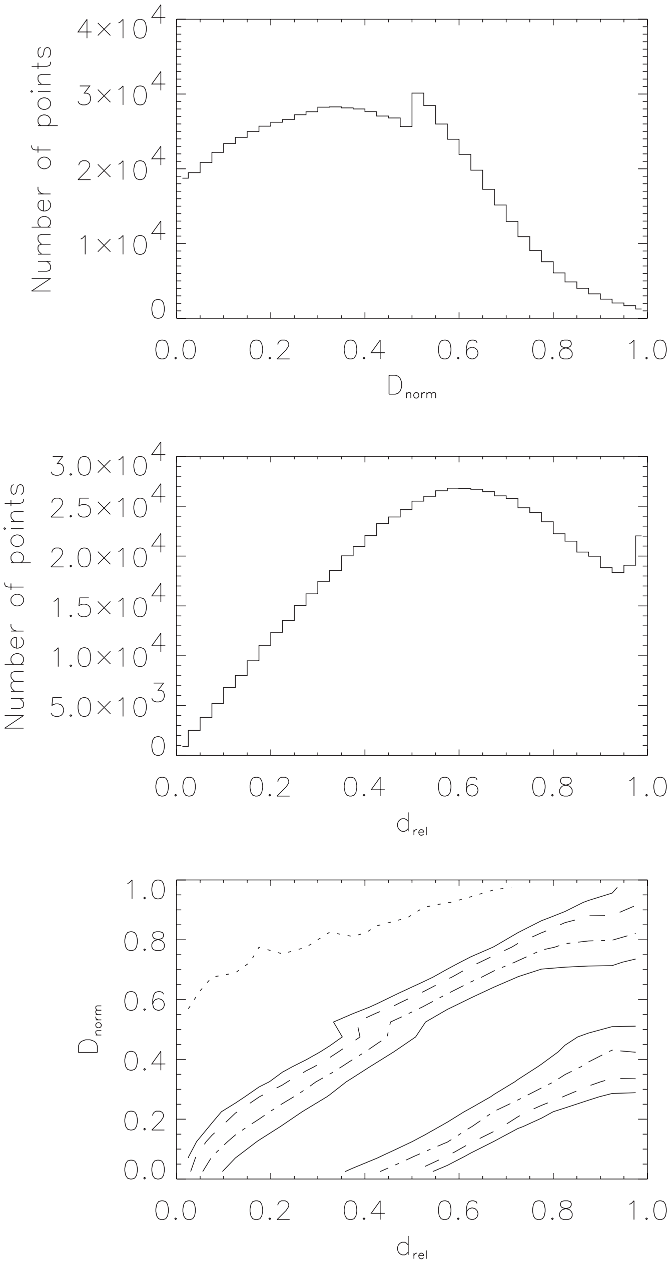

Fig. 7. *Top panel*: number of pixels versus $D_{\rm norm}$ for $N_{\rm box}$ larger than 40 and $|B| < 3$ G, where $N_{\rm box}$ is the number of pixels below 3 G in a 7×7 pixels box around the current pixel. *Middle panel:* number of pixels versus $d_{\rm rel}$ for $N_{\rm box}$ larger than 40. *Lower panel*: number of pixels versus $D_{\rm norm}$ and $d_{\rm rel}$ for $N_{\rm box}$ larger than 40. Contours correspond to 10 pixels (dotted line), 900 pixels (solid line), 1300 pixels (dashed line), 2200 pixels (dotted-dashed line) and 3500 pixels (dot-dot-dot-dashed line).

Figure 7 also shows the 2D distribution of the pixels in $D_{\rm norm}$ and $d_{\rm rel}$. As noted above there is a very large dispersion despite a good correlation factor. For $d_{\rm rel}$ close to 0.5, the *FWHM* of the $D_{\rm norm}$ distribution is of the order of 0.4, while for $D_{\rm norm}$ close to 0.5 the *FWHM* of the $d_{\rm rel}$ is also close to 0.4. When considering the boundary ($d_{\rm rel}$ close to 1), the *FWHM* of the $D_{\rm norm}$ distribution is similar. However it is much smaller (and no longer a Gaussian) when considering values of $D_{\rm norm}$ close to 1, as $d_{\rm rel}$ peaks around 1.

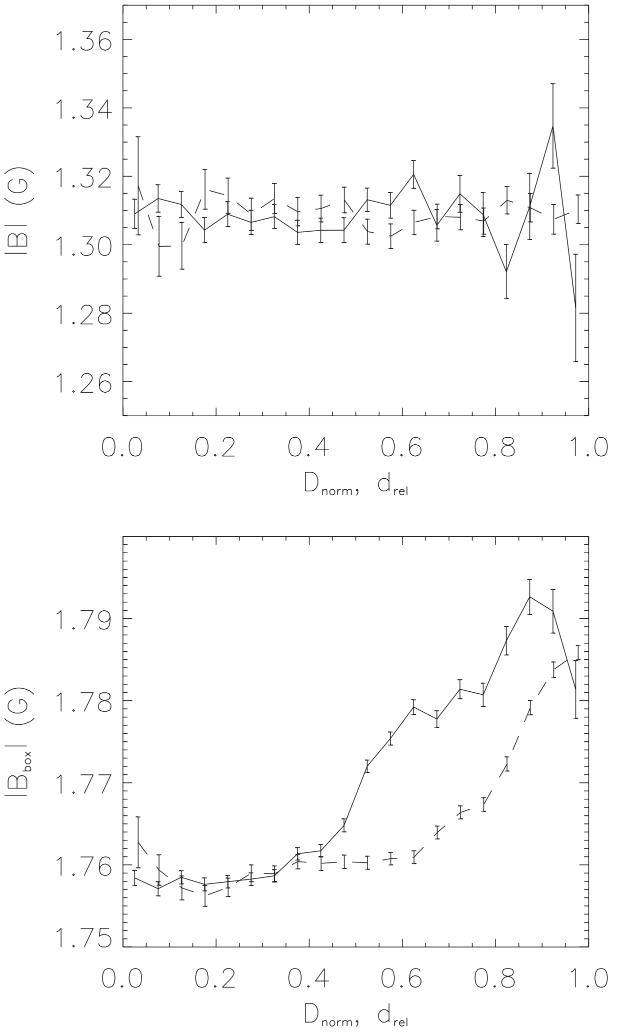

Fig. 8. *Top panel*: magnetic field $|B|$ in each pixel as a function of the normalized divergence $D_{\rm norm}$ (solid line) and of the relative distance to cell center $d_{\rm rel}$ (dashed line), for $N_{\rm box}$ larger than 40 and $|B| < 3$ G. *Lower panel*: same for the magnetic field $|B_{\rm box}|$ averaged over the 7 × 7 pixel box.

3.2.2. Magnetic field content

It is important to check the magnetic field variations for this pixel selection. This is shown in Fig. 8. The variations of $|B|$ are very small and not significant, so at least the variations of I are not expected to be affected by any residual magnetic field variations. Furthermore, the variation of $|B_{\rm box}|$, affecting mostly $I_{\rm min}$ and $I_{\rm max}$, is significant but still very small, with a variation of the order of 0.03 G, while $|B_{\rm box}|$ is always below 3.5 G. When looking at the variation of I with $|B|$, we see that the variation in that domain of $|B|$ is very small, and such a small variation of $|B|$ would correspond to an intensity variation of 0.006 only (for an average level of 3930 ADU), which is negligible.

3.2.3. Intensity variations

We have defined a selection of pixels for which the influence of the magnetic field should be very small. We can now study the intensity variations inside supergranules. Figure 9 shows the intensity variations as a function of the normalized divergence $D_{\rm norm}$ and of the relative distance to cell center $d_{\rm rel}$, for $N_{\rm box}$ larger than 40. I decreases from the center of the cell to the boundary, either using $D_{\rm norm}$ or $d_{\rm rel}$. $I_{\rm max}$ is also decreasing, while $I_{\rm min}$ is close to constant, leading to a smaller contrast at the cell boundary. Despite a consistent slope between the two approaches ($D_{\rm norm}$ and $d_{\rm rel}$), all intensities increase again very close to the edge (converging flows) for $D_{\rm norm}$ but decrease even more when using the geometrical approach. This may be due to the fact that even with a severe selection, there is still probably a small contamination from the network magnetic field in converging flows.

In order to quantify these variations, we have used two approaches. The first one is to compute the slope of these variations over the whole range. The results are shown in Table 1. For $N_{\rm box}$ larger than 40, the slopes are larger for $D_{\rm norm}$ than for $d_{\rm rel}$. Given their respective distribution, this means that the slope may be larger in the inner part of the cells. The slope for $I_{\rm min}$ is positive (showing an increase toward the boundary) for $D_{\rm norm}$ but is not very significant, and it is not significantly different from zero for $d_{\rm rel}$.

Another way to look at these variations is to consider what happens at the center and at the boundary. Here we compute the average intensities close to the cell center or maximum diverging flows (with $D_{\rm norm}$ and $d_{\rm rel}$ lower than 0.1), and close to the boundary or maximum converging flows (values above 0.9). Table 2 shows the intensity at the cell boundary minus the intensity at the cell center. Again for $N_{\rm box}$ larger than 40, the signs are consistant with the slopes of Table 1. However, the differences are now larger when using $d_{\rm rel}$ than when using $D_{\rm norm}$. This could be due to the observation made in Fig. 9 close to the boundary. This indicates that in that case, the variation may be reduced in the strong converging flows, but are strongly present everywhere else on the cell boundary.

3.2.4. Variations for a more drastic selection

Despite that the number of pixels available strongly decreases when a more severe selection is made using $N_{\rm box}$, we also shows the results for $N_{\rm box}$ larger than 44. This leads to 89509 pixels, covering only 0.3% of the surface. The results are shown in Tables 1 and 2. In this case, both the slopes and the intensity differences are increased, even if the errobars become larger. Another important fact is that $I_{\rm min}$ then also decreases from the cell center to the boundary when considering $D_{\rm norm}$. It is not significantly different from zero when considering $d_{\rm rel}$.

3.2.5. Discussion of errorbars and possible biases

For $N_{\rm box}$ larger than 40 for example, the slopes and intensity differences are very significant, with a S/N larger than 10 in many cases. So even if the errorbars are underestimated by a factor smaller than 2 as mentionned in Sect. 2.4, the results presented in this section remain very significant.

Because of the severe selection, it is important to consider possible biases that would affect the results. Indeed, we consider pixels with $|B|$ lower than 3 G only. Therefore, in more active areas, we will select a larger proportion of pixels *inside* granules (i.e. where the intensity is the greatest) because the small-scale magnetic structures (unresolved here) are more likely to be located in intergranules (e.g. Domínguez Cerdeña et al. 2003). This should be the case closer to the boundary and to the magnetic network, and therefore we might expect an increase of intensity there due to the selection effect. Since we observe the opposite, this possible selection bias cannot be responsible for our results.

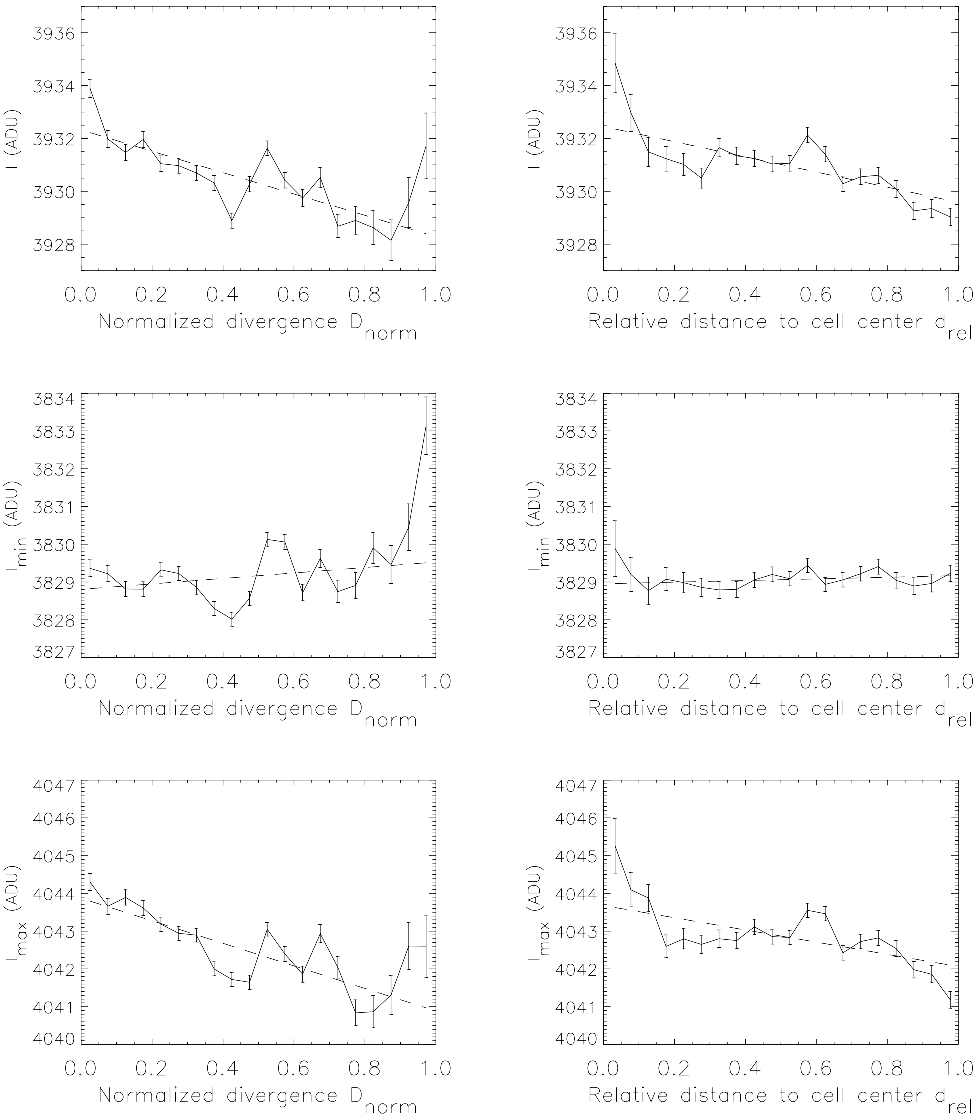

Fig. 9. *Left panels*: intensities versus the normalized divergence $D_{\rm norm}$, for $N_{\rm box}$ larger than 40 and $|B| < 3$ G. *Right panels*: same versus the relative distance to cell center $d_{\rm rel}$. *From top to bottom*: intensity I, $I_{\rm min}$, and $I_{\rm max}$. The dashed lines are linear fits. Note that for a given variable, the scale is the same for $D_{\rm norm}$ and $d_{\rm rel}$ in order to make the comparison easier.

Table 1. Slopes of intensity (I, $I_{\rm min}$, $I_{\rm max}$) versus the normalized divergence $D_{\rm norm}$ and versus the relative distance to cell center $d_{\rm rel}$, for $N_{\rm box}$ larger than 40 (Cols. 2 and 3) and larger than 44 (Cols. 4 and 5) . Intensities are expressed in ADU and the average intensity is 3930. $|B|$ is smaller than 3 G.

Int.	$D_{\rm norm}$, 40	$d_{\rm rel}$, 40	$D_{\rm norm}$, 44	$d_{\rm rel}$, 44
I	-4.04 ± 0.35	-2.87 ± 0.33	-6.33 ± 1.03	-2.07 ± 0.96
$I_{\rm min}$	0.72 ± 0.23	0.22 ± 0.21	-1.87 ± 0.68	-0.30 ± 0.62
$I_{\rm max}$	-2.99 ± 0.23	-1.62 ± 0.21	-2.25 ± 0.68	-0.09 ± 0.62

Table 2. Difference between intensities at the cell boundary and at the cell center (boundary intensity minus center intensity, see text), i.e. I, $I_{\rm min}$, $I_{\rm max}$, when using the normalized divergence $D_{\rm norm}$ and the relative distance to cell center $d_{\rm rel}$, for $N_{\rm box}$ larger than 40 (Cols. 2 and 3) and larger than 44 (Cols. 4 and 5). Intensities are expressed in ADU and the average intensity is 3930. $|B|$ is smaller than 3 G.

Int.	$D_{\rm norm}$, 40	$d_{\rm rel}$, 40	$D_{\rm norm}$, 44	$d_{\rm rel}$, 44
I	-2.50 ± 0.31	-4.34 ± 0.30	-7.87 ± 0.90	-2.87 ± 0.94
$I_{\rm min}$	2.27 ± 0.20	-0.25 ± 0.19	-2.60 ± 0.61	0.69 ± 0.61
$I_{\rm max}$	-1.26 ± 0.21	-2.99 ± 0.19	-4.06 ± 0.60	-2.74 ± 0.60

Decreasing further the threshold of 3 G does not change the results, so the results are quite robust. Furthermore, we have performed simulations to better test the significance of the results. We choose random pixels in the maps that will be considered as artificial "cell centers". Then we use the same pixel selection as on the real data. We derive slopes showing the variation of the intensity between the cell center and the cell boundary: these slopes are more than one order of magnitude smaller than the observed slopes. Finally, we have also added a new selection by choosing only the cells for which the perimeter-area relation is not too far from a circle. The results are not significantly different either.

3.3. Variation with cell size

As we have a large sample of pixels, we attempted to study possible variations of the results with cell size. When considering various categories of sizes, we find that the results are quite constant, except for very large cells. However, there are only a few of these very large cells so the results are not significant in that domain. We conclude that at this point it is difficult to identify any significant variation with the cell size. However, this approach is very interesting because it also shows that the results are very robust when considering completely independant data sets of cells.

4. Discussion and conclusion

When selecting the pixels associated with the lowest magnetic fields in order to avoid possible brightness enhancements due to the magnetic network, we observe a decrease of the intensity from the supergranule cell center to the boundary. The amplitude of the variation is of the order of 2–7 ADU depending on the more or less severe selection or on the type of computation (slope over the whole supergranule or difference between the intensities at the center and boundary), which corresponds to a variation of 0.05% to 0.18% in brightness. If we consider an average temperature of 5800 K, this corresponds to a significant variation in temperature in the range 0.8–2.8 K. This can be compared to the upper limit of 2–3 K on non-axisymmetric brightness inhomogeneities over scales between 5×10^4 and 2×10^5 km (i.e. in a range above the supergranule scale) found by Foukal & Fowler (1984). Furthermore, our results are very stable with respect to the selection, and there is a systematic increase of the intensity variation when the selection is more drastic. We have also noted that the variations are quite sharp at the center of the cells.

A new result has also been obtained concerning the variation of the intensity as a function of the magnetic field, as we observe a dependence on the localisation in the cell. Network magnetic fields are associated with a larger intensity close to the cell center compared to those close to the boundary, while it is the opposite for lower magnetic field structures, which are probably related to intranetwork magnetic fields.

Our work also examines in more detail the intensity variation across the supergranules. Is this variation the same everywhere? Is it different for granules and intergranules? To answer these questions we have also considered the minimum intensity (intergranule) and maximum intensity (granule center) in boxes around each pixel. We find that the behavior of the granules is close to the general variation, but tends to exhibit smaller slopes. On the other hand, the intergranules show a decrease from cell center to boundary only when the selection is very restrictive: in all cases the slope is very small.

It could be argued that the observed intensity variation could be due to a different size distribution of granules at the center of supergranules and at the boundary. For example, Brandt et al. (1991) found an excess of small granules in converging flows at the mesogranulation scale. As the magnetic field tends to be larger at the boundary of supergranule cells, we expect to have smaller granules (Hanslmeier et al. 1991; Hirzberger et al. 1999). However, Hirzberger et al. (1997) have observed that when the granule size increases, the maximum intensity also increases but the minimum intensity decreases. Granulation simulations (Gadun et al. 2000) confirm the observations of Hirzberger et al. (1997). So if the intensity variation is due to this size effect, we expect to observe a decrease in intensity and maximum intensity (which we do observe) and an increase in minimum intensity, which we do not observe (we find an almost constant minimum intensity, or a decreasing one).

We conclude that the intensity variations expected from smaller granules at the cell boundary are not sufficient to explain our results. It reinforces the possibility of a lower average temperature at the boundary of supergranules. A lower temperature at the boundary is compatible with a convective nature of solar granulation. However, an open question is now whether this intensity variation in granules and intergranules is the one that would be observed if one decreases the average temperature of region by a given amount, or if the behavior of intergranules and granules is expected to be different. Furthermore, the intensity profiles close to the cell center do not seem be flat as is the case for granules.

Comparison with large-scale simulations of the solar surface such as those performed by Rieutord et al. (2002) and Benson et al. (2006) will therefore be performed order to check that the observed profiles and intergranule and granule properties are compatible with convection. It will also have to be checked with higher spatial resolution observations on a large field-of-view, such as those that will soon be obtained with CALAS[1] at the Pic du Midi Observatory (Meunier et al. 2003, 2005). This should improve the measurements of granules and intergranules.

Acknowledgements. We thank M. Rieutord for useful comments on the manuscript. SOHO is a mission of international cooperation between the European Space Agency (ESA) and NASA.

References

Beckers, J. M. 1968, Sol. Phys., 5, 309
Benson, D., Stein, R. F., & Nordlund, A. 2006, AAS/Solar Physics Division Meeting, 37, 30.03
Brandt, P., Ferguson, S., Scharmer, G., et al. 1991, A&A, 241, 219
Domínguez Cerdeña, I., Sánchez Almeida, J., & Kneer, F. 2003, A&A, 407, 741
Foukal, P., & Fowler, L. 1984, ApJ., 281, 442
Frazier, E. N. 1970, Sol. Phys., 14, 89
Gadun, A. S., Hanslmeier, A., Pikalov, K. N., et al. 2000, A&AS, 146, 267
Hagenaar, H. J., Schrijver, C. J., & Title, A. M. 1997, ApJ., 481, 988
Hanslmeier, A., Nesis, A., & Mattig, W. 1991, A&A, 251, 307
Hart, A. B. 1954, MNRAS, 114, 17
Hirzberger, J., Bonet, J. A., Vázquez, M., & Hanslmeier, A. 1999, ApJ., 515, 441
Hirzberger, J., Vázquez, M., Bonet, J. A., Hanslmeier, A., & Sobotka, M. 1997, ApJ., 480, 406
Koutchmy, S., & Lebecq, C. 1986, A&A, 169, 323
Lin, H., & Kuhn, J. R. 1992, Sol. Phys., 141, 1
Meunier, N., Rieutord, M., & Beigbeder, F. 2003, in SF2A-2003: Semaine de l'Astrophysique Francaise, ed. F. Combes, D. Barret, T. Contini, & L. Pagani, 93
Meunier, N., Rondi, S., Tkaczuk, R., Rieutord, M., & Beigbeder, F. 2005, in Large-scale Structures and their Role in Solar Activity, ed. K. Sankarasubramanian, M. Penn, & A. Pevtsov, ASP Conf. Ser. 346, 53
Meunier, N., Tkaczuk, R., Roudier, T., & Rieutord, M. 2007, A&A, 461, 1141
Montagne, M., Muller, R., & Vigneau, J. 1996, A&A, 311, 304
Rast, M. P. 2003a, in GONG+ 2002. Local and Global Helioseismology: the Present and Future, ed. H. Sawaya-Lacoste, ESA SP-517: 163
Rast, M. P. 2003b, ApJ., 597, 1200
Rieutord, M., Ludwig, H.-G., Roudier, T., Nordlund, A., & Stein, R. 2002, Nuovo Cimento C Geophysics Space Physics C, 25, 523
Rieutord, M., Roudier, T., Malherbe, J. M., & Rincon, F. 2000, A&A, 357, 1063
Scherrer, P. H., Bogart, R. S., Bush, R. I., et al. 1995, Sol. Phys., 162, 129
Simon, G., & Leighton, R. 1964, ApJ., 140, 1120
Title, A. M., Tarbell, T. D., & Topka, K. P. 1987, ApJ, 317, 892
Title, A. M., Topka, K. P., Tarbell, T. D., et al. 1992, ApJ, 393, 782
van der Borght, R. 1979, MNRAS, 188, 615
Wang, H. 1988, Sol. Phys., 117, 343

---

[1] CAmera for the LArge Scales of the solar surface.

A&A 466, 691–696 (2007)
DOI: 10.1051/0004-6361:20066790

Astronomy
&
Astrophysics

The superrotation of solar supergranules

N. Meunier and T. Roudier

Laboratoire d'Astrophysique de l'Observatoire Midi-Pyrénées, Université Paul Sabatier, CNRS, 57 Avenue d'Azereix, BP 826, 65008 Tarbes Cedex, France
e-mail: `[meunier;roudier]@ast.obs-mip.fr`

Received 22 November 2006 / Accepted 19 January 2007

ABSTRACT

Context. Supergranules have long been believed to rotate faster than plasma and than magnetic structures. However, it has recently been shown that this could be due to a bias appearing when using Dopplergrams, which are strongly affected by projection effets.
Aims. Our purpose is to perform new measurements of supergranule angular velocities using a technique that would not be significantly influenced by projection effets.
Methods. We are therefore tracking horizontal divergence maps smoothed on the supergranular scale, either globally or on the scale of cells. Tracking the magnetic field using the same technique allows them to be used as a reference. Doppler tracking is performed for a direct comparison.
Results. We confirm that the tracking of Doppler features is not reliable when computing the dynamics on the supergranular scale. However, we find that divergence features are still rotating faster than the magnetic field, when using two independent time series.
Conclusions. We conclude that the long-standing puzzle of supergranular superrotation persists, and that interpreting it in terms of anchorage depth inside the convective zone may not be sufficient to explain it.

Key words. Sun: rotation – Sun: photosphere – Sun: general

1. Introduction

Supergranules have been found to rotate significantly faster than plasma, and even faster than the magnetic structures, including the network (Duvall 1980; Snodgrass & Ulrich 1990). Both these results have been obtained by tracking Doppler features on the solar disk. More recently, Beck & Schou (2000) found similar results by tracking the features on different scales in Fourier space. More puzzling properties of supergranules were also obtained by Schou (2003), in particular a wavelike behavior of supergranules, although this analysis has been questioned by Rast et al. (2004).

However, very recently, Hathaway et al. (2006) performed a simulation that showed that all these measurements, which were performed using Doppler features, were strongly biased by the projection effects on the observed signal. They concluded that supergranules may not be rotating as fast as previously thought and that the rotation could probably then be explained by the anchoring of supergranules in the convective zone at a depth rotating at the same rate.

It was therefore necessary to measure the angular velocity of supergranules again using a method without any projection effect. We therefore chose to track supergranules using horizontal divergence maps as determined by Meunier et al. (2007a,b,c). We used the same data sets as in Meunier et al. (2007a,b) while Meunier et al. (2007c) used only a subset. Tracking magnetograms is used for reference, and Doppler features are tracked for comparison. We describe the data in Sect. 2. The global tracking is presented in Sect. 3 and the feature tracking in Sect. 4. We discuss the results in Sect. 5.

2. Data and processing

2.1. MDI data

We used high resolution MDI/SOHO (Scherrer et al. 1995) intensity maps, magnetograms, and Dopplergrams obtained during the solar minimum in January 1997 and March 1997. The first series started on January 16, 1997 at 23:00 and lasted 46 h. The second series started on March 17, 1997 at 11:00 and lasted 15 h. A few images were missing in each time series, typically one or two images per hour. They were replaced by interpolating between adjacent images. The pixel size is 0.605 arcsec and the field-of-view $620'' \times 303''$. The temporal cadence is 1 min. All images are remapped on a grid with constant steps in longitude and latitude.

2.2. Divergence maps

For each of the 61 hourly data sets, the 60 intensity maps and magnetograms were aligned with the map at the center of the data set. Intensity maps were corrected for large-scale gradients and k-ω filtered (with a cut-off at 6 km s^{-1}). A local correlation tracking (LCT) algorithm was then applied to provide velocity and divergence maps. These divergence maps are averaged over 1 h and smoothed with a Gaussian whose full-width at half-maximum is 10.2 Mm to exhibit supergranular cells. The validity of this approach is discussed in Meunier et al. (2007b,c). The displacements between maps separated by a given time-lag (1 h or more) will be computed using several techniques described in Sect. 3.

2.3. Magnetogram reference

It is very important to compare the angular velocity derived from horizontal divergence maps with that obtained with other variables, such as the magnetic field, using the same technique, because there is a large dispersion of the magnetic structure's angular velocity in the literature. Here we consider the 1-h averaged magnetograms, with a low noise level (~3 G). These maps can be used exactly in the same way as the divergence maps, and the magnetic network angular velocity will be used as a reference. Note that the magnetic network is located in regions of strong converging flows as expected (Meunier et al. 2007a,b). A pore with active network surrounding it is in the field-of-view. Most of the large boxes used in Sect. 3 do not include it, however, except at the end of the sequence (but see discussion in Sect. 3.1), and cells close to the pore have been eliminated in Sect. 4.

2.4. Doppler maps

Because the previous results using Dopplergrams have been questionned by Hathaway et al. (2006), it was interesting to compare the displacements obtained in the same conditions for Dopplergrams. We therefore also consider 1-h averaged Dopplergrams, from which the fundamental rotation signal has been removed after an estimation using a linear fit for each line of the images. In this resulting Dopplergram, small-scale structures are still visible, as can be confirmed by comparing the Fourier transform of these images with the smoothed divergence maps used above. To deal with features on the same scale as the divergence maps of Sect. 2.2 (supergranulation), we spatially smooth these Dopplergrams with a Gaussian whose half-width at half-maximum is ~7 Mm, to obtain a spatial Fourier transform similar to the one in the divergence maps. The structures are also visually similar (except for the strong projection effects in Dopplergrams of course), as shown in Fig. 1. The resulting maps still contain some very large-scale variations due to the projection effects. Finally, it is interesting to note that the computation of the displacement between consecutive maps for various values of the spatial smoothing (from no smoothing to more than 10 Mm) shows that it is very sensitive to the smoothing and reaches a maximum around 5 Mm. This is probably due to the strong projection effects. We show in Sect. 3.2 that the angular velocity is strongly affected by these projection effects.

3. Global correlation tracking

3.1. Divergence map tracking

We first compute global displacements between two subsequent magnetograms or divergence maps by correlation. We consider square boxes (401 × 401 pixels, i.e. $14 \times 14^{\circ 2}$) centered on disk center. An example of the three kinds of maps is shown in Fig. 1. To illustrate the behavior of each type of data, Fig. 2 shows a cut in the longitude direction for a given latitude, and follows this cut in time for the January 1997 time series. The global magnetic field displacement is taken as the reference and removed in this figure. We can observe very long-lived divergence features, as already observed by DeRosa & Toomre (2004) for example, as well as long-lived network structures.

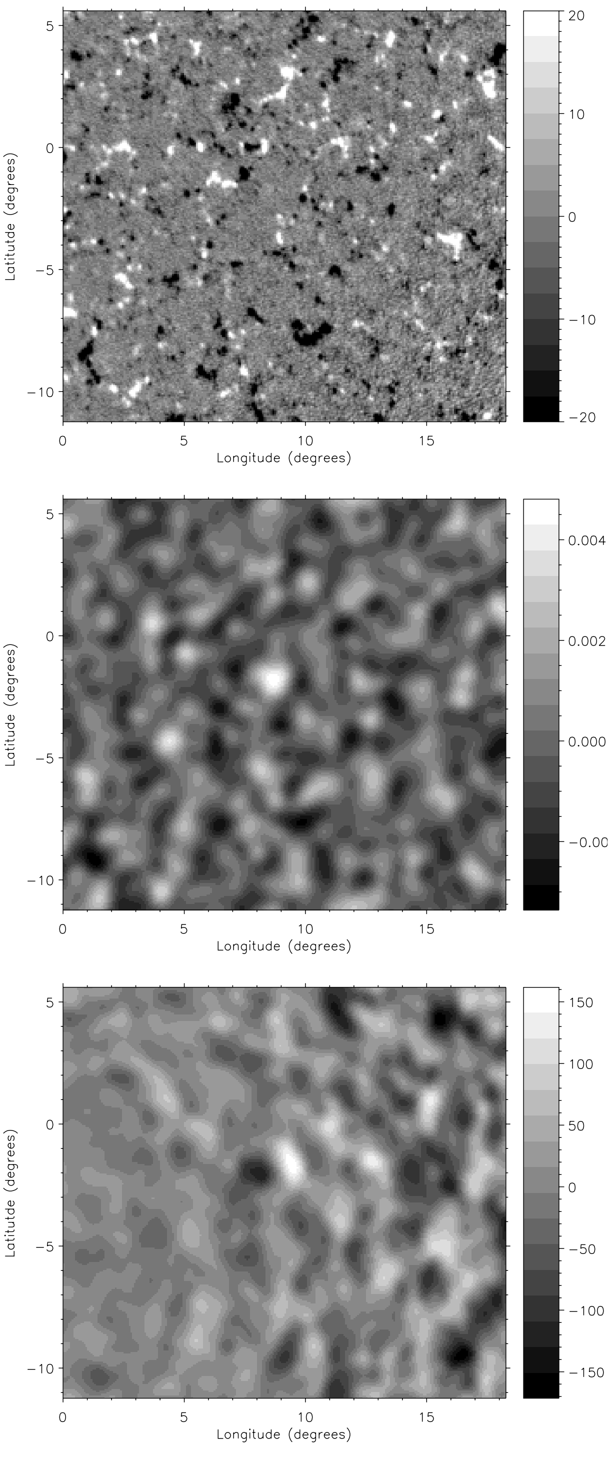

Fig. 1. *Upper panel*: magnetogram averaged over 1 h, after remapping, showing the line-of-sight magnetic field (in Gauss). Only half of the available field-of-view is shown. *Middle panel*: same for the horizontal divergence at the supergranular scale (in s^{-1}). *Lower panel*: same for the Dopplergram (line-of-sight velocity field in m/s), after angular correction and spatial smoothing (see text).

Table 1 shows the results for a time lag of 1 h for the two time series. The maximum correlation is smaller for the divergence maps (0.68 and 0.67 for the two time series) than for the magnetic field (0.93 and 0.82), indicating a stronger distortion on short time scales for horizontal divergences. In all cases, the amplitude of these correlations is sufficient for computing precise displacements. We therefore obtain a larger angular velocity for divergence maps compared to magnetograms, with a difference of 0.17 ± 0.08 deg/day for the January 1997 time series and of 0.35 ± 0.11 deg/day for the March 1997 time series, which is significantly different from zero at the 1σ level (2σ level in the case of the March time series). The amplitude of the difference

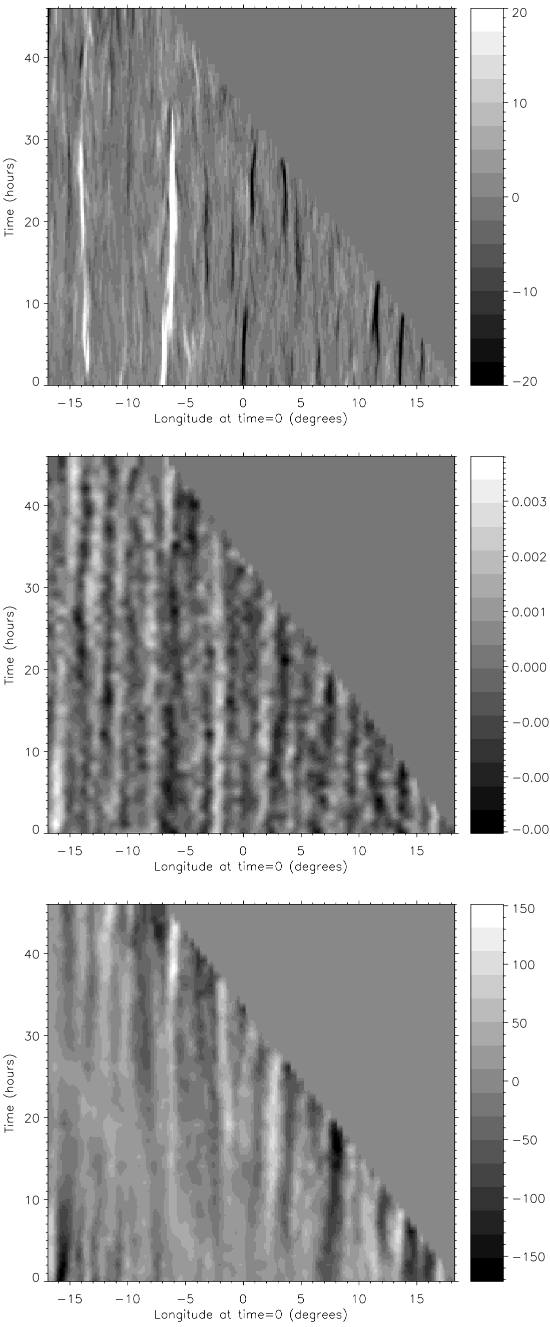

Fig. 2. *Upper panel*: line-of-sight magnetic field (in Gauss) versus longitude and time, after an averaging over 0.4° in latitude, for latitude –2.8° (crossing disk center). *Middle panel*: same for the horizontal divergence (in s^{-1}) on the supergranular scale. *Lower panel*: same for the Dopplergram (line-of-sight velocity in m/s), after angular correction and spatial smoothing (see text).

between the divergence map shift and the Carrington rotation is on the order of 36 m/s for the January time series, and very similar for the March time series, i.e. a factor of two smaller than the results of Lisle et al. (2004). A small variation with longitude is observed, as in previous works (e.g. Meunier 1999).

Despite coming to the same conclusion for the two data sets, i.e. a higher angular velocity for the divergence maps compared to the magnetic-field, there are few differences that are worth pointing out. The difference in the residual is mostly due to a magnetic field angular velocity variation, weaker in the case of the March 1997 time series. The origin of this discrepancy, as well as the difference in maximum correlation shown in Table 1, is illustrated in Fig. 3. The January 1997 time series exhibits a larger maximum correlation, which is due to the presence of the pore, except for the two first images, for which the pore was not present (corresponding to the two points in the lower left corner of the figure). The March 1997 time series exhibit an intermediate maximum correlation, likely to be due to an intermediate activity level. Therefore the higher angular velocity for the January time series is likely to be due to the presence of that pore, showing a significant variation in the angular velocity with the activity level, as already observed in previous works (see the discussion in the next section). However, the angular velocity derived from the divergence maps remains stable and the residual always has a positive sign.

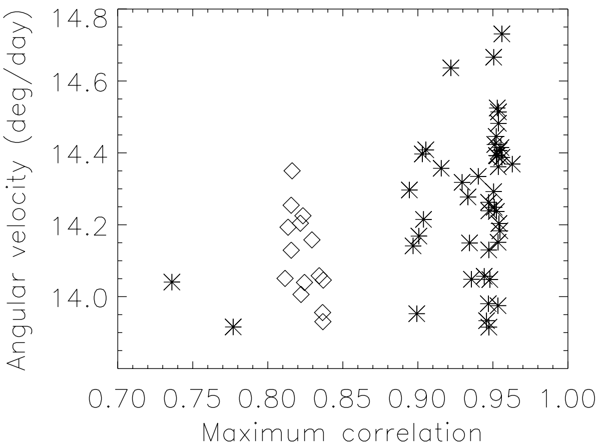

Fig. 3. Sidereal rotation rate derived from the global tracking of the magnetic field versus the maximum correlation between magnetograms, for January 1997 (stars) and March 1997 (diamonds).

To take the small differential rotation into account (expected to be of the order of 0.1 pixel given our pixel size and field-of-view), we also computed the correlation for latitude strips of 1 degree. The results are very similar, even when considering a larger field-of-view, i.e. for strips covering the whole longitude range. It also shows that the presence of the pore at the end of the sequence, in the 401 × 401 pixel box, does not affect the result much, as the residual angular velocities are similar at latitudes. In this case, the larger maximum correlation for the strip containing the pore is also observed, however, the variation in the angular velocity with the correlation is not significant.

When using different time lags, a small variation in angular velocity is observed, but is not very significant compared to the uncertainties on the measurements. However, the difference between the two types of structures, magnetic fields and divergences, remains similar. Our result therefore seems very robust.

3.2. Comparison with Doppler map tracking

In the case of Dopplergrams, surprisingly, we do not observe that the Doppler features are rotating faster than the magnetic field. On the contrary, they rotate slower, the residuals with respect to the magnetic-field angular velocity being −0.23 ± 0.04 deg/day for the January time series and −0.24 ± 0.08 deg/day for the March time series. Furthermore, we observe that the displacement computation is very sensitive to the size of the box and to the spatial smoothing, which is probably for the same reason as the bias discussed by Hathaway et al. (2006), i.e. strong

Table 1. Sidereal angular velocity (in deg/day) derived from the global tracking for magnetic field ($\Omega_{\rm B}$), for horizontal divergence maps ($\Omega_{\rm div}$), and for smoothed Dopplergrams ($\Omega_{\rm dop}$).

Series	# sets	$\Omega_{\rm B}$	$C_{\rm B}$	$\Omega_{\rm div}$	$\Delta\Omega_{\rm div}$	$C_{\rm div}$	$\Omega_{\rm dop}$	$\Delta\Omega_{\rm dop}$	$C_{\rm dop}$
January 1997	46	14.27 ± 0.03	0.93	14.44 ± 0.08	0.17 ± 0.08	0.68	14.04 ± 0.04	-0.23 ± 0.05	0.92
March 1997	15	14.11 ± 0.03	0.82	14.46 ± 0.11	0.35 ± 0.11	0.67	13.87 ± 0.07	-0.24 ± 0.08	0.88

projection effects that are absent from the horizontal divergence maps. For example, when changing the size of the box from 101^2 to 401^2 pixels, the angular velocity of the magnetic field and divergence maps remain within their errorbars, while the angular velocity derived from Dopplergrams varies from 13.45 ± 0.20 deg/day to 14.04 ± 0.04 deg/day in the January time series. It is also much more variable with longitude. This shows that the Dopplergrams are not very reliable when one wishes to compute the dynamics of supergranules.

4. Horizontal divergence feature tracking

To complete our analysis, we also performed a local tracking, centered on either the region of maximum divergence (diverging flows) or on the region of minimum divergence (converging flows). Here we focus on the diverging flows. This approach is therefore similar to a local correlation tracking (we consider a box of size 65×65 pixels, i.e. $\sim 2.3 \times 2.3$ degrees or 28×28 Mm^2), but is also close to a feature tracking, as the velocities are computed only at the position of supergranular cells. The size of the box is close to the supergranular's typical size. For each structure identified by the position of maximum divergence, for example, we also consider the value of this divergence, the magnetic field level. The magnetic level was computed using two different approaches (all on the absolute value): 1) average for all pixels in the box, 2) for pixels with magnetic fields larger than 10 G (typically network magnetic fields).

For a time lag of 1 h, a summary of the results is shown in Table 2. The average maximum correlation is indicated (respectively $C_{\rm mag}$ and $C_{\rm div}$), as well as the residual angular velocity (in deg/day) after substraction of the magnetic angular velocity for horizontal divergence maps ($\Delta\Omega_{\rm div}$). The results are shown for diverging flows (Div) and for converging flows (Conv). The average maximum correlation is indicated ($C_{\rm mag}$, $C_{\rm div}$, and $C_{\rm dop}$), as well as the residual angular velocity (in deg/day) after substraction of the magnetic angular velocity for horizontal divergence maps ($\Delta\Omega_{\rm div}$) and for smoothed Dopplergrams ($\Delta\Omega_{\rm dop}$). We consider 4979 boxes, or "cells", for the January 1997 time series, and 1622 cells for the March 1997 time series. Each of these cells is associated to a local maximum in the divergence map (and therefore to a supergranular cell). The difference in angular velocities between the magnetic field and the divergences is positive in both cases; i.e. the divergence features are again rotating faster than the magnetic field. As for the global tracking, we observe higher angular velocity for diverging flows compared to the magnetic network. The average maximum correlation is 0.73, i.e. slightly larger than for the global tracking, and the peak of the distribution of the maximum correlation is even higher (close to 0.80). The amplitude of the difference agrees with the result of the previous section, within the errorbars. We have not observed any significant variations in these residuals with the amplitude of the maximum divergence (which is correlated with the size of the cell, Meunier et al. 2007c) nor with the maximum correlation.

However, as for the global tracking, most of the difference comes from the variation in the angular velocity of the magnetic field, as illustrated in Fig. 4. In all cases strong fields are better correlated than weak fields, and are associated to higher angular velocities. The slope between the angular velocity and the magnetic field averaged over the cell is 0.0047 ± 0.0008 deg/day/G, which corresponds to a difference of 0.24 ± 0.04 deg/day between very weak fields and a 50 G field. The slope between the angular velocity and the maximum correlation is also very significant, with values of 0.83 ± 0.08 deg/day and 0.64 ± 0.18 deg/day respectively for the January 1997 and the March 1997 time series. The increase in angular velocity with increasing magnetic field inside the cell is in agreement with the results of Meunier (2005a).

When considering the average magnetic field in the box for fields larger than 10 G (i.e. corresponding mostly to the network, case #2 above), the slope of the residuals versus the magnetic field is significantly negative at the 1σ level (-0.02 ± 0.01 deg/day/G), for the January 1997 time series, indicating a larger residual for weaker magnetic network. The slope is smaller, -0.008 ± 0.004 deg/day/G, when considering all magnetic field values (case #1 above). However, the slopes for the March 1997 time series, despite having the same sign, are not significantly different from zero, due to the larger errorbars. This may be due to the the smaller range in magnetic fields in this quieter data set, which is illustrated in Fig. 4. By following each cell during its lifetime, we also determined that long-lived cells had a higher angular velocity. This should be studied further using a larger data set, as the uncertainties remain large. However, it may contradict the results of DeRosa & Toomre (2004), who found cells with longer life in a more active network, which they interpreted as a possible stabilization effect of the magnetic field on the cells.

The dispersion of the difference between the diverging flows and the magnetic field angular velocities is quite large, on the order of several deg/day, despite the small average residual. The illustration in Fig. 2 seems to indicate that this large dispersion is not due to uncertainties in the measurements but to actual drifts of the cells in one direction or another. Whether these drifts are random or are clues of systematic large-scale flows is the subject of future work.

When we increase the time lag, the angular velocity of diverences decreases. For long time lags, the selection is biased toward long-lived cells, which may have a higher angular velocity, so this does not agree with the observed variation with the time lag. The variation with the time lag may therefore be related to residual projection effects.

Finally, it should be pointed out that the computation performed on converging flows (and therefore selection location of minimum divergence), which is quite independent, provide very similar results, with a residual of 0.30 ± 0.06 deg/day (Table 2).

5. Conclusion and discussion

We have compared the angular velocity of supergranules defined by horizontal divergences with that of magnetic structures and Doppler features with similar techniques, either a global tracking or a local tracking. In all cases and for the two independent time

Table 2. Sidereal angular velocity (in deg/day) derived from the local tracking for magnetic field (Ω_B) and for horizontal divergence maps (Ω_{div}).

Serie	Type	# cells	Ω_B	C_B	Ω_{div}	$\Delta\Omega_{div}$	C_{div}
January 1997	Div	4979	14.18 ± 0.01	0.79	14.35 ± 0.07	0.26 ± 0.07	0.73
March 1997	Div	1622	14.02 ± 0.02	0.72	14.40 ± 0.13	0.47 ± 0.13	0.73
January 1997	Conv	5327	14.19 ± 0.01	0.80	14.38 ± 0.07	0.30 ± 0.06	0.73
March 1997	Conv	1775	14.03 ± 0.02	0.73	14.67 ± 0.12	0.61 ± 0.12	0.73

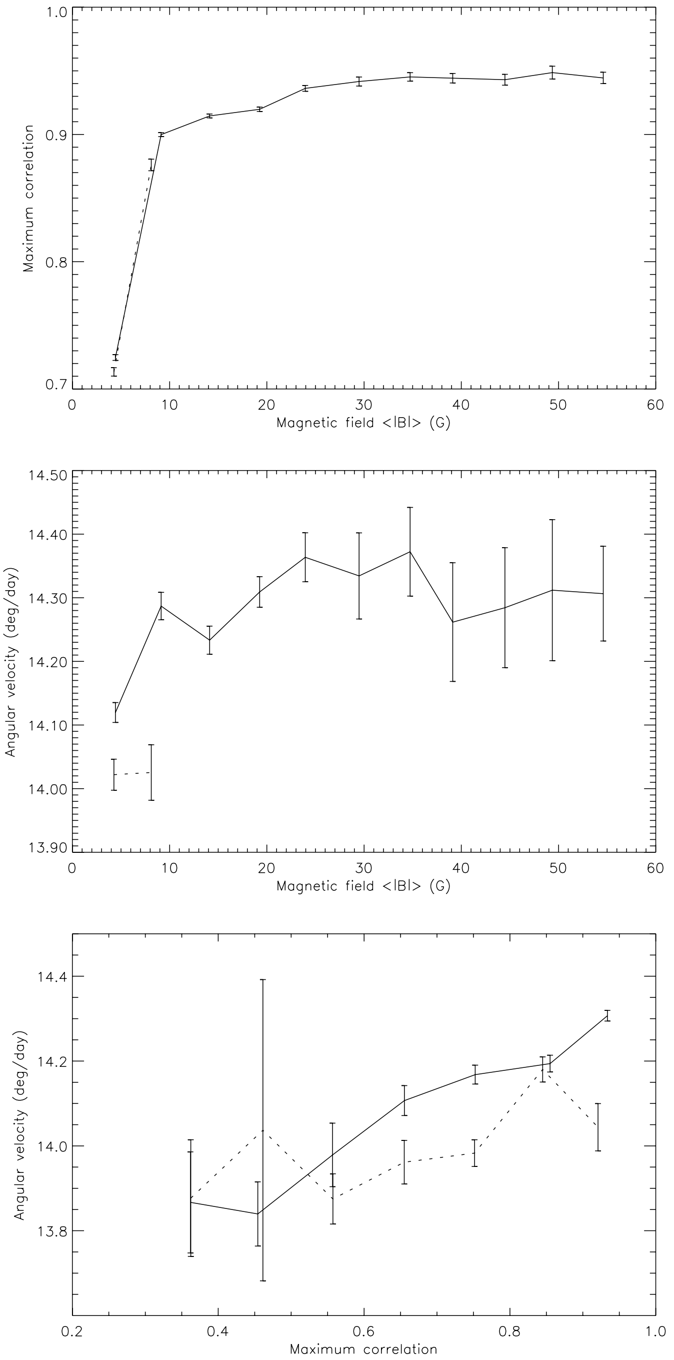

Fig. 4. *Upper panel*: maximum correlation versus the magnetic field averaged over the cells, derived from the feature tracking of diverging flows, for the January 1997 series (solid line) and for the March 1997 series (dotted line). Most of the signal above 10 G is due to the presence of a pore surrounded by active network in the January 1997 series. *Middle panel*: same for the sidereal rotation rate derived from the magnetograms versus the magnetic field averaged over the cells. *Lower panel*: same for the sidereal rotation rate derived from the magnetograms versus the maximum correlation.

series, we observe that supergranules do rotate faster than the magnetic field. The results are signicant at the 1σ level in the case of the global tracking and at the 3σ level in the case of the local tracking. Because we used the same data to compute the magnetic field angular velocity used as a reference, and not the published values, the residuals are free of the influence of temporal variations in the angular velocity.

Comparing the absolute values of the angular velocities is not easy, as magnetic tracers have been shown to exhibit a variable angular velocity during the solar cycle or with the properties of the structures (such as their size). This is the case for sunspots (Balthasar & Wöhl 1980; Gilman & Howard 1984; Balthasar et al. 1986; Lustig & Hanslmeier 1987; Hathaway & Wilson 1990; Nesme-Ribes et al. 1993; Nesme-Ribes et al. 1997; Brajša et al. 2006) or for the magnetic network (Komm et al. 1993; Meunier et al. 1997; Meunier 2005b) for example. Most of these works show a higher angular velocity at the time of maximum. The variation of the supergranular rotation rate has not been studied in the past, however. Here, we do find a velocity that is significantly lower than the rates derived by Duvall (1980); Snodgrass & Ulrich (1990). In the first case, this may be explained by the observations of Duvall (1980) done at a time having been of high activity, while we are using observations obtained during the cycle minimum. The difference with the results of Snodgrass & Ulrich (1990) may be due to the same reason, as they are averaged over approximately two solar cycles and therefore correspond to a higher activity level on average. The differences could also be due to the presence of large-scale patterns of velocities, like those described by Schroeter & Wöhl (1976) for example. This would not apply to the results of Snodgrass & Ulrich (1990), as they cover a very long period, but may apply to ours or to the results of Duvall (1980). Furthermore, the rate derived for boxes covering supergranules agrees well with the angular velocity obtained by Meunier (2005b) for 1997 using a similar method on full-disk magnetograms for the same period (1997). The results of Meunier (2005b) were averaged over the whole year and a more detailed analysis would be necessary to compare the absolute values of the angular velocities more precisely. However, the angular velocity of divergences determined globally is intermediate between this angular velocity and the one determined using small magnetic feature tracking. As discussed in Meunier (2005a), these angular velocities are too high to be explained by a simple anchoring depth of structures.

The angular velocity derived from Dopplergrams was found to be much more sensitive to the conditions (size of the box, time lag, smoothing) and to be in general smaller than the magnetic field angular velocity. This is surprising as the simulation performed by Hathaway et al. (2006) show that they should be overestimated due to the projection effects. It can also be pointed out that MDI velocity fields may be slightly underestimated, as shown by Wöhl & Schmidt (2000). However, this would bias the angular velocity of the plasma derived from the amplitude of the line-of-sight velocity, but not necessarily the angular velocity of the structures identified in the velocity field itself. It is also well-known that the local magnetic field may influence the estimation of the line-of-sight velocity. However, here again, as we are only considering the velocity patterns, it is likely that the projection effects are dominating the measurement of the amplitude of the velocity structure angular velocity.

Acknowledgements. SOHO is a mission of international cooperation between the European Space Agency (ESA) and NASA. We thank the referee for suggestions that helped to improve the paper.

References

Balthasar, H., & Wöhl, H. 1980, A&A, 92, 111
Balthasar, H., Vazquez, M., & Wöhl, H. 1986, A&A, 155, 87
Beck, J. G., & Schou, J. 2000, Sol. Phys., 193, 333
Brajša, R., Ruždjak, D., & Wöhl, H. 2006, Sol. Phys., 237, 365
DeRosa, M. L., & Toomre, J. 2004, ApJ, 616, 1242
Duvall, Jr., T. L. 1980, Sol. Phys., 66, 213
Gilman, P. A., & Howard, R. 1984, ApJ, 283, 385
Hathaway, D. H., Williams, P. E., & Cuntz, M. 2006, ApJ, 644, 598
Hathaway, D. H., & Wilson, R. M. 1990, ApJ, 357, 271
Komm, R. W., Howard, R. F., & Harvey, J. W. 1993, Sol. Phys., 145, 1
Lisle, J. P., Rast, M. P., & Toomre, J. 2004, ApJ, 608, 1167
Lustig, G., & Hanslmeier, A. 1987, A&A, 172, 332
Meunier, N. 1999, ApJ, 527, 967
Meunier, N. 2005a, A&A, 436, 1075
Meunier, N. 2005b, A&A, 442, 693
Meunier, N., Nesme-Ribes, E., & Grosso, N. 1997, A&A, 319, 673
Meunier, N., Roudier, T., & Tkaczuk, R. 2007a, A&A, in press
Meunier, N., Tkaczuk, R., & Roudier, T. 2007b, A&A, 463, 745
Meunier, N., Tkaczuk, R., Roudier, T., & Rieutord, M. 2007c, A&A, 461, 1141
Nesme-Ribes E., Ferreira E. & Mein P. 1993, A&A, 274, 563
Nesme-Ribes, E., Meunier, N., & Vince, I. 1997, A&A, 321, 323
Rast, M. P., Lisle, J. P., & Toomre, J. 2004, ApJ, 608, 1156
Scherrer, P. H., Bogart, R. S., Bush, R. I., et al. 1995, Sol. Phys., 162, 129
Schou, J. 2003, ApJ, 596, L259
Schroeter, E. H., & Wöhl, H. 1976, Sol. Phys., 49, 19
Snodgrass, H. B., & Ulrich, R. K. 1990, ApJ, 351, 309
Wöhl, H., & Schmidt, W. 2000, A&A, 357, 763

A&A 466, 1123–1130 (2007)
DOI: 10.1051/0004-6361:20066644

Astronomy & Astrophysics

Are supergranule sizes anti-correlated with magnetic activity?

N. Meunier, T. Roudier, and R. Tkaczuk

Laboratoire d'Astrophysique de l'Observatoire Midi-Pyrénées, Université Paul Sabatier, CNRS, 57 avenue d'Azereix, BP 826,
65008 Tarbes Cedex, France
e-mail: `[meunier;roudier]@ast.obs-mip.fr`

Received 26 October 2006 / Accepted 23 January 2007

ABSTRACT

Context. The variation of supergranule cell sizes with the magnetic environment is still controversial.
Aims. We study this relation in detail to understand the discrepancies observed between previous results.
Methods. We determine the cell size using divergence of horizontal flows derived from local correlation tracking of intensity maps (MDI/SOHO). We study the variation of the cell size as a function of the magnetic field inside the cell. We also consider which component of the magnetic field most influences the cell size.
Results. Our main conclusion is that there are no large cells when the magnetic field (in absolute value) averaged over the cell is large. This is mostly due to the magnetic field inside the cell (intranetwork fields), while strong network magnetic fields (at the cell boundary) are associated with larger cells. Further studies of the evolution of the cells and of the flux imbalance suggest that a high level of weak fields may prevent the formation of large cells. This is compatible with the expectation that strong magnetic fields should prevent large-scale flows.
Conclusions. The relation between the local activity level determined by the average magnetic field inside the cells and the supergranule size is not linear. Furthermore, it strongly depends on the definition of the activity level (magnetic field inside the cell or magnetic network) and on the magnetic sensitivity of the data. This last point probably explains at least partially the conflicting results obtained up to now.

Key words. Sun: activity – Sun: magnetic fields – Sun: granulation – Sun: photosphere – Sun: general

1. Introduction

The variation of granule sizes with the magnetic environment is well known (Schmidt et al. 1988; Muller et al. 1989; Title et al. 1992). However, it is quite controversial for supergranules as some authors (Table 1) found an increase in size with increasing activity, while others found either a decrease or no variation at all. The same controversy stands for the variation of supergranule sizes during the solar cycle. Table 1 gives a summary of the previous results obtained using two different approaches, namely the variation with the magnetic field at a given time over the field-of-view (spatial variation) and the variation during the solar cycle (temporal variation). In all previous works except that of DeRosa & Toomre (2004), the determination of the cells themselves or of the cell sizes has been made using the magnetic network, either directly from photospheric magnetograms or indirectly from Ca II K images (chromospheric level). Therefore the cell size determination and the activity level characterization were not determined independently. This is unfortunate as it can lead to some biases. For example, if the magnetic field inside a cell is large (which is likely to happen when the average activity level is larger), there is a risk to split that cell into at least two parts, which would lead to smaller cells. It is therefore easy to artificially bias the result toward smaller cells when the activity level is higher. The magnetic sensitivity of the data could also bias the results. The results of DeRosa & Toomre (2004), which have been obtained by tracking Doppler features, is probably the most reliable as the cell size determination is not made using data dominated by magnetic fields. However, they only give the average cell size for two periods, one being more active than the other, and do not study in detail the dependence of the cell sizes on the local magnetic field.

To address this long-standing question, we have determined supergranule cells using divergence of the horizontal flow velocity as in Meunier et al. (2007a,b). These measurements are independent of the magnetic fields. We will study the variation of the cell size with the magnetic field inside the cells at a given time (namely the solar cycle minimum). To get a complete picture, we also study the precise location inside the cells of the magnetic field influencing the cell size variations. We will show that the definition of the activity level is crucial, as it will be necessary to determine which component of the magnetic field influences the cell size variations. It will also be of interest to consider the temporal evolution of the cells: is the observed variation due to different initial condition for small and large cells, or is it the result of the development of the cells?

The data and processing are briefly described in Sect. 2. In Sect. 3, we study the variation of the cell size with the activity inside the cells, first by considering the magnetic field averaged over the cells or part of the cells, then by considering the magnetic field for each pixel of the images. In Sect. 4, we address the causality link leading to the observed relationship, through the study of the cell evolution and the degree of mixity between positive and negative magnetic fields. Finally, in Sect. 5, we study the dependence of the result on the magnetic sensitivity, which may provide an explanation for the incoherent results obtained in previous works. We discuss the results and conclude in Sect. 6.

Table 1. List of variations of supergranule sizes with the magnetic field from the literature. The first 5 references concern studies at a given time (spatial variations), while the last 6 references concern studies covering the solar cycle or part of it (temporal variations). FT means Fourier transform. The sign "+" means an increase of the cell size with increasing activity level, while the sign "–" means the opposite variation and "0" no variation.

Reference	Data	Method	Variation	Comments
Sýkora (1970)	Ca II K images	autocorrelation	+	
Wang (1988)	magnetograms	autocorrelation	+	Large errorbars
Wang et al. (1996)	magnetograms	autocorrelation	+	
Hagenaar et al. (1997)	Ca II K images	segmentation	0	
Raju & Singh (2002)	Ca II K images	autocorrelation	–	Via latitude variations
Sýkora (1970)	CaII K images	autocorrelation	+	
Singh & Bappu (1981)	Ca II K images	autocorrelation?	–	
Muenzer et al. (1989)	Ca II K images	2D TF	+	
Komm et al. (1995)	magnetograms	autocorrelation	+	FWHM of the autocorrelation curves
Berrilli et al. (1999)	Ca II K images	segmentation	–	Over 1 year only
DeRosa & Toomre (2004)	Doppler	segmentation	–	2 time series

2. Data processing

We use high resolution MDI/SOHO (Scherrer et al. 1995) intensity maps and magnetograms obtained during the solar minimum, in January 1997 and March 1997. The pixel size is 0.605 arcsec and the field-of-view $620'' \times 303''$. The temporal cadence is 1 min. We define hourly data sets, each containing 60 raw images. 61 such hourly data sets are available in our sample (46 in January 1997 and 15 in March 1997).

For each hourly data set, the 60 intensity maps and magnetograms are aligned with the map at the center of the data set. Magnetograms are averaged together to provide a single low-noise magnetogram per hour. Intensity maps are corrected for large-scale gradients and k–ω filtered. A local correlation tracking algorithm is then applied to provide velocity and divergence maps. These divergence maps are averaged over 1 h and smoothed with a Gaussian whose full-width at half-maximum is 10.2 Mm to exhibits supergranular cells. The validity of this approach is discussed in Meunier et al. (2007b).

The divergence maps are used for two purposes. First, a steepest descent algorithm is applied (see Hagenaar et al. 1997; Meunier et al. 2007a,b) to determine the boundary of the cells. This leads to a cell size defined by the maximum radius of the cell, hereafter R. The smoothed divergence maps also provide a way to determine the relative distance to cell center in each cell, noted $d_{\rm rel}$. The cell center corresponding to $d_{\rm rel} = 0$, is defined as the barycenter of the cell. Furthermore, a normalized smoothed divergence, noted $D_{\rm norm}$, is defined. It takes the value 0 at the location of maximum positive divergence in the cell (which in general does not coincide exactly with $d_{\rm rel} = 0$, although $d_{\rm rel}$ and $D_{\rm norm}$ are correlated), 0.5 at positions of zero divergence and 1 at position of maximum convergence. This normalized divergence provides an alternative way to take into account the localization of the magnetic field inside the cells. We refer to Meunier et al. (2007a,b) for more details about the processing.

3. Variation of the cell size with the activity level

We will use two different approaches. In the first one, we consider properties averaged over the cell: for each cell, we consider the size R and the absolute value of the magnetic field $|B_{\rm c}|$ averaged over the cell. A complementary analysis is to average $|B|$ over a specific part of the cell (for example close to the cell center or close to the cell boundary), using selections based on $d_{\rm rel}$ or $D_{\rm norm}$, to study which component of the magnetic field influences the cell size. This magnetic field is denoted $|B_{\rm r}|$.

Another approach will be to consider the absolute value of the magnetic field for each pixel, $|B_{\rm p}|$, and then to associate the size R of the cell to which the pixel belongs. This will be very useful to study for example the magnetic field variations inside the cells for various cell size ranges, i.e. radial profiles of the magnetic fields inside the cells.

The magnetic field we are considering is the line-of-sight component. A small projection effect is therefore present. For the magnetic network for example, expected to be mainly vertical, values in the corners of our fields of view should be smaller by a few percent than at disk center: $\cos(\theta)$ ranges from 1 at the center of the images to 0.95 in the corners. 90% of the pixels have values above 0.96, 61% above 0.98. This effect can however be neglected in what follows, as is the influence of the projection effect on the supergranule size, since the observed variations are larger than a few percent (see for example Figs. 2 or 3).

3.1. Magnetic properties averaged over the cells

3.1.1. Averages over the entire cell

We first consider properties averaged over each cell or over part of each cell. Figure 1 shows the cell size R versus the absolute value of the magnetic field averaged over the cell, $|B_{\rm c}|$. The solid curve (left panel) gives the mean cell size for each magnetic field bin. The errorbars are the uncertainties on the mean at the 1σ level, as for the other similar curves shown in this paper. A small decrease of the cell size is observed as the magnetic field in the cell increases, except for the smallest sizes and magnetic fields. However, this decrease seems to be due to the fact there is no large cell with a strong magnetic field rather than to an actual shift of distribution, as shown in the 1D histograms of Fig. 1 (middle and right panels). When considering the distribution of R values for various ranges of $|B_{\rm c}|$ for example, the tail of the distribution is smaller for strong magnetic fields, while the peak of the distribution correspond to an almost constant R. In the left panel, the solid curve shows a variation of the cell size on the order of 4 Mm, while the position of the peak of the distributions (middle panel) does not change by more than 1 Mm.

We also note that the left panel of Fig. 1 presents strong similarities with the scatter plot shown by Hagenaar et al. (1997) in their Fig. 9. They concluded that there was no variation of the cell size with the activity level, but in fact the distributions show that there is indeed a variation. This difference will also

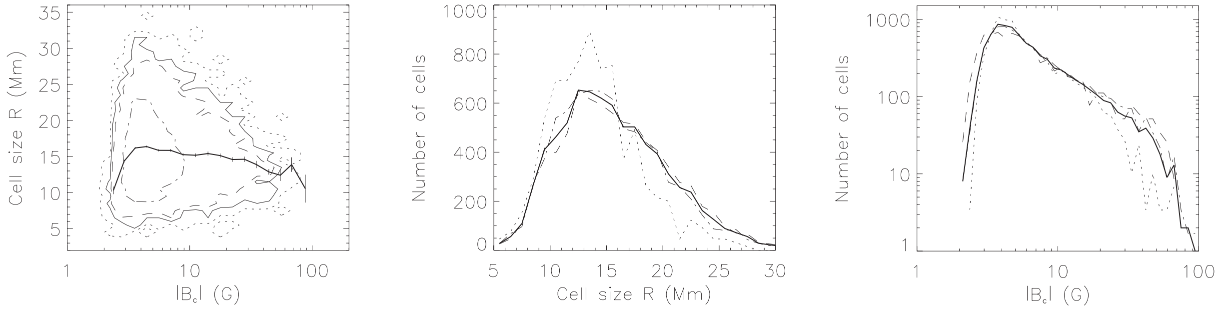

Fig. 1. *Left*: number of cells as a function of the absolute value of the magnetic field averaged over the cell $|B_\mathrm{c}|$ and of the cell size R. Contours are at the levels of 1 cell (dotted line), 5 (solid line), 10 (dashed line), and 50 (dotted-dashed line) cells. The thick solid line represents the average cell size in small $|B_\mathrm{c}|$ ranges. *Middle*: number of cells as a function of R, for various ranges of $|B_\mathrm{c}|$ averaged over the cell: all cells (thick solid line), cells with $|B_\mathrm{c}|$ smaller than 10 G (dashed line), cells with $|B_\mathrm{c}|$ in the range 10–18 G (dotted-dashed line) and cells with $|B_\mathrm{c}|$ larger than 18 G (dotted line). Histograms are normalized by the number of cells used to build the thick curve. *Right*: number of cells as a function of $|B_\mathrm{c}|$ averaged over the cell, for various size ranges: all cells (thick solid line), cells with R smaller than 6 Mm (dashed line), cells with R in the range 6–20 Mm (dotted-dashed line) and cells with R larger than 20 Mm (dotted line). Histograms are normalized by the number of cells used to build the thick curve.

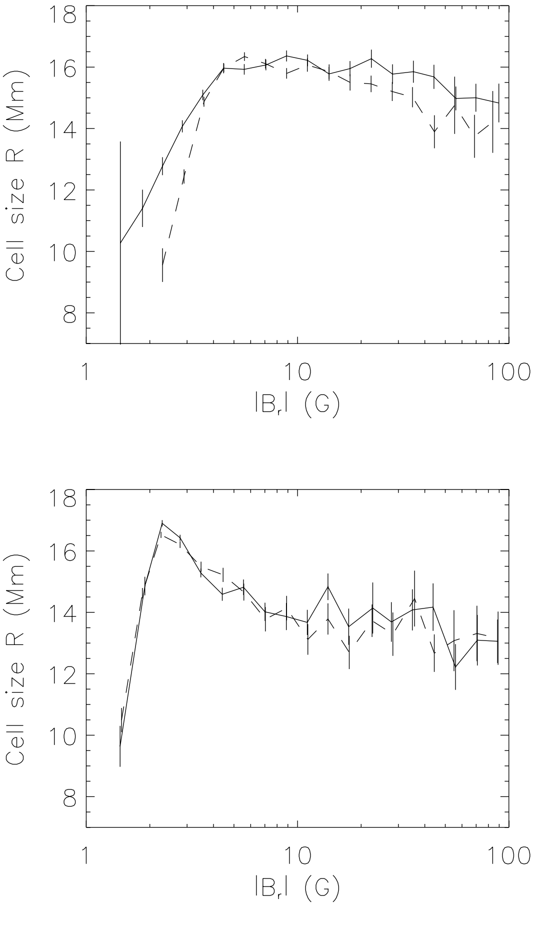

Fig. 2. Cell size R versus the absolute value of the magnetic field $|B_\mathrm{r}|$ averaged over various regions in each cell. *Upper panel*: in converging flows (solid line) and at cell boundary (dashed line). *Lower panel*: in diverging flows (solid line) and at cell center (dashed line).

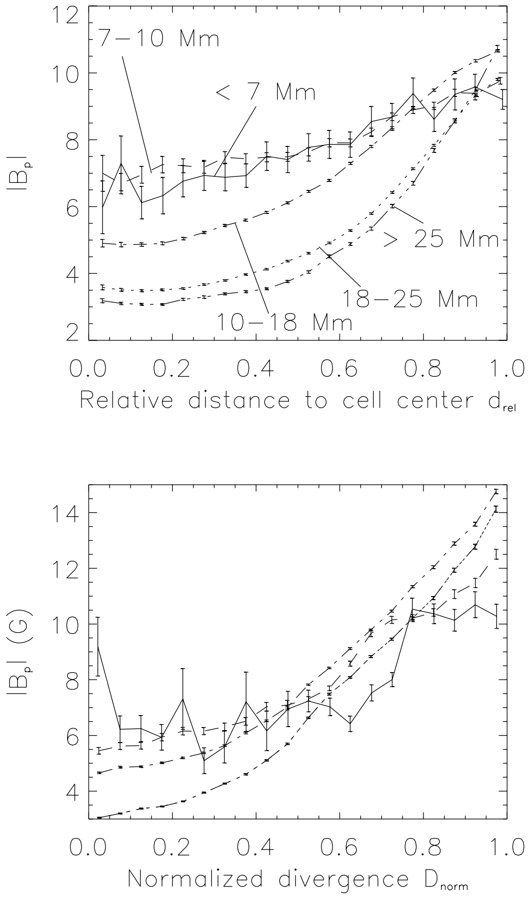

Fig. 3. *Upper panel*: absolute value of magnetic field at each pixel $|B_\mathrm{p}|$ versus the relative distance to cell center d_rel, for various size ranges: R lower than 7 Mm (solid line), in the range 7–10 Mm (dashed line), in the range 10–18 Mm (dotted-dashed line), in the range 18–25 Mm (dotted line), and larger than 25 Mm (dot-dot-dot-dashed line). *Lower panel*: same versus the normalized smoothed divergence D_norm.

be discussed in more detail in Sect. 5 as the flatter curve they observe may be due to the magnetic sensitivity.

3.1.2. Averages over particular areas of the cells

Our goal is now to understand the origin of this variation. To investigate this variation in more detail, we have computed the average magnetic field in various parts of the cell, $|B_\mathrm{r}|$: in the strong diverging flows (D_norm smaller than 0.2), in the strong converging flows (D_norm larger than 0.8), at cell center (d_rel smaller than 0.2) and at cell boundary (d_rel larger than 0.8). The variation of the cell size as a function of these new estimates of the magnetic field is shown in Fig. 2.

Two regimes are observed. First, for very small magnetic fields, we note that very weak field regions are associated with the smallest cells. This could be seen in Fig. 1, although less clearly. The amplitude of this variation does not seem to depend much on the localization of the magnetic field in the cell. However, the position of the maximum of the curves depends on the localization and varies between 3 G (diverging flows and cell center) and 7 G (converging flows and cell boundary). In the first case the peak in the curve is quite sharp and the uncertainty on the 3 G value is smaller than 1 G. In the second case, the maximum is well defined around 7 G for the cell boundary, with similar uncertainties, and it is rather a plateau starting at 7 G for converging flows. There is great similarity between curves for diverging flows and cell center. The same is true for converging flows and cell boundary curves.

Then a second regime, which concerns most of the cells, is observed for magnetic fields larger than a few Gauss and corresponds to the observation already discussed in Sect. 3.1.1. Here, we also observe a decrease of the cell size as the magnetic field increases. However, the amplitudes of the variations are different. A rough estimate from Fig. 2 shows that the strongest variation is observed for the magnetic field estimated in the diverging flows (variation of ~4 Mm) and in the cell center (~3 Mm), followed by the variation at the cell boundary (~2 Mm) and in the converging flows (~1 Mm).

The magnetic field at the cell boundary is well correlated with the magnetic field in converging flows (0.67) as well as the field at cell center with the field in diverging flows (0.66), which is expected. However, the correlation between the field at cell center and at cell boundary is much smaller (0.33) and it is even worse between the field in diverging flows and converging flows (0.17). This shows that to define an "activity level", even local, is not that easy. Which component of the magnetic field are we talking about? Do they have the same influence? We notice that the behavior for $|B_r|$ defined at cell center or at the boundary does not give the same result.

3.2. Radial profiles and magnetic field distributions inside cells

Given the results obtained when averaging the magnetic field in specific parts of the cells, we study further the dependence on the localization. Therefore, we now consider all the pixels of the maps. To each pixel we associate the size of the cell to which it belongs. We first consider the profiles of the magnetic field as a function of the relative distance to the cell center $d_{\rm rel}$ and as a function of the normalized divergence $D_{\rm norm}$, and then the distribution of the magnetic field values for various size ranges. $|B_{\rm p}|$ denotes the absolute value of the magnetic field at each pixel. These profiles are an extension of a "radial profile", as it is not only a geometrical definition (using $d_{\rm rel}$), but also correspond to a definitioni directly using the flows ($D_{\rm norm}$).

3.2.1. The magnetic field radial profiles inside the cell

We consider the profiles of $|B_{\rm p}|$ versus the relative distance to cell center $d_{\rm rel}$ and versus the normalized divergence $D_{\rm norm}$, for various cell size ranges. The results are shown in Fig. 3. Close to the cell center, a very strong decrease in magnetic field is observed as the cell size increases, and this is seen up to values of $d_{\rm rel}$ around 0.7. On the other hand, a small *increase* in magnetic field is observed at the cell boundary, for $d_{\rm rel}$ above 0.9. When considering the variation with the normalized divergence $D_{\rm norm}$, we also observe a strong decrease of the magnetic field in diverging flows, for $D_{\rm norm}$ up to ~0.3. However, above 0.5, the trend is reversed again, and the magnetic field *increases* as the cell size increases. This confirms that the variation in cell size is mostly dependent on the magnetic field *inside* the cell. There may also be a reversal at the cell boundary due to the magnetic network. It can indeed be expected that strong magnetic field network can be present only when the convergences are strong, in large and long-lived cells (DeRosa & Toomre 2004). The reversal is stronger for $D_{\rm norm}$ than for $d_{\rm rel}$, which is expected as the magnetic network exhibits a better correlation with the regions of strong convergence than with the entire boundary of the cells. Therefore this provides a coherent picture.

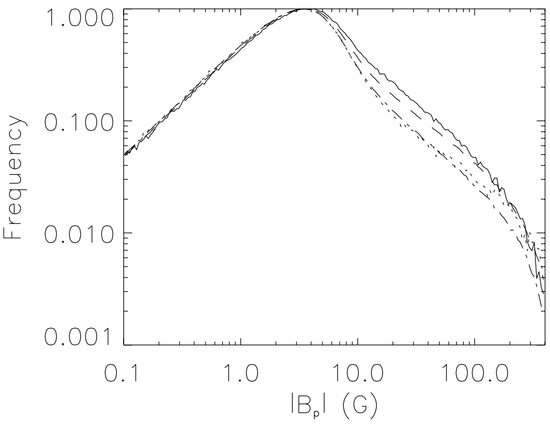

Fig. 4. Distribution of the absolute value of magnetic field at each pixel $|B_{\rm p}|$ in each pixel for different size ranges: R lower than 10 Mm (solid line), in the range 10–16 Mm (dashed line), in the range 16–20 Mm (dotted-dashed line) and larger than 20 Mm (dotted line). The histograms are normalized to their maximum.

3.2.2. The magnetic field distributions

Finally, we consider the magnetic field distribution for the whole surface, and when selecting specific regions inside the cells. The total distribution of $|B_{\rm p}|$ for various cell size ranges is shown in Fig. 4. The tail is shorter for large cells, as expected. Figure 5 now shows the same plots when considering the different categories of localization of the magnetic field in the cells: in strong diverging flows ($D_{\rm norm}$ smaller than 0.2), in strong converging flows ($D_{\rm norm}$ larger than 0.8), at cell center ($d_{\rm rel}$ smaller than 0.2) and at the cell boundary ($d_{\rm rel}$ larger than 0.8). The tail is smaller for diverging flows and for the cell center, which is expected as there is almost no magnetic network there. The tail of the magnetic field distribution is again reduced when the size increases, at the cell center and in diverging flows. In converging flows, the longest tail is for the largest cells, confirming the reversal observed in Fig. 3.

4. Evolution of the magnetic field in the cells, flux imbalance, and cell size

In the previous section, we have shown that a strong magnetic field inside the cells is associated with smaller cells, while the dependence on the magnetic field at the boundary (mostly magnetic network) is reversed. As the magnetic field inside the cells increases, the possible maximum value for R decreases, as was shown in Fig. 1. The main variation is then mostly a variation in

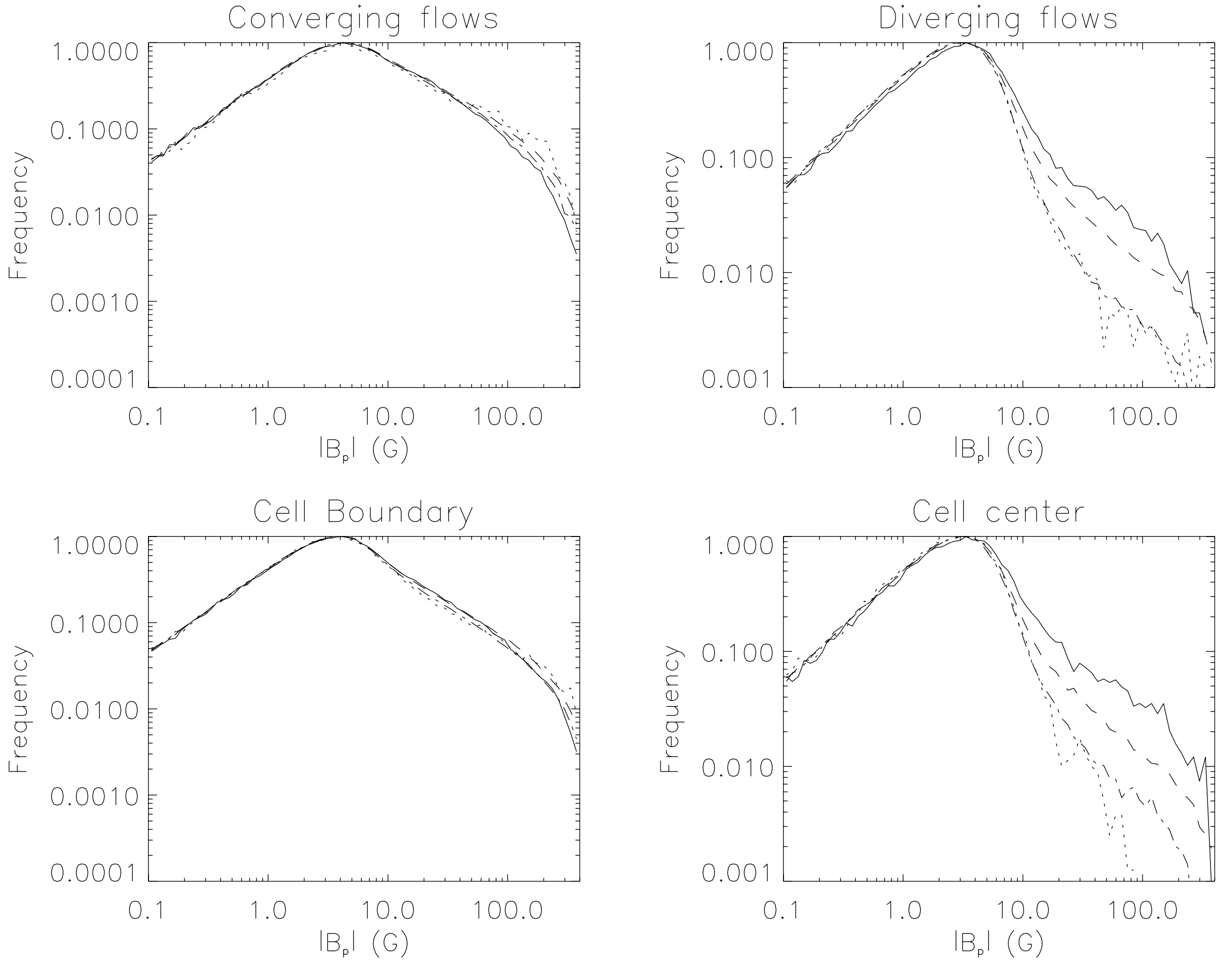

Fig. 5. Distribution of the magnetic field $|B_\mathrm{p}|$ in each pixel for different size ranges: R lower than 10 Mm (solid line), in the range 10–16 Mm (dashed line), in the range 16−20 Mm (dotted-dashed line) and larger than 20 Mm (dotted line). The magnetic field is considered in different regions of the cells: in converging flows (*upper left panel*), in diverging flows (*upper right panel*), at cell boundary (*lower left panel*), and at cell center (*lower right panel*). The histograms are normalized to their maximum.

the tail of the distributions. R and $|B_\mathrm{c}|$ are here defined at a given time during the cell lifetime.

Two interpretations are possible: (i) in regions with weak magnetic fields, it is possible to have large cells while strong magnetic fields prevent the formation of large cells; or (ii) in large cells the polarities cancel each other faster, with a more efficient concentration of magnetic fields, resulting in a smaller flux, and in a more concentrated field at the boundary of the cells. However, if large cells form preferentially in unipolar regions, the more concentrated field at the boundary would not be associated with a smaller flux, but there is currently no indication that this is the case. The first hypothesis may be examined by studying the evolution of B as a given cell evolves. The second hypothesis will be investigated by looking at the flux imbalance as a function of cell sizes as well as as by comparing this to the expected flux imbalance as a function of scale, independently of the cell determination.

4.1. Evolution of the cells

The question to answer is: when a cell is formed and increases in size to lead to a large cell, how does the magnetic field in that cell evolve? Is it weak at the beginning and then forms more concentrated features? Is it already larger at the beginning? It would be interesting to know if the results are related to the evolution of the cells (i.e. it is natural that when a small cell evolves toward a larger cell, the magnetic field decrease), or if they are related to their initial condition. Among small cells, there should be a large proportion of cells that remain small, and a few that lead to large cells. Thus, are the seeds of large cells found in regions with particularly weak magetic fields or not?

We have tracked supergranules as described in Meunier & Roudier (2007). This tracking is a combination of local correlation and feature tracking, as the local correlation is computed only at places where the divergence is maximum: we therefore track the positions of maximum divergence. From this analysis, we derive a list of structures that are tracked in time, and we also know their properties at any time during their lifetime (provided that their first identification is not on the first image of the series). The magnetic field at cell center (or in diverging flows) tends to decrease over time for long-lived structures. However, the magnetic field computed at their starting time (first identification) shows a larger variation, which shows that the differences already exist when the cell is first identified (at least at the temporal resolution of 1 h). We also note that long-lived structures have weaker magnetic fields inside the cells compared to short-lived cells, and have a constant field inside the network. This contradicts the results of DeRosa & Toomre (2004), who concluded that cells embedded in a more active region tend to live longer, which was interpreted as a possible stabilisation effect of

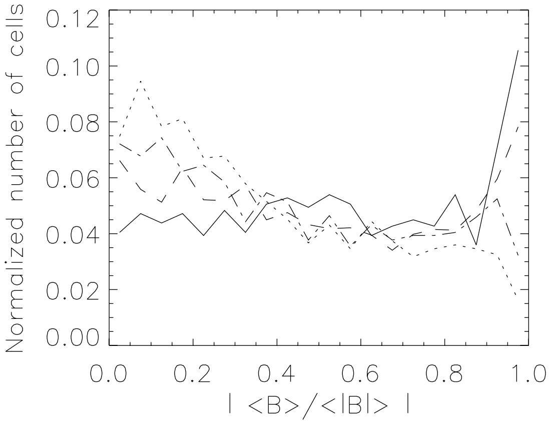

Fig. 6. Distribution of the flux imbalance $|\langle B\rangle/\langle|B|\rangle|$ for different size ranges: R lower than 10 Mm (solid line), in the range 10–16 Mm (dashed line), in the range 16–20 Mm (dotted-dashed line) and larger than 20 Mm (dotted line).

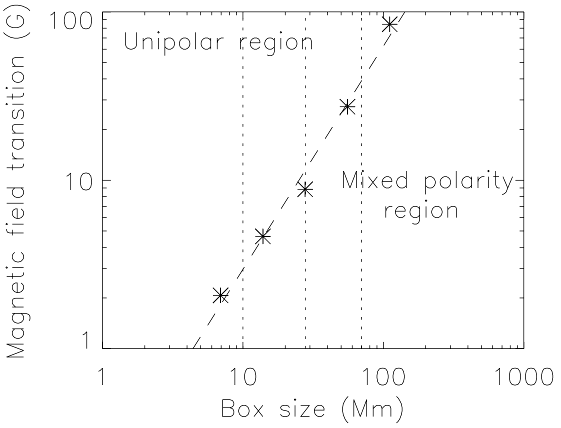

Fig. 7. Magnetic field threshold (stars) corresponding to an average flux imbalance of 0.5, versus the size of the box over which the imbalance is computed. The dashed line is a linear fit. The vertical dotted lines indicate the minimum and maximum size of detected cells ($2R$) studied here as well as the size corresponding to the peak of their distribution.

the magnetic field on the cells: from our analysis, this may not be the case.

A complete study of the evolution of cells is beyond the scope of the present paper and will be the subject of a future work. We can already conclude however that the evolution of the magnetic field inside the cells during their life is probably not at the origin of the observed relation between size and magnetic field in supergranular cells.

4.2. Flux imbalance

Let us consider the evolution of cells toward small or large cells starting from an initial distribution of the magnetic field. For a similar degree of magnetic field mixity and of average field strength, if the magnetic field in large cells tends to concentrate in strong magnetic field structures at the boundary, thus “emptying” the cells, one expects the magnetic field in these cells to be more unipolar, as more flux of opposite polarities will also cancel out. To check this, we computed the absolute value of the flux imbalance $|\langle B\rangle/\langle|B|\rangle|$ over each cell. Values around 0 mean a mixed polarity field, while values close to 1 mean unipolar field (of either polarity). Figure 6 shows the distribution of this imbalance for various size ranges. We observe that large cells are more often close to mixed polarity than smaller cells, while small cells are more often close to unipolar magnetic fields. Therefore we do not observe a larger unipolarity of the magnetic fields in large cells. This means that the initial conditions leading to cells of various sizes were probably different in field strength, in mixity, or both.

We compare these results with the imbalance computed over boxes of various sizes, independently of any image segmentation. We have chosen square boxes with size 16, 32, 64, 128 and 256 pixels, corresponding to 6.0 Mm for the smallest size and 111 Mm for the largest size. The value of 64 pixels is close to the supergranular size (27.7 Mm). Boxes are distributed regularly over the surface, so that for a given size, we pave the whole surface with adjacent boxes of that size. The imbalance is computed for various thresholds of the magnetic field, i.e. only magnetic fields larger than a certain value are considered. For high thresholds, this provides the mixity associated with magnetic network only, while the low thresholds also take into account the intranetwork magnetic field observed here down to the noise level of $\sim$3 G. Figure 7 shows the magnetic threshold for which the imbalance is around 0.5. The unipolarity seems stronger for high magnetic thresholds. The limit between the two regimes increases with the box size. In the supergranular regime, the threshold is in the range 2−40 G, and is typically around 10 G for a supergranule of 30 Mm. At a given threshold $|B_{\rm th}|$, more mixed polarity is observed for large scales. This is in good agreement with the imbalance computed as a function of the cell size. The two approaches are independent: the spatial distribution of the cells is probably close to random as the field-of-view corresponds to quiet sun (no active region to bias the distribution), while the square boxes cover the whole field of view and are therefore not biased. A possible explanation would be that the flux imbalance at the scale of the cell is not controled by the supergranular diffusion only, but also at a more global level, depending on large-scale motions such as the meridional circulation and on the distribution of active regions.

Note that the spatial resolution of the observation is important for this kind of study, because at low resolution, some flux is missed. Such a study should therefore be completed using large-scale observations made with very high resolution such as the one that will be performed by the CALAS[1] instrument at the Lunette Jean Rösch of the Pic du Midi Observatory (Meunier et al. 2003, 2005).

5. Influence of the magnetic sensitivity on the results

Our results could explain why contradictory results have been obtained in the past. If we consider good sensitivity magnetograms such as the one we are using here, we observe that no large cells can exist for strong magnetic fields, while there is a reversal when considering the magnetic field at the cell boundary (magnetic network). With a different sensitivity, we may be more sensitive to the influence of the magnetic network for example. We are now quantifying this effect.

As an indicator of the dependence, we compute the slope (derived from a linear fit on the scatter plot) of the cell size R versus $|B_{\rm c}|$ and $|B_{\rm p}|$ in various cases. The slope of $|B_{\rm c}|$ and $|B_{\rm p}|$ versus R is also computed for comparison. Instead of using all pixels in the cells, we consider the pixels with $|B_{\rm p}|$ larger than a

---

[1] CAmera for the LArge Scales of the solar surface.

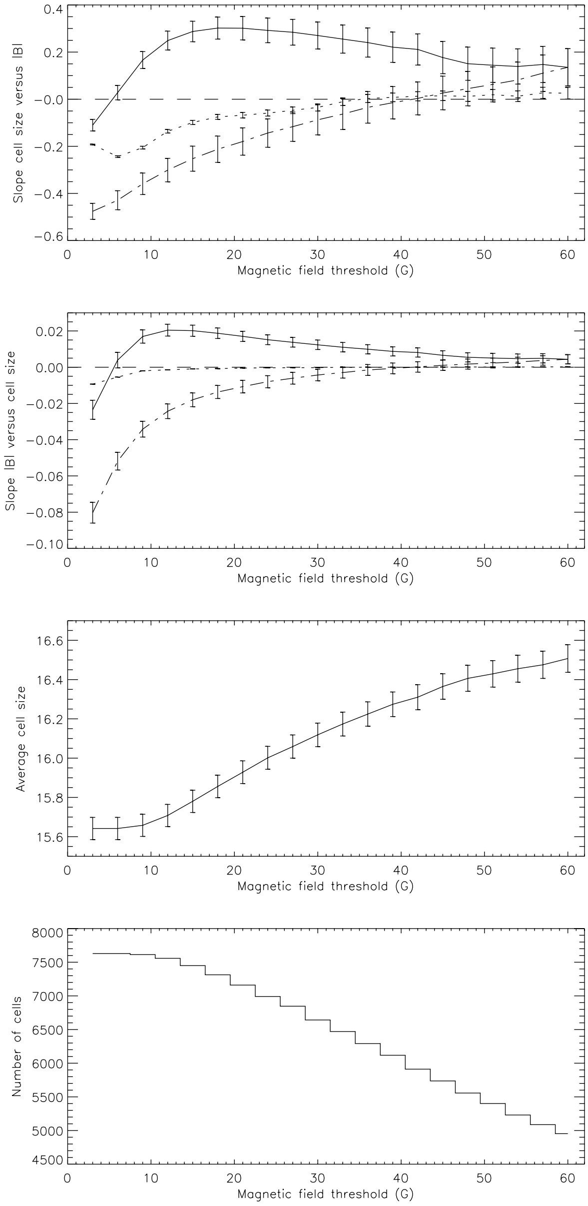

Fig. 8. *First panel*: slope of the cell size R versus the magnetic field $|B|$ as a function of the threshold B_{th}. $|B|$ is chosen larger than B_{th}. Plots are for cells such that $|B_{\mathrm{c}}|$ is larger than B_{th} (solid) and for cells such that $|B_{\mathrm{c}}|$ is larger than 60 G (dashed line). The dotted line corresponds to the computations made on all pixels with $|B_{\mathrm{p}}|$ larger than B_{th}. *Second panel*: same for the slope of the magnetic field $|B|$ versus the cell size R. *Third panel*: average cell size for each selection (cells such that $|B_{\mathrm{c}}|$ is larger than B_{th}). *Fourth panel*: number of cells for each selection (cells such that $|B_{\mathrm{c}}|$ is larger than B_{th}).

certain threshold $|B_{\mathrm{th}}|$, to simulate observations of various magnetic sensitivities. As some cells may not have any pixels with a magnetic field larger than the threshold, the sample is different for various $|B_{\mathrm{th}}|$: at larger thresholds, some cells are eliminated from the computation. Therefore, we have also considered the variation when considering the same sample, i.e. the sample for the largest threshold considered (60 G).

The results are shown in Fig. 8 as well as the average cell size and the number of cells for each sample. When using the same sample for all $|B_{\mathrm{th}}|$, we observe a negative slope for small $|B_{\mathrm{th}}|$ (as observed in Sect. 3). The sign of the slope changes around 40 G and then becomes positive. When selecting a different sample (i.e. the sample containing all cells for which the computation can be done), the reversal takes place much sooner, for $|B_{\mathrm{th}}|$ around 5 G. For comparison, the slope for $|B_{\mathrm{p}}|$ shows intermediary values. The differences are due to the different weightings of cells of different properties in the two approaches. With $|B_{\mathrm{p}}|$, more weight is given to cells with more pixels larger than the threshold. The size of the sample is also intermediate in the case of $|B_{\mathrm{p}}|$, since some cells may have a $|B_{\mathrm{c}}|$ lower than $|B_{\mathrm{th}}|$ but may contain pixels with $|B_{\mathrm{p}}|$ larger than $|B_{\mathrm{th}}|$.

The difference between the two types of sampling can be understood with Fig. 9, which shows the number of cells versus R and $|B_{\mathrm{c}}|$ simultaneously for the same sampling and a different sampling for four examples of $|B_{\mathrm{th}}|$. For small $|B_{\mathrm{th}}|$ (upper left panel), we see that the cells removed when restricting the sampling are mostly very small cells with small magnetic fields (cells in the lower left section of the panel), so it is easy to understand why the slope is closer to zero or is reversed (as shown by the two curves showing the mean magnetic field in each cell size bin). When increasing the threshold, the shape of the distribution is changed, and the limitation of large cells at strong magnetic fields seems less present. The slopes are only an *indicator*, as the relation between the cell size and the average magnetic field over the cell is not linear, and in all cases the distributions must be considered to get a clear picture, as the correlation between R and $|B_{\mathrm{th}}|$ is small.

Depending of the magnetic sensitivity of the observations, the weight given to the magnetic network and to the magnetic field inside the cells will be different, providing different dependences between R and $|B_{\mathrm{th}}|$. Furthermore, the magnetic field inside the cells may be missed for various reasons. For example, Hagenaar et al. (1997) have averaged their Ca II K images over several hours, and these weak field structures may then not be seen if their lifetime is not that long.

6. Conclusion

We have studied in detail the dependence of the supergranule size as a function of the local activity level in the cell. This is the first time that this work is performed with a determination of the cells independent of the magnetic field measurement, since previous authors have used either magnetograms or CaK images to identify the cell size, either by segmentation or by autocorrelation. An exception is the work of DeRosa & Toomre (2004) on Dopplergrams: they only give the average cell size for two periods, and do not study in detail the relationship between the activity level and the cell size.

We conclude that there are two answers to the original question: are supergranule sizes anti-correlated with magnetic activity? Our main conclusion is that there are no large cells when the average magnetic field (in absolute value) in the cell is large. This is mostly due to the magnetic field *inside* the cell (intranetwork fields), while strong network magnetic fields are associated with larger cells. Further studies of the evolution of the cells and of the flux imbalance suggest that the main explanation could be that high levels of weak fields may prevent the formation of large cells. This is compatible with the expectation that strong magnetic fields should prevents large scale flows, as observed for granules. This conclusion will have to be confirmed with studies at a higher temporal resolution.

We conclude that there is not a single answer to the long-standing question concerning the dependence of supergranule size on the activity level, as it strongly depends on the magnetic field definition. This also explains the apparent contradiction between previous results. It also means that the study of the

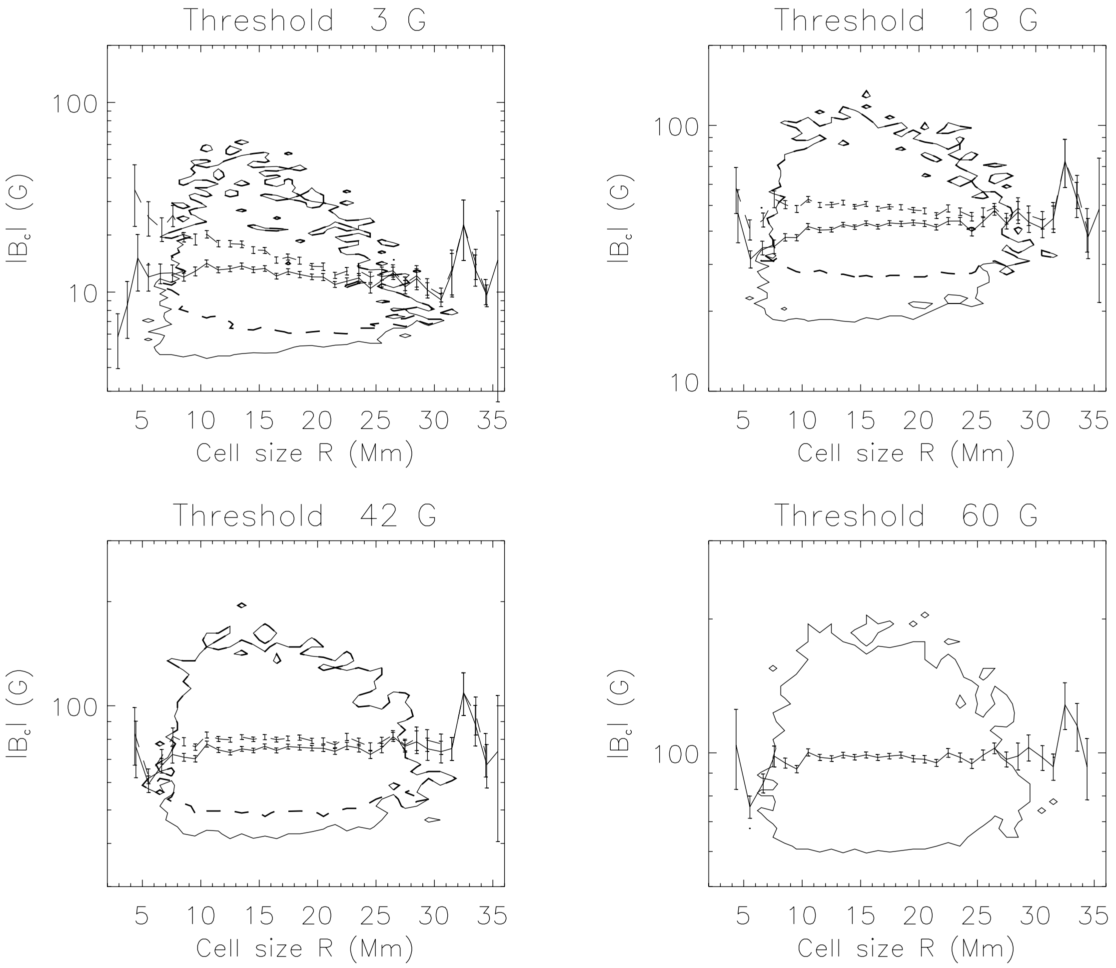

Fig. 9. Contour of the distribution of the magnetic field $|B_c|$ in the cell versus the cell size R, for 4 different magnetic field lower thresholds B_{th}. The thick solid line represents the contour for all cells with $|B|$ larger than the current threshold, while the thick dashed line represents the contour for a subset of cells corresponding to the 60 G threshold. The two thin curves with errorbars show the mean magnetic field for each cell size bin, for the subset corresponding to the current threshold (solid line) and for the subset corresponding to the 60 G threshold (dashed line). The errorbars show the uncertainty on the mean at the 1σ level.

possible variation of supergranule sizes during the solar cycle must carefully define the magnetic field. Such a study, which considers the activity level over the whole sun at the time of the observation and not the magnetic field strength inside the cell as done in the present work, will also provide complementary information that will help to interpret the relation between the activity level and the supergranule cell size.

An interpretation of the radial profiles inside the cells should also be provided by a comparison with the results of simulations of supergranulation in presence of magnetic fields. This remains to be done, as no simulation currently provides such profiles. The interpretation of these profiles is strongly related to the origin of the intranetwork and network magnetic fields. Depending on their origin, either generated by the global dynamo through active region remants or generated locally through a local dynamo action (e.g. Cattaneo et al. 2003), the resulting radial profiles may be different, and may have different correlations with the amplitude of the divergence in the cell. A complementary analysis using cork diffusion, similar to those performed by Krijger et al. (2002), should also be applied to these observations. This will be the subject of future work.

Acknowledgements. SOHO is a mission of international cooperation between the European Space Agency (ESA) and NASA.

References

Berrilli, F., Ermolli, I., Florio, A., & Pietropaolo, E. 1999, A&A, 344, 965
Cattaneo, F., Emonet, T., & Weiss, N. 2003, ApJ, 588, 1183
DeRosa, M. L., & Toomre, J. 2004, ApJ, 616, 1242
Hagenaar, H. J., Schrijver, C. J., & Title, A. M. 1997, ApJ, 481, 988
Komm, R. W., Howard, R. F., & Harvey, J. W. 1995, Sol. Phys., 158, 213
Krijger, J. M., Roudier, T., & Rieutord, M. 2002, A&A, 387, 672
Meunier, N., & Roudier, T. 2007, A&A, 466, 691
Meunier, N., Rieutord, M., & Beigbeder, F. 2003, in SF2A-2003: Semaine de l'Astrophysique Française, ed. F. Combes, D. Barret, T. Contini, & L. Pagani, 93
Meunier, N., Rondi, S., Tkaczuk, R., Rieutord, M., & Beigbeder, F. 2005, in Large-scale Structures and their Role in Solar Activity, ed. K. Sankarasubramanian, M. Penn, & A. Pevtsov, ASP Conf. Ser., 346, 53
Meunier, N., Tkaczuk, R., & Roudier, T. 2007a, A&A, 463, 745
Meunier, N., Tkaczuk, R., Roudier, T., & Rieutord, M. 2007b, A&A, 461, 1141
Muenzer, H., Schroeter, E. H., Wöhl, H., & Hanslmeier, A. 1989, A&A, 213, 431
Muller, R., Hulot, J. C., & Roudier, T. 1989, Sol. Phys., 119, 229
Raju, K. P., & Singh, J. 2002, Sol. Phys., 207, 11
Scherrer, P. H., Bogart, R. S., Bush, R. I., et al. 1995, Sol. Phys., 162, 129
Schmidt, W., Grossmann-Doerth, U., & Schroeter, E. H. 1988, A&A, 197, 306
Singh, J., & Bappu, M. K. V. 1981, Sol. Phys., 71, 161
Sýkora, J. 1970, Sol. Phys., 13, 292
Title, A. M., Topka, K. P., Tarbell, T. D., et al. 1992, ApJ, 393, 782
Wang, H. 1988, Sol. Phys., 117, 343
Wang, H., Tang, F., Zirin, H., & Wang, J. 1996, Sol. Phys., 165, 223

A&A 462, 731–741 (2007)
DOI: 10.1051/0004-6361:20054159

Astronomy & Astrophysics

Analysis of broad-band Hα coronagraphic observations

D. Romeuf[1,4], N. Meunier[2], J.-C. Noëns[2], S. Koutchmy[3], R. Jimenez[2], O. Wurmser[4],
S. Rochain[4], and "Observateurs Associés" Team[4]

[1] Centre de Ressources Informatiques, Université Lyon I, 8 avenue Rockfeller, 69373 Lyon Cedex 08, France
e-mail: `David.Romeuf@recherche.univ-lyon1.fr`
[2] Laboratoire d'Astrophysique de l'Observatoire Midi-Pyrénées, 57 avenue d'Azereix, BP 826, 65008 Tarbes Cedex, France
e-mail: `[noens;meunier]@ast.obs-mip.fr`
[3] Institut d'Astrophysique de Paris, CNRS and UPMC, 98 bis boulevard Arago, 75014 Paris, France
e-mail: `koutchmy@iap.fr`
[4] Observateurs associés/FIDUCIAL, Team of observers at the Pic du Midi coronagraph, `http://www.astrosurf.com/oa`
e-mail: `Odile.Wurmser@wanadoo.fr; s.rochain@aliceadsl.fr`

Received 6 September 2005 / Accepted 23 September 2006

ABSTRACT

Context. Daily broad-band full-limb Hα images of the inner corona were obtained during solar cycle 23 (1994–2005) using the 15 cm Pic-du-Midi coronagraph.
Aims. We want to automatically extract the properties and evolutions of the observed cool HI coronal structures over a wide range of sizes and light fluxes, from small jets and/or spikes to large prominences.
Methods. A tool was developed to process the complete set of stored images. This paper describes the recognition techniques implemented in our software and discusses its use. It includes the removal of the parasitic diffraction ring produced by the set of different occulting disks used throughout the year.
Results. We present and discuss selected results from a statistical analysis of the occurrence of parameters characterizing the observed structures applied to a large sample of observations. It illustrates the capabilities of this software when applied to our database. Strong asymmetries of the activity level over the solar poles become evident, confirming similar results from previous works. We also discuss the distribution of relative light fluxes of these structures over a wide range of sizes.
Conclusions. The complete series of FITS and calibrated images, the list of the detected structures, and their geometric and luminosity evolutions are stored in the BASS2000 solar database catalogue (`http://bass2000.bagn.obs-mip.fr`) and are made publicly available. The Hα HI structures observed over the limb of the sun present statistical properties of great interest for understanding its eruptive activity.

Key words. Sun: activity – Sun: corona – Sun: prominences – Sun: coronal mass ejections (CMEs)

1. Introduction

Since 1994, the 15 cm coronagraph at the Pic-du-Midi Observatory (Niot & Noëns 1997), called "HACO" (H Alpha COronagraph), has been used to perform a daily survey of the evolution of the cool structures in the inner corona. Cool coronal structures were episodically studied in the past (Leroy 1972), but no systematic quantitative analysis seems to exist. This is especially true when light fluxes of chromospheric and cool coronal HI structures, as measured over their entire line profiles, are considered.

Our full-limb coronagraphic Hα images are being collected using a broad-band filter, with a time cadence that depends on the observed events. This program has provided a database of more than 185 000 images covering the solar cycle XXIII. It was necessary to build special software in order to extract useful information about the HI structures and their time evolutions from this long time series. Tools generally used to treat the full disk images produced by solar telescopes are unfortunately not adapted to processing the full-limb images produced by coronagraphs. The difficulties come essentially from the non uniform distribution of the background intensity in the images produced by the sky brightness and from seeing effects, convolved with the instrumental background, and especially from the bright ring produced in the inner parts by the occulting system of the coronagraph. The objectives are to permit an automatic treatment of all images obtained by the daily survey. It must produce both series of calibrated images in relative units, corrected from the instrumental and seeing effects, and a list of the positions of the detected structures, in addition to their brightness and geometric properties. It must be able to show the time evolutions of all these parameters and must indicate about the activity in the detected regions at the time of observations.

Automatic recognition techniques have already been applied to Hα full disk images taken with narrower pass-bands by Collin & Nesme-Ribes (1995). Recent work has been done on this subject in the context of EGSO[1] by Zharkova et al. (2003). They studied a way to standardize such full narrow pass-band disk images with the purpose of performing some automatic recognition, for filaments in particular (Fuller et al. 2005). To our knowledge the only study aimed at automatically detecting coronal structures (outside the disk) is that of Robbrecht & Berghmans (2004), who propose a technique for recognizing CMEs on LASCO/SOHO images, i.e. much farther from the limb than what is considered here with HACO images. Here we built an automatic recognition software, called SCANPROTU,

---

[1] European Grid for Solar Observations.

in order to extract all data from the complete set of images provided by the daily survey, such as their behavior, size, luminosity, height, etc. This software includes a calibration procedure of images. All calibrated images, along with the raw data, will be made publicly available in the BASS2000 database in Tarbes–France[2]. The database containing the identified structures will be available in an SQL archive[3]. A large amount of information will be available on line (such as JPEG files or movies and some properties of the detected structures), while the original FITS files can be requested by all users.

This database enables the comparison of the time evolution of a given structure with other observations at various wavelengths (more particularly those obtained using SOHO instruments such as EIT, SUMER, UVCS, CDS, and LASCO). For example, a small sub-sample has been used by Innes et al. (1999) to perform a multi-wavelength study of a coronal mass ejection, including the dynamical "disparition brusque" (DB) events that play a fundamental role during CMEs. In addition, this database makes it possible to perform a statistical study of the cool structures of the lower corona. As an example of a study that is more extended in time, the initial years of this time series data were used by Noëns & Wurmser (2000), who identified small short-lived polar Hα spikes or cool "jets". They observed a rather strong asymmetry between the North and South Polar Regions and a possible relationship with the polar magnetic field reversal related to the solar cycle. However, considering the amount of data, it is clearly necessary to introduce some more automatic recognition software in order to extract as many structures as possible, using a single identification procedure. It is also important to be able to retrieve as much information as possible from the smallest and finest structures detected with our instrument, such as spikes in addition to large prominences. These fine structures are poorly understood but may take part in the general mass transport of material in the inner corona (Dere et al. 1989; Koutchmy & Loucif 1991; Delannée et al. 1998; Loucif et al. 1998).

The processing described in this paper may also be applied to series of full images produced by other coronagraphs, including space-borne ones (Koutchmy 1987). But it is not suitable for the usual images of the hot corona obtained in emission lines, partly because the structures of this part of the corona are often more diffused and larger in size compared to the dense Hα cool structures. In this paper, we describe observations (Sect. 2), the image processing, and the algorithm allowing the detection of the structures (Sects. 3 and 4). Then, in Sect. 5, we present a few new results to illustrate an efficient use of this database to analyze the so-called cool corona. Perspectives are discussed in Sect. 6.

2. Observations

The HACO coronagraph provides full-disk broad-band Hα images above the limb, covering a field up to 1.3 solar radius. The occulting disk is changed every month so as to adjust the amount of occultation to the changing apparent size of the solar image due to the yearly motion of the Earth around the sun along its elliptical orbit. Files are written in FITS format, with a set of keywords corresponding to the standards of solar databases like BASS2000, SOHO, and MEDOC. The instrument has evolved over time. Two CCD cameras have been successively used. A 1024 × 1024 Wright CCD 16 bits camera was used from 1994 till 2001. Since 2001, a 2048 × 2048, 14-bit, CCD Apogée AP10 camera is used. With the former camera, the pixel size corresponded to 2.8 arcsec. With the present camera, the pixel size is 1.4 arcsec. The theoretical angular resolution is 1.1 arcsec, although the actual angular resolution is often worse due to the seeing. Several Hα filters were successively used in order to optimize the S/N ratio, keeping in mind that the light fluxes we measure should not be too affected by effects due to Doppler shifts of the emission line when dynamical events are picked up. The former filter had a 1 nm *FWHM*. It was used from 1994 to the end of 1995. A second filter with a 0.33 nm *FWHM* was then used during the period 1995–2000. Finally, a third filter with a 0.17 nm *FWHM*, thermally stabilized, was used in the period 2000–2003. Since 2003 a new "improved in quality" (homogeneity, transparency) 0.15 nm FWMH filter is used. The software SCANPROTU takes these different parameters into account to provide homogeneous quantitative data.

Table 1. Number of observing days, number of images, and average number of images per day for each year from 1994 to 2004.

Year	# days	# images	Av. # images/day
1994	82	4635	56.5
1995	128	8175	63.8
1996	187	9363	50.1
1997	101	6281	62.2
1998	58	3075	53.0
1999	90	8502	94.5
2000	168	13 535	80.6
2001	191	27 170	142.2
2002	162	23 308	139.6
2003	182	31 754	174.5
2004	169	43 979	260.2

A team of observers, led by one of the authors (J.-C. Noëns), performs daily observations. The evolution of the capabilities of the coronagraph led to an improvement of the time resolution of the recorded images, see also Table 1. The frames are not taken with a fully automatic procedure: the observers indeed select the optimum rate adapted to the individual evolution of each observed dynamic event in real time, up to 5 images/min when a fast-evolving structure is identified. Only 1 image/min is taken during a period without any dynamical event. In addition, data is obtained for making the flat-field correction and the photometric calibration. For the flat-field measurement, five images are obtained using a white screen illuminated by the sun in front of the entrance objective of the coronagraph. Calibration images are obtained every hour by directly measuring the sun centers intensity through a neutral density placed in front of the objective. Dark currents are automatically corrected for each image. More details about the observations were given by Niot & Noëns (1997). Table 1 shows the number of observing days and the number of images produced annually, as well as the average number of images per day. The rate of observations clearly increased over time so more data was obtained for highly variable phenomena. The gap in the number of observing days in the period 1997–99 is due to a break in scientific activities during the reshaping of the Pic-du-Midi observatory.

3. Flat-fielding and calibrations

Each image is first accurately flat-fielded using a specially designed method. For this purpose, the five flat-field images are

---

[2] BASS2000 is a database for groundbased solar observations: `http://bass2000.obs-mip.fr/pageac_ang.htm`

[3] `http://bass2000.obs-mip.fr/New2003/Pages/Coro/interro_scanprotu.html`

normalized and reduced to a single flat-field image by taking, for each pixel, the median of the values over the five images at that pixel. Then, they are calibrated to remove the diurnal variations in the Earth atmospheric transmission. For this purpose, solar disk images are produced with a calibrated neutral density in order to provide intensities in units of the disk center intensity as measured with a 1 Å wide filter. We also removed effects due to the slow drifts of the narrow interference filters that were successively used. Finally, intensities are expressed in millionths of the solar central intensity of 10^{-5} times its surface, i.e. the luminance of a given pixel is a fraction of 10^{-11} L_s, with L_s the sun disk center's intensity at this wavelength, over a 1 Å passband and taken over a pixel. The purpose of this unit is to optimize the number of bits used to save the rather large number of images. Sources of uncertainties in this calibration are of two kinds. On a time scale of years, they include the replacements of the Hα filters, the filter aging and the effect of dust accumulation inside the instrument. On a time scale of a few hours, they include the variable atmospheric transmission due to the height of the sun in the sky, which is removed during the processing, and to local weather conditions. Our calibration is well-adapted to short term variation, but is more uncertain for long-term variations.

4. The SCANPROTU algorithm

The data is processed one image at a time, but a code is indeed applied to the whole daily time series. After the calibrations described above, the software SCANPROTU is used. It contains the following steps:

- 1. find the disk center and the solar radius in arbitrary units;
- 2. transform into polar coordinates;
- 3. compute the wavelet planes;
- 4. suppress the artefacts and parasitic fringes created by the occulting disk;
- 5. determine an average profile around the limb and filtering processing;
- 6. perform a “pyramidal” analysis;
- 7. compute a calibrated image;
- 8. analyze the properties of each detected structure.

Note that steps 3 to 6 are applied to the polar coordinate images, which are only used to determine the geometry of the structures (position, size). Step 7 is applied to the original image in order to get the intensities associated to each structure.

4.1. Disk center coordinates, radii of the occulting disk, and solar image

The image of the occulting disk is surrounded by a very bright fringe (Fig. 1) of parasitic origin, which is usually slightly asymmetric since the occulting disk and the solar disk do not have precisely the same center. This fringe is due to the light diffracted by the occulting disk. Therefore, the actual radius of the sun does not correspond to the size of this fringe, but is smaller, as illustrated in Fig. 2. For example, simultaneous observations of SOHO/EIT images and HACO images performed on June 14, 1999 (Noëns et al. 2004) have shown that there was a factor of ~0.985 between the estimated solar radius and the true solar radius.

First, the position and radius of the occulting disk is determined. Starting from the approximate image center, we search for the first maximum along each radial intensity profile. The center of gravity of the area enclosed inside the inner part of the bright fringe defined by the positions of these maximum values is used to determine the precise center and the radius of the occulting disk (Fig. 2). Note that the occulting disk may not be perfect and that its effective radius may change in time, due to dilatation and thermal shocks in case of interruption during cloud periods.

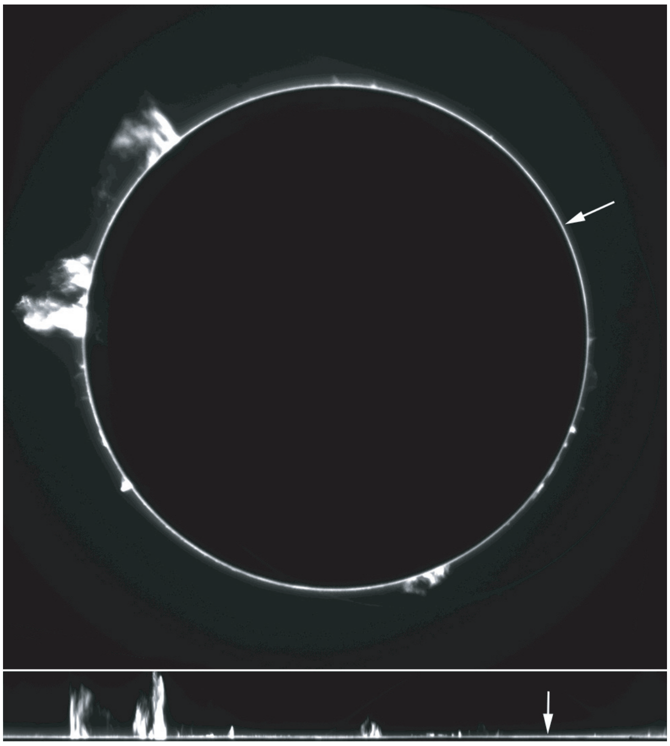

Fig. 1. *Upper panel*: raw image after the calibration described in Sect. 3 obtained on August 2, 2000 with the North pole at the top. *Lower panel*: same image in polar coordinates. The abscissa scale of the lower panel figure covers 360 degrees, and the ordinate scale covers 0.32 solar radius. On both panels the white arrow indicates the location of the bright fringe described in Sect. 4.1 and removed in Sect. 4.4.

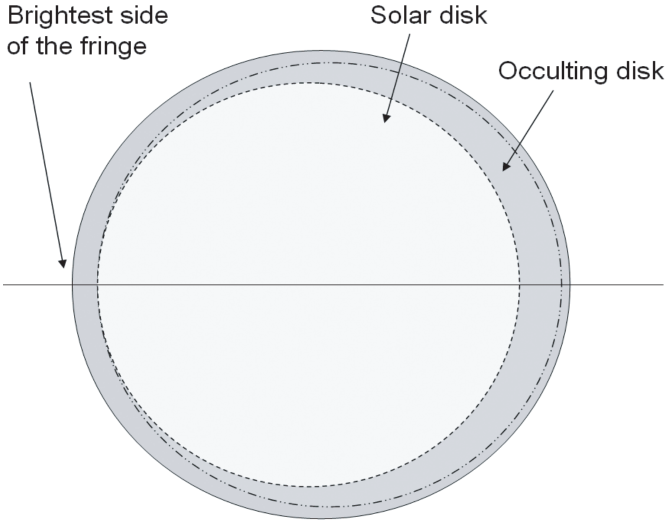

Fig. 2. Schematic to show the various elements to take into account: the occulting disk, the solar disk, the bright parasitic “diffraction” ring due to combined effects inside the instrument and to the seeing.

The second step is to determine the coordinates of the sun center and its radius. We search for its contour by fitting an

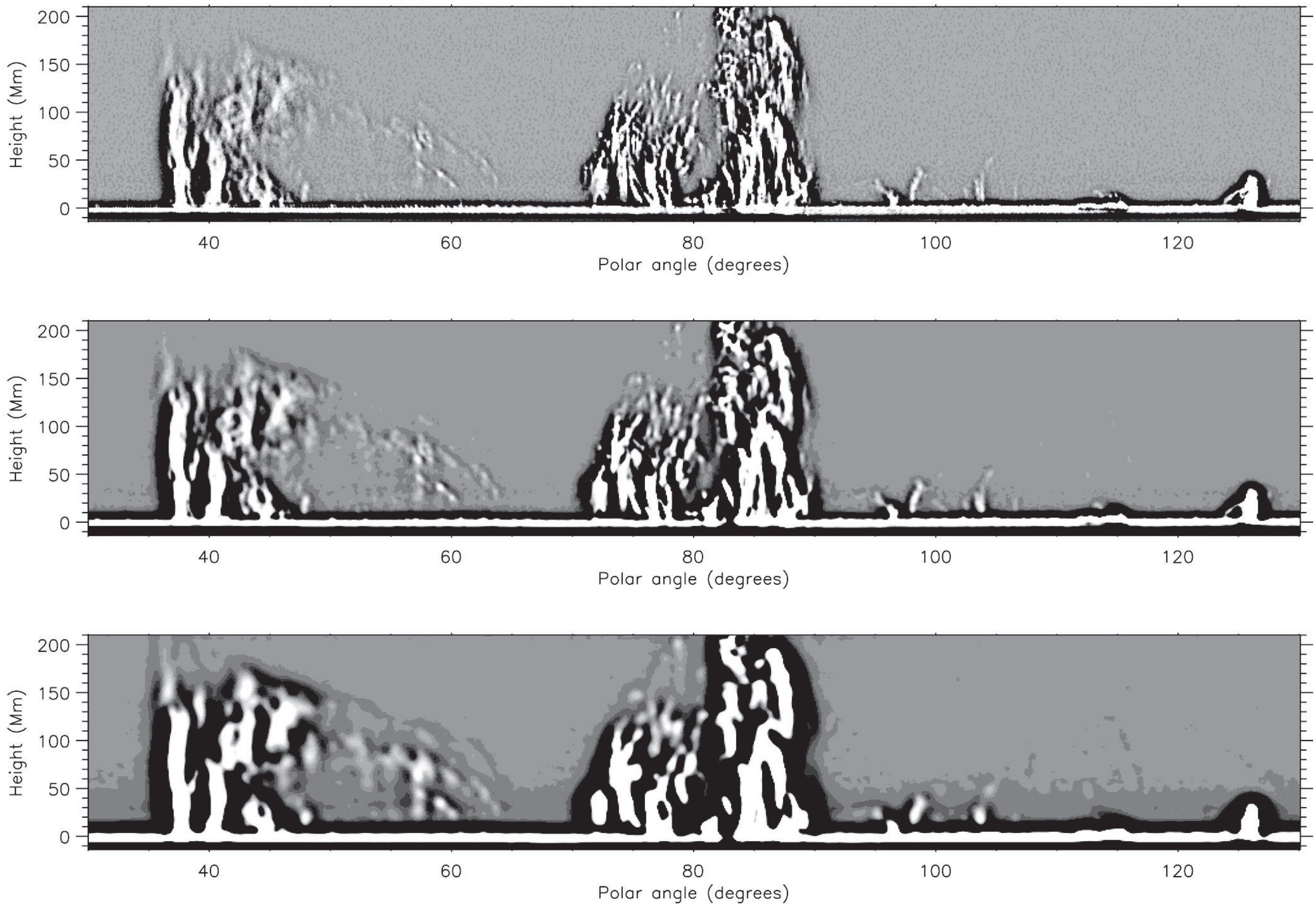

Fig. 3. Example of wavelet planes obtained for a part of the image of Fig. 1. The spatial scale changes by a factor of two between maps. The first map at the top is built with the finest details, including the noise. The last map at the bottom is built with larger structures. The middle map corresponds to intermediate scales. The bright limb fringe is visible on all the maps. Note also the dark artefact at the edges of the structures (Gibbs effect). The height is positive outward the sun.

ellipse using a least-square technique (Fitzgibbon et al. 1999) on the inflexion points along the external part of each radial profile (the inflexion points after the maximum intensity are considered). The parameters of the ellipse are used to define the center and the radius of the solar disk. This method proved to be robust to provide the best image-motion compensation. Normalized and compressed images remapped to 2048 × 2048 pixels, with the North Pole at the top, are used to create movies with different thresholds available at BASS2000.

4.2. Transformation into polar coordinates

Each image is transformed into polar coordinates. An example is shown at the bottom of Fig. 1. The x-axis represents the polar angle with a resolution of 0.1 degrees. The y-axis represents the distance from disk center, with values from 0.98 to 1.3 solar radius. The first column is centered on the North Pole, the angles being counted counter-clockwise. The algorithm described below to detect and select structures is based on the polar profiles deduced from this polar coordinates field. In the case of the 1024 × 1024 camera, the typical sun radius is around 400 pixels and 0.1 degrees then represents 0.7 pixels. In the case of the 2048 × 2048 camera, it represents 1.4 pixels, so there is a slight degradation of the spatial resolution in the second case. However, it is important to keep in mind that the polar coordinate images will be used only to identify structures and never to determine intensities. Furthermore, because of the seeing, this slight degradation is no concern for determining the geometry of the structures.

4.3. Wavelet plane analysis

Coronagraphic images contain details at various spatial scales (quiescent prominences, eruptive prominences, jets, spikes) from a few Mm to more than 50 Mm. The dynamical range of intensities can reach 4 orders of magnitude. Furthermore, these structures at different scales are often superimposed on each other. Since it is necessary to extract all the structures, even the small ones, a simple threshold on the images could be used, but a specific technique was developed. It was chosen to add to the image those wavelet planes corresponding to the finest details in order to increase the detection capabilities. This step is crucial for determining the positions of the structures. The result is an increased contrast and a better signal-to-noise ratio for fine structures, which will make the determination of the position of the structures more precise. Evidently the resulting image cannot be used for any photometric purpose.

Wavelet planes are computed using the classical “à trou” algorithm (Holschneider & Tchamitchian 1990; Shensa 1992). More details about wavelet techniques were published by Starck & Murtagh (1994). Illustrations of some of the obtained wavelet planes are shown in Fig. 3. The plan corresponding to the

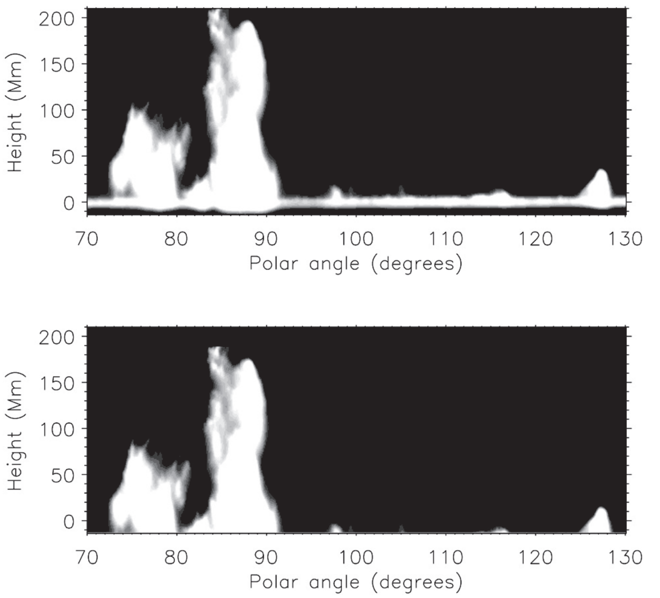

Fig. 4. Illustration of the ring removal processing (see Sect. 4.4) applied to the region shown in Fig. 3. *Upper panel*: image before the correction. *Lower panel*: image after the correction. The height is positive outward the sun.

smallest scale has been chosen to correspond to the finest details seen on our images, which correspond to ~2 Mm given the pixel size on the order of 1 Mm. The other plans are such that they sample the different scales up to the largest structures: at each step, the scale is twice the scale of the previous step. The top panel shows the wavelet plane with the finest details, i.e. a few Mm. It illustrates the fact that some of these finest structures are individual structures by themselves (cool "jets"), while other fine structures are included in larger prominences, which will have to be identified using wavelet planes such as those in the lower panel (showing only the large scales). On the other hand, it is obvious that the last wavelet plane would not be suitable for identifying the small jets. This will be discussed in Sects. 4.5 and 4.6. The image used in the next section is a combination of the different wavelet planes with a different weighting.

4.4. Suppression of the parasitic fringe

At this stage the enhanced image still contains the bright fringe described in Sect. 4.1, in addition to the solar structures. The accurate removal of this bright region situated at the bottom of the image is difficult. Several techniques were tested, and the following technique was selected. First, along each radial direction, the signal is convolved with a low-pass filter in order to smooth the profile and make the derivative of the signal less noisy. The fringe location is then defined as the position of the first maximum along the profile (using the first derivative). The center of the Gibbs artefact is determined using a similar technique where structures are not present. Positions where some activity is seen, leading to higher values for the width of the fringe, must be eliminated and replaced by another estimate. Let us call $p(x)$ the position of this minimum for each position x around the sun. The aberrant values in $p(x)$ are eliminated using a median filter, as each value is replaced by the median in p over 40 degrees centered on position x and zeros are added at the top of the position. The choice of the 40 degrees value results from a compromise between the typical size of a prominence on one side (it has to be larger) and the slow variation of the thickness of this fringe versus the polar angle (see Fig. 2). An example of an image before and after the correction is shown in Fig. 4. We can estimate the typical error on the shift determination to be close to the pixel size, which is small compared to the distortions of the limb shape due to the seeing, for example. The position of the structures should not be significantly affected by this error, which will mostly affect the detection of the smallest structures (a few pixels). This will therefore slightly affect the slopes of the distributions for the small structures (see Sect. 5.1).

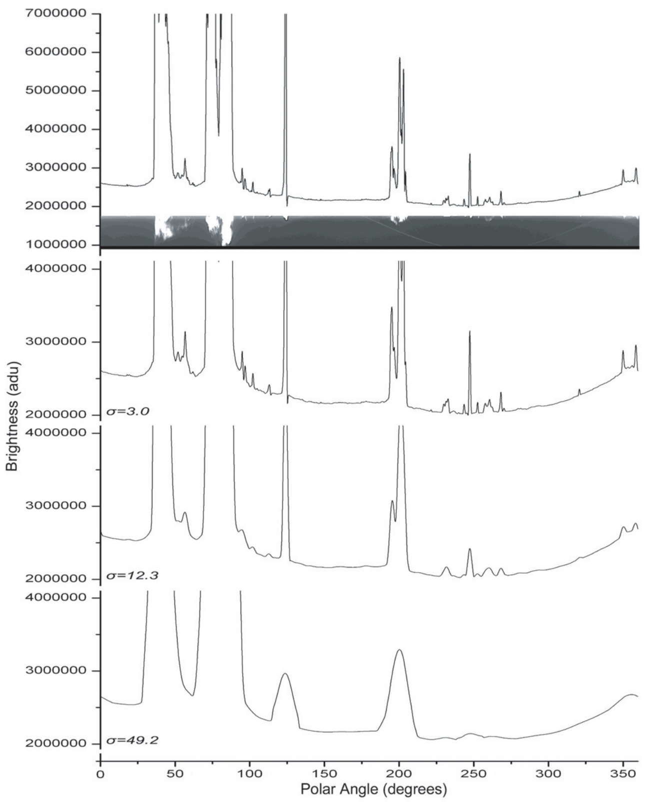

Fig. 5. Example of the scale analysis: profiles versus polar angle for the region selected in Fig. 3. *Top part*: original averaged profiles versus polar angle. The three subsequent rows correspond to profiles convolved with a low-pass filter, increasing the spatial smoothing with a width of 3.0, 12.3 and 49.2 pixels (see Sect. 4.5).

4.5. Average profile and scaling analysis

To detect off-limb solar structures, images in polar coordinates are averaged in the radial direction to produce a profile of the averaged brightness versus the polar angle. Note that the background outside actual structures strongly contributes to this average profile. An example is shown in Fig. 5 (upper panel). Its visual inspection shows that all scales are present from small features and spikes (a few Mm) to large quiescent prominences (several 10 Mm). However, small scales can either be present alone or superimposed on a larger-scale structure. The algorithm must therefore be able to separate the structures on various scales. Therefore, we generate a series of profiles where the small-scale structures are increasingly filtered. This is done using a low-pass filter, the original profile being convolved with Gaussian profiles of various widths: 1.5, 3.0, 6.1, 12.3, 24.6, 49.2 pixels are the half-widths at half-maximum (HWHM) of the Gaussian filters. The amplitudes of the Gaussian widths are chosen to cover the range of scales of the structures we have to identify (see in particular Fig. 3), from small structures (a HWHM of 1.5 pixels corresponds to a width of about 2 Mm) to large structures (49.2 pixels corresponds to a width of about 120 Mm).

An example of the processing is shown in Fig. 5. For each profile, the detection of structures is performed by detecting the profile maximum, derived from the first derivatives, and the location of their inflexion points, derived from the second derivatives. Note that in the case of very large eruption events, we must visually impose the position. This second step is important for studying evolution, such as the total brightness in the case of a large prominence leading to a CME. At this stage, we obtain for each profile 3 values of polar angles determining a structure: the center position and the upper and lower limit positions. A fourth quantity is also computed: we call it the "strength" of the detected structure. It is the sum of the absolute values of the derivative over the entire structure inside the upper and lower limits. This quantity is useful for determining the threshold between background values and actual solar structures. Such a threshold is experimentally defined for each spatial smoothing, as we visually checked on a small data set that we have not eliminated actual structures. Structures whose strengths are below the threshold are eliminated to avoid any false detection. The choice of the threshold has been made in a conservative way, as another algorithm will be applied in Sect. 4.8 to the daily time series in order to eliminate structures that might appear only once.

4.6. Pyramidal analysis

Structures detected on various scales must be analyzed in order to provide a single list of structures. Starting with the largest scale, a pyramidal analysis allows the elimination of the small structures located in a zone where a structure has already been detected at the upper level. More specifically, we first consider the structures defined on the largest scale. This identifies the largest structures, the smallest ones being absent. Then, at the following step (on a smaller scale), two categories of structures are present: those that overlaps an already identified large structure (therefore they are not to be considered) and those not overlapping such structures (they are added to the list of structures). This is repeated until the smallest scale is reached. This is called the "extraction process" or simply the "extraction" further on. A list of positions is derived from this analysis, and it provides the location of the structures described in Sect. 4.8.

4.7. Final products

To produce calibrated images in Cartesian coordinates and to precisely estimate the intensities of the structures, the original images (obtained at the end of Sect. 4.1) are normalized to the same standard. After properly subtracting the background, the data is made available at BASS2000. An example is shown in Fig. 6, where the bright fringe and the background were subtracted. In addition, the average activity level and its standard deviation (showing the temporal variability of the activity level) over a day are computed in order to use this as a selection criterion in database requests. These images are used to extract F_s, the light flux integrated over the whole structure, by summing the intensities of each pixel between the two limits determining the structure (see Sect. 4.8).

Fig. 6. *Upper panel*: the background with the ring computed from the image shown in Fig. 1 (see Sect. 4.7). *Lower panel*: the cleaned image obtained after applying the background plus ring correction.

4.8. Structure parameters

In addition to the positions of each detected structure (lower and upper limits P_1 and P_2, and central positions P_c), several parameters are computed using the images in polar coordinates, after suppression of the parasitic fringe:

– the height H determined in two steps. First, a fast algorithm provides an estimation by using the radial profile averaged between P_1 and P_2. Starting from the maximum of the intensity profile, the height where the profile reaches 10% of the maximum intensity gives a first estimate, H_0. This value is arbitrary in some cases when a prominence is very complex and presents fine structure in the radial direction. A threshold is therefore experimentally defined in order to extract the pixels belonging to the structure. To eliminate possible contamination from the parasitic fringes occurring far from the limb, only pixels below $2H_0$ are considered. The position

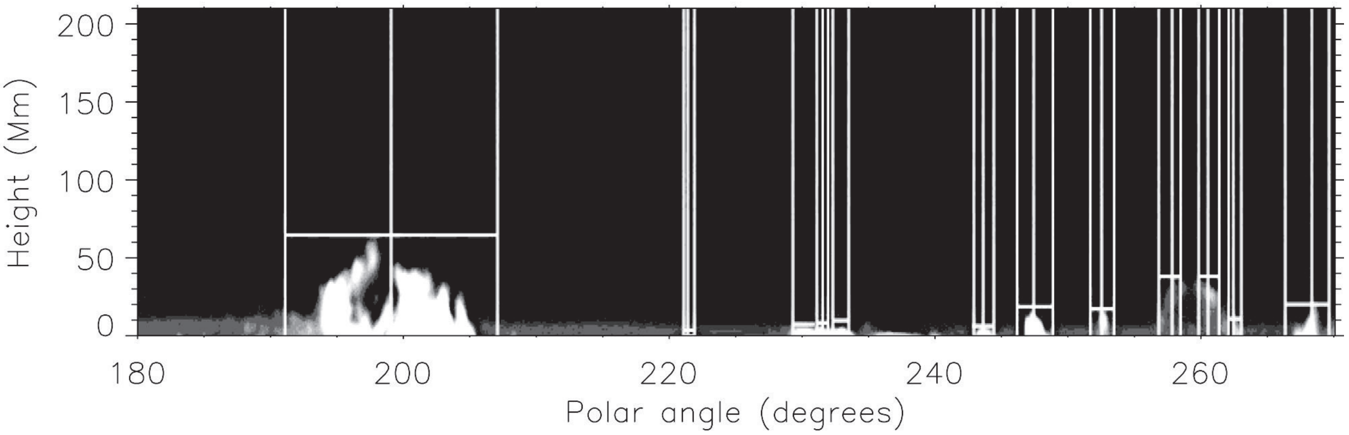

Fig. 7. Illustration to show how the height determination method works for the selected region of Fig. 3. The vertical lines show the limits P_1 and P_2, as well as the location of the center of the detection P_c of each structure. The horizontal lines show the height H corresponding to each structure.

of the highest pixel defines the new height H, which is expressed in fractions of the solar radius. An example of height determination is illustrated in Fig. 7;

- the effective surfaces in pixel number S_{pix} and in units of 10^{-5} of the solar surface S are estimated using the same experimental threshold, but it is applied to the image where the bright fringe has been removed (see Sect. 4.4). The coordinate transformation is taken into account in this computation;
- the center of gravity of the structure is defined using the same technique as for the effective surface. The coordinates are X in tenth of degrees and Y in pixels.

Note that the position is determined after the convolution described in Sect. 4.5; therefore, these positions slightly overestimate the angular extent of the structures. The set of widths was chosen in order to sample the size ranges of the observed structures as well as possible. Finally, a reliable estimation of the light flux, F_s, is performed on the calibrated image (Sect. 4.7). The intensity is summed between P_1 and P_2 and for heights up to $1.5H$. This represents the light flux in Hα with neither the background nor the parasitic fringe.

The errors introduced by the seeing and light conditions are difficult to determine. One possibility is to look at the temporal variation in the integrated flux in a given zone of the image, after removing the long-term variation (daily variation). For low fluxes, the variations are on the order of 5–10% of the flux. The proportion should be much lower for large-flux structures like prominences. However, part of these fluctuations have a solar origin. Furthermore, we do not observe any correlation between the flux variations in various locations along the limb, as could be expected from light variations of instrumental and/or atmospheric origin. This means that the errors on the fluxes due to the seeing and light conditions are quite small, in addition to being random. It is also likely that they affect all structures equally.

Once all detections for a given day are obtained, a filter eliminates structures that are not detected on more than two consecutive images. Additional parameters are obtained by tracking structures from a single image to the next, enabling the study of the evolution of a given structure. It allows the evaluation of a lower limit for the lifetime of the structure, as well as properties such as its maximum height, maximum light flux, or maximum effective surface. Other properties are also computed. This algorithm takes into account that several independent structures can occur at the same location. We call these new values extracted values. All these characteristics, in addition to other parameters, are stored in a SQL database made available at: `http://bass2000.bagn.obs-mip.fr/New2003/Pages/Coro/interro_scanprotu.html`. Briefly, the database can be retrieved as follows:

- a simple form can be filled out to provide the requested variables owing to various criteria (date, size, etc.). A large ascii file containing the list of structures and their properties can then be retrieved for subsequent analysis;
- ready-to-use codes are available. They use the database, make simple computations, and provide results mainly as plots such as histograms, plots showing the time evolution of the structure location (coronagram), curves showing the average value of a given parameter versus the polar angle, etc. For a given day, an example of a time sequence of coronagrams is shown in Fig. 8.

5. First results

The software described above was applied to the data set running from 1998 to 2000. During this period covering the last sunspot maximum, the Hα filter was stable. Here, we illustrate a few important results in order to show the capabilities of this public database, focusing our attention on the effective surface and light flux distributions, as well as on the apparent relationships between these parameters. Only structures larger than 10 pixels in size were considered in this analysis. This leads to a total of 480 913 individual structures. After the selection described in Sect. 4.8, a data set of 63 711 structures was left. Effective surfaces S were evaluated as a fraction of $10^{-5}\ S_\odot$ (with $S_\odot$ the surface of the solar disk) and light fluxes F_s were fraction of 10^{-11} $F_\odot$ (with $F_\odot$ the intensity of the solar disk center in the same spectral band and the same surface defined by the pixel size). As an example, a typical S value of 1 corresponds to a linear size of 3.9 Mm with 100 corresponding to a linear size of 39 Mm.

5.1. Effective surface and light flux distributions

Figure 9 shows the distribution of light fluxes F_s and effective surfaces S for all detected structures. Three regimes can be identified: for effective surfaces i) below 1; ii) between 1 and 10; and iii) above 10, with S expressed as a fraction of $10^{-5}\ S_\odot$.

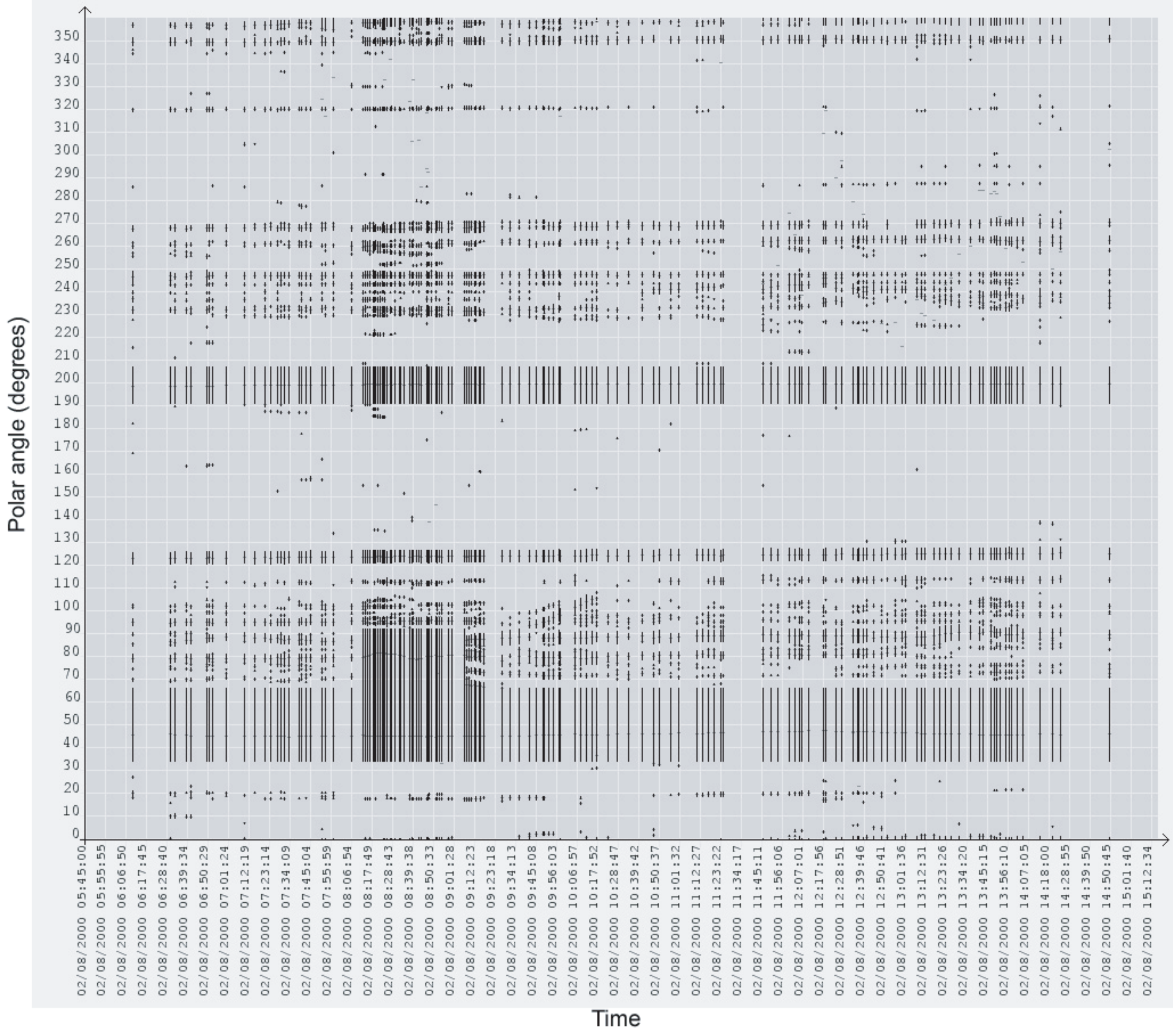

Fig. 8. "Coronagrams" to show the time variations in the location of the detected structures for a continuous typical observing sequence from 6:10 to 14:50 UT, taken on Aug. 2, 2000. The diagram shows all the recorded detections. Solar latitudes are shown along the vertical axis and the time runs along the horizontal axis. The structures are selected using the filtering process described on Sect. 4.8. For this day a "coherence" of the large prominence around the polar angle 48 degrees has been imposed (see Sect. 4.5).

For example, a small cool "jet", such as those observed in the right part of Fig. 3 (between polar angles 90 and 110°), corresponds to an effective surface S on the order of 10 to 20. Similarly three regimes can be seen in the flux distribution. Distributions are also shown for the values after the "extractions". In this case, the fluxes and effective surfaces correspond to the maximum value over the day and therefore each structure is counted only once a day.

Different regimes can also be observed there, although they are shifted slightly toward lower values. In the case of the distribution of effective surfaces S after selection (bottom of Fig. 9), we observe a power law for S in the range 0.2–30 and another power law, much steeper, for S larger than ~30, i.e. structures definitely larger than jets. This could be due to the fact that they are related to active regions rather than to the chromospheric network, as is the case for the smallest structures.

5.2. Relationships between structure parameters

Figure 10 shows the relationships between effective surfaces S and fluxes F_{s} on a log-log scale. The relationship is found to be approximately linear over almost three orders of magnitudes. It corresponds to a power law with a slope of 5/4. For larger structures (i.e. for S larger than ~60), the flux is smaller than expected from the linear fit. When looking into more details, there seems in fact to be two regimes in the linear domain, with two distinct slopes below an effective surface of 1 and above it. Below effective surfaces of 1, the slope is 1.108 ± 0.003 for all structures (0.999 ± 0.007 for the maximum values after the "extractions"), and it becomes 1.312 ± 0.001 (1.362 ± 0.007 for the maximum values after the "extractions") for S larger than 1. The slope is in general larger than 1, showing that in the linear regime, larger structures have a larger flux per square pixel than smaller ones. The exception is for small structures, with a slope consistent with 1, indicating a constant flux per square

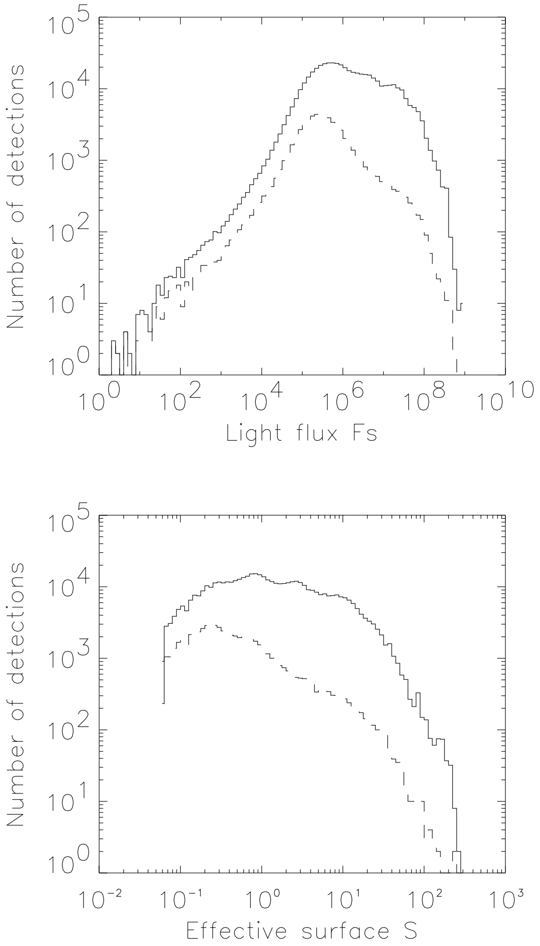

Fig. 9. *Upper panel*: distribution of light fluxes F_s for all structures (solid lines) and the maximum light flux per structure after the selection (dashed line), with F_s expressed as a fraction of 10^{-11} $F_\odot$, during the period 1998–2000. *Lower panel*: distribution in effective surface S for all structures (solid lines) and the maximum total light flux per structure after the selection (dashed line), with S expressed as a fraction of 10^{-5} $S_\odot$.

pixel for S up to 1. For large structures, the slope is significantly larger after the "extractions", showing that these parameters are more pronounced when considering only the maximum during the lifetimes of the structures. This suggests different evolutions for the structures depending on their size and a possible influence of the optical thickness on prominence elements. It could also be interesting to look further at the relationship with the level of activity of the analyzed prominences, with their latitudes, etc. We leave this research for a forthcoming paper. Finally, Fig. 10 also shows the variations with size of the rms dispersion of Log(F_s) in each size bin. It shows that the dispersion is much larger for small structures, as can also be seen on the 2D distribution showing the number of structures versus S and F_s. It is interesting to notice that for small structures, the total extension of F_s values for a given size can reach 4 orders of magnitude, including a long weak tail toward weak light fluxes, which can be seen at the top of Fig. 10.

5.3. Polar angle distribution

Figure 11 shows the distributions versus polar angle for various categories of sizes. The top row shows the distributions for structures identified on all images (i.e. before the selection

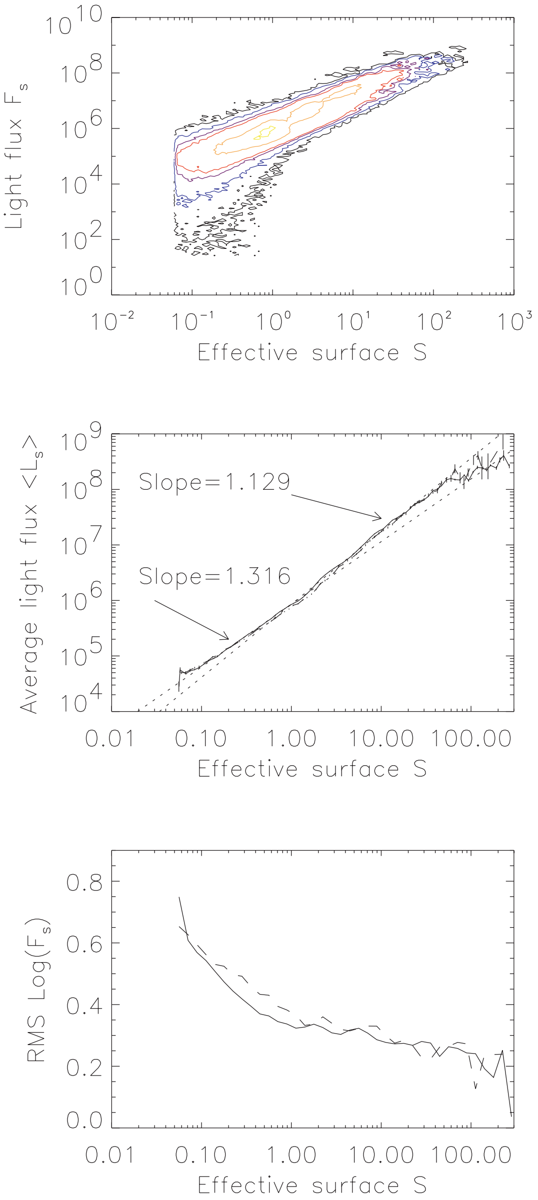

Fig. 10. *Upper panel*: light flux F_s versus effective surface S after the selection (maximum values over the lifetime are used), with S expressed as a fraction of 10^{-5} $S_\odot$ and F_s expressed as a fraction of 10^{-11} $F_\odot$, for the period 1998–2000. The levels correspond to 1 structure (black), 10 (blue), 50 (purple), 100 (red), 500 (orange), and 800 (yellow). *Middle panel*: light fluxes F_s versus the effective surface S after averaging in boxes of constant size in Log(S), for all structures (solid line) and after the extraction process (dashed line). The two dotted lines correspond to the linear fits over S in the range 0.1–1 and S larger than 1. *Lower panel*: rms dispersion of Log(F_s) in each S bin, for all structures (solid line) and after the selection (dashed line).

described in Sect. 4.8). In this case, a given structure is counted as many times as it appears. On the other hand, the distributions in the bottom row correspond to structures after the selection: this eliminates a few uncertain structures and, more important, a given structure is now counted only once per day. The differences between the two approaches is not easy to interpret, but it is in part related to the respective lifetimes of each category of structures. We are concentrating our analysis on the distribution after selection.

Let us first consider the smallest structures, with S smaller than 1. We observe a large number of structures in the activity

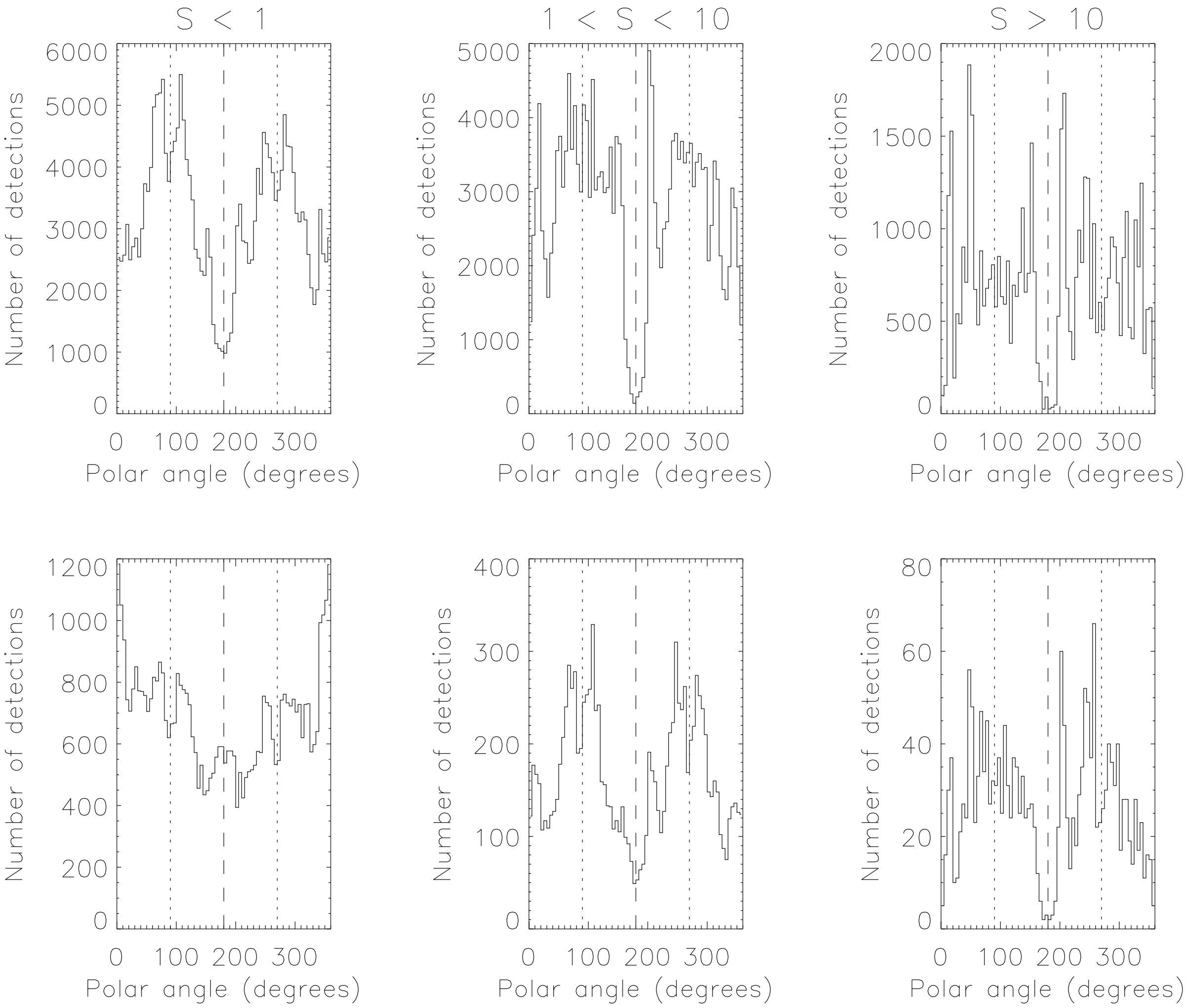

Fig. 11. Distribution of the number of structures versus the polar angle (counted positive counter-clockwise from the North pole), for all structures (*top*) and after the extraction, see 4.8 (*bottom*) over the period 1998–2000, for various size range S: smaller than $1 \times 10^{-5}\ S_\odot$ ($left$), between $1 \times 10^{-5}\ S_\odot$ and $1 \times 10^{-5}\ S_\odot$ (*middle*) and larger than $10 \times 10^{-5}\ S_\odot$ (*right*). The vertical dashed lines represent the solar South pole position, and the dotted lines represent the equator. Note the N-S asymmetry especially strong in polar regions for S smaller than $10 \times 10^{-5}\ S_\odot$.

belts, with a gap at the equator. A smaller gap is observed between the activity belts and the poles, which is much more pronounced in the Northern hemisphere as there is a very strong asymmetry between the two poles (twice as many structures at the Northern pole). The number of structures is also greater close to the poles than at lower latitudes. When considering larger structures, for S in the range 1–10, we observe a similar pattern in the activity belt, with the same gap at the equator. The gap poleward of the activity belts is quite pronounced, again with a definite asymmetry between the numbers of structures at the poles. However, the number of structures is now quite small, as the distribution is dominated by the activity belts. Large structures (S larger than 10) follow a pattern close to the structures in the 1–10 S range. In particular, they also show strong peaks in the 70–80° latitude range (especially in the Southern hemisphere), in addition to the activity belts and strong gaps at the poles. However, the distributions show a larger dispersion.

The dominating features for all structures are therefore small gaps in activity at the equator and just above the activity belt, as well as a strong asymmetry between hemispheres, especially close to the poles. Very small features are definitely more present at the poles, and they have their highest rate of occurence there.

The gap at intermediate latitudes could be related to the fact that it has been difficult to establish a connection between the high latitude branch of solar activity (observed in the corona and using filaments as tracers) and the low latitude one (activity belt), as illustrated for example in Leroy & Noëns (1983). This is of particular interest to the solar dynamo theories as it provides some constraints on the behavior of the dynamo waves. The North-South asymmetry may also be related to the dynamo action. The fact that it is more pronounced at high latitudes shows that the different components of the solar cycle (here the low-latitude branch and the high-latitude one) do not behave in the same way. We cannot go further because the data considered in this paper cover just a part of the solar cycle. It is our objective to study the evolution of the North-South asymmetry of the distribution of small structures during the whole solar cycle and its possible relationship with the polar magnetic field reversal in a forthcoming paper.

6. Conclusion

Special software was developed to process the large data set of coronagraphic data collected since 1994 in daily surveys at the Pic du Midi Observatory. This software allows the detection of structures over a wide range of sizes, from small spikes to large prominences. The preliminary results indicate interesting properties over this wide range of light fluxes, i.e. over almost eight orders of magnitude and over more than three orders of magnitude in effective surfaces.

The distributions of fluxes and effective surfaces show three different regimes. The variations in fluxes with structure size is close to linear over three orders of magnitude, with two slightly different slopes for structures below or above 1 (this threshold corresponds to a linear size of 3.9 Mm). The large amount of samples also allows the study of the latitude distribution for the different categories of set and shows a well-structured organization, as well as asymmetries between hemispheres, as already observed by Noëns & Wurmser (2000). This database can therefore potentially be used to study the parameters of small-scale structures in detail, such as their spatial distribution in latitude, their lifetime distribution, as well as the variation in their properties over the solar activity cycle and the relationship with the closest active regions, eruptions, etc., taking the difference between the Northern and Southern hemisphere distributions into account. In this context, we recall that prominences have disk-filament counterparts and, accordingly, they are good proxies of magnetic neutral sheets well inside the inner corona. This will be the subject of future work.

The statistical study of large structures such as prominences is then made possible, as it will be easy to follow their variations in brightness and height, including those leading to CMEs. In addition, these observations can easily be used in comparison to other data, such as that obtained by EIT and SUMER on SOHO in EUV and by LASCO at a much higher altitude above the limb. Finally, the tool developed in this work could be applied to any other coronagraphic data in Hα and partly to other coronagraphic data, including those obtained with externally occulted instruments in space (see Koutchmy 1988). It will, of course, be extensively used to process the data from the new coronagraphic and chromospheric instruments currently being developed for the corona at the Pic du Midi Observatory.

Acknowledgements. Living expenses of the large number of associated observers (O.A.) and most of the new equipment were covered by FIDUCIAL. Observations are also supported by PNST of the CNRS and INSU, Observatoire Midi-Pyrénées, Laboratoire d'Astrophysique of OMP and Institut d'Astrophysique de Paris, CNRS, and UPMC. We thank the BASS2000 technical staff, as well as the technical teams of the Pic du Midi Observatory, for their help. We thank C. Latouche for his permanent interest and confidence, G. Stellmacher for reviewing the manuscript, Th. Roudier for useful discussions, J.-M. Abbadie for help running Pic du Midi facilities for us, J.-C. Vial for his interest and the anonymous referee for meaningful suggestions that led to substantial improvements in the paper.

References

Collin, B., & Nesme-Ribes, E. 1995, C. R. Acad. Sci. Paris, 321(IIb), 77
Delannée, C., Koutchmy, S., Delaboudinière, J.-P., et al. 1998, in Solar jets and coronal plumes, ESA SP-421, 129
Dere, K. P., Bartoe, J. F., Brueckner, G. E., & Recely, F. 1989, ApJ, 95, L345
Fitzgibbon A., Pilu, M., & Fisher, R. B. 1999, IEEE Transactions on pattern analysis and machine intelligence, 21(5), 476
Fuller, N., Aboudarham, J., & Bentley, R. D., 2005, Sol. Phys., 227, 61
Innes, D. E., Inhester, B., Srivastava, N., et al. 1999, Sol. Phys., 186, 337
Koutchmy, S. 1988, Space Sci. Rev., 47, 95
Koutchmy, S., & Loucif, M. L. 1991, in Mechanism of chromospheric and coronal heating, Heidelberg Conf., ed. Ulmschneider, et al., 152
Leroy, J.-L. 1972, Sol. Phys., 25, 413
Leroy, J.-L., & Noëns, J.-C. 1983, A&A, L1
Loucif, M. L., Koutchmy, S., Stellmacher, G., et al. 1998, in Solar jets and coronal plumes, ESA SP-421, 299
Niot, J. M., & Noëns, J.-C. 1997, Sol. Phys., 173, 53
Noëns, J.-C., & Wurmser, O. 2000, Ap&SS, 273, 17
Noëns, J.-C., Balestat, M.-F., Jimenez, R., et al. 2004, in Multi-Wavelength Investigations of Solar Activity, Saint-Petersburg 14-19 june 2004, (Cambridge University Press), IAU Symposium, 223, 291
Holschneider, M., & Tchamitchian, P. 1990, Les ondelettes en 1989, ed. P.G Lemarié, (Springer Verlag), 102
Robbrecht, E., & Berghmans, D. 2004, A&A, 425, 1097
Romeuf, D., Rochain, S., Jimenez, R., et al. 2004, Atelier PNST, 26–29 Jan. 2004, Autrans, Livre des résumés, 109
Shensa, J. 1992, IEEE. Trans. Signal Process., 40(10), 2464
Starck, J.-L., & Murtagh, F. 1994, A&A, 288, 342
Zharkova, V. V., Ipson, S. S., Zharkov, S. I., et al. 2003, Sol. Phys., 214, 89

Astronomy & Astrophysics manuscript no. art4
April 27, 2007

Tracking granules at the Sun's surface and reconstructing velocity fields. II. Error analysis

R. Tkaczuk[1], M. Rieutord[1], N. Meunier[2], T. Roudier[2]

[1] Laboratoire d'Astrophysique de Toulouse et Tarbes, UMR 5572, CNRS et Université Paul Sabatier Toulouse 3, 14 avenue E. Belin, 31400 Toulouse, France
[2] Laboratoire d'Astrophysique de Toulouse et Tarbes, UMR 5572, CNRS et Université Paul Sabatier Toulouse 3, 57 Avenue d'Azereix, BP 826, 65008 Tarbes Cedex, France
e-mail: `tkaczuk@ast.obs-mip.fr, rieutord@ast.obs-mip.fr, meunier@ast.obs-mip.fr, roudier@ast.obs-mip.fr`

Received ; Accepted

ABSTRACT

Context. The determination of horizontal velocity fields at the solar surface is crucial to understand the dynamics and magnetism of the convection zone of the sun. Such measurements can be done by tracking granules.
Aims. Tracking granules from ground-based observations is however suffering from the Earth's atmospheric turbulence which induces image distortion. The focus of this paper is the evaluation of the influence of this noise on the maps of velocity fields.
Methods. We use the Coherent Structure Tracking algorithm developed recently and apply it to two independent series of images which contain the same solar signal.
Results. We show first that a $k-\omega$ filtering of the times series of images is highly recommended as a pre-processing to decrease the noise while, on the contrary, the use of destretching should be avoided. We also demonstrate that the lifetime of granules has a strong influence on the error bars of velocities and that a threshold on the lifetime should be imposed to minimize errors. Finally, although solar flow patterns are easily recognizable and image quality is very good, it turns out that a time sampling of two images every 21 s is not frequent enough, since image distortion still pollutes velocity fields at a 30% level at the 2500 km-scale, i.e. the scale at which granules start to behave like passive scalars.
Conclusions. The Coherent Structure Tracking algorithm is a tool useful for noise control on the measurement of surface horizontal solar velocity fields when, at least, two independent series are available.

Key words. Convection – Turbulence – Sun: granulation – Sun: photosphere

1. Introduction

Movies of the solar surface show that it is a place of intense turbulent fluid flows where three major scales (granulation, mesogranulation and supergranulation) have been pointed out. In order to better understand the underlying dynamics, it is crucial to be able to measure the velocity fields. As far as horizontal flows are concerned, the basic techniques have relied on the measurement of the displacement of granules which, as shown by Rieutord et al. (2001), trace the fluid flows at scales larger than 2.5 Mm.

Two algorithms have been devised to transform a time sequence of images into a sequence of horizontal velocity fields maps. These are the LCT algorithm (i.e. Local Correlation Tracking, see November & Simon 1988) and the CST algorithm (Coherent Structure Tracking, see Rieutord et al. 2007 hereafter referred to as Paper I).

When the surface velocity field are known, one is usually interested in identifying/following the dynamical structures of the flow like vortices, upwellings or downwellings. The identification of these structures demands however the computation of the velocity gradients like the divergence or the vorticity. In Paper I, it has been pointed out that such quantities are very sensitive to the noise induced by terrestrial atmospheric distortion, since they are derivatives of the velocity field. The use of the velocity field to describe the dynamics of the solar surface thus needs to be complemented by an error analysis which both evaluates the significance of the observed dynamical features and gives a way to eliminate, or at least reduce, the impact of errors.

The aim of this paper is to analyse the consequences of errors in the final result of velocity, vorticity and divergence fields. As mentioned above, the main source of errors comes from the distortion of images induced by the Earth's atmospheric turbulence. The case of errors or,

---

Send offprint requests to: M. Rieutord

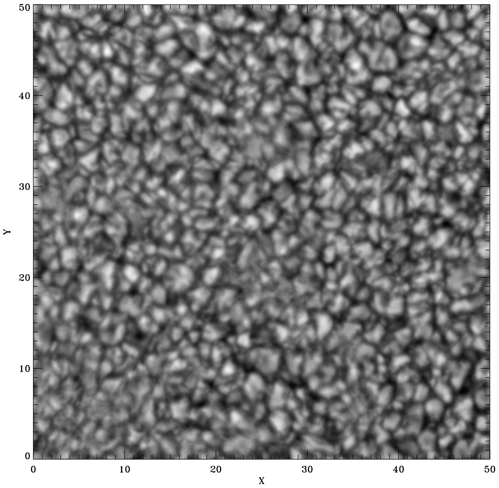

Fig. 1. View of the region used for the tests. X and Y scales are in arcsec.

equivalently, the precision of measurements has already been discussed for the LCT algorithm by November & Simon (1988) who mentioned errors of the order of 20 m/s on the velocity field. Further work by Simon et al. (1995) showed that this precision was certainly largely overestimated. More recently, Potts et al. (2003) investigated the case of interpolation errors, associated with the LCT algorithm, which also spoil the final result. Here, we will focus on the CST algorithm and try to give a neat picture of the influence of the Earth's atmospheric distortion on the measurement of the velocity fields at different scales.

We organized the paper as follows. Using two independent series of images of the solar surface, we first evaluate the noise induced on the positions of the granules and how image pre-processing can reduce it. We then focus on the way the noise influences the final velocity fields at different scales and analyze its propagation up to the curl and divergence maps. Conclusions and outlooks follow.

2. Observations

We use a time series of images obtained on June 5, 1993 at the SVST (Swedish Vacuum Solar Telescope), Observatorio Roque de los Muchachos, La Palma (data courtesy of P. Brandt, see also Simon et al. 1994). This data set has already been studied by many authors (Sobotka et al. 1997a,b; Sobotka et al. 1999a,b; Dorotovič et al. 2002; Getling & Brandt 2002; Roudier et al. 2003). The original series consists of 1868 image pairs of size 1310×970 pixels taken at $\lambda = 468 \pm 5$ nm. The time between two pairs of images is close to 21 seconds. Images from a pair are separated by a few seconds (3 s on average and always less than 14 s). The pixel size is $0.''125$, and the spatial resolution is near diffraction limit $0.''25$. The field of view is $2.'7 \times 2.'0$. However, the instrument leads to a rotation of the field of view, and the area observed on the Sun at the beginning of the time series is different from the one at the end. The rotation center is located on a pore at pixel coordinates $(590, 102)$ (not in the field-of-view used here).

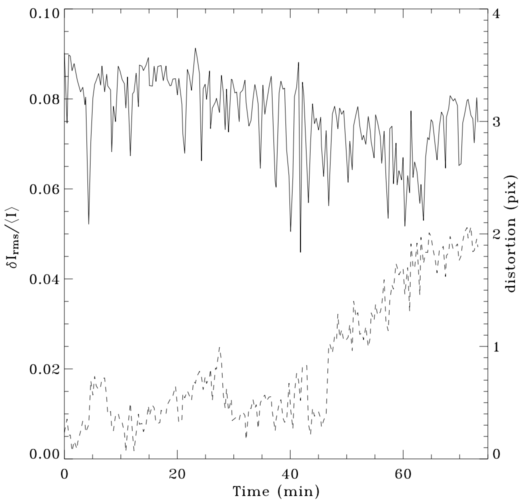

Fig. 2. Indices of image quality. Contrast (solid line) and distortion amplitude (dashed line, scale on right). Distortion is the rms displacement, evaluated with local correlation tracking, between two images of a pair.

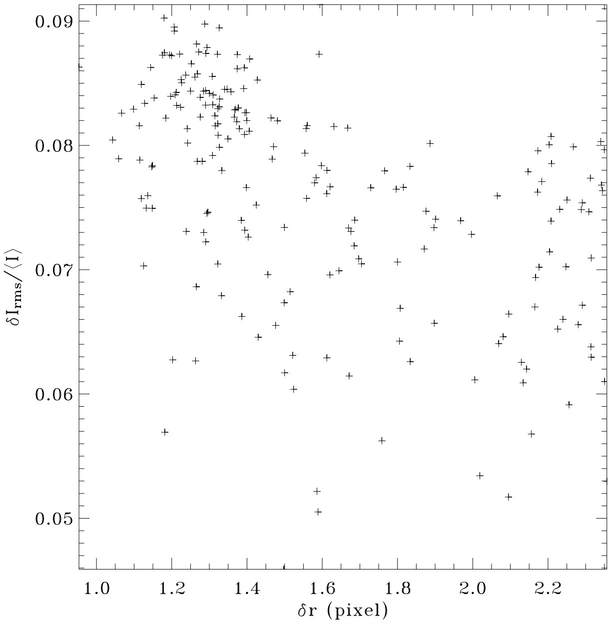

Fig. 3. The normalized intensity contrast versus the rms displacement of granules between the two images of each pair.

For our investigations described below, we used a subsample of 210 pairs of frames (images 841 to 1262), covering $\sim$ 77 minutes. In Sect. 6, slightly more data have been used (images 800 to 1298 corresponding to a $\sim$ 87 min sequence). As shown in Fig. 1, we extract a region of 401×401 pixels centered on a (magnetically) quiet zone.

The main advantage of this data set is that it contains two independent sequences of images which can be considered as representing the same solar signal. The only

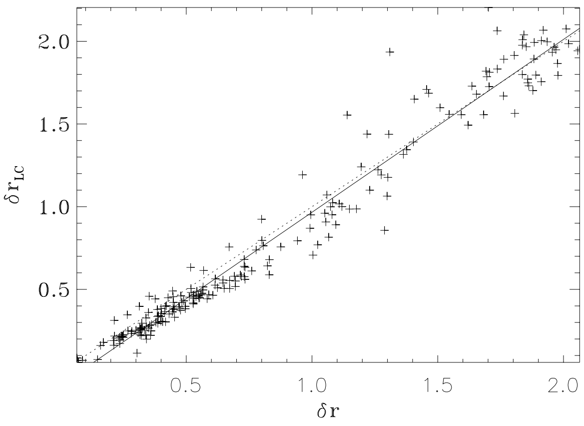

Fig. 4. Mean distance between granule centers of gravity for each image pair versus the mean displacement due to atmospheric turbulence estimated by local correlation (one point per image pair). Both displacements are in pixel. The solid line shows the line of equation $y = x$ and the dotted line is a linear fit over the points.

difference comes from the Earth's atmospheric distortion the effects of which can thus be analyzed. Moreover, as shown by Fig. 2, image quality varies during the sequence. Although the contrast remains almost constant, we see that the amplitude of distortion increases after t=45 min. We thus have at our disposal a "good" sequence where mean distortion is about 0.5 pixel and a "bad" sequence where mean distortion reaches an amplitude of 2 pixels; **in the following, when we refer to "good" data we will mean the first 45 min, while "bad" data will designate the remaining sequence.**

3. Sources of errors in CST

In the CST method, errors are introduced through the segmentation (i.e. through the determination of the granule positions) and through the interpolation made in order to obtain a velocity field sampled over a regularly-spaced grid. The precision at which the velocity field can be measured thus depends on :

- the precision at which a granule position is determined,
- the duration of granule tracking,
- the temporal resolution (time interval between velocity maps),
- the spatial resolution of the grid used to sample the velocity field.

This list shows that the CST algorithm allows us to identify all the crucial steps and thus to follow the propagation of errors from the beginning to the end of the computation.

4. Standard deviation of granule positions

The first step of the error analysis is to estimate the error on the granule positions[1]. We first apply it to the raw data, and then use it to estimate the performances of pre-processing steps which can be performed before granule segmentation, namely on the image sequences.

4.1. Method

In order to estimate the standard deviation on granule positions, we use pairs of images. Because of their quasi-simultaneity, they represent the same solar surface and all the differences between them come from atmospheric distortions, instrumental effects or processes applied on the data.

After the segmentation step, the algorithm identifies granules present on both images of the pair. We then simply measure the distance between two identical granules. More precisely, we consider that the position of a granule is controlled by two random variables (x_i, y_i) for which we have two realizations. We thus construct two other random variables $(\delta x_i, \delta y_i) = (x_{i,1} - x_{i,2}, y_{i,1} - y_{i,2})$ whose variance is just twice that of (x_i, y_i). Thus with a pair of images we can estimate the mean error over the field of view in each direction x and y by

$$\sigma_x = \sqrt{\frac{1}{2N}\sum_{i=1}^{N}(x_{i,1} - x_{i,2})^2},\ \sigma_y = \sqrt{\frac{1}{2N}\sum_{i=1}^{N}(y_{i,1} - y_{i,2})^2}$$

and the mean displacement $\delta r = \sqrt{\sigma_x^2 + \sigma_y^2}$.

These quantities are clearly estimates of the image quality through atmospheric distortion. Interestingly enough, we compared this estimate with the intensity contrast usually used to indicate image quality. As shown in Fig. 3, the correlation between the two indicators is rather poor, meaning that they are largely decoupled although they both come from atmospheric turbulence ! We interpret this result, tentatively, as showing that different layers of the Earth's atmosphere control the contrast and the distortion.

Furthermore, we compared (see Fig. 4) the displacement of granules with the displacement field derived from a local correlation tracking (using a FWHM of 20 pixels) between the two images of a pair. As expected, the correlation is much better (~ 0.96).

4.2. Application to pre-processing

One of the interesting applications of the error estimate on the granule position is to allow the evaluation of the effectiveness of various pre-processings applied to the images before estimating the granule position. A measure of σ_x before and after a given pre-processing indicates its

---

[1] By granule position we mean the position of the center of gravity of the granule in the segmented image.

	Good data		
	σ_x	σ_y	N_g
No processing	0.696 ± 0.081	0.701 ± 0.084	1077 ± 91
$k-\omega$	0.416 ± 0.037	0.418 ± 0.028	1096 ± 34
	Bad data		
	σ_x	σ_y	N_g
No processing	0.694 ± 0.075	0.727 ± 0.079	803 ± 150
$k-\omega$	0.470 ± 0.039	0.527 ± 0.045	972 ± 89

Table 1. Comparison of the performances obtained on time series with high and low quality images with and without $k-\omega$ filtering. Note that the errors only slightly increase from the "good" to the "bad" data, but the number of granules, and in other words the number of measuring points, is reduced by 20% without filtering, while the loss is 10% with filtering.

performance. We have applied this approach to the $k-\omega$ filtering and to the destretching.

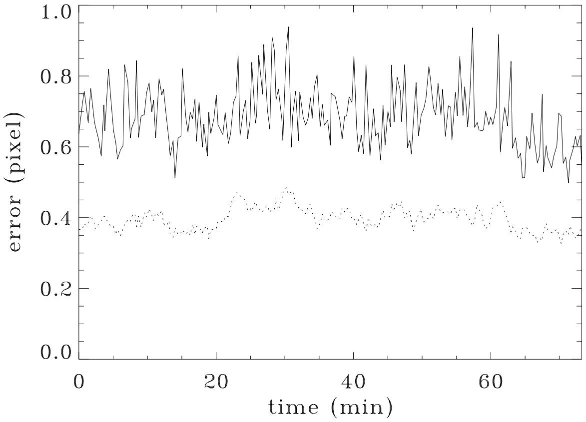

Fig. 5. Estimation of the error σ_x on the determination of the center of gravity position in the x direction as a function of time with no $k-\omega$ filtering (solid line) and with the filtering (dotted line).

4.2.1. $k-\omega$ filtering

The $k-\omega$ filtering (see for example Title et al., 1987) acts both spatially and temporally. In practice, it is a thresholding in the Fourier space: the contributions of all frequencies corresponding to a phase velocity larger than the threshold are eliminated.

Let us note that the data we use are irregularly sampled. The time step between two pairs of images is about 21 seconds, within a few seconds (the maximum deviation with respect to a periodic sampling is 15 s, while the average deviation is 6.3 s). The same data set has been used by Dorotovič et al. (2002), who interpolated them to get a regularly spaced time series. We consider that this is unnecessary refinement since, within a few seconds, the solar signal does not change. Hence, with a regular time step, images would differ from ours by just a different realization of the Earth's atmospheric turbulence.

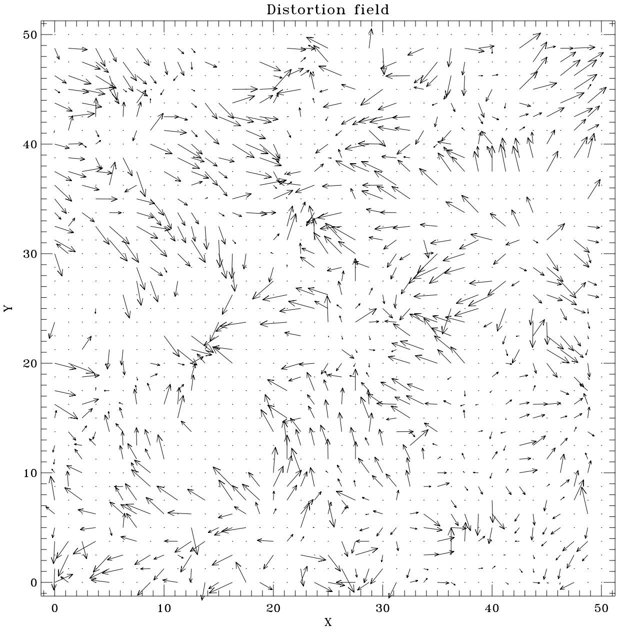

Fig. 6. An example of a map of displacements due to the Earth's atmospheric distortion as sampled by granules. Regions without data have a too low image quality for granule to be identified. X and Y are in arcsec.

Fig. 5 shows the average error in pixel on the x-position of the granules for data pre-processed with a $k-\omega$ filtering and data without pre-processing. We used a threshold for the phase velocity of 4 km/s. The figure shows that the performance is quite improved over the whole time series by the use of this filtering. The error for the y-component is of the same order of magnitude as the error for the x-component.

One may wonder why the increasing distortion seen after t=45 min in Fig. 2 does not appear in Fig. 5. This comes from the way the error is measured. Indeed, only granules close enough in a given pair of images are kept. The distortion map in Fig. 6 shows the lack of measurements in some regions; image quality is not good enough for granules to be identified from one frame to the other. With this method it is clear that high amplitude distortion does not show up with increased error in granule position; rather it appears in a reduction of the number of "valid granules". In Fig. 7 we see the loss of granules when conditions deteriorate and how $k-\omega$ filtering improves the situation. Numbers in Table 1 also illustrate this process.

4.2.2. Destretching

This method, introduced by November & Simon (1988), is based on the same principles as the LCT. It uses a local correlation scheme to determine the displacements with respect to a reference image. From these displacements, images are stretched by interpolation in order to be the closest possible to the reference image. This method aims

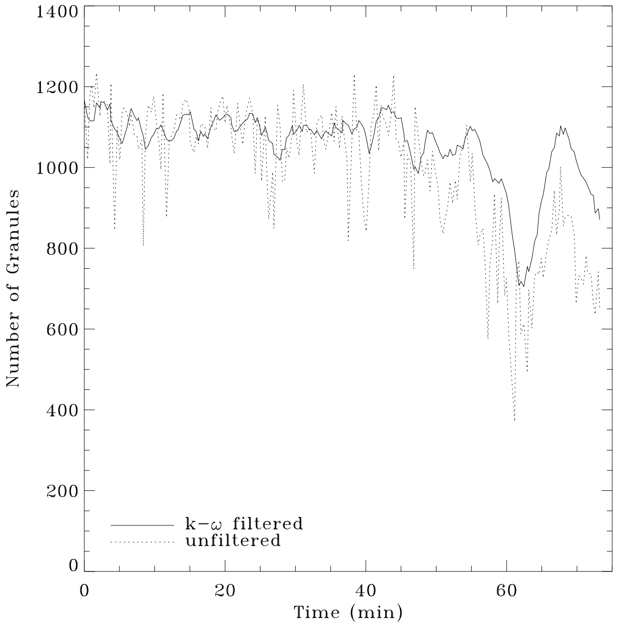

Fig. 7. Comparison of the number of granules for each image for raw data (dotted line) and for $k - \omega$ filtered data (solid line). The number of granules is defined as the number common to both images taken 'simultaneously'. We note that filtering attenuates the fluctuations and when atmospheric distortion increases, filtering reduces the losses of granules.

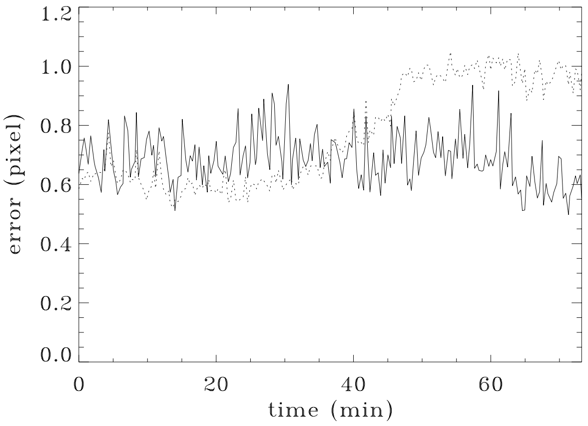

Fig. 8. Same as Fig. 5 but for destretching; solid line is for unprocessed data while dotted lines show the error (σ_x) with the destretched sequence. Note that when image quality is good ($t \leq 45$ min) errors remain of the same order of magnitude as in raw data but fluctuations are less important, while when image quality decreases ($t > 45$ min), errors increase.

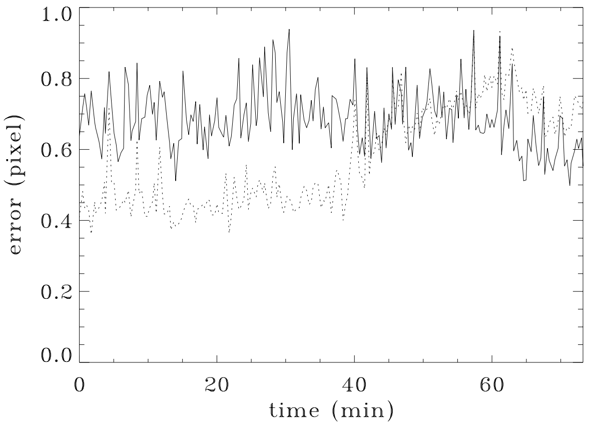

Fig. 9. Efficiency of destretching: the dotted line shows the difference between two simultaneous images when one has been destretched with other as reference. If destretching were perfect, this new error should be vanishing. Note that during the "bad sequence" there is no improvement at all.

at correcting the effects of atmospheric turbulence and allows us to compare images which are then plagued with the same distortion.

The pre-processing we use applies 4 successive corrections based on local correlation tracking with the following parameters: a FWHM of 31 pixels with a 62 pixel step, a FWHM of 62 pixels and a 31 pixel step, a 32 FWHM and a 16 pixel step, and then a FWHM of 20 pixels and a 10 pixel step. This combination has been established empirically and seems to give the best results. We remind that 62 pixels correspond to 7.75″ and 10 pixels to 1.25″.

Fig. 8 compares the error estimate on the granule positions in the x-direction between the destretched and raw time series. Quite clearly the destretched series does not compare favourably with the raw one. On the contrary, destretching seems to worsen the results when the image quality is slightly degraded (see in Fig. 2 the increase of distortion after t=45 min) as we see from the increasing error after t=45 min.

Actually, the poor performance of destretching on error reduction could be anticipated from the result displayed in Fig. 9. There we plot the mean distance between the granules in two simultaneous plates when one plate has been destretched to the other. If destretching were perfect the error would vanish. Clearly, this is not the case: in the sequence with 'intense' atmospheric turbulence the error is not reduced at all while during the good sequence a small factor 1.5 is gained. Therefore we interpret the error increase generated by destretching as the evidence that the destretching process decorrelates from the true displacement of granules and thus introduces a new random variable whose dispersion adds to the original signal as shown by the factor $\sqrt{2}$ taken by the error. This decorrelation may probably come from a change of scale of the distortion motions which is no longer matched by the destretching process optimized for the first frames of the sequence; **if this interpretation is correct, the destretching process would need a readjustment of the local correlation tracking parameters from time to time, making the whole processing very costly computationally**. The only good point introduced by destretching is the reduction of the fluctuations.

Resolution	σ_x	$\sigma_x(k-\omega)$
1.″25	0.72	0.42
2.″50	0.37	0.18
5.″00	0.28	0.11
10.″0	0.20	0.08

Table 2. Rms fluctuations of the position of granules on a typical pair of images shown for different resolutions with the multi-resolution analysis and with and without $k-\omega$ filtering. σs are given in image pixel. The 1.″25 resolution corresponds to unfiltered data.

4.2.3. Distortion noise at different scales

We have shown in Paper I that multi-resolution analysis was an interesting tool for the determination of flow structures. We may thus wonder how the distortion noise affects the different scales and therefore resists to wavelet filtering. Using maps such as the one in Fig. 6 we compute the different components of a multi-resolution decomposition as will be used in the analysis of the velocity field. Quantitatively we show in Table 2 the values of the distortion amplitude at different scales. This table shows again the importance of $k-\omega$ filtering in the reduction of errors, especially at large scales.

4.2.4. Conclusion

To conclude this section, two points should be underlined: on the one hand, destretching is certainly an unnecessary complication whose positive effect is only to reduce the noise fluctuations when correctly tuned to the distortion scales; otherwise it is likely to double the variance of the signal. On the other hand, $k-\omega$ filtering appears as the required pre-processing whose effect on noise reduction is clear. We surmise that when using time-sequences with a higher time-sampling the noise reduction by $k-\omega$ filtering will be even more efficient.

5. Propagation of errors from granule positions to the velocities

We have examined in the previous section the estimation of errors on the granule position. In this section, we study the propagation of these errors to the velocity of the granules, after averaging in time and over a given spatial range.

5.1. Error propagation

As seen above, the first step of the velocity computation in the CST algorithm is the determination of the position of granules on each image. The duration of the tracking of the k^{th} granule is given by $\Delta t_k = t_{n_f(k)} - t_{n_i(k)}$ where $n_i(k)$ and $n_f(k)$ are the image where the granule k appears and the image where it disappears, respectively.

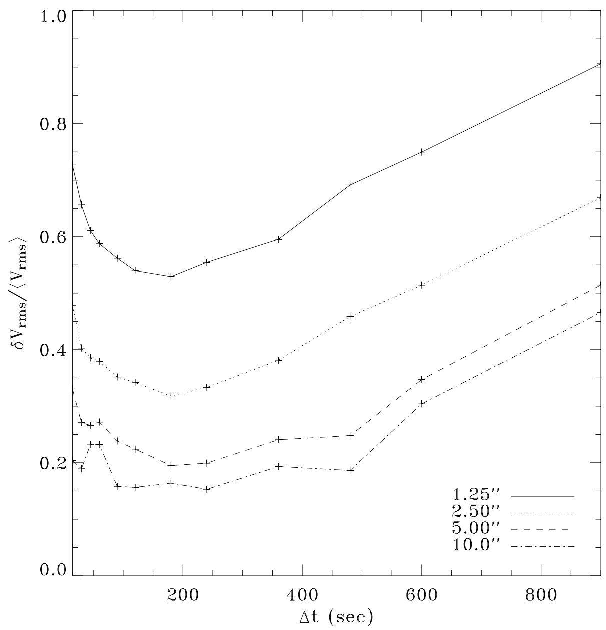

Fig. 10. Error on the x-component of the velocity as a function of the threshold on the granule lifetime. The different lines are for different resolution of the multi-resolution decomposition; the solid line shows the raw case (no wavelet filtering). The optimal threshold clearly appears around 3 min.

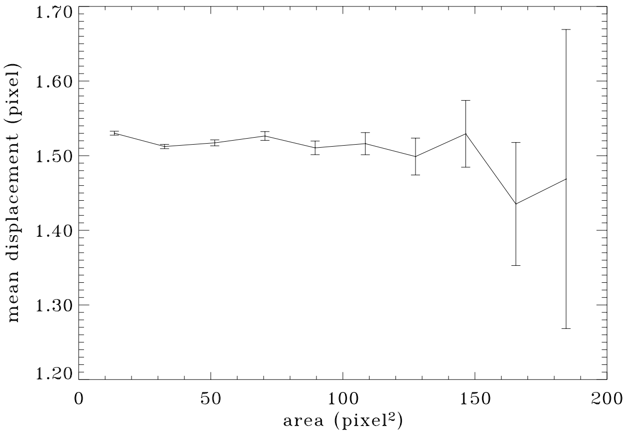

Fig. 11. Average distance between granule center of gravity of a pair of images as a function of the granule size.

Over an image granules are much less dense than pixels, thus the velocity field is sampled on a much coarser grid whose elements are of size δ. The velocity at a grid coordinate (x, y) is assumed to be the average of the velocity of granules whose average coordinates belong to the domain D around (x, y) (i.e. in $[x-\delta/2, x+\delta/2], [y-\delta/2, y+\delta/2]$). The spatial resolution of the velocity field is given by the mesh size δ. The x-component of the average velocity in D is given by:

$$V_{x_p} = \frac{1}{N}\sum_{k\in D} V_{x_k} = \frac{1}{N}\sum_{k\in D}\frac{x_{k,n_f(k)} - x_{k,n_i(k)}}{\Delta t_k}$$

where N is the number of trajectories falling in D. The uncertainty on the value of V_{x_p} is then:

$$\sigma^2_{V_{x_p}} = \frac{1}{N^2}\sum_{k\in D}\frac{\sigma^2_{k,n_i}+\sigma^2_{k,n_f}}{\Delta t_k^2}.$$

If we assume that the dispersion on the center of gravity remains the same for the whole time series (σ_x), and that the time interval Δt_k is the same for all granules (i.e. all granules have the same lifetime Δt), then the expression of the dispersion of the average velocity in x is:

$$\sigma^2_{V_{x_p}} = \frac{1}{N^2}\sum_{i\in D}\frac{2\sigma_x^2}{\Delta t^2} = \frac{2\sigma_x^2}{N\Delta t^2}.$$

In this case, the error on the velocity varies like

$$\delta V = \frac{\sqrt{2}\sigma_x}{\sqrt{N}\Delta t}. \qquad (1)$$

We see that precise velocity values need many granules in a grid element and a long time interval. In other words, errors are less if a coarse resolution in space and time is used. A trade-off must be found (see below) but it is clear that this technique will be more appropriate to slowly evolving large-scale flows than to rapidly varying small-scale ones.

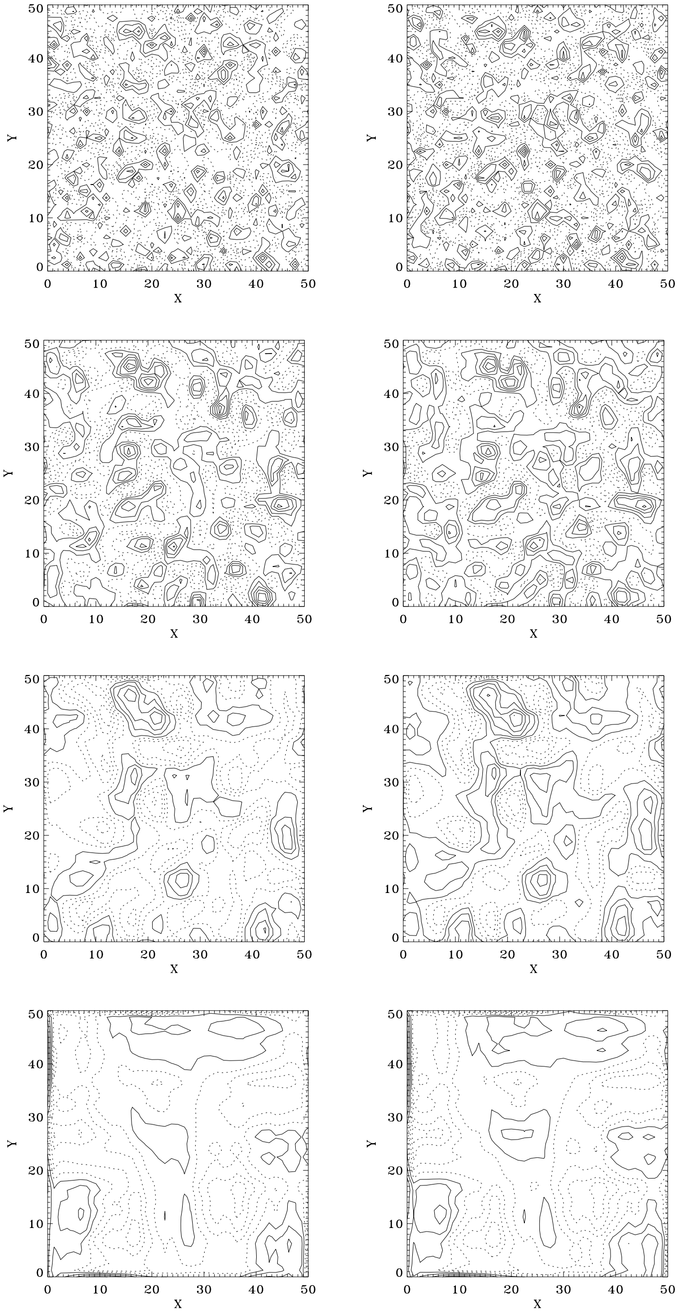

Fig. 12. Two views of the divergence field at different resolution. The difference between the left and right flow fields is the noise introduced by the Earth's atmosphere. In the first row no filtering has been applied and common features are barely identifiable. The following rows show filtered data according to multi-resolution representation (see Paper I) with a resolution divided by 2 from one row to the next. The mesh size is 10 pixels (1.″25) and the flow is an average over $\sim$ 1.5hr. X and Y are in arcsec.

5.2. Influence of the granule lifetime

However, all granules do not have the same lifetime (see for example Hirzberger et al. 1999 or Paper I). In this case, it may be more appropriate to select only a subsample of the granules. For example, in the simple case where half of the N granules have a lifetime Δa_t and the other half a lifetime $\Delta b_t = 2\Delta a_t$, the error on the velocity is:

$$\begin{aligned}\sigma^2_{a+b} &= \frac{1}{N^2}\left(\sum_{i\in D,\Delta t_i=\Delta a_t}\frac{2\sigma_x^2}{\Delta a_t^2}+\sum_{i\in D,\Delta t_i=\Delta b_t}\frac{2\sigma_x^2}{\Delta b_t^2}\right)\\ &= \frac{1}{N^2}\left(\frac{N\sigma_x^2}{\Delta a_t^2}+\frac{N\sigma_x^2}{4\Delta a_t^2}\right) = \frac{5\sigma_x^2}{4N\Delta a_t^2}.\end{aligned}$$

If we take into account only the $\frac{N}{2}$ granules with the largest lifetime Δb_t, we obtain:

$$\begin{aligned}\sigma_b^2 &= \frac{2^2}{N^2}\sum_{i\in D,\Delta t_i=\Delta b_t}\frac{2\sigma_x^2}{\Delta b_t^2} = \frac{4}{N^2}\frac{N\sigma_x^2}{4\Delta a_t^2}\\ &= \frac{\sigma_x^2}{N\Delta a_t^2} \le \sigma^2_{a+b}.\end{aligned}$$

Therefore, the errors are smaller when considering only the granules with the largest lifetime.

This result shows that some selection on "valid granules" may improve the quality of the velocity field. We thus impose a lower threshold on granule lifetime to eliminate short-lived structures. This threshold has to be determined empirically and depends on the filling factor of the grid (we need to avoid grid points with no data, see Paper I). This strategy may be improved by computing the average velocity for various thresholds, starting with the largest one. Since granules with long lifetimes are rare the number N is small and the error is large. By reducing

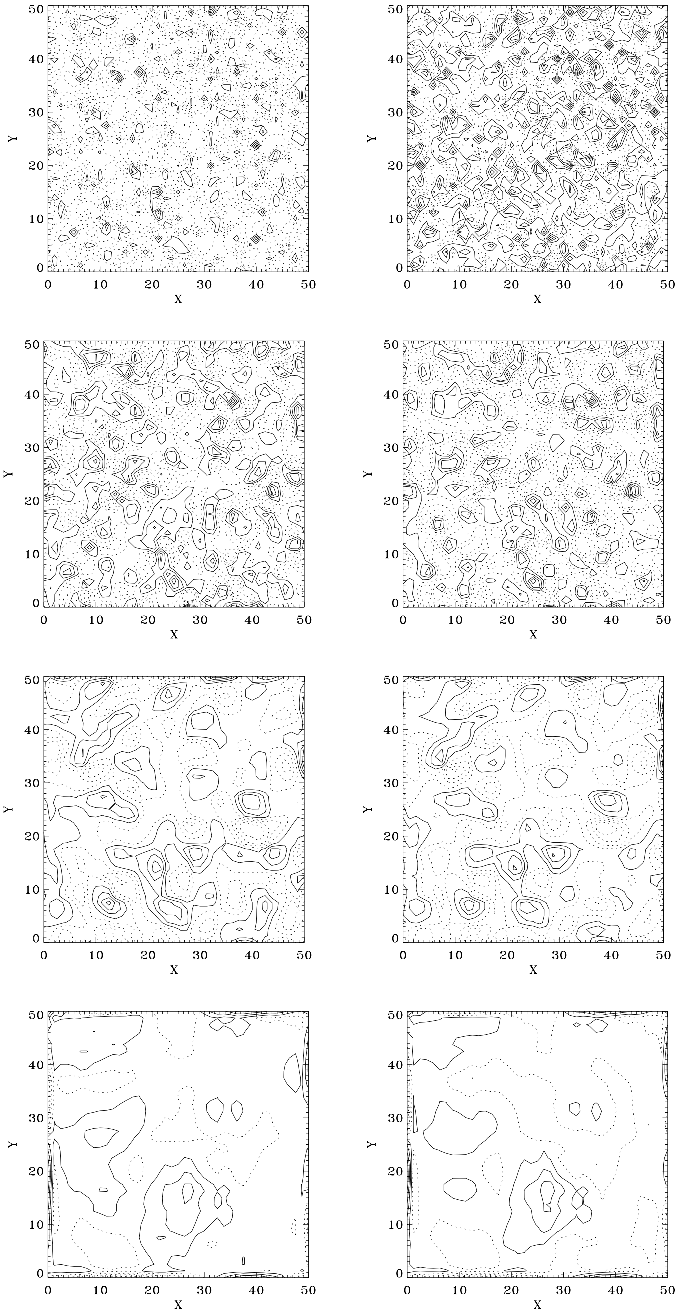

Fig. 13. Same as in Fig. 12 but for the z-component of the curl field.

the threshold, the number of granules increases rapidly and the error decreases. For some optimal threshold the error ceases to decrease as the increase in granules number no longer compensates the diminishing value of Δt (see Eq. 1). This process is illustrated in Fig. 10 where we show the dispersion of velocity differences between the two independent data sets as a function of the threshold on the granule lifetime. Clearly, for these data the optimal threshold is around 3 min.

5.3. Influence of the granule size

It is also interesting to study the influence of the granule size on the error on the granule center of gravity. We would expect a smaller error in the case of large granules, as these are defined by a larger number of pixels. A selection on the granule size could then also improve the precision on the velocity field. Fig. 11 shows an estimation of the error on the granule position for various granule size intervals. The precision increases only slightly with the granule size, the improvement is at most 0.05 pixels. This means that the error on the velocity will not change much either. This small improvement on the error is too weak to compensate the increase of the error on the velocity due to the decrease in the number of granules as their size increases.

6. Error propagation to the final maps

Following the algorithm described in Paper I (but see also Sect. 5.1), we now compute the velocity fields of the two independent time series at different resolution (see Paper I). A comparison between the two fields shows the influence of the distortion induced by the Earth's atmosphere and the efficiency of MRA in revealing the flow patterns at the different scales. The results are illustrated by Fig. 12 and Fig. 13 which show the horizontal divergences and the vertical component of vorticity respectively.This flow field is the average velocity over a $\Delta t = 87$ min time lapse including the preceding sequence and with no distinction between the "bad" and "good" sequences. Actually, we first computed the velocity fields using the "good" sequence and then extended the computation to the whole set. We observed that the dispersion between the two independent sequences was still reduced when using the whole set of data showing that, for the determination of the large-scale mean flow, the observed degradation in the distortion is not influential.

In Table 3, we summarize quantitatively the dispersion of the results as a function of the resolution for unfiltered images. This table shows the decreasing influence of distortion with increasing scale. It also shows that, as expected, velocity gradients (divergence and the z-component of the vorticity) suffer much more from the noise and that the curl is certainly the most sensitive quantity to image quality. The values of the correlations between the results issued from the two independent series indicate quantitatively the similarity of the fields. Here too, filtered fields are much better correlated, up to 90% on the velocity field. As shown below this correlation is still improved when using $k - \omega$ filtered data.

In this table, we also give a 'turbulent velocity'; this is the mean rms dispersion of granule velocities. Indeed, in each velocity pixel we take the mean velocity of the granules falling in this very pixel; however, while computing this mean velocity, we also have access to the dispersion around this mean. This mean (over the whole field-of-view) dispersion represents the random motion of granules around their drift by large-scale flows. This table shows

Resolution	(pixel size)	$V_{\rm rms}$	C_v	(Div V)$_{\rm rms}$	C_d	(Curl V)$_{\rm rms}$	C_c	Turbulence
1.25″	920 km	700±695	0.49	7.1±7.0	0.45	5.7±7.0	0.22	880±224
2.50″	1840	478±342	0.74	3.8±2.8	0.69	2.9±3.0	0.45	893±122
5.00″	3680	340±172	0.87	1.6±0.9	0.89	1.2±0.9	0.73	890±94
10.0″	7360	205±92	0.90	0.58±0.24	0.94	0.41±0.24	0.85	896±65

Table 3. With the whole time series (87 min), using a velocity pixel of 1.25″ and removing all granules with a lifetime less than 180 s, we compute the rms velocities, divergences and curls, of the maps issued from the multi-resolution decomposition. The first row shows raw data (no wavelet filtering) while the next rows shows the numbers issued from the wavelet-filtered maps. Velocities are in m/s, divergence and curl in 10^{-4}s^{-1}. C_v, C_d and C_c are the correlations between the results of the two independent series of images. The "uncertainties" shown along the numbers give the amplitude of the fluctuations generated by the Earth's atmospheric distortion. "Turbulence" indicates the mean rms velocity (in m/s) of granules around their mean trajectory.

Resolution	(pixel size)	$V_{\rm rms}$	C_v	(Div V)$_{\rm rms}$	C_d	(Curl V)$_{\rm rms}$	C_c	Turbulence
1.25″	920 km	597±330	0.85	6.8±4.2	0.81	5.0±4.2	0.66	680±193
2.50″	1840	466±162	0.94	4.0±1.7	0.91	2.7±1.7	0.81	692±105
5.00″	3680	350±80	0.97	1.8±0.4	0.97	1.2±0.4	0.95	689±78
10.0″	7360	209±40	0.98	0.63±0.1	0.98	0.42±0.1	0.96	694±53

Table 4. Same as Table 3 but for $k-\omega$ filtered data. Note the reduction of the dispersion of the results.

Resolution	(pixel size)	$V_{\rm rms}$	C_v	(Div V)$_{\rm rms}$	C_d	(Curl V)$_{\rm rms}$	C_c	Turbulence
0.″875	644 km	722±534	0.73	11±9.7	0.64	10±9.7	0.54	528±288
1.″75	1288	528±258	0.88	6.3±3.7	0.83	4.5±3.8	0.65	532±143
3.″50	2576	403±128	0.95	2.7±0.9	0.94	1.8±0.9	0.87	533±75
7″	5152	284±65	0.97	1.2±0.3	0.97	0.7±0.3	0.94	533±45

Table 5. Same as Table 4 but for a smaller velocity pixel. The more intense fluctuations compared to Table 4 come from the smaller scales involved. We give this table as it shows the parameters at the scale of ∼2500 km where granules trace the large scale motions. The weaker "Turbulence" values come from the empty bins which are more numerous.

that although this quantity suffers (also) from image quality, it is almost independent of scale. This independence of scale is expected since this quantity measures the proper motion of granules and therefore their intrinsic kinetic energy which should not vary from place to place.

Table 4 give the same quantities but for the $k-\omega$ filtered sequence. We note the strong reduction of the noise, almost a factor 2, at all scales and the strong improvement of correlation between the results of the two independent series. Moreover, the dispersion of the velocities is reduced in the same proportion as displacement of granules (i.e. $\frac{330\mathrm{m/s}}{695\mathrm{m/s}} \sim \frac{0.4\mathrm{pix.}}{0.7\mathrm{pix.}}$). The comparison of the values of turbulence in Tab. 4 and Tab. 3 shows the influence of the Earth's atmospheric noise on the random motion of granules.

Table 5 gives another view of this velocity field using a smaller mesh size. Here we computed the velocity amplitudes which are traced by granules when they can be considered as passive scalars, i.e. at a scale larger than 2500 km. Numbers show that at that scale the velocity field has an amplitude of 400 m/s and that such a measurement is still uncertain by 30%; this is about the same for the divergence but it rises to 50% for the vorticity.

These results show that, when independent images series are available, the use of the CST algorithm authorizes a tight control on the role of the noise induced by the Earth's atmospheric distortion.

7. Conclusions

In this paper we have tried to show the various influences of the noise generated by the Earth's atmosphere when one measures the horizontal velocity field at the surface of the sun through granule tracking.

For this purpose we compared two time series of images of the solar surface separated by at most a few seconds; they thus represent the same solar signal but with a different noise (essentially distortion from the Earth's atmosphere). We measured the position of the granules in the two time series and used these data to determine the amplitude of the noise. We could thus test the pre-processing that could be applied first to the images, namely a $k-\omega$ filtering and the destretching. The comparison between the pre-processed series and the raw one allowed us to evaluate the efficiency of the pre-processing. It turns out that $k-\omega$ filtering significantly reduces the noise while destretching, even if reducing the fluctuations, not only cannot reduce it, but amplifies it when distortion increased.

We also found that the CST algorithm which tracks coherent structures (essentially granules), could easily go across sequences of images with decreased image quality. This is because all granules are not affected evenly by distortion and granules whose trajectories are too much perturbed by atmospheric noise are eliminated; they thus do not input noise in the final velocity field. This is clearly a feature that algorithms based on local correlations of images cannot authorize.

We also studied how the distortion noise affecting granules positions introduces some noise on the interpolated velocity fields. We thus showed that the lifetime of granules was an important parameter and that short lived granules should be eliminated; the trade-off between granule number (the more numerous the granules, the better sampled the velocity field) and noise intensity seems to be, for our sequence, around 3 min. It is clear that if the atmospheric noise is more intense this threshold should be increased. With the decomposition of the velocity on the Daubechies wavelets (see Paper I), we could evaluate the impact of the noise at different scales and showed that errors on velocities decrease with increasing scale as expected. More precisely, we could show that at a scale of 2500 km, i.e. at the scale where granule motions trace the large scale flows (Rieutord et al., 2001), the typical velocities, around 400 m/s, are still noised at a 30% level. Nevertheless, one can recognize, on the wavelet-filtered maps, common patterns between the two time series, all the more easily that the scale is large.

The next steps are now obvious: with new cameras with fast reading sensors (like CMOS), it is easy to increase the time sampling by a factor 10. In this case the $k-\omega$ filtering will be much more efficient at reducing the noise on granule motion. Hence, with an increased time-sampling we expect to reduce the noise in two ways: first, by an improved efficiency of the $k-\omega$ filter and second by a factor $\sqrt{N}$ from the N images sharing the same solar signal.

The tools developed here seem to perform quite efficiently on the numerical side and therefore allow for the treatment of much larger fields of view.

Finally, we did not discuss the results in terms of solar turbulence. Let us mention that numbers, like the amplitude of velocity at a 2.5 Mm scale, are in agreement with previous determinations (e.g. Brandt et al., 1991). However, it is clear that (solar) fluid mechanics should be discussed, as for instance the scale dependence of flow features; this is beyond the scope of this paper but will be the subject of forthcoming work.

Acknowledgements. RT wishes to thank the French ministery of education for its financial support through the CALAS project. We are most grateful to Peter Brandt who kindly allowed us to use the extraordinary eleven-hours sequence obtained at the SVST of La Palma.

References

Brandt, P., Ferguson, S., Scharmer, G., et al. 1991, Astron. & Astrophys., 241, 219
Dorotovič, I., Sobotka, M., Brandt, P. N., & Simon, G. W. 2002, A&A, 387, 665
Getling, A. V. & Brandt, P. N. 2002, A&A, 382, L5
Hirzberger, J., Bonet, J. A., Vázquez, M., & Hanslmeier, A. 1999, ApJ, 515, 441
November, L. J. & Simon, G. W. 1988, Astrophys. J., 333, 427
Potts, H. E., Barrett, R. K., & Diver, D. A. 2003, Sol. Phys., 217, 69
Rieutord, M., Roques, S., Roudier, T., & Ducottet, C. 2007, submitted to AA, 1
Rieutord, M., Roudier, T., Ludwig, H.-G., Nordlund, Å., & Stein, R. 2001, Astron. & Astrophys., 377, L14
Roudier, T., Lignières, F., Rieutord, M., Brandt, P. N., & Malherbe, J. M. 2003, A&A, 409, 299
Simon, G. W., Brandt, P. N., November, L., Scharmer, G. B., & Shine, R. A. 1994, in Solar Surface Magnetism, ed. R. Rutten & C. Schrijver (Kluwer), 261
Simon, G. W., Brandt, P. N., November, L., Shine, R., & Strous, L. 1995, in Proc. of 4th SOHO Workshop: Helioseismology (ESA SP-376), 223
Sobotka, M., Brandt, P. N., & Simon, G. W. 1997a, A&A, 328, 682
Sobotka, M., Brandt, P. N., & Simon, G. W. 1997b, A&A, 328, 689
Sobotka, M., Brandt, P. N., & Simon, G. W. 1999a, A&A, 348, 621
Sobotka, M., Vázquez, M., Bonet, J. A., Hanslmeier, A., & Hirzberger, J. 1999b, ApJ, 511, 436
Title, A. M., Tarbell, T. D., & Topka, K. P. 1987, ApJ, 317, 892

A&A 467, 1289–1298 (2007)
DOI: 10.1051/0004-6361:20066649
© ESO 2007

Astronomy & Astrophysics

Photospheric flows around a quiescent filament

S. Rondi[1], Th. Roudier[1], G. Molodij[2], V. Bommier[3], S. Keil[5], P. Sütterlin[4], J. M. Malherbe[2], N. Meunier[1], B. Schmieder[2], and P. Maloney[5]

[1] Laboratoire d'Astrophysique de l'Observatoire Midi-Pyrénées, Université Paul Sabatier Toulouse III, CNRS, 57 Avenue d'Azeirex, BP 826, 65008 Tarbes Cedex, France
e-mail: `roudier@ast.obs-mip.fr`
[2] LESIA, Observatoire de Paris, Section de Meudon, 92195 Meudon, France
[3] LERMA, Observatoire de Paris, Section de Meudon, 92195 Meudon, France
[4] Sterrekundig Instituut Utrecht, Postbus 80 000, 3508 TA Utrecht, The Netherlands
[5] National Solar Observatory, Sacramento Peak, Sunspot, NM 88349, USA

Received 27 October 2006 / Accepted 1 March 2007

ABSTRACT

Context. The horizontal photospheric flows below and around a filament are one of the components in the formation and evolution of filaments. Few studies exist because they require multiwalength time sequences at high spatial resolution.
Aims. Our objective is to measure the horizontal photospheric flows associated with the evolution and eruption of a filament.
Methods. We present observations obtained in 2004 during the international JOP 178 campaign which involved eleven instruments both in space and at ground based observatories. We use TRACE WL, DOT and DST observation to derive flow maps which are then coaligned with intensity images and with the vector magnetic field map obtained with THEMIS/MTR.
Results. Several supergranulation cells cross the Polarity Inversion Line (PIL) and can transport magnetic flux through the PIL, in particular parasitic polarities. We present a detailed example of the formation of a secondary magnetic dip at the location of a filament footpoint. Large-scale converging flows, which could exist along the filament channel and contribute to its formation, are not observed. Before the filament's eruptive phase, we observe both parasitic and normal polarities being swept by a continuously diverging horizontal flow located in the filament gap. The disappearance of the filament initiates in this gap. Such purely horizontal motions could lead to destabilization of the filament and could trigger the sudden filament disappearance.

Key words. Sun: atmosphere – Sun: filaments – Sun: granulation – Sun: magnetic fields

1. Introduction

Filaments (prominences seen on the limb) which are common solar features always occur along lines where the underlying photospheric magnetic field changes sign. They represent regions where magnetic fields are interacting with the plasma in a subtle way in the different parts of the solar atmosphere. The filament's existence in the corona is mainly due to magnetic fields that support dense material against gravity inside dipped arcade loops or flux tubes (Kuperus & Raadu 1974). The filaments are structures of the solar corona which are anchored at footpoints in the solar photosphere. These footpoints connect with the photosphere with a periodicity of few tens of Mm, which relates to their connection with supergranules (Plocieniak & Rompolt 1973; Aulanier et al. 1998). Several theorical investigations have proposed models for the formation of filaments based on converging flows produced by turbulence convection in the photosphere (Van Ballegooijen & Marten 1989; Choe & Lee 1992; Ridgway & Priest 1993). Knowledge of photospheric motions over long periods is needed to understand the action of the plasma on the filament. In particular, barbs, footpoints of prominences when observed on the disk, are always associated with parasitic polarities (Martin & Echols 1994; Aulanier et al. 1998, 1999, 2000; Martens & Zwaan 2001) implying a reversal of the transverse horizontal magnetic field. The mechanism generating such magnetic configurations must take into account photospheric motions. Martres et al. (1981) found a photospheric velocity field beneath a filament in which lines of zero radial velocity were roughly perpendicular to the direction of the filament. Martin et al. (1985) observed that the formation and evolution of filaments is linked to converging photospheric motions perpendicular to the polarity inversion line (PIL). The successive emergence and cancellation of minor polarities in filament channels have been used to explain the formation and the disappearance of a part of a filament (Schmieder et al. 2006).

In reponse to these observations new theories of filament formation have been developped (Van Ballegooijen 2004; Martens & Zwaan 2001; Priest 1997; Aulanier et al. 1998; Kuijpers 1997; Ridgway & Priest 1993). From a theoretical point of view, the field line footpoints are subjected to shearing flows parallel to the PIL (Ridgway & Priest 1993; Mackay et al. 2000; Mackay & van Ballegooijen 2006). Some of these models include converging photospheric motions that allow the magnetic configuration to support a dense plasma in the corona.

Most observational studies of filaments have been carried out to describe their properties and structures in the corona and chromosphere. However, the magnetic field contributing to the formation of the filaments can transfer photospheric perturbations into the corona. Very few papers exist on the determination of photospheric motions beneath and in the vicinity of filaments. Such measurements require multi wavelength observations. We use the method described in Roudier et al. (1999) to measure the horizontal flows in the photosphere in the present paper.

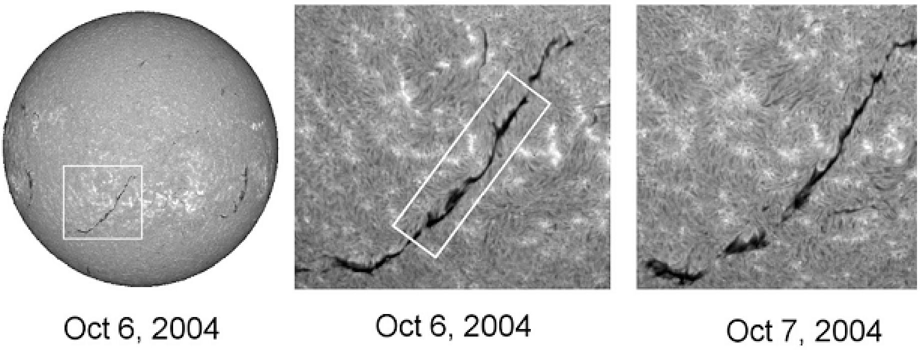

Fig. 1. (*Left*) The position of the target filament indicated on an Hα image observed by ISOON on October 6 2004 and (*middle and right*) the filament region in the ISOON data on October 6 and 7, 2004 showing how it evolved. The field of view of the DOT filament mosaic shown in Fig. 2 is indicated in the *middle* image.

The pioneering investigation carried out by Molowny-Horas (1994) on the dynamics of filaments and the underlying photosphere, using photospheric data with moderate resolution, revealed horizontal flows aligned with the direction of the filament and with similar velocity distributions on either side. As distance from the neutral line increases, Molowny-Horas found that parallel flows become less pronounced, and show more of the complex mesogranulation and supergranulation velocity fields. His investigation did not detect any systematic large-scale photospheric motion converging towards the neutral line. The detailed observations of Magara & Kitai (1999) show evolving, random photospheric motions around the filament channel. They also do not find any convergence toward the filament channel. On the other hand, they observed some unsteady shearing motions around the filament with lifetimes less than 6 h. Recently the OSLO group (Lin et al. 2005) used the Swedish Solar Telescope (SST) to study photospheric flows. They found that flows along network cell boundaries are directed predominantly from one side of the PIL to the other.

Using MSDP data, Malherbe et al. (1983a) found that long-lived upward motions often occur in the core of the quiescent filaments. They suggested that such flows (1 km s^{-1}) could be related to converging motions in the photosphere and that they are supported by the magnetic field when inverse polarity fields are present (as in the case for most filaments).

In this paper we investigate a filament observed over a large field of view with high spatial resolution. The observations and coalignment between all involved instruments are explained in Sect. 2. The description of horizontal photospheric flows below and in the neighborhood of the filament is illustrated in Sect. 3. The location of the filament relatively to the photospheric network is described in Sect. 4 and formation of parasitic polarities is discussed in Sect. 5. We present in Sect. 6 the photospheric and chromospheric context of the filament eruption on October 7, 2004. Finally, Sect. 7 contains a summary and discussions of the results.

2. Observations and data processing

2.1. Description of data and instrumentation

Our data come from a combination of ground and space based telescopes on October 6–8, 2004 during a JOP 178 campaign (`http://bass2000.bagn.obs-mip.fr/jop178/index.html`). The target was a quiescent filament seen in Fig. 1 at solar coordinates S16E11 (on Oct. 6). This target was observed by the Dutch Open Telescope (DOT), THEMIS, the Meudon Solar Tower (MST), The Dunn Solar telescope (DST), the Improved Solar Observing Optical Network (ISOON), TRACE and SOHO/MDI/EIT. All of these instruments tracked this target and observed its eruption on October 7 at approximately 16:30 UT.

Table 1 summarizes the characteristics of all the JOP 178 observations used for our analysis. The ground-based observations are summarized below. The four DOT cameras recorded the same field of view in the G-band, blue continuum, red continuum, Ca II H line center (passband 0.128 nm, Rutten et al. 2004; see Leenaarts et al. 2006, for detail). DOT Hα line center observations on October 6, 2004 at 8:50 UT were used to construct the mosaic in Fig. 2 (Rutten et al. 2004, `http://www.dot.iac.es/`). THEMIS (`http://www.themis.iac.es/`) obtained polarimetric and Doppler measurements of this region on October 6–8, 2004. The MSDP spectrograph at MST obtained Hα Doppler velocities of the target on October 6. The DST located at Sacramento Peak (`http://www.nso.edu/`) obtained high-resolution G-band and Hα time sequences of the target on Oct. 6 and 7, 2004. ISOON, also at Sacramento Peak, (`http://nsosp.nso.edu/isoon/`), observed the target in Hα full-disk mode on October 6 and 7, 2004.

Observations from space were obtained with TRACE (`http://trace.lmsal.com/`) and SOHO/MDI (`http://sohowww.nascom.nasa.gov/`) and are summarized below and in Table 1. TRACE observed the filament region almost continuously on October 6 and 7, 2004. The MDI on board SOHO provided a full-disk longitudinal magnetogram every minute and EIT full-disk observations on October 6 and 7, 2004.

2.2. Coalignment of the data

We have coaligned successively all of the data obtained by the different instruments. Our primary goal was to derive the horizontal flow field below and in the vicinity of the filament. Therefore, we had to coalign the white light (WL) TRACE data with the Hα observations from DOT, DST and ISOON. In order to achieve this coalignment, we applied different strategies for each of the ground-based instruments. For the DOT, we first coaligned the CaII H (3968 Å) and 1600 Å TRACE observations by using the chromospheric network as a reference. THEMIS and DOT data were coaligned by precisely overlapping the filament visible in Hα in both observations. The time difference between the DOT (8:35) and THEMIS (10:06 to 11:09)

Table 1. October 6–8 2004.

Telescope	Datatype	Field of view	Pixel size	Cadence	Time UT
DOT	G-band	85″ × 323″	0.071″	30 s	8:50 October 6
	blue Continuum				
	red Continuum				
	CaIIC H line center				
	Hα			60 s	
	(simultaneously)				
THEMIS	Magnetic field	120″ × 360″	0.43″ along the slit	irregular	10:06–11:09 October 6
	Doppler velocity		0.8″ in the		9:10–10:13 October 7
	(simultaneously)		scanning direction		10:44–11:35 October 7
	FeI 6302Å				14:30–15:17 October 7
	Hα				8:30–11:35 October 8
MEUDON MSDP	Hα Doppler velocity	240″ × 420″	0.5″	30 s	13:12–13:42 October 6
DST	G-band	83″ × 83″	0.101″	20–30 s	15:11–17:11 October 6
	Hα		0.171″		14:48–16:48 October 7
ISOON	Hα	full-disk	1.077″	1 min	14:05–22:35 October 6
					13:37–22:35 October 7
TRACE	white Light	384″ × 384″	0.5″	30–180 s	continuous October 6
	Continuum 1600 Å				continuous October 7
	Fe IX-X 171 Å				
	Fe XII 195 Å				
	(not simultaneously)				
MDI/SOHO	magnetogram	full-disk	1.96″	1 min	20:49–23:49 October 6
	Doppler velocity				9:44–22:50 October 7
	NiI 6768 Å			96 min continuous	October 6 and 7
EIT/SOHO	He II 304 Å	full-disk	2.63″	4 fr/h	continuous October 6
	Fe IX-X 171 Å				continuous October 7
	Fe XII 195 Å				

observations is small enough that the filament maintains its shape sufficiently to allow coalignment of these data at the ±1″ level. To control the quality of this coalignment, we also compared the bright regions in the CaII H and in the G-band, with the magnetic maps from THEMIS. To use TRACE WL data to measure horizontal flow with respect to the filament on ISOON observations, the alignment was performed in two steps: first we coaligned the DST G-band and 1600 Å TRACE data; second, we coaligned the Hα filament and the bright features visible simultaneously on DST and ISOON observations. This enabled us to coalign TRACE and ISOON data at ±1″.

The co-alignment between SOHO/MDI magnetograms and ISOON Hα images was performed by adjusting the chromospheric network visible in Hα (ISOON) and the amplitude of longitudinal magnetogram of MDI with an accuracy of one pixel (1.96″).

2.3. Filtering and velocity field

We have extracted time sequences of TRACE WL data to correspond with the respective Hα observations. The subsets of the TRACE WL sequence used to obtain the horizontal velocities are respectively: from 7:45 to 10:06 UT on October 6, 2004 corresponding to the DOT observations, from 14:48 to 17:31 UT on October 6, 2004 corresponding to ISOON observations and from 13:30 to 18:05 on October 7, 2004 also corresponding to ISOON observations. The TRACE WL images were rigidly-aligned and filtered for p-modes in $k - \omega$ space (threshold phase velocity of 4 km s^{-1}) to remove five-minute oscillations. Next, horizontal flow vectors were derived using local correlation tracking (LCT, November & Simon 1988). The flow velocities were derived using a correlation window of 3″ × 3″ corresponding to a scale that can faithfully track granules (Rieutord et al. 2001). As the (measured) velocity field is purely two-dimensional, two quantities are relevant to describe flow structures: these are the divergence $D = \partial_x v_x + \partial_y v_y$ and the z-component of the vorticity $\zeta = \partial_x v_y - \partial_y v_x$. The MDI data were also rigidly aligned and filtered for p-modes in $k - \omega$ space in the same manner used for the TRACE WL data.

3. The photospheric flow pattern below and in the neighborhood of the filament

Figure 2 shows a mosaic at 8:50 UT of the Hα filament structure that was observed in the southern solar hemisphere (S16E11) on October 6, 2004 during the decaying phase of the solar cycle. This filament has a sinistral chirality which is a normal configuration in that hemisphere. The smallest chromospheric features on the image show that the angular resolution is around 0.5″ over the field of view of 95″ × 323″. The 5″ radius circles indicate the region of apparent footpoints.

As a way to visualize the horizontal flow, we introduce passive scalars (corks), and allow them to move with the local horizontal velocity over extended time periods. The corks eventually arrange themselves into a network at supergranular scale. Figure 3 shows the cork trajectories resulting from the measured horizontal velocities over a period of 5 h superimposed on the location of the filament. The distribution of horizontal velocity amplitude lies between 0 and 1.2 km s^{-1} and peaks at 0.3 km s^{-1}. We observe that the corks are expulsed from diverging cells with dimensions corresponding from meso- to super-granular scales as expected. Some of the cork trajectories cross the filament at various locations along its length. The divergence map (Fig. 3) does not exhibit any peculiar behaviour below the filament and indicates that the horizontal flow is similar over the entire field of view.

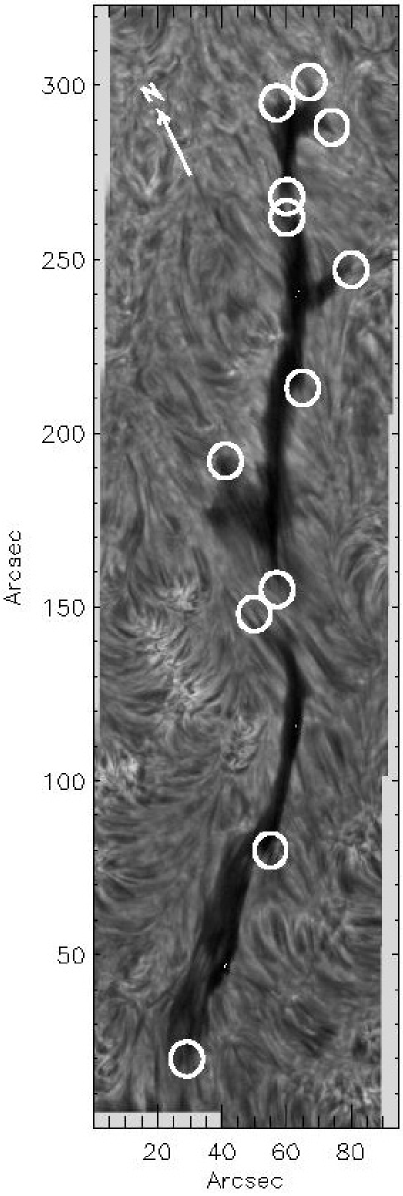

Fig. 2. A mosaic of the filament in Hα observed with the DOT, made from 6 frames selected at about 8:50 UT on October 6, 2004. The circles indicate the footpoint locations of the filament. The arrow indicates solar north.

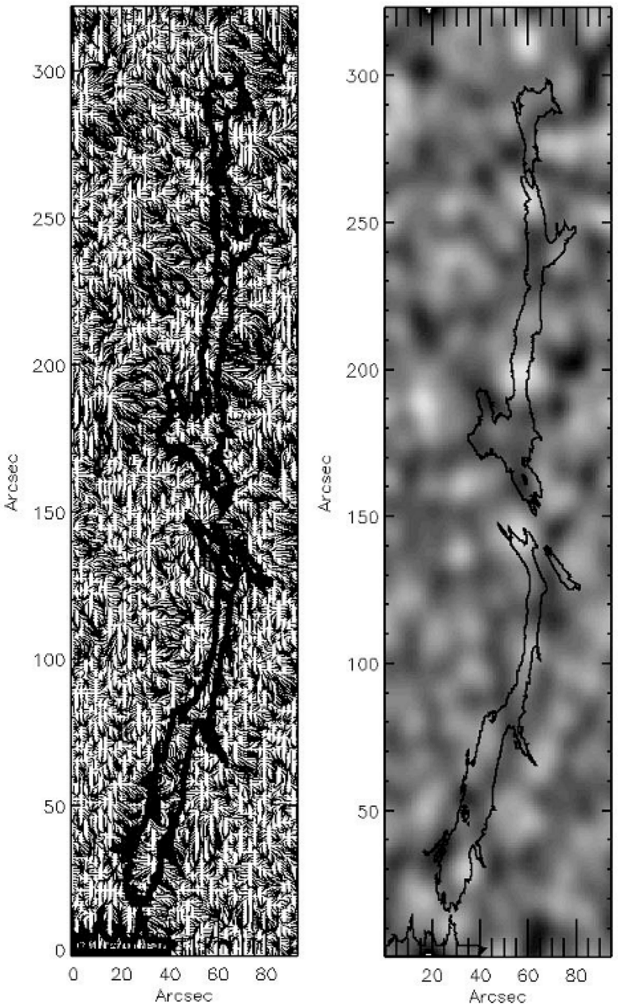

Fig. 3. (*Left*) cork trajectories (passive scalars) computed from horizontal velocities obtained by tracking the TRACE WL data over a 5 h period are superimposed on the location of the filament (thickline, isocontour in the Hα intensity map) observed with the DOT. *On the right*, divergence map computed from the horizontal photospheric velocities (TRACE data) superimposed on the location of the filament observed with the DOT. Bright are diverging and dark converging flow.

Figure 4 shows the location of the filament observed in Hα by ISOON later in the afternoon on October 6, 2004, superposed on the divergence field derived from the horizontal velocities measured on TRACE WL data. As was the case with the DOT data taken earlier on October 6, we do not observe peculiar photospheric motions below or in the neighborhood of the filament. We observe the well-known pattern of meso- and super-granular cells everywhere. In particular, neither set of observations reveal the predicted large-scale converging flows often invoked in filament formation. Using larger temporal windows for avering the horizontal flow window or using larger spatial windows to compute the velocity field with the LCT algorithm did not change the result. One explanation could be that we observed a mature filament that was not in its early formation phase. However, at a few locations along the filament, we observe areas of strong divergence, three of which particularly stand out in the top part of the filament. For example the structure at the coordinates (55, 149) in Fig. 3 (DOT data) remains visible in Fig. 4 at about 15–16 UT, i.e. 6 h later at the coordinates (210, 170) and also in the DST data (not shown). The divergence at (55, 149) is located in a gap of the filament which separates two main footpoints. The divergence at (58, 259) in the DOT data is located where the filament breaks up later in the afternoon, as seen in the ISOON data. This could indicate that divergent flow contributes to the creation and maintenance of the gap in the filament.

Finally, Fig. 5 shows the vorticity of the horizontal flow relatively to the filament. We note that in our observations the footpoints of the filament are generally located in areas of positive vorticity. However, we also see a strong negative vorticity in the lower part of the filament at the location (40, 60).

4. Filament and network, and chromospheric dynamic of the filament

In this section, we compare the network obtained by tracking passive corks in the measured photospheric flow field with

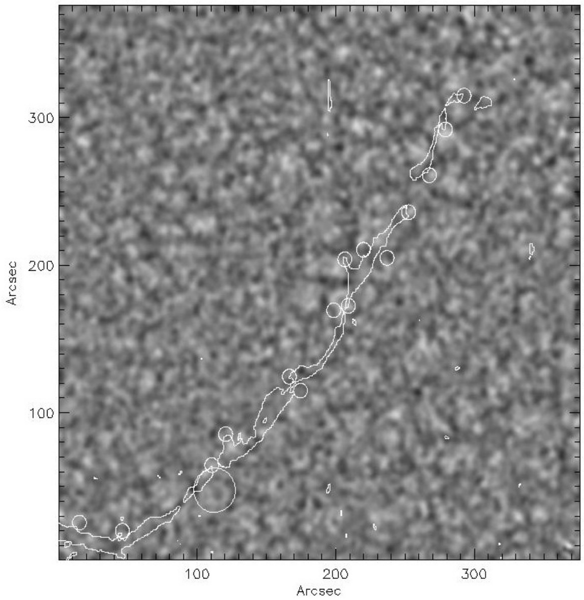

Fig. 4. A divergence map computed from the horizontal photospheric velocities on October 6, 2004 between 14:48 and 17:31 UT, using the TRACE WL data the location of the filament seen in Hα by ISOON superimposed. Bright areas are diverging and dark areas are the converging flow. Solar north is located at the top of the figure. The large white circle indicates the location of the divergence which is still visible on Oct. 7 2004, while the smaller circles show the filament footpoints.

properties of the chromosphere around the filament. Following Lin et al. (2005), we assume that sub-structure seen in Hα at semi-regular spacing pointing away from either side of the main filament body, the so-called barbs, represent magnetic footpoints that connect into the photosphere. Our objective in this section is two fold: to verify the quality of the coalignment between the various data sets, and to compare the location of the barbs with the network boundaries, irrespective of polarity considerations. We then describe the evolution of the chromospheric properties of the filament with respect to the filament footpoints in the photosphere. The following section discusses the magnetic field associated with the filament.

Figure 6 shows the final location of the corks after propagating for 5-h in the flow field (computed from TRACE data), superimposed on a CaII map. In this figure, we verify the colocation of the network formed by the corks with the bright CaII features representing the chromospheric network. The small differences between the cork positions and bright CaII features is partly due to the short interval (5 h) over which the corks were allowed to propagate compared to the much longer lifetime of the chromospheric network. The good correspondence between the corks and the CaII network confirms the alignment between the observations from the different ground and space-based instruments.

Similarly, Fig. 7 shows the final location of the corks superimposed on the Hα filament as seen by ISOON later on October 6, 2004. The figure shows a rather good correlation between cork location and the magnetic network visible as bright features at superganular boundaries.

At the photospheric level, the solar granulation does not exhibit any special behaviour below or near the filament. However, several supergranulation cells are seen to cross the PIL as observed by Lin et al. (2005). The 5″ radius circles in Fig. 6 indicate the locations of apparent end points of the filament barbs. We find that 75% of the observed barb end points fall within the network boundaries (defined both by corks and CaII), which is in good agreement the earlier findings of Lin et al. (2005).

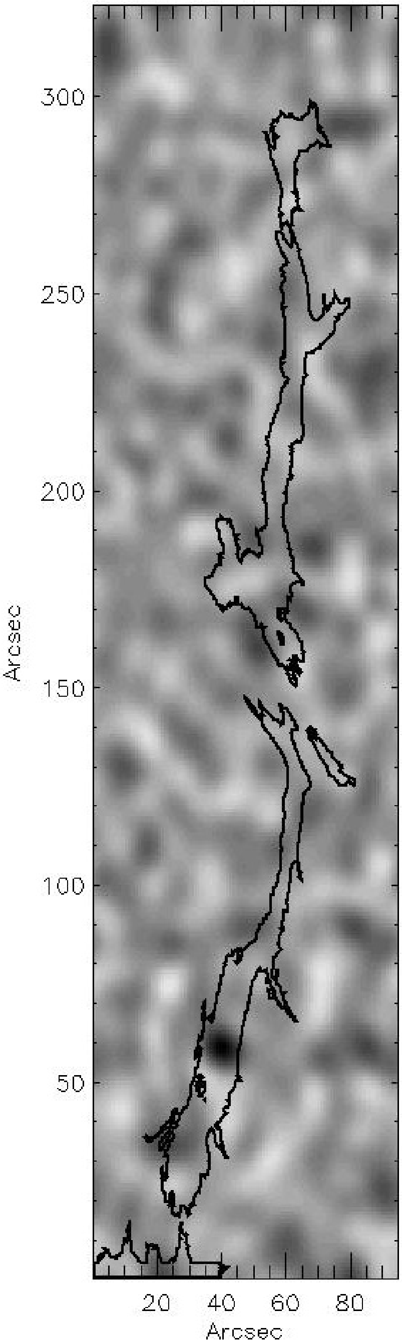

Fig. 5. A vorticity map computed from the horizontal photospheric velocities (TRACE data) with the location of the filament observed with DOT superimposed.

Figure 8 overlays Hα intensity isolines showing the location of the filament on chromospheric Doppler velocities observed in Hα at Meudon (13:36 UT). We observe a classical blueshift in the filament core indicating that the material is upflowing (between 0.5 and 2 km s^{-1}). We observe a strong upflow (4 km s^{-1}) at the location of the gap in the filament (210, 90) in Fig. 8. However, the dynamics in the filament footpoints are more complex with mixed, rapidly evolving, upflows and downflows (lying between −2 to 2 km s^{-1}). This is confirmed by Doppler velocities (Fig. 9) measured in Hα by THEMIS (10:06–11:09 UT) a few hours before the Meudon observation.

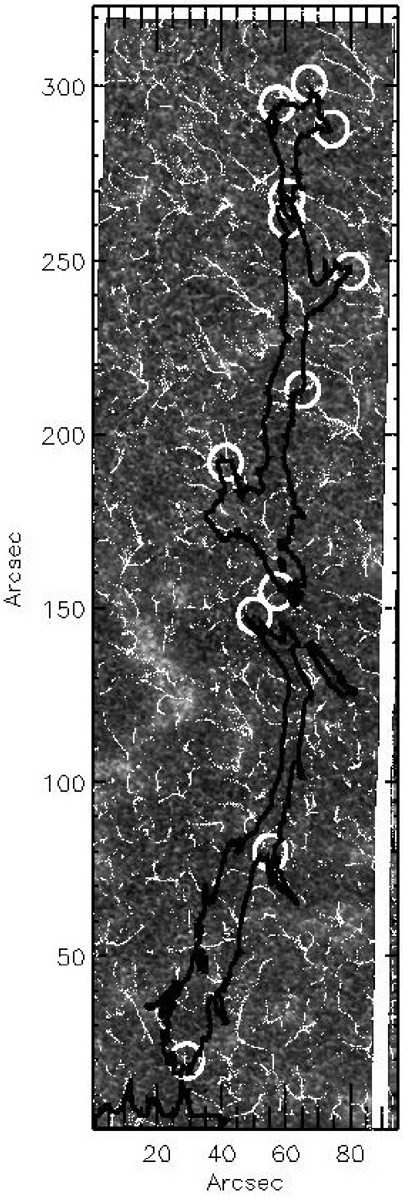

Fig. 6. A chromospheric image taken with the DOT in Ca II H (3968 Å), showing the atmosphere about 500 km above the photosphere. Superimposed are the final corks positions after 5-h of evolution of the flow field and an isophote showing the location of the filament in Hα with circles indicating the footpoints. The angular resolution is close to 0.2″ over the whole field.

In this earlier THEMIS data, we observe a general upflow at the footpoints of the filament. Both upward and downward flows are visible at the top of the filament position (64, 285) in Fig. 9, while no such motions are observed a few hours later in the Meudon data at the same location. Our observation for the upflowing material in the filament core and the complex dynamics associated with filament footpoint, confirm the previous results of Malherbe et al. (1983b), Schmieder et al. (1984) and Schmieder et al. (1991).

5. Parasitic polarities

We have directly measured the magnetic field with the THEMIS/MTR polarimeter (Fig. 9). A possible link between horizontal photospheric flows and the location of parasitic polarities was investigated using the THEMIS magnetic map and the horizontal flows computed with the TRACE WL data.

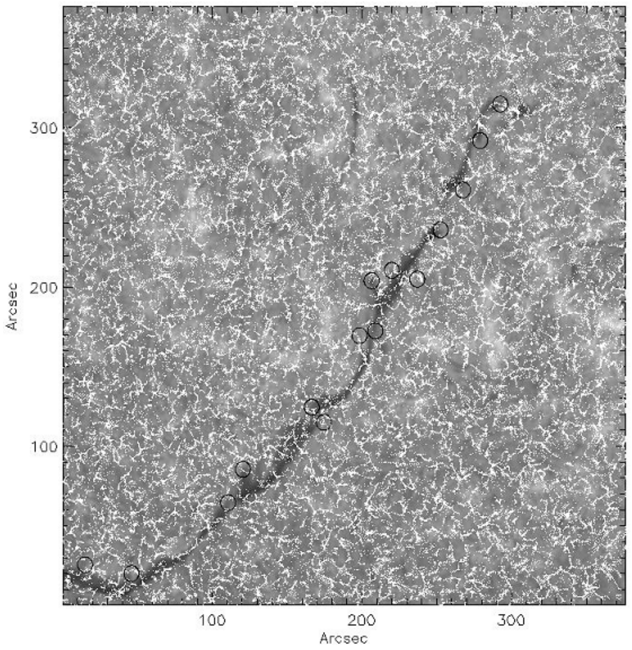

Fig. 7. The filament region observed in Hα by ISOON on October 6, 2004, between 14:48 and 17:31 UT. The final positions of the corks computed from 5-h of evolution of the flow field, are superimposed. Solar north is located at the top of the figure.

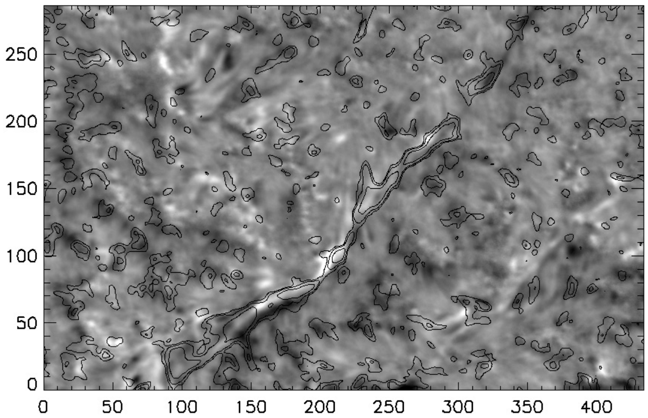

Fig. 8. Hα MSDP spectrograph observation from Meudon on Oct. 6, 2004 at 13:36 UT. Dark represents downflow and bright upflow. Solar north is located at the top of the figure.

THEMIS measured the magnetic field in the filament region in FeI 6302 Å between 10:06 and 11:09 UT on October 6. The amplitude of the longitudinal magnetic field shown in Fig. 9 lies between ±447 Gauss, with the highest absolute values being saturated on this map. The cork trajectories computed over a 5-h period and the filament as seen in Hα are superimposed on the magnetic map. We observe that the filament lies above the polarity inversion lines (PILs) seen within the filament channel. We also note the presence of parasitic polarities on both sides of the PIL as expected. For example in Fig. 9 we find strong positive parasitic polarities (shown in red) located at the coordinates (70, 248), (70, 190), (80, 250), (85, 130) and strong negative parasitic polarities (shown in green) at (20, 25), (48, 125).

We now examine the interaction between these parasitic polarities and the flows and in particular with the supergranules

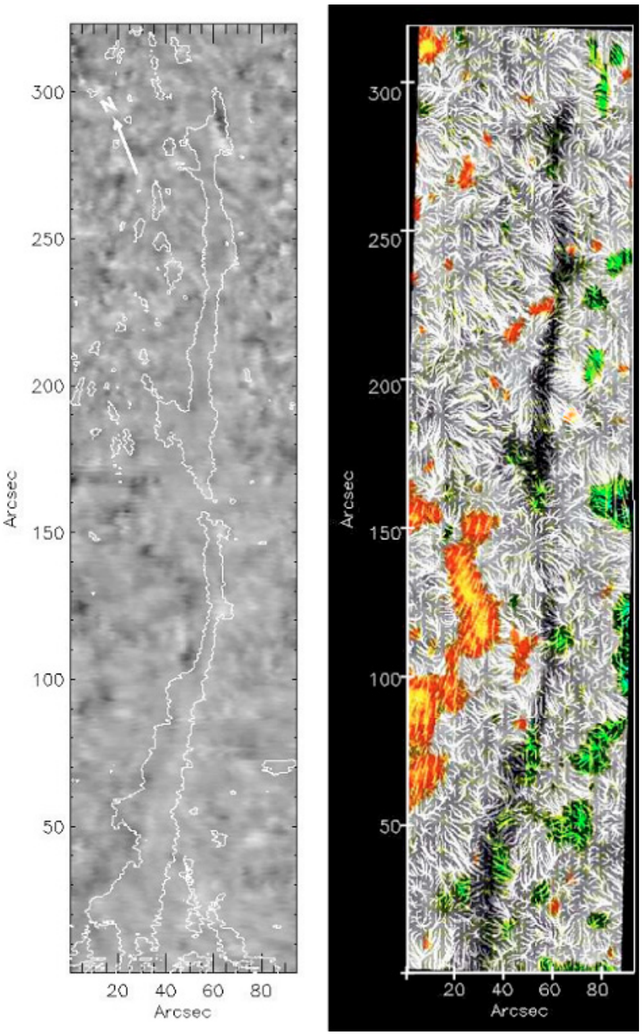

Fig. 9. (*Left*) Doppler velocity measured in Hα with THEMIS on October 6, 2004 between 10:06 and 11:09 UT. Dark represents downflow and bright upflow. The arrow indicates solar north. (*Right*) A THEMIS magnetogram from October 6, 2004 with cork trajectories computed from TRACE data superimposed. The longitudinal magnetic field lies between ±447 Gauss. The cold colors, green and blue, represent the field pointing into (negative) polarity) the Sun and the hot colors, red and yellow, indicate the field pointing out (positive polarity) of the sun. The Hα filament observed simultaneously with THEMIS is superimposed.

observed to cross the PIL. The two polarities at (70, 248) and (80, 250) in Fig. 9 are located at the extremity of the cork trajectories. Figure 10 shows some of the details at this location. The dotted circle indicates a center of divergence on the scale of a supergranule, while the small arrows show the direction of the flow field. The large arrows on the right of the figure point towards the parasitic polarity (in red) and the dominant polarity (of the weak background field) in green. The cork trajectories cross beneath the filament indicating that the flow transports corks (and thus flux tubes) across the filament channel and could in this manner create parasitic polarities. Convection could push opposite polarity fields, by the outward dispersal of magnetic flux, through the PILs. Thus supergranule cells could induce a significant flow into the polarity inversion zone thereby transferring field of opposite polarity from one side of the PIL to the other one.

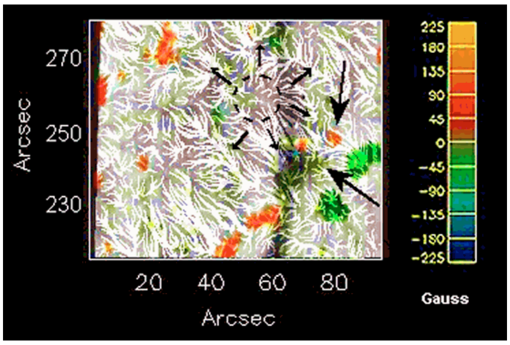

Fig. 10. Detail of a parasitic polarity extracted from Fig. 9. The longitudinal magnetic field lies between ±447 Gauss. The thick arrows show two parasitic polarities and the dotted circle indicates roughly the center of the divergence (while thin arrows indicate the direction) of the horizontal flow on the scale of a supergranule.

The parasitic polarity (in red) at (80, 250) in Fig. 10 forms a secondary inversion line with the dominate polarity (in green). The presence of such an inversion line in the filament channel could play a role in the formation of the filament footpoints in agreement with Aulanier et al. (1998), who suggest that barbs are always associated with parasitic polarities. The presence of the parasitic polarity implies an inverse configuration for the transverse horizontal magnetic field. Therefore, taking into account the model of Aulanier et al. (1998), we propose a plausible scenario for footpoint (barb) formation from our observation. Namely, the diffusion of the magnetic field through the PILs, driven by supergranular flows, forming parasite polarity over a time scale of 3 to 5 h (cork diffusion). When this parasitic polarity is located close to a dominant polarity feature, even with weak magnetic field, the coupling of magnetic structures forms a secondary inversion line with a dip where the dense material can be retained against gravity, on the side of the main prominence body. This agrees with the previous works of Aulanier & Schmieder (2002), López Ariste et al. (2006) and Schmieder et al. (2006) who show the importance of small polarities in the formation of dips.

However, since we have not observed the temporal evolution of the magnetic field, we cannot exclude the possibility that the parasitic polarities emerged locally and that they are not transported by the photospheric flows. Aulanier (1998) found that the angle barbs formed with the filament correlated with the motion of the parasitic polarity involved in its formation. This implies a relationship between polarity changes and photospheric motions. In Fig. 9 several supergranulation cells are seen to cross the PIL. We find several examples of parasitic polarities linked to divergent flow such as those in Fig. 9 at (48, 125) (green) or (70, 190) red, low amplitude). Three other examples appear to be related to the evolution of the convective flow: (43, 255) (green), (85, 130) (red) and, (20, 25) (green). In general the parasitic polarities are located close to maxima in the amplitude of the horizontal velocity.

We have also computed the photospheric horizontal velocities, on October 7, 2004, using the TRACE data between 9:40 and 11:00 UT. Figure 11 shows a THEMIS magnetogram (between 9:10 and 10:13 UT) and the final corks locations after 5-h. We note a very good correspondence between the position of the corks and the magnetic concentrations at the boundaries of the supergranules, indicating a good alignment between the different data as in Sect. 4. We observe from the cork trajectories (not shown) that corks are also transported through the filament

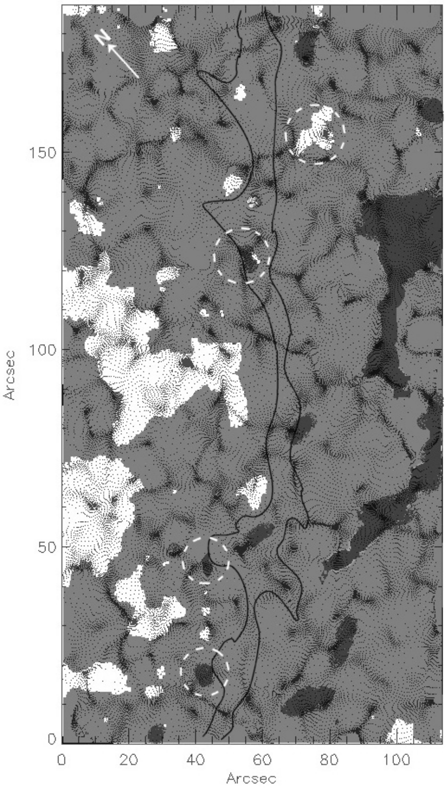

Fig. 11. A THEMIS magnetogram taken on October 7, 2004, between 9:10 and 10:13 UT, with cork final positions superimposed. Some parasitic polarities are indicated by dotted circles. The arrow indicates solar north.

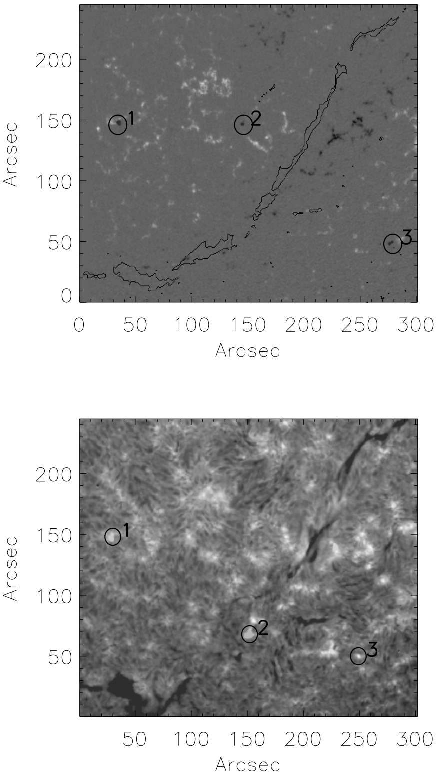

Fig. 12. *Top*: A MDI magnetogram observed on October 7, 2004 at 19:14 on which the three parasitic polarities are visible. *Bottom*: An ISOON Hα map on October 7, 2004 at 16:30 UT. Solar north is directed toward the top of the figure.

channel. The final position of some corks correspond to parasitic polarities (circles in Fig. 11), which appear to have been transported to the other side of the neutral line by the horizontal flows. Three of them, the lowest ones in Fig. 11 are located close to footpoints of the filament. This observation agrees well with the results obtained on the previous day. However, the pair of polarities described in Fig. 10 (Oct. 6) is no longer visible on the Oct. 7 THEMIS magnetogram, due to the evolution of the magnetic field.

6. Filament eruption

The filament erupted on October 7, 2004 in the manner most often observed. The filament completely disappears over about 3h between 16:30 and 19:40 UT. As described by Martin et al. (1985), at the start of the eruption, the centre of the filament first expands outward with the far ends remaining attached at their photospheric footings. Next it developed the classic arch form as it disappeared from view against the solar disc. The eruption of a filament often produces a coronal mass ejection (CME) and sometimes a large two-ribbon flare. In this case the filament erupted around 16:30 on October 7, 2004, and a CME was observed at around 19:00 UT with the LASCO-2/SOHO coranagraph and a two ribbon flare was observed with the SOHO/EIT. In this section we investigate the flows associated with this eruption.

6.1. Parasitic polarities and brightness enhancements

Before the filament erupts, we observe an increase in brightness at three separate locations in the ISOON Hα data. These three brightenings, visible in Fig. 12 (bottom) start to increase in brightness respectively at 17:04 (#1), 17:15 (#2) and 17:27 (#3). Only Feature #1 is near a parasitic polarity observed in the magnetogram. Features #1 and #2 have negative polarity while feature #3 is positive.

SOHO/MDI acquired magnetograms continuously throughout the filament eruption. No changes in the longitudinal magnetic field were detected during the eruption. Only three features with strong parasitic polarity (PP), relatively to the local background magnetic field, appeared before and after the eruption. The PP #1 in Fig. 12 (top) appears at 13:04 UT with the emergence of new field at around 16:30, which corresponds to a brightness increase in the ISOON Hα observation around 17 UT. PP #2 appears at about 18:29, after the eruption. Finally, PP #3 emerges before the eruption at 12:54 and appears to split at 19:04, after the eruption. PP numbers #1 and #3, which appear before the eruption, are located at distances of 137″ and 123″ from the filament, respectively. Both lie outside the TRACE 171 Å field of view, thus we cannot determine if a link exists between these features and the filament. Unfortunately TRACE did not observed in 171 Å between 16 and 18 UT, during the impulsive phase of the filament eruption. At 15:30 UT, before the eruption, only faint minor loops have formed over the filaments body, as seen in 171 Å. At 18:32 UT, the middle sections of the loops have brightened considerably and some appear to touch down at a newly created brightening located inside the filament while others continue to loop over the entire filament. From 18:32 to 23:12 UT the newly created brightening continues to brighten and grow in size while propagating down the length of the filament.

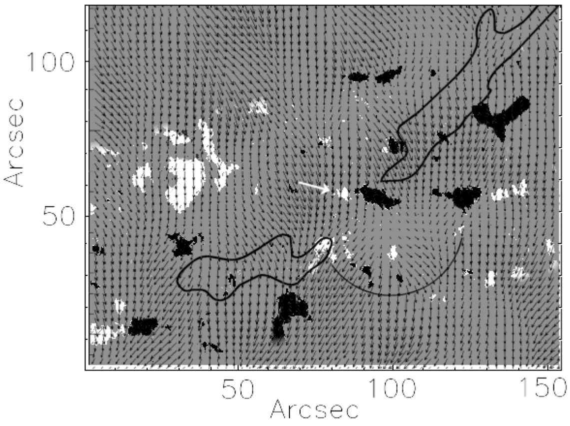

Fig. 13. Magnetic field measured by THEMIS on October 7, 2004 between 14:30–15:17 UT, with the SE extremity of the contour of the filament, and with horizontal photospheric flows, measured with TRACE data, superimposed. The arrow indicates a magnetic feature which is observed to move and interfer with the close opposite polarity (on its right) in the MDI magnetograms (see text). The highest absolute values beeing saturated on this map. The location of the persistent velocity divergence is shown by the arch of the circle. North is located at the top of the figure.

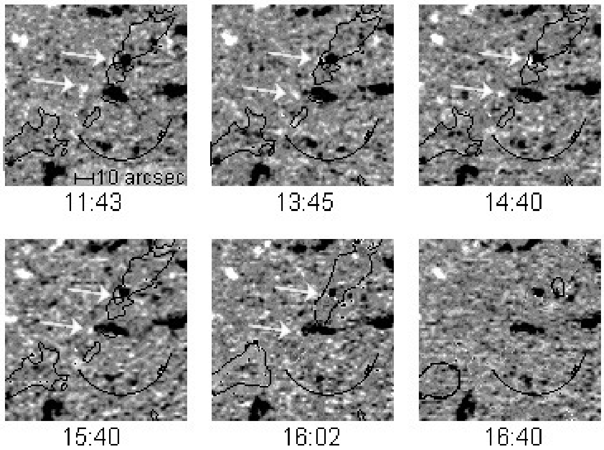

Fig. 14. A time sequence of the longitudinal magnetic field measured by MDI on October 7, 2004 between 11:43–16:40 UT, with the SE extremity of The filament superimposed, as in Fig. 13. The arrows indicate the structures which move with the photospheric flows towards regions of opposite polarity. The location of the persistent velocity divergence is shown by the arch of the circle. Solar north is located at the top of the figure.

The EIT observations in 284 Å, 195 Å and 171 Å taken before (at about 13 UT) and after (at about 19 UT) the filament eruption show a clear reorganization of the magnetic field in the corona and the classic two-ribbon flare configuration.

6.2. Photospheric flows during the eruption

To investigate the photospheric motions below and near the filament eruption, we used MDI Doppler data from 9:44 to 22:50 UT and the one-minute cadence TRACE WL observations. The time sequence of Doppler velocities shows only the expected slow evolution of supergranules throughout the entire field-of-view. There were no peculiar changes in the pattern associated with the eruption. To detect the presence of persistent large-scale horizontal flows, we applied LCT with a correlation window of $8'' \times 8''$ to 13h of the MDI Doppler data (between 9:50 and 22:50). The resulting horizontal velocities do not show any large-scale organization.

Following the same procedure used for the October 6, 2004 data, we coaligned the October 7, 2004 ISOON Hα and TRACE WL data in order to measure the horizontal velocities below and near the filament during its eruption. The horizontal flow vectors were derived by applying LCT with a correlation window of $3'' \times 3''$. A detailed inspection of the velocity vectors and their divergence and vorticity fields did not reveal any peculiar evolution or change of the horizontal flow before or during the filament eruption.

However, at the location where the filament starts to disappear, we observe a persistent divergence of the flow visible before and after the filament eruption. This divergent flow was also present on October 6, 2004, implying a strong continuous flow that remains at the same location over an extended time period.

Figure 13 shows the horizontal velocity measured with TRACE data superimposed on the line-of-sight (LOS) magnetic field measured by THEMIS on October 7, 2004 between 14:30 and 15:17 UT. We observe that parasitic and normal polarities are probably swept by the continuous diverging horizontal flow which is also where the filament gap appears at the beginning of the eruption. Such purely horizontal motions could destabilize the filament and lead to the sudden filament disappearance (Lin et al. 2001).

Inspection of the MDI magnetograms permits us to study the evolution of the stronger magnetic features seen in the THEMIS data, as was done in Schmieder et al. (2006). Figure 14 shows the time evolution of the MDI magnetograms between 11:43–16:40 UT, in the SE extremity where the eruption begins. We observed two magnetic structures, indicated by arrows on Fig. 14, that move with the photospheric flow towards regions of opposite polarities. The upper structure disappears between 16:05 and 16:10 UT and the lower one between 16:20 and 16:30 UT when they interact with the opposite polarities. These phenomena could initiate the reorganization of the magnetic field and could be candidates to start the destabilization of the filament, which begins erupting at about 16:30 UT.

However, from our observations, we cannot exclude the possibility that the eruption of the filament could be related to physical conditions in the upper atmosphere (chromosphere or corona) rather than the effects of the photospheric motions acting on the magnetic structures.

Finally, from the THEMIS vector magnetic field measurement, we observe a modification of the orientation of the transverse magnetic field before and after the filament eruption. The orientation of the transverse magnetic field in the network has changed between the magnetograms obtained on the 6–8 October, 2004. The azimuth is defined as the angle between the transverse component of the magnetic field and solar north. Figure 15 displays azimuth histograms of the network magnetic field obtained on October 6–8. These histograms have well defined peaks, indicating a strong homogeneity of the azimuth of the network magnetic field. The mean values are 155° (on October 6), 180° (or 0°) (on October 7) and 45° (on October 8). This change may relate to the activity of the filament which disappears on 7 October and reforms the following day. Projection effects, which change with solar rotation, are negligible relatively to the amplitude of the observed azimuth variation.

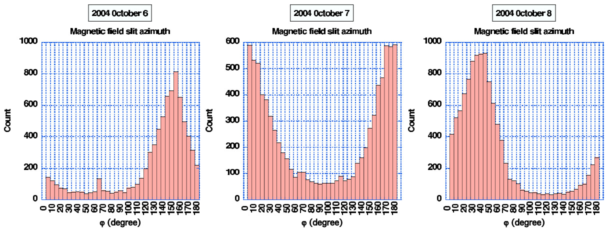

Fig. 15. Azimuth histograms of the network magnetic field obtained for the value of αB > 45 Gauss, where α is the magnetic filling factor, on October 6–8.

7. Discussion and conclusion

We have presented multi-wavelength observation of the evolution and eruption of a filament obtained during the JOP 178 campaign on October 6 through 8, 2004. We analyzed the photospheric motions below and in the immediate neighborhood of the filament to search for systematic flows that could both sustain the filament and lead to its eruption. We did not observe any large-scale flows converging toward the filament channel that might have contributed to its formation in agreement with the results of Magara & Kitai (1999). We found that the photospheric motions in the vicinity of the filament exhibit the same properties as those in the remainder of our field-of-view which contains mainly quiet sun. Perhaps motions converging toward the filament exist in the early phases of its formation, but neither our observation nor those of Magara & Kitai (1999) observe this phase. We observe that several supergranulation cells cross the Polarity Inversion Line. Our observations show that the supergranules can play a role in the transport of parasitic polarities through the filament channel and thus contribute to the formation of barbs (filament footpoints). We presented a detailed example in Sect. 5 where one clearly sees the formation of a secondary magnetic dip at the location of a footpoint.

We also investigate the evolution and eruption of the filament. Regarding the evolution of the filament, On October 7, 2004, we observed an eruption of the filament at approximately 16:30 UT which was followed by a CME visible with the LASCO2/SOHO coronagraph at about 19:00 UT. Before and during the eruption, we detected only a few changes in the MDI/SOHO magnetograms. The horizontal photospheric velocities are similar over the entire field of view and show only the classic evolution of the meso- and super-granulation. However, we observed two phenomena which could cause the filament eruption. The first is the transport of parasitic and normal polarities by a continuous diverging horizontal flow, lasting at least one day, located in the filament gap where the filament starts to disappear. Such a purely horizontal motion could lead to the destabilization of the filament and to the sudden filament disappearance (Lin et al. 2001). The second is the mixing of opposite polarities induced by the horizontal flows which in turn implies a reorganization of the magnetic field at the origin of the filament eruption.

However, since we do not have high spatial and temporal resolution measurements of the magnetic field needed to continuously observe its evolution, we cannot exclude the possibility that the eruption is triggered by physical conditions in the upper atmosphere (chromosphere or corona).

One very interesting observational result was the re-orientation by 70° (or 110°) of the transverse field after the eruption seen in the daily vector magnetograms obtained with THEMIS. Further observations of field changes are required to understand if such shifts in the direction of the field are commonly associated with filament eruptions, and if so, what causes them.

To further elucidate the contribution of photospheric motions to the formation, evolution and eruption of a filament, multi-wavelength observations over extended time periods, with both high temporal and spatial resolution, especially for the magnetic field, are needed. The HINODE (Solar B) satellite is equipped to provide such observations.

Acknowledgements. This work was supported by the Centre National de la Recherche Scientifique (C.N.R.S., UMR 5572 and UMR 8109), by the Programme National Soleil Terre (P.N.S.T.) and European OPTICON transnational Access Programme. SOHO is a mission of international cooperation between the European Space Agency (ESA) and NASA. This work was supported by the European commission through the RTN programme (HPRN-CT-2002-00313). We wish to thank THEMIS, DOT, DST, ISOON, SOHO/MDI, SOHO/EIT, TRACE Teams and Ch. Coutard for their technical help. We are indebted to G. Aulanier, P. Mein and N. Mein for many discussions.

References

Aulanier, G. 1998, Thesis Université Paris VI Pierre et Marie Curie
Aulanier, G., & Schmieder, B. 2002, A&A, 386, 1106
Aulanier, G., Demoulin, P., van Driel-Gesztelyi, L., Mein, P., & Deforest, C. 1998, A&A, 335, 309
Aulanier, G., Demoulin, P., Mein, N., et al. 1999, A&A, 342, 867
Aulanier, G., Srivastava, N., & Martin, S. F. 2000, ApJ, 543, 447
Choe, G. S., & Lee, L. C. 1992, Sol. Phys., 138, 291
Kuijpers, J. 1997, ApJ, 489, L20
Kuperus, M., & Raadu, M. A. 1974, A&A, 31, 189
Leenaarts, J., Rutten, R. J., Carlsson, M., & Uitenbroek, H. 2006, A&A, 452, 15
Lin, J., Forbes, T. G., & Isenberg, P. A. 2001, JGR, 106, 25
Lin, Y., Wiik, J. E., Engvold, O., Rouppe van der Voort, L., & Frank, Z. A. 2005, Sol. Phys., 227, 283
López Ariste, A., Aulanier, G., Schmieder, B., & Sainz Dalda, A. 2006, A&A, 456, 725
Mackay, D. H., Gaizauskas, V., & van Ballegooijen, A. A. 2000, ApJ, 544, 1122
Mackay, D. H., & van Ballegooijen, A. A. 2006, ApJ, 641, 577
Magara, T., & Kitai, R. 1999, ApJ, 524, 469
Malherbe, J. M., & Priest, E. 1983a, A&A, 123, 80
Malherbe, J. M., Schmieder, B., Ribes, E., & Mein, P. 1983b, A&A, 119, 197
Martens, P. C., & Zwaan, C. 2001, APJ, 558, 872
Martin, S. F., & Echols, C. R. 1994, Solar Surface Magnetism, NATO Advanced Science Institutes (ASI) Series C: Mathematical and Physical Sciences, Proceedings of the NATO Advanced Research Workshop, held Soesterberg, the Netherlands, November 1–5, 1993, ed. R. J. Rutten, & C. J. Schrijver (Dordrecht: Kluwer Academic Publishers), 339
Martin, S. F., Livi, S. H. B., & Wang, J. 1985, Aust. J. Phys., 38, 929
Martres, M. J., Mein, P., Schmieder, B., & Soru-Escaut, I. 1981, Sol. Phys., 69, 301
Molowny Horas, R. L. 1994, Thesis Institute of Theoretical Astrophysics University of Oslo
November, L. J., & Simon, G. W. 1988, ApJ, 333, 427
Plocieniak, S., & Rompolt, B. 1973, Sol. Phys., 29, 399
Priest, E. R. 1997, New Perspectives on Solar Prominences, proceedings of a meeting held in Aussois, France, 28 April–4 May 1997, ed. D. F. Webb, B. Schmieder, & D. M. Rust, ASP Conf. Ser. 150, IAU Colloq., 167, 453
Ridgway, C., & Priest, E. 1993, Sol. Phys., 146, 277
Rieutord, M., Roudier, T., Ludwig, H.-G., Nordlund, Å., & Stein, R. 2001, A&A, 377, 14
Roudier, Th., Rieutord, M., Malherbe, J. M., & Vigneau, J. 1999, A&A, 349, 301
Rutten, R. J., Hammerschlag, R. H., Bettonvil, F. C. M., Sütterlin, P., & de Wijn, A. G. 2004, A&A, 413, 1183
Schmieder, B., Malherbe, J. M., Mein, P., & Tandberg-Hanssen, E. 1984, A&A, 136, 81
Schmieder, B., Raadu, M. A., & Wiik, J. E. 1991, A&A, 252, 353
Schmieder, B., Aulanier, G., Main, P., & Ariste, A. Lopez 2006, Sol. Phys., 238, 245
Van Ballegooijen, A. A. 2004, ApJ, 612, 519
Van Ballegooijen, A. A., & Martens, P. C. H. 1989, ApJ, 343, 971

- Romeuf D., Meunier N., Noëns J.-C., Koutchmy S., Jimenez R., Wurmser O., Rochain S., et al., Analysis of broad-band Hα coronagraphic observations, 2006, 2007, A & A 462, 731
- Tkaczuk, R., Rieutord, M., Meunier, N., Roudier, T., Tracking granules at the Sun's surface and reconstructing velocity fields. II. Error analysis, 2007, A & A, sous presse
- Rondi S., Roudier T., Molodij, G., Bommier V., Sütterlin P., Malherbe J.-M., Keil S., Meunier N., Mein P., Mein N., Schmieder B., Maloney P., Photospheric general context around dark filament, 2007, A & A, sous presse

Bibliographie

Adams M., Hathaway D. H., Stark B. A., Musielak Z. E., 1997, Sol. Phys., 174, 341

Ambrož P., 2001, Sol. Phys., 198, 253

Antonucci E., Azzarelli L., Casalini P., Cerri S., Denoth F., 1979, Sol. Phys., 63, 17

Arnaud J., Briand C., Ceppatelli G., 1998, New Astronomy Review, 42, 499

Balke A. C., Schrijver C. J., Zwaan C., Tarbell T. D., 1993, Sol. Phys., 143, 215

Balthasar H., Wöhl H., 1980, A & A, 92, 111

Basu S., Antia H. M., 2003, Astrophys. J., 585, 553

Basu S., Schou J., 2000, Sol. Phys., 192, 481

Beck J. G., 2000, Sol. Phys., 191, 47

Beck J. G., Gizon L., Duvall T. L., Jr., 2002, Astrophys. J. Letter, 575, L47

Beck J. G., Schou J., 2000, Sol. Phys., 193, 333

Beckers J. M., 1968, Sol. Phys., 5, 309

Beckers J. M., Artzner G., 1974, Sol. Phys., 37, 309

Bellot Rubio L. R., Collados M., 2003, A & A, 406, 357

Belvedere G., Godoli G., Motta S., Paterno L., Zappala R. A., 1977, Astrophys. J. Letter, 214, L91

Berdyugina S. V., Usoskin I. G., 2003, A & A, 405, 1121

Berger T. E., Löfdahl M. G., Shine R. A., Title A. M., 1998, Astrophys. J., 506, 439

Berrilli F., Ermolli I., Florio A., Pietropaolo E., 1999, A & A, 344, 965

Bommier V., Landi Degl'Innocenti E., Landolfi M., Molodij G., 2007, accepted in A&A

Brajša R., Wöhl H., Vršnak B., et al., 2004, A & A, 414, 707

Brandt P. N., Greimel R., Guenther E., Mattig W., 1991, Turbulence, Fractals, and the Solar Granulation. Applying Fractals in Astronomy, edited by Andre Heck and Jean M. PErdang. Springer-Verlag Berlin Heidelberg New York. Also Lecture Notes in Physics, volume 3, p.77, p. 77

Chou D.-Y., Dai D.-C., 2001, Astrophys. J. Letter, 559, L175

Collier Cameron A., Donati J.-F., Semel M., 2002, Mon. Not. R. astr. Soc., 330, 699

Collin B., Nesme-Ribes E., Leroy B., Meunier N., Sokoloff D., 1995, Academie des Science Paris Comptes Rendus Serie B Sciences Physiques, 321, 111

Criscuoli S., Rast M. P., Ermolli I., Centrone M., 2007, A & A, 461, 331

Del Moro D., Berrilli F., Duvall T. L., Jr., Kosovichev A. G., 2004, Sol. Phys., 221, 23

del Toro Iniesta J. C., Bellot Rubio L. R., Collados M., 2001, Astrophys. J. Letter, 549, L139

DeRosa M. L., Toomre J., 2004, Astrophys. J., 616, 1242

Dikpati M., de Toma G., Gilman P. A., 2006, Geophys. Res. Letters, 33, 5102

Dikpati M., de Toma G., Gilman P. A., Arge C. N., White O. R., 2004, Astrophys. J., 601, 1136

Domínguez Cerdeña I., Kneer F., Sánchez Almeida J., 2003, Astrophys. J. Letter, 582, L55

Domínguez Cerdeña I., Sánchez Almeida J., Kneer F., 2003, A & A, 407, 741

Donati J.-F., Collier Cameron A., Petit P., 2003, Mon. Not. R. astr. Soc., 345, 1187

Duvall T. L., Gizon L., 2000, Sol. Phys., 192, 177

Duvall T. L., Jr., 1980, Sol. Phys., 66, 213

Duvall T. L., Jr., Jefferies S. M., Harvey J. W., Pomerantz M. A., 1993, Nat, 362, 430

Duvall T. L. J., D’Silva S., Jefferies S. M., Harvey J. W., Schou J., 1996, Nat, 379, 235

El-Ad H., Piran T., da Costa L. N., 1996, Astrophys. J. Letter, 462, L13

Fan Y., Abbett W. P., Fisher G. H., 2003, Astrophys. J., 582, 1206

Faurobert-Scholl M., 1993, A & A, 268, 765

Faurobert-Scholl M., Feautrier N., Machefert F., Petrovay K., Spielfiedel A., 1995, A & A, 298, 289

Fisk L. A., Zurbuchen T. H., Schwadron N. A., 1999, Astrophys. J., 521, 868

Foukal P., Fowler L., 1984, Astrophys. J., 281, 442

Foukal P., Harvey K., Hill F., 1991, Astrophys. J. Letter, 383, L89

Foukal P., Lean J., 1988, Astrophys. J., 328, 347

Fragos T., Rantsiou E., Vlahos L., 2004, A & A, 420, 719

Frazier E. N., 1970, Sol. Phys., 14, 89

Gaizauskas V., Harvey K. L., Harvey J. W., Zwaan C., 1983, Astrophys. J., 265, 1056

Gama S., Vergassola M., Frisch U., 1994, J. Fluid Mech., 260, 95

Gilman P. A., Howard R., 1985, Astrophys. J., 295, 233

Haber D. A., Hindman B. W., Toomre J., et al., 2002, Astrophys. J., 570, 855

Hagenaar H. J., Schrijver C. J., Title A. M., 1997, Astrophys. J., 481, 988

Hagenaar H. J., Schrijver C. J., Title A. M., Shine R. A., 1999, Astrophys. J., 511, 932

Hart A. B., 1954, Mon. Not. R. astr. Soc., 114, 17

Harvey J. W., 1977, Highlights of Astronomy, 4, 223

Harvey K. L., 1993, Ph.D. Thesis

Harvey K. L., Harvey J. W., Sheeley N. R., Jr., 1982, Sol. Phys., 79, 149

Harvey K. L., Recely F., 2002, Sol. Phys., 211, 31

Harvey K. L., Zwaan C., 1993, Sol. Phys., 148, 85

Hathaway D., Beck J., Bogart R., et al., 2000, Sol. Phys., 193, 299

Hathaway D. H., 1992, Sol. Phys., 137, 15

Hathaway D. H., 1996, Astrophys. J., 460, 1027

Hathaway D. H., Williams P. E., Cuntz M., 2006, Astrophys. J., 644, 598

Howard R. F., 1991, Sol. Phys., 135, 327

Howard R. F., 1992a, Sol. Phys., 142, 47

Howard R. F., 1992b, Sol. Phys., 137, 205

Howard R. F., 1992c, Sol. Phys., 137, 51

Howard R. F., 1996, Ann. Rev. Astron. Astrophys., 34, 75

Janßen K., Vögler A., Kneer F., 2003, A & A, 409, 1127

Kahler S. W., Hudson H. S., 2002, Astrophys. J., 574, 467

Keller C. U., Deubner F.-L., Egger U., Fleck B., Povel H. P., 1994, A & A, 286, 626

Khomenko E. V., Collados M., Solanki S. K., Lagg A., Trujillo Bueno J., 2003, A & A, 408, 1115

Komm R., Corbard T., Durney B. R., et al., 2004, Astrophys. J., 605, 554

Komm R., Mattig W., Nesis A., 1990, A & A, 239, 340

Komm R. W., Howard R. F., Harvey J. W., 1993a, Sol. Phys., 147, 207

Komm R. W., Howard R. F., Harvey J. W., 1993b, Sol. Phys., 145, 1

Komm R. W., Howard R. F., Harvey J. W., 1995, Sol. Phys., 158, 213

Krijger J. M., Roudier T., 2003, A & A, 403, 715

Krishan V., Paniveni U., Singh J., Srikanth R., 2002, Mon. Not. R. astr. Soc., 334, 230

Kuhn J. R., Lin H., Loranz D., 1991, PASP, 103, 1097

Labonte B. J., Howard R., 1982, Sol. Phys., 80, 15

Landolfi M., Arena P., Deglinnocenti E. L., 1984, Sol. Phys., 93, 269

Lean J. L., Cook J., Marquette W., Johannesson A., 1998, Astrophys. J., 492, 390

Leighton R. B., 1964, Astrophys. J., 140, 1547

Lin H., 1995, Astrophys. J., 446, 421

Lin H., Kuhn J. R., 1992, Sol. Phys., 141, 1

Lisle J. P., Rast M. P., Toomre J., 2004, Astrophys. J., 608, 1167

Lites B. W., Leka K. D., Skumanich A., Martinez Pillet V., Shimizu T., 1996, Astrophys. J., 460, 1019

Livi S. H. B., Wang J., Martin S. F., 1985, Australian Journal of Physics, 38, 855

Livingston W., Harvey J., 1971, The Kitt Peak Magnetograph. Iv: 40-CHANNEL Probe and the Detection of Weak Photospheric Fields, in Howard R. (ed.), IAU Symp. 43: Solar Magnetic Fields, p. 51

Livingston W. C., Harvey J., 1975, BAAS, 7, 346

Lustig G., Hanslmeier A., 1987, A & A, 172, 332

Madjarska M. S., Doyle J. G., van Driel-Gesztelyi L., 2004, Astrophys. J. Letter, 603, L57

Malherbe J.-M., Moity J., Arnaud J., Roudier T., 2007, accepted in A&A

Mandelbrot B. B., 1975, Journal of Fluid Mechanics, 72, 401

Martin S. F., 1988, Sol. Phys., 117, 243

McAteer R. T. J., Gallagher P. T., Ireland J., 2005, Astrophys. J., 631, 628

Meunier N., 1999a, Astrophys. J., 515, 801

Meunier N., 1999b, Astrophys. J., 527, 967

Meunier N., 2003, A & A, 405, 1107

Meunier N., 2004, A & A, 420, 333

Meunier N., 2005a, A & A, 437, 303

Meunier N., 2005b, A & A, 443, 309

Meunier N., 2005c, A & A, 436, 1075

Meunier N., 2005d, A & A, 442, 693

Meunier N., Arnaud J., Vigneau J., 2002, Nuovo Cimento C Geophysics Space Physics C, 25, 659

Meunier N., Jefferies S. M., 2000, Astrophys. J., 530, 1016

Meunier N., Kosovichev A., 2003, A & A, 412, 541

Meunier N., Nesme-Ribes E., Collin B., 1997, A & A, 319, 683

Meunier N., Nesme-Ribes E., Grosso N., 1997, A & A, 319, 673

Meunier N., Roudier T., 2007, Astron. & Astrophys., 466, 691

Meunier N., Roudier T., Tkaczuk R., 2007, Astron. & Astrophys., 466, 1123

Meunier N., Tkaczuk R., Roudier T., 2007, Astron. & Astrophys., 463, 745

Meunier N., Tkaczuk R., Roudier T., Rieutord M., 2007, Astron. & Astrophys., 461, 1141

Muenzer H., Schroeter E. H., Wöhl H., Hanslmeier A., 1989, A & A, 213, 431

Muller R., Roudier T., 1984, Sol. Phys., 94, 33

Nandy D., Choudhuri A. R., 2002, Science, 296, 1671

Nesme-Ribes E., Meunier N., Collin B., 1996, A & A, 308, 213

Nesme-Ribes E., Meunier N., Vince I., 1997, A & A, 321, 323

Nesme-Ribes E., Ferreira E. and Mein P. , 1993, A & A, 274, 563

Nesme-Ribes E., Ferreira E. and Vince I. , 1993, Preprint, 1

Nishikawa J., 1994, Sol. Phys., 152, 125

November L. J., 1994, Sol. Phys., 154, 1

Ortiz A., Solanki S. K., Domingo V., Fligge M., Sanahuja B., 2002, A & A, 388, 1036

Paletou F., 2001, C. R. Acad. Sc. Paris, 2, 885

Paletou F., Molodij G., 2001, Multi-line Spectropolarimetry at THÉMIS, in Sigwarth M. (ed.), ASP Conf. Ser. 236: Advanced Solar Polarimetry – Theory, Observation, and Instrumentation, p. 9

Parnell C. E., 2002, Mon. Not. R. astr. Soc., 335, 389

Pillet V. M., Lites B. W., Skumanich A., Degenhardt D., 1994, Astrophys. J. Letter, 425, L113

Raju K. P., Bromage B. J. I., Chapman S. A., Del Zanna G., 2005, A & A, 432, 341

Raju K. P., Singh J., 2002, Sol. Phys., 207, 11

Rast M. P., 2003, Astrophys. J., 597, 1200

Rees D. E., López Ariste A., Thatcher J., Semel M., 2000, A & A, 355, 759

Rempel M., 2006, Astrophys. J., 647, 662

Rieutord M., Roques S., Roudier T., Ducottet C., 2007, submitted to A&A

Rieutord M., Roudier T., Ludwig H.-G., Nordlund Å., Stein R., 2001, Astron. & Astrophys., 377, L14

Rieutord M., Roudier T., Malherbe J. M., Rincon F., 2000, Astron. & Astrophys., 357, 1063

Rincon F., 2004, Thèse de Doctorat

Romeuf D., Meunier N., Nöens J.-C., et al., 2007, accepted in A&A

Rondi S., 2006, Thèse de Doctorat

Rondi S., Roudier T., Molodij G., et al., 2007, Astron. & Astrophys., 467, 1289

Roudier T., Lignières F., Rieutord M., Brandt P. N., Malherbe J. M., 2003, A & A, 409, 299

Roudier T., Rieutord M., Malherbe J., Vigneau J., 1999, Astron. & Astrophys., 349, 301

Rüedi I., Solanki S. K., Livingston W., Stenflo J. O., 1992, A & A, 263, 323

Ruzmaikin A., Sokoloff D., Tarbell T., 1991, LNP Vol. 380: IAU Colloq. 130: The Sun and Cool Stars. Activity, Magnetism, Dynamos, 380, 140

Sainz Dalda A., López Ariste A., 2007, submitted to A&A

Sánchez Almeida J., Lites B. W., 2000, Astrophys. J., 532, 1215

Schou J., Antia H. M., Basu S., et al., 1998, Astrophys. J., 505, 390

Schou J., Howe R., Basu S., et al., 2002, Astrophys. J., 567, 1234

Schrijver C. J., 2001, Astrophys. J., 547, 475

Schrijver C. J., DeRosa M. L., Title A. M., 2002, Astrophys. J., 577, 1006

Schrijver C. J., Shine R. A., Hagenaar H. J., et al., 1996, Astrophys. J., 468, 921

Schrijver C. J., Zwaan C., 2000, Solar and Stellar Magnetic Activity. Solar and stellar magnetic activity / Carolus J. Schrijver, Cornelius Zwaan. New York : Cambridge University Press, 2000. (Cambridge astrophysics series ; 34)

Schrijver C. J., Zwaan C., Balke A. C., Tarbell T. D., Lawrence J. K., 1992, A & A, 253, L1

Schüssler M., 2005, Astron. Nachr., 326, 194

Seiden P. E., Wentzel D. G., 1996, Astrophys. J., 460, 522

Shine R., Simon G., Hurlburt N., 2000, Sol. Phys., 999, 999

Sigwarth M., 2001, Astrophys. J., 563, 1031

Simon G., Leighton R., 1964, Astrophys. J., 140, 1120

Simon G. W., Title A. M., Weiss N. O., 2001, Astrophys. J., 561, 427

Singh J., Bappu M. K. V., 1981, Sol. Phys., 71, 161

Snodgrass H. B., Ulrich R. K., 1990, Astrophys. J., 351, 309

Socas-Navarro H., Sánchez Almeida J., 2002, Astrophys. J., 565, 1323

Socas-Navarro H., Sánchez Almeida J., 2003, Astrophys. J., 593, 581

Solanki S. K., Zufferey D., Lin H., Rüedi I., Kuhn J. R., 1996, A & A, 310, L33

Srikanth R., Singh J., Raju K. P., 2000, Astrophys. J., 534, 1008

Stauffer E., 1985, Introduction to percolation theory. Taylor and Francis, London and Philadelphia

Stenflo J. O., 1982, Sol. Phys., 80, 209

Sýkora J., 1970, Sol. Phys., 13, 292

Tkaczuk R., Rieutord M., Meunier N., Roudier T., 2007, submitted to A&A

Usoskin I. G., Berdyugina S. V., Poutanen J., 2005, A & A, 441, 347

van der Borght R., 1979, Mon. Not. R. astr. Soc., 188, 615

van Driel-Gesztelyi L., Petrovay K., 1990, Sol. Phys., 126, 285

Vlahos L., Georgoulis M. K., 2004, Astrophys. J. Letter, 603, L61

Wang H., 1988, Sol. Phys., 117, 343

Wang H., Tang F., Zirin H., Wang J., 1996, Sol. Phys., 165, 223

Wang J., Wang H., Tang F., Lee J. W., Zirin H., 1995, Sol. Phys., 160, 277

Wang Y.-M., Hawley S. H., Sheeley N. R., Jr., 1996, Science, 271, 464

Wang Y.-M., Sheeley N. R., Andrews M. D., 2002, Journal of Geophysical Research (Space Physics), 107, 10

Wang Y.-M., Sheeley N. R., Jr., 1990, Astrophys. J., 365, 372

Wang Y.-M., Sheeley N. R., Jr., 2004, Astrophys. J., 612, 1196

Ward F., 1973, Sol. Phys., 30, 527

Wentzel D. G., Seiden P. E., 1992, Astrophys. J., 390, 280

White O. R., Livingston W. C., 1981, Astrophys. J., 249, 798

Yurchyshyn V. B., Abramenko V. I., Carbone V., 2000, Astrophys. J., 538, 968

Zhao J., Kosovichev A. G., 2004, Astrophys. J., 603, 776

Zhao J., Kosovichev A. G., Duvall T. L., Jr., 2001, Astrophys. J., 557, 384

Zhao J., Kosovichev A. G., Duvall T. L., Jr., 2004, Astrophys. J. Letter, 607, L135

Zirin H., 1987, Sol. Phys., 110, 101

Zwaan C., 1987, Ann. Rev. Astron. Astrophys., 25, 83